

University of Nevada, Reno

**Precast Column-Footing Connections for Accelerated Bridge
Construction in Seismic Zones**

A dissertation submitted in partial fulfillment of the
requirements for the degree of Doctor of Philosophy in
Civil Engineering

by

Zachary B. Haber

Dr. M. Saiid Saiidi / Dissertation Advisor

Dr. David H. Sanders / Dissertation Co-Advisor

May, 2013



University of Nevada, Reno
Statewide • Worldwide

THE GRADUATE SCHOOL

We recommend that the dissertation
prepared under our supervision by

ZACHARY B. HABER

entitled

**Precast Column-Footing Connections For Accelerated Bridge Construction In
Seismic Zones.**

be accepted in partial fulfillment of the
requirements for the degree of

DOCTOR OF PHILOSOPHY

M. Saiid Saiidi, Ph. D., Advisor

David H. Sanders, Ph. D., Committee Member

Ahmad M. Itani, Ph. D., Committee Member

Shen-Yi Luo, Ph. D., Committee Member

John Anderson, Ph. D., Graduate School Representative

Marsha H. Read, Ph. D., Dean, Graduate School

May, 2013

Abstract

Accelerated bridge construction (ABC) has become increasingly popular in the eyes of state and federal transportation agencies because of its numerous advantages. To effectively execute ABC projects, designers utilize prefabricated structural elements that can be quickly assembled to form functional structural systems. It is advantageous to the bridge designer if these systems emulate the design and behavior of conventional cast-in-place systems. If this can be achieved, typical analysis and design procedures can be used. The difficulty with developing emulative systems is usually encountered in the design and detailing of connections. Substructure connections are particularly critical in seismic zones because they must dissipate energy through significant cyclic nonlinear deformations while maintaining their capacity and the integrity of the structural system.

The research presented in this dissertation focused on developing and evaluating earthquake resistant connections for use in accelerated bridge construction. The project was comprised of three main components; testing of five large-scale precast reinforced concrete column models, a series of individual component tests on mechanical reinforcing bar splices, and extensive analytical studies.

Column studies included the design and construction of five half-scale bridge column models that were tested under reversed slow cyclic loading. Four new moment connections for precast column-footing joints were developed each utilizing mechanical reinforcing bar splices to create connectivity with reinforcing bars in a cast-in-place footing. Two different mechanical splices were studied: an upset headed coupler and grout-filled sleeve coupler. Along with the splice type, the location of splices within the

plastic hinge zone was also a test variable. All column models were designed to emulate conventional cast-in-place construction thus were compared to a conventional cast-in-place test model. Results indicate that the new connections are promising and duplicate the behavior of conventional cast-in-place construction with respect to key response parameters. However, it was discovered that the plastic hinge mechanism can be significantly affected by the presence of splices and result in reduced displacement ductility capacity.

In order to better understand the behavior of mechanical splices, a series of uniaxial tests were completed on mechanically-spliced reinforcing bars under different loading configurations: monotonic static tension, dynamic tension, and slow cyclic loading. Results from this portion of the project also aided the development of analytical models for the half- and prototype-scale column models. Results indicated that, regardless of loading configuration, specimens failed by bar rupture without damage to the splice itself.

The analytical studies conducted using OpenSEES included development of microscope models for the two mechanical reinforcing bars splices and full analytical models of the five half-scale columns, which were both compared with respective experimental results to validate the modeling procedures and assumptions. Prototype-scale analytical models were also developed to conduct parametric studies investigating the sensitivity of the newly developed ABC connections to changes in design details.

In general, the results of this study indicate that the newly developed ABC connections, which utilize mechanically-spliced connections, are suitable for moderate and high seismic regions. However, emulative design approaches are not suitable for all of the

connections develop. A set of design recommendations are provided to guide bridge engineers in the analysis and design of these new connections.

Dedication

To my mother, for inspiring me to pursue my potential. And to my fiancée, farral, for providing constant strength, love, and support during the course of my doctoral studies.

Acknowledgement

The research presented in this document was funded by the California Department of Transportation under contracts Nos. 65A0372 and 65A0425. The support of Dr. Saad El-Azazy and Dr. Charles Sikorsly, the Caltrans project managers, is appreciated. The interest and comments of Mike Keever, Mark Mahan and Ron Bromenschenkel are also much appreciated. The Nevada Department of Transportation provided partial student support.

The author would like to thank Headed Reinforcement Corp. (HRC) and Splice Sleeve North America (SSNA) for donation of the couplers and bars used in this study. The technical input from Christian Dahl and Joseph Morente from HRC, Masahiro Abukawa from Splice Sleeve Japan (SSJ), Toshikazu Yamanishi from SSNA, and Jim Schroder of Schroder & Associates, LLC is greatly appreciated. Special thanks are expressed to Dr. Patrick Laplace, Robert Nelson, and Mark Lattin for their help with testing, and to Mostafa Tazarv and Ali Mehrosoroush for their assistance with instrumentation and data collection. Mr. Don Newman and Brendan Morris are also thanked for efforts during the construction of the test models.

During the course of this research, the National Science Foundation's East Asia and Pacific Summer Institute (EAPSI) program and the National Science Council of Taiwan provided funding for a visiting researcher position at the National Center for Research on Earthquake Engineering (NCREE) in Taipei, Taiwan (R.O.C.). The assistance and guidance of NCREE Director Kuo-Chun Chang and Professor Yu-Chen Ou of National Taiwan University of Science and Technology are greatly appreciated. Dr. Raymond

Wang from Ruentex Engineering and Construction, and Mr. Ping-Hsiung Wang of NCREE are also thanked. Lastly, the friendship and moral support of James Ruppert, Alex Smith, Sarah Morton, Peter Greene, Cammie Crowder, Julia Stevens, and Johnson Chen were invaluable during the duration of the EAPSI program.

The author expresses a very special thanks to President Tomiro Kaya of SSJ for providing financial support (and unmatched hospitality) for a visit to Tokyo, Japan to discuss the finding of this research. Rocky Namiki, Soichi Kunoki, and Asao Sakuda are also thanked for their time, assistance, and kindness.

The dissertation committee members, Dr. Ahmad M. Itani, Dr. John Anderson, and Dr. Shen-Yi Luo, are thanked for their time, effort, and assistance during the development of this document. Finally, Dr. M. Saiid Saiidi and Dr. David Sanders cannot be thanked enough for the invaluable mentorship and guidance they provided during the past three years.

Table of Contents

Abstract.....	i
Dedication.....	iv
Acknowledgement.....	v
Table of Contents.....	vii
List of Tables.....	xx
List of Figures.....	xxvii
1. Introduction.....	1
1.1 Introduction.....	1
1.2 Past Research on Precast Substructure Connections for ABC in Seismic Zones.....	4
1.2.1 Socket (SO) Connections.....	4
1.2.2 Grouted Pocket (GP) Connections.....	7
1.2.3 Grouted Duct (GD) Connections.....	9
1.2.4 Hybrid (HY) Connections.....	11
1.2.5 Mechanically-Spliced (MS) Connections.....	12
1.3 Objectives and Scope.....	13
1.4 Document Outline.....	15
2. Mechanical Reinforcing Bar Splices.....	18
2.1 Introduction.....	18
2.2 Discussion of Selection Criteria.....	18
2.3 Review of Literature.....	22
2.3.1 Code Requirements.....	22
2.3.1.1 ACI.....	23
2.3.1.2 AASHTO.....	23

2.3.1.3 Caltrans	24
2.3.2 Research on Individual Coupler Performance.....	24
2.3.2.1 Army Corp [2009].....	24
2.3.2.2. FDOT [2007]	26
2.3.2.3 MDOT [2008]	26
2.3.2.4 NCHRP 10-35 [1991]	28
2.3.2.5 Nouredine [1994].....	29
2.3.2.6 WJE Associates [2000]	29
2.3.2.7 Summary	30
2.3.3 Summary of Research on Components	32
2.4 Final Coupler Selection	35
2.5 Experimental Program.....	35
2.5.1 Introduction	35
2.5.2 Description of Test Methods	36
2.5.2.1 Static Tensile Tests	36
2.5.2.2 Dynamic Tensile Tests.....	37
2.5.2.3 Cyclic Loading Tests	38
2.5.2.4 Single and Multi-Cycle Slip Testing.....	38
2.5.3 Specimen Preparation.....	39
2.5.3.1 HC Coupler Specimens.....	39
2.5.3.2 GC Coupler Specimens.....	39
2.5.4 Instrumentation and Data Acquisition.....	40
2.5.4.1 Static Tensile Tests	40
2.5.4.2 Dynamic Tensile Tests.....	41
2.5.4.3 Cyclic Loading Tests	41

2.5.4.4 Slip Tests.....	42
2.5.5 Test Results	42
3. Large-Scale Experimental Program	43
3.1 Introduction	43
3.2 Definition of Materials	44
3.2.1 Conventional Concrete	44
3.2.2 Self-Consolidating Concrete	45
3.2.2.1 ASTM C1611 - Slump Flow of Self-Consolidating Concrete.....	45
3.2.2.2 ASTM C1610 – Static Segregation of Self-Consolidating Concrete Using Column Technique.....	46
3.2.2.3 Caltrans Requirements on SCC	47
3.2.3 Cementitious Grouts.....	47
3.2.3.1 W. R. Meadows® 588-10K (Grout 1)	48
3.2.3.2 SikaGrout® 212 (Grout 2).....	48
3.2.3.3 SS Mortar® by Splice Sleeve (Grout 3)	48
3.2.4 Reinforcing Steel.....	49
3.3 Development of Benchmark Column	49
3.3.1 Introduction	49
3.3.2 Design Procedure	50
3.3.3 Final Benchmark Column Details	53
3.4 Cast-in-Place (CIP) Column Model	53
3.4.1 Introduction	53
3.4.2 Footing Design and Details	53
3.4.3 Loading Head Design and Details.....	54
3.4.4 Final Model Details.....	54

3.4.5 Construction	54
3.4.6 Instrumentation.....	55
3.5 Models with Upset Headed Coupler (HC) Connections.....	55
3.5.1 Details of HC Column Models.....	55
3.5.2 General Construction Sequence of HC Models.....	56
3.5.3 Construction of HC Models	59
3.5.3.1 HCNP Model Construction.....	59
3.5.3.2 HCPP Model Construction	62
3.5.4 Instrumentation.....	63
3.5.4.1 HCNP Model Instrumentation	63
3.5.4.2 HCPP Model Instrumentation.....	63
3.6 Models with Grouted Coupler (GC) Connections.....	63
3.6.1 General Details of GC Column Models	63
3.6.2 General Construction Sequence GC Models.....	64
3.6.3 Construction of GC Models	64
3.6.3.1 GCNP Model Construction.....	64
3.6.3.2 GCPP Model Construction	66
3.6.4 Instrumentation.....	67
3.6.4.1 GCNP Model Instrumentation	67
3.6.4.2 GCPP Model Instrumentation.....	68
3.7 Test Set-up and Loading Protocol	68
3.7.1 General Information	68
3.7.2 Placement of Column Model.....	68
3.7.3 Lateral Loading Configuration.....	69
3.7.4 Axial Load.....	69

3.7.5 Loading Protocol.....	70
3.7.6 Data Acquisition.....	70
4. Experimental Results: Individual Column Models	71
4.1 Introduction	71
4.2 Material Test Results.....	71
4.2.1 Conventional Concrete	72
4.2.1.1 Conventional Concrete 1 (CC1).....	72
4.2.1.2 Conventional Concrete 2 (CC2).....	72
4.2.1.3 Conventional Concrete 3 (CC3).....	72
4.2.1.4 Conventional Concrete 4 (CC4).....	73
4.2.1.5 Conventional Concrete 5 (CC5).....	73
4.2.1.6 Conventional Concrete 6 (CC6).....	73
4.2.2 Self-Consolidating Concrete	74
4.2.2.1 Self-Consolidating Concrete 1 (SCC1).....	74
4.2.3 Cementitious Grout	76
4.2.3.1 Cementitious Grout 1 (G1)	76
4.2.3.2 Cementitious Grout 2 (G2)	76
4.2.3.3 Cementitious Grout 3 (G3)	76
4.2.4 Reinforcing Steel.....	77
4.2.4.1 Number 3 Bar Reinforcing Steel (S3).....	77
4.2.4.2 Number 8 Bar Reinforcing Steel 1 (S8-1)	77
4.2.4.3 Number 8 Bar Reinforcing Steel 2 (S8-2)	78
4.2.4.4 Number 8 Bar Reinforcing Steel 3 (S8-3)	78
4.2.5 Summary of Material Properties	79
4.3 Data Processing Methods and Result Presentation Order	79

4.3.1 General Observations	79
4.3.2 Failure.....	79
4.3.3 Force-Displacement Response	80
4.3.4 Measured Strains	81
4.3.5 Measured Curvature and Bond Slip	82
4.3.6 Energy Dissipation	83
4.4 Model Results.....	83
4.4.1 CIP.....	83
4.4.1.1 General Observations.....	84
4.4.1.2 Failure	85
4.4.1.3 Force-Displacement Response.....	85
4.4.1.4 Measured Strains.....	86
4.4.1.5 Measured Curvature and Bond-Slip.....	87
4.4.1.6 Energy Dissipation.....	88
4.4.2 HCNP	88
4.4.2.1 General Observations.....	89
4.4.2.2 Failure	90
4.4.2.3 Force-Displacement Response.....	91
4.4.2.4 Measured Strains.....	92
4.4.2.5 Measured Curvature and Bond-Slip.....	93
4.4.2.6 Energy Dissipation.....	94
4.4.3 HCPP	94
4.4.3.1 General Observations.....	95
4.4.3.2 Failure	97
4.4.3.3 Force-Displacement Response.....	97

4.4.3.4 Measured Strains.....	99
4.4.3.5 Measured Curvature and Bond-Slip.....	100
4.4.3.6 Energy Dissipation.....	101
4.4.4 GCNP	101
4.4.4.1 General Observations.....	101
4.4.4.2 Failure	103
4.4.4.3 Force-Displacement Response.....	103
4.4.4.4 Measured Strains.....	104
4.4.4.5 Measured Curvature and Bond-Slip.....	105
4.4.4.6 Energy Dissipation.....	106
4.4.5 GCPP.....	106
4.4.5.1 General Observations.....	107
4.4.5.2 Failure	108
4.4.5.3 Force-Displacement Response.....	108
4.4.5.4 Measured Strains.....	109
4.4.5.5 Measured Curvature and Bond-Slip.....	110
4.4.5.6 Energy Dissipation.....	111
5. Comparison of Test Model Performance	112
5.1 Introduction	112
5.2.1 Presentation of Results	112
5.2 Comparison of Response of Models without Pedestals.....	113
5.2.1 Apparent Damage and Failure.....	113
5.2.2 Force-Displacement Relationships.....	114
5.2.3 Energy Dissipation	115
5.2.4 Measured Strains	116

5.2.5 Plastic Hinge Curvatures	118
5.3 Comparison of Response Models with Pedestals	119
5.3.1 Apparent Damage and Failure.....	119
5.3.2 Force-Displacement Relationships.....	120
5.3.3 Energy Dissipation	122
5.3.4 Measured Strains	122
5.3.5 Plastic Hinge Curvatures	124
5.3.6 Behavior of Pedestal Joints	125
5.4 Summary and Overall Evaluation.....	126
5.4.1 Model Performance	126
5.4.1.1 Apparent Damage and Failure	126
5.4.1.2 Force-Displacement Relationship.....	127
5.4.1.3 Energy Dissipation.....	128
5.4.1.4 Measured Strains.....	128
5.4.1.5 Moment-Curvature and Rotation	129
5.4.2 Effect of Couplers on Column Performance	129
5.4.2.1 Grouted Couplers (GC).....	129
5.4.2.2 Upset Headed Coupler (HC).....	130
5.4.3 Effect of Pedestal on Column Performance	131
6. Damage States and Response Parameters	133
6.1 Introduction	133
6.2 Background	133
6.3 Response Parameters	135
6.3.1 Maximum Drift Ratio (MDR)	135
6.3.2 Residual Drift Ratio (RDR).....	135

6.3.3 Frequency Ratio (FR).....	136
6.3.4 Inelasticity Index (II).....	136
6.3.5 Maximum Longitudinal (MLS) and Transverse (MTS) Steel Strain	137
6.4 Results	137
6.4.1 CIP.....	137
6.4.2 HCNP	138
6.4.3 GCNP	138
6.4.4 HCPP	139
6.4.5 GCPP	139
6.5 Discussion and Conclusions	140
7. Results from Couplers Tests	143
7.1 Introduction	143
7.2 Headed Coupler Tests.....	143
7.2.1 Static Tensile Tests.....	143
7.2.2 Dynamic Tests.....	145
7.2.3 Cyclic Tests	146
7.2.4 Slip Tests	149
7.3 Grouted Sleeve Coupler Tests	149
7.3.1 Static Tensile Tests.....	150
7.3.2 Dynamic Tensile Tests	151
7.3.3 Cyclic Tests	152
7.3.4 Slip Tests	154
7.4 Comparison and Discussion	154
8. Analytical Modeling of Column Models	162
8.1 Introduction	162

8.2 General Model Components.....	162
8.2.1 Elements.....	162
8.2.1.1 Rotational Springs.....	162
8.2.1.2 Elastic Beam-Column Elements.....	163
8.2.1.3 Nonlinear Beam-Column Elements.....	164
8.2.2 Material Models.....	164
8.2.2.1 Unconfined Concrete.....	165
8.2.2.2 Confined Concrete.....	166
8.2.2.3 Unconfined and Confined Grout.....	167
8.2.2.4 Reinforcing Steel.....	167
8.2.3 Bond-slip Rotation Modeling.....	168
8.2.3.1 Calculating M- θ Relationship.....	169
8.2.3.2 Implementing the M- θ Relationship in OpenSEES.....	170
8.2.4 General Details.....	171
8.3 Modeling of Low-Cycle Fatigue Failure.....	172
8.4 Analytical Modeling of CIP.....	176
8.4.1 General Model Details.....	176
8.4.2 Results.....	177
8.4.2.1 Force-Displacement Relationships.....	177
8.4.2.2 Energy Dissipation.....	178
8.4.2.3 Local Behavior.....	179
8.4.2.4 Modeling of Longitudinal Bar Fracture.....	180
8.5 Analytical Modeling of HCNP.....	181
8.5.1 Modeling of Headed Coupler Assembly.....	181
8.5.2 Model Details.....	184

8.5.3 Results	186
8.5.3.1 Force-Displacement Relationships	186
8.5.3.2 Energy Dissipation.....	187
8.5.3.3 Local Behavior.....	187
8.5.3.4 Modeling of Longitudinal Bar Fracture	188
8.6 Analytical Modeling of GCNP	189
8.6.1 Grouted Coupler Component Model.....	189
8.6.2 Model Details	196
8.6.3 Results	197
8.6.3.1 Force-Displacement Relationships	197
8.6.3.2 Energy Dissipation.....	199
8.6.3.3 Local Behavior.....	199
8.6.3.4 Modeling of Longitudinal Bar Fracture	201
8.7 Preliminary Analysis of the Pedestal.....	201
8.8 Analytical Modeling of HCPP.....	205
8.8.1 Model Details	205
8.8.2 Results	206
8.8.2.1 Force-Displacement Relationships	206
8.8.2.2 Energy Dissipation.....	207
8.8.2.3 Local Behavior.....	208
8.8.2.4 Modeling of Longitudinal Bar Fracture	209
8.9 Analytical Modeling of GCPP.....	210
8.9.1 Model Details	210
8.9.2 Results	212
8.9.2.1 Force-Displacement Relationships	212

8.9.2.2 Energy Dissipation.....	212
8.9.2.3 Local Behavior.....	213
8.9.2.4 Modeling of Longitudinal Bar Fracture.....	214
8.10 Summary and Discussion.....	215
8.10.1 Analytical Model of CIP.....	215
8.10.2 Analytical Model of HCNP.....	216
8.10.3 Analytical Model of GCNP.....	217
8.10.4 Analytical Models of Columns with Pedestals.....	218
8.10.4.1 HCPP.....	219
8.10.4.2 GCPP.....	219
8.10.5 Concluding Remarks.....	220
9. Parametric Studies and Design Recommendations.....	221
9.1 Introduction.....	221
9.1.1 Prototype Column Design.....	221
9.1.2 General Model Details.....	222
9.1.3 Description of Parametric Study.....	223
9.2 Parametric Study of Columns Grouted Coupler Connections.....	224
9.2.1 Target Design Displacement Ductility (DD) Study.....	224
9.2.1.1 Details of Study.....	224
9.2.1.2 Results.....	224
9.2.2 Aspect Ratio (AR) Study.....	227
9.2.2.1 Details of Study.....	227
9.2.2.2 Results.....	228
9.2.3 Longitudinal Steel Reinforcement Ratio (RR) Study.....	229
9.2.3.1 Details of Study.....	229

9.2.3.2 Results.....	230
9.2.4 Comparison and Discussion	232
9.3 Pedestal Geometry and Detailing	237
9.3.1 Details of Study	237
9.3.2 Results	238
9.3.3 Discussion	241
9.4 Design Recommendations	242
9.4.1 Development of Initial Design Details	243
9.4.2 Determination of Void Diameter.....	244
9.4.3 Columns Employing Headed Coupler Devices	245
9.4.4 Columns Employing Grouted Coupler Devices	246
9.4.5 Pedestal Design and Detailing.....	249
9.4.6 Additional Comments	251
9.5 Summary and Conclusions	252
10. Summary and Conclusions.....	255
10.1 Summary	255
10.2 Key Observations	256
10.2.1 Experimental Studies of Column Models.....	256
10.2.2 Direct Coupler Testing	258
10.2.3 Analytical Studies	260
10.3 Conclusions	262
References.....	265
Tables.....	274
Figures	328
Appendix A: Strain Gage Measurement Tables	585

List of Tables

Table 2-1 Summary of US code provisions for mechanical splices	275
Table 2-2 Code qualification for the five preliminary splices	275
Table 2-3 Summary of literature for individual coupler tests	275
Table 2-4 Cycle loading protocol defined by AC133 (2010)	276
Table 2-5 Tensile Test Nomenclature	276
Table 2-6 Loading protocol for HCC tests.....	277
Table 2-7 Loading protocol for GCC tests.....	277
Table 2-8 Caltrans maximum slip allowed for mechanical couplers	277
Table 3-1 Conventional concrete mix details	278
Table 3-2 Self-consolidating concrete mix details.....	278
Table 3-3 ASTM C1611 Visual inspection index.....	278
Table 3-4 Specific Caltrans requirements for SCC.....	279
Table 3-5 Summary of initial design parameters	279
Table 3-6 Final design parameters	279
Table 4-1 Conventional concrete 1 (CC1) material test results	280
Table 4-2 Conventional concrete 2 (CC2) material test results	280
Table 4-3 Conventional concrete 3 (CC3) material test results	280
Table 4-4 Conventional concrete 4 (CC4) material test results	281
Table 4-5 Conventional concrete 5 (CC5) material test results	281
Table 4-6 Conventional concrete 6 (CC6) material test results	281
Table 4-7 Self-consolidating concrete 1 (SCC1) material test results	282
Table 4-8 Self-consolidating concrete 2 (SCC2) material test results	282
Table 4-9 Cementitious grout 1 (G1) material test results.....	282

Table 4-10 Cementitious grout 2 (G2) material test results	283
Table 4-11 Cementitious grout 3 (G3) material test results	283
Table 4-12 Number 3 bar reinforcing steel 1 (S3) material test results	283
Table 4-13 Number 8 bar reinforcing steel 1 (S8-1) material test results.....	284
Table 4-14 Number 8 bar reinforcing steel 2 (S8-2) material test results.....	284
Table 4-15 Number 8 bar reinforcing steel 3 (S8-3) material test results.....	284
Table 4-16 Summary of conventional concrete material properties	285
Table 4-17 Summary of self-consolidating concrete material properties	285
Table 4-18 Summary of cementitious grout material properties	285
Table 4-19 Summary of reinforcing steel material properties	285
Table 4-20 Complete summary of material properties	286
Table 4-21 Day-of-test material properties for CIP	287
Table 4-22 Measured peak load and displacement for CIP	287
Table 4-23 CIP energy dissipation per drift level.....	288
Table 4-24 Day-of-test material properties for HCNP.....	288
Table 4-25 Measured peak load and displacement for HCNP.....	288
Table 4-26 HCNP energy dissipation per drift level.....	289
Table 4-27 Day-of-test material properties for HCPP	289
Table 4-28 Approximate locations of ruptured bars in HCPP	289
Table 4-29 Measured peak load and displacement for HCPP.....	290
Table 4-30 HCPP energy dissipation per drift level	290
Table 4-31 Day-of-test material properties for GCNP.....	291
Table 4-32 Approximate locations of ruptured bars in GCNP	291
Table 4-33 Measured peak load and displacement for GCNP	292
Table 4-34 GCNP energy dissipation per drift level.....	292

Table 4-35 Day-of-test material properties for GCPP	293
Table 4-36 Approximate locations of ruptured bars in GCPP	293
Table 4-37 Measured peak load and displacement for GCPP.....	294
Table 4-38 GCPP energy dissipation per drift level	294
Table 5-1 Summary of drift level comparison point.....	295
Table 5-2 Summary of damage for model without pedestal	295
Table 5-3 Parameters used to determine the elasto-plastic curve and displacement ductility for models without pedestal.....	296
Table 5-4 Summary of damage for models with pedestal.....	296
Table 5-5 Parameters used to determine the elasto-plastic curve and displacement ductility for models with pedestal.....	297
Table 5-6 Summary of damage for all models.....	298
Table 7-1 Static test results for headed couplers at yield.....	299
Table 7-2 Static test results for headed couplers at ultimate and failure	299
Table 7-3 Measured strain rates for headed couplers samples.....	299
Table 7-4 Dynamic test results for headed couplers at yield	300
Table 7-5 Dynamic test results for headed couplers at ultimate and failure	300
Table 7-6 Measurements taken from cyclic test HCC-1	301
Table 7-7 Measurements taken from cyclic test HCC-2.....	301
Table 7-8 Summary of test results for cyclic tests on headed couplers	302
Table 7-9 Results for single cycle slip tests on upset headed coupler	302
Table 7-10 Multi-cycle slip test results for HCS1	302
Table 7-11 Multi-cycle slip test results for HCS2	303
Table 7-12 Multi-cycle slip test results for HCS3	303
Table 7-13 Summary of multi-cycle slip tests on headed couplers	303

Table 7-14 Static test results for grouted couplers at yield.....	304
Table 7-15 Static test results for grouted couplers at ultimate and failure.....	304
Table 7-16 Measured strain rates for grouted coupler dynamic tensile tests.....	304
Table 7-17 Dynamic test results for grouted couplers at yield	305
Table 7-18 Dynamic test results for grouted couplers at ultimate and failure	305
Table 7-19 Summary of results for GCC-1.....	305
Table 7-20 Results for single cycle slip tests on grouted couplers	306
Table 7-21 Multi-cycle slip test results for GCS1	306
Table 7-22 Multi-cycle slip test results for GCS2	306
Table 7-23 Multi-cycle slip test results for GCS3	307
Table 7-24 Summary of multi-cycle slip tests on headed couplers	307
Table 7-25 Comparison of dynamic yield stress for headed couplers with available models	307
Table 7-26 Comparison of dynamic yield stress for grouted couplers with available models	308
Table 7-27 Comparison of dynamic ultimate stress for headed couplers with available models	308
Table 7-28 Comparison of dynamic ultimate stress for grouted couplers with available models	308
Table 8-1 Measured axial load data.....	309
Table 8-2 Low-cycle fatigue-life parameters based on plastic strain amplitude.....	309
Table 8-3 Low-cycle fatigue-life parameters based on total strain amplitude.....	309
Table 8-4 Longitudinal reinforcing steel properties for CIP.....	310
Table 8-5 Description of material properties for cementitious materials for CIP.....	310
Table 8-6 Rotational spring properties for modeling bond-slip in CIP	310
Table 8-7 Longitudinal reinforcing steel properties for HCNP	311
Table 8-8 Description of material properties for cementitious materials in HCNP.....	311
Table 8-9 Rotational spring properties for modeling bond-slip in HCNP	312
Table 8-10 Properties for bi-linear ductile cast iron material	312

Table 8-11 Longitudinal reinforcing steel properties for GCNP	312
Table 8-12 Description of material properties for cementitious materials in GCNP	313
Table 8-13 Rotational spring properties for GCNP	313
Table 8-14 Results from moment-curvature analysis of the pedestal	314
Table 8-15 Longitudinal reinforcing steel properties for HCPP	315
Table 8-16 Description of material properties for cementitious materials in HCPP	316
Table 8-17 Rotational spring properties for HCPP	317
Table 8-18 Longitudinal reinforcing steel properties for GCPP	317
Table 8-19 Description of material properties for cementitious materials in GCPP	318
Table 8-20 Rotational spring properties for GCPP	319
Table 9-1 Conventional column design details	320
Table 9-2 Typical material properties used for parametric study	321
Table 9-3 Parametric study matrix	322
Table 9-4 Model details used in parameter study of target design displacement ductility for GC columns	322
Table 9-5 Summary of results for ductility study	323
Table 9-6 Model details for aspect ratio study	324
Table 9-7 Summary of results for aspect ratio study	324
Table 9-8 Model details for reinforcement ratio study	325
Table 9-9 Summary of results for reinforcement ratio study	325
Table 9-10 Summary of results for HP columns with pedestals of height 0.5D	326
Table 9-11 Summary of results for HP columns with pedestals of height 1.0D	326
Table 9-12 Summary of results for GP columns with pedestals of height 0.5D	327
Table 9-13 Summary of results for GP columns with pedestals of height 1.0D	327
Table A-1 CIP longitudinal bar strain gages 1-5	586

Table A-2 CIP longitudinal bar strain gages 6-10	586
Table A-3 CIP longitudinal bar strain gages 11-15	587
Table A-4 CIP longitudinal bar strain gages 20-24	587
Table A-5 CIP longitudinal bar strain gages 29-33	588
Table A-6 CIP longitudinal bar strain gages 38-42	588
Table A-7 CIP transverse bar strain gages 16-19	589
Table A-8 CIP transverse bar strain gages 25-28	589
Table A-9 CIP transverse bar strain gages 34-37	590
Table A-10 CIP transverse bar strain gages 43-46	590
Table A-11 HCNP longitudinal bar strain gages 1-5	591
Table A-12 HCNP longitudinal bar strain gages 6-10	591
Table A-13 HCNP longitudinal bar strain gages 11-17	592
Table A-14 HCNP longitudinal bar strain gages 22-26	592
Table A-15 HCNP longitudinal bar strain gages 31-35	593
Table A-16 HCNP transverse bar strain gages 18-21	593
Table A-17 HCNP transverse bar strain gages 27-30	594
Table A-18 HCNP transverse bar strain gages 36-39	594
Table A-19 HCPP longitudinal bar strain gages 1-5	595
Table A-20 HCPP longitudinal bar strain gages 6-10	595
Table A-21 HCPP longitudinal bar strain gages 11-15	596
Table A-22 HCPP longitudinal bar strain gages 20-24	596
Table A-23 HCPP longitudinal bar strain gages 29-35	597
Table A-24 HCPP longitudinal bar strain gages 40-44	598
Table A-25 HCPP longitudinal bar strain gages 49-53	598
Table A-26 HCPP transverse bar strain gages 16-19	599

Table A-27 HCPP transverse bar strain gages 25-28.....	599
Table A-28 HCPP transverse bar strain gages 36-39.....	600
Table A-29 HCPP transverse bar strain gages 45-48.....	600
Table A-30 HCPP transverse bar strain gages 54-57.....	601
Table A-31 GCNP longitudinal bar strain gages 1-5.....	601
Table A-32 GCNP longitudinal bar strain gages 6-10.....	602
Table A-33 GCNP longitudinal bar strain gages 29-33.....	602
Table A-34 GCNP longitudinal bar strain gages 38-42.....	603
Table A-35 GCNP transverse bar strain gages 25-28.....	603
Table A-36 GCNP transverse bar strain gages 34-37.....	604
Table A-37 GCNP transverse bar strain gages 43-46.....	604
Table A-38 GCNP grouted coupler strain gages 11-17.....	605
Table A-39 GCNP grouted coupler strain gages 18-24.....	606
Table A-40 GCPP longitudinal bar strain gages 1-5.....	606
Table A-41 GCPP longitudinal bar strain gages 6-10.....	607
Table A-42 GCPP longitudinal bar strain gages 11-15.....	607
Table A-43 GCPP longitudinal bar strain gages 20-24.....	608
Table A-44 GCPP longitudinal bar strain gages 47-31.....	608
Table A-45 GCPP longitudinal bar strain gages 56-60.....	609
Table A-46 GCPP transverse bar strain gages 16-19.....	609
Table A-47 GCPP transverse bar strain gages 25-28.....	610
Table A-48 GCPP transverse bar strain gages 43-46.....	610
Table A-49 GCPP transverse bar strain gages 52-55.....	611
Table A-50 GCPP grouted coupler strain gages 29-35.....	611
Table A-51 GCPP grouted coupler strain gages 36-42.....	612

List of Figures

Figure 1-1 Precast columns connection types for ABC (adapted from Marsh et al., 2011)	329
Figure 2-1 Schematic for commonly used terms	330
Figure 2-2 Shear-screw coupler	330
Figure 2-3 Grout-filled sleeve coupler.....	331
Figure 2-4 Upset headed coupler	331
Figure 2-5 Straight threaded coupler	332
Figure 2-6 Tapered threaded coupler.....	332
Figure 2-7 Failure of shear screw splices other than bar rupture.....	333
Figure 2-8 Failure of grouted sleeve splices other than bar rupture	333
Figure 2-9 Failure of upset headed splices other than bar rupture.....	333
Figure 2-10 Failure of tapered thread splices other than bar rupture.....	334
Figure 2-11 Strain measurement region defined by ASTM A1034.....	334
Figure 2-12 Cyclic loading protocol	334
Figure 2-13 Support frame for construction of grouted coupler specimens	335
Figure 2-14 Grouted coupler test specimens ready for grouting.....	335
Figure 2-15 Grouted coupler test specimens after grouting and bar insertion.....	335
Figure 2-16 Instrumentation plan for HC couplers (Static and High Rate Tests).....	336
Figure 2-17 HC tensile test specimen set-up	336
Figure 2-18 Instrumentation plan for GC couplers (Static and High Rate Tests).....	337
Figure 2-19 GC tensile test specimen set-up	337
Figure 2-20 Instrumentation for HC slip test.....	338
Figure 2-21 HC slip test set-up	338
Figure 2-22 Instrumentation for GC slip test.....	339

Figure 2-23 GC slip test set-up	339
Figure 3-1 Static segregation column	340
Figure 3-2 Benchmark column cross-section details	340
Figure 3-3 Footing dimensions and reinforcement details.....	341
Figure 3-4 Loading head dimensions and reinforcement details	342
Figure 3-5 CIP full column model details.....	343
Figure 3-6 Bottom steel in footing form	344
Figure 3-7 CIP footing ready for casting concrete.....	344
Figure 3-8 Form-work for column ready for head construction	345
Figure 3-9 CIP column head formwork and reinforcement.....	345
Figure 3-10 Completed CIP column model	346
Figure 3-11 CIP strain gage schematic	347
Figure 3-12 Instrumented cast-in-place column cage	348
Figure 3-13 CIP displacement and curvature instrumentation.....	349
Figure 3-14 General details of headed coupler connection.....	350
Figure 3-15 Column shell connection details for HC models.....	351
Figure 3-16 HCNP full column reinforcement drawing	352
Figure 3-17 HCNP full column reinforcement drawing.....	353
Figure 3-18 HCNP pedestal reinforcement details	354
Figure 3-19 HC connection construction procedure	355
Figure 3-20 Longitudinal reinforcing bar template.....	356
Figure 3-21 Placement of HCNP footing column cage	356
Figure 3-22 HCNP footing reinforcement and form-work prior to casting concrete.....	356
Figure 3-23 Footing after casting showing HRC headed dowels	357
Figure 3-24 Prepared form-work for HC column base segment.....	357

Figure 3-25 Construction of column cage base segment	358
Figure 3-26 Column cages and internal PVC form.....	358
Figure 3-27 HCNP column sell ready for casting concrete	359
Figure 3-28 HCNP column shell after removal of formwork.....	360
Figure 3-29 Transition bar with male threaded ends	360
Figure 3-30 Initial setting of HCNP column shell	361
Figure 3-31 Steel spacers for HRC couplers.....	361
Figure 3-32 Spacer inserted between upper heads.....	362
Figure 3-33 Torqueing HRC couplers	362
Figure 3-34 Connection region after tightening of couplers and tying spiral	363
Figure 3-35 Connection region ready for closure grouting.....	363
Figure 3-36 Grout ready for pumping.....	364
Figure 3-37 Flow table test for grout (ASTM C1437).....	364
Figure 3-38 Casting of grout cubes.....	365
Figure 3-39 Void left from bleed material	365
Figure 3-40 Void region prepared for epoxy injection	366
Figure 3-41 Final slump-flow test of SCC.....	366
Figure 3-42 Filling SCC segregation column	367
Figure 3-43 Collection of segregation column top and bottom contents	367
Figure 3-44 Sieving segregation column contents	368
Figure 3-45 Segregation column contents after sieving.....	368
Figure 3-46 Cast SCC in column core	369
Figure 3-47 HCPP footing reinforcement and form-work.....	369
Figure 3-48 HCPP footing dowels and placement of corrugated ducts for pedestal	370
Figure 3-49 Pedestal reinforcement and form-work	370

Figure 3-50 HCPP pedestal after casting concrete.....	371
Figure 3-51 Voids found in HCPP coupling region.....	371
Figure 3-52 Repair form-work and casting of new concrete	372
Figure 3-53 Completed repair.....	372
Figure 3-54 HCNP strain gage instrumentation plan.....	373
Figure 3-55 HCNP instrumented footing dowel cage.....	374
Figure 3-56 HCNP instrumented column cage.....	374
Figure 3-57 Instrumentation of closure region	375
Figure 3-58 HCNP displacement and curvature gage instrumentation plan.....	376
Figure 3-59 HCPP strain gage instrumentation plan	377
Figure 3-60 HCPP displacement and curvature gage instrumentation plan	378
Figure 3-61 General GC connection detail	379
Figure 3-62 GCNP column model geometry and reinforcement details.....	380
Figure 3-63 GCPP column model geometry and reinforcement details	381
Figure 3-64 GCPP pedestal details	382
Figure 3-65 Construction sequence of GC column connection	383
Figure 3-66 GCNP footing dowel reinforcement cage	384
Figure 3-67 GCNP completed footing form and reinforcement	384
Figure 3-68 GCNP footing casting concrete.....	385
Figure 3-69 Measurement of GCNP footing dowel.....	385
Figure 3-70 GCNP footing after removal of formwork.....	386
Figure 3-71 Installation of NMB couplers on GCNP column cage	386
Figure 3-72 Tying spiral around GCNP coupler region	387
Figure 3-73 GCNP column shell platform with NMB Sleeve Setters	387
Figure 3-74 NMB Sleeve Setters	388

Figure 3-75 GCNP column cage on platform with PVC form in the center.....	388
Figure 3-76 Grout ports protruding through form	389
Figure 3-77 Complete GCNP column shell	389
Figure 3-78 Grout sleeve ports below GCNP column shell.....	390
Figure 3-79 GCNP footing dowel bars after cleaning	390
Figure 3-80 GCNP column shell after placement on footing dowels	391
Figure 3-81 Steel shim between column shell and footing	391
Figure 3-82 Temporary formwork for grouting column shell-to-footing interface	392
Figure 3-83 Grout after placement.....	392
Figure 3-84 GCNP footing formwork and reinforcement	393
Figure 3-85 GCNP pedestal formwork and reinforcement.....	393
Figure 3-86 GCNP pedestal ducts after grouting and cleaning dowels	394
Figure 3-87 Temporary grout form and grout washers.....	394
Figure 3-88 Placement of the GCNP column shell	395
Figure 3-89 GCNP strain gage instrumentation plan.....	396
Figure 3-90 Wiring of GCNP footing cage.....	397
Figure 3-91 Strain gage installation on NMB couplers	397
Figure 3-92 Instrumented couplers	398
Figure 3-93 GCNP column cage instrumentation.....	398
Figure 3-94 GCNP Displacement and curvature instrumentation	399
Figure 3-95 GCNP strain gage instrumentation plan	400
Figure 3-96 GCNP displacement and curvature instrumentation plan	401
Figure 3-97 Schematic of experimental set-up	402
Figure 3-98 Photo of test set-up.....	403
Figure 3-99 Placement of column model.....	403

Figure 3-100 Construction of reaction pylon.....	404
Figure 3-101 Spreader beam and loading rams	404
Figure 3-102 Nitrogen accumulator.....	405
Figure 3-103 Loading protocol	405
Figure 4-1 CIP material schematic.....	406
Figure 4-2 HCNP material schematic	407
Figure 4-3 HCPP material schematic.....	408
Figure 4-4 GCNP material schematic	409
Figure 4-5 GCPP material schematic.....	410
Figure 4-6 SCC1 slump flow test results	411
Figure 4-7 SCC2 slump flow test results	411
Figure 4-8 Stress-strain behavior of #3 reinforcing steel 1 (S3-1).....	412
Figure 4-9 S3-1 reinforcing bars after testing.....	412
Figure 4-10 Stress-strain behavior of #8 reinforcing steel 1 (S8-1).....	413
Figure 4-11 S8-1 samples after testing	413
Figure 4-12 Stress-strain behavior of #8 reinforcing steel 2 (S8-2).....	414
Figure 4-13 S8-2 samples after testing	414
Figure 4-14 Stress-strain behavior of #8 reinforcing steel 3 (S8-3).....	415
Figure 4-15 S8-3 samples after testing	415
Figure 4-16 Reference orientation of the test set-up.....	416
Figure 4-17 Variables used in the determination of section curvature	416
Figure 4-18 Observed damage for CIP at drift levels less than 1%	417
Figure 4-19 CIP damage at 1% drift	417
Figure 4-20 CIP damage at 2% drift.....	418
Figure 4-21 CIP damage at 3% drift.....	418

Figure 4-22 CIP damage at 4% drift	419
Figure 4-23 CIP damage at 5% drift	419
Figure 4-24 CIP damage at 6% drift	420
Figure 4-25 CIP damage at 8% drift	420
Figure 4-26 CIP damage at 10% drift	421
Figure 4-27 Failure mechanisms of CIP	421
Figure 4-28 CIP hysteretic force-displacement response.....	422
Figure 4-29 CIP average force-displacement backbone curve	422
Figure 4-30 CIP Measured longitudinal tensile strain profiles	423
Figure 4-31 CIP plastic hinge curvatures for lower drift levels.....	424
Figure 4-32 CIP plastic hinge curvatures for higher drift levels.....	424
Figure 4-33 CIP moment vs. bond-slip rotation relationship.....	425
Figure 4-34 CIP cumulative energy dissipation.....	425
Figure 4-35 Damage observed for HCNP at drift levels less than 1%.....	426
Figure 4-36 HCNP observed damage at 1% drift	426
Figure 4-37HCNP observed damage at 2% drift	427
Figure 4-38HCNP observed damage at 3% drift	427
Figure 4-39 HCNP observed damage at 4% drift	428
Figure 4-40 HCNP observed damage at 5% drift	428
Figure 4-41 HCNP observed damage at 6% drift	429
Figure 4-42 HCNP observed damage at 8% drift	429
Figure 4-43 HCNP observed damage at 10% drift	430
Figure 4-44 HCNP observed damage at 12% drift	430
Figure 4-45 Removal of concrete from plastic hinge and footing	431
Figure 4-46 Fractured bar located on the east face of HCNP (left bar)	431

Figure 4-47 HCNP hysteretic force-displacement response	432
Figure 4-48 HCNP average force-displacement backbone curve	432
Figure 4-49 HCNP Measured longitudinal strain profiles	433
Figure 4-50 HCNP plastic hinge curvatures for lower drift levels	434
Figure 4-51 HCNP plastic hinge curvatures for higher drift levels	434
Figure 4-52 HCNP moment vs. bond-slip rotation relationship	435
Figure 4-53 HCNP cumulative energy dissipation	435
Figure 4-54. HCNP damage at drift levels less than 1%	436
Figure 4-55. HCNP observed damage at 1.0% drift.....	436
Figure 4-56. HCNP observed damage at 2.0% drift.....	437
Figure 4-57 HCNP observed damage at 3.0% drift.....	437
Figure 4-58. HCNP observed damage at 4.0% drift.....	438
Figure 4-59 HCNP observed damage at 5.0% drift.....	438
Figure 4-60. HCNP observed damage at 6.0% drift.....	439
Figure 4-61. HCNP observed damage at 8.0% drift.....	439
Figure 4-62. HCNP observed damage at 10.0% drift.....	440
Figure 4-63. . HCNP observed damage at 12.0% drift.....	440
Figure 4-64 Locations of fractured bar on the west face of HCNP	441
Figure 4-65 Location of fractured bar on the east face of HCNP	441
Figure 4-66 Bars and pedestal ducts removed from HCNP.....	442
Figure 4-67 HCNP hysteretic force-displacement response.....	443
Figure 4-68 HCNP average force-displacement backbone curve.....	443
Figure 4-69 Measured longitudinal tensile strain profiles for HCNP.....	444
Figure 4-70 HCNP plastic hinge curvatures for lower drift levels	445
Figure 4-71 HCNP plastic hinge curvatures for higher drift levels	445

Figure 4-72 HCPP moment vs. bond-slip rotation relationship.....	446
Figure 4-73 HCPP moment vs. pedestal joint rotation	446
Figure 4-74 HCPP cumulative energy dissipation.....	447
Figure 4-75 Damage observed for GCNP at drift levels less than 1%.....	448
Figure 4-76 GCNP observed damage at 1.0% drift	448
Figure 4-77 GCNP observed damage at 2.0% drift	449
Figure 4-78 GCNP observed damage at 3.0% drift	450
Figure 4-79 GCNP observed damage at 4.0% drift	451
Figure 4-80 GCNP observed damage at 5.0% drift	452
Figure 4-81 GCNP observed damage at 6.0% drift	453
Figure 4-82 GCNP observed damage at 8.0% drift	453
Figure 4-83 Location of removed grouted coupler (center bar west face).....	454
Figure 4-84 Couplers removed from GCNP	454
Figure 4-85 Grout cone due to strain penetration	454
Figure 4-86 GCNP hysteretic force-displacement response	455
Figure 4-87 GCNP average force-displacement backbone curve	455
Figure 4-88 Measured average longitudinal tensile strain profiles for GCNP.....	456
Figure 4-89 GCNP plastic hinge curvatures for lower drift levels	457
Figure 4-90 GCNP plastic hinge curvatures for higher drift levels	457
Figure 4-91 GCNP moment vs. bond-slip rotation relationship	458
Figure 4-92 GCNP cumulative energy dissipation	458
Figure 4-93 Damage observed for GCPP at drift levels less than 1%	459
Figure 4-94 GCPP observed damage at 1.0% drift.....	459
Figure 4-95 GCPP observed damage at 2.0% drift.....	460
Figure 4-96 GCPP observed damage at 3.0% drift.....	461

Figure 4-97 GCPP observed damage at 4.0% drift.....	462
Figure 4-98 GCPP observed damage at 5.0% drift.....	463
Figure 4-99 GCPP observed damage at 6.0% drift.....	464
Figure 4-100 GCPP observed damage at 8.0% drift.....	465
Figure 4-101 Bar fracture location of west face of GCPP.....	466
Figure 4-102 Bar fracture location of east face of GCPP.....	466
Figure 4-103 GCPP hysteretic force-displacement response.....	467
Figure 4-104 GCPP average force-displacement backbone curve.....	467
Figure 4-105 GCPP measured longitudinal strain profiles.....	468
Figure 4-106 GCPP plastic hinge curvatures for lower drift levels.....	469
Figure 4-107 GCPP plastic hinge curvatures for higher drift levels.....	469
Figure 4-108 GCPP moment vs. bond-slip rotation relationship.....	470
Figure 4-109 GCPP moment vs. pedestal joint rotation relationship.....	470
Figure 4-110 GCPP cumulative energy dissipation.....	471
Figure 5-1 Comparison of damage in models without pedestal after second push cycle of 0.75% drift.....	472
Figure 5-2 Comparison of damage in models without pedestal after second push cycle of 2.0% drift.....	472
Figure 5-3 Comparison of damage in models without pedestal after second push cycle of 4.0% drift.....	473
Figure 5-4 Comparison of damage in models without pedestal after second push cycle of 6.0% drift.....	473
Figure 5-5 Comparison of damage in models without pedestal after second push cycle of 8.0% drift.....	474
Figure 5-6 Comparison of damage in models without pedestal after 10.0% drift.....	475

Figure 5-7 Comparison of the hysteretic force-displacement response of CIP and HCNP	476
Figure 5-8 Comparison of the hysteretic force-displacement response of CIP and GCNP	476
Figure 5-9 Comparison of the hysteretic force-displacement response of HCNP and GCNP	476
Figure 5-10 Average pushover response for models without pedestal	477
Figure 5-11 Elasto-plastic response of models without pedestal	477
Figure 5-12 Energy dissipation capacity of models without pedestal.....	477
Figure 5-13 Comparison of energy dissipation for models without pedestals.....	477
Figure 5-14 Comparison of plastic hinge longitudinal strain profiles for models without pedestal	478
Figure 5-15 Average transverse strain profiles due to compression zone dilation	479
Figure 5-16 Average transverse strain profiles due to shear deformation	480
Figure 5-17 Nomenclature for curvature measurement locations for models without pedestals .	481
Figure 5-18 Average moment-curvature response of models without pedestal at Section 0.....	481
Figure 5-19 Average curvature per drift level for models without pedestals	481
Figure 5-20 Moment-curvature response of models without pedestal Sections 1 - 4.....	482
Figure 5-21 Comparison of damage in models with pedestal after second push cycle of 0.75% drift.....	483
Figure 5-22 Comparison of damage in models with pedestal after second push cycle of 2.0% drift	483
Figure 5-23 Comparison of damage in models with pedestal after second push cycle of 4.0% drift	484
Figure 5-24 Comparison of damage in models with pedestal after second push cycle of 6.0% drift	484
Figure 5-25 Comparison of damage in models with pedestal after second push cycle of 8.0% drift	485

Figure 5-26 Comparison of damage in models with pedestal after 10.0% drift	486
Figure 5-27 Comparison of the hysteretic force-displacement response of CIP and HCPP	487
Figure 5-28 Comparison of the hysteretic force-displacement response of CIP and GCPP	487
Figure 5-29 Comparison of the hysteretic force-displacement response of HCPP and GCPP	487
Figure 5-30 Average pushover response of models with pedestals	488
Figure 5-31 Elasto-plastic response of models with pedestals.....	488
Figure 5-32 Energy dissipation capacity of models with pedestals	488
Figure 5-33 Comparison of energy dissipation for models with pedestals	488
Figure 5-34 Comparison of plastic hinge strain profiles for models with pedestal	489
Figure 5-35 Average transverse strain profiles due to compression zone dilation	490
Figure 5-36 Average transverse strain profiles due to shear deformation	491
Figure 5-37 Shear cracking mechanism in CIP	492
Figure 5-38 Shear cracking mechanism in models with precast pedestal.....	492
Figure 5-39 Nomenclature for curvature measurement locations for models with pedestals	493
Figure 5-40 Average moment-curvature response of models with pedestal at Section 0	493
Figure 5-41 Average curvature per drift level for models with pedestals.....	493
Figure 5-42 Moment-curvature response of models with pedestal Sections 1 – 4	494
Figure 5-43 Rotation behavior of the pedestal-column joint	494
Figure 5-44 Pedestal-column joints at 4.0% drift	495
Figure 5-45 Rotation behavior of the pedestal-footing joints	495
Figure 5-46 Pedestal-footing joints at 6.0% drift.....	495
Figure 5-47 Summary of force-displacement relationships:	496
Figure 5-48 Summary of energy dissipation behavior.....	497
Figure 5-49 Summary of longitudinal strain profiles.....	497
Figure 5-50 Observed hinge mechanisms	498

Figure 6-1 Damage states as defined by Vosooghi and Saiidi (2010)	499
Figure 6-2 Response parameters for standard columns under near- and far-field motions	500
Figure 6-3 Damage states for CIP	501
Figure 6-4 Response parameters for CIP	502
Figure 6-5 Damage states for HCNP	503
Figure 6-6 Response parameters for HCNP	504
Figure 6-7 Damage states for GCNP	505
Figure 6-8 Response parameters for GCNP	506
Figure 6-9 Damage states for HCPP	507
Figure 6-10 Response parameters for HCPP	508
Figure 6-11 Damage states for GCPP	509
Figure 6-12 Response parameters for GCPP	510
Figure 6-13 Comparison of damage states for all columns	511
Figure 6-14 Correlation between average push-over response and apparent damage states	512
Figure 7-1 Static test result for sample HS1	513
Figure 7-2 Static test result for sample HS3	513
Figure 7-3 Static test result for sample HS4	513
Figure 7-4 Monotonic stress-strain behavior of the headed coupler region	514
Figure 7-5 Sample HS3 disassembled after testing	514
Figure 7-6 Dynamic test result for sample HSR1	514
Figure 7-7 Dynamic test result for sample HSR2	515
Figure 7-8 Dynamic test result for sample HSR3	515
Figure 7-9 Dynamic test result for sample HSR4	515
Figure 7-10 Cyclic test results for headed coupler sample HCC-1	516
Figure 7-11 Cyclic test results for headed coupler sample HCC-2	517

Figure 7-12 Measured relationship between peak stress in the bars and gap length	517
Figure 7-13 Static test result for sample GS1	518
Figure 7-14 Static test result for sample GS2	518
Figure 7-15 Static test result for sample GS3	518
Figure 7-16 Monotonic stress-strain behavior of the grouted coupler region.....	519
Figure 7-17 Evidence of strain penetration into the grouted sleeve.....	519
Figure 7-18 Dynamic test result for sample GSR1	519
Figure 7-19 Dynamic test result for sample GSR2.....	520
Figure 7-20 Dynamic test result for sample GSR3.....	520
Figure 7-21 Dynamic test result for sample GSR4.....	520
Figure 7-22 Cyclic test results for grouted coupler sample GCC-1.....	521
Figure 7-23 Comparison of static and dynamic stress-strain behavior for headed coupler tests .	522
Figure 7-24 Comparison of static and dynamic stress-strain behavior for grouted coupler tests	522
Figure 7-25 Comparison of static and cyclic stress-strain behavior for headed coupler tests	522
Figure 7-26 Comparison of static and cyclic stress-strain behavior for grouted coupler tests	523
Figure 7-27 Comparison of the bar-to-coupler region strain ratio for static loading.....	523
Figure 7-28 Comparison of the bar-to-coupler region strain ratio for dynamic loading.....	524
Figure 8-1 Constitutive behavior for “Hysteretic” material.....	525
Figure 8-2 Constitutive model for unconfined concrete	525
Figure 8-3 Constitutive model for confined concrete	525
Figure 8-4 Constitutive model for reinforcing steel.....	526
Figure 8-5 Wehbe’s method for calculating bond-slip rotation.....	526
Figure 8-6 Moment-rotation relationship for bond-slip.....	526
Figure 8-7 General details of analytical column models	527
Figure 8-8 Parameters that define a stable hysteresis loop	528

Figure 8-9 Total strain amplitude – fatigue-life relationship.....	528
Figure 8-10 Data reported by Brown and Kunnath (2000) for No. 8 A615 Gr. 60 bars.....	528
Figure 8-11 Data reported by Zhou et al. (2010) for No. 8 A706 Gr. 60 bars.....	528
Figure 8-12 Schematic for description of low-cycle fatigue determination.....	529
Figure 8-13 Algorithm for determining fatigue fracture.....	529
Figure 8-14 Analytical model of CIP.....	530
Figure 8-15 Moment-curvature response for CIP (Section A-A shown in Fig. 8-14).....	530
Figure 8-16 Calculated bond-slip behavior for CIP.....	530
Figure 8-17 Hysteresis curves for CIP.....	531
Figure 8-18 Average envelope curves for CIP.....	531
Figure 8-19 Energy dissipation for CIP.....	532
Figure 8-20 Comparison between measured and calculated strains.....	532
Figure 8-21 Bond-slip rotation hysteresis for CIP up to 6% Drift.....	532
Figure 8-22 Moment-rotation of the 14-in [356-mm] section above the footing for CIP.....	532
Figure 8-23 Cumulative damage as a function of drift for CIP.....	533
Figure 8-24 Cumulative damage plotted with drift and load for CIP.....	533
Figure 8-25 HC gap opening/closing mechanism.....	534
Figure 8-26 Analytical model for HC uxi-axial test.....	534
Figure 8-27 Constitutive behavior for spring 1 (S_1).....	534
Figure 8-28 Constitutive behavior for spring 2 (S_2).....	535
Figure 8-29 Constitutive behavior for spring 3 (S_3).....	535
Figure 8-30 Combine behavior of the gap spring system.....	535
Figure 8-31 Results using displacement history from HCC1 test.....	536
Figure 8-32 Results using modified displacement history compared to data from HCC1 test....	536
Figure 8-33 Analytical model of HCNP.....	537

Figure 8-34 Moment-curvature response from HCNP grouted region	537
Figure 8-35 Calculated bond-slip behavior for HCNP	537
Figure 8-36 Hysteresis curves for HCNP	538
Figure 8-37 Average envelopes for HCNP	538
Figure 8-38 Energy dissipation for HCNP.....	539
Figure 8-39 Comparison between measured and calculated strains for HCNP	539
Figure 8-40 Comparison between measured and calculated moment-rotation relationships for HCNP	540
Figure 8-41 Cumulative damage as a function of drift for HCNP	540
Figure 8-42 Cumulative damage plotted with drift and load for HCNP.....	541
Figure 8-43 Component model details for individual grouted coupler	542
Figure 8-44 Observed cyclic strain behavior from GCC1	542
Figure 8-45 Proposed stress-strain model for ductile cast iron.....	543
Figure 8-46 Comparison between bi-linear models and measured data	543
Figure 8-47 Strain distribution along the grout-filled sleeve (Matsuzaki et al., 1987)	543
Figure 8-48 Determination of equivalent strain for the grouted sleeve	544
Figure 8-49 Stress-strain behavior for the grouted sleeve	544
Figure 8-50 Strain distribution along the reinforcing bar within the grout-filled sleeve (Matsuzaki et al., 1987)	544
Figure 8-51 Calculation of bond-slip behavior of reinforcing bar embedded in the grouted sleeve	545
Figure 8-52 Identification of the unsupported length for the grouted coupler.....	545
Figure 8-53 Calculated stress-slip response for the	546
Figure 8-54 Calculated coupler region response compared to test result	546
Figure 8-55 Analytical model of GCNP	547

Figure 8-56 Determination of an equivalent section for the grouted coupler region.....	548
Figure 8-57 Forces at the column-footing interface for GCNP	548
Figure 8-58 Moment-curvature response from GCNP fiber section shown in Figure 8-55d.....	548
Figure 8-59 Calculated bond-slip behavior at the column-footing interface for GCNP	549
Figure 8-60 Moment-curvature response from GCNP fiber section shown in Figure 8-55a.....	549
8-61 Calculated bond-slip behavior at the top of the grouted coupler for GCNP.....	549
Figure 8-62 Hysteresis curves for GCNP	550
Figure 8-63 Average envelope curves for GCNP	550
Figure 8-64 Energy dissipation for GCNP.....	551
Figure 8-65 Comparison between measured and calculated strains for GCNP	551
Figure 8-66 Hysteretic bond-slip rotation for GCNP up to 4% drift	552
Figure 8-67 Moment-rotation relationships for GCNP	552
Figure 8-68 Cumulative damage as a function of drift for GCNP	553
Figure 8-69 Cumulative damage plotted with drift and load for GCNP	553
Figure 8-70 Pedestal geometry, details and equivalent cross-section.....	554
Figure 8-71 Measured strain within the pedestal for GCNP	554
Figure 8-72 Pedestal sections investigated using moment-curvature analysis.	554
Figure 8-73 Constitutive model for corrugated steel ducts.....	555
Figure 8-74 Moment-curvature response of different pedestal section configurations	555
Figure 8-75 Definition of pedestal element	555
Figure 8-76 Analytical model of HCPP.....	556
Figure 8-77 Moment-curvature response from HCPP fiber section shown in Figure 8-76d	557
Figure 8-78 Moment-rotation relationships for bond-slip at the pedestal-footing interface for HCPP	557
Figure 8-79 Moment-curvature response from section shown in Figure 8-76b.....	557

Figure 8-80 Bond-slip rotation at the pedestal-column interface.....	557
Figure 8-81 Hysteresis curves for HCPP	558
Figure 8-82 Average envelope curves for HCPP	558
Figure 8-83 Energy dissipation for HCPP	559
Figure 8-84 Comparison between measured and calculated strains for HCPP.....	559
Figure 8-85 Moment-rotation relationship for bond-slip at the pedestal-footing interface up to 5% drift.....	560
Figure 8-86 Comparison between measured and calculated moment-rotation relationships for HCPP	560
Figure 8-87 Cumulative damage as a function of drift for HCPP.....	561
Figure 8-88 Cumulative damage plotted with drift and load for HCPP	561
Figure 8-89 Analytical model for GCPP.....	562
Figure 8-90 Moment-curvature response for the GCPP fiber-section shown in Figure 8-89e	563
Figure 8-91 Moment-rotation relationships for bond-slip at the pedestal-footing interface.....	563
Figure 8-92 Moment-curvature response for the GCPP fiber-section shown in Figure 8-89d	564
Figure 8-93 Moment-rotation relationships for bond-slip at the column-pedestal interface	564
Figure 8-94 Hysteresis curves for GCPP	565
Figure 8-95 Average envelope curves for GCPP	565
Figure 8-96 Energy dissipation for GCPP	566
Figure 8-97 Comparison between measured and calculated strains in the pedestal for GCPP....	566
Figure 8-98 Comparison between measured and calculated strains within the precast column for GCPP	567
Figure 8-99 Comparison between measured and calculated moment-rotation relationships for HCPP	567
Figure 8-100 Cumulative damage as a function of drift for GCPP.....	568

Figure 8-101 Cumulative damage plotted with drift and load for GCPP	568
Figure 9-1 Cross-sections for the conventional columns	569
Figure 9-2 Moment-curvature response of the prototype column	569
Figure 9-3 General details of the prototype OpenSEES models	569
Figure 9-4 General Connection details for parameter study of target design ductility of GC columns	570
Figure 9-5 Force-displacement relationships for DD7 models	570
Figure 9-6 Force-displacement relationships for DD6 models	570
Figure 9-7 Force-displacement relationships for DD5 models	571
Figure 9-8 Relationships between rotation and drift from ductility study models	571
Figure 9-9 Force-displacement behavior of AR6 columns	572
Figure 9-10 Relationships between rotation and drift from aspect ratio study models	572
Figure 9-11 Proposed GC column detail to reduce strain concentrations within the footing	573
Figure 9-12 Force-displacement behavior of RR1 columns	573
Figure 9-13 Relationships between rotation and drift from reinforcement ratio study models	574
Figure 9-14 Generalized force-displacement relationships	574
Figure 9-15 Critical sections and generalized curvature distributions	575
Figure 9-16 Flexural contribution to tip displacement	575
Figure 9-17 Flexure components from GN columns	575
Figure 9-18 Bond-slip rotation contribution to tip displacement	576
Figure 9-19 GN-to-C rotation ratios	576
Figure 9-20 Comparison of key calculated results for all models	577
Figure 9-21 Damage index (<i>DI</i>) in extreme reinforcing bar as a function of cycle	577
Figure 9-22 Comparison of peak tensile strain	578
Figure 9-23 Pedestal detail configurations investigated	578

Figure 9-24 Hysteretic behavior of columns in HC pedestal detail study	579
Figure 9-25 Hysteretic behavior of columns in GC pedestal detail study	580
Figure 9-26 Average envelope curves of columns in HC pedestal detail study	580
Figure 9-27 Average envelope curves of columns in GC pedestal detail study	581
Figure 9-28 Flexural contribution to tip displacement of models with pedestal.....	581
Figure 9-29 Contribution of pedestal rotation to tip displacement	581
Figure 9-30 Contribution of bond-slip rotation to tip displacement of models with pedestal	582
Figure 9-31 Maximum stress-strain occurring in grout above the pedestal region in HP models	582
Figure 9-32 Maximum stress-strain occurring in concrete above the pedestal region in HP models	582
Figure 9-33 Maximum steel stress-strain occurring above the pedestal region.....	583
Figure 9-34 Determination of circumferential stress due to concrete fluid head.....	583
Figure 9-35 Plastic hinge formation in conventional and GC columns	583
Figure 9-36 Suggested detailing near the footing surface.....	584

1. Introduction

1.1 Introduction

Challenges in bridge engineering include aging bridge infrastructure, increased focus on sustainable and resilient design and construction practices, and increased demand for more highways and bridges to be delivered in a timely manner. Thus, there is a need for development of newer more innovative bridge design, construction, and management practices to supplement these new demands and challenges.

As of 2012, approximately 11% of the nearly 610,000 bridges in United States have been rated “structurally deficient” according to the metrics used by the Federal Highway Administration (FHWA, 2012). This rating does not necessarily indicate nor imply that these bridge structures are unsafe, but that they require significant and frequent maintenance, and may require posted weight restrictions to reduce service loads. Furthermore, another 14% are rated “functionally obsolete”, which means that they do not meet current traffic and safety requirements. Thus, approximately 25% of all bridges in the United States are rated as deficient. The high percentage of deficient bridges is mostly a reflection of the fact the majority of bridges in the US were built soon after World War II for a design life of 50 years, and these bridge have reached their intended design life. Many of those structures require major rehabilitation or replacement.

Our bridge infrastructure is crucial for the transport of goods, they facilitate commerce, and they are important to daily commute of our traveling public. The bridge inventory in the US continues to age while the number of drivers has been constantly increasing from 1945 to present day at a rate of 2.5 million drivers per year.

The American Society of Civil Engineers (ASCE) indicates that deficient surface infrastructure i.e. bridges, cost users approximately \$10 billion US dollars in 2010 (ASCE, 2011). If substantial action is not taken to upgrade bridges and roads, this user cost is projected to increase to \$58 billion in 2020, and \$651 billion in 2040. Yet, current US funding for highways is only accounting for 50% of the amount required to meet demands. Thus, our transportation infrastructure, which is critical to economic stability and daily life, has reached a critical point where limited funding and increased impact of society require engineers, contractors, state, and federal transportation agencies to develop innovative methods to address these important issues.

Given these new challenges, there has been a substantial effort by federal transportation agencies to reduce the impact that bridge construction has on the general public, environment, and economy. Prime examples of such initiatives are “Every Day Counts (EDC)” and “Highways for Life (HFL)” initiatives, which are programs developed by the Federal Highway Administration to integrate innovation, technology, and rapid project delivery into bridge design and construction practices; This practice has been termed “Accelerated Bridge Construction” or ABC.

As briefly stated above, accelerated bridge construction can provide many advantages to bridge owners, contractor and construction workers, the economy, the environment, and the travelling public. Some of the specific advantages include, but are not limited to:

- 1) Reduced traffic interruption and less risk to the traveling public
- 2) Reduced effect on the environment due to expedited construction and application of more efficient constructions technologies requiring less energy
- 3) Reduced cost of new and replacement bridge construction and

- 4) Maximized work-zone safety for construction crews.
- 5) Higher quality of construction for structural elements and application of more durable, innovative materials due to prefabrication of in plants.

Given the advantages and support from the FHWA, many state DOTs have begun to develop their own ABC programs. Prime examples of such states are Utah, Massachusetts, and Washington State. Although some states have developed full-fledged ABC programs, the majority of states have implemented some form of accelerated bridge construction technology in bridge replacement or new bridge construction.

There is a common element to ABC projects that is independent of which state the projects are being completed and whether or not FHWA is directly involved. That is, to effectively execute ABC projects, designers use prefabricated bridge elements and systems (PBES) that can be manufactured in parallel with on-site construction and can be quickly assembled to form a functional structural system. Both FHWA programs mentioned above promote the use of PBES to minimize the impact of construction and expedite project completion. Furthermore, many states have or are currently developing standardized PBES details such that bridge designers are equipped with readily-available tools for ABC projects.

The use of prefabricated elements in bridge design and engineering is not a new practice. For example, precast girders have been used in many bridges for over 50 years. However, ABC projects typically require other components of the bridge structure to be prefabricated, which can create some new design challenges.

Despite the numerous advantages, ABC has not been extensively used in areas subject to moderate and high seismic hazards for good reason. There is a great deal of

uncertainty about the seismic performance of the connections used to join precast elements. Of specific concern are substructure connections (column-footing, column-shaft, and column-bent-cap) because they must dissipate energy through significant cyclic nonlinear deformations under seismic loading while maintaining their capacity and the integrity of the structural system.

1.2 Past Research on Precast Substructure Connections for ABC in Seismic Zones

To date, there have only been limited studies that investigated precast substructure connections for resisting seismic loading. Marsh et al. (2011) provides an excellent summary of the available literature and groups connections that have been tested or implemented into categories based on configuration. Figure 1-1 provides a schematic that identifies the five ABS connection types discussed in this section, which were adapted from Marsh et al. (2011). The following sections discuss each connection type individually and provide a review of relevant literature. It should be noted that many of the laboratory study conducted focused on ABC connections have focused on the connection between precast (or cast-in-place) columns and precast bent-caps. However, there have been a few studies on column-footing connections.

1.2.1 Socket (SO) Connections

The first connection, which is shown in Figure 1-1a, is defined as a socket (SO) connection. SO connections can be used for precast-to-precast (PC-to-PC) or precast-to-cast-in-place (PC-to-CIP) construction. In either case, an entire member can be inserted into an adjacent member and the remaining space can be filled with grout or concrete. In some cases, the walls of the inserted member and/or the socket are roughened because

vertical loads must be transferred via bond. It is critical in this connection that sufficient embedment length is provided to develop full capacity of the connected members.

Furthermore, bending is transmitted through prying action thus if the embedded length too short failure could occur from concrete break out. One of the benefits of this connection type is that blocks can be designs to provide significant construction tolerances, which aid rapid construction.

Socket connections have been investigated for use in column-footing and column-bent-cap connections. Ziehl et al. (2011) investigated using SO connections to join precast bent-caps with driven precast piles. Two full-scale subassemblies were tested under slow cyclic loading in a single cantilever configuration using a displacement-based loading protocol. Both full-scale models used 18 in by 18 in [457 mm by 457 mm] concrete piles that were prestressed with strands in a circular configuration. Two different bent-cap block configurations were used: one to represent an interior connection; and the second to represent an exterior connection. Each bent-cap block incorporated a 36-in [914-mm] diameter corrugated steel tube, which functioned as the socket. Piles were embedded 26 in [660 mm] into the bent-cap blocks, which corresponded to 1.44 pile diameters. The sockets were filled with a flowable 4000 psi [27.5 MPa] concrete mix. During testing, the interior joint model was subjected to a constant compressive axial load, while the exterior joint model was subjected to variable axial tension and compression.

Tests indicated good performance of both interior and exterior joint models. Both connections sustained numerous cycles of large, inelastic deformations with only minor cracking within the capacity-protected bent-cap blocks. Furthermore, both models

formed plastic hinge mechanisms within the pile itself. It was concluded that these connections were suitable for precast bent-cap-to-pile joints in regions of moderate seismicity. One disadvantage was noted, which was that bent-caps with SO connections were required to be larger than corresponding CIP bent-caps due to requirement tolerance of the SO connection.

Similar connections have been used at the column-footing and have been investigated by Marsh et al. (2010) and Motaref et al. (2011). The tests conducted by Marsh et al. (2010) focused on variation of the socket connection shown in Fig. 1a, which employed a precast concrete column and a cast-in-place footing. Two 42%-scale column-to-footing subassemblies were tested under slow cyclic loading at the University of Washington (UW). The models employed different reinforcement details at the base of the embedded column shaft; one employing hooked reinforcing bars (Specimen A), and the other employing headed bars (Specimen B). The embedded stubs of both precast columns were roughened prior to casting the footing, and where both embedded 1.2 column diameters into the cast footing.

Both specimens exhibited good energy dissipation, stable hysteresis loops up to approximately 7% drift, and force-displacement behavior that was similar to a conventional CIP column that was previously tested. There was minimal damage at the interface of the column and the footing. Following flexural testing, monotonically increasing axial load was applied to Specimen A to evaluate the efficacy of the PC-CIP socket connection. The connection was able to resist an axial load that corresponded to 3.5 times the factored dead and live load for the column, prior to punching failure at the base.

Motaref et al. (2011) tested a 0.3-scale precast two-column bridge bent on a shake-table. Each precast column employed a different novel material, fiber-reinforced polymer (FRP) composites in one and engineered-cementitious composite (ECC) in the other. Both used socket connections to the footing with an embedment length of 1.5 column diameters. The embedded portion of each column was not roughened prior to installation. Results indicated that both columns failed above the footing surface by formation of plastic hinges and achieved an average displacement ductility capacity of 6.7. Thus, the SO connection was effective and the columns with novel materials were found to perform well.

1.2.2 Grouted Pocket (GP) Connections

The second connection type is the grouted pocket (GP), which is shown in Figure 1-1b. GP connections use an opening formed in either a bent-cap or footing, similar to the SO connection, in which longitudinal reinforcing bars from a precast column can be inserted. The difference between the GP and SO connections is that bare column reinforcing bars are inserted into the adjacent members in GP compared to a fully cast member in the case of SO. The pocket is filled with cementitious grout or concrete after placement of the adjoining member. Similar to a CIP system, force is transferred between the column and bent-cap/footing by bond of the reinforcing bars. Thus, sufficient development of bar is required. GP connections can be designed to provide large construction tolerances. In most cases, these connections are typically employed between precast bent caps and adjoining columns. This is because the pocket is easily filled from the top and the cementitious filler materials can be consolidated properly.

Restrepo et al. (2011) tested two 42%-scale interior bent-cap subassemblies that employed GP connections. The columns were designed according to AASHTO Guide Specifications for LRFD Seismic Design such that plastic hinging would occur adjacent to the cap connection. The main difference between the two models was the reinforcement details within the joint and bent-cap stubs. One bent, denoted “CPFD”, incorporated more reinforcement within the joint and bent-cap than the second model, which was denoted “CPLD”. The models were tested under cyclic loading at increasing displacement ductility levels.

Both test models exhibited stable hysteresis loops and force-displacement envelopes that were similar to the conventional model. CPFD, which was more heavily reinforced in the joint and cap beams, developed a full plastic hinge within the column near the joint. Furthermore, the damage in the bent-cap was limited to a few vertical and inclined cracks that occurred near the end of the tests at a displacement ductility of 8.0. CPLD, which was lightly reinforced in the joint, did not exhibit plastic hinging until higher drift levels due to significant damage and deformation in the joint. By the time the model reached a displacement ductility of 8.0, large inclined shear cracks had developed in the joint and bond-slip deformations were larger than CPFD. It was concluded that both models behaved similar to respective conventional model details. It was suggested that additional analysis be completed to develop a model that would describe the behavior of the GP connection joint region.

1.2.3 Grouted Duct (GD) Connections

The grouted duct (GD) connection is shown in Figure 1-1c. This is similar to the SO and GP connections in that bars from adjacent members are not joined. Rather, bars are inserted into the adjacent member through a series of ducts. The ducts are typically made from galvanized steel and are corrugated to improve bond between the reinforcing bars and the adjacent member. Unlike the GP connection, in a GD connection, bars are individually anchored within a single duct. The ducts are filled with flowable cementitious grout. Similar to GP connections, force transfer is achieved through bond. Thus, sufficient duct-length must be provided to ensure full development of the bar. These connections have been used for both column-to-bent-cap and column-to-footing connections.

Grouted duct connections have been employed in bridge projects for non-seismic and seismic regions. Examples of the application of GD connections for non-seismic and seismic regions are the Lake Belton Bridge on SR 36 in Texas (Brenes et al., 2006) and the SR 520/SR 202 bridge in Washington State (Marsh et al., 2011), respectively. In both examples, the grouted ducts were used to connect precast bent-caps to columns. Grouted ducted column-to-bent-cap connections for seismic regions have been evaluated extensively by the Washington State Department of Transportation (WashDOT) in collaboration with researchers at the University of Washington (Raynor et al., 2002; Pang et al., 2008; Steuck et al., 2009). Initial studies by Raynor et al. (2002) and Steuck et al. (2009) focused on determining the behavior of reinforcing bar grouted within corrugated steel ducts. In both studies, it was determined the bars could be anchored in grouted ducts with relatively short bonded lengths (between 6 and 10 bar diameters, d_b).

Pang et al. (2008) built on previous work at UW, and conducted three 0.4-scale cantilever column tests where precast columns were connected to precast bent-caps segments using GD connections. The precast models were compared with a conventional column that had approximately the same geometric and reinforcement details. Two of the three precast models employed longitudinal bars that were debonded over $8d_b$ at the column-cap interface. Static lateral loading was applied according to recommendations from the NEHRP (Building Seismic Safety Council, 2003).

The precast model exhibited global response parameters, i.e. force-displacement relationship and energy dissipation that were similar to the conventional column model. Furthermore, all four models exhibited wide, stable hysteresis loops and failed by bar buckling followed by fracture. Although plastic hinging formed outside the bent-cap, the precast model exhibited concentrated deformations at the column-cap interface compared to the more distributed deformations observed within the conventional model. This action was predominately caused by the intentional debonding of longitudinal bar within the bent-cap. In general, it was concluded the connections were sufficient for use in precast column-to-bent-cap connections.

A similar connection configuration was investigated Restrepo et al. (2011). It was also found that the GD connection behavior similar to the corresponding conventional model.

Tazarv and Saiidi (2013) tested a single half-scale reinforcement concrete precast bridge column that employed a grouted duct connection to a CIP footing, denoted PNC. The half scale model had a 24-in [610-mm] diameter circular cross-section and an aspect ratio of 4.5. The column was reinforced with 11 No. 8 [D25] ASTM A706 Grade 60 bars

in the longitudinal direction, and a No. 3 [D9.5] spiral with a 2-in [51-mm] pitch in the transverse direction; these reinforcement quantities results in longitudinal and transverse volumetric reinforcement ratios of 1.92% and 0.98%, respectively. Longitudinal reinforcing bar dowels protruded from the base of the columns and were embedded 28 in [711 mm] into a 3-in [76-mm] diameter corrugated steel ducts, which were filled with ultra-high performance concrete (UHPC). The longitudinal bars were debonded 4 in [102 mm] above and below the column-footing interface to improve the ductility of the column. The column was tested under reversed slow cyclic loading, and was compared to a conventional CIP column with the same details.

PNC behaved approximately the same as the conventional model. The models had similar hysteretic and force-displacement relationship envelopes. Furthermore, the displacement ductility capacity of PNC and CIP had ductilities of 6.30 and 7.36, respectively, and were comparable. Both models also exhibited similar apparent damage per drift level. However, damage accumulated more rapidly in PNC due to lower concrete compressive strength. Nevertheless, the behavior of the models was comparable and there was no apparent damage to the GD connection, which indicated satisfactory performance of UHPC-filled ducts.

1.2.4 Hybrid (HY) Connections

Hybrid (HY) connections are those that employ unbonded or bonded prestressing tendons to join a precast column element with the adjacent substructure elements (Figure 1-1d). In HY connections, the precast column can be a single unit or segmented in multiple units that may or may not incorporate mild steel reinforcement to connect the

segments. The purpose of prestressing tendons is to provide a self-centering mechanism and the mild steel reinforcement is typically placed in plastic hinge zone to provide energy dissipation. Tendons are typically anchored in the adjacent member and are designed to remain elastic to maximum re-center capabilities. Some of the disadvantage of this connection type include difficulty in accessing anchorages placed in footing, reliance on discrete tendon anchorages, relatively small energy dissipation, and potential for corrosion of unbonded tendons.

There have been a number of analytical and experimental studies to investigate the behavior of HY connections (Billington and Yoon, 2004; Palermo et al., 2005; Hewes, 2007; Ou et al., 2010a; Ou et al., 2010b; Motaref et al., 2011). However, this type of connection fundamentally differs from the others discussed in this section due to the presence of initial prestressing force. Thus, the design procedures for HY connections differ significantly from those used for conventional columns compared to the other ABC connections discussed in this section.

1.2.5 Mechanically-Spliced (MS) Connections

Mechanically-spliced (MS) connections entail using mechanical reinforcing bar splices to directly create continuity between longitudinal bars in a precast column element and the adjacent substructure elements (Figure 1-1e). MS connections can provide a unique feature that other connections discussed cannot: reinforcing details within the column and adjacent members can be approximately the same as conventional cast-in-place systems. Thus, minimal deviation from the design procedure may be

required. However, depending on the connection details and splice type, tolerances can be rather tight compared to other connection types.

In the United States, mechanical reinforcing bar splices have been used in low and moderate seismic zones for bridge substructure connections (Edison Bridge in Fort Meyers, Florida and the Riverdale Rd. Bridge over I-84 outside Salt Lake City, Utah) but not in high seismic zones. Because the focus of the present study was on MS a comprehensive review of this type of connection was conducted and a separate chapter was dedicated to that review. Chapter 2 provides a thorough discussion of mechanical splices, their applications in building and bridge structures, and the relevant literature.

1.3 Objectives and Scope

The main objective of this study was to develop, test, analyze, and evaluate precast column-footing connections for ABC in moderate and high seismic zones. Unlike the majority of connections tested by previous researchers, which would require some analysis or design considerations that would deviate from conventional systems, the goal of this study was to develop connections that closely resembled conventional cast-in-place systems with respect to design and performance. That is, the connections were to be emulative of conventional cast-in-place construction such that designer would not require specialized design methods or analysis. To achieve emulative detailing, mechanical reinforcing bar splices were used to connect precast columns to cast-in-place footings. Furthermore, to reduce transportation and erection costs, the precast column elements were initially hollow but served as stay-in-place forms that were filled with concrete once installation was complete.

This project was made-up of three major components: half-scale column model experimental testing, individual coupler component testing, and extensive analytical modeling and parametric studies. Five half-scale reinforced concrete bridge column models with circular sections were designed, constructed, and tested until failure. One column was a conventional cast-in-place (CIP) benchmark model, which was designed using a displacement-based approach, and was used to evaluate the performance of four precast columns each with a different column-footing connection detail. Precast models used one of two different mechanical reinforcing bar splices and were connected to the CIP footing at one of two locations. The models were constructed as they would be in the field to assess rapid constructability of each connection type. The objective of the column model study was to characterize the behavior of columns utilizing mechanical splices in column plastic hinge zones.

The component studies were conducted on individual mechanical splices and consisted of numerous uniaxial tests. The objective was to characterize the component behavior of each splice type under different loading configurations. Results from this portion of the project also aided the development of analytical models for the half-scale column models. The testing program developed included monotonic static and dynamic tension tests, single- and multi-cycle elastic slip tests, and slow cyclic loading tests.

The analytical studies included development of individual element models for the two mechanical reinforcing bars splices used in the experimental studies. These elements were incorporated in the analytical models of the five half-scale column models using OpenSEES, and the results were compared with experimental results from the cyclic column model experiments to validate the modeling procedures and assumptions.

Prototype-scale analytical models were also developed to conduct parametric studies investigating the sensitivity of the newly developed ABC connections to changes in design details. Subsequent to parametric studies, a set of recommendations were developed for design and detailing of the ABC connections.

1.4 Document Outline

The following section briefly describes the contents of each chapter contained in this document:

Chapter 2 – Mechanical Reinforcing Bar Splices: This chapter describes the selection criteria used to develop a short list of coupler devices for the new connections; the available literature and code requirements for mechanical splices, the mechanical performance of individual splice assemblages, and performance of structural members that utilize splices in plastic hinge zones; and the experimental program developed to characterize the component behavior of the two selected splices.

Chapter 3 – Large-Scale Experimental Program: This chapter describes the materials used for column design and construction; the relevant standards associated with the materials; the design procedure for the benchmark column; the details of precast columns; the construction procedures followed for each model; and the testing protocols and instrumentation.

Chapter 4 – Experimental Results for Individual Column Models: This chapter presents descriptions of the measured material properties for each column; a discussion of data processing methods; and a detailed discussion of the experimental results for each of the half-scale column models.

Chapter 5 – Comparison of Test Model Performance: This chapter presents a comparison between the conventional benchmark column and the precast columns. Different response parameters are reviewed and compared. The chapter is concluded with a general discussion of the key factors affecting each model.

Chapter 6 – Damage States and Response Parameters: This chapter presents the apparent damages states and response parameters from the column models tested in this study. The results are compared with the data set compiled by Vosooghi and Saiidi (2010) and similarities and differences with conventional construction are highlighted.

Chapter 7 – Results from Individual Coupler Tests: This chapter presents the experimental results from the individual coupler testing program discussed in Chapter 2. Results are discussed for each test completed for individual coupler types. Experimental data is then compared for the two coupler types and the effect of static versus dynamic loading is presented.

Chapter 8 – Analytical Modeling of Column Models: The chapter presents the development and validation of two sets of element analytical models idealizing the behavior of couplers for incorporation in OpenSEES. The first set of models were developed for reinforcing bars spliced with mechanical splices, which were validated using the experimental results discussed in Chapter 7. The second set, which employed the techniques developed for an each splice type, consisted of nonlinear frame-element models for the half-scale columns. Column analytical model results were compared with the experimental results from Chapter 4 to evaluate the elements and the analytical modeling techniques for of the test models.

Chapter 9 – Parametric Studies and Design Recommendations: This chapter discusses the development of prototype-scale analytical models that were used to conduct parametric studies on mechanically-splice connection details. The effects of critical design parameters such as target design displacement ductility, aspect ratio, and longitudinal reinforcement ratio were studied along with an investigation focused on splice location in the plastic hinge zones. A set of design details are also discussed.

Chapter 10 – Summary and Conclusions: This chapter provides key observations from the coupler component and column model experimental studies, which were presented in Chapters 4, 5, 6, and 7, along with those from analytical studies presented in Chapters 8 and 9. This chapter also provides a set of conclusions that address the broader findings of the results from this study.

2. Mechanical Reinforcing Bar Splices

2.1 Introduction

As discussed in Chapter 1, the focus of the study was on cast-in-place footing to precast column connections made using mechanical reinforcing bar splices. This Chapter provides a review of relevant literature and discusses the two mechanical splices used in this study. The objectives and organization of the chapter is as follows:

- 1) Describe the selection criteria that were employed to develop a short list of possible coupler devices.
- 2) Review available literature related to code requirements for mechanical reinforcing bar splices, the mechanical performance of individual splice assemblages, and performance of structural members that utilize splices in plastic hinge zones.
- 3) Based on review of literature, identify the two mechanical splices that were used in the column models.
- 4) Describe the experimental program developed to characterize the component behavior of the two selected splices. The results from component studies are presented in Chapter 7.

2.2 Discussion of Selection Criteria

There is a wide variety of commercially available mechanical reinforcing bar splices. ACI Committee 439 published a document that provides a detailed description of splices available in the United States (ACI-439, 2007). Prior to discussing the selection criteria used in this study, the commonly used terms and definitions related to mechanical splices

are presented. Figure 2-1 provides a schematic identifying relevant terms and how they are associated to the mechanical splice. It should be noted that some definitions provided vary slightly from those described by ACI Committee 439.

- Coupler - A mechanical device that joins two separate reinforcing bars for the purpose of transferring axial compression and/or tension.
Note ACI439 defines a “coupler” as a threaded device and this document identifies a coupler in a more general manner.
- Splice - The complete assembly of a coupler and any additional intervening material or other components required to accomplish the splicing of reinforcing bars.
- Coupler Region - The region including the coupler that extends 2 reinforcing bar diameters beyond the ends of the coupler device.
- Position Coupler - Threaded coupler devices must be rotated to engage and tighten. In some cases, the reinforcing bar cannot be rotated i.e. if it is tied to an adjacent bar. A position coupler has a built-in mechanism that allows rotation of the device, without rotation of the bar for engaging the threads
- Position Lock Nut - An additional nut(s) that can be used to lock a threaded coupler device into a tightened state.

There were four considerations that made up the criteria used to identify the initial set of coupler devices for further investigation; they are as follows:

- 1) Caltrans Prequalification – Caltrans has a prequalified list of available couplers. These devices are mechanically tested and accepted for use in Caltrans projects

without additional consent as long as placement of the splice adheres to Caltrans bridge design code provisions. There are two main splice categories: 1) “Service Splice”; and 2) “Ultimate Splice”. The difference between these two designations is discussed in the following sections.

- 2) Ease of Installation – The devices selected are to be used in accelerated construction. Thus, it is critical that they are easy to install and provide appropriate tolerances such that construction will not be slowed if reinforcing bars are misaligned slightly.
- 3) Minimal Loss of Ductility – It is critical that the spliced bars be able to undergo significant axial deformation prior to failure.
- 4) Consistent/Desirable Failure Modes – Many coupler manufactures report that a device results in ductile failure of the reinforcing bar, which is not always the case. It is important that the coupler behavior is consistent with respect to the reported failure mode.

A preliminary list of five coupler devices was compiled for further investigation based on points 1 and 2. The first device is referred to as a “Shear Screw” coupler, denoted “SSC”, and is shown in Figure 2-2. This device connects reinforcing bars through a series of steel screws that are housed in steel sleeve; this fully assembly is the coupler. The bars are inserted into either end of the device until they reach a “bar-stop” at the mid-height of the steel sleeve. The screws are then tightened to a specified torque. Once the target torque is reached the screw heads shear-off and the screws are firmly embedded with the reinforcing bars and the connection is complete.

The second coupler selected was a grout-filled ductile iron sleeve, denoted “GC”, and is shown in Figure 2-3. This device is commonly used in conventional and precast building construction. At a precasting plant, reinforcing bars are inserted into the tapered end of the sleeve and the device is then cast within the concrete member. On site, the precast element is positioned such that reinforcing bar dowels protruding from the adjacent member enter the open ports of the sleeves. The connection is completed by pumping a proprietary high-strength (with compressive strength exceeding 14 ksi [96 MPa]) cementitious grout into the sleeve. Force is transmitted through formation of compression struts in the grout which transfer force in the sleeve.

The third coupler, denoted “HC”, is referred to as an upset headed coupler and is shown in Figure 2-4. The coupler consists of male and female threaded steel collars used to join bar segments having deformed heads. The heads can be created off-site at the manufacturer’s facility or on-site with manufacturer-provided equipment. To make the heads, the bar-end is heated to a specified temperature and then compressed using a specially designed hydraulic ram. The threaded steel collars are positioned over the deformed heads and torqued according to manufacturer specification, which depends on the bar size. This splice transfers compression directly through the deformed heads and tension through the threaded collars.

The fourth coupler device is referred to as a “straight-thread” coupler, denoted “STC”, and is shown in Figure 2-5. This splice requires the bar-ends to be threaded prior to installing the coupler. Threads can be installed one of two ways: 1) threads machined directly on the bar-end reducing the cross-sectional area of the bar, or 2) diameter of the bar-end is first enlarged using a hydraulic ram (Figure 2-5b) followed by installation of

the threads. The second installation method ensures that the nominal area of the threaded section is larger than the nominal area of the bar itself to prevent premature rupture at the threads. To create the connection, a female threaded collar is installed over the threaded bar-ends. A position lock nut(s) can be used if the reinforcing bar cannot be rotated.

The final device that was considered is referred to as a “tapered thread” coupler, denoted “TTC”, and is shown in Figure 2-6. Installation of the threads results in the bar having a reduced cross-section. There are a few different variations of this device. Most commonly, the connection is made with a single threaded male bar-end and a female socket that is installed on the second reinforcing bar. In many cases, male and female connections are friction welded to each bar-end. Friction welding is a process that involves spinning one component at a high rate and contacting the second component to create high enough heat to result in joining of the two components. Furthermore, the devices can be manufactured as a position coupler so the reinforcing bars do not need to be rotated to install the device.

2.3 Review of Literature

2.3.1 Code Requirements

Most building and bridge seismic design codes have provisions that place minimum performance requirements on mechanical reinforcing bar splices. Usually in the form of predetermined stress or strain ranges that must be achieved prior to failure, these performance standards are used to specify the type of splice and location where the device can be used depending on the expected demand. Table 2-1 outlines the code requirements for mechanically spliced bars that are covered in this section. Furthermore,

Table 2-2 identifies the performance designation for the aforementioned five splices prescribed by each code.

2.3.1.1 ACI

The American Concrete Institute places mechanical reinforcing bar splices into two performance categories for seismic detailing. A “Type 1” splice must be able to develop 1.25 times the specified yield strength (f_y) of the spliced reinforcing bar prior to failure. Type 1 couplers are only permitted to be placed a distance equal to twice the member depth from sections where large inelastic deformations will occur. A “Type 2” splice must meet the Type 1 criteria and also be able to develop the specified ultimate tensile strength of the spliced reinforcing bars. Unlike the Type 1 designation, a Type 2 device may be placed in any given section of a structural member regardless of the deformation demand unless stated otherwise in other provisions. Note that there is no explicit strain capacity criterion placed on either type.

2.3.1.2 AASHTO

The American Association of State Highway and Transportation Officials (AASHTO) define a single designation for mechanical splices; “Full-Mechanical Connection (FMC)”. In order to be classified as an FMC a mechanically spliced bar must be able to achieve 1.25 times the specified yield stress of the coupled bars and the coupling device must meet a slip requirement as defined in Table 2-1. Slip within the coupler is measured by loading the spliced bar to 30 ksi (207 MPa) and then unloading to 3 ksi (20.7 MPa). Displacement is measured over the coupler region for each loading. The difference between these two measurements is the slip. The AASHTO provisions for

seismic design prohibit the placement of splices in regions expected to undergo large inelastic deformation.

2.3.1.3 Caltrans

Caltrans places splices in two categories: “Ultimate Splice” and “Service Splice”. Capacity and demand as well as the maximum slip are specified and location of splice is restricted, resulting in the strictest provision. Splices used in elements that undergo significant nonlinear deformations and dissipate energy during an earthquake must be categorized as an “Ultimate Splice” even though the coupler is not allowed in the plastic hinge zone. The use of a “Service Splice” in such elements is prohibited altogether. Similar to AASHTO, Caltrans also requires splices to have a minimum slip resistance.

2.3.2 Research on Individual Coupler Performance

The following section provides a review of relevant literature on the performance of reinforcing bar splices tested under uniaxial loading. Each study is separated into a subsection and concluding remarks about each splice are made in the final subsection. Table 2-3 provides a summary of the studies surveyed.

2.3.2.1 Army Corp [2009]

This report discusses monotonic tensile testing of five different mechanical couplers for steel reinforcing bars under different loading rates. Of the five systems tested, four are considered in this literature review: GC, HC, TTC, and SSC devices. Specimens were constructed using No. 10 Gr. 60 ASTM A615 reinforcing bars and were subjected to three different strain-rates: “slow” = 1,000-6,000 $\mu\epsilon/\text{sec}$; “intermediate” = 10,000-

70,000 $\mu\epsilon/\text{sec}$; and “rapid” = 3 – 3.8 million $\mu\epsilon/\text{sec}$. Three samples were tested per loading rate per coupler type along with three control reinforcing bar for each rate.

Under slow loading, the average ultimate strength of all the splice systems other than the SSC splice were comparable to the control bars. The average ultimate load of the SSC splices was 28% lower than that of the control bars. Similarly, at the intermediate loading rate, the average ultimate strength of all the splice systems other than the SSC device were comparable to the control bars. All splices did, however, exhibit reduced ductility at failure compared to the control bar. At the rapid loading rate, the average ultimate load of the HC and GC splices were within $\pm 10\%$ of the control bars, while the SSC and TTC splices exhibited reduced ultimate tensile strength by 68% and 23% compared to control bars, respectively. The ductility of all four splices was reduced significantly under rapid loading.

There were a number of different failure modes exhibited by test specimens. All HC specimens failed due to rupture of the reinforcing bar under the slow loading rate. Under the intermediate and rapid loading rates, bar rupture was also observed but tended to be closer to or at the base of the deformed head likely due to stress concentration. The GC splices failed by bar rupture, rupture at the mid-height of the sleeve, or bar pullout. There was not a distinct correlation between the failure modes of the GC splice and the rate of loading. However, a fourth failure mode was observed during the rapid loading rate where the sleeve violently broke apart. The SSC specimens tended to fail due to rupture of the reinforcing bar at the first or second screw due to stress concentration. A single sample failed by pullout of the reinforcing bar from the steel sleeve containing the shear screws under the rapid loading rate. All of the TTC specimens failed due to bar rupture

away from the splice under the slow loading rate. As the rate increased, samples began to fail prematurely by fracture of the bar at the beginning of the tapered threads. This was the failure mode observed by all three TTC samples under the rapid loading rate.

2.3.2.2. FDOT [2007]

The focus of this study was to investigate the effect of improper grouting on the mechanical performance of GC splices. Six specimens were constructed using Gr. 60, No. 9 reinforcing bars. Of the six specimens, three were grouted using a rodding technique for consolidation to represent the proper grouting scenario and two were constructed without rodding to represent a “poor grouting” scenario. The sixth sample was subjected to further agitation of the installed rebar after grouting. Specimens were subjected to monotonic static tensile loading 12 days after grouting. Results showed that 5 out of the 6 specimens failed by fracture of the sleeve with little variance in load at failure. However, there was a decrease in strain at rupture for specimens that failed within the sleeve region. It was concluded that the mechanical performance GC splice is not sensitive to the grouting technique.

2.3.2.3 MDOT [2008]

This report presents the experimental evaluation of two grout-filled splices. The first utilized a ductile cast iron sleeve where the connectivity of both spliced bars was made using grout. The second also utilized a ductile iron sleeve but the connection of the spliced bar was grouted at one end and used a tapered threaded connection at the other. The experimental program included evaluating the splices for slip resistance, creep, fatigue and ultimate loading.

Specimens were constructed with epoxy-coated, Gr. 60, No. 6 and 11 bars. Three samples per splice and bar size were tested resulting in 12 samples per splice. The samples were first tested for slip resistance according to ASTM A1034 followed by fatigue testing. Each sample was subjected to one million cycles of tension at a rate of 9 Hz from 6 to 24 ksi [41.3 to 165 MPa]. If samples endured the full one million cycles, a second slip test was conducted followed by monotonic tensile loading to failure at a rate of 10 ksi/min 68.9 [MPa/min].

Both splices passed the slip test according to the AASHTO LRFD criteria with the slip for No. 6 and 11 bars being less than 0.01 in [0.254 mm]. Both splices also endured the one million cycles of fatigue loading from 6 to 24 ksi [41.3 to 165 MPa] and passed the post fatigue slip test. The average ultimate load for the splice that was grouted on one side was $1.69f_y$ and $1.48f_y$ for No. 6 and 11 bar, respectively. Samples that were spliced with the coupler grouted at both sides had an average ultimate load of $1.66f_y$ and $1.75f_y$ for No. 6 and 11 bar, respectively. Although, both splices performed consistently in the slip and fatigue tests, the failure modes resulting from monotonic tension testing were not consistent. The splice that was grouted on a single side exhibited two different failure modes both occurring at the tapered thread connection: 1) rupture of the reinforcing bar at the section where the taper began; and 2) shear failure of the threads on the reinforcing bar. The splice that was grouted on both sides exhibited three different failure modes: 1) pullout of the reinforcing bar from the grouted sleeve, 2) fracture of the reinforcing bar away from the coupler, and 3) fracture at the mid-height of the ductile iron sleeve.

2.3.2.4 NCHRP 10-35 [1991]

This report discusses results from a series of finite- and long-life fatigue tests on conventional spliced and unspliced bars. Seven different mechanical splices were investigated. Of the seven, three are relevant to this literature review: the GC, TTC, and STC systems. Specimens were constructed from Gr. 60, No. 8 reinforcing bars that met the requirements of ASTM A615. The measured yield stress, ultimate stress, and elongation at failure for control bars was 69.1 ksi [476 MPa], 111.7 ksi [769 MPa], and 15%, respectively.

Finite-life fatigue tests, which were only conducted on TTC splices, subjected samples to stress ranges of 40.0 and 47.5 ksi [275 and 327 MPa] at 5 to 15 Hz until failure. Long-life fatigue tests were conducted on GC, TTC, and STC splices using a staircase test sequence. In a staircase test sequence, the stress range applied to a given sample depends on performance of the preceding sample. That is, if a sample endures the selected cycle-count target, the stress range for the following sample is increased. The converse is also applied. The stress range was incremented by 1.0 ksi [6.89 MPa] in successive tests. A minimum stress of 3 ksi [20.6 MPa] was used for all tests.

Results indicate that the fatigue limit of the spliced bars was consistently lower than that of the unspliced bar. The GC specimens exceeded the fatigue performance of all other mechanical splices followed by the TTC and STC splices, respectively. The mean using the long-life fatigue tests for the GC, TTC, and STC splices was 24 ksi [165 MPa], 20 ksi [137 MPa], and 13 ksi [89 MPa], respectively. The observed failure modes for GC samples were bar rupture and fracture at the mid-height of the grout-filled sleeve. The

TTC and STC splices failed by fracture of the reinforcing bar at the threaded sections. In some cases, STC specimens failed by fracture of the coupler itself.

2.3.2.5 Nouredine [1994]

Nouredine investigated plastic strain capacity of mechanically spliced bars. The goal of the study was to develop strain-based performance criteria to compliment Caltrans existing strength-based criteria. A number of different mechanical splices were studied including the GC and TTC splices. Test specimens were construction from both ASTM A615 and A706 Gr.60 No. 18 bars. Two specimens per bar type were tested under monotonic tensile loading until failure. The GC specimens achieved better overall performance compared to TTC specimens. The average ultimate load recorded for the GC and TTC specimens was $1.68f_y$ and $1.46f_y$, respectively, where f_y is the specified yield strength of the spliced bars. The GC splice was defined as a “Class I” splice, which indicates that the spliced bars can achieve strains in excess of 7% and 10% for ASTM A615 and A705, respectively. The TTC splice was defined as “Class III”, which indicates that a strength requirement of 80 ksi [551 MPa] can be met but the splice has poor ductility. TTC samples achieved less than 4% elongation in the spliced bars prior to failure. The observed failure modes of GC specimens were reinforcing bar rupture away from the coupler region and rupture at the mid-height of the grout filled sleeve. The TTC specimens all failed by stripping of the threads.

2.3.2.6 WJE Associates [2000]

A study conducted by Wiss, Janney, Elstner Associates, Inc (WJE) investigated the compressive, tensile, and cyclic behavior of GC splices. The objective of the study was

to determine if GC splices conformed to the performance and acceptance criteria defined by AC133 (2010), which is a testing and acceptance criteria defined by the International Code Council Evaluation Service (ICC-ES). Test specimens were constructed with No. 5 through No. 11 bars, and No. 14 Gr. 60 ASTM A615 bars. Specimens were also constructed using No. 18 bar and transition splices, which are not covered in this review. The influence of bar deformation patterns was also investigated by using different patterns for each bar size. All splices were tested in accordance with specification defined by AC133 [2010]. The grout in each specimen was allowed to cure for at least 28 days prior to testing.

Results indicated that all specimens exceeded the AC133 “Type 2” requirements in monotonic tension to failure, which is to exceed the lesser of $0.9f_u$ or $1.6f_y$ of the unspliced bar. All specimens also passed the compression requirement, exceeding $1.25f_y$ monotonic compression. Lastly, all specimens endured the full cyclic loading protocol defined by AC133, which is listed in Table 2-4. There were three distinct failure modes observed during monotonic tensile tests: 1) pullout of the reinforcing bar from the grouted sleeve; 2) fracture of the reinforcing bar away from the coupler; and 3) fracture at the mid-height of the ductile iron sleeve. These failure modes were also observed in the MDOT tests.

2.3.2.7 Summary

Based on a review of six previous studies on individual couplers, the following observations can be made regarding each of the five splice systems reviewed:

Shear Screw Coupler (SSC) - This device was only studied by the Army Corp. of Engineers

under different loading rates. The failure modes associated with this splice, other than bar rupture outside the coupler region, are shown in Figure 2-7. It was evident that as loading rate increased the splice had a tendency to fail prematurely due to bar fracture caused by stress concentrations at the shear screws. This resulted in lower ultimate stress and strain compared to the control bars. Bar pullout from the steel sleeve which contained the shear screws was also observed under blast-like strain rates.

Grouted
Coupler (GC)

- The GC splice was investigated in all six of the studies reviewed. These splices exhibited good resistance against slip, cyclic, and fatigue loading along with good performance under static and dynamic loading. The failure modes that were observed other than bar rupture outside the coupler region are shown in Figure 2-8. These modes were pullout of the bar from the grouted sleeve and fracture of the ductile iron sleeve. Nevertheless, in most cases, the GC splices could develop the full tensile capacity of the spliced bars

Upset Headed
Coupler (HC)

- This splice was only investigated in the Army Corp. study but exhibited good performance under static and dynamic loading rates. The HC splice showed little reduction in ultimate stress and

minimum reduction in ductility under the different loading rates.

The only failure mode observed other than bar rupture away from the coupler region was fracture of the bar at the base of the deformed heads, which is shown in Figure 2-9.

- Straight Thread Coupler (STC) - This splice was only investigated in the NCHRP study. The splice did not perform well under fatigue loading. In most cases, the splice failed prematurely due to fatigue fracture at the threads or fracture of the coupler. This resulted in a fatigue limit stress range of 13 ksi [89 MPa], which was the lowest among the GC, TTC, and STC splices.
- Taper Thread Coupler (TTC) - The TTC splice was tested in four of the studies reviewed. In most cases the splice failed prematurely due to fracture of the reinforcing bar at the threaded section or by stripping of the threads from the reinforcing bar. These failure modes are shown in Figure 2-10.

2.3.3 Summary of Research on Components

Mechanical splices have traditionally been used to splice reinforcing bars or prefabricated reinforcement cages in construction projects that require long bars for cast-in-place construction. Most studies that focus on the performance of mechanical reinforcing bar splices in plastic hinge zones were performed in Japan (Takaine et al.

(2008), Splice Sleeve Japan (19??), Sato et al. (1993), Kawabata et al. (1990), and Ikadai et al. (1999)) and Taiwan (Huang et al. (1997)). These studies focused on applications of GC splices in precast column or beam connections for high-rise building construction. Among the various studies, there was not substantial difference between test specimens. Most test columns had square cross-sections and low aspect ratios ($AR < 3$); thus shear-flexure or pure shear dominated behavior. The general conclusion of these studies was that that precast columns with GC splices in the hinge zones had comparable or better performance than corresponding conventional cast-in-place columns.

The performance of GC splice in bridge columns was investigated in one study. Aida et al. (2005) conducted cyclic loading tests on three scaled column models to validate the column design for a railway viaduct in Japan. Of the three models tested, one column was cast-in-place and the other two were precast. Precast columns utilized GC splices to connect the precast column to the footing. Other test parameters included the type of anchorage used for longitudinal reinforcing bars within the footing and the reinforcing bar lug configuration. Instead of conventional hooks, longitudinal bars were anchored by a welded steel plate or heads. Two different lug configurations were also tested a threaded-style lug and a bamboo (ring) style lug.

The test columns had 29.5 in [750 mm] square cross-sections, an aspect ratio of 3.33, an ALI of 0.092 (ALI is defined as the ratio of the axial load to the product of the gross cross-section area and the concrete compressive strength), and longitudinal and transverse reinforcement ratios of 4.70% and 0.83%, respectively. The columns with reinforced longitudinally with 40 – 1.14 in [29 mm] diameter bars and transversely were 0.51 in [19 mm] diameter bars spaced at 3.3 in [83 mm]. Models were subjected to

reverse cycling loading in displacement control. Displacement increments were under terms of the yield displacement (Δ_y). All models were subjected to 3 cycles for each displacement increment from Δ_y to $6\Delta_y$ incremented by Δ_y . After which point, the loading protocol was changed during the test based on the performance of the model.

All models exhibited similar hysteretic behavior: good energy dissipation and minimal strength degradation under 5% drift. Strength degradation began in the baseline cast-in-place model at 5% drift due to bar buckling. Bar buckling did not begin in the models with grouted couplers until after 6% drift. Comparison of force-displacement envelopes showed that the precast models had slightly higher lateral load capacity compared to that of the baseline model. It was concluded that columns with GC splice performed better than the conventional cast-in-place column.

Reetz et al. (2004) investigated that application of TTC splice in beam plastic hinge zones. Two specimens were tested under reversed cyclic loading using a drift-based loading protocol. Specimens "A1" and "B1" had rectangular cross-sections measuring 24 in by 12 in [610 mm by 305 mm] and 16 in by 10 in [406 mm by 254 mm]. Both specimens were reinforced longitudinally with four No. 7 bars [D23], which results in reinforcement ratios of 0.47% and 0.92% for specimens A1 and B1, respectively. The transverse reinforcement was designed according to Chapter 21 of ACI 318-02. The longitudinal reinforcing bars were spliced 3 in [76 mm] above the simulated beam-column joint using a TTC splice. Results indicated that failure of A1 and B1 was due to longitudinal bar buckling and fracture of longitudinal bars, respectively. In B1, the fracture of longitudinal bars occurred at the interface between the threaded bar and the coupler.

In conclusion, there has not been a study focused on the application of mechanical splices in plastic hinge zones of bridge columns that conform to modern US design standards. The studies available only provide limited to no information on how the presence of the mechanical splices effect the behavior of the member.

2.4 Final Coupler Selection

Based on preceding review of literature and discussions with the research sponsor (Caltrans), the upset headed coupler (HC) and grout-filled ductile iron sleeve coupler (GC) devices were selected for further investigation and use in precast columns. The HC-type splice that was used in this study was the HRC 500/510 Series coupler produced by the Headed Reinforcement Corp. The GC-type coupler selected was the NMB Splice Sleeve produced by Splice Sleeve North America, a subsidiary of Splice Sleeve Japan.

2.5 Experimental Program

2.5.1 Introduction

In order to understand the behavior of the mechanical couplers selected for use in precast columns, a testing program was developed. Five tests were used to determine various properties of the mechanical couplers: 1) monotonic static tension; 2) monotonic dynamic tension; 3) reversed static cyclic loads; 4) single cycle slip; and 5) multi-cycle slip. Table 2-5 provides a list of the nomenclature used to identify the tests conducted. All tests were conducted at the Large-Scale Structures Lab (LSSL) at the University of Nevada, Reno on an MTS servo-hydraulic universal testing machine with hydraulically-actuated grips.

2.5.2 Description of Test Methods

2.5.2.1 Static Tensile Tests

Static tensile tests were conducted in accordance with the following standards:

- 1) ASTM A370 – 03: Standard test methods and definitions for mechanical testing of steel products.
- 2) ASTM A1034/A1034M – 10: Standard test methods for testing mechanical splices for steel reinforcing bars.
- 3) Caltrans Test 670 (CT670): Method of testing for mechanical and welded reinforcing steel splices.

The length of each tensile test sample was selected using the provisions described in CT670. That is, the minimum length of each specimen was determined using Eq. 2-1.

$$L_{\min} = 8d_b + 16" + L_{coupler} \quad (2-1)$$

Where

L_{\min} = Minimum length of tensile test sample measured as the clear distance between test machine grips.

d_b = Diameter of the reinforcing bar in inches.

$L_{coupler}$ = Total length of the coupler device in inches.

This resulted in specimen lengths for the HC and GC couplers of 26.5 in [673 mm] and 38 in [965 mm], respectively. Samples were loaded using displacement control. Given that the length of HC and GC samples were different, two sets of loading rates were selected based on ASTM A370 such that samples would be loaded at approximately the same static strain rate. For HC test samples, pre- and post-yield displacement rates

were 0.00625in/sec [0.159mm/sec] and 0.05in/sec [1.27mm/sec], respectively. For GC test samples, pre- and post-yield displacement rates were 0.01875in/sec [0.476mm/sec] and 0.15in/sec [3.81mm/sec], respectively. For each coupler type, three static tensile tests were completed. The location and dimension of extensometers used for measuring elongation over the coupler region were determined using ASTM 1034. Figure 2-11 shows the general requirement for the length of the extensometer; specific details regarding extensometer dimensions for HC and GC tests are provided in subsequent sections.

2.5.2.2 Dynamic Tensile Tests

The loading protocol for the dynamic tensile tests was selected such that samples would be exposed to strain-rates similar to those that would be experienced during an earthquake event. Therefore, the initial target strain rate range was selected to be 50,000-100,000 $\mu\epsilon$ /sec. A study conducted by Zadeh and Saiidi [2007] used the same MTS loading frame at UNR for high strain-rate tests on #8 bars and found that the achieved strain-rates were approximately 80% of the target rate. Therefore the target rate used in this study was 70,000 $\mu\epsilon$ /sec with the expectation of achieving strain rates within the target range. The displacement loading rates that correspond to 70,000 $\mu\epsilon$ /sec for HC and GC couplers were 1.575 in/sec [40 mm/sec] and 2.695 in/sec [68 mm/sec], respectively. It was also noted by Zadeh and Saiidi that during strain-rate tests the hydraulic grips of the MTS test frame had a tendency to slip. A dial gage was used to monitor grip slippage. If it was observed that the grips were slipping, the test would be stopped.

2.5.2.3 Cyclic Loading Tests

Cyclic loading tests were conducted in load control at rates of 1 kip/sec [4.45 kN/sec] and 0.5 kip/sec [2.23 kN/sec] for tension and compression, respectively. Figure 2-12 shows the general loading protocol that was used for all samples. Each tension cycle was incremented by $0.2f_y$, where f_y was the measured yield stress of the reinforcing bar, from $0.5f_y$ to $1.1f_y$ followed by increments of $0.1f_y$ thereafter. After the tension target was reached for each cycle the load was reversed until the sample was in compression at a stress of 3 ksi [20.7 MPa]. A low compression stress target was selected to prevent buckling. The slight differences in the ultimate strength of bars used for HC and GC samples dictated that the GC sample be subjected to one extra tension cycle.

2.5.2.4 Single and Multi-Cycle Slip Testing

Two different types of slip tests were conducted. In the context of this study, “slip” is defined as a permanent deformation that occurs over the coupler region after a specified stress-level has been applied and then released. The first slip test conducted was the single-cycle slip test. The loading protocol for the single-cycle slip was developed by following guidelines in CT670 and ASTM A1034/A1034M. Once a sample was loaded into the testing frame, an initial load of 3 ksi [20.7 MPa] was applied and the elongation over the sample measurement gage length ($\Delta_{initial}$) was recorded along with the minimum and maximum loads recorded by the loading frame. The sample was then stressed to 30 ksi [207 MPa] and held while elongation and load measurements were recorded. Subsequently, the sample was de-stressed to 3 ksi [20.7 MPa] and the final elongation (Δ_{final}) and load measurements were recorded. The single-cycle slip is defined by Eq. 2-2.

$$Slip = \Delta_{final} - \Delta_{initial} \quad (2-2)$$

The maximum permissible slip allowed by Caltrans is a function of bar size. Once the single-cycle slip test was completed, slip loading and measurement procedures were repeated 3-5 times per sample to investigate if multiple loading cycles increase the slip. A total of 3 samples were tested per coupler type.

2.5.3 Specimen Preparation

2.5.3.1 HC Coupler Specimens

HC coupler specimens were prepared using two 16-in [406-mm] No. 8 [D25] bar segments. One end of each segment had a deformed head that was installed by the Headed Reinforcement Company. The two segments were joined using a male HRC500 and a female HRC510 coupling collar. The two collars were initially tightened by hand and were then tightened to a torque of 150 ft-lbs [2.44k N-m] using a pipe wrench. Once the final torque was applied, strain gages were installed.

2.5.3.2 GC Coupler Specimens

In order to aid in the construction of GC coupler specimens, a special wooden frame was constructed. The main purpose of this frame was to orient reinforcing bars and couplers to ensure that the final coupler/bar assembly was straight. After the basic frame was constructed, plumb vertical lines were drawn onto the wood to use as a guide for securing bars and couplers (Figure 2-13). Once the coupler and form-end bar were tied to the frame, small wooden shims were nailed to the frame for alignment of the second bar (Figure 2-14) after the couplers had been filled with grout.

All couplers were filled with a high-strength, non-metallic, cementitious grout provided by the manufacture of the coupler; this material is discussed in more in Chapter 3. The grout was mixed according to specifications provided by the manufacturer. After the grout was properly mixed, the GC sleeves were filled to approximately three-fourths of their height. The grout was then rodded 10 times using a smooth 0.25-in [6.4-mm]-diameter rod to ensure good consolidation. The second reinforcing bar was then inserted in the field-end of the coupler and tied to the support frame to ensure that no movement would occur during curing of grout (Figure 2-15). Any excess grout was cleaned from the coupler sleeves with a damp cloth. The specimens were allowed to cure for 7 days before being removed from the support frame. During preparation of GC specimens, grout cubes were cast according to ASTM C109-02 to measure the compressive strength of the grout.

2.5.4 Instrumentation and Data Acquisition

2.5.4.1 Static Tensile Tests

Static tensile test specimens were instrumented with both electronic resistance strain gages and an extensometer. The placement and gage-length of the extensometers used to capture strain and elongation over the coupler region was selected in accordance with ASTM A1034. Data was recorded using National Instruments hardware and Labview software. Data from the MTS frame load cell was also recorded. All data for static tests was acquired at a rate of 4 Hz. During all tests, continuous video was recorded to capture the failure.

HC specimens were instrumented with four 120 Ohm YFLA-2 strain gages produced by Texas Measurements (TML). Gages were installed using CNY adhesive also produced by TML. Strain gages were located above and below the HC coupler. The extensometer used for HC specimens was an Epsilon 3543-0600-200T. This extensometer had a 2 in [50 mm] measurement length and a 6 in [152 mm] total gage length. Figure 2-16 depicts the instrumentation for the HC static tensile tests. A photo of the final test set-up is shown Figure 2-17.

GC specimens were instrumented using six 120-Ohm YFLA-2 strain gages produced by TML. Gages were installed using CNY adhesive also produced by TML. Strain gages were located above and below the GC coupler along with two gages located on the coupler itself. The extensometer used for GC specimens was an Epsilon 3543-1800-800T. This extensometer had a 4-in [102-mm] measurement length and an 18-in [457-mm] total gage length. Figure 2-18 depicts the instrumentation for the GC static tensile tests. A photo of the final test set-up is shown in Figure 2-19.

2.5.4.2 Dynamic Tensile Tests

The instrumentation and test set-up used to perform the dynamic tensile tests were the same as those used for the static tensile tests, and the same data acquisition system was used. The only difference between the tests was that the data acquisition rate used for dynamic tests was 16 Hz.

2.5.4.3 Cyclic Loading Tests

The instrumentation, test set-up, and data acquisition system used in the cyclic loading tests were the same as those used for the static tensile tests.

2.5.4.4 Slip Tests

The instrumentation used for the slip tests was a single spring action dial gage. For both HC and GC coupler specimens the dial gage was mounted on a threaded rod that was welded to the lower spliced bar. The lower threaded rod was located 4 in [102 mm] below the coupler. A second L-shaped threaded rod was welded 4 in [102 mm] above the coupler and extended down to contact the measurement tip of the dial gage. An instrumentation schematic for the HC slip tests and test set-up are shown in Figure 2-20 and Figure 2-21, respectively. Similarly, the instrumentation schematic for the GC slip tests and test set-up are shown in Figure 2-22 and Figure 2-23, respectively. The slip data was recorded manually in a notebook.

2.5.5 Test Results

The results from the experiments described in this chapter are presented in Chapter 7.

3. Large-Scale Experimental Program

3.1 Introduction

This chapter describes the elements necessary to conduct the experimental portion of this study. Five half-scale reinforced concrete column models were constructed and tested. The order of the sections in this chapter and purpose of each is described below.

- Definition of Materials:

There were a number of different materials utilized in the design and construction of column models. Basic characteristics of each material are discussed i.e. expected material properties and constituents. Furthermore, all test practices and/or standards that were employed for each material are presented.
- Development of a Benchmark Column:

A benchmark column model was designed as the basis for the precast models. The general procedure by which the benchmark was designed and detailed is discussed.

All precast columns design details were developed from a conventional cast-in-place column. The precast columns were to be emulative of conventionally designed columns.
- Cast-in-Place (CIP) Column Model:

The cast-in-place (CIP) column model was the baseline model used to evaluate the performance of the precast models. The structural details, construction procedure, and

instrumentation are discussed. CIP used the exact details that were developed for the benchmark model.

- **Headed Coupler (HC) Column Models:** Two column models incorporated upset-headed mechanical couplers. The structural details, construction procedure, and instrumentation are discussed for both models. Emphasis has been placed on the construction sequence.
- **Grouted Coupler (GC) Column Models:** Two column models incorporated cast iron grout-filled sleeve couplers. The structural details, construction procedure, and instrumentation are discussed for both models. Emphasis has been placed on the construction sequence.
- **Test Set-up and Loading Protocol:** The final sections of the chapter discuss the experimental set-up, loading protocol, and data acquisition used during testing.

3.2 Definition of Materials

3.2.1 Conventional Concrete

The conventional concrete used for construction of column models was a 3/8-in [10-mm] maximum course aggregate Portland cement concrete mix with a specified 28-day compressive strength of 4500 psi [31 MPa] and slump of 6 in [152 mm]. The

constituents of the conventional concrete mix design are listed in Table 3-1. The following standards were used in evaluating the slump and compressive strength of conventional concrete:

- 1) ASTM C39 – Test Method for Compressive Strength of Cylindrical Concrete Specimens [ASTM International, 2003a].
- 2) ASTM C143 – Test Method of for Slump of Hydraulic-Cement Concrete [ASTM International, 2003b].

3.2.2 Self-Consolidating Concrete

Self-consolidating concrete (SCC) as defined by the American Concrete Institute (2007) is highly flowable, nonsegregating concrete that can spread into place, fill formwork, and encapsulate the reinforcement without any mechanical consolidation. The SCC used in this study had design strength of 4000 psi [27.6 MPa] and an expected strength exceeding 5000 psi [34.4 MPa]. The constituents of the SCC mix design are listed in Table 3-2. The standards, guidelines, and test methods used to characterize the SCC mix are described in subsequent sections.

3.2.2.1 ASTM C1611 - Slump Flow of Self-Consolidating Concrete

Given that SCC is highly flowable, a traditional slump test is not appropriate nor results in useful information. ASTM C1611 [ASTM International, 2009] provides an alternative test method that is appropriate for SCC. The slump flow test is used to determine the flow potential of an SCC mix along with means of visually inspecting the consistency of the mix. The slump flow test is started by filling a standard slump cone that is inverted on a flat, dampened, non-porous surface. The cone is then lifted up

allowing the SCC to flow out the bottom of the cone and spread outward. Once the concrete has spread, two measurements are taken, d_1 and d_2 . The slump flow is then determined using Eq. 3-1.

$$\text{Slump Flow} = (d_1 + d_2) / 2 \quad (3-1)$$

Where

d_1 = Largest diameter of the circular spread of concrete

d_2 = Spread of concrete in the direction perpendicular to that of d_1

ASTM C1611 also describes a method by which the consistency and stability of an SCC mix can be assessed. After the slump flow test has been completed, the spread concrete is to be inspected visually and given a score between 0 and 3 that corresponds to the consistency and stability of the mix. Table 3-3 provides a description of the criteria used to score the mix.

3.2.2.2 ASTM C1610 – Static Segregation of Self-Consolidating Concrete Using Column Technique

Self-consolidating concrete can have a tendency to segregate if the mix is not proportioned to be cohesive. ASTM C1610 [ASTM International, 2007a] provides a method by which the segregation of an SCC mix can be determined. This method uses a 3-segment 26 in [660 mm] tall PVC column to determine segregation. A schematic of the segregation column is shown in Figure 3-1. Before SCC is cast, the column is filled with SCC and allowed to sit undisturbed for 15 min. After the 15-min wait period has elapsed, the top and bottom sections of the column are emptied into separate collection containers. The concrete contents of the collection containers is then washed out through

a No. 4 [4.75 mm] sieve and weighed. The percentage of segregation is then determined using Eq. 3-2.

$$S = \begin{cases} 2 \left[\frac{CA_B - CA_T}{CA_B + CA_T} \right] \cdot 100 & \text{if } CA_B > CA_T \\ 0 & \text{if } CA_B \leq CA_T \end{cases} \quad (3.2)$$

Where

S = Static segregation, percent

CA_B = Mass of course aggregate in the bottom section of the column

CA_T = Mass of course aggregate in the top section of the column

3.2.2.3 Caltrans Requirements on SCC

Caltrans currently has specific requirements that must be met for the tests described above; slump flow, visual inspection index, and static segregation. The requirements for these tests are listed in Table 3-4.

3.2.3 Cementitious Grouts

The cementitious grouts used in this study were all pre-packaged grouts. The constituents of the grouts were water, hydraulic cement, fine aggregate, and some chemical additives. The following test methods and specifications were followed when using cementitious grout materials.

- 1) ASTM C1107 – Standard Specification for Packaged Dry, Hydraulic-Cement Grout (Nonshrink) [ASTM International, 2011].
- 2) ASTM C1437 – Test Method for Flow of Hydraulic Cement Mortar [ASTM International, 2007b].

3) ASTM C109 – Test Method for Compressive Strength of Hydraulic Cement

Mortars (Using 2 in or [50 mm] Cube Specimens) [ASTM International, 2002].

Three separate grouts were used and are described in subsequent sections

3.2.3.1 W. R. Meadows® 588-10K (Grout 1)

W. R. Meadows 588-10K is a non-shrink, non-corrosive, non-metallic, mineral-based grout that can be mixed to plastic, flowable, or fluid consistency. For the applications of this study, this grout was mixed to a fluid state (addition of 1 gal [3.9 L] of water), which results in a 28-day manufacturer specified strength of 8,200 psi [56.5 MPa].

3.2.3.2 SikaGrout® 212 (Grout 2)

SikaGrout 212 is a high performance, non-shrink, non-metallic, low-bleed grout that contains no chlorides. Similar to the 588-10K grout, Sika 212 can be mixed to plastic, flowable, or fluid consistencies. For the applications of this study, this grout was mixed to a fluid state (addition of 1.06 gal [4.0 L] of water) which results in a 28-day specified strength of 5,800 psi [40 MPa].

3.2.3.3 SS Mortar® by Splice Sleeve (Grout 3)

SS mortar was a special grout that was provided by the Splice Sleeve Company for use with the NMB grout sleeve coupler. The SS mortar is a non-metallic grout that has a high early strength. It is recommended that the SS mortar be mixed with 0.98 – 1.0 gal [3.7 - 3.9 L] of water. Furthermore, it is recommended that only full bags be mixed.

When mixed to manufacture specification, the SS mortar has a specified 28-day strength of 12.5-14.6 ksi [86-100 MPa] depending on cure temperature.

3.2.4 Reinforcing Steel

Standard Gr. 60 deformed mild reinforcing steel bars were used in this study. Three of the five column models used ASTM A615 bars, and the remaining two models used ASTM A706 bars; specifics are discussed in subsequent sections. Both bar types have an expected yield strength of 68ksi [468MPa] and ultimate strengths that varying between 95 ksi [655 MPa] and 110 ksi [758 MPa]. The following standards were used as reference:

- 1) ASTM E8 – Test Methods for Tension Testing of Metallic Materials [ASTM International, 2004a].
- 2) ASTM A370 – Test Methods and Definitions for Mechanical Testing of Steel Products [ASTM international, 2003c].
- 3) ASTM A706 – Standard Specification for Low-Alloy Steel Deformed and Plain Bars for Concrete Reinforcement [ASTM International, 2004b].

3.3 Development of Benchmark Column

3.3.1 Introduction

As was mentioned in the introduction of this chapter, the precast column models developed were to be of emulative design. That is, the connection mechanism for the precast column-to-footing assembly is to behave like that of a conventional cast-in-place column-to-footing assembly. Therefore, a benchmark column was designed such that the details of the connection region could be adapted to incorporate mechanical coupler connections. Furthermore, the benchmark column details were also used to construct a conventional (cast-in-place) column model with which the precast models could be

compared. The following sections describe the design procedure and performance objectives for the benchmark model.

3.3.2 Design Procedure

The benchmark model was designed according to Caltrans Seismic Design Criteria (SDC) version 1.4. The SDC outlines the minimum criteria for seismic design of ordinary bridges in the State of California. In developing the design details for the benchmark column model, focus was put on closely following the specification outlined in Chapter 3 (Capacities of Structure Components) of the SDC. This section presents the requirements for displacement-based capacity of ductile concrete members. Section 3.1.4.1 of the SDC imposes a minimum calculated local displacement ductility capacity of $\mu_c = 3.0$ for ductile column members. Displacement ductility is defined by Eq. 3-3.

$$\mu_c = \frac{\Delta_c}{\Delta_Y^{col}} \quad (3-3)$$

Where:

Δ_c = Column member displacement capacity determined using rotation capacity which is determined from curvature capacity from moment-curvature ($M-\phi$) analysis.

Δ_Y^{col} = Effective yield displacement of the column.

Three main components contribute to lateral displacement of a column; (1) flexural deformation, (2) shear deformation, and (3) bond-slip rotation at column ends. The displacements Δ_c and Δ_Y^{col} in Equation 3-3 only include the flexural component of displacement. It was desired that the benchmark column be able to undergo large inelastic deformations. Therefore, a minimum design displacement ductility capacity of

$\mu_c = 7.0$ was selected. The selection of initial design parameters was based on creating a representative half scale column model, the testing capabilities of the Large-Scale Structure Laboratory (LSSL) at the University of Nevada, Reno (UNR), and ability to adapt the benchmark design to incorporate mechanical couplers into the plastic hinge region.

It was critical that the behavior of the mechanical couplers be accurately represented. As described in Chapter 2, research has shown that bar diameter can have an effect on the performance of mechanical couplers. Since the majority of California bridges are built with large diameter bars (No. 11 [D39] or No. 14 [D43]) it was critical that larger diameter bars be used. Therefore No. 8 [D25] bars were selected for the longitudinal reinforcement. The second parameter determined was the amount of longitudinal reinforcement. It was desired that the longitudinal reinforcing steel ratio be representative of those in modern bridges. Therefore it was decided that a ratio of approximately 2% be used. It is common for California bridge columns to have circular cross-section. Therefore, assuming a prototype bridge column with a 48-in [1220 mm] diameter circular cross-section, the resulting half-scale benchmark column had a 24-in [610-mm] circular cross-section and 11 – No. 8 [D25] longitudinal reinforcing bars. It was desired that the behavior of the benchmark column be flexural-dominated with relatively high shear. Therefore an aspect ratio (column height / cross-section diameter) of 4.5 was selected. The column models were to be tested under a constant axial load. The axial load was determined using Eq. 3-4 and an ALI = 0.10.

$$P_{axial} = ALI \cdot f'_c \cdot A_g \quad (3-4)$$

Where

ALI = Axial load index.

f'_c = Specified compressive strength of concrete at 28 days.

A_g = Gross column cross sectional area.

Based on the cross-section dimensions and an expected f'_c of 5000 psi [34 MPa], the design axial load was 226 kip [1005 kN]. The concrete cover was the final design parameter determined. The minimum cover specified by Section 8 (Reinforced Concrete) of the Caltrans Bridge Design Specification (2003) is 2 in [50 mm], which is typically used in bridge columns. The test models in this study were to be of half-scale. Therefore the minimum concrete cover would be 1 in [25 mm]. To maintain the same column diameter and location for the longitudinal reinforcement, the benchmark model cover had to be increased to 1.75 in [44.5 mm]. This enabled the columns with couplers to maintain the minimum concrete cover of 1 in [25 mm]. A summary of the initial design parameters is listed in Table 3-5.

Once the initial design parameters were selected, the transverse reinforcement was designed. The transverse reinforcement was to resist shear and provide adequate confinement to achieve a displacement ductility of at least 7.0. Moment-curvature analysis was used to determine the effective yield and ultimate curvatures. The displacement ductility was then determined using the equations in Section 3.1.3 in the SDC. The moment-curvature models developed used the parameters in Table 3-5 and then varied the pitch and size of the transverse reinforcement such that the calculated displacement ductility capacity was at least 7.0.

3.3.3 Final Benchmark Column Details

A summary of the design details and cross-section for the benchmark column are shown in Table 3-6 and Figure 3-2, respectively. The transverse steel was No. 3 spiral with a 2-in [50-mm] pitch. This resulted in a transverse reinforcement ratio of 1.05%. The final calculated displacement ductility capacity was 7.04.

3.4 Cast-in-Place (CIP) Column Model

3.4.1 Introduction

The cast-in-place (CIP) column model was detailed and constructed according to the benchmark model details. It should be noted that the footing and loading head described in this section were used for all models. The following sections will discuss the construction and instrumentation associated with the CIP model.

3.4.2 Footing Design and Details

Column footings were designed to remain elastic during testing. The main considerations in design of the footing were moment and shear capacity, resistance against sliding, and prevention of overturning. These factors were used to determine the main footing reinforcement and dimensions. The main reinforcement for the footing consisted of No. 6 [D19] Gr. 60 mild steel bars, and the main dimensions for the footing were 70 in [1778 mm] wide, 70 in [1778 mm] long, and 32 in [813 mm] deep. Geometry and reinforcement details are shown in Figure 3-3.

3.4.3 Loading Head Design and Details

The loading head was also designed to remain elastic during testing. The dimensions of the loading head were controlled by dimensions of the lateral load actuator. The loading head consisted of No. 3 [D10], #4 [Ø13 mm], and No. 6 [D19] mild steel bars for reinforcement. The dimensions for the loading head were 32 in [813 mm] wide, 45 in [114 mm] long, and 24 in [610 mm] deep. Geometry and reinforcement details are shown in Figure 3-4.

3.4.4 Final Model Details

The final geometric and reinforcement details for the fully assembled CIP column model are shown in Figure 3-5.

3.4.5 Construction

Construction of CIP began by building the formwork and laying out the bottom mat of reinforcing steel for the footing (Figure 3-6). Once the bottom mat was placed, the reinforcing cage for the column was built and placed onto the bottom mat of the footing reinforcement cage. The longitudinal reinforcing bars used to construct CIP were ASTM A615 bars. After the column cage was placed, the remainder of the reinforcing steel for the footing was placed (Figure 3-7) and the footing concrete was cast. Prior to casting, the slump of concrete was measured and standard 6 in x 12 in [152 mm x 305 mm] cylindrical samples were taken. After 3 days of curing, construction began on the column form and falsework for the loading head (Figure 3-8). The reinforcement configuration of the loading head can be observed in Figure 3-9. After the formwork and reinforcement were placed, the concrete was cast for the column and loading head. Similar to the

procedure in casting the footing, the slump was measured and concrete compression cylinders samples were taken. After 3 days all form-work was removed. A photo of the completed CIP column model is shown in Figure 3-10.

3.4.6 Instrumentation

The CIP column reinforcing cage was instrumented with 120-Ohm electronic resistance strain gages prior to casting concrete. Gages were placed in 6 layers from below the footing surface and through the plastic hinge zone. Figure 3-11 shows the strain gage instrumentation plan for the CIP column. A photo of the completed strain gage installation is presented in Figure 3-12. During testing, CIP was also instrumented with string pot displacement transducers to record column head displacements and linear-variable displacement transducers (LVDT) used to record plastic hinge curvatures and bond-slip. A schematic of these displacement and curvature transducers is shown in Figure 3-13.

3.5 Models with Upset Headed Coupler (HC) Connections

3.5.1 Details of HC Column Models

HC models utilized a hollow precast concrete shell that contained longitudinal and transverse reinforcing steel. The longitudinal reinforcing bars used to construct the HC models were ASTM A706 bars. The column was initial hollow to reduce weight for transportation and erection purposes. A similar practice could be applied in the field. The column-to-footing connection for HC models was made with HRC 500/510 series mechanical couplers. Connectivity between the longitudinal reinforcement in the column shell and footing was achieved by using a transition bar and two HRC up-set headed

couplers. Once the connection was made, formwork was placed around the open region that contained the couplers and the connection zone was pressure grouted. Two HC column models were tested: one with connection made directly to the footing, denoted “HCNP”, and the second with the column mounted on precast pedestal, denoted “HCPP”, which was used to reduce the demand over the connection region and investigate if this method would affect the ductility capacity of the column. The height of the pedestal was determined by discussions between the research team at UNR and Caltrans. Each pedestal was 12-in [305-mm] high (one half column diameter) and was match cast to the footing. Reinforcing bar dowels passed through the pedestal via 2.25-in [57-mm] inner diameter corrugated steel-sheet ducts that were filled with cementitious grout prior to installing the precast column shells.

A general schematic of the HC connection can be observed in Figure 3-14, which shows details with and without the precast pedestal. The specific dimensions of the connection region in the column shell are shown in Figure 3-15. The geometric and reinforcement layouts for the HC models without and with pedestals can be found in Figure 3-16 and Figure 3-17, respectively. The details for the pedestal can be found in Figure 3-18. The precast pedestal dimensions and reinforcement details were the same for HCPP and GCPP.

3.5.2 General Construction Sequence of HC Models

This section presents the general construction sequence for the HC column models with the focus placed on the construction of the column-to-footing connection. The construction sequence presented assumes that the footing and precast column have been

cast and the column is ready to be placed. Figure 3-19 illustrates the 6-step construction sequence for the HC models as described below.

- 1) Placement of shims: Shims must be placed between the footing and the precast column for two reasons. First, shims are used to aid the process of plumbing the column shell. Second, shims create a void that will be filled with grout to create a flush connection between the precast shell and footing/pedestal (Figure 3-19a).
- 2) Placing precast column shell: Once shims have been placed, the column shell can be lifted and placed onto the shims. Prior to setting the column shell, the transverse reinforcement (hoops or spiral) must be set over the bottom connection dowels. After placement, the column shall be plumbed and supported to restrain movement. A drawing of this step can be found in Figure 3-19b.
- 3) Grouting column-to-footing/pedestal interface: Once the column shell has been plumbed and supported, the interface between the shell and footing/pedestal can be grouted. A temporary form should be placed and the concrete surfaces should be pre-wetted such that water from the grout is not absorbed and the grout flowability is not compromised. The grout should be mixed to fluid state and poured from a single location. Once the grout has been poured, it should be left undisturbed for 24 hours. A drawing of this step is shown in Figure 3-19c.

- 4) Placing transition bars and transverse steel: A transition bar was used to connect the column to the footing/pedestal. Each transition bar was fabricated according to measurements taken between the column and footing/pedestal dowels. After the grout has had time to set, the transition bars can be placed. The initial connection of the transition bar is made at the bottom dowel. In some cases there will be a small gap (less than 0.25 in [6 mm]) between the heads at the column connection dowel; that is, the transition bar is slightly too short. In this case a small circular steel shim must be inserted prior to torquing the couplers. Couplers shall be torqued to the manufacture's specifications. Once the transition bars have been installed the transverse reinforcement can be tied into place (Figure 3-19d). Note, transverse reinforce must be placed prior to connecting the transition bar to the column dowel bars.
- 5) Construct closure formwork: Once Step 4 has been completed, the formwork for closure grouting can be constructed. This formwork must be constructed such that fluid pressure from the grout can be resisted and such that minimum grout is lost due to leakage. The grout inlet should be constructed at the base of one side of the formwork and a grout outlet should be built into the precast column shell to ensure that the closure region is completely filled with grout (Figure 3-19e).
- 6) Pump grout and pour SCC: The final steps in completing the HC column connection are filling the closure region with grout and filling the hollow column shell with SCC. When preparing for the grout pumping operation, the grout pump

should be cleaned thoroughly prior to mixing grout. Grout should be mixed to a fluid consistency based on manufacturer's specifications. Once the grouting procedure begins, it should not be stopped until closure region is completely filled. After completing the closure, the grout should be allowed to cure for 24 hours prior to filling the column with SCC (Figure 3-19f).

3.5.3 Construction of HC Models

3.5.3.1 HCNP Model Construction

Construction of HCNP began with the footing. A wooden template (Figure 3-20) was used to align the longitudinal reinforcing bars such that the footing dowel cage and column cage would meet in the correct locations. Once the footing dowel cage was constructed, it was placed onto the reinforcement mat at the bottom of footing form (Figure 3-21). The remainder of the footing reinforcement was then placed (Figure 3-22). The concrete was cast and allowed to cure for 3 days prior to removal of the formwork. Figure 3-23 shows the completed footing after removal of formwork. The threaded female HRC coupler collars and headed bars can be seen protruding from the footing surface.

Once the footing was completed, the column shell reinforcement cage was constructed. The same wooden template that had been used in the footing was used to align longitudinal reinforcement. A platform (Figure 3-24) was constructed to provide support to the primary longitudinal and traverse reinforcing cage. The platform was also used to construct the formwork and reinforcement for the base segment of the HCNP shell (Figure 3-25). Once the base segment formwork was completed, the main shell

reinforcement cage and internal PVC form were placed (Figure 3-26). Figure 3-27 shows HCNP column shell ready for casting concrete. The column shell was allowed to cure for 3 day prior to removal of the formwork. A photo of the completed shell is presented in Figure 3-28.

Connectivity between the longitudinal reinforcement in the column shell and reinforcement in the footing was made by using a transition bar (Figure 3-29). The transition bars were inserted between the connection dowels protruding from the column shell and those protruding from the footing with the base segment of the column shell resting on steel shims. Figure 3-30 shows the column shell placed on the footing with transition bars inserted. Initially, only three transition bars were fully connected to stabilize and plumb the column shell prior to grouting the shell-to-footing interface. This interface was grouted using Grout 1 (Section 3.2.3.1). Once the grout had cured for 24 hours, all the transition bars were fully connected. Although each transition bar was specifically sized, some bars still had small gaps that remained between the heads at the upper connections. Small circular steel shims (Figure 3-31) provided by HRC were used to fill these gaps prior to connecting the threaded collars (Figure 3-32). Once all collars had been tightened by hand, two pipe wrenches and a linear scale were used to apply 150 lbs-ft [203 N-m] torque to the collars as specified by HRC (Figure 3-33). After completing the installation of the transition bars, the transverse reinforcement in the closure region was tied (Figure 3-34) and formwork was constructed for grouting (Figure 3-35).

The closure region was pressure grouted using an Airplaco HG-9 manual grout pump. Grout 2 (Section 3.2.3.2) was used to fill the closure region. Figure 3-36 shows grout in

the pump hopper ready to be pumped into the closure region. A portion of the first batch of grout mixed was set aside for flow table measurements per ATSM 1437. A flow table test was conducted every 5 min over a 20-min time frame to make sure there was no change in the flowability of the grout with time. Figure 3-37 shows the set-up of the flow table test and the table after the completion of the test. All four tests resulted in the grout completely covering the table indicating no change in fluidity. During the grout closure, cube samples were cast for compression testing (Figure 3-38). Once the closure form was completely full, the inlet and outlet grout ports were sealed off and the grout was allowed to cure for 24 hours prior to removal of the formwork.

After the formwork was removed from the grout closure region, a thin ring measuring approximately 0.2 – 0.4 in [5 – 10 mm] in thickness of void space and/or loose material was found at the top of the closure region. This was caused by bleed water and segregation of the grout. Figure 3-39 shows the location and condition of the void area. It was decided to remove all poor quality materials and fill the remaining space with a high strength, high modulus epoxy. Figure 3-40 shows the column prepared for epoxy injection. After epoxy injection, the falsework for the loading head was constructed.

Once the formwork and reinforcement for the loading head were placed, the head and core of the column shell were ready to be filled with SCC. Prior to casting, the slump flow of the SCC was measured (Figure 3-41) and the static segregation column was filled (Figure 3-42). After 15 min the contents of the segregation column were separated (Figure 3-43) and sieved (Figure 3-44). Figure 3-45 shows the sieved contents of the static segregation column. The tests showed that the SCC met the Caltrans specification and therefore the SCC was cast (Figure 3-46).

3.5.3.2 HCPP Model Construction

The construction procedures and sequence of HCPP, which is the column with an HC connection and a precast pedestal, was similar to that of HCNP; the difference being the construction of the pedestal. Figure 3-47 shows formwork and connection dowel cage for the HCPP footing. The footing was cast and allowed to cure for 3 days prior to removing the formwork. Once the formwork was removed, the pedestal was constructed. Figure 3-48 shows the HCPP connection dowels protruding from the surface of the footing and placement corrugated steel ducts for the pedestal. After placement of the ducts, the transverse reinforcement was tied and a Sonotube form was placed (Figure 3-49). A photo of the cast pedestal before grouting ducts can be seen in Figure 3-50. The pedestal ducts were grouted with Grout 1. The grout was poured into each duct using a plastic cup. The ducts were filled half way, rodded 15 times, then filled completely, and rodded another 15 times. Any excess grout around the perimeter of the ducts was cleaned off.

The reinforcement and formwork for the HCPP column shell were constructed in the same fashion as described for HCNP. However, when the formwork was removed it was noticed that concrete had not reached the bottom segment of the form, which would be in the closure region (Fig. 3-51). The poor concrete was removed, and this region was re-formed with a Sonotube and new conventional concrete was cast (Figure 3-52). The completed repair can be observed in Figure 3-53.

HCPP encountered the same issue with the upper part of the grout closure region as HCNP. The same repair method, as described in the previous section, was used to repair the column.

3.5.4 Instrumentation

3.5.4.1 HCNP Model Instrumentation

The longitudinal and transverse reinforcing steel in HCNP was instrumented with strain gages. The strain gage instrumentation plan for HCNP is shown in Figure 3-54. Photos of the instrumented footing dowels and column cages can be seen in Figure 3-55 and Figure 3-56, respectively. After the column shell was placed and the transition bars were installed, the closure region was instrumented with strain gages (Figure 3-57). Prior to testing, string pot displacement gages and LVDTs were also installed on the column to capture head displacement and plastic hinge curvature, respectively. The instrumentation plan for string pots and LVDTs is presented in Figure 3-58.

3.5.4.2 HCPP Model Instrumentation

The instrumentation in HCPP was similar to that of HCNP. The strain gage instrumentation plan is presented in Figure 3-59, and the string pot / LVDT plan is presented in Figure 3-60.

3.6 Models with Grouted Coupler (GC) Connections

3.6.1 General Details of GC Column Models

Similar to the HC column models, the GC models utilized a hollow precast concrete shell that contained longitudinal and transverse reinforcing steel. The longitudinal reinforcing bars used to construct the GC models were ASTM A615 bars. The connection of the column-to-footing connection for GC model was made with NMB grout sleeve couplers. The column shells were lowered onto reinforcing bar dowels that

protruded from the footing. Once the shell was lowered onto the dowels the sleeves were pressure grouted through plastic ducts that protruded from the column shell. The grout used was a high strength proprietary mix that was supplied by the grout sleeve manufacturer. Once the precast column shells were connected to the footing, the core was filled with SCC. Two GC column models were tested; one where the connection was made directly to the footing and the second where the column was mounted on a 12-in [305 mm] precast pedestal. The pedestal was used to shift the location of the couplers by one-half the column diameter to investigate if this method would affect the ductility capacity of the column.

A general schematic of the GC connection can be seen in Figure 3-61. The geometric and reinforcement layouts for the GC models without and with pedestals can be seen in Figure 3-62 and Figure 3-63, respectively. The details for the pedestal can be found in Figure 3-64.

3.6.2 General Construction Sequence GC Models

This section presents the general construction sequence for the GC column models with focus placed construction of the column-to-footing connection.

3.6.3 Construction of GC Models

3.6.3.1 GCNP Model Construction

Construction of the GCNP model began by building the footing dowel cage, which provided the protruding connection dowels for the column shell (Figure 3-66). In order to ensure that the footing dowels and grout sleeve ports in the column would line up, a wooden template was used to position longitudinal bars. The dowel cage was placed

onto the bottom mat of footing reinforcement, and the remainder of the footing reinforcement cage was constructed (Figure 3-67). The footing was then cast (Figure 3-68) and allowed to cure for 3 days prior to removal of formwork. During casting, the lengths of the connection dowels were measured (Figure 3-69) to ensure that no movement had occurred and that they were of a proper length of 7.25 in to 7.5 in [184 mm-190 mm]. The completed GCNP footing, after removal of formwork, can be observed in Figure 3-70.

The GCNP shell was constructed following the footing. Using the same wooden template, the longitudinal and transverse reinforcement for the shell were placed and tied. The NMB sleeves were not installed until after the shell reinforcement cage was fully constructed. Figure 3-71 shows NMB sleeves being installed on the reinforcement cage. After all sleeves were installed, a spiral was placed and tied over the coupler region (Figure 3-72).

Special formwork was constructed to secure the GCNP column cage. Figure 3-73 shows a platform with NMB Sleeve Setters to secure the couplers and a wooden disc in the center to secure the inner PVC form. A Sleeve Setter is a device developed by Splice Sleeve to lock NMB couplers into formwork. Figure 3-74 shows a photo of the Sleeve Setters from underneath the formwork. A photo of the GCNP reinforcement cage mounted on the Sleeve Setters is shown in Figure 3-75. Once mounted, a Sonotube form was placed over the reinforcing cage. Holes were then drilled into the form to allow placement of the PVC grout ports (Figure 3-76). Concrete was cast and the column shell was allowed to cure for 3 days prior to removal of the formwork. A photo of the completed shell is shown in Figure 3-77. Figure 3-78 shows the grout sleeve openings on

the underside of the GCNP column shell prior to the removal of the inner form work and the round plug. The grout tubes for the couplers can also be seen.

The footing dowels were cleaned with a wire-bristle grinder wheel prior to placing the GCNP column shell (Figure 3-79). The column shell was lowered over the footing dowels and placed on steel shims using a forklift. The column shell and steel shims can be seen in Figure 3-80 and Figure 3-81, respectively. A temporary form was constructed around the base of the GCNP column shell for grouting the interface between the shell and the footing (Figure 3-82). Grout 1 was used to fill the interface. Figure 3-83 shows the completed grouting prior to removal of formwork. Excess grout was removed after 24 hours.

The NMB couplers were grouted using a Airplaco HG-9 manual grout pump. The grout used to fill the sleeves was the SS Mortar (Grout 3[Section 3.2.3.3]). Grout was pumped into the sleeves from the bottom port. Pumping was not stopped until grout began to exit the top port. A stopper was then placed in the top port and the grout pump hose was removed from the bottom port and replaced with a stopper. Cube samples from the grout were cast at the time of sleeve grouting for later testing. Grout within the sleeves was allowed to cure for 24 hours prior to constructing the loading head falsework. Once the loading head formwork was placed and reinforcement cage built, the column shell core and head were filled with SCC.

3.6.3.2 GCPP Model Construction

The construction procedures and sequence of GCPP were similar to that of GCNP. The only differences were the construction of the pedestal and the placement of the

column shell. The reinforcement for the footing and connection dowels can be seen in Figure 3-84. After the footing was cast and cured for 3 days, the corrugated ducts and reinforcement for the pedestal were placed. Wooden spacers were used to position the corrugated ducts and the transverse reinforcement. A Sonotube was used for forming the pedestal. Figure 3-85 shows a photo of the GCPP pedestal ready for casting. Once the pedestal had cured for 3 days, the wooden shims were removed from the pedestal ducts and the ducts were grouted with Grout 1. The grout was poured in each duct using a plastic cup. The ducts were filled half way, rodded 15 times, then filled completely, and rodded another 15 times. Any excess grout around the perimeter of the ducts was cleaned off. Figure 3-86 shows a photo of the completed pedestal.

Prior to lowering the column shell over the connection dowels, a temporary form was constructed around the pedestal using a Sonotube (Figure 3-87) to create a form for bedding grout. Steel shims were placed on the footing and GRW washers were slid onto connection dowels. A layer of bedding grout (Grout 1) was placed on the pedestal and the GCPP column shell was lowered over the connection dowels (Figure 3-88). After the column shell was placed and plumbed the same procedure as described in Section 3.6.3.1 for completing construction was followed i.e. grouting couplers and casting SCC.

3.6.4 Instrumentation

3.6.4.1 GCNP Model Instrumentation

Strain gages were placed on longitudinal and transverse reinforcing steel along with couplers. The strain gage instrumentation plan for GCNP can be found in Figure 3-89. A photo of the instrumented dowel cage can be seen in Figure 3-90. Two strain gages were

installed at the mid-section of seven of the NMB couplers in the GCNP model (Fig. 3-91). Figure 3-92 shows a group of couplers after strain gage installation has been completed. The final instrumented reinforcement cage can be seen in Figure 3-93.

During testing, GCNP was also instrumented with string pot displacement transducers and LVDTs to capture the head displacement and plastic hinge curvatures, respectively. The string pot and LVDT instrumentation plan can be found in Figure 3-94.

3.6.4.2 GCPP Model Instrumentation

The instrumentation plan for GCPP was very similar to that of GCNP. The strain gage instrumentation plan can be found in Figure 3-95. The displacement and curvature instrumentation plan can be found in Figure 3-96.

3.7 Test Set-up and Loading Protocol

3.7.1 General Information

All column models were tested at the Large-scale Structures Laboratory at the University of Nevada, Reno. Tests were conducted outdoors on a portion of a newly constructed strong-floor. All models were tested by slow cyclic loading in a single cantilever configuration. During loading procedures, a nominally constant axial load was applied. A general schematic showing the details of the experimental set can be seen in Figure 3-97. Figure 3-98 shows a photo of the actual testing configuration.

3.7.2 Placement of Column Model

Each column model was placed using a forklift (Figure 3-99). Models were lowered onto 2 in [51 mm] wooden shims that provided a void between the underside of the

model footing and the strong floor. Temporary formwork was constructed, and this interface region was filled with cementitious grout. After 24 hours, 6 high-strength 1-3/8 in [35 mm] post-tensioning rods were used to secure the footing to the strong floor. Each rod was post-tensioned to 100 kip [448 kN].

3.7.3 Lateral Loading Configuration

Load was applied to the column model using a 220 kip [978 kN] MTS servo-controlled hydraulic actuator. The actuator was mounted to a reaction pylon that was constructed of seven 20 kip [89 kN] modular reaction blocks (Fig. 3-100). Each block was 4 ft [1.2 m] x 4 ft [1.2 m] x 8ft [2.4 m]. After the blocks were placed, sixteen 1-3/8 in [35 mm] high-strength DSI post-tensioning rods were used to post-tension the blocks to the strong floor. Each rod was tensioned to 100 kips [44 8 kN].

3.7.4 Axial Load

Axial load was applied to the column model using two Enerpac hollow-core hydraulic rams and a spreader beam (Figure 3-101). During testing, the axial load was monitored using an annular low-profile load cell. The spreader beam was placed atop the loading head of the column model and secured using four 0.5-in [13-mm] diameter threaded anchor rods. Once the spreader beam was in place, the hollow-core rams were positioned. A high-strength 1-3/8 in [35 mm] diameter threaded rod was fed through the center of each ram and locked-off using a bearing plate and nut. The other end of the threaded rod passed through the column footing and strong floor and was locked-off under the strong floor. Both hydraulic rams were pressurized with the same pump and system pressure was maintained using a nitrogen accumulator (Figure 3-102).

3.7.5 Loading Protocol

Lateral load was applied to the column model in a slow cyclic fashion. The loading was displacement controlled. Figure 3-103 depicts the drift-based loading protocol that was used. For each drift level, two full push and pull cycles were planned. The displacement rate of the actuator was determined such that the rate of strain in longitudinal bars was within the static testing limits set by ASTM A370. Therefore up to 3.0% drift ratio, the rate of actuator displacement was set at 1 in/min [25.4 mm/min]. For drift levels greater than 3.0% the rate of travel was set at 5 in/min [127 mm/min]. The loading was paused at key drift levels to mark cracks, inspect the column, and take photos. Loading was terminated after a model experienced multiple abrupt drops in lateral load.

3.7.6 Data Acquisition

Data from instruments was acquired continuously during all loading procedures at a rate of 1Hz using a national instrument data acquisition system and Labview software. The column loading was video recorded.

4. Experimental Results: Individual Column Models

4.1 Introduction

This chapter presents the test results for the five column models that were tested in this study. Test results are presented one model at a time and include measured lateral force-displacement hysteresis curves, the average backbone and idealized elasto-plastic curves, plastic hinge strain profiles, plastic hinge curvatures, and other forms of data. Prior to presenting results from column tests, Section 4.2 provides a detailed discussion of results from tests on properties of the column model material constituents. The methodologies to process data for each column model were similar and are presented in Section 4.3, followed by the measured data.

4.2 Material Test Results

Four different materials were used in the construction of column models; (1) conventional concrete, (2) self-consolidating concrete, (3) cementitious grout, and (4) reinforcing steel. For each material type, such as conventional concrete, there were multiple castings generally resulting in different material properties. Therefore, each batch of concrete, type of grout, and type of reinforcing steel are discussed separately and are given an individual identification code. A color-coded material schematic is presented for CIP, HCNP, HCPP, GCNP, and GCPP in Figure 4-1 through Figure 4-5, respectively. The material schematic indicates the material used in each portion of the column model. At the end of this section, a summary of all material properties is provided.

4.2.1 Conventional Concrete

The specified 28-day compressive strength of concrete was 4500 psi [31 MPa], and the target slump was 6 in [152 mm]. Prior to casting, the slump of concrete was measured according to ASTM C143. If the measured slump was not within ± 1.0 in [25 mm] of the target value, water and/or plasticizer were added until the slump reached the satisfactory range.

4.2.1.1 Conventional Concrete 1 (CC1)

Conventional concrete 1 (CC1) was used to construct the footings for CIP and GCNP. The slump of the concrete was 5 in [127 mm], and this was considered satisfactory. The measured 7-day and 28-day compressive strengths of CC1 were 3350 psi [23.1 MPa] and 4695 psi [32.3 MPa], respectively. The compressive strength test data for CC1 is shown in Table 4-1.

4.2.1.2 Conventional Concrete 2 (CC2)

Conventional concrete 2 (CC2) was used to construct the footings for HCNP and HCPP. The initial slump of the concrete was 4.5 in [114 mm]. Five gallons [18.9 L] of water were added to the mix and the slump increased to 5 in [127 mm], which was satisfactory. The measured 7-day and 28-day compressive strengths of CC2 were 3751 psi [25.8 MPa] and 5006 psi [34.5 MPa], respectively. The compressive strength test data for CC2 is shown in Table 4-2.

4.2.1.3 Conventional Concrete 3 (CC3)

Conventional concrete 3 (CC3) was used to construct the column and loading head for CIP. The initial slump of the concrete was 4.5 in [114 mm]. Three gallons [11.4 L]

of water was added to the mix and the slump increased to 5.5 in [133 mm]. The measured 7-day and 28-day compressive strengths of CC3 were 2759 psi [19.0 MPa] and 4115 psi [28.3 MPa], respectively. The compressive strength test data for CC3 is shown in Table 4-3.

4.2.1.4 Conventional Concrete 4 (CC4)

Conventional concrete 4 (CC4) was used to construct the footing for GCPP. The slump of the concrete was 6 in [152 mm]. The measured 7-day and 28-day compressive strengths of CC4 were 3666 psi [25.3 MPa] and 4871 psi [33.6 MPa], respectively. The compressive strength test data for CC4 is shown in Table 4-4.

4.2.1.5 Conventional Concrete 5 (CC5)

Conventional concrete 5 (CC5) was used to construct the precast column shells and pedestals for GCNP, GCPP, and HCNP. The initial slump of the concrete was 4.0 in [102 mm]. Two gallons [7.6 L] of plasticizer was added to the mix and the slump increased to 6.0 in [152 mm]. The measured 7-day and 28-day compressive strengths of CC5 were 2974 psi [20.5 MPa] and 3826 psi [26.4 MPa], respectively. The compressive strength test data for CC5 is shown in Table 4-5.

4.2.1.6 Conventional Concrete 6 (CC6)

Conventional concrete 6 (CC6) was used to construct the precast column shell for HCNP. The initial slump of the concrete was 4.0 in [102 mm]. One gallon [3.8 L] of plasticizer was added to the mix and the slump increased to 6.5 in [165 mm]. The measured 7-day and 28-day compressive strengths of CC6 were 2599 psi [17.9 MPa] and

3495 psi [24.1 MPa], respectively. The compressive strength test data for CC6 is shown in Table 4-6.

4.2.2 Self-Consolidating Concrete

The specified 28-day compressive strength of SCC was 4000 psi [27.5 MPa]. Caltrans minimum criteria (Table 3-4) was used to select target values for other critical SCC parameters: slump flow diameter ≥ 18 in [457 mm], visual inspection index (VSI) = 0.0, and static column segregation $\leq 15\%$. Prior to casting, the slump flow diameter and VSI were measured according to ASTM C1611. If the target values were not met, water and/or plasticizer were added to mix and the measurements were repeated until the target was reached. Per ASTM C1610, a static segregation test was complete once the target slump flow and VSI were reached.

4.2.2.1 Self-Consolidating Concrete 1 (SCC1)

Self-consolidating concrete (SCC1) was used to fill the hollow precast column shells of the GC models and to repair the bottom portion of the HCPP column shell. The initial slump flow diameter of SCC was 17.3 in [438 mm], which did not meet the target requirements. This slump flow did not conform to Caltrans SCC specifications thus 0.25 gal [0.95 L] of superplasticizer was added to the mix, and the slump flow increased to 20.3 in [514 mm]. The visual inspection index (VSI) for the first and second slump flow tests were 1.0 and 0.0, respectively. Figure 4-6 shows photos taken from both slump flow tests. A static segregation column test was also completed, and the coarse aggregate weights measured from the contents of the top and bottom segments of the static segregation column were 8.32 lb [37 N] and 10.3 lb [45.8 N], respectively,

resulting in a segregation of 21.1%. Although this percent segregation exceeded the target range, it is suspected that there was error in collecting the contents of the segregation column segments. When the contents of the middle column segment were discarded, some content volume flowed into the base segment. The measured 7-day and 28-day compressive strengths of SCC1 were 3612 psi [24.9 MPa] and 4303 psi [29.6 MPa], respectively. The compressive strength test data for SCC1 is shown in Table 4-7.

4.2.2.2 Self-Consolidating Concrete 2 (SCC2)

Self-consolidating concrete (SCC2) was used to fill the hollow precast column shells of HCNP and HCPP. The initial slump flow diameter was 16.5 in [419 mm] and the VSI was 1.0. In order to achieve the target slump flow diameter and VSI, 6 gal [22.7 L] of water and 2 gal [7.6 L] of superplasticizer were added to the mix in two separate iterations, respectively. The slump flow and VSI after the addition of water were 17 in [432 mm] and 1.0, respectively. After addition of superplasticizer, the slump flow and VSI were 25.3 in [643 mm] and 0.0, respectively. Figure 4-7 shows photos taken from first and final slump flow tests. The course aggregate weights measured from the contents of the top and bottom segments of the static segregation column were 10.3 lb [45.8 N] and 11.1 lb [49.4 N], respectively, resulting in a segregation of 7.5%. The average measured 7-day and 28-day compressive strengths of SCC2 were 3505 psi [24.1 MPa] and 5240 psi [26.1 MPa], respectively. The compressive strength test data for SCC2 is shown in Table 4-8.

4.2.3 Cementitious Grout

Three different pre-packaged cementitious grouts were used with different manufacturer specified 28-day compressive strengths: G1 = 8,200 psi [56.5 MPa], G2 = 5,800 psi [40 MPa], and G3 = 12.5-14.6 ksi [86-100 MPa]. Per ASTM C109, the compressive strength of grout was measured using the average of three 2-in [51-mm] cube samples.

4.2.3.1 Cementitious Grout 1 (G1)

Cementitious grout 1 (G1) was used to fill the corrugated steel ducts in the pedestals of HCPP and GCPP and was also used for grouting the interface between column shells and footings or pedestals for all precast models. The average 7-day and 28-day cube compressive strengths for G1 were 5724 psi [39.4 MPa] and 7713 psi [53.1 MPa], respectively. Table 4-9 lists the results from the individual cube tests of G1.

4.2.3.2 Cementitious Grout 2 (G2)

Cementitious grout 2 (G2) was used to fill the coupler region of HCNP and HCPP. The average 7-day and 28-day cube compressive strengths for G2 were 5942 psi [40.9 MPa] and 7319 psi [50.4 MPa], respectively. Table 4-10 lists the results from the individual cube tests of G2.

4.2.3.3 Cementitious Grout 3 (G3)

Cementitious grout 3 (G2) was the proprietary grout provided by the Splice Sleeve Company used to fill the grout-filled sleeve couplers in GCNP and GCPP. The average 7-day and 28-day cube compressive strengths for G3 were 12837 psi [88.4 MPa] and

15638 psi [107.7 MPa], respectively. Table 4-11 lists the results from the individual cube tests of G3.

4.2.4 Reinforcing Steel

4.2.4.1 Number 3 Bar Reinforcing Steel (S3)

A single lot of No. 3 reinforcing bars was used in the construction of column models. Referred to as “S3, these bars were used to construct spirals for the transverse reinforcement in all models. The average measured yield stress, ultimate stress, and percent elongation at rupture for S3 bars were 81.8 ksi [564 MPa], 112 ksi [768 MPa], and 15.4%. S3 bars did not have a defined yield point thus a 0.2% offset was used to determine the stress at yield. The average elongation at rupture was determined using strain from samples that failed within the specified extensometer gage length (samples 2 and 3). The measured stress-strain behavior of the S3 samples is shown in Figure 4-8. Photos of the tension samples after testing are shown in Figure 4-9. A summary of material properties for S3 is listed in Table 4-12.

4.2.4.2 Number 8 Bar Reinforcing Steel 1 (S8-1)

The first lot of No. 8 reinforcing bars (S8-1) was used for longitudinal reinforcement in CIP, GCNP, and GCPP; these bars were ASTM A615 bars. The average measured yield stress, ultimate stress, and percent elongation at rupture for S8-1 bars were 66.8 ksi [460 MPa], 111.3 ksi [767 MPa], and 15.8%. The average elongation at rupture was determined using strains from samples 1, 2, and 4, which fractured within the extensometer gage length. The measured stress-strain behavior of the S8-1 samples is

shown in Figure 4-10, and photos samples after testing are shown in Figure 4-11. A summary of material properties for S8-1 is shown in Table 4-13.

4.2.4.3 Number 8 Bar Reinforcing Steel 2 (S8-2)

The second lot of No. 8 reinforcing bars (S8-2) was used for longitudinal reinforcement in the column shells and footings of the HC models. These bars were ASTM A706 bars provided by HRC and came with deformed heads for the 500/510 couplers. The average measured yield stress, ultimate stress, and percent elongation at rupture for S8-2 bars were 68.0 ksi [468 MPa], 95.1 ksi [655 MPa], and 18.2%. The average elongation at rupture was determined using measured strains from samples 1, 2, and 5, which fractured within the extensometer gage length. The stress-strain behavior for S8-2 samples is shown in Figure 4-12, and the samples after testing are shown in Figure 4-13. A summary of material properties for S8-2 is listed in Table 4-14.

4.2.4.4 Number 8 Bar Reinforcing Steel 3 (S8-3)

The third lot of No. 8 reinforcing bars (ASTM A706), denoted S8-3, was also provided by HRC. S8-3 bars were used for the transition bars between the HC model shells and footing dowels. The average measured yield stress, ultimate stress, and percent elongation at rupture for S8-3 bars were 67.5 ksi [465 MPa], 95.1 ksi [655 MPa], and 15.9%. The average elongation at rupture was determined using measured strains from samples 3 and 5, which fractured within the extensometer gage length. The measured stress-strain behavior for S8-3 samples is shown in Figure 4-14, and photos of the tension samples after testing are shown in Figure 4-15. A summary of material properties for S8-3 is shown in Table 4-15.

4.2.5 Summary of Material Properties

A summary of the average final slump measurements, 7-day compressive strengths, and 28-day compressive strengths for the conventional concretes is presented in Table 4-16. A summary of average materials properties for the self-consolidating concretes is shown in Table 4-17. The average 7-day and 28-day compressive cube strength results for the cementitious grouts are shown in Table 4-18. A summary of the average measured reinforcing steel properties is shown in Table 4-19.

4.3 Data Processing Methods and Result Presentation Order

Each type of experimental result is presented in a separate section. There are a number terms or phrases used to describe the direction of loading, locations on the surface of the column, and locations of the internal reinforcing steel. A drawing is provided in Figure 4-16, which indicates the orientation of the test set-up and commonly used terms or phrases associated with discussion of the test results. Note that “left” and “right” designation depend on the view point.

4.3.1 General Observations

The observed damage at various drift levels, drops in the measured lateral load, adjustments in axial load during the tests, and any deviation from the target loading protocol are discussed in this section.

4.3.2 Failure

The primary failure mechanism for all models was rupture of longitudinal bars. The locations of bar rupture were not evident during the tests for most models. Therefore, concrete was removed in parts of the plastic hinge region and footing of select models

after testing to locate ruptured bars. This section presents the findings after concrete removal. Furthermore, couplers were removed from HCNP and GCNP in order to inspect them for damage. These findings are also presented in this section.

4.3.3 Force-Displacement Response

This section presents the measured force-displacement relationships. The full hysteresis response of the column is shown first. Hysteresis curves are plotted as force (y-axis) versus percentage drift (x-axis). The force shown in these plots was recorded directly from the load cell on the actuator used to apply lateral load to the column. The column drift was calculated by taking the average of the data from the four string pot displacement transducers that recorded the deflection of the column loading head and dividing that average by the column height (footing surface to the lateral loading point) of 108in [2743mm]. In the hysteresis curves, positive force and drift correspond to push cycles where the column head was traveling from West to East.

An average hysteresis backbone curve was calculated by taking the average of the envelopes on the first push and pull cycle for each drift level. In some instances, in order to get a smoother backbone curve, extra points were taken between maximum drift levels. To determine the effective yield point, the backbone envelope was idealized by an elasto-plastic curve. This was accomplished by balancing the areas enclosed by the idealized and actual force-displacement envelopes. The ascending branch of the idealized curve was defined by a line that passed through the origin and a point corresponding to the average force associated with the first longitudinal bar yielding on the backbone curves.

The idealized force-displacement response was used to determine the displacement ductility capacity of each column model.

4.3.4 Measured Strains

During each imposed drift cycle, strains were recorded continuously from gages on reinforcing steel bars and grouted couplers in the GC models. This section presents the maximum and minimum strains for each cycle of various drift levels and the tensile strain profiles within the plastic hinge region. Positive strains indicate tension and vice versa.

The peak strain data are presented in tables in Appendix A. Each table lists strains at a single level of longitudinal, transverse, or coupler strain gages. Tables identify the strain gages by numbers corresponding to those shown in the Chapter 3 strain gage instrumentation schematics. Strains exceeding the measured yield strains are shown in **bold**. The word “Dead” identifies gages that were unresponsive, did not function properly prior to the beginning of testing, or malfunctioned shortly after loading commenced. Furthermore, a “-” is shown if a gage malfunctioned later during the test.

The plastic hinge strain profiles shown in this section reflect the average recorded strains during the first cycle of each drift level. For example, during push cycles, strains recorded from the right, center, and left reinforcing bars (refer to Figure 4-16) located on the West side of the column were averaged. The average strains that occurred at peak drift levels are the ones shown in the profile plots. Similarly, during pull cycles, these average strains were determined with measurements from the right and left bars on the East side of the column.

4.3.5 Measured Curvature and Bond Slip

The curvatures, bond-slip rotations, and pedestal joint rotations were measured using LVDTs mounted on the East and West faces of the column. The nominal gage length for each LVDT was 7 in [178 mm]. The actual gage lengths, due to construction tolerances and misplacement, were slightly different. Therefore prior to each test, the actual gage lengths were measured to be used during data processing. The distance between each LVDT rod and the face of the column was also measured. The curvature calculated for a given location of LVDT gage pairs was determined by Equation 4-1. A representative diagram depicting the variables used in Eq. 4-1 is shown in Figure 4-17. The curvatures are presented in the form of profiles that depict location above the footing versus curvature. The location of each data point relative to the footing surface is defined by the average height of the LVDT gage lengths used to calculate the curvature. This is indicated in Figure 4-17 by h_{avg} .

$$\varphi = \tan^{-1} \left(\frac{\frac{\Delta L_1}{L_1} - \frac{\Delta L_2}{L_2}}{D + d_1 + d_2} \right) \quad (4-1)$$

Where

- φ = Average curvature
- $\Delta L_1, \Delta L_2$ = Displacement measurement from LVDT
- L_1, L_2 = Initial gage length of transducers
- D = Diameter of the column
- d_1, d_2 = Distance between the column face and the LVDT rod

The bond-slip and pedestal joint rotations were calculated using an approach similar to that used for curvature. The difference was that the numerator in Eq. 4-1 was ΔL_1 less ΔL_2 . Both bond-slip and pedestal joint rotations were plotted versus the moment that occurred at the column base and pedestal joint, respectively. Moment was calculated by multiplying the measured actuator load by the distance from the loading point to the location of interest. These distances from the loading point to the column base and pedestal joint were 108 in [2.74 m] and 96 in [2.44 m], respectively.

4.3.6 Energy Dissipation

The energy dissipation capacity was determined by calculating the area enclosed by the force-displacement hysteresis loops. For each model, the energy dissipated per cycle and the cumulative energy dissipated are presented in a table. A plot of the cumulative energy dissipation is also presented.

4.4 Model Results

Prior to discussing model results, the day-of-test properties for cementitious material are discussed. Table 4-20 provides a complete summary of material properties for each model.

4.4.1 CIP

CIP was constructed with conventional concrete CC1 (footing) and CC3 (column and loading head). The day CIP was tested the average compressive strengths for CC1 and CC3 were 5413 psi [37.3 MPa] and 4446 psi [30.6 MPa], respectively. A summary of these material properties is shown in Table 4-21 and the material schematic is shown in Figure 4-1. During testing, the measured axial load from CIP varied from 187-222 kips

[832-987kN], which corresponds to a maximum difference of 11% compared to the target of 200 kip [890 kN].

4.4.1.1 General Observations

Figure 4-18 through Figure 4-26 depict the damage in CIP at various drift levels. Below 1% drift, well-distributed flexural hairline cracking was observed (Figure 4-18 and Figure 4-19). By 2% drift (Figure 4-20), flexural cracks began to open to approximately 0.04 in (1.0 mm) in width and inclined shear cracks began to form. Cracks also began to form in footing radiating outward from the column at this drift level. The axial load was adjusted to 199 kip (885 kN) to account for slight increases during the larger drift cycles prior to the 3% drift cycles. Minor spalling occurred on the East and West faces of the column during the first full cycle of +3% drift (Figure 4-21). At the end of the 4% drift cycles (Figure 4-22), spalling had become more extensive and transverse bars were visible on the East and West faces of the column. Numerous transverse reinforcing bars were visible, crack widths were in excess of 0.08 in (2 mm), and shear cracks propagated at the end of the 5% drift cycles (Figure 4-23). Strain penetration into the footing was also evident at the end of the 5% cycles. The longitudinal bars first became visible during the 6% drift cycles (Figure 4-24). Prior to beginning cycles of 8%, the axial load was adjusted to 195 kip (867 kN) to avoid excessive overshoot of the axial load when 8% drift is applied. After completing the 8% drift cycles, multiple longitudinal bars were visible on both sides of the column, cracks had become very wide, and delamination of footing concrete had occurred due to strain penetration. Damage began to penetrate into the confined concrete core after the first full cycle of 10% drift. During the second cycle

of +10% drift, longitudinal bars began to buckle on the East side of the column. When subjected to the following cycle of -10% drift, a longitudinal bar fractured on the East side of the column at -8%. It was decided to subject CIP to one extra half cycle of +10% drift. During this cycle, two longitudinal bars fractured on the West side of the column and a transverse bar fractured on the East side.

4.4.1.2 Failure

Figure 4-27 depicts the failure mechanisms in CIP. Failure was governed by buckling of the longitudinal reinforcing steel, followed by rupture of longitudinal bars. Rupture of longitudinal bars occurred 3 in (76 mm) to 12 in (305 mm) above the surface of the footing

4.4.1.3 Force-Displacement Response

The hysteretic lateral force-displacement response of CIP is shown in Figure 4-28, and the peak loads and displacements for each drift level are listed in Table 4-22. The hysteresis behavior is stable with minimal strength degradation occurring during the second full drift cycles. The loops of the hysteresis curve are wide, which indicates good energy dissipation. The curve is symmetric except for a small hump at approximately 2.5% drift where the lateral load drops slightly. This drop in load is due to spalling of concrete on the East side of column. After completion of the test, it was observed that the column reinforcing cage was offset to the West by approximately 0.75 in (19 mm). This means that the cover on the East side of the column was greater than that of the West side. This increased cover explains the hump in the hysteresis curve and drop in load at +2.5% drift. A drop in lateral load can be observed at -8% drift during the second

cycle of -10.0% drift, which corresponds to the first longitudinal bar rupture. Two more drops are shown at +7.5% and +9.5% drift during the third cycle of +10%. These correspond to transverse and longitudinal bar fractures, respectively.

The envelopes of hysteresis curves were determined to develop push-over response of the column. The average envelope for the positive and negative regions and elasto-plastic curves are shown in Figure 4-29. The envelope is approximately linear until 1.5% drift. After this point, the force tends to increase slightly until 10% drift where a maximum lateral load capacity of 69.2 kip (308 kN) was reached. The first yield point was determined by examining the strain measurement from the longitudinal reinforcing bars and recording the displacement and load at which the strain exceeded yield. The measured first yield of CIP occurred at a displacement of 0.86 in (21.8 mm). The effective yield displacement was determined by balancing the areas between the plastic branch of the elasto-plastic curve and the force-displacement envelope. The effective yield displacement was 1.46 in (37mm). The corresponding effective yield force and moment were 66 kip (294 kN) and 7128 kip-in (805 kN-m), respectively. The displacement ductility capacity of CIP was 7.36, which was based on the displacement the first longitudinal reinforcing bar fractured.

4.4.1.4 Measured Strains

The longitudinal reinforcing bar strain profiles is shown in Figure 4-30. Figure 4-30a and b represent that average profile from the push cycles. This reflects measurements from the West face of the column. Figure 4-30c and d represent the average profile from the pull cycles. This reflects measurements from the East face of the column. The strains

recorded for each cycle at peak drift are shown in Table A-1 through A-10. It can be observed that for drift cycles less than 1%, the strains are low and evenly disburse. This is because the onset of yielding begins during the end of 1% drift cycles. At 2% drift, yielding occurred in the bars on both East and West faces of the column thus the strains increased significantly. It can be observed in Figure 4-30b and d, that after 3% drift the plastic hinge strains are well distributed and substantial yielding has occurred throughout the lower 24 in [610 mm] of the column and penetrated into the footing.

4.4.1.5 Measured Curvature and Bond-Slip

The plastic hinge curvature profiles are shown in Figure 4-31 through Figure 4-32. At the lower drift levels (Figure 4-31), the curvatures are concentrated in the 1-in (25.4-mm) region above the footing. Below 1% drift the curvature in this region is small because the longitudinal bars have not yielded and bond-slip is not yet significant. The curvatures at the column base double in magnitude at 2% drift because of reinforcement yielding. At the higher drift levels (Figure 4-32), the curvatures at the base of the column are greatest due to yielding and bond-slip. Yet, it can be observed that the curvatures 4 in (102 mm) to 15 in (351 mm) above the footing increase significantly during the higher drift cycles. Due to the spread of yielding through the plastic hinge, these curvature profiles above 4 in [102 mm] become fairly well distributed.

Figure 4-33 depicts the relationship between moment and bond-slip rotation at the base of the column. The maximum rotation is 0.032 rad.

4.4.1.6 Energy Dissipation

The energy dissipation for CIP was calculated by integrating the area enclosed by each hysteresis loop. Table 4-23 shows the calculated energy dissipation at each drift level for both cycles and the cumulative energy dissipation. Figure 4-34 depicts the cumulative energy as a function of drift. The main energy dissipation source in CIP was yielding of reinforcing steel. Therefore, it can be observed that at low drift levels the cumulative energy dissipation is low. At 4% drift, the cumulative energy dissipation begins to increase linearly for yielding has occurred in numerous bars. The total cumulative energy dissipated by CIP by the end of the second full cycle of 10% drift was 7869 kip-in (888 kN-m).

4.4.2 HCNP

The footing of HCNP was constructed with concrete CC2, which had a measured day-of-test compressive strength of 5646 psi (38.9MPa). Concrete CC6 was used to construct the precast column shell and had a day-of-test compressive strength of 3860 psi (26.6 MPa). The region where the coupler connection was made was grouted with G2, which had a cube compressive strength of 8303 psi (57.2 MPa) on the day of testing. Finally, the core of HCNP was filled with SCC2. On the day of testing, SCC2 had a measured compressive strength of 5835 psi (40.2 MPa). A summary of the measured day-of-test material properties is shown in Table 4-24. During testing, the measured axial load from HCNP varied from 187-222 kips [832-987kN], which corresponds to a maximum difference of 11% compared to the target of 200 kip [890 kN].

4.4.2.1 General Observations

Figure 4-35 through Figure 4-44 show photos of damage observed in HCNP at the various drift levels. Two dashed lines can be observed on the columns. These lines indicate the approximate location of the center of the HRC couplers within the column. During the drift levels below 1% (Figure 4-35), thin and well distributed flexural cracks were observed to form. During 0.75% drift, some of the cracks in the precast column began to become inclined and formed shear cracks. By 1.0% drift (Figure 4-36), shear cracks were connected to the flexural cracks on the other side above the grouted closure region. Cracks in the footing also began to form in the radial direction outward from the column base at the 1% drift level. During the 2.0% drift cycles (Figure 4-37), concentrated cracks began to form directly above the lower coupler indication line and at the joint between the footing and column. The widths of these cracks at 2.0% were 0.04 in [1 mm] and 0.08 in [2 mm], respectively. A few vertical cracks had also begun to form in the grouted closure region. During the second cycle of -2.0% drift, minor spalling of grout occurred on the West side of the column. Spalling can be observed in Figure 4-38, which depicts the second cycle of 3.0% drift. During these cycles, transverse reinforcing bars and couplers became visible. The widths of the concentrated cracks at the base of the column and above the coupler indication line were 0.12 in [3 mm] and 0.08 in [2 mm], respectively. At 4.0% drift (Figure 4-39), spalling on the West face of the column had extended upwards, the concentrated crack at the column base had a width of approximately 0.14 in [3.5 mm], and multiple transverse bars were visible. Substantial strain penetration into the footing had occurred by 5.0% drift (Figure 4-40). Figure 4-40a depicts the concentrated crack that developed above the lower coupler layer.

After 5.0% drift, the width of this crack was approximately 0.16 in [4 mm]. When 6.0% drift was reached (Figure 4-41), the lower part of headed coupler had become completely visible on the East face of the column along with longitudinal bars. By 8.0% drift (Figure 4-42), it was apparent that damage to the confined grout core began to occur. Extensive damage had been accumulated in the footing near the column base due to strain penetration. During the second cycle of -10%, a load noise was heard originating from the East side of the column and a drop in lateral load bearing capacity was observed. The damage sustained to the column by 10.0% drift is shown in Figure 4-43. After the second cycle of -10.0% drift, it was decided to push the column to +12.0%. During this cycle, a second loud noise was heard and a drop in lateral load was observed. Buckling of longitudinal bars and kinking of transverse bars was also observed during 12.0% drift (Figure 4-44).

4.4.2.2 Failure

In order to locate where the bars had ruptured, concrete was removed from the plastic hinge region and portions of footing of HCNP (Figure 4-45). One bar (center bar) was found to have ruptured just below that surface of the footing on the West side of the column. Figure 4-46 depicts the second ruptured bar that was found. This bar was located on the East side of the column and had fractured approximately 2 in [51 mm] above the surface of the footing.

In order to examine if any damage had been sustained to the couplers, the lower HRC coupler was removed from the center bar on the West face of the column. This bar had ruptured as noted above. There was no apparent damage in the coupler. Although no

damage was apparent, there was a considerable amount of play within the threaded collar. That is, the portions of bar that protruded from the coupler could move freely over the length of approximately 0.08 in [2 mm] in longitudinal direction. This finding confirms the hypothesis that opening and closing of a gap between the deformed heads of the HRC coupler occurs during load thus causing slight pinching in the hysteretic loops, which will be discussed in the next section.

4.4.2.3 Force-Displacement Response

The hysteretic force-displacement response of HCNP is shown in Figure 4-47. The peak force and displacement measurements for each drift level are shown in Table 4-25. The force-displacement behavior of HCNP is approximately linear up to 1.5% drift. At 2.0% drift, the force-displacement relationship begins to flatten out at 65.7 kip [292 kN] and 62.7 kip [279 kN] for the push and pull cycles, respectively. After 2.0% drift, the peak forces in the hysteresis loops remain stable. It can be observed that the loops are wide, indicating good energy dissipation, and there is minimal strength degradation at the higher drift levels. During the return to zero load, a small pinch can be identified on each loop. The reason for the pinching is as follows: when the longitudinal bars are under tension, the headed ends separate from the filler washers that were inserted between the heads during construction and a gap is formed. Upon reversal of the load, these bars go into compression, but the compression occurs after the gap is closed. The column rotates without significant resistance during the gap closure leading to the pinching. The first longitudinal bar rupture is reflected in the drop in the lateral load during the second cycle

of -10.0%. The second bar rupture corresponds the drop in lateral load that occurs during the cycle to +12.0% drift.

The average hysteresis envelope and elasto-plastic curves for HCNP are shown in Figure 4-48. The curve is approximately linear until 1.5% drift. After this point, the curve tends to increase only slightly until 10% drift where a maximum average lateral load capacity of 68.8 kip [306kN] was reached. The idealized elasto-plastic behavior is shown in black. The idealized curve was obtained using the same procedure as that used in CIP. From the idealized elasto-plastic curve, the effective yield displacement was 1.64 in [42 mm]. The corresponding effective yield force and moment were 67.5 kip [300 kN] and 7290 kip-in [823 kN-m], respectively. The displacement ductility capacity of HCNP was 6.49.

4.4.2.4 Measured Strains

A summary of the recorded longitudinal and transverse reinforcing bar strains for each drift level is shown in Tables A-11 through A-15 and Tables A-16 through A-18, respectively. Figure 4-49 depicts the average longitudinal tensile strain profiles. There are two horizontal solid lines shown that represent the approximate locations of HRC coupler centers in the column. Up to 1.0% drift, the measured strains are evenly distributed and small for yielding of reinforcement has not yet occurred. As mentioned in the previous section, the average first yield point occurred during the 2.0% cycles at 1.2% drift. It can be observed that the longitudinal bar strains near the column-footing interface become substantially larger (in excess of 9000 $\mu\epsilon$) during the 2.0% drift cycles. By 3.0% drift, yielding of reinforcement has propagated throughout the plastic hinge and

into the footing. Furthermore, the distribution of strains within the hinge is evenly disbursed. A maximum average strain of 50,435 $\mu\epsilon$ was recorded during the push cycles (+12.0% drift) and occurred 11 in [280 mm] above the surface of the footing. The maximum average measured strain was 66,395 micro-strains and was recorded during the pull cycles at 4 in [102 mm] below the footing surface. This occurred during -10.0% drift.

4.4.2.5 Measured Curvature and Bond-Slip

The curvature profiles in the plastic hinge zone are shown in Figure 4-50 and Figure 4-51. The two horizontal solid lines shown represent the approximate locations of the center of HRC couplers within the column. Before 2.0%, there is a uniform curvature profile from 4 in [102 mm] to 27.5 in [698 mm] above the footing. The curvatures within the bottom 1 in [25.4 mm] gage length remained under 0.002 in^{-1} (0.0508 mm^{-1}). During the 2.0% cycles, curvatures at the base of the column began to increase significantly due to yielding of reinforcement and initiation of bond-slip. Furthermore, the curvature gages in proximity to the coupler layers display higher curvatures due to slight gap opening of the headed reinforcing bars within the threaded coupler collars. This behavior continues until 8.0% drift when the distribution of curvature above the 4 in [102 mm] gage location become approximately linear. For all drift levels the maximum curvature occurs at the base of the column within the 1 in [25.4 mm] gage length. By 12% drift, the data from this location is no longer reliable because of significant delamination of footing concrete.

The moment versus bond-slip rotation relationship for HCNP is shown in Figure 4-52. It can be observed that significant bond-slip rotation begins to occur after 5000 kip-

in [565 kN-m] of applied moment or 1.0% drift. That maximum rotation due to bond-slip was 0.025 rads.

4.4.2.6 Energy Dissipation

The energy dissipation calculated for each cycle and the cumulative energy dissipation are listed in Table 4-26. There is not a substantial difference in the amount of energy dissipated in the first and second cycles of loading. A plot of the cumulative energy dissipation as a function of drift level is shown in Figure 4-53. Similar to CIP, the main energy dissipation mechanism in HCNP was yielding of longitudinal reinforcement. After 4.0% drift, the relationship between cumulative energy dissipation and drift is linear indicating that the hysteresis loops are stable. At 10% drift, the cumulative energy that was dissipated by HCNP was 7044 kip-in [795 kN-m]; 5.3% less than that of CIP.

4.4.3 HCPP

HCPP was constructed using conventional concrete CC2 for the footing and CC5 for the pedestal and a portion of the precast shell. The measured day-of-test compressive strengths for CC2 and CC5 were 5692 psi [39.2 MPa] and 4300 psi [29.6 MPa], respectively. SCC1 was used to repair the bottom portion of the precast shell that was found to have poorly consolidated concrete. SCC2 was used to fill the core of the precast shell and cast the loading head. The measured day-of-test strengths for SCC1 and SCC2 were found to be 5139 psi [35.4 MPa] and 5240 psi [36.1 MPa], respectively. Cementitious grout G1 was used in the pedestal ducts and G2 was used for closure of the coupler region. The measured day-of-test compressive cube strength for G1 and G2 were 7058 psi [48.6 MPa] and 7186 psi [49.5 MPa], respectively. These material properties

are summarized in Table 4-27. The material schematic for HCPP is shown in Figure 4-3. During testing, the measured axial load from HCPP varied from 190-224 kips [845-996 kN], which corresponds to a maximum difference of 7% compared to the target of 200 kip [890 kN].

4.4.3.1 General Observations

The damage that was accumulated by HCPP during testing can be observed in Figure 4-54 through Figure 4-63. In these photographs, three lines can be seen on the column; a solid line and two dashed lines. The solid line represents the top of the precast pedestal and the dashed lines indicate the approximate locations of the center of the HRC couplers. At drift levels below 1.0% (Figure 4-54), the column sustained only minor cracking damage. After the first full cycle of 0.25% drift, cracking at the pedestal-column joint had occurred. A crack had also formed at the top interface between the grout-closure region and the precast column shell (Figure 4-54a). By the end of the 0.75% drift cycles, well distributed flexural cracks had developed above the pedestal and opening began to occur at the pedestal-column joint. During the 1.0% drift cycles (Figure 4-55), flexural cracks began to turn to shear cracks in the precast column shell. Also a crack formed at the pedestal-footing joint. During the first cycle of +2.0%, the width of opening at the pedestal-footing and pedestal-column joints was approximately 0.04 in [1 mm]. Shear cracks had fully formed in the precast column shell during the 2.0% drift cycles (Figure 4-56). Spalling of concrete at the mid-height of the pedestal occurred during the first cycle of 3.0% drift (Figure 4-57). Figure 4-57a shows the pedestal-footing joint opening during the first cycle of +3.0% drift. The width of this

opening was approximately 0.12 in [3mm]. This increased to 0.19 in [5 mm] during the second cycle of -3.0% drift. Similarly, the opening of the pedestal-column joint was measured to be approximately 0.08 in [2 mm] and 0.12 in [3 mm] during the first and second cycles of 3.0%, respectively. Photos of the pedestal-footing and pedestal-column joints after the first cycle of 4.0% drift can be observed in Figure 4-58a and Figure 4-58b. After two full cycles of 4.0% drift (Figure 4-58c and d), several shear cracks were formed throughout the entire height of the column (including the pedestal), multiple spirals were visible on the East face of the pedestal, and some vertical cracks had formed in the grouted closure region. The corrugated steel ducts within the pedestal were visible after the 5.0% drift cycles (Figure 4-59). Spalling began within the grouted closure region on the East face of the column and concentrated cracking was observed in proximity to the lower coupler identification line. During the 6.0% drift cycles (Figure 4-60), delamination of concrete on the footing surface began to occur, and the crack widths at the pedestal-footing and pedestal-column joints were 0.39 in [10 mm] and 0.16 in [4 mm], respectively. The damage to the footing became more severe during 8.0% drift (Figure 4-61), and significant spalling had occurred within the grouted closure region such that multiple spirals were visible. After 8.0% drift, it was also observed that damage was beginning to penetrating into the confined core of the pedestal. Three consecutive drops in lateral load capacity were observed during the second cycle of +10.0% drift (Figure 4-62). It was also evident that damage was penetrating in the confined core of the grouted closure region (Figure 4-62b), longitudinal bar had become visible in the grouted region, and longitudinal bars began to buckle at the pedestal-footing joint due to

loss of cover concrete. The column was then subjected to a single cycle of -12.0% drift (Figure 4-63). During this cycle the lateral load dropped.

4.4.3.2 Failure

After testing, portions of concrete from the pedestal and footing were removed to locate fractured bars. It was found that all four drops in lateral load were caused by fractured bars. Furthermore, the location of fracture was found to be the same for all bars. Figure 4-64 depicts the location of 3 of the bar fractures on the West face of HCPP. It can be observed that all three bars broke within the footing just below the top mat of reinforcing steel. Figure 4-65 shows the location of the fractured bar on the East face of HCPP. It can be seen that fracture occurred just below the top mat of reinforcement.

Each pedestal duct containing a fractured bar was removed for inspection and documentation. The removed bars and pedestal ducts are shown in Figure 4-66. An arrow on the right-hand side of each photo indicates the location where fracture occurred. Measurements were taken to determine how deep within the footing fracture occurred. The results are listed in Table 4-28. The average approximate depth at which fracture occurred was 5.13 in [130 mm].

4.4.3.3 Force-Displacement Response

The hysteresis force-displacement response of HCPP is shown in Figure 4-67. The measured peak force and displacement for each drift level are listed in Table 4-29. Figure 4-67 shows that HCPP exhibits good hysteretic response with wide, stable loops and negligible strength degradation. The hysteresis curve displays symmetric linear behavior up to approximately 1.5% drift. After this point, yielding of reinforcing steel

and spalling of the concrete cover occurs. After yielding, the peak lateral forces for different drift levels increased slightly due to strain hardening. The ultimate load in the positive and negative portions of the curve is approximately ± 70 kip [311 kN]. Similar to HCNP, slight pinching occurs in the response for drift levels after the 0.75% drift. The pinching is caused by closing of the gap in the headed bars within the HRC coupler.

The first drop in lateral load was recorded during the second cycle of +10.0% and occurred as the column passed +6.0%. Two more drops in lateral load were subsequently recorded during the same cycle at +7.0% and +9.5% drift. Once +10.0% drift was reached, the lateral load capacity of HCPP had decreased by 43%. The column was then pulled to a second cycle of -10.0%. During this cycle, the load-displacement response of HCPP was stable, thus it was decided to continue loading until the actuator ran out of stroke. A drop in load was recorded at -12.0% drift. The test was concluded as the actuator reached -13.0% drift.

The average force-displacement envelope is shown in Figure 4-68. The response is approximately linear up to 1.5% drift. The curve then flattens out and concludes at an ultimate load of 71 kip [316 kN]. The displacement ductility was calculated by idealizing the envelope with an elasto-plastic curve. Based on test data, the average first yield point occurred at 0.95 in [24.1 mm] (0.87% drift) displacement with corresponded to a lateral load of 40.2 kip [179 kN]. The effective yield displacement and load were 1.57 in [39.9 mm] (1.45% drift) and 66.4 kip [295 kN], respectively. The displacement ductility capacity of HCPP was 7.07, which was based on the displacement at which first longitudinal bar fracture occurred.

4.4.3.4 Measured Strains

The maximum recorded longitudinal and transverse reinforcing bar strains are listed in Tables A-19 through A-25 and Tables A-26 through A-30, respectively. Figure 4-69 depicts the average longitudinal tensile strain profiles. There are three solid lines shown on the strain profile plots. The lower most of these lines represents the top of the 12 in [305 mm] precast pedestal. The second two indicate the approximate center of the HRC coupler layers. There is an even distribution of strain throughout the hinge region up to 1.0% drift. Longitudinal reinforcement yielded during the 1.0% drift cycles causing a significant increase in strain during 2.0% drift. Initially, larger strains (10,000 $\mu\epsilon$ and greater) are only exhibited at the pedestal-footing joint just above the top of the pedestal. As the drift increases, yielding begins to spread upward along the length of the column and deeper into the footing. A well distributed strain profile is exhibited above the pedestal for drifts greater than 5.0%. The maximum average tensile strains occur at the pedestal-footing interface and exceed 35,000 $\mu\epsilon$. This result suggests that strain concentrations in proximity to the pedestal-footing joint caused bar ruptures below the surface of the footing. This is supported by the results presented in Section 4.6.2; all bar breaks occurred beneath the footing surface. The strain at the mid-height of the precast pedestal tends to remain lower than other locations within the plastic hinge. This suggests that the corrugated steel ducts and high-strength grout impede spread of strain in the reinforcing bars that pass through the pedestal.

4.4.3.5 Measured Curvature and Bond-Slip

The calculated curvature profiles at the base of the column are shown in Figure 4-70 and Figure 4-71. There are two horizontal solid lines shown. The lower line represents the top of the precast pedestal and the second indicates the approximate location of HRC coupler centers directly above the pedestal. The second layer of HRC couplers is not shown because they are outside the upper curvature gage lengths. Similar to HCNP, there is a uniform distributing of curvature up to 2.0% drift with the maximum curvatures occurring at the base of the column. Curvatures at the base begin to increase substantially after 1.0% drift due to yielding and strain penetration into the footing. Subsequently, between 2.0% and 8.0% drift, the highest curvatures outside the base segment occur at the pedestal-column joint. These large curvatures at the pedestal-footing and pedestal-column joints are consistent with the large gap opening that was observed at these joints during the test.

The moment versus bond-slip rotation and moment versus pedestal joint rotation relationships are shown in Figure 4-72 and Figure 4-73, respectively. Once yielding of reinforcement begins, which occurs between 1.0% and 2.0% drift under a moment of 4500 kip-in [508 kN-m], the bond-slip rotation begins to increase more with each drift level. The maximum calculated rotation due to bond-slip was 0.037 rads. The rotation at the pedestal-column joint begins to increase substantially after a moment (calculated at the joint) of 4000 kip-in [448 kN-m]. The majority of rotation occurring at the pedestal-column joint can be attributed to opening of the joint. The maximum calculated rotation at this joint was 0.0112 rads.

4.4.3.6 Energy Dissipation

Table 4-30 lists the calculated energy dissipation per drift cycle and cumulative values per cycle. A plot of the cumulative energy dissipation versus drift level can be observed in Figure 4-53. Similar to CIP, the main energy dissipating mechanism in HCPP was yielding of steel. At 10.0% drift the cumulative energy dissipated by HCPP was 7080 kip-in [799 kN-m].

4.4.4 GCNP

Conventional concrete CC1 was used to cast the footing of GCNP and CC5 was used for the precast shell. The measured compressive strengths of these two concretes on the day of testing were 5500 psi [37.9 MPa] and 4228 psi [29.1MPa], respectively. The core of the column shell and the loading head were cast with SCC1, which had a measured day-of-test compressive strength of 4997 psi [34.4 MPa]. The compressive cube strength of the grout used for the NMB couplers was 16,410 psi [113.1 MPa] on test day. A summary of these material properties is listed in Table 4-31. The material schematic for GCNP is shown in Figure 4-4. During testing, the measured axial load from GCNP varied from 196-221 kips [872-983kN], which corresponds to a maximum difference of 10.5% compared to the target axial load of 200 kip [890 kN].

4.4.4.1 General Observations

Figure 4-75 through Figure 4-82 depict the damage that was accumulated by GCNP during testing. A solid line in the columns indicated the top of the grouted coupler. During the 0.25% to 0.50% drift cycles, only minor flexural cracking was observed. Several cracks were observed above the coupler but within the coupler region cracking

was minor. Shear cracks began to form above the coupler region during the 0.75% drift cycles. Furthermore, a concentrated crack began to form near the solid line that indicated the top of the grouted couplers. Figure 4-76 depicts the damage during the cycles of 1.0% drift. Flexural cracks still appear well-distributed, shear cracks have extended, and more pronounced cracking begin to occur within the coupler region. After the 2.0% drift cycles (Figure 4-77), the crack above the coupler became visible with a width of approximately 0.06 in [1.5 mm]. All other cracks at the 2.0% drift level were of hairline width. It was also observed that a concentrated crack was forming at the column-footing joint. The crack width at the coupler line was 0.12 in [3 mm] during the 3.0% drift cycles (Figure 4-78). At this drift level, extensive shear cracking had formed and minor spalling of concrete had occurred at the base of the column. During cycles of 4.0% drift (Figure 4-79), spalling within the coupler region occurred, transverse reinforcement became visible, and cracking in the footing at the base of the column began to occur. The width of the concentrated crack at the top of the coupler region (Figure 4-79a) was 0.19 in [5 mm]. After the 5.0% drift cycles, multiple transverse bars on both sides of the column and a single couple sleeve on the West side were visible (see Fig. 4-79)., A concentrated crack width existed above the coupler region of 0.26 in [6.5 mm] after the 5.0% drift cycles. During the 6.0% drift cycles (Figure 4-80), extensive damage to the footing occurred due to strain penetration and spalling propagated above the coupler region. Subsequently, a large gap formed between the column and the footing (Figure 4-81a). A drop in the lateral load capacity was observed and a noise indicating bar fracture was heard from the East face of the column during the second cycle of -6.0% drift. During the first cycle of -8.0% drift a second drop in load was observed along with a sharp noise

form the West face of the column. After this cycle, severe damage to the footing was observed and numerous transverse bars became visible above the coupler region (Figure 4-82).

4.4.4.2 Failure

As described in the previous section, there were two drops in the lateral load during testing of GCNP. To determine the cause of load drops, some of the couplers were removed from the column after the test. Figure 4-83 depicts one of the locations where an NMB coupler was removed from the column. It was found that two bars had fractured below the surface of the footing. Figure 4-84 shows the couplers and fracture locations (indicated by the arrow) of these bars. A measurement from the base of the coupler to the end of the fractured bar indicates that both ruptures occurred approximately 4.25 in [108 mm] below the surface of the footing. These measurements are summarized in Table 4-32. Each coupler was inspected, and there was no indication of bar pull-out. Both coupler exhibited a shallow cone-shape region where grout had fractured adjacent to the opening of the coupler (Figure 4-85). This indicates that strain penetration occurred within the coupler.

4.4.4.3 Force-Displacement Response

The measured hysteretic force-displacement response of GCNP is shown Figure 4-86. The displacement and load measurements taken at the peak drift levels are listed in Table 4-33. GCNP exhibits a well-behaved hysteretic response with wide, stable loops. The response is approximately linear up to 1.5% drift and plateaus thereafter. The peak load in GCNP was 72.1 kip [321 kN], which occurred on the positive drift side of the curve.

The first drop in lateral load capacity experienced by GCNP occurred during the second cycle to -6.0%. A loss of 38% lateral load bearing capacity was recorded at -5.5% drift. The column was then subjected to a third full cycle of 6.0% without any abrupt changes in lateral load. It was then decided to push the column to a single cycle of +8.0% drift. During this cycle, a drop in lateral load was recorded at +7.0% drift. The cycle was completed and the column was returned to zero lateral load to conclude the test.

The average force-displacement envelope of the hysteresis curves for GCNP is shown in Figure 4-87. The response is approximately linear up to 1.0% drift. The curve rolls over to a plateau between 1.0% and 3.0% concluding at an ultimate load of 70.0 kip [311 kN]. The displacement ductility was calculated by idealizing the envelope with an elasto-plastic curve. Based on test data, the average first yield point occurred at 0.81 in [20.6 mm] (0.75% drift) displacement, which corresponded to a lateral load of 38.1 kip [169 kN]. The resulting effective yield displacement and load were 1.42 in [36.1 mm] (1.31% drift) and 66.9 kip [298 kN], respectively. The displacement ductility capacity of GCNP was 4.52.

4.4.4.4 Measured Strains

A summary of the maximum recorded longitudinal and transverse reinforcing bar strains is shown in Tables A-32 through A-34 and Tables A-35 through A-37, respectively. The maximum longitudinal strains recorded from the mid-height of the grouted couplers are listed in Tables A-38 and A-39. Figure 4-88 depicts the average longitudinal tensile strain profiles. The solid line shown in each plot represents the top of

the grouted coupler. The data point between 5 in [127 mm] and 10 in [254 mm] indicates the strain on the grouted coupler sleeve at mid-depth. Below 0.75% drift, strains are fairly well distributed throughout the plastic hinge region. The average first yield point for GCNP occurred just below the surface of the footing during the 0.75% drift cycles. The average strains above and below the coupler region increase substantially during the 2.0% drift cycles. By this drift level, yielding has penetrated into the footing and propagated well above the coupler region. It is evident from the profiles shown in Figure 4-88 that the presence of the grouted coupler causes the strains within the hinge to redistribute above and below the coupler regions. The largest average strain occurred within the footing for both push and pull cycles. Both the push and pull cycles achieved strains greater than 25,000 $\mu\epsilon$ within the footing. This result is consistent with the observed failure location of longitudinal reinforcing bars in GCNP, which occurred in the footing.

4.4.4.5 Measured Curvature and Bond-Slip

The curvature profiles at the base of the column are shown in Figure 4-89 and Figure 4-90. A single horizontal solid line is shown to represent the top of the grouted coupler sleeves. Below 2.0%, the distribution of curvature is uniform throughout the length of the plastic hinge region except for at the base where curvatures are larger due to bond-slip. After 2.0% drift, curvatures at the base continue to remain larger than those in other section due to yielding and strain penetration. The curvatures within the coupler region (below the solid line) tend to remain smaller due to the higher relative stiffness of the section. The data point set directly above the coupler line captures the concentrated

cracking that occurred in this location. That is, the curvatures tend to be larger in this location relative to other sections.

The calculated moment versus bond-slip rotation relationship for GCNP is shown in Figure 4-91. It can be observed that bond-slip rotation begins to increase substantially after 5000 kip-in [565 kN-m] of applied moment or 1.0% drift. This is because strain penetration begins to develop within the footing and into the grouted coupler sleeve. The maximum rotation due to bond-slip was 0.0129 rads.

4.4.4.6 Energy Dissipation

Table 4-34 lists the calculated energy dissipation per drift cycle and cumulative values per cycle. A plot of the cumulative energy dissipation versus drift level can be observed in Figure 4-92. Even with the presence of the ductile-iron grout-filled sleeve, GCNP exhibits good energy dissipation behavior. Similar to CIP, the main energy dissipating mechanism in GCNP was yielding of longitudinal reinforcement. Yet, this yielding predominately occurred above the coupler region and within the footing. At 6.0% drift the cumulative energy dissipated by GCNP was 3115 kip-in [352 kN-m].

4.4.5 GCPP

Conventional concrete CC4 was used in the construction of the GCPP footing, and CC5 was used for the precast pedestal and column shell. The day-of-test compressive strength for these two concretes were 5722 psi [39.4 MPa] and 4203 psi [29.0 MPa], respectively. The column shell core and loading head were cast with SCC1, which had a compressive strength of 5139 psi [35.4 MPa]. Grouts G1 (pedestal ducts) and G3 (NMB couplers) had compressive cube strengths of 7015 psi [48.8 MPa] and 15,840 psi [109.2

MPa], respectively. A summary of the day-of-test material properties for GCPP is shown in Table 4-35. The material schematic for GCPP is shown in Figure 4-5. During testing, the measured axial load from HCNP varied from 198-218 kips [881-970kN], which corresponds to a maximum difference of 9% compared to the target of 200 kip [890 kN].

4.4.5.1 General Observations

The apparent damage sustained by GCPP can be observed in Figure 4-93 through Figure 4-100. Two solid lines are drawn to indicate the pedestal-column joint (the lower line) and the top of the grouted coupler region (the upper line). Below 1.0% drift, evenly distributed flexural cracking occurred throughout the plastic hinge length (Figure 4-93). This included the formation of a crack at the pedestal-column joint. Flexural cracks continued to develop within the column during the 1.0% drift cycles, and some flexural cracks began to extend into shear cracks (Figure 4-94). The concentrated crack at the pedestal-column joint widened to measure 0.08 in [2 mm] wide during the 2.0% drift cycles (Figure 4-95). By this drift level, there was also a noticeable crack forming at the pedestal-footing interface, which measured 0.06 in [1.5 mm]. Shear cracks covering the face of the column and cracks in the footing were also observed during 2.0% drift. During 3.0% drift (Figure 4-96), spalling occurred on both sides of the pedestal, and the crack width at the pedestal-footing and pedestal-column interfaces became approximately 0.16 in [4 mm] and 0.14 in [3.5 mm], respectively. Multiple transverse bars within the pedestal were visible after two cycles of 4.0% drift, and the cracks at the pedestal-footing and pedestal-column joints continued to widen to the width of 0.28 in [7 mm] and 0.19 in [5 mm], respectively. Furthermore, spalling progressed into the East face of the column

shell. A crack became apparent during 5.0% drift (Figure 4-98) at the top of the coupler region. This is similar to that observed in GCNP. During this drift level, the cracks at the pedestal-footing and pedestal-column joints were 0.35 in [9 mm] and 0.19 in [5 mm] wide, respectively. Delamination of concrete on the surface of the footing began to occur during the first cycle of 6.0% drift (Figure 4-99) due to substantial strain penetration. The lateral load capacity of the column dropped during the first and second cycles of -6.0% drift. After two full cycles, severe damage in the footing had occurred and corrugated ducts within the pedestal became visible. The column was then subjected to two cycles of +8.0% drift (Figure 4-100). A third drop in later load was recorded during the second cycle.

4.4.5.2 Failure

After testing, portions of GCPP pedestal and footing were removed in order to identify the cause of the drops in lateral load. It was determined that rupture of longitudinal reinforcing steel was the reason for the drops in load. Another possible cause of failure could have been the pull-out of the bars from the couplers, however this did not occur. Similar to HCPP, the rupture location of the bars was in the footing. These ruptured bars are identified in Figure 4-101 and Figure 4-102. Rupture occurred approximately 4.94 in [125 mm] below the surface of the footing on average. Table 4-36 lists the approximate rupture location for each bar.

4.4.5.3 Force-Displacement Response

The measured peak load and displacement per drift cycle for GCPP are listed in Table 4-37. The hysteretic force-displacement relationship can be observed in Figure 4-103.

GCPP exhibits a stable hysteretic load-displacement response with wide loops and minimal strength degradation. The behavior is symmetric and approximately linear up to 1.0% drift. The curve then tends to flatten with a slight positive slope due to strain hardening. The measured maximum lateral load was 69.4 kip [309 kN], which occurred during the first cycle of +6.0% drift.

The first drop in lateral load capacity was recorded at -6.0% drift during the first cycle at that drift level. Loading continued and a second drop in load was observed during the second cycle of -6.0% drift. The column was then pushed to +8.0% drift followed by a return to -6.0% drift (third cycle). There were no abrupt changes in the lateral load bearing capacity during this cycle. The final drop in lateral load was recorded at approximately +7.0% drift during the second cycle of +8.0%.

The average force-displacement envelope for GCPP is shown in Figure 4-104. The response is approximately linear up to 1.0% drift. Thereafter, the curve exhibits a slight increasing slope due to strain hardening of the reinforcing steel, and the ultimate point is 69.2 kip [308 kN]. The displacement ductility was calculated by idealizing the envelope with an elasto-plastic curve. Based on test data, the average first yield point was 0.96 in [24.4 mm] (0.89% drift) displacement, which corresponded to a lateral load of 43.1 kip [192 kN]. The effective yield displacement and load were 1.41 in [35.8 mm] (1.3% drift) and 63.8 kip [284 kN], respectively. The displacement ductility of GCPP was 4.53.

4.4.5.4 Measured Strains

A summary of the maximum recorded longitudinal and transverse reinforcing bar strains is shown in Tables A-40 through A-45 and Tables A-46 through A-49,

respectively. The maximum longitudinal bar strains were recorded at the mid-height of the grouted couplers and are listed in Tables A-50 and A-51. Figure 4-105 depicts the average longitudinal bar tensile strain profiles. The two solid lines shown in each plot represent the top of the pedestal (lower line) and the top of the grouted coupler region (upper line). Below 1.0% drift, the average strain within the hinge region is below yield and the profile is uniform. As yielding occurs, the strains near the surface of the footing and within the precast pedestal begin to increase substantially. Similar to HCPP, the strain at the mid-height of the pedestal tends to be lower than that near the joints and within the footing. For the drift levels greater than 1.0%, the maximum strain occurs at the interface between the footing and pedestal. This suggests that strain concentrations within the footing caused the bar ruptures. For all drift levels, the strains within and above the coupler region remain below 11,000 $\mu\epsilon$.

4.4.5.5 Measured Curvature and Bond-Slip

The calculated curvature profiles within the plastic hinge region of the column are shown in Figure 4-106 and Figure 4-107. The two solid lines shown in each plot represent the top of the pedestal (lower line) and the top of the grouted coupler region (upper line). For all drift levels, the maximum curvatures are at the pedestal-footing interface (base of the column). Between 0.25% and 1.0% drift, the curvatures in the other portions of the column are small and uniformly distributed. The cracking that occurred at the pedestal-column joint is captured as the drift exceeds 1.0%. That is, there is an increase in the curvature represented by the data point just below the pedestal line.

Similar to GCNP, the curvatures at the mid-height of the grouted coupler region tend to be small. This indicates higher section rigidity relative to other sections in the column.

The moment versus bond-slip rotation and moment versus pedestal joint rotation relationships are shown in Figure 4-108 and Figure 4-109, respectively. Once yielding of longitudinal reinforcement begins, which occurs between 1.0% and 2.0% drift (moment of 5000 kip-in [565 kN-m]), the bond-slip rotation begins to increase more with each drift level. The maximum calculated rotation due to bond-slip was 0.0222 rads. The rotation at the pedestal-column joint begins to increase substantially after a moment (calculated at the joint) of 4291 kip-in [484 kN-m]. The majority of rotation occurring at the pedestal-column joint can be attributed to opening of the joint. The maximum calculated rotation at this joint was 0.0077 rads.

4.4.5.6 Energy Dissipation

Table 4-38 lists the calculated energy dissipation per drift cycle and cumulative values per cycle. A plot of the cumulative energy dissipation versus drift level can be observed in Figure 4-110. The presences of the pedestal and grout sleeve couplers forced yielding of the reinforcing steel, the main energy dissipating mechanism, to occur below the footing surface and at the pedestal-column joint. Yet, GCPP exhibits good energy dissipation capacity. At 6.0% drift the cumulative energy dissipated by GCPP was 3201 kip-in [362 kN-m].

5. Comparison of Test Model Performance

5.1 Introduction

This chapter compares the performance of the five column models. Similar to Chapter 4, each performance indicator used to compare column performance is briefly discussed prior to presenting data. The models will be compared in two groups: (1) models without pedestals (HCNP, and GCNP), and (2) those with pedestals (HCPP and GCPP). The performance of the models within each group are evaluated and compared with respect to CIP and between each other. The chapter is concluded by summarizing the comparison of the column models, identifying the effect of couplers within the plastic hinge, and the effect of using a pedestal.

5.2.1 Presentation of Results

The results are compared in the same order as those in Chapter 4: (1) apparent damage and failure, (2) force-displacement behavior, (3) energy dissipation, (4) strain measurements, and (5) moment-curvature relationships. Within Section 5.3, which compares models with pedestals, a sixth section is provided to investigate the behavior of the pedestal-footing and pedestal-column joints. In sections discussing damage, strain, and moment-curvature behavior, six significant drift levels were selected to compare performance of the models. The first two drift levels examined are 0.75% and 2.0% drift, which represent points prior to and after the first yield of the column models, respectively. The third comparison point is 4.0% drift because Caltrans SDC indicates the minimum required displacement ductility capacity for a seismic critical element is $\mu_D = 3.0$, which corresponds to approximately 4.0% drift for all the test models. Failure of

the GC and HC models occurred during 6.0% and 10.0% drift, respectively, thus these two points are discussed. Finally, 8.0% drift was selected as another point of comparison because it was a data point intermediate to the failure points of the GC and HC models. Table 5-1 provides a summary of the drift levels used for comparison and the significance of each drift level.

5.2 Comparison of Response of Models without Pedestals

5.2.1 Apparent Damage and Failure

Figure 5-1 through Figure 5-6 compare the apparent damage from models without a precast pedestal (HCNP and GCNP) with that of CIP, and Table 5-2 provides a summary of the damage once each drift level was reached. Prior to first yielding, all models exhibited well-distributed flexural cracking (Figure 5-1) and slightly inclined cracks. By 2.0% drift (Figure 5-2), the dispersion of flexural cracks among the models was still very similar. During the 4.0% drift, spalling of concrete occurred leaving transverse reinforcing bars visible and many shear cracks were formed in the three models (Figure 5-3). Furthermore, numerous cracks had formed in the top surface of footings at the base of the columns. The compressive strength of concrete in the footings was similar for the three models; the strengths for CIP, HCNP, and GCNP were 5413 psi [37.3 MPa], 5646 psi [38.9 MPa], and 5500 psi [37.9 MPa], respectively. The apparent damage within the plastic hinge region at 6.0% drift between the precast models and CIP was also very similar (Figure 5-4). All three models exhibited extensive spalling, wide cracks, and multiple transverse and longitudinal bars had become visible. The height of the spalled concrete in CIP, HCNP, and GCNP were approximately 14 in

[356 mm], 14 in [356 mm], and 18 in [457 mm], respectively. However, there were some differences observed from GCNP after the 6.0% drift cycles. Longitudinal bars fractured and extensive delamination of footing concrete was observed both of which were not observed in HCNP or CIP. Figure 5-5 depicts the damage that occurred during the 8.0% drift cycles. Although GCNP was considered to have failed during 6.0% drift, it is still shown because it was pushed to 8.0% drift after it had failed. Similar to the damage observed during 6.0% drift, all three models exhibit the same apparent damage except for the more severe damage in the footing of GCNP. Lastly, by the completion of the 10.0% drift (Figure 5-6), CIP and HCNP both exhibited damage to the confined core of concrete, longitudinal bar buckling, transverse bar kinking, and the rupture of multiple longitudinal bars resulting in failure.

The progression and amount of damage occurring in the precast models compared to that of CIP was similar. This is particularly true for HCNP, which exhibited identical progression and level of damage per drift level as CIP. The same can be said for damage accumulated by GCNP in comparison to CIP until 5.0%. After this point, GCNP began to exhibit extensive damage in the footing, buckling of bars below the footing, and bar fracture within the footing.

5.2.2 Force-Displacement Relationships

The hysteretic force-displace response of HCNP and GCNP are compared with CIP in Figure 5-7 and Figure 5-8, respectively. It can be observed that the hysteretic behavior of HCNP and GCNP are similar to that of CIP. The differences that can be observed include small variations in peak load per drift level and slight pinching that occurs during

the unloading portions of the HCNP curve. The similarities indicate that both HCNP and GCNP have approximately the same energy dissipation capacity as CIP up to certain drift levels. Figure 5-9 shows the superimposed hysteretic responses of HCNP and GCNP and indicates that both models have similar hysteretic behavior prior to failure of GCNP.

Figure 5-10 shows the force-displacement envelopes for CIP, HCNP, and GCNP. The ascending branches for the three curves are identical up to 2.0% drift. After 2.0% drift, the trajectory of each curve varies slightly, but the curves conclude at approximately the same ultimate load. Using the pushover envelopes, an idealized elasto-plastic curve was created for each model. The elasto-plastic curves are shown in Figure 5-11 along with the resulting displacement ductilities. Compared to CIP and GCNP the first yield load and displacement are higher for HCNP. This can be attributed to slight slippage occurring within the headed couplers, which results in displacement without increasing the lateral. It can be concluded that placing the mechanical couplers directly within the plastic hinge zone did not significantly affect the force-displacement relationships.

5.2.3 Energy Dissipation

Figure 5-12 depicts the cumulative energy dissipation as a function of drift. Having only minor differences, both precast models follow the trend exhibited by CIP. Below 3.0% drift, the three models appear to have the same energy dissipation capacity. After 3.0% drift, the energy dissipation in GCNP tends to be approximately the same as CIP while HCNP tends to have a slightly lower dissipated. As mentioned in Chapter 4, the main energy dissipation mechanism in all models was plastic deformation of steel. Figure 5-13 depicts the percent difference in energy dissipation of HCNP and GCNP relative to

CIP. For all drift levels, the energy dissipated by GCNP remains within $\pm 5\%$ of CIP. Prior to yielding of steel ($< 2.0\%$ drift), the amount of energy dissipated by HCNP tends to be significantly larger ($> 15\%$) than CIP. Yet, this is misleading because prior to yielding of reinforcing steel the energy dissipated per drift level is low, and it is not until 3.0% drift that the hysteresis loops begin to widen. At this point, the energy dissipated by HCNP tends to be lower than that of CIP by $5\% - 10\%$, a difference that could be due to experimental scatter.

5.2.4 Measured Strains

Figure 5-14 depicts the average longitudinal tensile strain profiles for CIP, HCNP, and GCNP. Discussion of how longitudinal strains were averaged is presented in Chapter 4, Section 4.3.4 “Measured Strains”. The data point at 7.25 in [184 mm] above the footing surface indicates the mid-height of the grouted coupler on the GCNP profiles. Other than the smaller strains measured at the coupler mid-height location, there is not a substantial difference between the profiles prior to 6.0% drift. This point can be more clearly seen in the graphs by considering the broken line that bypasses the strain in the grouted coupler show in the dash line. Once 6.0% drift is reached, a clear difference between HCNP and GCNP can be identified. HCNP exhibits a well distributed strain profile similar to that of CIP whereas GCNP exhibits concentrations of strain above the coupler region and within the footing. The strain concentration ultimately resulted in failure of the GCNP due to bar rupture within the footing. Although HCNP also failed due to bar rupture, the rupture locations were similar to that of CIP because of the similarities in strain distribution at larger drift levels.

Figure 5-15 presents the average transverse reinforcement strain profiles due to dilation of concrete in the compression zone. A diagram in the lower left-hand corner of Figure 5-15a denotes the locations where strain was recorded. The data in the plots reflects the average of the two gages during the first cycle of compression. Note that the measured yield strain in the transverse bars was 5072 microstrains. The maximum strains measured in the transverse bars were well below the yield strain; the only exception was the strains on their 8% and 10% drifts in CIP. There is not a substantial difference among the profiles until 4.0% drift is reached. At this point, the transverses strains measured in GCNP at 17.5 in [444 mm] above the footing begin to exceed those of CIP by a factor of 2 – 3. This area is just above the cast iron grout-filled couplers, and the increased strains indicate that dilation of concrete within the plastic hinge compression zone is being shifted above the couplers similar to the longitudinal strains. In contrast, the HCNP and CIP strains are comparable for all drift levels.

Figure 5-16 presents the average transverse reinforcement strain profiles caused by shear cracking and deformation. The diagram in the lower left-hand corner of Figure 5-16a depicts the locations where strain was recorded. The data shown in each plot reflects the average of these two gages for the first push and pull cycle of each drift level. No yielding of the transverse bars at these locations was noted for any of the drift levels in any of the specimens. HCNP and GCNP exhibit similar profiles and strain magnitudes for all drift levels compared to CIP.

5.2.5 Plastic Hinge Curvatures

Figure 5-17 shows the locations where curvature measurements were measured and the corresponding plastic hinge details for precast models without pedestals. Moments were calculated by multiplying the average lateral load recorded from the actuator and the distance between the loading point and mid-height of each respective section shown in Figure 5-17. The curvatures in subsequent figures are an average that was taken at peak displacement for the first push and pull cycle of each drift level. Figure 5-18 shows the average moment-curvature response recorded at Section-0, which captures the section response and the bond-slip within the footing. The moment-curvature behavior of HCNP and GCNP are approximately identical to that of CIP. Yet, if the curvature is plotted versus drift level, as shown in Figure 5-19, GCNP exhibits larger curvatures after 3.0% drift while HCNP and CIP exhibit approximately the same curvature-drift relationship. The higher curvatures in GCNP compared to HCNP and CIP come from higher bond-slip and strain penetration in the footing. Figure 5-20 depicts the moment-curvature behavior of Sections 1 to 4. As shown in Figure 5-17, both precast models contain couplers within Section-1, and the effect of these couplers is reflected in Figure 5-20a. Compared to Section-1 of CIP, HCNP tends to undergo higher curvature under the same applied moment indicating that after first yield (5000 kip-in [565 kN-m]) the section becomes slightly softer than CIP. The reduced section stiffness is a result of slight bar-slip occurring within the headed coupler. GCNP exhibited the same approximate section stiffness as CIP up to the yield point (≈ 6600 kip-in [745 kN-m]). After this point, GCNP exhibits significantly reduced curvature compared to CIP as a result of the substantially higher stiffness of the cast-iron grout-filled sleeves. Figure 5-20b depicts the response of

Section-2. Again, GCNP exhibits reduced section curvature due to the presence of the grouted couplers. Section-3 captures the effect of the second layer of headed couplers in HCNP and a small upper portion of the grouted couplers in GCNP (Figure 5-20c). After yielding occurs around 5000 kip-in [565 kN-m], the curvatures in the precast models are slightly higher than those measured in CIP. For HCNP, this is because of the slight slippage between the deformed heads with the threaded collars. Nevertheless, the behavior is similar to that of CIP. In the case of GNCP, the higher post-yield curvatures are a result of concentrated plasticity occurring above the grouted coupler region. The curvatures in Section-4 are comparable and small because the section is outside the hinge zone (Figure 5-20d)

5.3 Comparison of Response Models with Pedestals

5.3.1 Apparent Damage and Failure

Figure 5-21 through Figure 5-26 compare the apparent damage sustained by CIP, HCNP, and GCNP, and Table 5-4 provides a summary of damage at the selected drift levels. In these figures, the lower solid line on the precast models indicates the interface between the pedestal and the precast column shell. Prior to first yielding (Figure 5-21), thin, well distributed flexural cracks can be observed on the three models and a similar crack pattern can be observed on both pedestals. After yielding (Figure 5-22), shear cracks begin to form on the three models including the pedestals of both HCNP and GCNP. It was evident that gap opening began to occur at the pedestal-column joint in both precast models during 2.0% drift. By 4.0% drift (Figure 5-23), joint opening was also beginning to occur at the pedestal-footing interface in both precast models. By the

conclusion of this drift level, spalling had occurred and cracks had formed in the footings of all three models. Also, spalling was concentrated within the pedestal of the precast models. Upon the conclusion of 6.0% drift (Figure 5-24), spalling had occurred throughout the height of the precast pedestals and began to spread to the precast shells of HCPP and GCPP. Furthermore, numerous spirals and corrugated ducts within the pedestals had become visible and the joint openings at the pedestal-column and pedestal-footing interfaces had become quite large. During 6.0% drift, the longitudinal bars in GCPP ruptured within the footing resulting in significant delamination of concrete at the pedestal-footing interface. All three models exhibited damage in the footing by the conclusion of 8.0% drift but the extent of damage in the precast models was more significant than that of CIP (Fig. 5-25). The failure of HCPP was due to rupture of longitudinal bars within the footing during 10.0% drift. Figure 5-26 compares the apparent damage to HCPP and CIP. Both columns exhibit similar damage consisting of extensive spalling, visible bars, and damage penetration into the confined concrete core.

After the tests, broken bars within the footings of the precast model were located by removing concrete. It was discovered that rupture occurred at a depth of approximately 5 in [127 mm] in both HCPP and GCPP. Along with longitudinal strain data that will be presented in subsequent sections, these findings indicate that the pedestal with grouted ducts alters the hinging mechanism and results in strain concentrations within the footing.

5.3.2 Force-Displacement Relationships

The hysteretic force-displacement curves for HCPP and GCPP are compared with those of CIP in Figure 5-27 and Figure 5-28, respectively, and then superimposed in

Figure 5-29. The hysteresis data in Figure 5-27 and Figure 5-29 for HCPP was truncated at the second cycle of -10.0% drift for comparison purposes. Figure 5-27 shows that HCPP and CIP have approximately identical hysteretic behavior in terms of peak force per cycle and shape of each hysteretic loop. Similar to HCNP, the only difference between the two is slight pinching that occurs on the unloading cycles for HCPP due to slippage of the heads within the threaded coupler collar. It can be observed in Figure 5-28 that GCPP also exhibits hysteretic behavior similar to that of CIP prior to failure of GCPP. Yet, in the case of GCPP, there is no pinching during the unloading cycles and thus GCPP and CIP have same unloading branch trajectories. Comparing the response of HCPP and GCPP (Figure 5-28), it can be observed that both models have similar hysteresis behavior. This would indicate that, despite the different couplers used, the pedestal tends to govern the force-displacement relationship.

The average envelopes of the hysteresis curves and elasto-plastic curves are shown in Figure 5-30 and Figure 5-31, respectively. Table 5-5 lists the parameters and corresponding values that were used to construct the elasto-plastic curves and the displacement ductility capacities. CIP and the precast models have similar envelopes. The ascending branches of the curves are approximately the same until 1.0% drift and there is little difference in the stiffness thereafter. The three curves also tend to conclude at the same ultimate load but at different drift levels. Similarities in the envelopes and measured first yield points (Figure 5-31) resulted in very similar elasto-plastic curves. The main difference was the displacement ductility capacity for CIP and HCPP compared with GCPP, which were 7.36, 7.07, and 4.53, respectively.

5.3.3 Energy Dissipation

Figure 5-32 depicts the cumulative energy dissipation as a function of drift for the CIP, HCPP, and GCPP. The precast models follow the same trend exhibited by CIP with minor differences. Prior to 3.0% drift, the models appear to have the same energy dissipation capacity. After 3.0% drift, the energy dissipated by GCPP tends to be approximately the same as CIP, while the energy dissipation in HCPP is slightly lower compared to CIP. Figure 5-33 depicts the percent difference in energy dissipation of HCPP and GCPP relative to CIP. The energy dissipated by GCPP remains larger than that of CIP for all drift levels. Prior to yielding ($< 2.0\%$ drift), the energy dissipated by HCPP tends to be significantly larger ($> 15\%$) than CIP. Yet, this is misleading because prior to 2% drift the energy dissipated per drift level is low, and it is not until 3.0% drift that the hysteresis loops begin to widen. The energy dissipated by HCPP tends to be lower than that of CIP by 5% - 14% after 2.0%, which is in the range of experimental scatter.

5.3.4 Measured Strains

Figure 5-34 presents the average longitudinal bar strain profiles within the plastic hinge of HCPP and GCPP compared with those of CIP. The solid black line at 12 in [305 mm] above the footing surface indicates the pedestal-column joint on the precast models. The data point at 19.5 in [495 mm] above the footing on GCPP indicates the mid-height of the grouted coupler sleeve. The distribution of strain in the precast models above the pedestal tends to be similar to that of CIP neglecting the data from the mid-height of the grouted coupler on GCPP. For all drift levels, the average strain measured at the mid-

height (6 in [152 mm] above the footing) of the pedestals was significantly lower than that of CIP at the same location. Longitudinal bars passed through the pedestal via corrugated steel ducts that were filled with grout that had a compressive strength of 7000+ psi [48.2 MPa]. The high strength of the grout and confinement provided by the corrugated ducts improved the bond substantially and prevented spread of plasticity of the reinforcing bars within the ducts. By 6.0% drift, it can be observed that the presence of the pedestal results in increased strains within the footing of the precast models and these strains ultimately resulted in the rupture of bars. This observation is consistent with the finding from removing concrete within the precast model footings.

Figure 5-35 presents the average transverse strain profiles due to dilation of concrete in the compression zone. A diagram in the lower left-hand corner of Figure 5-35a indicates the locations where strain was recorded. The data in the plots reflects the average of the two gages during the first cycle of any drift level. It can be seen that all the strains were relatively small and did not reach the yield strain of 5072 microstrains. There is not an explicit trend in the data that would indicate that the pedestal or couplers alter the strain distribution because the profiles are similar. Figure 5-36 depicts the average transverse strains of HCPP and GCPP due to formation of shear cracks and shear deformation compared with those of CIP. The diagram located in the lower left-hand corner of Figure 5-36a depicts the locations where strain was recorded from transverse bars. The data shown in each plot reflects the average of these two gages for the first push and pull cycle of each drift level. There are three general observations that can be made from these profiles: (1) the maximum strain for the precast models tends to occur 8 – 12 in [203 – 305 mm] above the pedestal-column joint compared to those of CIP, which

occur 12 in [305 mm] above the footing, 2) the maximum strains are small and well below the yield strain, and (3) the strains measured within the pedestal substantially smaller than those of the CIP strains especially at higher drift ratios. In order for strain to accumulate in a transverse bar used for shear reinforcement a crack must be present. Figure 5-37 present the shear crack that occurs in columns dominated by flexure, like CIP. Beginning as a flexural crack, a shear crack tends to form within approximately one column diameter from the footing. As this crack attempts to open, transverse bars that bridge the crack accumulate strain while inhibiting crack opening. The data from the precast models with pedestals indicate that conventional shear crack does not form. Figure 5-38 presents the shear cracking mechanism for the columns with pedestal. The pedestal contains steel ducts that increase the shear strength, thus preventing the formation of wide inclined cracks. The spiral strains above the pedestal, however, are relatively high and indicating inclined cracks above the pedestal as reflected in Fig. 5-36.

5.3.5 Plastic Hinge Curvatures

Figure 5-39 provides a schematic detailing the names and location where curvature measurements were taken, and the corresponding plastic hinge details for precast models with pedestals. Moments were calculated by taking the product of the average lateral load recorded from the actuator and the distance between the loading point and mid-height of each respective section shown in Figure 5-39. Figure 5-40 shows the average moment-curvature response recorded from Section-0, which captures the section response and the bond-slip occurring within the footing, and Figure 5-41 depicts the relationship between curvature and drift. The shape of the moment-curvature curves for the precast

models are identical to that of CIP for Section-0, but Figure 5-41 shows that after 4.0% drift the precast models reach slightly higher curvatures. This is due to the rigidity of the pedestal that forces behavior plastic deformations to concentrate at the pedestal-footing interface during the higher drift levels; an observation that is consistent with the observed longitudinal strain profiles. The moment-curvature relationships from Sections 1 to 4 can be observed in Figure 5-42. All sections exhibit moment-curvature relationships similar to CIP. Section-1 reflects response from the mid-height of the precast pedestal, and although the models follow the same trend as CIP, they tend to reach higher curvatures by the time the effective yield curvature is reached (≈ 6600 kip-in [745 kN-m]). CIP achieves a larger ultimate curvature than the precast models. The effect of the presence of the couplers can be observed in the response of Section-3 where GCNP exhibits greater section stiffness but lower curvature, and HCPP response is slightly softer during the ascending portion of the curve.

5.3.6 Behavior of Pedestal Joints

HCPP and GCPP each had two pedestal joints: (1) the pedestal-footing joint located at the footing surface and (2) the pedestal-column joint that was located 12 in [305 mm] above the footing. It was observed that these joints had a tendency to open as wide as 0.4 in [10 mm]. The rotational behavior of the pedestal-column joint is presented in Figure 5-43, and Figure 5-44 depicts representative photos taken during testing of this joint. It can be observed in Figure 5-43a that the pedestal-column joint of HCPP and GCPP exhibit similar moment-rotation relationships. By examining the rotation of the joint versus drift, it can be observed that GCPP undergoes larger rotations for some drift levels

compared to HCPP. Nevertheless, these differences are not substantial, and it can be concluded that the type of coupler used does not have a significant impact of the behavior of the pedestal-column joint.

The rotational behavior of the pedestal-footing joint is presented in Figure 5-45, and Figure 5-46 depicts representative photos taken during testing. The moment-rotation behavior of the pedestal-footing joint is similar for HCPP and GCPP. The data for HCPP is only shown up to 6% drift because extensive damage to the footing concrete occurred in subsequent drift levels, making the data unreliable. By examining the rotation-drift relationships, it can be observed that GCPP tends to experience a larger rotation per drift level compared to HCPP. This increased joint rotation can be attributed to the presence of the pedestal and grouted coupler region, which force hinging behavior to occur elsewhere in the column i.e. pedestal joints.

5.4 Summary and Overall Evaluation

This section provides a brief summary and discussion of the comparisons between column models. A summary of results is presented followed by discussions covering the effect of couplers and precast pedestal on model performance.

5.4.1 Model Performance

5.4.1.1 Apparent Damage and Failure

A complete summary of the apparent damage sustained by each model at selected drift levels is provided in Table 5-6. The progression of damage in the precast models was similar to that of CIP. By 2.0% drift, all models experienced flexural cracking extending into shear cracks. Transverse reinforcing bars became visible due to spalling

of concrete and there were cracks in footing by 4.0% drift. By 6.0% drift, longitudinal bars and/or couplers were visible, spalling became extensive, and strain penetration into the footing was evident. It was at this drift level that the longitudinal bars in both GC models fractured within the footing. Furthermore, both GC model exhibited severe damage to the footing during 6.0% drift due strain penetration including extensive cracking and delamination of concrete. This was not observed the HC models or CIP until 8.0% drift. By 8.0% drift, damage began to penetrate into the confined concrete core of CIP and both HC models, and was followed by longitudinal bar rupture during 10.0% drift.

All models experienced longitudinal bar rupture as the dominate failure mode, but there were some distinct trends observed regarding the location of these failures. Similar to CIP, the majority of the longitudinal bar rupture locations in HCNP were above the surface of the footing. In the case of the GCNP and the models with precast pedestal the bars fractured at approximately 5 in [127 mm] below the surface of the footing.

5.4.1.2 Force-Displacement Relationship

Figure 5-47 depicts the hysteretic, pushover (envelope of the hysteresis curves), and elasto-plastic force-displacement relationships for all models. All of the precast models exhibited similar hysteresis behavior compared to that of CIP (Figure 5-47a-d). The only difference was the slight pitching that occurred during the unloading portions of the hysteresis loops for the HC models. Similarly, when the precast models are compared against one another (Figure 5-47e-f) similar hysteresis loops can be identified. The similarities in hysteresis behavior of precast models compared to CIP indicate that

couplers and precast pedestal located within the plastic hinge region do not have a significant effect on hysteretic behavior. The same can be said for the average pushover and elasto-plastic responses which are shown in Figure 5-47g and Figure 5-47h, respectively.

5.4.1.3 Energy Dissipation

The cumulative energy dissipated per drift level is in Figure 5-48a for all models, and the percent difference of the precast models relative to CIP is shown in Figure 5-48b. All four precast models followed the same energy dissipation trend per drift cycle as CIP. Prior to yielding ($< 2.0\%$ drift), both headed coupler models and GCPP dissipated within 5-23% more energy per drift level than CIP, while GCNP was within $\pm 5.0\%$ of CIP. After 3.0% drift, the energy dissipation capacity of the GC models remains within $\pm 5.0\%$ of CIP while the HC models dissipate 7- 14% less energy than CIP.

5.4.1.4 Measured Strains

Figure 5-49 depicts a graphical summary of the longitudinal strain profiles within the plastic hinge region at 4, 6, and 10% drift. As noted previously, CIP exhibited well distributed strain throughout the plastic hinge resulting in a large region over which plastic rotation occurred. HCNP also displayed well distributed strains throughout the plastic hinge region and the magnitude of the strains were approximately the same as CIP. The plot for GCNP identifies the grouted coupler region with a green shaded box. Strains measured at the mid-height of the grouted coupler were low because the coupler cross section area was substantially more than the bar area thus reducing the strain in the coupler itself. A similar phenomenon occurred in HCPP and GCPP due to the grout-

filled corrugated steel duct located within the precast pedestal. For most cases, the presence of couplers within the plastic hinge did not have a substantial effect of the maximum transverse bar strains. As discussed in Section 5.3.4, the presence of the corrugated ducts in the pedestal increased the shear strength and reduced shear cracking.

5.4.1.5 Moment-Curvature and Rotation

The moment-curvature relationships were found to be affected by the presence of couplers within the column cross-section. The HC models exhibited slightly higher curvatures in sections where couplers were located due to very slight bar-slip within the headed coupler collars. Although variations were obvious, the differences were small compared with CIP and are within experimental scatter. The grouted couplers had the opposite effect and GC models experienced reduced curvature in sections where the grouted coupler sleeves were located thus increasing rotational stiffness. In the case of GCNP, this forced increased rotation to occur at the footing-column interface and above the coupler region. Although large gaps were observed to form at the pedestal-column and pedestal-footing interfaces, the curvatures measured at these locations did not differ substantially from those of CIP. Yet, there was a slight increase in the maximum rotation at the pedestal-footing joint observed in GCPP.

5.4.2 Effect of Couplers on Column Performance

5.4.2.1 Grouted Couplers (GC)

The grouted couplers had one significant effect on the behavior of columns. The addition of the 14.5-in [368-mm] cast-iron grout-filled sleeve resulted in increased section-stiffness within the coupler region thus not adequately contributing to plastic

rotation. Instead, plastic rotation was forced to outside the grouted coupler region forming a plastic hinge mechanism that differed from that of CIP.

Figure 5-50 depicts the observed hinging mechanisms for the five column models. The plastic hinge regions are represented by hatched areas on the longitudinal reinforcing bars. CIP is shown at the top of the figure and as expected exhibited plastic rotation that occurred over a large length resulting in well distributed hinge behavior. Plastic hinging in GCNP occurred in two regions: (1) above the grouted coupler region and (2) below this region within the footing. A similar mechanism was observed in GCPP, yet the lengths over which the hinges form is small due to the location of the grouted couplers and presence of the pedestal. The presence of the grouted coupler in GCNP also initiated longitudinal bar buckling below the footing surface after delamination of footing concrete. The limited plasticity over the plastic hinge region in GC columns led to a lower drift capacity (6% vs. 10%). Other than the effect on plastic hinge formation and its effect on the drift capacity, the presence of the grouted coupler sleeves did not seem to have a substantial effect of the progression of damage, the force-displacement relationships, or the energy dissipation capacity.

5.4.2.2 Upset Headed Coupler (HC)

The HC column models both employed two layers of 11 upset-headed couplers. These couplers caused the columns to exhibit hysteretic force-displacement and energy dissipation responses that were essentially the same as that of CIP with slight pinching due to slippage of the upset headed bars within the threaded coupler collars. The observed hinge mechanisms for the HC columns can be observed on the lower right-hand

side of Figure 5-50. It was found that the couplers had no significant effect on the formation of plastic hinging when the couplers were immediately above the footing. That is, HCNP exhibited a large, well-distributed plastic hinge mechanism similar to that of CIP. Neglecting the presence of the pedestal, there was no significant change in the plastic hinge behavior above the pedestal near the headed couplers in HCPP. The only difference in the hinge behavior caused by the headed couplers was very slight concentrated rotation within the coupler layers caused by the minor slippage of the headed bars within the coupler. This action is identified in Figure 5-50 by hatched dots indicating the slippage points and by a hitched line indicating the location of slight concentrated rotation.

5.4.3 Effect of Pedestal on Column Performance

The precast pedestals were used to shift the coupler locations away from the footing by 12 in [305 mm] thus reducing the moment demand on the connection region. Longitudinal reinforcing bar passed through corrugated steel ducts that were filled with high strength cementitious grout. The pedestals did not seem to significantly affect the drift capacity, the progression of damage, energy dissipation capacity, or the force-displacement behavior of the column models. The pedestal did however cause redistribution of longitudinal tensile strains to occur within the footing. The grout-filled corrugated steel ducts acted similar to the cast-iron grout-filled couplers by increasing the section stiffness slightly that resulted in concentrated hinging at the pedestal-footing interface, which is reflected in Figure 5-50 HCPP and GCPP. This behavior results in strain concentrations below the footing and ultimately causes premature bar rupture. This

mode of failure was observed in both HCPP and GCPP for all bar rupture locations.

Lastly, the pedestals caused shear cracks to form further from the footing compared to

CIP thus also shifting the location of the maximum transverse bar strain.

6. Damage States and Response Parameters

6.1 Introduction

This chapter presents apparent damages states and response parameters from the column models tested in this study and compares them with a data set compiled by Vosooghi and Saiidi (2010). The objective was to determine whether the visual evaluation and repair strategies developed in the aforementioned study are applicable to the precast columns tested in this study. Prior to discussing results for precast columns, a brief review of the work by Vosooghi and Saiidi (2010) is presented followed by explanation of how response parameters were determined for the present study. Discussion and concluding remarks are provided at the end of the chapter.

6.2 Background

In modern seismic design of bridge structures the target response under strong earthquakes is “no-collapse”. This performance objective implies that the bridge structure could undergo significant damage that may or may not be repairable. Under less severe earthquakes with shorter return periods, damage to the bridge structures is expected to be repairable in a timely fashion. In order to assess such damage, engineers must visually inspect the structure and make recommendations for remedial action.

The study conducted by Vosooghi and Saiidi (2010) provides engineers with a methodology to correlate visual column damage with performance parameters in order to prescribe a repair procedure. Five distinct visual damage states (DS) were defined (Figure 6-1):

- DS-1: Flexural cracks

- DS-2: First spall and shear cracks
- DS-3: Extensive cracking and spalling of concrete
- DS-4: Visible longitudinal and/or transverse reinforcement
- DS-5: On-set of damage to the confined concrete core (imminent failure)

These damage states were considered to be repairable without major reconstruction of columns. Columns at DS-1 to DS-5 were the focus of the study by Vosooghi and Saiidi. A sixth damage state (DS-6) would be associated with fractured longitudinal and/or transverse reinforcement, which was outside the scope of that study. A database of 33 scaled bridge column models, mostly tested using shake tables, was compiled to correlate damage states with external and internal seismic response parameters, which are described in the next section: maximum drift ratio (MDR), residual drift ratio (RDR), frequency ratio (FR), inelasticity index (II), maximum longitudinal steel strain (MLS), and maximum transverse steel strain (MTS).

Of the 33 columns, the current study only considered columns that had modern seismic detailing and low shear intensity (SI); low shear intensity was considered $SI < 4$. The former filter was used because the columns tested in this study were of modern seismic design and had low shear level. The shear intensity is defined in Eq. 1 and 2 for US and SI units, respectively. The columns in this study had an average $SI \approx 3.0$.

$$SI = V / A_e \cdot \sqrt{f'_c} \quad lbs, in \quad (6.1)$$

$$SI = V / A_e \cdot \sqrt{f'_c} \cdot 0.083 \quad N, mm \quad (6.2)$$

Where

- V = Shear demand
 A_e = Effective cross-section area = 80% of the gross area
 f'_c = Compressive strength of concrete

6.3 Response Parameters

The response parameters from the reference data set compiled by Vosooghi and Saiidi (2010) are shown in Figure 6-2. The data reflects the response parameters both near- and far-field motions for each given damage state. Variation indicators on the graph bar represent data for \pm one standard deviation.

6.3.1 Maximum Drift Ratio (MDR)

The *MDR*, which is an external response parameter, was determined using Eq. 6.3.

$$MDR = \frac{D_{max}}{H} \quad (6.3)$$

Where D_{max} = the maximum displacement for a given damage state, and H is the height of the column from the surface of the footing to the point of lateral load.

6.3.2 Residual Drift Ratio (RDR)

The *RDR*, also an external response parameter, was determined using Eq. 6.4.

$$RDR = \frac{D_{res}}{H} \quad (6.4)$$

Where D_{res} = the residual displacement of the column after the motion leading up to a given damage state. In shake-table studies, this parameter is measured directly from the column after a given run. In the present study, the residual displacement of the column was considered to the displacement at which zero lateral load was measured during the

returning portion after maximum drift. The average of the residual displacement for the first push and pull cycle was used in the current study.

6.3.3 Frequency Ratio (FR)

The FR is defined in Eq. 6.5, and is an external response parameter.

$$FR = \frac{F_{\text{eff}}}{F_{\text{uncracked}}} \quad (6.5)$$

Where F_{eff} = effective natural frequency of the column, and $F_{\text{uncracked}}$ = uncracked natural frequency of the column. F_{eff} was determined using the chord stiffness, which was calculated by dividing the peak lateral force by the corresponding displacement. The uncracked natural frequency was determined using the initial slope of the measured force-displacement curve for stiffness. The average stiffness of the first push and pull cycles were used for both parameters to estimate frequencies.

6.3.4 Inelasticity Index (II)

The II is an external response parameter used to determine residual plastic displacement capacity, and was calculated using Eq. 6.6.

$$II = \frac{D_{\text{max}} - D_Y}{D_U - D_Y} \quad (6.6)$$

Where D_{max} is the average maximum lateral displacement for a given damage state. Parameters D_Y and D_U represent the effective yield and ultimate displacement, respectively, as determined using elasto-plastic idealizations of the measured force-displacement envelope curves.

6.3.5 Maximum Longitudinal (MLS) and Transverse (MTS) Steel Strain

The *MLS* was determined using strain measured on the longitudinal reinforcing bars within the column. The maximum strain was determined by taking the average of the maximum strain recorded on several extreme bars during the first push and pull cycle leading up to a given damage state. A similar method was employed for the *MTS* except that the maximum strain could occur within the compression zone due to dilation of concrete or on the sides of the column due to shear deformation. If the maximum was found to occur within the compression zone, an average of the push and pull cycles was used. If the maximum was due to shear deformation, the strains in the two gages within the same layer were averaged for the first push and pull cycles. For both *MLS* and *MTS*, unreliable data was not considered.

6.4 Results

6.4.1 CIP

The damage states for CIP can be observed in Figure 6-3. CIP was designed with modern seismic detailing; therefore, as expected all five damage states were achieved. The response parameters for CIP are shown in Figure 6-4 along with those from the reference data set. For majority of damage states, the response parameters for CIP tend to be within one standard deviation of the far-field motion data. The residual drift ratio does, however, tend to be higher for damage states DS-2 through 4 when compared to the columns subjected to far-field motions. As described previously, the residual drift was defined as the displacement where the unloading branch of the hysteresis loop crossed the horizontal axis (zero load). In most cases, this method could overestimate the residual

drift that would occur from a ground motion. In shake-table tests, residual column displacement is measured *after* the shaking of the columns has stopped. Far field motions typically include reverse pulses that tend to reduce residual displacement, while near field motions usually include a single strong, non-reversing pulse that results in large residual displacements (Choi, et al 2010). Thus at DS-4 and 5, the *RDR* is in between the near and far field motion data from the reference data set.

6.4.2 HCNP

Similar to CIP, HCNP achieved all five damage states, which are shown in Figure 6-5. There are only a few slight differences in some of the damage states compared to those defined in Figure 6-1. Instead of spalling of concrete, spalling of grout is observed in DS-2 and DS-3. Furthermore, couplers become visible along with the transverse and longitudinal bars in DS-4 and DS-5. The response parameters are shown in Figure 6-6. There is little difference between the response parameters for HCNP and those from the far-field data set. Similar to CIP, the *RDR* is larger than that from the far-field data set due to the method of determination as mentioned earlier. Nevertheless, the response factors determined for HCNP correlate very well with the reference data set with respect to each damage state.

6.4.3 GCNP

The damage states for GCNP are shown in Figure 6-7. GCNP achieved all damage states except for DS-5 because failure of the column occurred prior to concrete core damage. Once DS-4 was achieved, grouted couplers were visible along with the transverse reinforcement, and significant delamination of footing concrete had also

began. The corresponding response parameters are shown in Figure 6-8. Similar to other models, most response parameters were within one standard deviation of the far-field motion data with respect to each damage state. The inelasticity index however was significantly different for DS-2 and higher damage states compared to both far- and near-field data sets, exceeding three times the standard deviation for both data sets. This is because GCNP had a lower ductility capacity compared to the average of the reference data set.

6.4.4 HCPP

Each damage states for HCPP are shown in Figure 6-9. Similar to HCNP, all five damage states were achieved. The only visual differences between the damage states observed for HCPP and those shown in Figure 6-1, were spalling of grout in DS-3, visible corrugated ducts in DS-4, and damage to the footing in DS-5. The corresponding response parameters are shown in Figure 6-10. Similar to HCNP, the measured response parameters correlate very well with the reference data set for far field motions.

6.4.5 GCPP

The damage states for GCPP are shown in Figure 6-11. Similar to GCNP, GCPP only achieved DS-1 through DS-4 prior to failure. There is no difference in the observed damage compared to that shown in Figure 6-1 until DS-4 was reached. At this damage state, corrugated ducts were visible instead of longitudinal bars, and there was extensive damage to the footing at the base of the column. The corresponding response parameters are shown in Figure 6-12. Similar to GCNP, there was not a significant difference between the measured response parameters per damage state and those from the reference

data set for far field motions except for the inelasticity index. The II was more than three standard deviations higher in DS-2 and higher compared to the reference data set. Once again, this can be related to the reduced ductility capacity of GCPP compared to average response of the reference data set.

6.5 Discussion and Conclusions

The objective of this chapter was to determine whether the precast columns tested in this study conform to the damage states and corresponding response parameters established by Vosooghi and Saiidi (2010). As expected, CIP achieved all five damage states, and the majority of response parameters were within one standard deviation of the reference data set for a given damage state. For most damage states, the only discernible difference was the RDR due to the method of determination compared to the reference data set; the difference in the RDR for a given damage state was similar for CIP and all precast column models. Both HC models achieved all five damage states and the response parameters were comparable to reference data set with respect to each damage state. The only difference in apparent damage compared to that shown in Figure 6-1 was the spalling of grout during DS-3 and the visible ducts and headed couplers during DS-4 and DS-5. The GC models only achieved DS-1 through DS-4 prior to failure but still had good correlation with the response parameters from the reference data for the majority of damage states. The one significant exception was the inelasticity index (II). After DS-1, the II for a given damage state was higher by more than three-times the standard deviation of both far- and near-field data. This is due to the reduced lateral displacement capacity of the GC models compared to CIP, which is a good representation of the

reference data set. This was one major implication. In a post-earthquake inspection, a damaged bridge column employing grouted coupler within the plastic hinge could be assumed to have higher residual drift capacity using the damage state metric developed by Vosooghi and Saiidi (2010). More than likely, this would result in a unsatisfactory repair strategy and the repaired column could have a higher probability of failure.

Figure 6-13 provides a comparison of the response parameters among the five column models tested in this study. The *MDR* for a given damage was the same for all five column models except at DS-3 for GCNP, which was slightly higher compared to the other models. Similarly, the *RDR* is comparable among the five column models for all damage states except at DS-3 for GCNP, where the *RDR* tends to be slightly higher. Nevertheless, the difference can be attributed to experimental scatter and is not significant. The *FR* and *MLS* are comparable for all models and given damage states. The only two response parameters that exhibit significant differences when comparing the five models are the *II* and *MTS*. As describe above, *II* for the GC models was much higher after DS-1 given the lower lateral displacement capacity of these columns, whereas, the *II* for CIP and the HC models are comparable for all damage states. The *MTS* for CIP tended to higher for DS-2 through 5 compared to the precast models. The plastic hinge regions for the precast models contained materials that added to the shear resistance of the column i.e. grouted sleeves, corrugated steel ducts, and grout that was twice as strong as the concrete used in CIP; therefore, this result is not surprising. Lastly, Figure 6-14 provides the average push-over curves for each column model and the corresponding damage states. These plots give a visual correlation between the force-displacement/ductility and the apparent damage states.

In conclusion, the HC column models exhibit response parameters for a given damage state that have good correlation to the reference data set. This indicates that the post-earthquake evaluation, decision-making and repair strategies developed by Vosooghi and Saiidi (2010) could be applied. However, this is not entirely the case for GC columns. It is recommended that if the methods developed by Vosooghi and Saiidi (2010) are to be used for GC columns, that the definition of DS-4 rather than DS-5 be labeled as the point of imminent failure.

7. Results from Couplers Tests

7.1 Introduction

As described in Chapter 2, a series of tensile tests were conducted to characterize the static, dynamic, cyclic loading and slip behavior of the couplers used in the precast column models tested in this study. This chapter presents the results from those tests. The test results are discussed in the following order: 1) static tests; 2) dynamic tests; 3) cyclic loading tests; and 4) single- and multi-cycle elastic slip tests. At the end of the chapter a brief summary of the performance of each coupler is provided and compared with the performance of other couplers.

7.2 Headed Coupler Tests

The reinforcing bars used for each headed coupler test came from S8-2, which were ASTM A706 bars (described in Section 4.2.4.3 in Chapter 4). The average measured yield stress, ultimate stress, and percent elongation at rupture for these bars were 68.0 ksi [468 MPa], 95.1 ksi [655 MPa], and 18.2%, respectively. Just like those used in the column tests, each headed coupler was torqued to 150 ft-lbs [203 N-m] as specified by the manufacturer.

7.2.1 Static Tensile Tests

Static tensile test were conducted in displacement control mode such that strains in the sample did not exceed those specified in ASTM A1034. The pre- and post-yield displacement rates were 0.00625in/sec [0.159mm/sec] and 0.05in/sec [1.27mm/sec], respectively. The results from static tests are summarized in Table 7-1 and Table 7-2. The measured stress-strain behavior and photos of the test specimen after failure are

shown in Figure 7-1 through Figure 7-2. A small diagram is included in each plot to identify the locations where measurements were taken. The solid lines represent the average of two strain gage measurements taken at each respective location. The dashed line indicates the strain measured from the extensometer in the coupler region. A white arrow indicates the location of bar rupture. The stress-strain behavior of sample HS2 is not shown because of extensometer malfunction. Thus, a fourth sample (HS4) was tested.

All four samples achieved nearly the same yield stress, ultimate stress, and strain at failure as measured in the control bar samples discussed in Chapter 4. Furthermore, all samples failed by rupture of reinforcing bars outside the coupler region. The stress-strain response of the reinforcing bar was as expected for a mild steel bar under monotonic static loading. That is, a steep linear ascending branch, a well-defined yield point and post-yield plastic region, followed by strain-hardening and rupture.

Figure 7-4 depicts the generalized monotonic stress-strain behavior of the coupler region, which can be broken into three distinct branches: (1) the initial elastic branch prior to gap-opening; (2) the elastic post gap-opening branch; and (3) the post-yield branch. As mentioned in Section 3.5.3.1 the manufacturer of headed couplers specifies a predetermined torque to be applied to the threaded collars when installing the device. As a result of this torque, a pre-compression force is applied to the deformed heads within the steel collar. Within branch 1, the linear response of the coupler (K_1) region reflects the stiffness of the mild steel reinforcing bars in series with the stiffness of the steel collar. The “gap-opening point” marks the end of branch 1 and beginning of branch 2 where a significant decrease in the stiffness occurs (K_1 to K_2) because the gap between

the heads begins to open. Within branch 2, the force in the mild steel bars overcomes the initial pre-compression of the steel collars and the bars separate. Theoretically, if the load were to be removed while on branches 1 or 2, the stress-strain curve would return to the origin via the original path. Branch 2 concludes when the bars begin to yield (referred to as the “yield point”). Branch 3 reflects the interaction of the bars undergoing plastic deformation and deformations within the steel collar. The average elongation within the coupler region at failure was 7.7%.

The coupler assemblies were inspected for damage after completion of the tests. Figure 7-5 shows the HS3 sample disassembled. There was no apparent damage to the deformed heads or threaded steel collars. However, there was slack between the deformed heads within the collar prior to disassembling the coupler. As mentioned in Section 4.4.2.2, this same observation was made for the couplers removed from HCNP. Furthermore, unscrewing the two threaded collars after the test was difficult and in some cases was not possible. This is attributed to permanent deformation of the threads.

7.2.2 Dynamic Tests

The loading protocol initially called for samples to be loaded in displacement control at 0.42 in/sec [10.7 mm/sec] which equates to a strain rate of 70,000 microstrain/sec based on the initial gage length of the extensometer. Based on the research of Zadeh and Saiidi (2007), this would result in an achieved rate between approximately 50,000 and 100,000 microstrain/sec. After testing of the first sample, HSR1, the achieved strain rates were checked and were between 7000 and 22,000 microstrain/sec, which were too low relative to the target strain rates. The loading rate was increased to 1.575 in/sec [40

mm/sec], which corresponded to a 70,000 microstrain/sec rate based on the clear length of the sample. The strain rates for subsequent samples were found to be between 9000-112,000 microstrain/sec, which was acceptable. Table 7-3 lists the achieved strain rates during three different portions of test: (1) zero stress to yield [$\sigma_0 - \sigma_Y$]; (2) yield to ultimate stress [$\sigma_Y - \sigma_{ULT}$]; and (3) ultimate stress to bar fracture [$\sigma_{ULT} - \text{fracture}$].

The results from dynamic tests are summarized in Table 7-4 and Table 7-5. The measured stress-strain behavior and photos of the test specimens after failure are shown in Figure 7-6 through Figure 7-9. The average (not including HSR1) measured yield stress and ultimate stress were 71.6 ksi [493 MPa] and 98.1 ksi [676 MPa], respectively. These stresses are slightly higher than those measured during static tests. This is likely due to the effect of dynamic loading and will be addressed at the end of the chapter. All samples failed due to bar rupture and away from the coupler. After the loading rate was increased for HSR2, HSR3, and HSR4 the yield point was not well defined because the sampling frequency of 16 Hz was too low. Thus, this value is not shown in Table 7-4. Nevertheless, the coupler region displayed the same stress-strain behavior as observed in the static tests; a three branch curve was observed similar to that shown in Figure 7-4.

7.2.3 Cyclic Tests

Cyclic loading tests were performed to quantify the effect of strain reversals and the relation between gap-opening and applied stress. Mainly tensile loading was applied with small compressive stresses to avoid buckling. Two HC samples were tested; one sample, HCC-1, with the manufacturer specified torque applied to the threaded collars, and the second, HCC-2, without the manufacturer specified torque, which was hand

tightened prior to testing. HCC-2 was studied to investigate the sensitivity of gap-opening to the initial torque applied to the collars. Load was applied at 1 kip/sec [4.45 kN/sec] during travel to the tension target stress, which corresponds to a rate of 1.27 ksi/sec [8.72 MPa/sec]. During travel to the compression stress target, load was applied at 0.5 kip/sec [2.22 kN/sec], which corresponds to a loading rate of 0.635 ksi/sec [4.36 MPa].

The results from cyclic tests are listed in Table 7-6 through Table 7-8. The yield stress, ultimate stress, and elongation at failure of the reinforcing bar and coupler region for HCC-1 were 68.5 ksi [472 MPa], 93.3 ksi [643 MPa], 16.9%, and 7.8%, respectively. The yield stress, ultimate stress, and elongation at failure of the reinforcing bar and coupler region for HCC-2 were 67.7 ksi [466 MPa], 94.6 ksi [652 MPa], 12.6%, and 8.48%, respectively. Both HCC samples failed by reinforcing bar rupture away from the coupler region. Furthermore, fractured bars exhibited necking and ductile failure. The main differences between the two samples were the strain in the coupler region at failure and the stress at which the gap began to open. The strain over the coupler region of HCC-2 was 8.7% greater than that of HCC-1, and gap-opening occurred at approximately 6 ksi [41 MPa] for HCC-1 compared to almost immediately after loading for HCC-2. Both of these differences can be attributed to the lack of pre-compressive force between the deformed heads of HCC-2.

The measured stress-strain response and failure location for HCC-1 and 2 are shown in Figure 7-10 and Figure 7-11, respectively. The stress-strain envelopes of both HCC samples exhibited the behavior described in Section 7.2.1 and shown in Figure 7-4. It was proposed in Section 7.2.1 that if load was removed within the post gap-opening

branch (branch 2 in Figure 7-4) the stress-strain curve would return to the origin via the original path. It is evident in both HCC tests that this is clearly not the case. That is, after the gap opens, permanent deformation occurs within the threaded collars rather than the bars because the reinforcing bars have yet to reach the yield point.

The closure of the gap between the heads can be observed as the stress in the specimen transitions from tension to compression. Point 1 in Fig. 7-10b indicates where stress in the specimen is approximately zero and the gap between the heads begins to close. The gap is fully closed at point 2 and compressive stress begins to develop. Once the compression cycle is nearly completed and the stress in the specimen is approximately zero, the gap between the heads begins to open again. When point 3 is reached, the heads are once again in contact with the steel collar and tension begins to accumulate.

The distance between points 1 and 2, considered to be the gap length, was determined for each cycle for both HCC samples. The measurements used in determining the gap-opening behavior are listed in Table 7-6 and Table 7-7 for HCC-1 and 2, respectively. The relationship between the stress in the bar and the measured gap length is shown in Figure 7-12. There is an obvious linear relationship between the length of the gap and the stress in the bar. The trend line for each data set was obtained using linear regression. There was little difference between the slope of the trend line for HCC-1 and 2, which were 1043 ksi/in [284 MPa/mm] and 1008 ksi/in [272 MPa/mm], respectively. This indicates that the level of torque applied to the coupler has little influence on the gap-opening behavior once the gap is open, but does impact when the opening occurs. This

data was used to develop an analytical model for the HC splice. Further details are provided in the next chapter.

7.2.4 Slip Tests

Table 7-9 lists the results from the single cycle slip tests. As discussed in Chapter 2, samples were preloaded to 3 ksi [20.7 MPa], loaded to 30 ksi [207 MPa] for and held for 60 sec, and the test was completed by returning the load to 3 ksi [20.7 MPa]. At each point, displacement was measured over the coupler region. The slip is defined as the difference between the final and the initial displacements. Caltrans maximum allowable slip (listed in Table 2-1) for a coupler splicing #8 bars is 0.014 in [0.356 mm]. All three samples passed the single-cycle slip test.

Table 7-10 through Table 7-12 list the measured data and results for the multi-cycle slip tests, and Table 7-13 provides a summary of these tests along with the cumulative slip for each sample. A minimum of 3 cycles were applied to each sample. Additional cycles were applied until the measured slip was zero for two consecutive cycles. All samples had less slip than the Caltrans maximum allowable slip of 0.028 in [0.7112 mm] after multiple cycles.

7.3 Grouted Sleeve Coupler Tests

The reinforcing bars used for each grouted coupler test came from S8-1, which were ASTM A615 bars (described in Section 4.2.4.2). The average measured yield stress, ultimate stress, and percent elongation at rupture for S8-1 bars were 66.8 ksi [460 MPa], 111.3 ksi [767 MPa], and 15.8%, respectively. Each coupler was grouted with cementitious grout 3 (G3), which was described in Section 4.2.3.3. The average 7-day

and 28-day cube compressive strengths for G3 were 12,837 psi [88.4 MPa] and 15,638 psi [107.7 MPa], respectively. Cube tests were also conducted on the day of tensile testing and the average compressive strength of the grout was 18,874 psi [127.7 MPa].

7.3.1 Static Tensile Tests

The pre- and post-yield displacement rates were 0.01875 in/sec [0.476 mm/sec] and 0.15 in/sec [3.81 mm/sec], respectively. The results from static tests are summarized in Table 7-14 and Table 7-15. The measured stress-strain behavior and photos of the test specimen after failure are shown in Figure 7-13 to Figure 7-15. A small diagram is shown to identify the locations where measurements were taken. The solid lines represent the average of two strain gage measurements taken at each respective location. The thick dashed line indicates the strain measured from the extensometer over the coupled region, and the thin dashed line indicates the average of the data from the two strain gages mounted at the mid-height of the ductile iron sleeve. A white arrow indicates the location of the bar rupture in each sample.

All samples failed due to bar rupture away from the coupler region, which indicates excellent performance of the couplers. The average yield and ultimate stresses were 66.2 ksi [456 MPa] and 108.5 ksi [747 MPa], respectively, which corresponds to differences of -0.89% and -2.5% compared to the control bars. The stress-strain behavior of the reinforcing bars was as expected. Measurements from the mid-height of the ductile cast-iron sleeves indicated significantly reduced elongation at failure compared to the reinforcing bars and coupler region due to the large cross-sectional area of the sleeves.

The average elongation at failure was 0.68%, and the stress-strain behavior of the sleeve appeared approximately linear throughout the test.

Figure 7-16 displays the observed monotonic stress-strain behavior in the grouted coupler region. Two distinct branches were identified: (1) a linear-elastic branch with stiffness K_1 ; and (2) a non-linear inelastic branch that continued until rupture of the reinforcing bar. The slope of branch 1 is a combination of the axial stiffness of the cast-iron sleeve and the reinforcing bars. This branch concludes at the yield point of steel. Branch 2 exhibits non-linear behavior and is where permanent deformation occurs. The shape of branch 2 is controlled by a combination of the approximately linear behavior of the sleeve, non-linear deformation of steel, and strain penetration of the bar into the grout within the sleeve. The average elongation of the grouted coupler region at failure was 5.3%, which is a 66.7% lower than the elongation in the bar.

The couplers were inspected after each test, and there was no apparent damage to cast-iron sleeves. There was however evidence of strain penetration into both the field and factory ends of the coupler. Figure 7-17 shows the field and factory ends of GS1 after testing. A small region of grout-cone pull out can be observed on both ends. This observation was typical of all grouted coupler samples tested.

7.3.2 Dynamic Tensile Tests

The loading rate for the grouted coupler dynamic tests was 2.695 in/sec [68.5 mm/sec], which corresponded to 70,000 microstrain/sec. During the first test (GSR1) the grips on the loading frame slipped, and the test was stopped. The loading rate for subsequent tests was 1.75 in/sec [44.5 mm/sec], which corresponds to 45,455

microstrain/sec, and no issues were encountered. The test for GSR1 was repeated with a new specimen denoted GSR4. Table 7-16 lists the strain-rates achieved during dynamic tests. The strain-rates achieved at the new loading rate were between 70,000 and 200,000 microstrain/sec, which were satisfactory.

The results from dynamic tests are summarized in Table 7-17 and Table 7-18. The measured stress-strain behavior and photos of the test specimens after failure are shown in Figure 7-18 to Figure 7-21. The average (not including GSR1) measured yield stress and ultimate stress were 70.4 ksi [485 MPa] and 110.7 ksi [763 MPa], respectively. These stresses are slightly higher than those measured during static tests, which is likely due to the effect of dynamic loading and will be addressed at the end of the chapter along with the corresponding results from HC tests. All samples failed due to bar rupture with three of the four samples failing outside the coupler region. Sample GSR3 failed by bar rupture within the coupler region approximately two bar-diameters from the factory end of the coupler. The strains within the bar, coupler region, and sleeve were all comparable to those measured during static tests, and the stress-strain behavior of the coupler region was as depicted in Figure 7-16. Similar to the headed coupler dynamic tests, the yield point of the bars was not well-defined because the data sampling frequency of 16 Hz was too low.

7.3.3 Cyclic Tests

A single grouted coupler sample (GCC-1) was subjected to cyclic loading, mostly under tension with small stress levels in compression cycles to avoid buckling. Similar to the HCC tests, load was applied at 1 kip/sec [4.45 kN/sec] during tensile loading, which

corresponds to a stress rate of 1.27 ksi/sec [8.72 MPa]. During compression loading, the load was applied at 0.5 kip/sec [2.22 kN/sec], which corresponds to a stress rate of 0.635 ksi/sec [4.36 MPa].

The results from the GCC -1 test are summarized in Table 7-19. The measured yield and ultimate stresses for GCC-1 were 66.1 ksi [455 MPa] and 98.7 ksi [680MPa], respectively. The elongation at failure of the reinforcing bar, coupler region, and the sleeve were 5.59%, 2.69%, and 0.46%, respectively. The measured stress-strain response and failure location are shown in Figure 7-22. The stress-strain envelope of the coupler region exhibited the behavior described in Section 7.3.1 and shown in Figure 7-16. After the first two full cycles, slight stiffness degradation begins to occur within the coupler region during re-loading from compression to tension. This is most likely due to slight degradation of the bond between the grout and the reinforcing bars for there is no reduction in unload/re-loading stiffness of the reinforcing bar (Figure 7-22a) or coupler sleeve (Figure 7-22c). Slight slippage of the reinforcing bars into the sleeve occurred during compression cycles. As shown in the upper corner of Figure 7-22b, a small region of approximately zero stiffness can be observed as the stress in the bars approaches the compression target. This behavior was subtle and is believed to have a minor effect on the cyclic behavior of the splice. Failure of GCC-1 occurred due to rupture of the upper spliced bar away from the coupler region. The failed bar did not exhibit necking around the fractured area; instead the fracture surfaces were flat (Figure 7-22e), which indicates a non-ductile failure.

7.3.4 Slip Tests

The results for the single-cycle slip tests are summarized in Table 7-20. All three grouted coupler samples met the Caltrans slip requirement, which is measured slip less than 0.014 in [0.356 mm]. The results from each multi-cycle slip are summarized in Table 7-21 through Table 7-23, and the cumulative slip results are shown in Table 7-24. Similar to the cyclic slip tests conducted on the headed couplers, samples were cycled until the initial and final displacement measurements equated to zero. All samples had less slip than the Caltrans maximum allowable slip of 0.028 in [0.7112 mm] after multiple cycles.

7.4 Comparison and Discussion

Figure 7-23 and Figure 7-24 compare the static and dynamic test results for HC and GC splice, respectively. For each coupler type a representative plot from the static and dynamic tests were used. For each respective coupler type, similar stress-strain behavior within the coupler region was observed under static and dynamic loading. That is, the behavior each device was independent of loading rate. This result is important because the large-scale tests conducted in this study were done under slow cyclic loading. This result suggests that the plastic hinge behavior in the large-scale column tests should not change substantially under dynamic ground excitation. The main difference between the static and dynamic tests is in the yield and ultimate stresses. In both sets of coupler tests, the average yield and ultimate stress were higher likely due to the effect of high strain-rate.

The effect of loading rate on mild steel reinforcing bars has been studied by several researchers. A good summary of previous works is provided by Zedah and Saiidi (2007). It has been well documented that as the rate of applied strain increases so does the yield stress and ultimate stress of the bar. Many equations have been developed and calibrated with experimental data to estimate these increases in stress. Two existing equation sets were selected to compare with tests results.

The first set, Equations 7.1 through 7.4, were proposed by Zedah and Saiidi (2007) to estimate the amplification factors for yield and ultimate stresses due to dynamic loading. Equations were calibrated with test data on No. 3, 8, and 11 Gr. 60 ASTM A615 bars subjected to monotonic tensile loading under constant and variable strain rates. The parameter K (Eq. 7.2) was introduced to account for the change in strain rate during loading up to yield. Values of 1, greater than 1, and less than 1 correspond to a constant, increasing, and decreasing strain rate, respectively.

$$\frac{f'_y}{f_y} = \left(\frac{K \dot{\epsilon}_{Y,avg}}{10^{-4}} \right)^\alpha \quad (7.1)$$

$$K = \left(\frac{\dot{\epsilon}_y}{\dot{\epsilon}_{0.5y}} \right)^{\frac{1}{2}} \quad (7.2)$$

$$\frac{f'_u}{f_u} = \left(\frac{\dot{\epsilon}_{U,avg}}{10^{-4}} \right)^{\frac{2}{3}\alpha} \quad (7.3)$$

$$\alpha = 0.022 \left(\frac{\phi}{\phi_8} \right)^{0.15} - 0.006 \left(\frac{f_y}{60} \right) \quad (ksi) \quad (7.4)$$

$$\alpha = 0.022 \left(\frac{\phi}{\phi_8} \right)^{0.15} - 0.006 \left(\frac{f_y}{414} \right) \quad (MPa)$$

Where

f'_y, f_y = dynamic and static yield strength of steel (ksi or MPa), respectively

f'_u, f_u = dynamic and static ultimate strength of steel (ksi or MPa), respectively

$\dot{\epsilon}_{Y,avg}$ = average rate of strain between $0.5\epsilon_y$ and ϵ_y

$\dot{\epsilon}_y, \dot{\epsilon}_{0.5y}$ = strain rate at yield and 50% of yield, respectively

$\dot{\epsilon}_{U,avg}$ = average rate of strain between zero and the strain at ultimate stress

ϕ, ϕ_8 = bar diameter of the bar of interest and a No. 8 bar, respectively

The second set of equations were proposed by Malvar (1998) and are based on tests conducted by a number of different researchers. Equation 7.5 is used to evaluate the dynamic to static ratios for yield and ultimate using different α -factors shown in Equations 7.6 and 7.7. These equations were calibrated from monotonic tension tests on Gr. 40, 60, and 75 of different sizes.

$$\frac{f'}{f} = \left(\frac{\dot{\epsilon}}{10^{-4}} \right)^\alpha \quad (7.5)$$

$$\alpha_{fy} = 0.074 - 0.040 \frac{f_y}{60} \quad (ksi) \quad (7.6)$$

$$\alpha_{fy} = 0.074 - 0.040 \frac{f_y}{414} \quad (MPa)$$

$$\alpha_{fu} = 0.019 - 0.009 \frac{f_y}{60} \quad (ksi) \quad (7.7)$$

$$\alpha_{fu} = 0.019 - 0.009 \frac{f_y}{414} \quad (ksi)$$

Where

- f', f = dynamic and static yield or ultimate strength of steel (ksi or MPa), respectively
- α = exponent equal to α_{fy} or α_{fu} for yield stress or ultimate stress, respectively
- f_y = yield stress of steel
- $\dot{\epsilon}$ = strain-rate in strain per second. For yield strength calculations, $\dot{\epsilon}$ was taken as the average strain rate from zero to ϵ_y , and from zero to the strain at ultimate stress for ultimate strength calculations.

The dynamic yield and ultimate strengths were calculated using average yield and ultimate stresses from static testing, and strain-rates measured during dynamic testing for respective coupler types. Table 7-25 and Table 7-26 show the comparison between the measured and calculated dynamic yield stress for the HC and GC samples, respectively. The average difference between the measured and calculated dynamic yield stress, according to the Zadeh and Saiidi model, was 5.2% for HC samples, and between 4.3-13.3% for GC sample. A range is given for the GC tests because the strain rate data between zero strain and yield was unreliable; thus, a single value of K could not be determined with confidence. The maximum difference between the measured and calculated dynamic yield stresses for the HC and GC tests using the Malvar model were 8.2% and 14.4%, respectively.

Table 7-27 and Table 7-28 show the comparison between measured and calculated dynamic ultimate stress for HC and GC samples, respectively. For both coupler types, the Zadeh and Saiidi model resulted in a slightly higher average percent difference compared to the Malvar model. The average percent difference between measured and calculated dynamic ultimate strain according to the Zadeh and Saiidi model was 3.8%

and 7.2 for HC and GC samples, respectively. The Malvar model resulted in average differences of 2.9% and 4.2% for the HC and GC samples, respectively.

The two models used to compare measured and calculated dynamic strengths both had good agreement with test results. Therefore it can be concluded that the increase in yield and ultimate strengths observed from dynamic tests compared to static results can be mainly attributed to the effect of loading rate.

The measured stress-strain envelopes for the coupler region of HC samples tested under cyclic loading are compared to the monotonic static behavior in Figure 7-25. The envelope responses for both HCC samples exhibit the same behavior as the monotonic static tests. As expected, the main difference between HCC-1 (with torque) and HCC-2 (without torque) was the stress at which the gap opened. Figure 7-26a and b show the comparison between the cyclic loading stress-strain envelopes and monotonic static curves for the coupler region and sleeve, respectively. The cyclic loading envelopes for both the coupler region and sleeve are comparable to the respective monotonic curves. The most significant difference between static and cyclic tests was the load and strains at failure. The ultimate load and strain at failure for GCC-1 was 11% and 52% lower than the average for the static tests. All samples tested under static loading failed by bar fractures that exhibited ductile failure i.e. necking of the bar in the fractured zone, while GCC-1 exhibited a brittle bar fracture. The data suggests that cyclic loading caused less ductile fracture and the reduced ultimate load and strain compared to the static tests. However, no conclusive statement can be made because of the very limited data and the fact that compressive stresses were limited. It should be noted that failure of GCC-1 was not caused by the splice.

Both coupler devices exhibited reduced ductility in the coupler region compared with the reinforcing bars. The differences between the deformation behavior of the coupler regions and reinforcing bar were quantified by plotting the strain over the coupler region (y-axis) against the strain in the reinforcing bar (x-axis). Strain-ratio plots are shown in Figure 7-27 for both coupler types under static loading. The strain ratio is the slope of the lines in the plot. Four indicator lines show the various strain ratios (slopes) i.e. 1:1, 1:2 etc. Prior to yield, which is shown for 68 ksi [469 MPa] reinforcing steel with an elastic modulus of 29,000 ksi [200 GPa], the behavior of the headed (Figure 7-27a) and grouted (Figure 7-27b) coupler samples were very different relative to one another. The gap between the heads occurs in the headed coupler region shortly after loading begins thus the slope of the strain-ratio curve is large. This indicates that more deformation occurs within the coupler regions relative to the reinforcing bars prior to yield. This was not the case in the grouted coupler region, where the strain ratio was between 1:1 and 1:1.5. This indicates that the grouted coupler assembly is slightly stiffer than the reinforcing bar, which is to be expected because of the sleeve. After yielding, both coupler types exhibit distinct trends in the relationship between bar strain and strain within the coupler region. Once 20,000 microstrain was exceeded within the reinforcing bar, the strain ratio for the headed coupler (Figure 7-27c) samples was between 1:1 and 1:1.5 until approximately 85,000 microstrain. After which point, the strain ratio was between 1:1.5 and 1:2 when failure occurred. The strain ratio for the grouted couplers (Figure 7-27d) remained approximately constant after yielding between 1:2 and 1:3, which was lower than the headed coupler.

Strain-ratio plots are shown in Figure 7-28 for the dynamic load case. All plots are similar to those from the static loading case except for Figure 7-28b, which depicts the grouted couplers prior to yield. The strain ratios were between 1:1.5 and 1:3 for one sample and less than 1:3 for the other two. Although this indicates that the grouted coupler region was stiffer in the case of dynamic loading, the strain ratio exceeds 1:3 after yielding, which was similar to the static loading case.

In conclusion, both coupler types exhibited consistent results for static and dynamic tests. All HC samples failed outside the coupler region with no damage observed in the couplers themselves. All of the GC samples failed by bar rupture outside the coupler region except for one, which failed approximately two bar diameters from the sleeve. Both devices were able to sustain increased demand caused by the strain rate effect of dynamic loading without adverse effect to failure locations, measured strains, coupler region behavior, and ductility. Using two existing models for strain-rate effect, the increase in yield stress and ultimate stress under dynamic loading were quantified. The cyclic loading tests on HC samples quantified the gap opening and closing behavior during load reversals. Cyclic loading of a grouted coupler sample showed comparable results to static tests except for the ultimate load and strain, which were lower compared to static tests due to premature bar rupture. The reason for the lower ultimate strain is not evident. Had the compressive strains been higher, low-cycle fatigue could be the reason. However, the compressive strains were too small to cause buckling. A larger number of test specimens would need to be studied to determine if the observed behavior presents a pattern. Lastly, strain-ratio plots, which depict the relationship between strain over the coupler region and strain in the reinforcing bar, indicate consistent reductions in strain

over the coupler region compared to the bar. For example, the coupler region of GC sample achieves approximately one third the strain of the bar for the duration of loading.

8. Analytical Modeling of Column Models

8.1 Introduction

This chapter presents the analytical models developed for each of the five half-scale column models tested in this study. All of the analytical models were created using OpenSEES, which is an object-oriented, open-source program that can be used to conduct finite element analysis. Created by researchers at UC Berkeley, OpenSEES provides a robust platform for analyzing structural and geotechnical systems subjected to earthquakes.

The analytical models had a number of similarities i.e. geometry, material properties and constitutive models, and reinforcement configuration. Thus, prior to discussing each individual analytical model, the basic components used to develop the models are discussed i.e. element types, material constitutive models, and calculations for bond-slip rotation. Two-dimensional analytical modeling was used for all the columns. Discussion of the general model components is followed by description and results for each individual model. Unique features of the individual models are discussed in respective subsections. The chapter concludes with discussions and concluding remarks.

8.2 General Model Components

8.2.1 Elements

8.2.1.1 Rotational Springs

Rotational spring elements were used for modeling bond-slip rotations caused by strain penetration of longitudinal bars into cementitious material. The “Hysteretic”

material available in OpenSEES was used for describing the moment-rotation behavior of these springs. Figure 8-1 provides a schematic that defines the constitutive behavior of the “Hysteretic” material. The envelope curve for the “Hysteretic” material is defined by two or three points for each loading direction that define a bi-linear or tri-linear primary curves, respectively. These points not only provide the definition of the envelope curve but also information required to define the unloading branch of the curve. The slope of the returning branch, K_r , is a function of the initial slope, K_o , the ductility, μ , and an exponent, β . Equation 8-1 defines the relationship of these constants to the slope of the unloading branch, and Eq. 8-2 provides the definition of ductility.

$$K_r = \mu^{-\beta} K_o \quad (8-1)$$

$$\mu = \frac{e}{e_1} \quad (8-2)$$

Where

- β = exponent used to determine the degraded unloading stiffness
- e = strain or deformation achieved by the spring upon reversal of load
- e_1 = effective yield strain or deformation, which is defined as the first point in the bi-linear (or tri-linear) curve

8.2.1.2 Elastic Beam-Column Elements

Elastic beam-column elements were used to model the loading head atop each column. For two-dimensional analysis, these elements only require that the area, moment of inertia, and elastic modulus of the material be defined. The geometric and material properties of elastic beam-column elements used in this study were selected to provide rigid behavior in the loading head.

8.2.1.3 Nonlinear Beam-Column Elements

The force-based beam-column elements available in OpenSEES were used to model the shaft of the column. This element considers the spread of plasticity along the length of the element. Although lumped plasticity models have been shown to provide good correlation with experimental result and reduced computation time, a discrete plastic hinge length, L_p , must be defined. As discussed in Chapter 4, some of the test columns in this study did not exhibit conventional plastic hinge formation. Thus, distributed plasticity elements were employed. The behavior of the distributed plasticity element is defined by fiber sections that are defined at the integration points along the length of the element. In cases where materials, geometry, or reinforcement change throughout the column, different fiber sections can be assigned to each integration point. The integration scheme used in this study is based on the Gauss-Lobatto quadrature rule, which is the default for the force-based beam-column. The number of integration points used for the different column models varied from five to nine depending on the length of the element. The number of integration points used for each model will be discussed in respective subsections.

8.2.2 Material Models

Many of the uniaxial material models used in the analytical models for the columns were similar. The constitutive models employed for concrete, longitudinal reinforcing steel, and cementitious grout are discussed first. Material models specific to individual analytical models are discussed in respective subsections.

8.2.2.1 Unconfined Concrete

Unconfined concrete was modeled using the “Concrete01”, which requires four input parameters to define the constitutive behavior (Figure 8-2). This material follows the Kent-Scott-Park concrete model and incorporates degrading linear unloading/loading stiffness according to the work of Karsan and Jirsa (1969). Concrete01 has no tensile strength and behaves perfectly-plastic after ϵ_{cu} is reached. Instead of using the common ACI-318 equation (Eq. 8-3), the elastic modulus of concrete, E_c , is defined by Eq. 8-4 using compressive strength of concrete, f'_c , and the corresponding strain, ϵ_{co} .

$$E_{c,ACI} = 57,000\sqrt{f'_c} \quad \text{psi} \quad (8-3)$$

$$E_{c,ACI} = 4700\sqrt{f'_c} \quad \text{MPa}$$

$$E_c = 2 \frac{f'_c}{\epsilon_{co}} \quad (8-4)$$

The numerical values for three of the four input parameters required to define the Concrete01 material were selected to be constant for all the column models: 1) strain at concrete crushing, $\epsilon_{co} = 0.002$; 2) strain at failure, $\epsilon_{cu} = 0.005$; and 3) stress at failure, $f'_{cu} = 0$. The aforementioned strains correspond to the strain at peak stress, which is a widely accepted value, and spalling of cover concrete, which was taken according to recommendations in Caltrans SDC, respectively. The Concrete01 material behaves perfectly plastic at a stress of f'_{cu} after ϵ_{cu} is reached. In this study, unconfined concrete is only present in the cover layer of concrete that surrounds the reinforcing cage. Once the cover has spalled off there would be no residual capacity, thus the stress, f'_{cu} ,

corresponding to spalling of concrete was selected to be zero. The compressive strength of concrete was determined by compression tests, which are discussed in Section 4.2.

8.2.2.2 Confined Concrete

Confined concrete was modeled using the “Concrete04” material, which requires six input parameters to define the constitutive behavior when tensile strength of concrete is included (Figure 8-3). The backbone of the stress-strain curve is defined by Popovic’s (Popovic, 1973) concrete model when the material is in compression. If the elastic modulus of concrete, E_c , is defined by Eq. 8-3 the compression stress-strain backbone is identical to Mander’s (Mander et al., 1988) model. Once the ultimate compression strain, ϵ_{cu} , is passed, the compression stress capacity goes to zero. There is an option to include or exclude tensile capacity of concrete when using Concrete04. If included, the tensile rupture stress and strain can be defined by the user. Once the tensile rupture strain, ϵ_t , is reached, the tensile capacity degrades exponentially to zero with increased tensile strain. Similar to Concrete01, Concrete04 incorporates degrading linear unloading/loading stiffness in both tension and compression according to the work of Karsan and Jirsa (1969).

The properties for the Concrete04 material were determined using Mander’s model. Mander’s confined concrete model uses the material properties of unconfined concrete, section geometry, and the transverse reinforcement material properties, spacing, and geometry to determine the confined constitutive behavior of concrete. All column models used the same transverse reinforcing steel and spiral pitch. The confined core diameters were slightly different between CIP/GC model and the HC model. The

compressive strength of unconfined concrete was determined by compression testing. Mander's model also requires the strains that correspond to failure of unconfined concrete. These strains were constant among the different concretes: strain at peak concrete stress, $\epsilon_{co} = 0.002$; the strain at failure, $\epsilon_{cu} = 0.005$. The elastic modulus of concrete was determined using Eq. 8-3.

8.2.2.3 Unconfined and Confined Grout

Cementitious grout was used for closing the connection regions in the HC column models. Currently, there are no models available to describe the unconfined and confined constitutive behavior of grout. Thus, the constitutive behavior of grout was defined using the previously discussed models for concrete. That is, Concrete01 was used for the constitutive behavior for unconfined grout, and Concrete04 was used for confined grout. The confined properties of grout were determined using Mander's model. For both confined and unconfined grouts, the strain at peak stress and failure were defined as $\epsilon_{go} = 0.002$ and $\epsilon_{gu} = 0.006$, respectively.

8.2.2.4 Reinforcing Steel

The stress-strain behavior of longitudinal reinforcing steel fibers was defined using the "ReinforcingSteel" material. This is a robust material model that can not only describe the stress-strain behavior of mild steel reinforcing bars but also incorporates the effects of buckling or low-cycle fatigue using available models from literature. The input parameters for ReinforcingSteel can be determined from a monotonic tension testing. Figure 8-4 shows the general monotonic curve for a mild steel reinforcing bar under tensile loading, and the six required input parameters for ReinforcingSteel.

The properties for steel fibers were determined from monotonic tension testing of reinforcing bar samples. As discussed in Section 4.2.4, there were three different lots of reinforcing bars used to construct column models. Five out of the six required input parameters were determined from testing bar samples from each lot. The only input parameter that remained constant for different bar types was the elastic modulus, E_s , which was selected to be 29,000 ksi [200 GPa]. Once the ultimate stress is reached, the stress remains constant.

8.2.3 Bond-slip Rotation Modeling

As moment is applied to the column, the bar tensile stress must be transferred into the footing through bond between the bar and footing concrete. If the bar is well anchored, force transfer will occur over a length, l_d , which is referred to as the “development length”. As the bond strength of concrete is overcome, strain begins to accumulate in the reinforcing bar and the bar starts to deform or “slip” relative to the concrete in the footing. This slip causes a concentrated rotation at the column-footing interface, which results in additional displacement in the column. Studies have indicated that bond-slip rotation at the column-footing interface can account for as little as 15-20% (Wehbe et al., 1999) and as much as 50% (Lehman and Moehle, 1998) of the lateral displacement of a column. Thus it is critical to account for this behavior when developing analytical models. The analytical models developed in this study employ the method developed by Wehbe et al. (1999) to account for the bond-slip rotation at the column-footing interface.

8.2.3.1 Calculating M- θ Relationship

Figure 8-5 provides a schematic for the bond-slip rotation calculation procedure. Wehbe's method assumes that the bond-slip rotation occurs about the neutral axis of the member, and that the bond stress over the development length is constant, which results in a linear or bilinear distribution of bar strain. The tensile stress/strain in the extreme reinforcing bar and the neutral axis location, c , are determined using moment-curvature analysis. The slip in the extreme tension bar can then be calculated by integrating the strain from the surface of the footing over the development length, l_d , (Eq. 8-5). Since, the strain distribution is linear up to yield and bilinear after yield, Eq. 8-5 can be rewritten as Eq. 8-6.

$$\delta_{slip} = \int_0^{l_d} \epsilon \, x \, dx \quad (8-5)$$

$$\delta_{slip} = \begin{cases} \frac{\epsilon_s l_1}{2} & \text{if } \epsilon_s \leq \epsilon_y \\ \frac{\epsilon_s l_1}{2} + \frac{\epsilon_s + \epsilon_y}{2} l_2 & \text{if } \epsilon_s > \epsilon_y \end{cases} \quad (8-6)$$

The lengths l_1 and l_2 are determined using Eq. 8-7 and 8-8, respectively.

$$l_1 = \frac{f_s d_b}{4u} \quad (8-7)$$

$$l_2 = \frac{f_s - f_y}{4u} d_b \quad (8-8)$$

Where

$$u = \frac{9.5\sqrt{f'_c}}{d_b} \leq 800 \quad \text{psi}$$

$$u = \frac{20\sqrt{f'_c}}{d_b} \leq 5.5 \quad \text{MPa}$$
(8-7)

Once the slip is known, the resulting rotation at the base of the column can be calculated using Eq. 8-8 for each corresponding moment from M- ϕ analysis.

$$\theta_{slip} = \tan^{-1} \left(\frac{\delta_{slip}}{c - d} \right)$$
(8-8)

Where

c = neutral axis location determined from moment-curvature analysis

d = column diameter

8.2.3.2 Implementing the M- θ Relationship in OpenSEES

As discussed in Section 8.2.1.1, bond-slip rotations were modeled in OpenSEES using rotational springs. The constitutive behavior of these springs was provided by the “Hysteretic” material model, which uses two to three force-deformation points to describe the response envelope. After the full M- θ relationship was determined by Wehbe’s method described in the previous section, an equivalent bi-linear curve was determined for implementation in OpenSEES. Figure 8-6 provides a schematic depicting the calculated M- θ determined by Wehbe’s method and the equivalent bi-linear curve. The initial slope of the bi-linear curve was determined by passing a straight line through the first yield point (M_y, θ_y) of the longitudinal steel determined from moment-curvature analysis. The effect yield point ($M_{y,eff}, \theta_{y,eff}$) was determined by balancing the area of the calculated and bi-linear curves after the first yield point. The second point of the bi-

linear curve was selected as the moment and rotation that corresponded to onset of core concrete crushing as determined from the moment-curvature models.

The slope of the returning branch of the bi-linear curve (Eq. 8-1), as mentioned previously, is a function of the initial stiffness (K_o), the ductility upon load reversal (Eq. 8-2), and an exponent β , which controls of the degradation of the returning slope. In initial trials, β was set at 0.5. The final value of β was between 0.3 and 0.4, which resulted in better correlation with experimental result.

8.2.4 General Details

Figure 8-7 presents the general details of each column model. The 96-in [2438-mm] shaft of each column consisted of distributed plasticity beam-column elements. A single element was used in CIP, while the precast models utilized multiple elements. Atop the column shaft was the loading head, which was modeled with three elastic beam-column elements. The material properties of these elements were selected such that rigid behavior would be achieved. Load was applied to each model using displacement control. Displacements were applied to the left-hand node of the loading head and the corresponding displacements were recorded from the right-hand center node. Each analytical model was subjected to the displacement history until the first bar fracture. Axial load was assigned to the upper-most node of the loading head. Due to the nature of the axial loading configuration used in the experimental tests, all models neglected the P- Δ effect. Although a nitrogen accumulator was used to maintain constant axial load on each model during testing, the load did vary slightly during the test. Table 8-1 shows a summary of the measured axial load data from each test. The average measured axial

load (all axial load data was included) from each of the five column tests was applied to each analytical model, respectively. Specific details regarding the axial load applied to each analytical model is discussed in respective subsections.

The rotational spring for bond-slip behavior at the column-footing interface (Section 8.2.3) was a zero-length element placed between the fixed column-footing interface node and the bottom node of one of the column shaft elements.

8.3 Modeling of Low-Cycle Fatigue Failure

One of the primary failure mechanisms of reinforced concrete columns subjected to a strong seismic event is low cycle fatigue fracture of longitudinal reinforcing bars (assuming adequate confinement to prevent substantial core damage and/or excessive longitudinal bar buckling is provided). During these events, large inelastic strain reversals occur in the longitudinal bars with strain amplitudes in excess of 0.06 in some cases [Mander et al., 1994]. Experimental studies on ASTM A706 and A615 bars have indicated that as little as seven full cycles of 0.06 strain can result in low-cyclic fatigue fracture of bars [Hawileh et al., 2010]. Although bar buckling was found to have occurred in most of the columns tested, it is not incorporated into the determination of failure.

The fatigue life of a material subjected to any strain range can be estimated by Eq. 8-9, which is known as the generalized Coffin-Manson relationship [Coffin 1954; Manson 1953]. This relationship accounts for the effects of both high-cycle (elastic range strain reversals) and low-cycle (plastic strain reversals) fatigue. A series of constants can be experimentally determined to develop a fatigue-life model for a given

material. These constants are typically determined using strain-based uniaxial tension/compression testing, which are conducted such that strain reversals form stable hysteresis loops. A representative schematic shown in Figure 8-8 identifies key points on the hysteresis loop.

$$\varepsilon_a = \frac{\Delta\varepsilon_a}{2} = \underbrace{\frac{\sigma_f'}{E}(2N_f)^b}_{\text{Elastic Component}} + \underbrace{\varepsilon_f'(2N_f)^c}_{\text{Plastic Component}} \quad (8-9)$$

Where

ε_a = total strain amplitude

$\Delta\varepsilon_a$ = total strain range ($\varepsilon_{\max} + |\varepsilon_{\min}|$)

σ_f' = fatigue strength coefficient

E = elastic modulus

N_f = number of full cycles to failure (thus $2N_f$ is the number of half-cycles)

b = fatigue strength exponent

ε_f' = fatigue ductility coefficient

c = fatigue ductility exponent

The original Coffin-Manson relationship, which is shown in Eq. 8-10, did not include a term for the high-cycle (elastic) fatigue. Although, this model is commonly used and the data is available for determining the constants, there can be some difficulties. First, due to Bauschinger effects, the plastic strain amplitude ε_p can be somewhat difficult to define. Second, it is more simplistic and straightforward to use the total strain amplitude, ε_a , for developing an algorithm to determine low-cycle fatigue fracture based on results from an analytical model. The total strain amplitude is defined as the width of the stress-

strain hysteresis loop, which is the summation of the maximum positive strain and the absolute value of the maximum negative strain. Equation 8-11 is a variant of Eq. 8-10, and uses the total strain amplitude rather than the plastic strain amplitude for defining fatigue-life parameters. This expression was suggested by Koh and Stephens (1991). As described above, the constants for Eq. 8-11 can be determined by testing the material of interest. Multiple tests need to be conducted at different strain amplitudes. The strain amplitude would then be plotted against the corresponding number of half-cycles to failure, $2N_f$. Based on this plot, which is shown in Figure 8-9, the required constants ϵ'_{fa} and c_a can be determined.

$$\epsilon_p = \frac{\Delta\epsilon_p}{2} = \epsilon'_{fp} (2N_f)^{c_p} \quad (8-10)$$

$$\epsilon_a = \frac{\Delta\epsilon_a}{2} = \epsilon'_{fa} (2N_f)^{c_a} \quad (8-11)$$

Since CIP and the GC models were reinforced with A615 bar and the HC models with A706 bars, two sets of low-cycle fatigue constants were required; one for each bar types. For A615 bars, fatigue constants were determined from data reported by Brown and Kunnath (2000). Tests conducted by Brown and Kunnath were on ASTM A615 Gr. 60 No. 8 bars. For A706 bars, fatigue constants were determined from data reported by Zhou et al. (2010) on tests using ASTM A706 Gr. 60 No. 8 bars. The data sets for the two studies are shown in Figure 8-10 and Figure 8-11, respectively. For reference, fatigue parameters determined by different researchers for plastic and total strain amplitude are listed in Table 8-2 and Table 8-3 respectively. It can be observed that the fatigue ductility coefficient, ϵ_f , and exponent, c , vary among the reported data. The large

variation is because these parameters depend on the material type and tend to vary with the size of the reinforcing bar. The cumulative damage in a given longitudinal bar subjected to any loading pattern can be calculated using Eq. 8-12. The damage index D is the sum of the reciprocal of the number of half-cycles to failure (Eq. 8-13) for the maximum strain recorded from the analytical model during each cycle of loading (ε_{a_i}).

When the sum equals unity, the bar is considered to have failed.

$$D = \sum_i \frac{1}{2N_{f_i}} \quad (8-12)$$

Where

$$2N_{f_i} = \left[\frac{\varepsilon_{a_i}}{\varepsilon_{f_a}} \right]^{c_a} \quad (8-13)$$

A procedure was written using Matlab to determine the point of first longitudinal bar fracture. A schematic and a flowchart shown in Figure 8-12 and Figure 8-13, respectively, accompany the explanation of how failure was determined. In each model, strain was recorded from the extreme longitudinal reinforcing bar fibers in critical sections within the column. The damage index was calculated for the maximum strain occurring at the i^{th} peak displacement. Once $D_i > 1$, the procedure returns to the previous peak strain ($i-1$) and damage index D_{i-1} . Beginning with $D = D_{i-1}$, the damage index is calculated for each intermediate strain ε_k between ε_{i-1} and ε_i until $D > 1$. Once D exceeds unity the corresponding load and displacement are reported, which indicate the failure point.

8.4 Analytical Modeling of CIP

8.4.1 General Model Details

A detailed schematic of the analytical model for CIP is shown in Figure 8-14a, and the fiber section at each nonlinear beam-column integration point is shown in Figure 8-14b. The model was composed of six nodes, two elements with nonlinear behavior, and three stiff elastic elements. The nonlinear beam-column element used to model the shaft of the column had nine evenly-spaced (12 in [305 mm] on center) integration points. Although five points would have been sufficient according to Neuenhofer and Filippou (1997), nine points were used in order to extract information from sections that were instrumented in the tests. A single, three-material fiber-section was used at each integration point. The number of sectors within the fiber section was determined by sensitivity analysis. That is, the number of sectors was incrementally reduced until there was little apparent change in the force-displacement response of the model. The material properties for longitudinal reinforcing steel and unconfined and confined concrete are listed in Table 8-4 and Table 8-5, respectively.

As discussed in Section 8.2.4, the axial load applied to each model was determined by averaging the measured axial loads. For CIP, the average measured axial load was 208 kip [923 kN], which was applied to node 5 of the model.

Moment-curvature analysis was conducted in OpenSEES using the section shown in Figure 8-14b to calculate the stresses and strains required for bond-slip rotation calculations. The moment-curvature responses from the push and pull directions are shown in Figure 8-15. Although the maximum moment in the push direction was only

4.2% larger than that in the pull direction, bond-slip rotation was still calculated in each direction in order to capture the difference in loading directions. The moment-rotation relationship for bond-slip rotation at the column-footing interface is shown in Figure 8-16. The values for the idealized moment-rotation relationship, which were used to define the behavior of the rotational spring at the column-footing interface, are listed in Table 8-6.

8.4.2 Results

8.4.2.1 Force-Displacement Relationships

Figure 8-17 compares the measured and calculated hysteresis curves for CIP. In general, there was very good correlation between the two curves. The most apparent difference between the measured and calculated response were the peak forces between 2.0% and 3.0% drift. At 2.0% and 2.5% drift, the peak measured force was approximately 10% larger than the calculated value. This difference was caused predominately by the location of the reinforcement cage within the column and the cover concrete. It was determined after testing that the reinforcement cage for CIP was slightly off-center to the west, which resulted in 0.25 – 0.5 in [6 – 12 mm] of extra cover concrete on the east face of the column. This explains the peak that at 2.5% drift in the measured data and the subsequent decrease in lateral force due to spalling. The only other apparent difference in peak load in the push direction occurred at 10%, where the calculated load was 5.6% larger than the measured load. Similarly, the largest difference in the peak lateral load in the pull direction occurred at 2.0%, in which the measured load was 3.2% larger than the calculated value. In the pull direction, the calculated load at all other peak

drifts was approximately the same as measured data. Good correlations between the two curves were also observed in the returning paths from peak drift, the residual displacements, and the location of pinching due to closure of cracks.

The average envelopes for CIP are shown in Figure 8-18. The ascending branches of the two curves were the same until 1.0% drift. Furthermore, there was little difference in the measured and calculated yield points of the longitudinal reinforcing steel. The average percent difference of the calculated load and displacement at first yield, relative to measured data, were -2% and 11%, respectively. After 1.0% drift, the calculated curve tends to soften at a higher rate than the measured curve. As mentioned above, this discrepancy can be attributed to misalignment of the reinforcement cage and cover thickness, which could not be fully incorporated into the analytical model. After 3.0% drift, the difference between the two curves was negligible. In general, there was good agreement between the measured and calculated envelopes.

8.4.2.2 Energy Dissipation

The energy dissipation was determined by calculating the area enclosed by each hysteresis loop. Figure 8-19 shows a comparison between the results for measured and calculated energy dissipation. The cumulative energy dissipated per drift level is shown in Figure 8-19a in which there was no apparent difference between measured and calculated energy dissipation. This result is to be somewhat expected given the similarity between the measured and calculated hysteresis loops. The percent difference between the measured and calculated energy dissipation is shown in Figure 8-19b for both cycles along with the cumulative dissipation per drift level. The results are shown after 2% drift

because before this drift level in elastic deformations were insignificant. After 4% drift, there was less than $\pm 5\%$ difference between the calculated and measured dissipated energies.

8.4.2.3 Local Behavior

The ability of the analytical model to duplicate the local behavior such as bond-slip rotation, curvature, and strains was evaluated by comparing the calculated and measured results. Figure 8-20 shows a comparison between the measured and calculated strains for two locations within CIP. At the column-footing interface (Figure 8-20a) there is good correlation between the measured and calculated tensile strains for each drift level. This is especially true as the drift becomes larger than 4%. On the other hand, the compressive strains do not correlate as well as the drift becomes large. At some points the difference is greater than 100%. In the experiment, damage to core concrete began at 8% drift. Therefore, the longitudinal reinforcing bars were subjected to higher stresses. Crushing of core concrete was not captured in the analytical model; therefore the large compressive strains are not seen in the hinge zone. Away from the hinge zone, the correlation between the measured and calculated strains is relatively close (Figure 8-20b), because the extent of non-linear deformations is relatively small.

Figure 8-21 depicts the bond-slip moment-rotation relationship at the column-footing interface. The measured and calculated responses are only shown up to 6% drift because measurements became unreliable due to delamination of concrete in the footing. Note that the measured bond-slip is influenced by local yielding of the longitudinal bars over the gauge length. This effect is not included in the theoretical model. The

calculated bond-slip rotation tends to overestimate the measured rotation after the effective yield point. This is especially true for the pull cycles in which rotations are negative. Yet, this is not unexpected because bond-slip in the actual column occurs more gradually compared to the calculation, which uses an effective yield point than a rather flat post-yield branch. Furthermore, the pinch that occurs near zero rotation is not captured. These differences are acceptable because Wehbe's method provides an approximation to the bond-slip behavior and that the measured bond-slip is not purely due to slippage of the bars.

Figure 8-22 shows the measured and calculated moment-rotation relationships over a 14-in [356-mm] length directly above the footing. This was the region where the majority of plastic rotation occurred in CIP. It can be observed that peaks and shape of the hysteresis loops are similar. Furthermore, there was little difference between the two curves with regard to the location of pinching. Good correlation indicates that the CIP analytical model can reasonably predict the rotations within the plastic hinge zone.

8.4.2.4 Modeling of Longitudinal Bar Fracture

The longitudinal bar fracture for CIP was modeled using the Coffin-Manson constants determined by Brown and Kunnath (2000) for ASTM A615 steel. Figure 8-23 shows the cumulative damage D as a function of the drift level. At each drift level, a vertical line segment is shown, which indicates the damage that occurred during cycles of that magnitude. The plot indicates that the damage index exceeds unity between 8% and 10% drift, which means that first fracture occurs during that first cycle of 10% drift. In reality, the first fracture occurred in the extreme west reinforcing bar at 6.6% drift during

the first push cycle to +10% drift. On the east side, the first longitudinal bar fractured during the second pull cycle to -10% drift. It can be seen that the prediction of low-cycle fatigue fracture is within the range of the experimental result. Figure 8-24 can be used to determine the cycle, drift, and load for a given damage index.

8.5 Analytical Modeling of HCNP

8.5.1 Modeling of Headed Coupler Assembly

Prior to developing a full analytical model of HCNP, an effort was made to develop a method to capture the behavior of the headed coupler assembly. As discussed in Section 7.2.3, a distinct gap opening/closing mechanism occurred in the headed coupler assembly when subjected to load reversals. Figure 8-25 illustrates the four states that were defined to describe this behavior and develop a simple analytical model.

- State 1: The pre-compression of the deformed heads, which is the result of the torque applied to tighten the threaded collars and join the two bars, has not been exceeded. Transition from State 1 to State 2 begins when net tension is present in the bars.
- State 2: The pre-compression of the bar is overcome and a gap begins to form. The length of the gap was found to be proportional to the stress in the bars (Fig. 7-12). Transition from State 2 to State 3 begins as the load is reversed and approaches zero.
- State 3: As the load in the bars becomes approximately zero, the assembly has zero stiffness. During this time the gap must close prior to compression force is transferred between the bars. Transition between State 3 and State

4 begins as the gap begins to close.

State 4: Compression is transferred directly between the heads without any interaction with the threaded collars.

Using this four-state model, a gap-opening element was developed with a group of parallel springs. Figure 8-26 shows the analytical model that was used to validate the parallel spring configuration for the gap-opening element. The component was composed of four nodes, two 3-in [76.3-mm] reinforcing bar truss elements (ReinforcingSteel material), and a zero-length gap-opening element, which was composed of three spring in parallel (S1, S2, and S3). The geometry and material properties used in the model were identical to those from the HC cyclic loading tests discussed in Chapter 2.

The constitutive behavior of springs S1-S3 is shown in Figure 8-27 through Figure 8-29, respectively. Spring S1 was used to describe the behavior of State 1 and 2 along with the transition to State 3 (Figure 8-27). The constitutive behavior of S1 was defined using the “Elastic-Perfectly Plastic Gap Material” in OpenSEES. A large initial stiffness, K_1 (with $E=10 \times E_s$), was used for S1 to simulate rigid behavior. S1, which acts like a lock mechanism and transfers force directly to the reinforcing bars. The stiffness of Branch 2, K_2 , otherwise known as the stress-displacement relationship for gap-opening, was 1040 ksi/in [282 MPa/mm]. This was determined experimentally (Section 7.2.3). The stiffness of the returning branch to zero load (Branch 3) was equal to K_1 . Branch 4, which controlled the return to zero displacement, had zero stiffness.

State 3 and the transition to State 4 were controlled by S2 (Figure 8-28), which had linear elastic behavior with an approximately zero stiffness. This spring was used to

prevent the system from reaching a point of zero stiffness during return cycles, which results in convergence issues. Figure 8-29 shows the constitutive behavior for S3, which was a rigid ($10x E_s$), compression only spring used to represent State 4 and transmit compression directly between the reinforcing bar elements. The combined behavior of the spring systems can be observed in Figure 8-30, which also identifies the spring that controls each part of the curve. Since the springs are in parallel, their stiffness is additive. The stiffness of each branch in the combined curve is approximately the same at the controlling spring.

The component model was subjected to the displacement history that was measured from the cyclic tensile test of HCC-1. Node 4 of the model was loaded to the displacement corresponding to the peak stress for a given cycle. Once the peak displacement was reached the load was reversed until the corresponding displacement in compression was reached. Figure 8-31a shows the analytical and experimental results for HCC-1. The response of the gap element is shown in Figure 8-31b. The proposed model captures the envelope response of HCC-1 and the unloading branch of the stress-strain curve once yielding begins. However, it can be observed in both plots that the gap does not close completely, which indicates that the gap length was overestimated. A second displacement history was applied to the models, in which the displacement applied in the compression direction was lengthened slightly to capture the complete gap closure.

Figure 8-32 shows the response of the model under the modified displacement history in comparison with the test results from HCC-1, and the response of the zero-length gap element. Using a modified displacement history, the closure of the gap is captured in the post-yielding region. If the stress in the bar has not exceeded yield,

compression stress is only generated once the strain in the model completely returns to zero. This indicates that there is some permanent deformation that occurs with the coupler assembly prior to yielding.

This gap element was implemented into the model of HCNP (discussed in the next section). Preliminary analysis showed that inclusion of the gap element resulted in significant over-estimation of the displacement of the column and formation of a concentrated hinging mechanism. It is believed that in the actual HCNP column, grout enters the couplers and retards the gap-opening behavior. The gap element was not included in the final HCNP analytical model.

8.5.2 Model Details

The detailed schematic of the analytical model for HCNP is shown in Figure 8-33. The model was composed of seven nodes, three elements with nonlinear behavior, and three stiff elastic elements simulating the loading head. The grouted cover region, which was 22 in [559mm] long, was modeled using a single nonlinear beam-column element with five integration points. The fiber section at each integration point was the same and is represented in Figure 8-33c. The remainder of the column shaft was also modeled using a single nonlinear beam-column element with five integration points. The fiber section used in this region is shown in Figure 8-33b.

The material properties for longitudinal reinforcing steel and the various cementitious materials are listed in Table 8-7 and Table 8-8, respectively. The axial load applied to the model was 206 kip [918 kN], which was the average measured axial load from the HCNP column test (the axial load ranged from 188 kip [836 kN] to 222 kip [987 kN]).

The bond slip rotation at the base of the column was determined using moment-curvature analysis of the fiber section shown in Figure 8-33c. The moment-curvature response of this section and the corresponding moment-rotation curves from bond-slip are shown in Figure 8-34 and Figure 8-35, respectively. The moment and rotation values used to define the response of the rotational spring at the column-footing interface are listed in Table 8-9.

There were three differences between the analytical model used for HCNP and the physical model tested:

- 1) During construction of the precast column shell, No. 3 [Dia. 10] longitudinal bars were used in constructing the geometry changes at the base of the shell.

Preliminary analytical models of HCNP indicated that these bars did not have a significant effect on the behavior of the model. Thus, they were not included in the final model.

- 2) The precast column shell incorporated a change in geometry at 8-in [43-mm] directly above the grouted region, which facilitated the flow of SCC into the base of the hollow shell. The section was excluded from the final model because the short element used to model this region resulted in convergence problems.
- 3) As mentioned in Section 8.5.1, the individual couplers were not included in the final model.

8.5.3 Results

8.5.3.1 Force-Displacement Relationships

Figure 8-36 shows a comparison between the measured and calculated hysteresis curves for HCNP. There was very good correlation between the measured and calculated hysteresis behavior for HCNP. Specifically, the general shape of the hysteresis loops are very similar, as are the unloading branch paths from peak drift, the residual displacements, and the location of pinching due to crack closure. There are two apparent differences between the measured and calculated curves: 1) the slight pinching caused by gap closure within the couplers is not present in the calculated curve; 2) the load at peak drift for pull cycles tends to be larger in the calculated curve compared to the measured values during pull cycles. As described in Section 8.5.1, the gap-opening element was not incorporated into the model of HCNP. Therefore it is not expected that the pinching effect to be present. The maximum difference in load at peak drift was 9.0%, which occurred during -10% drift. During push cycles the maximum difference between the measured and calculated curves was 2.9% at +2% drift.

The average envelopes for HCNP are shown in Figure 8-37. The ascending branches of the two curves are the same until 0.75% drift. At which point the measured curve begins to soften slightly, while the calculated curve maintains the initial stiffness. Between 2% and 8% drift the two curves are approximately the same. By 10% drift the measured curve has softened while the calculated load continues to increase, which results in a slight difference in the overall capacity between the two. In general, the hysteresis and envelopes are very similar.

8.5.3.2 Energy Dissipation

A comparison between the measured and calculated energy dissipation for HCNP is shown in Figure 8-38. It can be seen that the calculated dissipated energy exceeds the measured data slightly. This difference was expected since the gap opening/closing behavior was not incorporated in the analytical model of HCNP and the associated slight pinching was not captured. Prior to 5% drift the calculated cumulative energy dissipation was 25% greater than the measured result. By 8% drift, the difference between the calculated and measured energy dissipation was less than 10%. Given the known differences between the analytical and physical model, these differences are acceptable.

8.5.3.3 Local Behavior

The measured and calculated strains within the grouted region are shown in Figure 8-39. The largest calculated strain within the grouted region occurs at the column-footing interface (Figure 8-39a). The measure strain data is only shown up to 6% drift due to gage malfunction. It can be observed that strain at this location is being overestimated by the analytical model compared to the test results. Yet, this is similar to what was observed at the same location for CIP. That is, for the lower drift levels, the calculated strain tended to be larger than the measured strain. It was not until 8% that the difference became small. Conversely, in the remainder of the grouted region the difference between the measured and calculated tensile strains was negligible up to 4% drift, and there was little difference in the compressive strains for all drift levels. The most significant discrepancy between the strains occurs at the top of the grouted region (Figure 8-39d). The calculated strain indicates that very little plastic deformation occurs within the

section, while the test result indicates that tensile yielding of steel occurs at +4% drift and strain as large as 35,000 microstrain were recorded.

Figure 8-40 depicts the moment-rotation relationships for the column-footing interface and over the entire grouted region. The measured and calculated moment-rotation hysteresis curves due to bond-slip at the column-footing interface are compared up to 6% drift in Figure 8-40a. In general the calculated bond-slip rotation tends to overestimate the measured rotation by as much as 100% at 6% drift. The calculated and measured moment-rotation behavior over the grouted region is comparable (Fig. 8-40b) despite the differences that were observed in the strains along the same length. These results indicate that although the global response of HCNP can be determined with good correlation with the test result, the accuracy at the local level is not as good. One major contributing factor could be the material properties and constitutive models employed for the confined and unconfined grout.

8.5.3.4 Modeling of Longitudinal Bar Fracture

The prediction of longitudinal bar fracture for HCNP was done using the Coffin-Manson constants determined by Zhou et al. (2008) for ASTM A706 steel. Figure 8-41 shows the cumulative damage D as a function of the drift level for HCNP, which provides an estimate of how rapid damage occurs in the critical reinforcing bar. Fracture of the first longitudinal bar was predicted to occur on the west face of the column at +7.6% drift during the second push cycle to +10%. In the test of HCNP, the first longitudinal bar fracture occurred on the east side of the column during the second pull cycle to -10% drift and was in reasonable agreement with the experimental result. The

relationship between the calculated damage index, drift, and load can be observed in Figure 8-42.

The calculated strain history for the extreme bars in HCNP was also analyzed using the Coffin-Manson parameters experimental determined by Hawileh et al. (2010). It was determined that using these parameters in the low-cycle fatigue analysis significantly underestimated the life of the bars. Failure of the first reinforcing bar was predicted to occur during the first cycle of +5% drift. One possible explanation for the discrepancy is that the tests conducted by Hawileh et al. were completed using No. 6 bars.

8.6 Analytical Modeling of GCNP

8.6.1 Grouted Coupler Component Model

Prior to developing the full GCNP model, a brief study was conducted to determine effective section and material properties for the grouted couplers. Effective material properties and sleeve geometry are of interest because the cross-section of the sleeve changes with length and the material properties for the ductile iron material that composes the sleeve are not provided by the manufacturer.

Based on the test results and observations discussed in Section 7.3, the uniaxial force-deformation response of the GC splice over the coupler region was governed by combined behavior of reinforcing bars, the ductile iron sleeve, the grout filling, and strain penetration of the reinforcing bars into the sleeve. Figure 8-43 shows the general details of the GC component model that was used to validate the modeling methodology for the grouted coupler system. The component model for the grouted coupler was based on the geometry and testing configuration of the individual tensile test samples discussed in

Chapter 2. The model was composed of six nodes and five nonlinear truss elements; two reinforcing bar elements, two strain penetration elements, and a single grouted sleeve element.

The constitutive model for the reinforcing bar elements was defined using the “ReinforcingSteel” material and material properties determined by tension testing. The center element represents the grout-filled sleeve. The stress-strain behavior of the sleeve, as measured from experiment, was non-linear and lacked a well-defined yield point (Figure 8-44). The material properties for ductile cast iron vary greatly depending on the chemical constituents (Rio Tinto Iron & Titanium, 1990). For example, ductile cast iron with a specified yield stress of 40 ksi [275 MPa] will typically be able to undergo more than 18% elongation at failure, while a ductile cast iron with a specified yield stress of 90 ksi [620 MPa] may only achieve 2% elongation at failure (ASTM A536). The sleeves used in this study were composed of Grade 85-60-6 (nomenclature: [minimum ultimate strength] - [minimum yield strength] - [minimum percent elongation within 2-in [50-mm] gage length]) ductile cast iron conforming to ASTM A536 specification. This data was provided by the manufacturer of the coupler and is valid for couplers joining bar sizes greater than No. 6. According to the study conducted by the Michigan Department of Transportation (MDOT) (Jansson, 2008), the measured tensile properties for the ductile cast iron from a Grade 85-60-6 splice were significantly greater than the minimum specifications. The reported ultimate stress, yield stress, and elongation at failure were 131 ksi [903 MPa], 76 ksi [523 MPa], and 12.9%, respectively. Given the variability of material properties for the sleeve, an idealized tri-linear constitutive model is proposed

for the cast-iron material that composes the grouted sleeve, based largely on experimental results from this study and available literature.

Figure 8-45 shows the proposed idealized model for the ductile cast-iron material. Data from tensile tests of individual couplers and column tests indicated that the maximum recorded strain in the sleeve was 7500 microstrains prior to reinforcing bar fracture. It should be noted that in both cases the sleeve was filled with grout. However, the contribution of the grout to the tensile/compressive stiffness of the coupler assembly is minimal compared to the iron sleeve. Thus, the grout is neglected in the determination of sleeve properties. The elastic modulus of ductile cast iron has been reported between 23,500 ksi [162 GPa] and 24,500 ksi [169 MPa] (Rio Tinto Iron & Titanium Inc., 1990). The ascending branch of the constitutive model, E_{sleeve} , was taken as the highest reported value, 24,500 ksi [169 MPa], which correlated well with experimental results. The effective yield, $\sigma_{y,eff}$, and ultimate, σ_u , stresses were determined according to the minimum material properties specified in ASTM A536 for Grade 85-60-6 ductile cast iron along with the ultimate strain, ϵ_u . Thus, the effective yield stress, ultimate stress, and ultimate strain were 60 ksi [413 MPa], 85 ksi [586 MPa], and 6%, respectively. Table 8-10 list the properties that define the tri-linear constitutive model for ductile cast iron according to the points identified in Figure 8-45.

Figure 8-46 shows a comparison among the proposed model, a similar tri-linear model based on MDOT tests, and measured data from the tensile test of GS3. The proposed model is shown as described in the previous section. The MDOT model was created using the same tri-linear format as the proposed model and the reported material properties; the effective yield stress, ultimate stress, and ultimate strain were 76 ksi [523

MPa], 131 ksi [903 MPa], and 12.9%, respectively. Both tri-linear curves have the same elastic modulus. Within the range of observed strains from testing, the proposed model is the most reasonable. Although the proposed model overestimates the stress-strain curve compared to the observed behavior of the sleeve, it is not as significant as the tri-linear MDOT model.

A study conducted by Matsuzaki et al. (1987) investigated the strain distribution along the length of the coupler sleeve when subjected to uniaxial tension. Figure 8-47 shows that the strain distribution could be interpreted as parabolic or triangular in nature. Achieving this non-linear strain distribution in an analytical model would require numerous elements and is not practical. It is more practical to use a single element to represent the sleeve with uniform force-deformation properties; thus capturing the deformation response. The simplified constitutive relationship for the sleeve was developed by assuming that the same deformation would be achieved under a given uniaxial load. Figure 8-48 provides a schematic that illustrates the “actual” and uniform strain distributions. Assuming that actual and uniform distributions produce that same deformation δ , a relationship between the actual strain at the mid-height of sleeve and the corresponding uniform strain distribution can be established (Eq. 8-14). Thus, the stress-strain relationship for the uniform element can be defined by scaling the strains of the bi-linear curve by the coefficients shown in Eq. 8-15. The resulting equivalent stress-strain relationships for the sleeve are shown in Figure 8-49. The solid line represents the constitutive behavior of the ductile cast-iron material, and the dashed lines represent the equivalent stress-strain behavior as determined by Eq. 8-15.

$$\delta = \underbrace{\int \varepsilon(x)_{Actual} dx}_{Actual \ Dist.} = \underbrace{\int \varepsilon(x)_{Uniform} dx}_{Uniform \ Dist.} \quad (8-14)$$

$$\varepsilon_{eq} = \begin{cases} S_R \varepsilon_{mid}, S_R = 0.667 & \text{for Parabolic Distribution} \\ S_R \varepsilon_{mid}, S_R = 0.5 & \text{for Triangular Distribution} \end{cases} \quad (8-15)$$

The deformation within the coupler region is also caused by slip of the reinforcing bar from the grout-filled sleeve due to strain penetration. Note that there was no bar pull-out from the couplers, and the couplers provided full anchorage through the cementitious materials. However, there is local bar slippage due to straining of the bar. Several models have been proposed to describe the relationship between the stress in the bar and the resulting slip of the bar from concrete, but past work on bars anchored in cementitious grout within metallic ducts is limited (Raynor et al., 2002; Brenes et al., 2006; Steuck et al., 2009; Ou et al., 2010). Matsuzaki et al. (1987) showed that the distribution of strain along the reinforcing bars within the sleeve was linear prior to yielding and bi-linear after yielding (Figure 8-50). Thus, the slip of the reinforcing bar from the coupler was calculated using Wehbe's method (Figure 8-51). The uniform bond strength proposed by Wehbe (Eq. 8-7) did not produce development lengths consistent with the physical geometry of the sleeve and the tests results shown in (Figure 8-50). That is, a development length greater than the embedded length would be required using the uniform bond strength in Eq. 8-7 because the bond strength in Wehbe's method is for unconfined concrete and not confined grout. Therefore the bond strength was modified according to experimental testing conducted by Ou et al. 2010 on reinforcing bars anchored in grout-filled corrugated steel ducts (Eq. 8-16). The modified bond strength resulted in strain penetration lengths similar to those reported by Matsuzaki et al. (1987).

$$u_{\text{Grout}} = 32.5\sqrt{f'_c} \quad \text{psi}$$

$$u_{\text{Grout}} = 2.7\sqrt{f'_c} \quad \text{MPa}$$
(8-16)

The last component that was factored into the bond-slip calculation was elongation due to the supported length at each end of the coupler. Unsupported compression struts develop in the grout near the ends of the sleeve as tension builds within the bar, which results in grout cone pullout. This action is illustrated in Figure 8-52. These additional free lengths of reinforcing bar were incorporated in the bond-slip behavior of the reinforcing bar from the sleeve. A similar approach was described by Steuck et al., 2009, to describe the penetration effect of reinforcing bar anchored in grout-filled corrugated steel ducts. The unsupported length L_U can be calculated using Eq. 8-17a by assuming the angle θ of the cone failure plane. For this study the failure plane was assumed to be $\theta=45^\circ$. Thus the unsupported length can be calculated by Eq. 8-17b. The total slip δ_T of the reinforcing at a given end of the coupler sleeve can be calculated by summing the deformations due to strain penetration δ_{slip} and elongation of the unsupported length δ_{UL} (Eq. 8-18).

$$L_U = 0.5(d_D - d_b) \frac{1}{\tan \theta} \quad \text{Eq. 8-17a}$$

$$L_U(45^\circ) = 0.5(d_D - d_b) \quad \text{Eq. 8-17b}$$

Where

d_D = nominal inner diameter of the sleeve or duct in which the reinforcing bar is anchored

d_b = nominal diameter of the reinforcing bar

θ = angle between the reinforcing bar and the failure plane of the grout cone

$$\delta_T = \delta_{slip} + \delta_{UL} \quad (8-18)$$

Where

δ_T = Total deformation of the reinforcing bar from the sleeve

δ_{slip} = Deformation due to strain penetration. Defined by Eq. 8-6.

δ_{UL} = Deformation due to the elongation of the unsupported length, which can be approximated by the product of the strain in the bar, ε_s , and the unsupported length, L_U . Expression: $\delta_{UL} = \varepsilon_s \cdot L_U$

Figure 8-53 shows the calculated stress-slip relationship with and without the contribution of the unsupported length. The slip at a given stress was approximately twice as large when the unsupported length was incorporated into the bond-slip behavior.

Figure 8-54 compares the monotonic stress-strain behavior of the analytical model discussed in this section with the experimental result from GS3. In general, there was good correlation between the calculated and measured stress-strain behavior. The truss model indicates that prior to yielding more than 50% of the deformation of the coupler assembly come from the sleeve, while there are only minor contributions from the reinforcing bars and bond-slip. After yielding, plastic straining of the reinforcing bars and bond-slip deformation accounted for 85% of the total deformation of the assembly. These results confirm that the added stiffness of the sleeve and the concentrated deformations due to bond-slip must be considered when modeling columns that utilize these devices.

8.6.2 Model Details

A detailed schematic of the analytical model for GCNP is shown in Figure 8-55a. The model was composed of eight nodes, four elements with nonlinear behavior, and three stiff elastic elements. The column shaft was modeled using a nonlinear beam-column element with five evenly-spaced integration points. The fiber section at each of these points is represented in Figure 8-55b. The coupler region, which measured approximately 14.6 in [370 mm], was modeled using a distributed plasticity frame element with five integration points and two different fiber sections. To account for the presence of the grouted sleeves, the corresponding concrete area was excluded from the section definition, which can be observed in Figure 8-55c and Figure 8-55d by the presence of a trapezoidal void at each sleeve/steel fiber location. Although some commercially available structural analysis software packages can easily create circular voids, OpenSEES does not have such capabilities; thus, trapezoidal voids of equivalent area were used. The procedure used to determine the equivalent section is illustrated in Figure 8-56. There were two different fiber sections used in the coupler region element. The first, shown in Figure 8-55c, was used for the central three integration points (s2-s4), and utilizes the effective material property formulation for the grouted sleeve discussed in the previous section. The sleeve fiber in this section was allowed to carry both tension and compression. The second fiber section, shown in Figure 8-55d, utilized the bi-linear constitutive model with true material properties of the cast-iron sleeve. As shown by Matsuzaki et al., 1987, the grouted coupler assembly did not develop tension in the outer portions of the sleeve. A similar response would be observed if compression were applied because the force would still need to develop into the sleeve. However, at the

column-footing interface, the sleeve bares directly against the concrete surface of the footing as illustrated in Figure 8-57. Therefore, at the column-footing interface and the top of the sleeve, nodes two and four, respectively, the sleeve was only allowed to carry compression.

The material properties for longitudinal steel are listed in Table 8-11, and the properties of the various cementitious materials are listed in Table 8-12. The axial load applied to the model, which was the average measured load from the test of GCNP, was 209 kip [929 kN].

The rotation at the base of the column due to bond-slip was determined using moment-curvature analysis of the fiber section shown in Figure 8-55. The moment-curvature response of this section is shown in Figure 8-58. The resulting moment-rotation curves corresponding to bond-slip from the footing and base of the grouted coupler sleeve are shown in Figure 8-59. These two components were lumped in series into a single rotational spring. The bond-slip behavior occurring at the top of the grouted sleeve was determined using the moment-curvature response of the section shown in Figure 8-55b. The response of this section and the corresponding moment-rotation due to bond-slip are shown in Figure 8-60 and 8-61, respectively. The moment and rotation values for used to define the response of the rotational springs are listed in Table 8-13.

8.6.3 Results

8.6.3.1 Force-Displacement Relationships

The calculated hysteresis behavior for GCNP is compared with the test result in Figure 8-62. In general, there was good correlation between the calculated and measured

curves in regard to the shape of the loops and the loads at each drift level. There are two subtle differences between the measured and calculated curves. First, the location of pinching during pull cycles occurs at higher load than the measured result. This causes the loops to be wider and results in slightly more energy dissipation compared with the measure result, which is discussed in the following section. Second, the calculated load achieved at each negative drift cycle was slightly higher than the measured result. On average, the calculated load was 7% higher than the measured load. Although these are noticeable discrepancies, the calculated hysteresis response of GCNP is acceptable because the general behavior was captured.

Figure 8-63 compares the average and measured envelope curves for GCNP. The curves are the same up to approximately 0.75% drift. At which point the measured envelope curve begins to soften, while the calculated envelope does not begin to soften until 1.0% drift. This minor difference is caused by the discrepancy between the measured and calculated curves during pull cycles. After 3% drift, there was little differences between the curves. One possible explanation for the slightly higher capacity exhibited by the calculated response is the equivalent materials properties used for the grouted sleeve. Section 8.6.1 describes that the central region of the sleeve was stiffer to account for the varying strain that was observed in the Japanese studies. These sections would result in higher moment required to achieve that same deformation as the actual system. Nevertheless, both calculated force-displacement responses are acceptable.

8.6.3.2 Energy Dissipation

Figure 8-64 shows a comparison between the measured and calculated energy dissipation for GCNP. The calculated energy dissipation tends to exceed the measured data. After yielding occurs, there was approximately 20% difference between the calculated energy dissipated per cycle relative to the measured energy dissipation. As discussed in the previous section, the pinch that occurred during the cycle returning from positive drift was located at a slightly higher load than the measured pinch. This resulted in wider loops causing greater energy dissipation. The difference in energy dissipation for each cycle resulted in -15% to +18 difference in the cumulative dissipation.

8.6.3.3 Local Behavior

Figure 8-65 shows a comparison between measured and calculated strains at different locations within the column. The calculated strains shown in the Figure 8-65a and b were extracted from uniaxial steel fibers placed with the column-footing interface. The strains calculated at these fibers were compared with those measured at the column-footing interface (SG8 location) and 4-in [102-mm] below the surface of the footing (SG2 location). In both cases, the calculated tensile and compressive strains were comparable with those measured during the test. This indicates that using uniaxial steel fibers within the fiber section at the column-footing interface can predict not only that strain that occur at that location but can adequately represent the strains that occur within the footing at large drifts.

Figure 8-65c shows a comparison between the calculated and measured strains at the mid-height of one of the grouted couplers. It should be noted that the calculated strain

response reflects the equivalent material formulation for the sleeve assembly.

Nonetheless, there was very good correlation between the measured and calculated strain behavior at the location. It can be observed that there are some very slight difference in the tensile yield point and maximum compressive strains per drift level. Yet, these differences are minor. The strains directly above the grouted coupler region are compared in Figure 8-65d. Unlike the other locations investigated, there was rather poor correlation between the measured and calculated strain at this point. The calculated tensile strain was much larger than the measured strain for all drift levels. Conversely, the measured compressive strain was larger than calculated values for all drift levels.

Figure 8-66 depicts the moment-rotation relationship due to bond-slip for the column-footing interface. The measured and calculated responses are only shown up to 4% because after this point the measurements became unreliable due to delamination of concrete in the footing. In general, the calculated bond-slip rotation tends to overestimate the measured rotation. Yet, this is not unexpected because bond-slip in the actual column occurs more gradually compared to the calculation, which uses an effective yield point than a rather flat post-yield branch. Thus, this is an acceptable difference.

The moment-rotation relationships over the coupler region and the 14-in [356-mm] column section above the coupler region are shown in Figure 8-67a and b, respectively. Although it was shown that strains within these two regions were overestimated, the calculated rotation of each region was very similar to the measure response. In both regions, the general envelope behavior of the measured curve is captured along with the shape of the hysteresis loops. This is a good correlation, which indicates that the GCNP

analytical model can reasonably predict the rotations within both the coupler region and in the sections just above this region.

8.6.3.4 Modeling of Longitudinal Bar Fracture

Similar to CIP, GCNP was reinforced with ASTM A615 bars. Therefore, the prediction of longitudinal bar fracture was done using the Coffin-Manson constants determined by Brown and Kunnath (2000). Figure 8-68 shows the cumulative damage D as a function of the drift level. For comparison with test results, the analytical model was subject to two full cycles of 6% drift. The maximum calculated damage index was 0.85 after two cycles of 6% drift, which indicates that the bars are nearing failure. Thus, the model was pushed to a single cycle of +8% drift. The plot indicates that the damage index exceeds unity between 6% and 8%. The calculated first fracture occurred in the extreme west reinforcing bar at 6.6% drift during the first push cycle to +8% drift. In the test of GCNP, the first longitudinal bar fracture on the east side of the column during the second pull cycle to -6% drift. It should be noted that a second bar fracture occurred in the test at +7% during the first cycle to +8% drift. Thus, the prediction of low-cycle fatigue fracture is reasonable compared with the experimental result. Figure 8-69 shows the damage index plotted along with the drift and load for each cycle.

8.7 Preliminary Analysis of the Pedestal

Prior to developing analytical models for HCPP and GCPP, a fiber section was created for the pedestal and some preliminary moment-curvature analysis was conducted. Similar to the method that was discussed in Section 8.6.2, an equivalent section was developed in OpenSEES to account for the grout-filled duct in the pedestal section. The

pedestal section details and true geometry are shown in Figure 8-70 along with the geometry that was used for the equivalent cross section.

Experimental results suggested that presence of the corrugated steel grout-filled ducts added stiffness to the pedestal section. This was particularly evident by examining the longitudinal strain distribution within the pedestal. Figure 8-71 shows a representative plot of the measured strains within the pedestal of GCPP. Near the mid-height, the strains tend to be approximately 10% – 30% lower than those near the footing below and column joint above the pedestal. The purpose of the preliminary moment-curvature analysis was to determine the influence of the different materials in the pedestal. Five different fiber sections were developed and are shown in Figure 8-72. The description of each section is as follows:

- Version 1: This version represents an assumed conventional cast-in-place (CIP) section with the same geometry and reinforcement detailing as the precast pedestal.
- Version 2: This version represents a precast pedestal and utilizes an equivalent cross-section to account for the area of the corrugated steel grout-filled ducts (as shown in Figure 8-71). The steel ducts and grout are not included.
- Version 3: This section is the same as Version 2 but incorporates the steel ducts and the grout filling. Both the steel ducts and corresponding grout filling were modeled using individual uniaxial fibers. In this version, the steel ducts only carry compression. Material properties for the ducts and grout are discussed below.

- Version 4: All section properties and materials are the same as Version 3 except the steel ducts have been excluded.
- Version 5: All section properties and materials are the same as Version 3 except the grout has been excluded.
- Version 6: All section properties and materials are the same as Version 3 except the steel ducts can carry both tensile and compressive stress.

The corrugated steel ducts were composed of ASTM A653 Type CS sheet steel. The manufacture indicated that both Type CS-A and CS-B were used in producing that ducts. The only difference between the two types is the yield stress, which is specified as 25 ksi [175 MPa] and 30 ksi [207 MPa] for CS-A and CS-B, respectively. Both materials had a specified ultimate stress of 55 ksi [379 MPa], and elongation at rupture of 20%. A bilinear stress-strain model was used for the ducts, which is shown in Figure 8-73. The yield stress was taken as the average of the two material types ($f_y = 27.5$ ksi [189 MPa]). The elastic modulus was selected as that for typical steel $E = 29000$ ksi [200 GPa]. A straight line connected the yield point and the ultimate point, which was defined at a stress of 55 ksi [379 MPa] and strain of 0.2.

The grout was considered to be confined. Concrete01 was used for the constitutive models and the properties were determined using Mander's model. As described in Section 8.2.2., which discussed the general material models, confined and unconfined concrete within the pedestal sections were defined using Concrete04 and Concrete01, respectively. For the preliminary analysis presented in this section, the material properties for GCPP were used. Curvature was applied to each section until the crushing of the extreme confined concrete fibers occurred.

The moment-curvature responses of different sections are shown in Figure 8-74 for both push and pull directions. Table 8-14 provides a comparison of results for different versions and the percent difference compared with the CIP pedestal (Version 1). There was very little difference among Versions 1, 2, and 5 with regard to moment and curvature capacities. These sections did not contain the grout fibers, which were found to have the greatest influence on the moment capacity of the sections. Version 3, which contained both grout and steel duct fibers, had a moment capacity that was 5.6% (push direction) higher than the CIP pedestal (V1). The moment capacity of Version 6, which had grout fibers with compression-only behavior and steel duct fibers with both compressive and tensile behavior, was 9% (push direction) higher than the CIP pedestal.

Based on these results and the results from experimental testing, a two-node, five-integration point, nonlinear beam-column element is proposed to model the pedestal (Figure 8-75). The Version 3 section is used for integration points at Node two and three, and the Version 6 section is used for the central three integration points.

Similar to the grouted coupler sleeve, strain penetration also occurs into the grouted pedestal ducts. For calculating the bond-slip due to penetration into the pedestal ducts, Wehbe's method was used with the uniform bond strength equation proposed by Ou et al. (2010) for bars anchored in grout-filled corrugated steel ducts (Eq. 8-16). Furthermore, the unsupported length was also considered in the bond-slip calculations according to procedure discussed in Section 8.6.1. The cone failure plane angle was taken at $\theta = 45^\circ$.

8.8 Analytical Modeling of HCPP

8.8.1 Model Details

The detailed schematic of the analytical model for HCPP is shown in Figure 8-76. The model was composed of nine nodes, four elements with nonlinear behavior, and three stiff elastic elements. As described in Section 8.6, the pedestal was modeled using a single non-linear beam-column element with five integration points. At the outer-most integration points (at Node two and three), pedestal section Version 3 was employed, which only accounted for compressive stress in the grout and steel ducts. At the central three integration points, pedestal section Version 6 was employed, which also accounted for tension in the ducts but not in the grout. The other column components, the grouted region and the precast shaft, were modeled the same way as HCNP. That is, the grouted closure region was modeled using a single nonlinear beam-column element with five integration points. The fiber section at each integration point was the same and is represented in Figure 8-76c. The remainder of the column was also modeled using a nonlinear beam-column element with five integration points. The fiber section used in this region is shown in Figure 8-76b. Bond-slip rotation was included at the pedestal-footing interface due to strain penetration in the footing and into the grouted ducts within the pedestal. Bond-slip rotation was also considered at the pedestal-column joint due to strain penetration into the top of the grouted ducts in addition to bond slip rotation in the pedestal.

The material properties for longitudinal reinforcing steel and the various cementitious materials are listed in Table 8-15 and Table 8-16, respectively. The material properties

and constitutive model for the corrugated steel duct were the same as those discussed in Section 8.6 and are shown in Figure 8-73. The axial load applied to the model was 206.5 kip [919], which was the average measured axial load from the HCPP column test.

The rotation at the base of the column due to bond-slip was determined using moment-curvature analysis of the fiber section shown in Figure 8-76d. The moment-curvature response of this section and the corresponding moment-rotation curves for bond-slip are shown in Figure 8-77 and Figure 8-78, respectively. Similarly, bond-slip rotation at the pedestal-column joint was determined using the moment curvature response of the section shown in Figure 8-76c. The moment-curvature response of this section and the corresponding moment-rotation curves for bond-slip at the joint are presented in Figure 8-79 and Figure 8-80, respectively. The moment and rotation values used to define the response of the rotational springs at the column-footing interface and at the pedestal-column joint are listed in Table 8-17.

Similar to HCNP, the headed couplers, No. 3 reinforcing bars within the grouted region, and the short section where the geometry changes in the precast shell were not incorporated in the model for HCPP.

8.8.2 Results

8.8.2.1 Force-Displacement Relationships

The measured and calculated hysteretic force-displacement curves for HCPP are shown in Figure 8-81. There was very little difference between the measured and calculated responses except for the final push. The load at each drift increment was approximately the same for both push and pull directions. Furthermore, there was very

good correlation between the location of pinching and the unloading stiffness in the measured and calculated curves. Similar to HCNP, the only difference between the widths of the hysteresis loops was that the calculated curved did not have a pinch due to gap closure within the couplers. In general, there was very good correlation between the two curves.

The average envelopes of the force-displacement hysteresis curves are shown in Figure 8-82. There is little difference in the measured and calculated envelope curves prior to 0.75% drift. After this point, the measured envelope begins to soften slightly, while it is not until 1.0% that calculated curve begins to soften. Although the curves begin to soften at different points, the difference was small and acceptable. Both curves begin to reach a plateau at nearly 2% and are approximately the same all the way to failure at 10% drift.

8.8.2.2 Energy Dissipation

A comparison between the measured and calculated energy dissipation for HCPP is shown in Figure 8-83. The calculated cumulative energy dissipation tends to exceed the measured data for the majority of drift levels. Similar to HCNP, this was expected since the longitudinal bar gap opening/closing behavior at the couplers was not incorporated in the analytical model, which caused reduced energy dissipation. Thus, the energy dissipated by analytical model was slightly higher than the experimental result. Between 2% and 5% drift, the difference in cumulative energy dissipated by the analytical model varied from -20% to +18% relative to the experimental result. After 6% drift, the differences between cumulative and energy dissipated per cycle were between +18% and

0% compared to the experiment. Given the known differences between the analytical and physical model, these differences are acceptable.

8.8.2.3 Local Behavior

Figure 8-84 shows a comparison between the measured and calculated strains within the pedestal (Figure 8-84a), the grouted closure region above the pedestal (Figure 8-84b), and within the precast concrete shell above the closure region (Figure 8-84c). At the pedestal-footing interface strains were compared up to 6% drift. There is good correlation between the measured and calculated compressive strain up to 6% drift. The calculated tensile strains tend to be larger than the measured strain at drift levels up to 6%. However, the difference becomes smaller as drift increases, which was observed in analytical models for other columns presented in this chapter. Prior to 10% drift, the maximum calculated strain within the grouted region above the pedestal was below 7000 microstrains, which indicates that strain hardening did not occur. Yet, measured strains from the same location exceed 50,000 microstrain prior to 10% drift. Thus, the correlation between the measured and calculate strain within the grouted region is not good for the analytical model tends to underestimate the strains. The discrepancy between strains within this region could be in part due to the constitutive model used for the unconfined and confined grout. The measured strains above the grouted region are just beyond yield. Although the calculated strain at the same location exceeds yield by 3% drift, the maximum difference is less than an order of magnitude, which was the case within the grouted region. Furthermore, the measured and calculated strains above the

grouted region were much lower compared to other locations within the column that experienced significant nonlinear deformation.

The measured and calculated moment-rotation hysteresis curves due to bond-slip at the column-footing interface are compared up to 5% drift in Figure 8-85. In general the calculated bond-slip rotation tends to overestimate the measured rotation. This was observed for both HCNP and GCNP, and, as describe in previous sections, this could be caused by the bi-linear approximation of Wehbe's method. Moment-rotation relationships for the pedestal and grouted region above the pedestal are shown Figure 8-86a and b, respectively. In general, the calculated moment-rotation response over the pedestal correlates very well with the measured response with respect to the peak values, pinch location, and unloading stiffness. The calculated rotation within the grouted region was significantly underestimated compared with the measured result. Plastic rotation in the analytical model did not begin to occur until after 6% drift compared to 3% in the test model. These results indicate that although the global response of HCPP can be determined with good correlation with the test result, the accuracy at the local level is questionable within the grouted region above the pedestal. Similar to the analytical results for HCNP, one of the major contributing factors could be the material properties and constitutive models employed for the confined and unconfined grout.

8.8.2.4 Modeling of Longitudinal Bar Fracture

The prediction of longitudinal bar fracture for HCPP was done using the Coffin-Manson constants determined by Zhou et al. (2008) for ASTM A706 steel. After two full cycles of 10% drift, the maximum damage indices on the east and west face of the

column were $D_{east} = 0.814$ and $D_{west} = 0.884$, respectively. Similar to the experimental loading protocol, the analytical model was then pulled until -13% drift. Fracture of the extreme bars on the east side of the column was estimated at -11.7%. The test model experienced first fracture on the east side of the column at -12% drift. However, this was after three successive bar fractures on the west side at +6.2%, +7.2%, and +9.5% drift during the second push cycle to +10% drift. Figure 8-87 shows the cumulative damage D as a function of the drift level for HCPP using the modified loading protocol. It is evident that the prediction of low-cycle fatigue fracture is unreasonable compared with the experimental result and requires some improvement. The relationship between the calculated damage index, drift, and load can be observed in Figure 8-88.

8.9 Analytical Modeling of GCPP

8.9.1 Model Details

The detailed schematic of the analytical model for GCPP is shown in Figure 8-89. The model was composed of ten nodes, six elements with nonlinear behavior, and three stiff elastic elements. As described in Section 8.6, the pedestal was modeled using a single non-linear beam-column element with five integration points. At the outer-most integration points, pedestal section Version 3 was employed, which only accounted for compressive stress occurring in the grout and steel ducts. At the center integration point, pedestal section Version 6 was employed, which also accounted for tension in the ducts but not in the grout. Both versions employed the same fiber section (Figure 8-89e). The grouted sleeve element and the remainder of the column shaft were modeled in the same manner as GCNP. That is, the grouted coupler was modeled using a single nonlinear

beam-column element with five integration points. The fiber section at the central three integration points is shown in Figure 8-89c, while the section for the exterior integration points is in Figure 8-89d. The remainder of the column shaft was also modeled using a nonlinear beam-column element with five integration points. The fiber section used in this region is shown in Figure 8-89b. Bond-slip rotation was included at the pedestal-footing interface due to strain penetration in the footing and into the grouted ducts within the pedestal. Bond-slip rotation was also included at the pedestal-column joint due to strain penetration into the top of the grouted ducts and into base of the grouted coupler. In initial models, rotation from bond-slip at the top of the grouted coupler was included but was neglected in the final model because it was found to have a minor effect on the behavior of the model.

The material properties for longitudinal reinforcing steel are shown in Table 8-18, and the description and properties for the cementitious materials are listed in Table 8-19. The axial load applied to the model was 208 kip [925 kN], which was the average measured axial load from the GCPP test.

The rotation at the base of the column due to bond-slip was determined using moment-curvature analysis of the fiber section shown in Figure 8-89e. The moment-curvature response of this section is shown in Figure 8-90, and the resulting moment-rotation curves corresponding to bond-slip from the footing and base of the grouted coupler sleeve are shown in Figure 8-91. These two components were lumped in series into a single rotational spring. The bond-slip behavior at the top of the pedestal and base of the grouted sleeve were determined using the moment-curvature response of the section shown in Figure 8-89b, which is shown in Figure 8-92. The corresponding

moment-rotation relationships due to bond-slip at the pedestal-column interface are shown in Figure 8-93. The moment and rotation results that were used to define the response of the rotational springs are listed in Table 8-20.

8.9.2 Results

8.9.2.1 Force-Displacement Relationships

The measured and calculated hysteretic force-displacement relationships for GCPP are shown in Figure 8-94. There was very little difference between the measured and calculated response. The load at each drift increment was approximately the same for both push and pull directions. The largest discrepancy in load at peak drift between the two curves was at -2% drift, where there was a +5.8% difference relative to the measure response. Both curves exhibited very good correlation with regard to the location of pinching, residual displacements, and unloading stiffness. In general, there was very good correlation between the two curves.

The average envelope curves for GCPP are shown in Figure 8-95. There was little difference between the measured and calculated curves prior to 1.5% drift. Between 2% and 3% drift, the average calculated load was slightly higher than the measured envelope. Yet, after 3% drift the two curves once again become approximately the same until 6% drift, which corresponds to failure. Thus, the global force-displacement behavior of the GCPP model correlates well with the tests results.

8.9.2.2 Energy Dissipation

Figure 8-96 shows a comparison between the measured and calculated energy dissipation. There was little apparent difference in the cumulative energy dissipated per

drift level (Figure 8-96a). Given the similarities between the measured and calculated hysteresis loops, this result is not surprising. The percent difference between the measured and calculated energy dissipation is shown in Figure 8-96b for the first second cycles along with the cumulative dissipation per drift level. The difference in energy dissipated for the first and second cycle was between -5% and 15% after 2% drift, which resulted in a $\pm 10\%$ difference in the cumulative dissipation.

8.9.2.3 Local Behavior

Figure 8-97 shows a comparison between measured and calculated strains within the pedestal. At the pedestal-footing interface strains were compared up to 6% drift. There was good correlation between the measured and calculated compressive and tensile strains. Similar to the results from other analytical models, calculated strain at the interface with the footing tended to be larger than measured strain until higher drift levels. At the mid-height of the pedestal, there was very good correlation between the strains prior to 4% drift. After 4% drift, the measured strains began to exceed the calculated values in both tension and compression; however, the difference was not significant. For most drift levels, the tensile strains were significantly overestimated at the pedestal-column interface

The measured and calculated strains within the grouted coupler region and within the precast shell above the coupler region are shown in Figure 8-98. The calculated strains at the mid-height of the grouted coupler sleeve correlated fairly well in compression but tended to underestimate the plastic strains in tension. It was discussed in Section 8.6.1 that the material properties of the grouted sleeve are subject to large variability. Thus,

the difference in the measured and calculated tensile strain is not unexpected. Directly above the grouted coupler region, there was not a large difference between the measured and calculated strains until +5% drift. At which point, the longitudinal reinforcing steel in the test model begins to yield. Although there were some differences at higher drift, the section does not undergo large inelastic deformations. Therefore, these differences are acceptable.

Moment-rotation relationships for the pedestal and within grouted coupler region above the pedestal are shown Figure 8-99a and b, respectively. In general, the calculated moment-rotation response over the pedestal correlates very well with the measured response with respect to peak forces, pinch location, and unloading stiffness. The calculated rotation within the grouted coupler region was significantly underestimated compared with measurements from the experiment (Figure 8-99b). There was very little plastic rotation calculated by the analytical model. By 6% drift the measured rotation was approximately twice that of the calculated rotation over the grouted coupler region.

8.9.2.4 Modeling of Longitudinal Bar Fracture

Similar to CIP and GCNP, GCPP was reinforced with ASTM A615 bars. Therefore, the prediction of longitudinal bar fracture was done using the Coffin-Manson constants determined by Brown and Kunnath (2000). For comparison with test results, the analytical model was subjected to the same loading protocol as used in the test until first fracture, which occurred at -6% during the first cycle to -6% drift. The calculated damage indices for the extreme bars on the east and west faces of the column after the first cycle to -6% were $D_{east} = 0.41$ and $D_{west} = 0.44$, which indicates the bars are not

close to fracture. The model was then subjected to a second full cycle of 6% drift followed by a push to +8% , a third pull to -6%, and a second push to +8% drift, which was the same the loading protocol. After the modified loading, the calculated damage indices for the extreme bars on the east and west faces of the column were $D_{east} = 0.79$ and $D_{west} = 0.58$, which indicates that the east extreme bar is close to fatigue fracture. Yet, by this point in the experiment three bars had fractured. The analysis was re-run following the loading protocol used for CIP, and fracture occurred at +8.9% drift during the first cycle of +10% drift. Figure 8-100 shows the cumulative damage D as a function of the drift level for the last loading protocol, and Figure 8-101 shows the damage index plotted along with the drift and load for each cycle. In general, the prediction of low-cycle fatigue fracture did not correlate well with experimental result. This is in part due to exclusion of buckling in the analytical model. By 6% drift, the longitudinal bars began to buckle at the interface between the pedestal and the footing, which contributed to bar fracture in the tests.

8.10 Summary and Discussion

This chapter presented the development and results of an analytical model for each column tested in this study. A summary of each model is provided in subsequent sections and concluding remarks are presented at the end of the section

8.10.1 Analytical Model of CIP

The analytical model for CIP provided very good global results such as force-displacement relationships and energy dissipation compared to the measured data. Similarly, the strains and curvatures calculated at the section level were also comparable

to the local behavior measured from the test. The prediction of low-cycle fatigue fracture for CIP was found to occur during the first cycle of +10% drift compared to the experiment where first fracture occurred during the second cycle of -10% drift. Thus, there was good correlation between the predicted and actual fracture cycles.

8.10.2 Analytical Model of HCNP

Using a four-state model and data from cyclic uniaxial tests, a multi-spring element was developed to describe the gap-opening behavior of the headed coupler assembly, which was observed in experimental results. Using a simple three-element component model with the same geometry as the HCC test specimens, the cyclic behavior of the gap element was evaluated and compared with test results. There was good correlation between the calculated and measured response of the coupler-reinforcing bar assembly. Yet, when implemented into preliminary models of HCNP, there was poor correlation between the calculated and measure response. It is believed that intrusion of grout into the collar assembly and interaction with other materials in the column test model resulted in significant differences between the component and system behavior of the coupler. Thus, the gap element was not implemented in the final HCNP analytical model.

Despite the differences between the physical and analytical model, the HCNP model exhibited hysteresis and envelope curves that were very similar to the test result. The energy dissipation was slightly higher than that determined from the measured data due to exclusion of the couplers form the model. The strains and rotations within the grouted region were typically underestimated, which was likely due to the constitutive models used to describe the uniaxial fiber behavior of the grout. Since there was no available

research on the stress-strain behavior of confined and unconfined cementitious grout, concrete models were applied, which may not accurately describe the behavior of grout. The prediction of low-cycle fatigue fracture for GCNP occurred during the second cycle of +10% drift compared closely to the experiment in which fracture first occurred during the second cycle of -10% drift.

8.10.3 Analytical Model of GCNP

Prior to developing the analytical model for GCNP, a simple component model was developed to validate material and strain penetration models for the grouted coupler assembly. Based on test results and the available literature, a bi-linear constitutive model was proposed for the ductile cast-iron material that composed the coupler sleeve. Using that bi-linear model, equivalent material properties were developed such that the grouted sleeve could be modeled as a single element. The effect of strain penetration into the sleeve and elongation due to the unsupported length were defined using Wehbe's method with a modified bond strength equation of grouted ducts proposed by Ou et al. (2010). The component model showed good correlation with the monotonic tension tests described in Chapter 7.

The grouted sleeve component model was incorporated in the analytical model of GCNP. Furthermore, bond-slip rotations at the column-footing interface and both ends of the grouted sleeve were modeled using rotational springs. The resulting model exhibited good correlation with the test results in terms of force-displacement relationships and the local behavior, but overestimated energy dissipation by 9%. Lastly, the prediction of low-cycle fatigue rupture of longitudinal steel was very reasonable compared to the

observed response. The calculated first fracture occurred in the extreme west reinforcing bar at 6.3% drift during the first push cycle to +8% drift. In the test of GCNP, the first longitudinal bar fractured on the east side of the column during the second pull cycle to -6% drift.

8.10.4 Analytical Models of Columns with Pedestals

Prior to developing models for HCPP and GCPP, a study was conducted on the influence of the different materials within the pedestal. Moment-curvature analysis was conducted on six different fiber sections; one which represented a cast-in-place pedestal and the other five represented a precast pedestal each with different material components incorporated i.e. steel ducts and the confined grout filling. Similar to the procedure used for GCNP, the concrete fiber section for the precast pedestal was modeled using an equivalent section. It was determined that the grout within the pedestal ducts resulted in a 5% increase in the moment capacity of the section compared to the CIP pedestal. Furthermore, when the compression and tension behavior of the corrugated steel ducts was included the resulting section had a moment capacity that was 9% higher than a CIP pedestal. Based on the preliminary results, a two-node, five-integration point, nonlinear beam-column element was proposed to model the behavior of the pedestal. Results from HCPP and GCPP both indicated that that moment- rotation response of the pedestal regions correlated well with the measured response. However, there were some discrepancies between the calculated and measured strains within the pedestal. This was particularly true above the pedestal-footing interface.

8.10.4.1 HCPP

In general, there was very good correlation between the measured and calculated force-displacement relationships and energy dissipation for HCPP. Although, the calculated energy dissipation overestimated the measured result, the difference was less than 25% after 4% drift. The measured and calculated local response in the pedestal region exhibited good correlation in terms of total rotation and strain at the pedestal-footing interface. However, the calculated strains above the pedestal-footing interface exceeded the measured data. Similar to HCNP, the calculated strains and rotations within the grouted region were much smaller than the measured quantities. Lastly, the prediction of longitudinal bar fracture was close to the observed behavior. The first bar fracture was predicted on the east face of the column during the first cycle of -12%, while experimental results indicates that fracture first occurred on the west face during the second cycle of +10% drift.

8.10.4.2 GCPP

The analytical model for GCPP exhibited very good global response i.e. force-displacement relationships and energy dissipation compared to test results. Similar to HCPP, there was also good correlation between the measured and calculated response within the pedestal region. The calculated local behavior of the grouted coupler region did not match the test results closely. Also, there was significant difference between the predicted and actual cycle at first fracture. In the test of GCPP, the first longitudinal bar fractured during the first of -6%, whereas the low-cycle fatigue prediction did not indicate fracture until the first cycle of +10% drift.

8.10.5 Concluding Remarks

Five analytical models were developed in this chapter. Based on the comparison of the analytical and measured results, the following general conclusions can be made:

- 1) Analytical models exhibited similar force-displacement relations compared with test results.
- 2) In most cases, the correlation between the calculated and measured local behavior was acceptable.
- 3) The constitutive models used to define the uniaxial behavior of confined (Mander's Model for confined concrete) and unconfined grouts (Kent-Park-Scott Model concrete model) may not result in accurate uniaxial behavior for grout. Further investigation should be conducted on the stress-strain behavior of confined and unconfined cementitious grout.
- 4) The Coffin-Manson low-cycle fatigue fracture model resulted in reasonable estimate of longitudinal bar fracture for CIP, HCNP, GCNP, and HCPP.
- 5) The single element pedestal model exhibited good correlation with test results despite underestimating strains above the pedestal.
- 6) The bi-linear constitutive model proposed for the ductile cast-iron material that composed the grouted coupler sleeve provided a reasonable approximation of the actual behavior. A similar statement can be made regarding the equivalent materials properties used to define the behavior of the grouted coupler as a single element with uniform material properties.

9. Parametric Studies and Design Recommendations

9.1 Introduction

This chapter presents a parametric study investigating the sensitivity of the precast columns to changes critical design parameters. Based on analytical models presented in Chapter 8, a set of prototype-scale models were studied. Prototype-scale models were used because they provide data which is directly relevant to engineering practice. The chapter is concluded with design recommendations for the precast columns that were developed, tested, and studied analytically in this investigation.

9.1.1 Prototype Column Design

The cross section details of the 24-in [610-mm] diameter half-scale model and the 48-in [1220-mm] prototype column are shown in Figure 9-1a and b, respectively. The prototype column was designed using the same procedure described in Section 3.3.2, which was a ductility-based design method prescribed by Caltrans SDC. Similar to the half-scale model, the prototype was designed to achieve a target displacement ductility $\mu_C = 7.0$. Moment-curvature analysis was conducted using OpenSEES to determine the transverse reinforcement details required to achieve the target displacement ductility. The design details for the half-scale and prototype models are listed in Table 9-1. The final prototype column was reinforced longitudinally with 16 - No. 14 [D43] bars and transversely with a No. 6 [D19] spiral with a 3.75-in [95-mm] pitch. These reinforcement details correspond to longitudinal and transverse reinforcement ratios of 1.98% and 1.08%, respectively. These ratios were 1.92% and 1.05%, respectively, for the half-scale model. The design axial load for the prototype was 905 kip [4025 kN],

which corresponded to $ALI = 0.1$. The material properties used in the analysis, and for the remainder of the models discussed in this chapter, are listed in Table 9-2. Material properties were selected based on the recommendations provided in Caltrans SDC (concrete and reinforcing steel) or based on properties determined from laboratory tests (grouts and ductile cast-iron). The moment-curvature response for the prototype model can be observed in Figure 9-2. The design displacement ductility and moment capacity for the prototype were $\mu_C = 7.3$ and 58,940 kip-in [6654 kN-m].

9.1.2 General Model Details

There were a few slight differences between the analytical models used in the parametric study and those described in Chapter 8. Figure 9-3 shows a schematic of the conventional prototype-scale analytical model. There were two main differences compared to the half-scale analytical models: 1) the loading head, which was modeled using rigid frame elements, was not included in the prototype-scale models, and 2) P- Δ effects were included. All other model components were the same as those discussed in Chapter 8. A prototype model was created for each of the four precast columns, which was based on the details described above. The prototype analytical models for the precast columns had the same configuration as the schematic shown in Figure 9-3 with the exception of extra elements for modeling different features within the connection region. The loading history applied to each analytical model followed the drift-based protocol that was applied to the test models. Column failure was based on crushing of the extreme concrete fibers within the confined core. Although low-cycle fatigue was shown to govern the failure of test models described in previous chapters, the models

described in this chapter had lower curvature capacities due to the properties of confined concrete, which make them more susceptible to core crushing rather than low-cycle fatigue. The half-scale models used a No. 3 [9.5] spiral that had a yield stress, ultimate stress, and rupture strain that were higher than what would be expected from a larger diameter ASTM A706 bar. Thus, the failure strain of confined concrete in the test models was higher, which resulted in higher curvature capacity of the section. Furthermore, crushing of concrete was taken as the failure point because this is the typical method employed in design practice. Nonetheless, to determine if low-cycle fatigue controlled the failure mode of the prototype columns, the tensile strains calculated at each longitudinal steel fiber location were monitored and were evaluated using the low-cycle fatigue algorithm discussed in the previous chapter.

9.1.3 Description of Parametric Study

There were two main foci of the parametric study. The first was to investigate the sensitivity of GC-type precast columns to changes in critical design parameters such as target design displacement ductility, μ_C , aspect ratio, and longitudinal reinforcement ratio. An alternative detail for GC columns is also presented and discussed, which would reduce strain concentrations at the connection interface and damage within adjacent member i.e. footings and bent-caps. The second focus was to investigate the design details of the pedestal that was used to shift the connection region and reduce moment demand over the mechanical splices. Two different pedestal heights were studied; one-half column diameter, $0.5D$, and a full column diameter, $1.0D$. For each height, a precast and cast-in-place detail was investigated. Table 9-3 provides a description of each

variable investigated in the parametric study case along with nomenclature. HC and GC connection configurations were investigated for pedestal detail.

9.2 Parametric Study of Columns Grouted Coupler Connections

9.2.1 Target Design Displacement Ductility (DD) Study

9.2.1.1 Details of Study

Three target design displacement ductilities (DD) were selected for investigation: 7.0, 6.0, and 5.0. For each ductility, a conventional column, denoted “C”, and a column with a grouted coupler column connection (without a pedestal), denoted “GN”, were designed. The design details for the conventional columns were the same as the prototype model discussed Section 9.1.1 except that the transverse reinforcement was varied to achieve the required ductility. The GN columns were designed and detailed using the same emulative approach as the half-scale test models. General details for GN columns are shown in Figure 9-4, and the design details for specific columns that were studied are listed in Table 9-4. The calculated displacement ductility for the DD7, DD6, and DD5 columns were 7.3, 6.17, and 5.16, respectively. The ultimate moment capacity, which was based on the conventional section, for the DD7, DD6, and DD5 columns were 58,940 kip-in [6683 kN-m], 56,270 kip-in [6353 kN-m], and 53,935 kip-in [6089 kN-m], respectively.

9.2.1.2 Results

Table 9-5 provides a summary of key results from the ductility study. The force-displacement relationships for DD7, DD6, and DD5 columns are shown in Figure 9-5

through Figure 9-7. On each hysteresis loop, a marker identifies the point where confined concrete core crushing began to occur. After this point, the data is presented showing the pull cycle returning to the column to zero displacement. The average envelope curves are shown only up to the point where core crushing initiated, which were used to determine the displacement ductility. One common feature shared by the three sets of plots was that the lateral force capacity of the GN model was greater than that of the corresponding conventional model by an average of 11.7%. For DD7 and DD6, the drift capacity of the GN models exceeded that of the conventional models, whereas the converse occurred in DD5. Furthermore, it is observed that as the target design displacement ductility decreases, so does the difference between the drift capacity of the conventional and GN models. That is, there is a point where the drift capacity of the GN column will be exceeded by that of the conventional case. Due to the stiffness of the grouted coupler section, which is not sensitive to changes in level of confinement, initiation of core crushing in the GN models always occurred above the coupler region and controlled the failure of the GN columns. The properties of the section above the coupler can be calculated explicitly using moment-curvature analysis. Yet, the column tip displacement at failure cannot be calculated based on failure of this section alone because the column displacement has contributions from the coupler region, bond-slip in addition to flexure above the coupler region.

The differences in displacement ductility between the GN and conventional models were +10.9%, +7.1%, and -20.8%, for the DD7, DD6, and DD5 cases, respectively. In general, the GN columns had lower effective stiffnesses, K_{Eff} , compared with the convention models (Eq. 9.1). This is caused by higher plastic moments, M_P , and

effective yield displacements, which was due to GN columns requiring more force (and displacement) to initiate yielding of the longitudinal reinforcement.

$$K_{Eff} = \frac{M_P}{\Delta_Y \cdot L} \quad (9.1)$$

Where

M_P = plastic moment capacity as determined by elasto-plastic idealization of the average force-displacement envelope

Δ_Y = effective yield displacement determined by idealization of the average force-displacement envelope

L = cantilever height of the column; distance between the footing node and the free end

The relationships between rotations within different regions of the models and drift are compared in Figure 9-8. Figure 9-8a shows a schematic illustrating where rotations were calculated. For each model, rotations were determined by integrating the section curvatures between the footing surface and $0.5D$ and between $0.5D$ and $1.0D$. Rotations due to bond-slip at the column-footing interface were extracted directly from the rotational spring at the base of the column. Prior to first yielding of longitudinal reinforcement, which occurred approximately at 1.0% in all models, there was little difference between the rotations in GN and conventional model at all locations. After yielding of steel, the rotation within the first half column diameter of the conventional models began to increase rapidly due to plastic deformation of longitudinal reinforcing steel fibers. On the other hand, the rotation at the same location in the GN models continued to increase linearly after yielding of steel and was significantly smaller

compared to the conventional models because of the relatively high stiffness of the couplers. Within the half column diameter above the coupler region, the GN models experienced more rotation than the conventional models due to the higher lateral load capacity. The bond-slip at the column-footing interface (Fig. 9-8d) was comparable between each GN and corresponding conventional model for each drift level.

The additional stiffness provided by the coupler sleeve relieved the amount of compressive strain in the confined concrete. In the case of GN-DD7, which underwent 10% drift prior to crushing of the extreme concrete fiber above the coupler regions, the maximum calculated compressive strain within the confined core of the coupler region was 80% of the capacity, ε_{cu} ($\varepsilon_{cu} = 0.0217$). Similar observations were made in GN-DD6 and GN-DD5. This indicates that, even at large drift ratios, the extent of damage to the confined core within the coupler region would be minimal.

9.2.2 Aspect Ratio (AR) Study

9.2.2.1 Details of Study

The columns discussed in Section 9.2.1 had an aspect ratio (AR) of 4.5. A second set of columns, one conventional and one GN model, were designed with an AR = 6.0. The height of the prototype column, which was 216 in [5486 mm], was increased to 288 in [7315 mm]. The target displacement ductility for the column was the same as the prototype. In order to achieve this ductility, the amount of confining steel was increased slightly compared to the 4.5 A.R. columns. The calculated displacement ductility and moment capacity for the conventional column with an aspect ratio AR = 6.0, denoted “C-

AR6”, were 7.09 and 60,886 kip-in [6874 kN-m], respectively. The details for the prototype and AR6 columns are listed in Table 9-6.

9.2.2.2 Results

Table 9-7 provides a summary of key results from the study of aspect ratio on GC columns. The force-displacement relationships for C-AR6 and GN-AR6 are shown in Figure 9-9. Similar to the difference between the C-DD and GN-DD columns, GN-AR6 had a lateral load capacity that was greater than that of C-AR6. However the difference was smaller, +6.9%, than observed in the DD study, which was +11.7% on average. Similarly, the drift capacity of GN-AR6 was 9.1% greater than C-AR6. However, GN-AR6 had a slightly lower effective stiffness, K_{Eff} , and larger plastic moment, M_P , than the C-AR6, which resulted in displacement ductilities that were approximately the same for the two models; C-AR6 and GN-AR6 had displacement ductilities of 7.78 and 7.76, respectively.

The relationships between rotation and drift for C-AR6 and GN-AR6 are presented in Figure 9-10. Similar to observations regarding the DD7 models (aspect ratio = 4.5), the calculated rotations in the first half column diameter after yielding of steel ($\approx 1.0\%$ drift) were much larger in the conventional case compared to the GN-AR6. For drift levels after 2.0%, the rotation in C-AR6 was two times greater than GN-AR6 because the couplers did not yield and their high stiffness limited the rotation. On the other hand, the rotations between 0.5D and 1.0D for both AR models were comparable for all drift levels along with the rotations due to bond-slip.

Similar to the GN-DD models, the calculated strains at individual fiber sections indicated that crushing of concrete initiated above the grouted coupler region in GN-AR6. Within the coupler region, the calculated strain in the confined core reached 65% of the crushing strain at the extreme fibers.

9.2.3 Longitudinal Steel Reinforcement Ratio (RR) Study

9.2.3.1 Details of Study

The minimum and maximum longitudinal steel reinforcement ratios (RR) prescribed by Caltrans SDC are $\rho_{\text{Long}} = 1.0\%$ and $\rho_{\text{Long}} = 4.0\%$, respectively. The prototype column had a longitudinal steel reinforcement ratio (RR) of $\rho_{\text{Long}} \approx 2.0\%$. Since many bridge columns designed in California have longitudinal reinforcement ratios less than 2.0%, the model used to investigate the effect of longitudinal reinforcement ratio was designed with $\rho_{\text{Long}} \approx 1.0\%$. The reinforcement configuration used for conventional column with $\rho_{\text{Long}} \approx 1.0\%$, denoted “C-RR1”, was 12 - No. 11 [D39], which corresponds to a longitudinal reinforcement ratio of 1.03%. The calculated displacement ductility and moment capacity for C-RR1 were 7.04 and 37,563 kip-in [4240 kN-m], respectively. Another difference between GN-RR1 and the prototype GN-DD7 model was the length of grouted coupler sleeve. The coupler length in GN-RR1 was shorter because the longitudinal bars in that column were smaller. The sleeve height for GN-RR1 was 19.5 in [495 mm] compared to 24.41 in [620 mm] for GN-DD7. Table 9-8 lists the properties for the RR1 columns along with the corresponding details for the prototype model.

As was shown in previous chapters, the GCNP test model connection resulted in large strains and damage at the column-footing interface. A design detail is presented in this

section that would reduce the likelihood of large strains and deformation at the column-footing interface. It is presented in this section because it is a modification of the GN-RR1 column; thus, denoted “GN-RR1-M”. Figure 9-11 shows the configuration of the modified detail, which employed No. 11 bars [D39] above the coupler region and No. 14 [D43] footing dowels. This connection detail uses a grouted splice sized for No. 14 bars [D43]. Based on testing conducted by the manufacturer of the grouted coupler, transitions between larger and smaller bar sizes can be made using a splice corresponding to the large bar size. That is, bars that vary one bar size can be spliced with a grouted coupler for the larger bar. However, it is suggested that this detail only be used to transition No. 11/14 bars (D39/D43) and No. 14/18 bars (D43/D57) configurations. The reinforcement ratios above and below the coupler region for GN-RR1-M were 1.03% (same as GN-RR1) and 1.49%, respectively. Due to the use of a larger grouted coupler, the clear cover above the coupler region was slightly larger than that of GN-RR1. Thus, the moment capacity of this section, which was 36,633 kip-in [4135 kN-m], was slightly lower than C-RR1. The details for this configuration are also listed in Table 9-8.

9.2.3.2 Results

Table 9-9 provides a summary of key results from the study of longitudinal reinforcement ratio. The force-displacement relationships for the RR1 column models are shown in Figure 9-12 including GN-RR1-M. Similar to other studies, the maximum lateral load achieved by the GN models was slightly larger than those achieved by the conventional models with a difference of 8.7% in GN-RR1 and 7.7% in GN-RR1-M. However, the displacement ductilities for the GN models were lower than the

conventional model ductility. In GN-RR1, the ductility (5.4) was 18.5% lower due to a higher effective yield displacement (+8.4%) and a lower ultimate displacement (-11.6%) compared to the conventional model. The ductility of C-RR1 was 6.62. The ductility for GN-RR1-M was 2.37, which corresponded to a -64.2% difference compared to C-RR1. The differences among the models can be attributed to the post-yielding force-displacement behavior, which is governed by initiation of yielding and eventual strain-hardening of steel. This is greatly affected by the relative stiffness of the coupler region, which can delay yielding and results in higher lateral loads. The coupler region of GN-RR1-M was much stiffer than the other models. Thus, the post-yielding slope of the force-displacement curve was larger compared to the other models, which resulted in the ultimate moment being reached directly above the region at lower displacement.

A comparison of the rotation-drift relationships among the three models is shown in Figure 9-13. Similar to results from the other studies, the conventional model achieves greater rotations within the first half column diameters compared to the GN models. Furthermore, there was a significant difference between GN-RR1 and GN-RR1-M, which was not unexpected. The details for GN-RR1 and GN-RR1-M are shown in Figure 9-13a. The rotation within the first half-diameter of GN-RR1-M was significantly lower than that of GN-RR1 due to difference in the height and cross-sectional area of the grouted coupler sleeve. GN-RR1-M used a No. 14 [D43] sleeve with a length of $0.5D$ compared to the No. 11 [D39] sleeve which is $0.4D$ long. Furthermore, the No. 14 [D43] coupler has an effective cross-sectional area that is 35% larger than the No. 11 [D39] coupler. Thus, GN-RR1-M experienced very little rotation compared to C-RR1 and GN-RR1. Figure 9-13c shows the rotation in the region $0.5-1.0D$ above the footing. Prior to

first yielding ($\approx 1.0\%$ drift), there was little difference in the calculated rotation among the three models. After first yielding, the rotation in GN-RR1-M increases dramatically. This was because flexure above the coupler region accounted for the majority of the column deformation. The rotation in GN-RR1 increased dramatically after 2% drift for the same reason. The bond-slip rotation (shown in Figure 9-13d) prior to yielding was similar among the three models. After yielding, the calculated bond-slip of C-RR1 and GN-RR1 began to increase more rapidly and were comparable. On the other hand, the bond-slip of GN-RR1-M remained small compared to the other models and approximately constant (0.0025 rad) after yielding. The difference is because the majority of bond-slip rotation occurs after yielding of steel and once the bar have begun strain hardening and the footing bars of GN-RR1-M reach this point due to larger area.

Similar to other GN models, failure of concrete occurred above the coupler region. Within the coupler region the maximum calculated confined concrete strains for GN-RR1 and GN-RR1-M were 84% and 15% of the ultimate confined concrete strain.

9.2.4 Comparison and Discussion

There are a number of trends that can be identified from the parametric study on columns with GC connection. Recall, that all column models with GC connection were design using an emulative approach (standard column design with no special considerations to take into account the presence of the grouted sleeve). Also note that column failure was assumed to be the initiation of confined concrete core crushing.

Figure 9-14 depicts the generalized envelope force-displacement relationships that were observed. The GN models consistently exhibited higher lateral load capacities than

their conventional counterparts. GN models with $AR = 4.5$ had lateral load capacities 7.7% to 12.8% higher than conventional models with the same AR , and GN-AR6 had a lateral load capacity 6.9% greater than C-AR6. Despite the difference in capacity, the initial stiffness, K , of conventional and GN columns were approximately the same. The higher lateral force observed in GN models is related to the point where the force-displacement curve begins to soften. Softening of the curve occurs after several reinforcing bars yield and begin to undergo strain-hardening. In both conventional and GN cases (excluding GN-RR1-M), yielding and steel hardening first occur at the column-footing. However, the added stiffness of the grouted couplers results in the GN columns requiring higher forces to initiate yielding and strain-hardening due to a shorter moment arm (effective cantilever height) between the loading point and the top of the coupler region. Thus, it is the section at the top of the coupler in the GN models that governs when the force-displacement curve will soften. Figure 9-15 depicts the critical sections in conventional (section A-A) and GN (section B-B) columns, which are located at the column-footing interface and just above the coupler region, respectively, and the expected curvature distribution at failure.

Calculated rotations were used to identify which portion of each model contributed the most to the lateral column tip displacement. Since shear deformation was not considered in the analysis, the tip displacement of conventional models, $\Delta_{T,C}$, (Eq. 9.2) is composed of a component due to flexure, $\Delta_{Flexure}$, and a component due to bond-slip rotation, Δ_{BS} . The tip displacement of the GN models, $\Delta_{T,GN}$, (Eq. 9.3) is caused by the same two components, but the component due to flexure was broken down further into

the contribution from flexure above the coupler region, $\Delta'_{Flexure}$, and contribution from rotation of the coupler region, Δ_{CR} .

$$\Delta_{T,C} = \Delta_{Flexure} + \Delta_{BS} \quad (9.2)$$

Where

- $\Delta_{T,C}$ = total tip displacement of the conventional columns
- $\Delta_{Flexure}$ = contribution of column flexure to tip displacement
- Δ_{BS} = contribution of bond-slip rotation to tip displacement

$$\Delta_{T,GN} = \Delta_{Flexure} + \Delta_{BS} \quad \text{Where} \quad \Delta_{Flexure} = \Delta'_{Flexure} + \Delta_{CR} \quad (9.3)$$

Where

- $\Delta_{T,GN}$ = Total tip displacement of the columns with grouted coupler connections. The definitions of $\Delta_{Flexure}$ and Δ_{BS} are the same as described for Eq. 9.2.
- $\Delta'_{Flexure}$ = Contribution of column flexure above the coupler region to tip displacement.
- Δ_{CR} = Contribution of coupler region rotation to tip displacement.

Figure 9-16 shows the ratio of $\Delta_{Flexure}$ to Δ_T for both model sets. Data is shown up to 5.0% drift at which point most models had not experienced core crushing. Prior to yielding ($\approx 1.0\%$ drift), the contribution of flexure to tip displacement was comparable among all models. After yielding, differences in the flexural contribution for conventional and GN models becomes more apparent. The maximum difference between the conventional and GN models occurred at 3.0% drift for the RR1 models (excluding GN-RR1-M); GN-RR1 was 37% greater than the corresponding conventional model. One significant difference that can be observed is that at 2.0% and 3.0% drift flexure

accounts for 82% and 91%, respectively, of the tip displacement for GN-RR1-M. The larger footing dowel bars yield but do not achieve strain hardening. Thus, the bond-slip contribution to displacement is very small, which results in flexure controlling the column displacement. The flexural contribution of the GN models was decomposed into the portions due to flexure above coupler region and rotation of the coupler region. These quantities were also normalized by Δ_T and are shown in Figure 9-17. Although the coupler region is stiffer than the conventional section, it still consistently accounts for 10% to 23% of the tip displacement, which is significant enough to warrant inclusion in the design procedure. Lastly, the displacement contribution from bond-slip is shown in Figure 9-18. This portion is the complement to the flexural contribution thus similar trends and differences can be observed. The bond-slip contribution was comparable for both C and GN models, and 20-60% of the tip deflection depending on the drift ratio

The rotation over the coupler region and rotation due to bond-slip were normalized using the corresponding data from conventional models. This data is shown as a function of drift in Figure 9-19. Despite changes in reinforcement and geometry, there was a similar trend observed among the models. Prior to yielding, the rotation over the coupler region was between 60% and 80% percent of the rotation that would occur over an equivalent length in corresponding conventional models. After yielding, there was a dramatic decrease in the rotation ratio. Excluding RR1-M case, the rotations achieved by the GN models after yield were consistently 30% to 40% of the conventional models. There was no obvious trend in the bond-slip rotation ratios. After yielding, the rotation ratios for GN-RR1-M decreased dramatically due to the high relative stiffness of the

coupler region and the reduced bond-slip due to larger footing bars compared with C-RR1.

A comparison between the elasto-plastic characteristics of the conventional and GN models is made in Figure 9-20. The results for GN and conventional models are plotted on the x- and y-axis, respectively. Thus, if a data point lies to the right of the dashed equivalence line it indicates that the value of the parameter was greater for the GN model compared with the corresponding conventional models and vice versa. A few distinct trends can be identified, many of which are interrelated. Yielding of steel in the GN models requires greater force (and displacement given similar initial stiffness) than conventional models. This characteristic, coupled with higher lateral load capacity, results in the GN models having slightly larger effective yield displacements, plastic lateral force capacity, and plastic moment capacity. However, this also results in GN models having lower effective stiffness. On the other hand, there is not a distinct trend regarding the ultimate displacement and ductility.

Test results indicated that large strains accumulate at the column-footing interface of the GNCP model. The longitudinal reinforcement strains calculated at the column-footing interface for each model were evaluated using the low-cycle fatigue (LCF) damage model presented in Chapter 8. The damage index (DI) was calculated using LRC parameters determined by Zhou et al (2010) for ASTM A706 No. 10 [D32] bars and by Hawileh et al. for ASTM A706 No. 6 [D19] bars, and are shown as a function of cycle number in Figure 9-21a and Figure 9-21b, respectively. These plots were not used to predict bar fracture, but to quantify the effect of LCF. Thus, it is expected that the DI determined using Hawileh's parameters to accumulate more rapidly for they are

numerical more conservative. In general, damage accumulates more rapidly in the GN models compared with the conventional models except for the GN-AR6. It should be noted that the DI is determined based on both tensile and compressive strains. By examining only peak tensile strains at each drift level (Figure 9-22), it can be observed that after yielding the strains in GN models begin to increase more rapidly than those in conventional models. Furthermore, the peak strain calculated for GN-RR1-M was significantly lower than the other GN models. Thus, confirming that modified detail can reduce the strains that would occur at the column-footing interface because of the larger bar size.

9.3 Pedestal Geometry and Detailing

9.3.1 Details of Study

The results from experimental testing of HCPP and GCPP indicated that the pedestal had a significant role in the behavior of the columns. It was found that rotations within the pedestal were relatively small, forcing much of the plastic deformation to the pedestal-footing and column-pedestal interfaces. The objective of this parametric study was to investigate the effect of pedestal height and detailing on the performance of precast columns.

As was stated in Section 9.1.2, two different pedestal heights were studied: one-half column diameter, $0.5D$, and a full column diameter, $1.0D$. For each height, a precast and a cast-in-place detail were investigated. The precast pedestal details were the same as those discussed in previous chapters only scaled-up to prototype size. The details for cast-in-place pedestals were the same as the precast counterpart except the grout-filled

corrugated steel ducts were excluded. Figure 9-23 shows the different pedestal details that were investigated and the corresponding nomenclature. Models were identified by the coupler type (H or G), use of precast or cast-in-place details (PC or CIP), and pedestal height (05D or 1D). For example, the model with grouted couplers and a one-half diameter precast pedestal would be denoted “GP-PC-05D.”

9.3.2 Results

The force-displacement curves for HP and GP models were compared with that of C-DD7, which was the conventional model with the same design details as models with pedestals. Similar to the other results presented in this chapter, failure was defined as initiation of confined concrete crushing, which is identified on each hysteresis plot with a marker. Hysteresis plots for the HP and GP models are shown in Figure 9-24 and Figure 9-25. For each pedestal configuration, the shape of the hysteresis loops was approximately the same as the conventional column model, and did not appear sensitive to the precast column type i.e. HP or GP. Furthermore, each precast models experienced failure at approximately the same point as the conventional model. The only apparent difference was that the capacity of models with PC pedestals was slightly higher than the conventional model. However, this is not unexpected because the grout-filled corrugated steel ducts within the pedestal cause longitudinal steel to yield at a larger lateral load and displacement; thus, causing the curves to soften at higher lateral load. The differences in lateral load capacity are more evident in the average envelopes shown in Figure 9-26 and Figure 9-27 for HP and GP models, respectively. The envelopes clearly indicate that there is little difference between the force-displacement relations of columns with

difference pedestals heights, and that detailing (PC or CIP) has more effect on the force-displacement relationships.

The force-displacement results for HP and GP models are summarized in Table 9-10 through Table 9-11 and Table 9-12 through Table 9-13, respectively. Models with PC pedestals consistently had lower displacement ductilities compared to C-DD7. Furthermore, ductilities were lower when the PC pedestal was $1.0D$ in height. On average, models with PC pedestals $0.5D$ and $1.0D$ in height had ductilities that were 8.7% and 11.5% lower than the conventional column. This was because these models had lower effective stiffness and higher plastic lateral load capacities with ultimate displacements similar to the conventional model. In general, HP models with CIP pedestals exhibited force-displacement results that were approximately the same as the conventional model. The greatest difference occurred in the HP-CIP-1D model, where the effective yield displacement was 3.1% greater than C-DD7. Although some parameters had greater differences compared to HP models, GP models as compared with CIP pedestals also exhibited similar key force-displacement parameters. The greatest difference was the displacement ductility for GP-CIP-05D, which was -5.3% lower than C-DD7.

Similar to the study of the GN models, calculated rotations were used to identify which portion of each model contributed most the lateral tip displacement. Equation 9.2 (repeated below for reader's convenience), which defined that the tip displacement, Δ_T , was composed of a component due to flexure, $\Delta_{Flexure}$, and a component due to bond-slip rotation, Δ_{BS} . The component due to flexure was broken down further into a contribution

from flexure above the pedestal, $\Delta'_{Flexure}$, and contribution from rotation of the pedestal region, Δ_{PED} , (Eq. 9.4).

$$\Delta_T = \Delta_{Flexure} + \Delta_{BS} \quad (9.2)$$

$$\Delta_{Flexure} = \Delta'_{Flexure} + \Delta_{PED} \quad (9.4)$$

Where

$\Delta'_{Flexure}$ = contribution of column flexure above the pedestal region to tip displacement

Δ_{PED} = contribution of pedestal region rotation to tip displacement

Figure 9-28 depicts the flexural contribution to column tip displacement for both HP and GP models. All models failed during the 8% drift cycle therefore data is only shown up to 6% drift. The flexural contribution to tip displacement was comparable among the models for each drift level. The flexural contribution for each model increased until yielding of steel then decreases to approximately $50\% \pm 5\%$ after 3% drift. As shown in Eq. 9.4., the flexural component was decomposed to investigate the contribution from the pedestal region. This is shown for both model sets in Figure 9-29. Both model sets exhibited the same trend for different pedestal configurations. That is, pedestals of similar size made approximately the same contribution (within 5%) to the tip displacement of the column. It can be observed and is expected that the taller pedestals make a larger contribution to the displacement. The contribution of bond-slip rotation, which is complementary to the flexural component, is shown in Figure 9-30.

Pedestals were used to reduce demand over the coupler region. Thus, the stress and strain in concrete and steel reinforcement were examined to determine the demands placed on the materials within the coupler region. Data was extracted from the extreme

longitudinal reinforcement, unconfined cover concrete, and the edge of confined core concrete fibers located at the nodal location directly above the pedestal. Data extracted from concrete fibers is shown in Figure 9-31 and Figure 9-32 for HP and GP models, respectively. The maximum stress and strain are plotted as data points on the full stress-strain envelope curve for each material. The data suggests that spalling of concrete (or grout) above the pedestal would likely occur using a 0.5D PC pedestal for both HP and GP columns, which is consistent with observations made during testing of HCPP and GCPP. Data from CIP-05D and both 1.0D models suggest that spalling would be less likely to occur due to lower demand. In regard to the confined core, using a 0.5D pedestal indicates the stress in concrete/grout would approach or just exceed the confined concrete strength, ϵ_{cc} . The stress in the confined core is significantly reduced (approximately $0.6\epsilon_{cc}$) as the height of the pedestal increased to 1.0D. The maximum stresses and strains in steel fibers directly above the pedestal are shown in Figure 9-33. This data provides an estimate of the demand that would be put on the splices. Caltrans MTD 20-9 states that the maximum allowable strain demand on an “Ultimate” splice is 0.02, which is identified in each plot shown in Figure 9-33. It can be observed that the limit prescribed by MTD 20-9 is met by all models except those with PC pedestals 0.5D in height. Furthermore, when a 1.0D pedestal was used, the demand on the bars was reduced significantly.

9.3.3 Discussion

The parametric study of pedestal details identified that, similar to columns with grouted coupler connections at the column-footing interface, the use of a PC pedestal that

incorporates grout-filled steel ducts increases the lateral load capacity of the columns by 5-6%. Furthermore, the resulting displacement ductilities are typically lower than a corresponding conventional column. On the other hand, the use of a CIP pedestal can result in the same approximate lateral load capacity, force-displacement relationships, and displacement ductility as a conventional column. For the most part, the height of the pedestal had little effect on the global response of the columns, but had greatest effect on the stress-strain demands in the coupler region. Thus, using a taller pedestal would reduce the likelihood of damage in the coupler region. Although numerical data indicates that spalling would likely occur when using a $0.5D$ CIP pedestal, localization of damage in an actual column may prevent damage from progressing above the pedestal. This would especially be the case for columns with grouted coupler connections due to increased rigidity in the coupler region. Lastly, using a pedestal greater than $1.0D$ in height may be impractical, and results from parametric study suggest that it would not provide further enhancement to the performance of the column.

9.4 Design Recommendations

The following section presents design recommendations based on the experimental and analytical studies presented in this document. Recommendations focus on developing the initial design details for the column, consideration of bursting stresses that would occur during filling the hollow core of the column with SCC, the effect of couplers on the column behavior, and design considerations for pedestals.

9.4.1 Development of Initial Design Details

It has been shown that the behavior of precast columns employing mechanical reinforcing bar splice within the plastic hinge behave similar to conventional columns with the same details. However, results indicate that the type of splice and whether or not a pedestal is incorporated into the column can alter the behavior from that of a corresponding conventional column. Even with these behavioral differences, an emulative approach can be used for the initial design phase of a precast column. Moment curvature analysis can be used to determine the preliminary longitudinal and transverse steel details such that the moment and ductility capacities meet the demands on the column. If reinforcement details are determined prior to selecting the mechanical splice, a second round of analysis should be completed using updated spacing. That is, when couplers are placed within a section, in order to meet clear cover provisions, typically this could require modification to the transverse reinforcement details such that the target design displacement ductility is met. On the other hand, if a splice is selected at the beginning of the design procedure, it should be incorporated into the initial set of cross section details for the following reasons:

- 1) Some splices have maximum cross-section diameters that are $1.5-2.75d_b$, and can congest the connection region. Depending on the number of longitudinal bars, this can cause violation of spacing requirements.
- 2) Selection of the splice from the beginning of the design procedure will reduce the number of iterations required.

- 3) As shown with the splices used in this study, each required different installation procedures. In the case of the HC device, the column was required to have a number of geometry changes to create working space for splice installation.

Once the initial reinforcement details of the column have been determined, the mechanical splice selected, and a decision has been made regarding whether or not a pedestal and/or internal void will be employed, the designer can begin to address the specific issues related to splice type, void design, and pedestal details.

9.4.2 Determination of Void Diameter

The precast column models developed in this study were initially hollow and were filled with SCC after installation. Such a feature allows for reduced weight during the transportation and erection of the precast column. The void in the center of the column should be proportioned such that the weight of the column is reduced significantly without causing excessive stresses in the shell as it is filled with SCC. As the shell is filled concrete, a fluid pressure head is created. Figure 9-34 shows a schematic of the hollow columns shell and the internal pressure, p_i , caused by filling the shell. The critical stress occurs at the outer-most portion of the shell. The circumferential stress, which would cause the shell to crack, can be approximated using the theory of thick-walled cylinders [Boresi and Schmidt, 2003]. Equation 9.5 can be used to determine the maximum tensile stress that occurs in the shell due to fluid pressure. It is suggested, as shown in Eq. 9.6, that the shell be designed such that the maximum circumferential tensile stress be less than the modulus of rupture for concrete, which can be determined using Eq. 9.7 (ACI-318.08R).

$$f_{\theta} = \gamma \cdot h \cdot \frac{2r_i^2}{\left(\frac{D}{2}\right)^2 - r_i^2} \quad (9.5)$$

Where

- γ = specific weight of fluid concrete to fill the shell
 h = height of the hollow shell to be filled with fluid concrete
 r_i = radius of the internal void
 D = diameter of the column

$$f_{\theta} < f_r \quad (9.6)$$

Where

$$f_r = 6.0\sqrt{f'_c} \quad \text{psi} \quad (9.7)$$

$$f_r = 0.56\sqrt{f'_c} \quad \text{MPa}$$

In most cases, the fluid head pressure will result in stresses that are significantly less than the modulus of rupture of concrete.

9.4.3 Columns Employing Headed Coupler Devices

The experimental results for columns with HC splices indicated that there was very little difference between the conventional column (CIP) and those employing HC splices (HCNP and HCPP). Furthermore, the analytical investigation presented in Chapter 8 indicated that columns with HC splices could be modeled excluding the splice to achieve comparable results to the experimental model. Based on these observations the following design recommendations are made:

- 1) A precast column, which is to use HC splices for connections in hinge zones, does not require any special analysis to account for the presence of the device. These

splices have little effect on the force-displacement behavior of the column and the formation of the plastic hinge mechanism.

- 2) In this study, the HC columns incorporated an open region (commonly referred to as the grouted connection region) used to provide working space for transition bar and coupler installation. This region was pressure grouted using hydraulic Portland cement grout, mixed to achieve a fluid consistency. Although the grout had a specified compressive strength of 5.8 ksi [40 MPa], the 28-day strength was 26% higher than expected (7.25 ksi [50 MPa]) and was approximately twice the compressive strength of the concrete in the precast shell of the column. The higher grout strength resulted in a slightly higher lateral load capacity. Thus, it is recommended that properties and presence of connection region closure material be considered in the analysis of the precast column. Furthermore, the cementitious closure material should be selected (and mixed) such that compressive strength is similar to that of the surrounding concrete.
- 3) Given the lack of available data, if hydraulic cement grout is selected as the closure materials, Mander's confined concrete model should be used to determine the confined properties.

9.4.4 Columns Employing Grouted Coupler Devices

It was evident from experimental and analytical studies that grouted couplers located within the plastic hinge zone have an effect on both the local and global behavior of column members. Specifically, these columns exhibit slightly higher lateral load

capacities and reduced deformation within the grouted coupler region. Based on the results of this study, the following design recommendations are made:

- 1) Columns with GC couplers that are embedded in the column should be designed to take into account that the plastic hinge forms adjacent to the couplers and not at the base of the column. For example, if a single-column bent is employed with a GC connection at the base, the member should be design such that hinge occurs above the coupler region; this is illustrated Figure 9-35. The plastic hinge in the conventional column would be expected to form at Section A-A, and the hinge in the GC column should be design to form at Section B-B.
- 2) As described in Section 9.4.1, an emulative approach can be used to determine the initial reinforcement details for precast column with mechanically-spliced connection. If grouted couplers are to be employed, the shear resistance of the column should be checked against the maximum expected increased lateral load capacity. That is, experimental and analytical studies both indicated that GC connections have a tendency to increase the lateral load capacity of the column due to the shifting of the plastic hinge. The increased shear force can be assessed by assuming the column is fixed at the top of the grouted coupler connection region (Section B-B in Figure 9-35) and determining the shear associated with the plastic moment, M_P , at the same section. This can be expressed mathematically by Eq. 9.8. Figure 9-35 illustrated this method on a single-column bent.

$$V'_P = \frac{M_P}{L'} \quad (9.8)$$

Where

M_P = plastic moment capacity of the corresponding conventional column
determined moment curvature analysis

L' = distance between the top of the coupler region to the center of mass of the
superstructure (or point of contraflexure assuming the column is fixed at the
top of the grouted coupler region)

- 3) Currently, there are no simplified or direct design methods for columns employing grouted coupler connections. Results from parametric study indicate that the response GC columns, when designed using an emulative approach, have a similar response to conventional columns, but ultimate displacement and ductility may not be accurately predicted. That is, in some cases GC columns had lower ductilities and ultimate displacements than a corresponding conventional column and vice versa. Thus, a fully emulative design procedure is not appropriate for columns with GC connections. Once the initial design parameters have been determined, the performance of the column should be verified using the analytical models presented in Chapter 8. A full frame-element analytical model must be used to determine the post-yielding behavior of the column because it was shown in that chapter that failure above the coupler region can occur prior to or after failure of a corresponding conventional model depending on reinforcement ratio, geometry, and confinement.
- 4) Experimental tests showed that after cycles of 6% drift, buckling occurred in the longitudinal bar within the footing. The bars did have a transverse reinforcement in the form of a spiral. However, once delamination of concrete occurred near the surface of the footing, transverse bar were no longer effective. The effective

unsupported length, which can be defined as the distance between the column base and the top mat of footing reinforcement, was 4 in [102 mm] or $4d_{bl}$. It is recommended that if the distance between the column base and the top mat of footing reinforcement is greater than $4d_{bl}$, then a butt-welded transverse hoop should be placed as intermediate support for longitudinal bars. Thus, in the event of large deformations and numerous cycle, which could cause delamination, longitudinal bar are restrained from buckling. This is illustrated in Figure 9-36.

9.4.5 Pedestal Design and Detailing

The geometry and detailing of the pedestal has been shown to have an effect on the force-displacement behavior of precast columns. Specifically, precast pedestal detail has been shown to slightly increase lateral load capacity while decreasing displacement ductility capacity compared with a conventional column or one with a CIP pedestal. This is caused by the presence of grout-filled steel ducts. Although, some differences exist, the pedestal can be used to reduce demand and possibly damage over the coupler region. The parametric study on pedestal details indicated that elasto-plastic behavior of columns with CIP pedestals was similar to a corresponding conventional column. Thus, a conventional design approach, with some modification, can be applied to columns with pedestals.

When determining the reinforcement details for columns with pedestals, moment-curvature analysis and the standard plastic hinge length, L_P , equation (Eq. 9.8) can be applied with the following considerations:

- 1) If the proposed pedestal height is greater than $0.08L$, which represents the contribution of geometry to plastic hinge formation, Eq. 9.8 can be used to generate the elasto-plastic force-displacement response of the column. The portion of the plastic hinge length due to bond-slip is considered to be the same for both conventional columns and columns with pedestals; this was observed in the parametric study.
- 2) In precast pedestals, any material that may alter the moment-curvature response of the pedestal section needs to be included. For example, a moment-curvature analysis was carried out on the C-DD7 and the PC pedestal sections. Equation 9.8 and elasto-plastic idealization were used to determine the plastic moment and displacement ductility. The precast section, which incorporated the presence of grout-filled corrugated steel duct, had a plastic moment capacity 5.1% greater than the C-DD7 section, and a ductility that was 3.3% smaller. These were similar to the differences observed in the analyzing full non-linear fiber models.

$$L_p = \underbrace{0.08L}_{\text{Geometry}} + \underbrace{0.15 f_{yl} d_{bl}}_{\text{Bond-slip}} \quad (9.8)$$

Where

L = length of the column or the distance between the fixed-end and point of contraflexure.

f_{yl} = yield strength of longitudinal reinforcing steel

d_{bl} = diameter of the longitudinal reinforcing bars

- 3) It is recommended that for flexure-dominated columns, the pedestal height be between 0.5 - 1.0 column diameters. Furthermore, it is recommended that CIP pedestals be used instead of PC pedestal. Pedestals heights less than $0.5D$ would increase the demand over the coupler region and the likelihood of damage. Furthermore, as the pedestal height becomes smaller, the behavior of the spliced zone has a greater effect of the local and global response of the column. On the other hand, as the pedestal height increases above $1.0D$, PC configurations could have lower ductility and CIP configurations would not provide any further enhancement. Heights above $1.0D$ would also become impractical.
- 4) If a CIP pedestal is selected with a height equal to or above $0.5D$, an emulative design approach can be applied. That is, moment-curvature and frame element analysis can be carried out using a corresponding conventional column.
- 5) If a PC pedestal is selected, the force-displacement behavior of column should be verified by analysis. The methods described in Chapter 8 can be applied.

9.4.6 Additional Comments

The study presented in this document focused on precast columns that were mechanically spliced with either HC or GC splices. Half-scale column tests and tensile tests on individual splices indicated that these devices have very good performance under static, dynamic, and cyclic loading. However, there are a number of different commercially available splices that have not been subjected to such thorough testing. Most splices have been evaluated to meet one (or more) of the many criteria (ACI, AASHTO, Caltrans, ICC-ES) to provide engineers with a means to assess the

performance of the device. However, all of the current performance/acceptance criteria focus on the behavior of these devices under the following conditions:

- 1) Monotonic static loading until failure
- 2) Elastic, single-cycle slip
- 3) Elastic-range fatigue (10,000+ cycles)
- 4) Limited cyclic loading in the plastic strain range (5 – 20 cycles at strains less than 1.5%)

Although the tests listed above provide some information regarding splice behavior, they are focused on the use of these devices in elements (or regions of element) that will not undergo repeated cycles of large non-linear deformations at high strain rates. Therefore, if the use of mechanical splices within hinge zone is to become common practice, additional testing should be required to evaluate the performance of splices under dynamic loading and cyclic loading in which the splice is subjected to large plastic strain reversals.

9.5 Summary and Conclusions

This chapter presented a parametric study investigating the sensitivity of the precast columns to changes in critical design parameters. A set of prototype-scale analytical models were developed based on the half-scale models presented in Chapter 8. Prototype-scale models were used to investigate the sensitivity of GC-type precast columns to changes in critical design parameters and to investigate different design details for pedestals used to reduce moment demand over the connection region. Lastly,

a set of design recommendations were presented. The following conclusions can be made:

- 1) The coupler region of GC columns provides additional stiffness that increases the lateral load capacity and shear demand. Furthermore, the rotation of the coupler region, although not as substantial as bond-slip and flexure outside the coupler region, makes enough of a contribution to the displacement of the column to warrant inclusion in the design procedure.
- 2) The additional stiffness provided by the grouted coupler sleeve relieves the amount of compressive strain experienced by confined concrete in the coupler region. Upon initiation of core crushing above the coupler region, strains in core concrete within the coupler region are expected to be 20-25% lower. In practice the strains are expected to be even smaller because the sleeves provide an increased cage effect.
- 3) Using modified detailing, in the form of larger bars (footing) being spliced with smaller bars (column), at the column-footing interface can reduce the accumulation of strain within footing dowels. However, this detail results in a very stiff coupler region relative to the column section. Thus, the majority of deformation is expected to occur within the column, which can result in premature crushing of concrete above the coupler region.
- 4) The use of a pedestal can reduce the demand on the connection region of the column. The use of a PC pedestal results in increases in lateral load capacity and lower displacement ductilities compared with corresponding conventional columns. The use of a CIP pedestal with a height between $0.5D$ and $1.0D$ results

in force-displacement behavior that is approximately the same as a corresponding conventional column. Furthermore, the use of CIP pedestal greater than $1.0D$ in height may be impractical, and would likely not provide further enhancement to the performance of the column.

10. Summary and Conclusions

10.1 Summary

Accelerated bridge construction (ABC) is gaining substantial momentum in the US because of its many advantages, including but not limited to:

- 1) Higher quality of construction for structural elements and application of more durable, innovative materials due to fabrication in plants.
- 2) Parallel execution of design, fabrication, and construction tasks.
- 3) Reduced traffic interruption and less risk to the traveling public and construction crews.
- 4) Reduced effect on the environment due to expedited construction and application of more efficient constructions technologies requiring less energy.

Despite the numerous advantages, ABC has not been extensively used in areas subject to moderate and high seismic hazards for good reason. In order for many ABC projects to be successful, extensive use of prefabricated bridge elements and systems (PBES) is required. There is a great deal of uncertainty about the seismic performance of the connections used to join elements together. Of specific concern are substructure connections (column-footing, column-shaft, and column-bent-cap), because they must dissipate energy through significant cyclic nonlinear deformations while maintaining their capacity and the integrity of the structural system.

The purpose of this study was to develop precast column-footing connections that are practical, could resist seismic loading, and be used in ABC projects. Four different connection details were developed using mechanical reinforcing bar splices to create

continuity between longitudinal bars within the precast column and a CIP footing. Columns employed either up-set headed couplers (HC) or grout-filled ductile cast-iron sleeve couplers (GC). Precast pedestals, which were one half-column diameter in height, were used in some of the models to shift the connection region reducing the moment demand over the mechanically-spliced connection. Precast columns were designed with a hollow core that would reduce the weight of the element during transportation and erection, and could be filled with self-consolidating concrete (SCC) or conventional concrete after installation.

The following sections describe the key observations and conclusions that were drawn from this study. Research summaries and observations are discussed individually for each of the three main components of this study, which were half-scale column model testing, direct coupler testing, and analytical studies.

10.2 Key Observations

10.2.1 Experimental Studies of Column Models

Five half-scale reinforced concrete bridge column models with circular sections were designed, constructed, and tested until failure. One column was a conventional cast-in-place (CIP) benchmark and was used to evaluate the performance of four precast columns each with a different connection detail. The benchmark column was designed using Caltrans' SDC for a target design displacement ductility of $\mu_C = 7.0$ such that large inelastic deformations would occur prior to failure. Two precast models were connected directly to the footing, HCNP and GCNP, and two models were connected atop a precast pedestal, HCPP and GCPP. The models were constructed as they would be in the field to

assess rapid constructability of each model. All the models were subjected to the same slow cyclic loading at increasing drift levels (two cycles per drift level) in a single cantilever configuration. Testing was stopped after significant drop in the lateral load was observed at which point the model was considered to have reached failure. The following key observation can be made regarding large-scale experimental studies:

- 1) Under drift ratios of 6% or less, all four precast models exhibited similar force-displacement relationships, energy dissipation, and damage progression as CIP.
- 2) The precast column elements employing GC connections required significantly less installation time than those employing HC connections. Grouted couplers had higher construction tolerances and field dowels that protruded from the footing/ pedestal allowed for easier placement of columns. The transition bar used between headed coupler required tight tolerance, more construction time, and adjustments during installation of the precast columns to the footings.
- 3) After testing, couplers were removed from HCNP and GCNP for inspection. There was no apparent external or internal damage to couplers even after numerous load reversals.
- 4) Pedestals were intended to reduce the moment demand over the coupler region and improve ductility. However, no improvement in the drift or displacement ductility capacity was observed. The grout-filled corrugated steel ducts in the pedestal increased section rigidity causing plastic rotations to occur predominately at the column-pedestal and pedestal-footing joints. In the CIP model, the maximum strains occurred within the first one-half column diameter from the footing surface, which is expected. Whereas, pedestals shifted the

- maximum transverse reinforcement strain to the region above the pedestal.
- 5) The presence of grouted couplers in GCNP resulted in concentrated plastic hinging mechanisms at the column-footing interface. Once delamination of footing concrete occurred bars began to buckle and subsequent fracture occurred.
 - 6) The plastic hinge mechanism for HCNP was essentially the same as that of CIP. Both experienced well-distributed plastic deformation within the first column diameter above the footing.
 - 7) The primary failure mode in all the columns was fracture of the longitudinal bars. The bars fractured above the footing surface in CIP and HCNP, and approximately 4-5 in [102-127 mm] below the footing surface in the GC models and HCPP due to concentrated plastic rotations.
 - 8) Internal and external response parameters of precast models were similar to the averages presented by Vosooghi and Saiidi (2010) for a given damage state (DS). The exception being that GC columns did not achieve DS-5 and both experienced inelasticity indices (II) that were higher for a given DS compared with the average data.

10.2.2 Direct Coupler Testing

These studies consisted of uniaxial testing of 29 total individual HC and GC devices. The objective was to characterize the component behavior of each splice type under static and dynamic loading. Results also aided the development of analytical models for the half-scale columns. Samples were constructed using No. 8 [D25] ASTM A706 or A615 Grade 60 reinforcing bars for HC and GC samples, respectively. Tests included

monotonic static and dynamic tension, single- and multi-cycle elastic slip, and slow cyclic loading. Dynamic tests were conducted to achieve strain rates similar to those that would be expected during a moderate-to-severe earthquake, and cyclic tests subjected the samples to a single cycle of tension which was increased following application of a compressive stress of 3 ksi [21 MPa]. The following observations were made:

- 1) Regardless of the loading type, all samples failed due to bar fracture, which occurred away from the coupler itself. Furthermore, there was no apparent damage to the couplers themselves in any of the tests.
- 2) Both coupler types were able to sustain increased demand caused by the strain-rate effect of dynamic loading without adverse effect to failure locations, measured strains, coupler region behavior, and ductility.
- 3) Both coupler types exhibited reduced overall ductility in the coupler region compared with the reinforcing bars. After strain in the reinforcing bar reached 20,000 $\mu\epsilon$, the average strains measured over the coupler regions for HC and GC samples were between 67-100% and 33-50% that of the reinforcing bar up to failure.
- 4) Although HC devices passed the Caltrans (and AASHTO) elastic single-cycle slip tests and the supplementary multi-cycle slip tests, cyclic loading indicated that increased stress in bars resulted in formation of a permanent gap between the deformed heads within the threaded steel collars, which accumulated linearly with stress.
- 5) GC devices exhibited a small grout-cone pull out at the ends of the grouted sleeve. Strain penetration into the sleeve ends formed an unsupported

compression strut, which resulted in a shallow wedge of grout pulling out from each end of the coupler sleeve.

10.2.3 Analytical Studies

The analytical studies included development of individual component models of reinforcing bars spliced with HC and GC devices. The proposed modeling methods and material models for components were validated using experimental results, and then were used to develop analytical models of the five half-scale columns. Half-scale columns were modeled with OpenSEES using distributed plasticity frame-elements with uniaxial fiber-sections. These models incorporated the effects of bond-slip rotation at various locations, depending on column type, and predicted longitudinal bar fracture due to low-cycle fatigue (LCF) using the Coffin-Manson LCF model and a linear damage accumulation model. The analytical results were compared with experimental results from the cyclic column model tests to validate the analytical models. Once good correlation between experimental and calculated results was achieved, prototype-scale analytical models were developed to conduct a parametric study with two main focuses: 1) sensitivity of GC-type precast columns to changes in critical design parameters such as target design displacement ductility, μ_C , aspect ratio, and longitudinal reinforcement ratio, and 2) investigation of the design details for the pedestal used to shift the connection region and reduce moment demand over the mechanical splices. The following key observations were made in the analytical studies:

- 1) The analytical models led to similar force-displacement relations compared with test results along with, in most cases, good correlation between the calculated and measured local behavior i.e. strains and rotations.
- 2) There was evidence that the methods to define the uniaxial behavior of confined (Mander's model) and unconfined (Kent-Park-Scott model) concrete may not be appropriate for accurately modeling the stress-strain behavior of grouts.
- 3) The Coffin-Manson low-cycle fatigue fracture model resulted in reasonable estimate of longitudinal bar fracture for CIP, HCNP, GCNP, and HCPP.
- 4) The single-element pedestal model exhibited good correlation with global test results despite underestimating strains near the pedestal-column joint.
- 5) The parametric studies showed that PC pedestals result in increases in lateral load capacity but lower displacement ductilities compared with corresponding conventional columns. CIP pedestals with the height between $0.5D$ and $1.0D$ (D = column diameter) result in force-displacement behavior that is approximately the same as that of a conventional column.
- 6) The bi-linear constitutive model proposed for the ductile cast-iron material that composed the grouted coupler sleeve provided a reasonable approximation of the actual behavior of the sleeve assembly. Furthermore, a similar statement can be made regarding the equivalent materials properties used to define the behavior of the grouted coupler as a single element with uniform material properties.
- 7) The modified uniform bond strength equation for bars in grouted ducts proposed by Ou et al. (2010) leads to reasonable estimate of bond-slip behavior due to strain penetration in bars anchored in grouted couplers.

- 8) A corresponding conventional column model can approximate the global force-displacement behavior of columns with GC connections. However, the conventional model cannot predict ultimate lateral load capacity, which is typically 6-12% larger in the GC column, and does not result in a reliable approximation of displacement ductility capacity or local behavior
- 9) After yielding, rotational deformations over the GC connection region are typically 30-40% of that in a corresponding conventional column. Although the rotation is relatively small, the coupler region still accounts for 15-25% of the post-yield top deflection of the column.

10.3 Conclusions

Based on the experimental and analytical studies present in this document the following conclusions are made:

- 1) Mechanical bar splices are a viable option for use in ABC substructures in seismic zones, because they can be effective for rapid construction and require detailing that is similar to conventional cast-in-place column.
- 2) The test and analytical results of this study have shown that the existing provisions in the Caltrans and AASHTO bridge seismic design documents disallowing the use of couplers in plastic hinges are not warranted.
- 3) Although test results indicated a lower drift capacity in columns with embedded grouted couplers (GC) compared to that of the CIP column, with a drift capacity of 6% the seismic performance of such columns is acceptable.
- 4) Headed reinforcement coupler connections (HC) fully emulate the response of

standard CIP construction in essentially all aspects of the seismic performance.

However, these couplers require tight construction tolerances and longer construction time compared with GC couplers.

- 5) The initial design parameters and reinforcement details for precast columns with mechanical-spliced can be reasonably determined using moment-curvature analysis and lumped-plasticity models.
- 6) The behavior of precast columns with mechanically spliced connections can be approximated using an analytical model for a corresponding conventional column. However, depending on the length of the splice and relative stiffness to reinforcing bars, an analytical model for a corresponding conventional column may not be able to reliably approximate displacement ductility capacity or localized plastic deformations.
- 7) Mechanical splices used within a plastic hinge zone can alter the plastic hinge mechanism. Shorter splices, less than 4 bar diameters, will not have a significant effect on the distribution of plasticity whereas larger splices (greater than 14 bar diameters), will have an effect plastic hinge formation and behavior depending of the relative stiffness of the splice.
- 8) The use of a pedestal can be effective in reducing the demand over the connection region, and can be used to achieve similar performance to a conventional column. However, the effectiveness of the pedestal depends on its height and detailing.
- 9) Strain concentrations and localized deformation at the column-footing interface can be reduced in GC columns using modified detailing, which employ larger

footing dowels. However, this method will result in increased post-yielding stiffness that must be taken under consideration in design.

- 10) Current code provisions for performance evaluation and acceptance of mechanical splices need to be expanded to reflect cyclic behavior under earthquake loading.

References

- 1) ACI333 (2010). "Acceptance Criteria for Mechanical Connector Systems for Steel Reinforcing Bars," International Code Council Evaluation Service.
- 2) ACI Committee 439 (2007). "Types of Mechanical Splices for Reinforcing Bars (ACI439.3R-07)," American Concrete Institute, Farmington Hills, MI.
- 3) ACI Committee 318 (2002). "Building Code Requirements for Structural Concrete (ACI318-02) and Commentary," American Concrete Institute, Farmington Hills, MI.
- 4) ACI Committee 237. (2007). "Self-consolidating concrete (ACI 237R-07)," American Concrete Institute, Farmington Hills, MI.
- 5) American Association of State Highway and Transportation Officials (AASHTO) (2010). "AASHTO Guide Specifications for LRFD Seismic Bridge Design," Washington, D.C.
- 6) ASTM International (2002). "Standard Test Method for Compressive Strength of Hydraulic Cement Mortars (Using 2-in. or (50-mm) Cube Specimens)," C109/C109M-02, West Conshohocken, PA.
- 7) ASTM International (2003a). "Standard Test Method for Compressive Strength of Cylindrical Concrete Specimens," C39/C39M-03, West Conshohocken, PA.
- 8) ASTM International (2003b). "Standard Test Method for Slump of Hydraulic-Cement Concrete," C143/C143M-03, West Conshohocken, PA.
- 9) ASTM International (2003c). "Standard Test Methods and Definitions for Mechanical Testing of Steel Products," A370-03a, West Conshohocken, PA.

- 10) ASTM International (2004). "Standard Specification for Low-Alloy Steel Deformed and Plain Bars for Concrete Reinforcement," A706/A706M-04, West Conshohocken, PA.
- 11) ASTM International (2007a). "Standard Test Method for Static Segregation of Self-Consolidating Concrete Using Column Technique," C1610/C1610M-06a, West Conshohocken, PA.
- 12) ASTM International (2007b). "Standard Test Method for Flow of Hydraulic Cement Mortar," C1437-07, West Conshohocken, PA.
- 13) ASTM International (2009). "Standard Test Method for Slump Flow of Self-Consolidating Concrete," C1611/C1611M-09b, West Conshohocken, PA.
- 14) ASTM International (2010). "Standard Test Methods for Testing Mechanical Splices for Steel Reinforcing Bars," A1034/A1034M-10, West Conshohocken, PA.
- 15) ASTM International (2011). "Standard Specification for Packaged Dry, Hydraulic-Cement Grout (Nonshrink)," C1107/C1107M-11, West Conshohocken, PA.
- 16) Billington, S. L. and Yoon, J. K. (2004). "Cyclic Response of Unbonded Posttensioned Precast Columns with Ductile Fiber-Reinforced Concrete." *Journal of Bridge Engineering*, Vol. 9, No. 4, pp. 353-363.
- 17) Brenes, F. J., Wood, S. L., and Kreger, M. E. (2006). "Anchorage requirements for grouted vertical-duct connectors in precast bent cap systems," Report No. 4176-1, Center for Transportation Research, University of Texas at Austin.
- 18) Boresi, A. P. and Schmidt, R. J. (2003). "Advanced Mechanics of Materials," Sixth Edition. John Wiley & Son, Inc.

- 19) Brown, J. and Kunnath, S. K. (2000). "Low cycle fatigue behavior of longitudinal reinforcement in reinforced concrete bridge columns," MCEER Technical Report 00-0007, pp. 87.
- 20) California Department of Transportation (2001). "Memo to Designers (MTD) 20-9," Division of Engineering Services, Sacramento, Calif., 16 pp.
- 21) California Department of Transportation (2003). "Bridge Design Specifications (BDS)." Division of Engineering Services, Sacramento, California.
- 22) California Department of Transportation (2010). "Seismic Design Criteria (SDC) Version 1.6," Division of Engineering Services, Sacramento, Calif., 160 pp.
- 23) Choi, H., Saiidi, M., Somerville, P., and El-Azazy, S. (2010). "An Experimental Study of RC Bridge Columns Subjected to Near-Fault Ground Motions," ACI Structural Journal, Vol. 107, No. 1, pp. 3-12.
- 24) Coffin, L. F. (1954). "A study of the effects of cyclic thermal stresses on a ductile metal," Transactions, American Society of Mechanical Engineers, New York, N.Y., 76, pp. 931-950.
- 25) Culmo, M. P. (2009). "Connection details for prefabricated bridge elements and systems," Federal Highway Administration Report No. FHWA-IF-09-010.
- 26) Federal Highway Administration (FHWA) (2012). "Deficient Bridges By State and Highway System," April, 29, 2013, <http://www.fhwa.dot.gov/bridge/deficient.cfm>
- 27) Hawileh, R., Rahmen, A., and Tabatabai, H. (2010). "Evaluation of the low-cycle fatigue life in ASTM A706 and A615 grade 60 steel reinforcing bars," Journal of Materials in Civil Engineering, V. 22, No. 1, pp. 65-76.

- 28) Hewes, J. T (2007). "Seismic Tests on Precast Segmental Concrete Columns with Unbonded Tendons." *Bridge Structures*, 3(3-4). pp. 215-227.
- 29) Hironobu, A. et al. (2005). "Cyclic Loading Experiment of Precast Columns of Railway Rigid-Frame Viaduct Installed with NMB Splice Sleeves," *Proceedings of the Japan Concrete Institute*, V. 27, No. 2.
- 30) Huang, S .W., Yu, J. T., Chiou, H. D., Asakawa, T., and Tsai, K. C. (1997). "Final Report of Experiment on Precast Reinforced Concrete Beam-Column Assemblage," Report, Chinese Society of Structural Engineering.
- 31) Ikadai, F., Kobayashi, K., Ase, M., and Abukawa, M. (1999). "Deformation Behavior of PCa Columns with Mortar Grouted Sleeve Joint," *Proceedings of the Architectural Institute of Japan*. (In Japanese)
- 32) International Code Council Evaluation Service, (2010). "Acceptance Criteria for Mechanical Connector Systems for Steel Reinforcing Bars," *Acceptance Criteria 133 (AC133)*.
- 33) Jansson, P.O. (2008). "Evaluation of Grout-filled Mechanical Splices for Precast Concrete Construction." Report R-1512, Michigan Department of Transportation.
- 34) Karsan, I. D., and Jirsa, J. O. (1969). "Behavior of concrete under compressive loading." *Journal of Structural Division ASCE*, 95(ST12).
- 35) Kawabata, I., et al. (1990). "Test of Centrifugal Precast Concrete Column – Part 1: Splice Sleeve System," *Proceedings of the Architectural Institute of Japan*. (In Japanese)
- 36) Kavianipour, F., and Saiidi, M. (2012). "Shake Table Testing of a Quarter-Scale 4-Span Bridge with Composite Piers," *Proceedings, The 6th International Conference on*

- Bridge Maintenance, Safety and Management (IABMAS). Stresa, Lake Maggiore, Italy, July 8-12.
- 37) Koh, S. K., and Stephens, R. I. (1991). "Mean stress effects on low cycle fatigue for a high-strength steel." *Fatigue Fract. Eng. Mater. Struct.*, V. 14, No. 4, pp. 413–428.
- 38) Lehman, D. E., and Moehle, J. P. (2000). "Seismic Performance of Well-Confined Concrete Bridge Columns," PEER Report 1998/01.
- 39) Lehman, D. E.; Gookin, S. E.; Nacamuli, A. M.; and Moehle, J. P. (2001). "Repair of Earthquake-Damaged Bridge Columns," *ACI Structural Journal*, V. 98, No. 2.
- 40) Malvar, L.J. (1998). "Review of Static and Dynamic Properties of Steel Reinforcing Bars," *ACI Materials Journal*, V. 95, No. 5.
- 41) Mander, J. B., Panthaki, F. D., Kasalanati, A. (1994). "Low-cycle fatigue behavior of reinforcing steel." *Journal of Materials in Civil Engineering*, V. 6, No. 4, pp. 453–468.
- 42) Mander, J. B., Priestley, M. J. N., and Park, R. (1988). "Theoretical stress-strain model for confined concrete." *Journal of Structural Engineering ASCE*, 114(8). 1804-1825.
- 43) Manson, S. S. (1953). "Behavior of materials under conditions of thermal stress," *Heat Transfer Symposium*, University of Michigan Engineering Research Institute, Ann Arbor, MI., pp. 9-75.
- 44) Marsh, M. L., Wernli, M., Garrett, B. E., Stanton, J. F., Eberhard, M. O., and Weinert, M. D. (2011). "Application of Accelerated Bridge Construction Connections in Moderate-to-High Seismic Regions," NCHRP Report 698.

- 45) Matsuzaki, Y., et al. (1987). "Effects of the performance of individual splice on member properties- Part 2: Study on the behavior of reinforced concrete beams with grout-filled steel splice sleeves," Architectural Institute of Japan. In Japanese.
- 46) Motaref, S., Saiidi, M. A., and Sanders, D. H. (2011). "Seismic Response of Precast Bridge Columns with Energy Dissipating Joints," Center for Civil Engineering Earthquake Research, Department of Civil and Environmental Engineering, University of Nevada, Reno, Nevada, Report No. CCEER-11-01, May 2011.
- 47) Neuenhofer, A., and Filippou, F. C. (1997). "Evaluation of nonlinear frame finite-element models," *Journal of Structural Engineering*, V. 123, No. 7, pp. 958-966.
- 48) Noureddine, I. M. (1996). "Plastic Energy Absorption Capacity of No. 18 Reinforcing Bar Splices Under Monotonic Loading," MS Thesis, California State University, Sacramento, pp. 108.
- 49) Ou, Y. C., Tsai, M. S, Chang, K. C., and Lee, G. C. (2010a). "Cyclic behavior of precast segmental concrete bridge columns with high performance or conventional steel reinforcing bars as energy dissipation bars," *Earthquake Engineering and Structural Dynamics*, V. 39, pp. 1181-1198.
- 50) Ou, Y. C., Wang, P. H., Tsai, M. S., Chang, K. C., and Lee, G. C. (2010b). "Large-scale Experimental Study of Precast Segmental Unbonded Posttensioned Concrete Bridge Columns for Seismic Regions," *Journal of Structural Engineering*, V. 136, No. 3, pp. 255-264.
- 51) Palermo, A., Pampanin, S., and Calvi, G. M. (2005). "Concept and Development of Hybrid Solutions for Seismic Resistant Bridge Systems." *Journal of Earthquake Engineering*, Vol. 9, No. 6, pp. 899-921.

- 52) Pang, B. K., Steuck, K. P., Cohagen, L., Stanton, J. F., and Eberhard, M. O. (2008). "Rapidly Constructible Large-Bar Precast Bridge-Bent Seismic Connection. WSDOT Research Report WA-RD 684.2.
- 53) Paulson, C. and Hanson, J. M. (1991). "Fatigue Behavior of Welded and Mechanical Splices in Reinforcing Steel." NCHRP 10-35.
- 54) Popovics, S. (1973). "A numerical approach to the complete stress strain curve for concrete." *Cement and Concrete Research*, V. 3, No. 5, pp. 583-599.
- 55) Potter, W. (2007). "Test Report for NMB Splice System for Sound Barrier Wall Foundation Connection." Final Report, Florida Department of Transportation.
- 56) Precast/Prestressed Concrete Institute (PCI) Northeast (2006). "Guidelines for Accelerated Bridge Construction using Precast/Prestressed Concrete Components," Report PCINER-06-ABC.
- 57) Raynor, D. J., Lehman, D. E., and Stanton, J. F. (2002). "Bond-slip response of reinforcing bars grouted in ducts," *ACI Structural Journal*, V. 99, No. 5, pp. 568-576.
- 58) Reetz, R. J.; Ramin, M. V.; and Matamoros, A. (2004). "Performance of Mechanical Splices within the Plastic Hinge Region of Beams Subject to Cyclic Loading," Proceedings, 13th World Conference on Earthquake Engineering, August 1-6.
- 59) Restrepo, J. I, Tobolksi, M. J., and Matsumoto, E. E. (2011). "Development of a Precast Bent Cap System for Seismic Regions," NCHRP Report 681.
- 60) Rio Tinto Iron & Titanium, Inc. (1990). "Ductile iron data for design engineers."
- 61) Rowell, S. P., Grey, C. E., Woodson, S. C., and Hager, K. P. (2009). "High Strain-rate Testing of Mechanical Couplers." Report ERDC TR-09-8, US Army Corps of Engineers.

- 62) Sato et al. (1993). "Experimental Study on Influence of Rebar Splice to Seismic Behaviors of Hollow Precast Concrete Column," Proceedings of the Architectural Institute of Japan. (In Japanese)
- 63) Soroushian, A.M., and Choi, K.B. (1987). "Steel Mechanical Properties at Different Strain Rates," ASCE Journal of Structural Engineering, V. 113, No.4, April, 1987.
- 64) Splice Sleeve Japan (19??). "Tests on Re-bar Splices in Reinforced Concrete Columns using NMB Splice Sleeves." NPD – 024.
- 65) Steuck, K. P., Eberhard, M. O., and Stanton, J. F. (2009). "Anchorage of large-diameter reinforcing bars in ducts," ACI Structural Journal, V. 106, No. 4, pp. 506-513.
- 66) Takaine, T., Nagai, S., Maruta, M. (2008). "Structural Performance of RC Beam and Beam-Column Subassemblages Using Reinforcement with Sleeve Joints at the End of Beams," Proceedings, 14th World Conference on Earthquake Engineering, October 12-17.
- 67) Tazarv, M. and Saiidi, M.S. (2013). "Emulative Moment-Resistant RC Bridge Column-Footing Connection for Accelerated Bridge Construction in High Seismic Zone," 7th National Seismic Conference on Bridges & Highways, Oakland. Paper No. 136, 2013, 10 pp.
- 68) Vosooghi, A., and Saiidi M. (2010). "Seismic Damage States and Performance Parameters for Bridge Columns," ACI Special Publication Series SP-271, Structural Concrete in Performance-Based Seismic Design of Bridges, May 2010, pp. 29-46.

- 69) Wehbe, N. I., Saiidi, M., and Sanders, D. H. (1999). "Seismic Performance of Rectangular Bridge Columns with Moderate Confinement," *ACI Structural Journal*, V. 96, No. 2, pp. 248-258.
- 70) Yamashita, R. and Sanders, D. H. (2005). "Shake Table Testing and an Analytical Study of Unbonded Prestressed Hollow Concrete Columns Constructed with Precast Segments." Center for Civil Engineering Earthquake Research, Department of Civil and Environmental Engineering, University of Nevada, Reno, Nevada, Report No. CCEER-05-09, August 2005.
- 71) Zadeh, M.S. and Saiidi, M.S. (2007). "Effect of Constant and Variable Strain Rates on the Stress-Strain Properties and Yield Propagation in Steel Reinforcing Bars," Report No. CCEER-07-02, Center for Civil Engineering Earthquake Research, Department of Civil Engineering. University of Nevada, Reno, NV.
- 72) Zhou, Y., Ou, Y. C., Lee, G. C., and O'Conner, J. S. (2008). "A Pilot Experimental Study on the Low Cycle Fatigue Behavior of Stainless Steel Rebars for Earthquake Engineering Applications," MCEER Internal Report, pp. 56.
- 73) Ziehl, P. H., Caicedo, J. M., Rizos, D., Mays, T., Larosche, A., El-Batanouny, M., and Mustain, B. (2011). "Testing of Connections Between Prestressed Concrete Piles and Precast Concrete Bent Caps," Final Report to Federal Highway Administration and South Carolina Department of Transportation.

Tables

Chapter 2 Tables

Table 2-1 Summary of US code provisions for mechanical splices

Code	Splice Designation	Stress Criterion for Spliced Bar	Strain Criterion for Spliced Bar		Maximum Slip Criterion	Location Restriction
ACI	Type 1	1.25f _y	none		none	Yes
	Type 2	1.0f _u				No
AASHTO	Full-mechanical connection (FMC)	1.25f _y	none		No. 3 - 14 = 0.01" No. 18 = 0.03"	Yes
Caltrans	Service	none	Minimum Capacity	Maximum Demand	No. 3 - 6 = 0.01" No. 7 - 9 = 0.014" No. 10 - 11 = 0.018" No. 14 = 0.024" No. 18 = 0.03"	
	Ultimate		> 2% 6% for No. 11 and larger 9% for No. 10 and smaller	< ε _v < 2%		

1" = 25.4mm

Table 2-2 Code qualification for the five preliminary splices

Identification	Code Qualification		
	Caltrans	ACI	AASHTO
SSC	Ultimate or Service (Dependent on bar size and manufacturer)	Type 2	FMC
GC	Service	Type 2	FMC
HC	Ultimate	Type 2	FMC
STC	Ultimate	Type 2	FMC
STC	Ultimate or Service (Dependent on bar size and manufacturer)	Type 2	FMC

Table 2-3 Summary of literature for individual coupler tests

Study Name	Year	Loading Type	Bar Size	Coupler Type				
				SSC	GC	HC	STC	TTC
Army Corp.	2009	S,D	10	X	X	X	-	X
FDOT	2007	S	9	-	X	-	-	-
MDOT	2008	Sp, F, S	6,11	-	X ¹	-	-	X ²
NCHRP 10-35	1991	F	8	-	X	-	X ³	X
Noureddine	1994	S	18	-	X	-	-	X
WJE Associates	1999	C	5-11,14	-	X	-	-	-

Loading Type: S - Monotonic Static; D - Dynamic; F - Fatigue; C - Cyclic; Sp - Slip

¹ Tests were performed on epoxy-coated couplers

² Tapered threads were only employed at one end of the splice, while the other end employed a grouted connection

³ The bar end was not derfmed prior to installation of the threaded.

Table 2-4 Cycle loading protocol defined by AC133 (2010)

Loading Stage	Tension	Compression	Number of Cycles
1	$0.95f_y$	$0.5f_y$	20
2	$2\varepsilon_y$	$0.5f_y$	4
3	$5\varepsilon_y$	$0.5f_y$	4
4	Load in tension to failure		
Note:			
f_y is the specified yield strength of the steel reinforcing bar			
ε_y is the strain of the steel reinforcing bar at actual yield stress			

Table 2-5 Tensile Test Nomenclature

ID	Coupler Type	Description	Note
HS	HC	Monotonic Static Tensile Test	-
HSR	HC	Monotonic Dynamic Tensile Test	-
HCC-1	HC	Cyclic Static Tension - Compression	Torqued
HCC-2	HC	Cyclic Static Tension - Compression	Not Torqued
HSS	HC	Slip Test - Single Cycle	-
HCS	HC	Slip Test - Multiple Cycles	-
GS	GC	Monotonic Static Tensile Test	-
GSR	GC	Monotonic Dynamic Tensile Test	-
GCC	GC	Cyclic Static Tension - Compression	-
GSS	GC	Slip Test - Single Cycle	-
GCS	GC	Slip Test - Multiple Cycles	-

Table 2-6 Loading protocol for HCC tests

Cycle	Force		Stress in the bar		Description
	[kip]	[kN]	[ksi]	[MPa]	
0	0	0	0	0	-
0.5	26.9	119	34	234	50% Yield
1	-2.4	-10.5	-3	-20.7	
1.5	37.6	167	47.6	328	70% Yield
2	-2.4	-10.5	-3	-20.7	
2.5	48.3	215	61.2	422	90% Yield
3	-2.4	-10.5	-3	-20.7	
3.5	59.1	263	74.8	515	110% Yield
4	-2.4	-10.5	-3	-20.7	
4.5	64.5	287	81.6	562	120% Yield
5	-2.4	-10.5	-3	-20.7	
5.5	69.8	311	88.4	609	130% Yield
6	-2.4	-10.5	-3	-20.7	
6.5	Fail				

Table 2-7 Loading protocol for GCC tests

Cycle	Force		Stress in the bar		Description
	[kip]	[kN]	[ksi]	[MPa]	
0	0	0	0	0	-
0.5	26.4	117	33.4	230	50% Yield
1	-2.4	-10.5	-3	-20.7	
1.5	36.9	164	46.76	322	70% Yield
2	-2.4	-10.5	-3	-20.7	
2.5	47.5	211	60.12	414	90% Yield
3	-2.4	-10.5	-3	-20.7	
3.5	58.0	258	73.48	506	110% Yield
4	-2.4	-10.5	-3	-20.7	
4.5	63.3	282	80.16	552	120% Yield
5	-2.4	-10.5	-3	-20.7	
5.5	68.6	305	86.84	598	130% Yield
6	-2.4	-10.5	-3	-20.7	
6.5	73.9	329	93.52	644	140% Yield
7	-2.4	-10.5	-3	-20.7	
7.5	Fail				

Table 2-8 Caltrans maximum slip allowed for mechanical couplers

Bar Size	Total Slip (in)
#3 - #6	0.010
#7 - #9	0.014
#10 - #11	0.018
#14	0.024
#18	0.030

Chapter 3 Tables

Table 3-1 Conventional concrete mix details

Component	Weight	
	US	SI
Cement - Nevada Type II	675 lbs	3002 N
Water	272 lbs	1210 N
Course Aggregate	320 lbs	1423 N
Fine Aggregate	1620	7000N
BASF Polyheed 997	48 oz	1419 mL
w/c	0.4	

Table 3-2 Self-consolidating concrete mix details

Component	Weight	
	US	SI
Cement - Nevada Type II	529 lbs	2352 N
Flyash Bridger	176 lbs	782 N
Water	282 lbs	1254 N
No. 7 Stone	1150 lbs	5115 N
No. 8 Stone	320 lbs	1423 N
Sand	1392 lbs	6191 N
BASF Polyheed 997	21 oz	620 mL
BASF Glanium 7500	99 oz	2927 mL
BASF VMA 362	11 oz	325 mL
BASF Delvo	49 oz	1448 mL
Air Content (3.2%)	-	-

Table 3-3 ASTM C1611 Visual inspection index

Visual Stability Index (VSI)	Description
0 = Highly Stable	No clear evidence of segregation or bleeding
1 = Stable	No clear evidence of segregation and slight bleeding observed as a sheen on the concrete mass
2 = Unstable	A slight mortar halo and/or aggregate pile in the center of the concrete mass
3 = Highly Unstable	Clearly segregated as observed as a large mortar halo and/or a large aggregate pile in the center of the concrete mass

Table 3-4 Specific Caltrans requirements for SCC

Property	Requirement	Test Method
Slump Flow	≥ 20 in [508mm]	ASTM C1611
Visual Stability Index	≤ 1.0	ASTM C1612
Static Segregation	$\leq 15\%$	ASTM C1610

Table 3-5 Summary of initial design parameters

DESIGN PARAMETER	SELECTION
Longitudinal Reinforcing Bar Size	#8 [25.4mm Diameter]
Longitudinal Reinforcing Ratio	1.92%
Cross-section Diameter	24in [610mm]
Aspect Ratio	4.5
Axial Load Index	0.10
Clear Concrete Cover	1.75in [44.5mm]

Table 3-6 Final design parameters

DESIGN PARAMETER	FINAL SELECTION
Column Cross-Section	Circular - 24in [610mm] Diameter
Longitudinal Reinforcement	11 - #8 Bars [25.4mm Diameter]
Longitudinal Reinforcement Ratio	1.92%
Transverse Reinforcement	#3Spiral at 2in Pitch [9.5mm Diameter Bars at 51mm Pitch]
Transverse Reinforcement Ratio	1.05%
Aspect Ratio	4.5
Design Axial Load	226kip [1005kN]
Clear Concrete Cover	1.75in [44.5mm]

Chapter 4 Tables

Table 4-1 Conventional concrete 1 (CC1) material test results

Test	7 Day		28 Day	
Date	5/30/2011		6/20/2011	
Sample	[psi]	[MPa]	[psi]	[MPa]
1	3315	22.8	4910	33.8
2	3556	24.5	4501	31.0
3	3180	21.9	4673	32.2
Average	3350	23.1	4695	32.3
Std Dev	190.2	1.31	205.3	1.41
C.O.V.	0.0568			

Table 4-2 Conventional concrete 2 (CC2) material test results

Test	7 Day		28 Day	
Date	5/30/2011		6/20/2011	
Sample	[psi]	[MPa]	[psi]	[MPa]
1	3737	25.7	5107	35.2
2	3673	25.3	5123	35.3
3	3843	26.5	4787	33.0
Average	3751	25.8	5006	34.5
Std Dev	85.6	0.59	189.3	1.30
C.O.V.	0.0228			

Table 4-3 Conventional concrete 3 (CC3) material test results

Test	7 Day		28 Day	
Date	6/3/2011		6/24/2011	
Sample	[psi]	[MPa]	[psi]	[MPa]
1	2752	19.0	4046	27.9
2	2668	18.4	4155	28.6
3	2856	19.7	4143	28.5
Average	2759	19.0	4115	28.3
Std Dev	94.1	0.65	59.8	0.41
C.O.V.	0.0341			

Table 4-4 Conventional concrete 4 (CC4) material test results

Test	7 Day		28 Day	
Date	6/10/2011		7/1/2011	
Sample	[psi]	[MPa]	[psi]	[MPa]
1	3659	25.2	4879	33.6
2	3640	25.1	4862	33.5
3	3699	25.5	Bad	Bad
Average	3666	25.3	4871	33.6
Std Dev	30.2	0.21	12.1	0.08
C.O.V.	0.0082			

Table 4-5 Conventional concrete 5 (CC5) material test results

Test	7 Day		28 Day	
Date	7/1/2011		7/22/2011	
Sample	[psi]	[MPa]	[psi]	[MPa]
1	2910	20.1	3764	25.9
2	2998	20.7	3726	25.7
3	3014	20.8	3987	27.5
Average	2974	20.5	3826	26.4
Std Dev	56.1	0.39	141.2	0.97
C.O.V.	0.0189			

Table 4-6 Conventional concrete 6 (CC6) material test results

Test	7 Day		28 Day	
Date	7/2/2011		7/23/2011	
Sample	[psi]	[MPa]	[psi]	[MPa]
1	2569	17.7	3504	24.1
2	2650	18.3	3420	23.6
3	2579	17.8	3563	24.5
Average	2599	17.9	3495	24.1
Std Dev	43.8	0.30	72.0	0.50
C.O.V.	0.0169			

Table 4-7 Self-consolidating concrete 1 (SCC1) material test results

Test	7 Day		28 Day	
Date	7/15/2011		8/5/2011	
Sample	[psi]	[MPa]	[psi]	[MPa]
1	3550	24.5	4090	28.2
2	3634	25.0	4091	28.2
3	3650	25.2	4728	32.6
Average	3612	24.9	4303	29.6
Std Dev	53.7	0.37	368.0	2.54
C.O.V.	0.0149			

Table 4-8 Self-consolidating concrete 2 (SCC2) material test results

Test	7 Day		28 Day	
Date	8/12/2011		9/2/2011	
Sample	[psi]	[MPa]	[psi]	[MPa]
1	3314	22.8	4967	34.2
2	3585	24.7	5510	38.0
3	3615	24.9	5244	36.1
Average	3505	24.1	5240	36.1
Std Dev	165.9	1.14	272.0	1.87
C.O.V.	0.0473			

Table 4-9 Cementitious grout 1 (G1) material test results

Test	7 Day		28 Day	
Date	7/7/2011		7/28/2011	
Sample	[psi]	[MPa]	[psi]	[MPa]
1	5981	41.2	7214	49.7
2	6091	42.0	7865	54.2
3	5099	35.1	8061	55.5
Average	5724	39.4	7713	53.1
Std Dev	544.1	3.75	443.6	3.06
C.O.V.	0.0951			

Table 4-10 Cementitious grout 2 (G2) material test results

Test	7 Day		28 Day	
Date	8/10/2011		8/31/2011	
Sample	[psi]	[MPa]	[psi]	[MPa]
1	6243	43.0	8606	59.3
2	6431	44.3	7440	51.3
3	5151	35.5	5910	40.7
Average	5942	40.9	7319	50.4
Std Dev	691.0	4.76	1352.2	9.32
C.O.V.	0.1163			

Table 4-11 Cementitious grout 3 (G3) material test results

Test	7 Day		28 Day	
Date	7/8/2011		7/29/2011	
Sample	[psi]	[MPa]	[psi]	[MPa]
1	12341	85.0	15971	110.0
2	12951	89.2	15294	105.4
3	13218	91.1	15650	107.8
Average	12837	88.4	15638	107.7
Std Dev	449.2	3.10	338.9	2.34
C.O.V.	0.0350			

Table 4-12 Number 3 bar reinforcing steel 1 (S3) material test results

Sample	Yield Stress		Ultimate Stress		Ultimate Strain
	[ksi]	[MPa]	[ksi]	[GPa]	
1	82.2	566	111.3	767	-
2	80.8	557	111.1	766	0.1496
3	82.2	566	111.8	770	0.1590
4	82.2	566	111.9	771	-
Average	81.8	564	111.5	768	0.1543
Std Dev	0.7	5	0.37	3	0.0066
C.O.V.	0.01		0.003		0.043

Table 4-13 Number 8 bar reinforcing steel 1 (S8-1) material test results

Sample	Yield Stress		Ultimate Stress		Ultimate Strain
	[ksi]	[MPa]	[ksi]	[GPa]	
1	67.3	464	111.5	769	0.1553
2	66.9	461	111.2	766	0.1632
3	66.2	456	111.1	766	0.1558
Average	66.8	460	111.3	767	0.1581
Std Dev	0.5	4	0.23	2	0.0044
C.O.V.	0.01		0.002		0.028

Table 4-14 Number 8 bar reinforcing steel 2 (S8-2) material test results

Sample	Yield Stress		Ultimate Stress		Ultimate Strain
	[ksi]	[MPa]	[ksi]	[MPa]	
1	67.1	462	95.1	655	0.1745
2	68.2	470	95.5	658	0.2024
3	68.3	470	94.9	654	0.1322
4	68.2	470	95.1	655	0.1944
5	68.2	470	95.0	655	0.2083
Average	68.0	468	95.1	655	0.1824
Std Dev	0.5	4	0.23	2	0.0308
C.O.V.	0.01		0.002		0.169

Table 4-15 Number 8 bar reinforcing steel 3 (S8-3) material test results

Sample	Yield Stress		Ultimate Stress		Ultimate Strain
	[ksi]	[MPa]	[ksi]	[MPa]	
1	67.3	464	95.2	656	0.1242
2	67.3	464	94.9	654	0.1885
3	67.8	467	95.1	656	0.1292
4	67.8	467	95.2	656	0.1948
5	67.1	463	94.9	654	0.1565
Average	67.5	465	95.1	655	0.1587
Std Dev	0.3	2	0.15	1	0.0326
C.O.V.	0.00		0.002		0.206

Table 4-16 Summary of conventional concrete material properties

ID	Final Slump		7 Day Average Strength		28 Day Average Strength	
	[in]	[mm]	[psi]	[MPa]	[psi]	[MPa]
CC1	5	127	3350	23.1	4695	32.3
CC2	5	127	3751	25.8	5006	34.5
CC3	5.25	133	2759	19.0	4115	28.3
CC4	6	152	3666	25.3	4871	33.6
CC5	6	152	2974	20.5	3826	26.4
CC6	6.5	165	2599	17.9	3495	24.1

Table 4-17 Summary of self-consolidating concrete material properties

ID	Final Slump Flow		Final VSI	Segregation [%]	7-Day Average Strength		28-Day Average Strength	
	[in]	[mm]			[psi]	[MPa]	[psi]	[MPa]
SCC1	20.3	514	0	21.17	3612	24.9	4303	29.6
SCC2	25.3	641	0	7.48	3505	24.1	5240	36.1

Table 4-18 Summary of cementitious grout material properties

ID	7 Day Average Strength		28 Day Average Strength	
	[psi]	[MPa]	[psi]	[MPa]
G1	5724	39	7713	53
G2	5942	41	7319	50
G3	12837	88	15638	108

Table 4-19 Summary of reinforcing steel material properties

Steel ID	Yield Stress		Ultimate Stress		Ultimate Strain
	[ksi]	[MPa]	[ksi]	[MPa]	
S3	81.8	564	111.5	768	0.1543
S8-1	66.8	460	111.3	767	0.1581
S8-2	68.0	468	95.1	655	0.1824
S8-3	67.5	465	95.1	655	0.1587

Table 4-20 Complete summary of material properties

Model	CIP		HCNP		HCPP		GCNP		GCCP											
	28-Day Strength	Day-of-Test Strength	28-Day Strength	Day-of-Test Strength	28-Day Strength	Day-of-Test Strength	28-Day Strength	Day-of-Test Strength	28-Day Strength	Day-of-Test Strength										
Concrete	[psi]	[MPa]	[psi]	[MPa]	[psi]	[MPa]	[psi]	[MPa]	[psi]	[MPa]										
	3350	23.1	5413	37.3	3751	25.8	5646	38.9	5006	34.5	5692	39.2	4695	32.3	5500	37.9	4871	33.6	5722	39.4
Footing	4115	28.3	4446	30.6	n/a	n/a	n/a	n/a	n/a	n/a	n/a	n/a	n/a	n/a	n/a	n/a	n/a	n/a	n/a	n/a
Column/Head	n/a	n/a	n/a	n/a	3495	24.1	3860	26.6	3826	26.4	4300	29.6	4871	33.6	4228	29.1	4871	33.6	4203	29.0
Shell	n/a	n/a	n/a	n/a	5240	36.1	5835	40.2	5240	36.1	5240	36.1	4303	29.6	4997	34.4	4303	29.6	5139	35.4
Core/Head*	n/a	n/a	n/a	n/a	n/a	n/a	n/a	n/a	3826	26.4	4300	29.6	n/a	n/a	n/a	n/a	4871	33.6	4203	29.0
Pedestal	n/a	n/a	n/a	n/a	n/a	n/a	n/a	n/a	n/a	n/a	n/a	n/a	n/a	n/a	n/a	n/a	n/a	n/a	n/a	n/a
Grout	28-Day Strength	Day-of-Test Strength	28-Day Strength	Day-of-Test Strength	28-Day Strength	Day-of-Test Strength	28-Day Strength	Day-of-Test Strength	28-Day Strength	Day-of-Test Strength	28-Day Strength	Day-of-Test Strength	28-Day Strength	Day-of-Test Strength	28-Day Strength	Day-of-Test Strength	28-Day Strength	Day-of-Test Strength	28-Day Strength	Day-of-Test Strength
	[psi]	[MPa]	[psi]	[MPa]	[psi]	[MPa]	[psi]	[MPa]	[psi]	[MPa]	[psi]	[MPa]	[psi]	[MPa]	[psi]	[MPa]	[psi]	[MPa]	[psi]	[MPa]
Pedestal Ducts	n/a	n/a	n/a	n/a	n/a	n/a	n/a	n/a	7713	53.1	7058	48.6	n/a	n/a	n/a	n/a	7713	53.1	7015	48.3
Closure Region	n/a	n/a	n/a	n/a	7319	50.4	8303	57.2	7319	50.4	7186	49.5	n/a	n/a	n/a	n/a	n/a	n/a	n/a	n/a
NMB Couplers	n/a	n/a	n/a	n/a	n/a	n/a	n/a	n/a	n/a	n/a	n/a	n/a	15638	108	16410	113.1	15638	108	15849	109
Reinforcing Steel	Yield Stress	Ultimate Stress	Yield Stress	Ultimate Stress	Yield Stress	Ultimate Stress	Yield Stress	Ultimate Stress	Yield Stress	Ultimate Stress	Yield Stress	Ultimate Stress	Yield Stress	Ultimate Stress	Yield Stress	Ultimate Stress	Yield Stress	Ultimate Stress	Yield Stress	Ultimate Stress
	[ksi]	[MPa]	[ksi]	[MPa]	[ksi]	[MPa]	[ksi]	[MPa]	[ksi]	[MPa]	[ksi]	[MPa]	[ksi]	[MPa]	[ksi]	[MPa]	[ksi]	[MPa]	[ksi]	[MPa]
Longitudinal Bars	66.8	460	111	767	68.0	468	95.1	655	68.0	468	95.1	655	68.0	468	111	767	66.8	460	111	767
Transverse Bars	81.8	564	112	768	81.8	564	112	768	81.8	564	112	768	81.8	564	112	768	81.8	564	112	768
Transition Bars	n/a	n/a	n/a	n/a	67.5	465	95.1	655	67.5	465	95.1	655	n/a	n/a	n/a	n/a	n/a	n/a	n/a	n/a

* Self-consolidating concrete

Table 4-21 Day-of-test material properties for CIP

Material	Component	Average Compressive Strength		Standard Deviation	
		[psi]	[Mpa]	[psi]	[Mpa]
CCI	Footing	5413	37.3	111	0.77
CC3	Column and loading head	4446	30.6	46	0.31

Table 4-22 Measured peak load and displacement for CIP

Drift [%]	Cycle 1						Cycle 2						Cycle 3							
	Push			Pull			Push			Pull			Push							
	Load		Displacement	Load		Displacement	Load		Displacement	Load		Displacement	Load		Displacement					
	[kip]	[kN]	[in]	[mm]	[kip]	[kN]	[in]	[mm]	[kip]	[kN]	[in]	[mm]	[kip]	[kN]	[in]	[mm]				
0.25	17.3	77.0	0.24	5.98	-17.8	-79.2	-0.25	-6.45	17.8	79.0	0.23	5.83	-16.3	-72.3	-0.27	-6.82	-	-		
0.50	30.6	136	0.46	11.8	-26.6	-118	-0.55	-13.9	30.4	135	0.45	11.5	-25.3	-113	-0.55	-14.0	-	-		
0.75	40.6	181	0.72	18.2	-35.0	-156	-0.82	-20.9	39.8	177	0.71	17.9	-33.8	-150	-0.83	-21.1	-	-		
1.00	49.0	218	0.97	24.6	-42.4	-189	-1.09	-27.7	47.9	213	0.96	24.4	-41.5	-185	-1.10	-28.0	-	-		
2.00	66.8	297	2.02	51.3	-60.1	-267	-2.14	-54.3	64.4	286	2.01	51.2	-57.9	-258	-2.15	-54.6	-	-		
3.00	66.6	296	3.09	78.4	-61.5	-273	-3.25	-82.7	63.2	281	3.06	77.6	-59.2	-263	-3.25	-82.6	-	-		
4.00	67.9	302	4.13	105	-62.7	-279	-4.39	-111	64.1	285	4.12	105	-60.7	-270	-4.39	-111	-	-		
5.00	67.6	301	5.17	131	-64.3	-286	-5.49	-139	65.0	289	5.18	132	-62.4	-277	-5.48	-139	-	-		
6.00	67.4	300	6.20	157	-65.6	-292	-6.61	-168	65.4	291	6.20	158	-63.5	-282	-6.59	-167	-	-		
8.00	68.6	305	8.29	210	-68.1	-303	-8.88	-226	65.9	293	8.23	209	-65.8	-293	-8.92	-227	-	-		
10.00	68.8	306	10.25	260	-69.6	-310	-11.20	-284	65.0	289	10.24	260	-57.1	-254	-11.25	-286	46.1	205	10.29	261

Table 4-26 HCNP energy dissipation per drift level

Drift	Cycle 1		Cycle 2		Cumulative	
	kip-in	kN-m	kip-in	kN-m	kip-in	kN-m
0.25	2.73	0.31	2.19	0.25	5.23	0.59
0.5	9.45	1.07	5.70	0.64	21.5	2.42
0.75	12.9	1.46	10.1	1.13	45.9	5.18
1	18.2	2.06	15.1	1.70	81.2	9.17
2	80.1	9.04	47.9	5.41	218	24.6
3	181	20.4	138	15.5	557	62.9
4	283	32.0	246	27.8	1118	126
5	400	45.2	376	42.4	1938	219
6	542	61.2	517	58.3	3058	345
8	887	100	858	96.9	4904	554
10	1235	139	1178	133	7457	842

Table 4-27 Day-of-test material properties for HCPP

Material	Component	Average Compressive Strength		Standard Deviation	
		[psi]	[Mpa]	[psi]	[Mpa]
<i>CC2</i>	Footing	5692	39.2	138	0.95
<i>CC5</i>	Pedestal/Shell	4300	29.6	195	1.34
<i>SCC 1</i>	Portion of the shell	5139	35.4	99	0.68
<i>SCC 2</i>	Shell core and loading head	5240	36.1	272	1.87
<i>G1</i>	Pedestal ducts	7058	48.6	366	2.52
<i>G2</i>	Closure region	7186	49.5	262	1.81

Table 4-28 Approximate locations of ruptured bars in HCPP

Bar Identification			Location of break below footing surface	
			[in]	[mm]
HCPP	West	L	4.75	121
HCPP	West	C	5.38	137
HCPP	West	R	5.38	137
HCPP	East	R	5.00	127
Average			5.13	130

Table 4-29 Measured peak load and displacement for HCPP

Drift [%]	Cycle 1								Cycle 2							
	Push				Pull				Push				Pull			
	Load		Displacement		Load		Displacement		Load		Displacement		Load		Displacement	
	[kip]	[kN]	[in]	[mm]	[kip]	[kN]	[in]	[mm]	[kip]	[kN]	[in]	[mm]	[kip]	[kN]	[in]	[mm]
0.25	15.0	66.7	0.24	5.97	-20.1	-89.3	-0.23	-5.95	15.3	68.1	0.23	5.89	-19.4	-86.2	-0.24	-6.12
0.50	26.2	117	0.46	11.8	-28.0	-125	-0.47	-11.9	27.2	121	0.48	12.1	-26.9	-120	-0.48	-12.2
0.75	35.9	160	0.73	18.6	-34.4	-153	-0.74	-18.7	34.8	155	0.73	18.6	-33.0	-147	-0.75	-19.0
1.00	42.8	191	0.99	25.2	-39.8	-177	-1.02	-25.9	41.7	186	1.00	25.3	-38.7	-172	-1.03	-26.0
2.00	60.7	270	2.04	51.7	-58.4	-260	-2.07	-52.6	58.5	260	2.04	51.7	-55.8	-248	-2.08	-52.9
3.00	66.0	294	3.11	79.0	-62.9	-280	-3.19	-81.0	62.4	277	3.10	78.7	-60.7	-270	-3.21	-81.5
4.00	67.8	301	4.13	105	-65.0	-289	-4.29	-109	64.2	286	4.13	105	-63.0	-280	-4.29	-109
5.00	67.6	301	5.19	132	-65.6	-292	-5.38	-137	64.7	288	5.20	132	-63.6	-283	-5.37	-136
6.00	68.9	307	6.25	159	-66.5	-296	-6.25	-159	66.4	295	6.28	159	-64.9	-289	-6.26	-159
8.00	71.5	318	8.63	219	-69.3	-308	-9.07	-230	68.1	303	8.63	219	-67.1	-298	-9.06	-230
10.00	71.5	318	10.78	274	-70.5	-314	-11.43	-290	41.3	184	10.78	274	-62.1	-276	-11.44	-291
12.00	-	-	-	-	-49.0	-218	-13.82	-351	-	-	-	-	-	-	-	-

Table 4-30 HCPP energy dissipation per drift level

Drift	Cycle 1		Cycle 2		Cumulative	
	kip-in	kN-m	kip-in	kN-m	kip-in	kN-m
0.25	2.49	0.28	3.91	0.44	6.40	0.72
0.5	4.77	0.54	5.48	0.62	16.7	1.88
0.75	12.6	1.43	10.1	1.15	39.4	4.45
1	17.8	2.01	14.3	1.61	71.5	8.07
2	76.4	8.62	47.2	5.33	195	22.0
3	172	19.4	135	15.2	501	56.6
4	274	31.0	245	27.7	1021	115
5	397	44.8	376	42.4	1794	203
6	545	61.6	513	57.9	2852	322
8	915	103	875	98.8	4642	524
10	1281	145	1157	131	7080	799

Table 4-31 Day-of-test material properties for GCNP

Material	Component	Average Compressive Strength		Standard Deviation	
		[psi]	[Mpa]	[psi]	[Mpa]
<i>CC1</i>	Footing	5500	37.9	346	2.38
<i>CC5</i>	Shell	4228	29.1	284	1.96
<i>SCC 1</i>	Shell core and loading head	4997	34.4	138	0.95
<i>G3</i>	Couplers	16410	113.1	950	6.54

Table 4-32 Approximate locations of ruptured bars in GCNP

Bar Identification			Location of break below footing surface	
			[in]	[mm]
GCNP	West	C	4.25	108
GCNP	East	L	4.25	108
Average			4.25	108

Table 4-33 Measured peak load and displacement for GCNP

Drift [%]	Cycle 1						Cycle 2						Cycle 3					
	Push			Pull			Push			Pull			Push			Pull		
	Load [kip]	Load [kN]	Displacement [in]	Load [kip]	Load [kN]	Displacement [in]	Load [kip]	Load [kN]	Displacement [in]	Load [kip]	Load [kN]	Displacement [in]	Load [kip]	Load [kN]	Displacement [in]	Load [kip]	Load [kN]	Displacement [in]
0.25	15.0	66.7	0.08	2.00	-18.3	-81.3	-0.50	-12.82	14.3	63.8	0.07	1.79	-18.5	-82.4	-0.51	-12.93	-	-
0.50	27.0	120	0.35	8.9	-29.5	-131	-0.81	-20.7	26.4	118	0.35	8.9	-29.0	-129	-0.81	-20.5	-	-
0.75	36.6	163	0.64	16.2	-39.6	-176	-1.11	-28.2	35.3	157	0.63	16.0	-38.7	-172	-1.11	-28.2	-	-
1.0	44.4	198	0.93	23.5	-47.7	-212	-1.43	-36.3	43.7	194	0.93	23.5	-46.4	-206	-1.44	-36.5	-	-
2.0	63.9	284	2.14	54.3	-62.7	-279	-2.63	-66.7	61.7	274	2.15	54.5	-60.7	-270	-2.62	-66.4	-	-
3.0	70.2	312	3.38	85.8	-66.7	-297	-3.86	-97.9	66.2	294	3.40	86.3	-64.4	-287	-3.85	-97.8	-	-
4.0	72.0	320	4.60	117	-67.3	-299	-5.11	-130	68.1	303	4.57	116	-65.2	-290	-5.09	-129	-	-
5.0	72.1	321	5.77	147	-68.7	-306	-6.34	-161	68.7	305	5.75	146	-66.3	-295	-6.36	-162	-	-
6.0	71.5	318	6.93	176	-69.6	-310	-7.59	-193	68.1	303	6.91	176	-69.1	-174	-7.64	-194	62.3	277
8.0	57.4	255	8.13	207	-	-	-	-	-	-	-	-	-	-	-	-	153	6.04

Table 4-34 GCNP energy dissipation per drift level

Drift	Cycle 1		Cycle 2		Cumulative	
	kip-in	kN-m	kip-in	kN-m	kip-in	kN-m
0.25	2.31	0.26	1.93	0.22	4.24	0.48
0.5	5.55	0.63	4.84	0.55	14.6	1.65
0.75	9.8	1.11	8.5	0.96	33.0	3.72
1	16.1	1.82	13.4	1.52	62.5	7.06
2	88.6	10.01	65.7	7.42	217	24.5
3	196	22.1	164	18.5	576	65.0
4	314	35.4	278	31.4	1167	132
5	427	48.2	402	45.4	1997	225
6	560	63.2	559	63.1	3115	352

Table 4-35 Day-of-test material properties for GCPP

Material	Component	Average Compressive Strength		Standard Deviation	
		[psi]	[Mpa]	[psi]	[Mpa]
<i>CC4</i>	Footing	5722	39.4	221	1.52
<i>CC5</i>	Pedestal / Shell	4203	29.0	227	1.56
<i>SCC 1</i>	Shell core and loading head	5139	35.4	99	0.68
<i>G1</i>	Pedestal ducts	7015	48.3	336	2.31
<i>G3</i>	Couplers	15849	109.2	1510	10.40

Table 4-36 Approximate locations of ruptured bars in GCPP

Bar Identification			Location of break below footing surface	
			[in]	[mm]
GCPP	West	C	4.88	124
GCPP	East	R	5.00	127
Average			4.94	125

Table 4-37 Measured peak load and displacement for GCPP

Drift [%]	Cycle 1						Cycle 2						Cycle 3							
	Push			Pull			Push			Pull			Push			Pull				
	Load		Displacement	Load		Displacement	Load		Displacement	Load		Displacement	Load		Displacement	Load		Displacement		
	[kip]	[kN]	[in]	[mm]	[kip]	[kN]	[in]	[mm]	[kip]	[kN]	[in]	[mm]	[kip]	[kN]	[in]	[mm]	[kip]	[kN]	[in]	[mm]
0.25	18.3	81.4	0.23	5.84	-19.8	-88.1	-0.26	-6.55	18.1	80.5	0.23	5.85	-19.0	-84.7	-0.26	-6.55	-	-	-	-
0.50	29.3	130	0.49	12.4	-28.1	-125	-0.51	-12.9	18.1	80	0.23	5.9	-19.0	-85	-0.26	-6.5	-	-	-	-
0.75	38.1	169	0.74	18.7	-37.4	-166	-0.77	-19.5	36.9	164	0.73	18.6	-36.5	-162	-0.79	-20.0	-	-	-	-
1.0	45.3	201	0.98	24.9	-44.1	-196	-1.04	-26.5	44.3	197	0.97	24.7	-42.6	-189	-1.05	-26.7	-	-	-	-
2.0	59.8	266	2.01	51.1	-58.9	-262	-2.14	-54.3	57.2	255	2.00	50.9	-56.4	-251	-2.15	-54.5	-	-	-	-
3.0	64.9	289	3.10	78.8	-62.6	-278	-3.22	-81.9	61.1	272	3.12	79.3	-60.2	-268	-3.23	-82.1	-	-	-	-
4.0	66.8	297	4.15	105	-64.9	-289	-4.36	-111	63.6	283	4.15	105	-62.9	-280	-4.34	-110	-	-	-	-
5.0	68.3	304	5.18	132	-67.5	-300	-5.44	-138	65.5	291	5.16	131	-65.4	-291	-5.48	-139	-	-	-	-
6.0	69.4	309	6.23	158	-69.0	-307	-6.58	-167	66.6	296	6.21	158	-50.5	-225	-6.63	-168	-49.1	-218	-6.68	-170
8.0	69.2	308	8.29	211	-	-	-	-	48.4	215	8.29	211	-	-	-	-	-	-	-	-

Table 4-38 GCPP energy dissipation per drift level

Drift	Cycle 1		Cycle 2		Cumulative	
	kip-in	kN-m	kip-in	kN-m	kip-in	kN-m
0.25	2.57	0.29	2.16	0.24	4.73	0.53
0.5	6.82	0.77	5.52	0.62	17.1	1.93
0.75	11.9	1.35	9.1	1.02	38.0	4.29
1	16.6	1.87	13.8	1.56	68.4	7.73
2	94.8	10.71	71.1	8.03	234	26.5
3	198	22.3	173	19.5	605	68.3
4	315	35.5	288	32.5	1207	136
5	440	49.6	419	47.3	2066	233
6	596	67.3	539	60.9	3201	361

Chapter 5 Tables

Table 5-1 Summary of drift level comparison point

Comparison Drift Level [%]	Description of Significance
0.75	Drift level prior to yielding of longitudinal steel
2.0	Drift level after yielding of longitudinal steel
4.0	Drift level corresponding to minimum Caltrans SDC displacement ductility for seismic critical elements ($\mu_D = 3.0$)
6.0	Drift level corresponding to failure of GCNP and GCPP
8.0	Drift level intermediate to failure of GC and HC models
10.0	Drift level corresponding to failure of HCNP, HCPP, and CIP

Table 5-2 Summary of damage for model without pedestal

Drift [%]	CIP	HCNP	GCNP
0.75	- Flexural cracking - Some inclined cracks	- Flexural cracking - Some inclined cracks	- Flexural cracking - Some inclined cracks
2.0	- Formation of shear cracks	- Formation of shear cracks - Concentrated crack near couplers - Vertical cracks in grout	- Formation of shear cracks - Concentrated crack above coupler region
4.0	- Spalling of cover - Visible transverse bars - Cracking in footing	- Spalling of cover - Visible transverse bars - Cracking in footing - Extensive cracking in grout	- Spalling of cover in coupler region - Visible transverse bars - Cracking in footing - Shear cracking in coupler region - Widening of concentrated crack above coupler region
6.0	- Extensive spalling - Multiple visible transverse bars - Visible longitudinal bars - Strain penetration into footing evident	- Lower coupler layer visible - Wide crack near lower coupler layer - Strain penetration into footing evident	- Extensive spalling in coupler region - Multiple transverse bars visible - Visible couplers - Damage to footing - Longitudinal bar rupture - Large gap between footing and column
8.0	- Damage beginning to penetrate into confined core - Wide cracks - Multiple visible longitudinal bars - Delamination of footing concrete	- Damage beginning to penetrate into confined grout core - Wide cracks - Multiple visible longitudinal bars - Delamination of footing concrete	- Longitudinal bar rupture - Spalling above coupler region - Extensive damage to footing concrete
10.0	- Longitudinal bar rupture - Longitudinal bar buckling - Transverse bar rupture - Core damage	- Longitudinal bar rupture - Longitudinal bar buckling - Transverse bar kinking - Grout core damage	N/A

Table 5-3 Parameters used to determine the elasto-plastic curve and displacement ductility for models without pedestal

Model	First Yield Point					Effective Yield Point					Ultimate Point			Ultimate Displacement Ductility
	Drift	Displacement		Load		Drift	Displacement		Load		Drift	Displacement		
	[%]	[in]	[mm]	[kip]	[kN]	[%]	[in]	[mm]	[kip]	[kN]	[%]	[in]	[mm]	
<i>CIP</i>	0.796	0.86	21.8	38.8	173	1.35	1.46	37.1	66.0	294	9.93	10.7	272	7.36
<i>HCNP</i>	1.167	1.26	32.0	51.8	230	1.52	1.64	41.7	67.5	300	9.85	10.6	270	6.49
<i>GCNP</i>	0.75	0.81	20.6	38.1	169	1.31	1.42	36.1	66.9	298	5.95	6.4	163	4.52

Table 5-4 Summary of damage for models with pedestal

Drift [%]	CIP	HCPP	GCPP
0.75	- Flexural cracking - Some inclined cracks	- Flexural cracking - Opening at pedestal-column joint	- Flexural cracking - Opening at pedestal-column joint
2.0	- Formation of shear cracks	- Formation of shear cracks - Vertical cracking in grouted region - Opening at pedestal-footing joint	- Formation of shear cracks - Opening at pedestal-footing joint - Cracking in footing
4.0	- Spalling of cover - Visible transverse bars - Cracking in footing	- Extensive shear cracking - Spalling in pedestal - Cracking in footing	- Extensive shear cracking - Spalling in pedestal - Transverse bars visible - Wide openings at pedestal-footing and pedestal-column joints
6.0	- Extensive spalling - Multiple visible transverse bars - Visible longitudinal bars - Strain penetration into footing evident	- Spalling in grout region - Multiple transverse bars visible - Strain penetration into footing evident - Wide opening at pedestal-footing and pedestal-column joints	- Spalling in coupler region - Strain penetration into footing evident - Multiple transverse bars visible - Longitudinal bar rupture
8.0	- Damage beginning to penetrate into confined core - Wide cracks - Multiple visible longitudinal bars - Delamination of footing concrete	- Delamination of footing concrete - Damage beginning to penetrate in pedestal confined core - Pedestal ducts visible	- Extensive damage to footing concrete - Pedestal ducts visible - Wide gaps at pedestal-footing and pedestal-column joint - Longitudinal bar rupture
10.0	- Longitudinal bar rupture - Longitudinal bar buckling - Transverse bar rupture - Core damage	- Longitudinal bar rupture - Longitudinal bar buckling in footing - Extensive damage to footing concrete - Longitudinal bars visible in grout region - Extensive spalling in grouted region	N/A

Table 5-5 Parameters used to determine the elasto-plastic curve and displacement ductility for models with pedestal

Model	First Yield Point					Effective Yield Point					Ultimate Point			Ultimate Displacement Ductility
	Drift	Displacement		Load		Drift	Displacement		Load		Drift	Displacement		
	[%]	[in]	[mm]	[kip]	[kN]	[%]	[in]	[mm]	[kip]	[kN]	[%]	[in]	[mm]	
<i>CIP</i>	0.796	0.86	21.8	38.8	173	1.35	1.46	37.1	66.0	294	9.93	10.7	272	7.36
<i>HCPP</i>	0.88	0.95	24.1	40.2	179	1.45	1.57	39.9	66.4	295	10.28	11.1	282	7.07
<i>GCPP</i>	0.889	0.96	24.4	43.1	192	1.31	1.41	35.8	63.8	284	5.93	6.4	163	4.53

Table 5-6 Summary of damage for all models

Drift [%]	CIP	HCNP	GCNP	HCPP	GCPP
0.75	- Flexural cracking - Some inclined cracks	- Flexural cracking - Some inclined cracks	- Flexural cracking - Some inclined cracks	- Flexural cracking - Opening at pedestal-column joint	- Flexural cracking - Opening at pedestal-column joint
2.0	- Formation of shear cracks	- Formation of shear cracks - Concentrated crack near couplers - Vertical cracks in grout	- Formation of shear cracks - Concentrated crack above coupler region	- Formation of shear cracks - Vertical cracking in grouted region - Opening at pedestal-footing joint	- Formation of shear cracks - Opening at pedestal-footing joint - Cracking in footing
4.0	- Spalling of cover - Visible transverse bars - Cracking in footing	- Spalling of cover - Visible transverse bars - Cracking in footing - Extensive cracking in grout	- Spalling of cover in coupler region - Visible transverse bars - Cracking in footing - Shear cracking in coupler region - Widening of concentrated crack above coupler region	- Extensive shear cracking - Spalling in pedestal - Cracking in footing	- Extensive shear cracking - Spalling in pedestal - Transverse bars visible - Wide openings at pedestal-footing and pedestal-column joints
6.0	- Extensive spalling - Multiple visible transverse bars - Visible longitudinal bars - Strain penetration into footing evident	- Lower coupler layer visible - Wide crack near lower coupler layer - Strain penetration into footing evident	- Extensive spalling in coupler region - Multiple transverse bars visible - Visible couplers - Damage to footing - Longitudinal bar rupture - Large gap between footing and column	- Spalling in grout region - Multiple transverse bars visible - Strain penetration into footing evident - Wide opening at pedestal-footing and pedestal-column joints	- Spalling in coupler region - Strain penetration into footing evident - Multiple transverse bars visible - Longitudinal bar rupture
8.0	- Damage beginning to penetrate into confined core - Wide cracks - Multiple visible longitudinal bars - Delamination of footing concrete	- Damage beginning to penetrate into confined grout core - Wide cracks - Multiple visible longitudinal bars - Delamination of footing concrete	- Longitudinal bar rupture - Spalling above coupler region - Extensive damage to footing concrete	- Delamination of footing concrete - Damage beginning to penetrate in pedestal confined core - Pedestal ducts visible	- Extensive damage to footing concrete - Pedestal ducts visible - Wide gaps at pedestal-footing and pedestal-column joint - Longitudinal bar rupture
10.0	- Longitudinal bar rupture - Longitudinal bar buckling - Transverse bar rupture - Core damage	- Longitudinal bar rupture - Longitudinal bar buckling - Transverse bar kinking - Grout core damage	N/A	- Longitudinal bar rupture - Longitudinal bar buckling in footing - Extensive damage to footing concrete - Longitudinal bars visible in grout region - Extensive spalling in grouted region	N/A

Chapter 7 Tables

Table 7-1 Static test results for headed couplers at yield

Sample ID	Yield					
	Within the Bars			Coupler Region		
	Stress		Strain	Deformation		Strain
	ksi	MPa		in	mm	
HS1	67.4	464	0.00321	0.068	1.73	0.01138
HS2	67.2	463	0.00269	-	-	-
HS3	67.2	463	0.00425	0.081	2.07	0.01360
HS4	67.1	462	0.00296	0.072	1.82	0.01201
Average	67.2	463	0.00328	0.074	1.87	0.01233

Table 7-2 Static test results for headed couplers at ultimate and failure

Sample ID	Ultimate		Fracture			
	Reinforcing Bar		Reinforcing Bar	Coupler Region		
	Stress		Strain	Deformation		Strain
	ksi	MPa		in	mm	
HS1	95.4	657	0.14466	0.453	11.50	0.07568
HS2	94.9	654	0.19236	-	-	-
HS3	94.7	653	0.15272	0.486	12.35	0.08123
HS4	95.4	657	0.16565	0.443	11.25	0.07413
Average	95.1	655	0.16384	0.461	11.70	0.07701

Table 7-3 Measured strain rates for headed couplers samples

Test	Sample ID	Average Strain Rate		
		$\sigma_0 - \sigma_Y$	$\sigma_Y - \sigma_{ULT}$	$\sigma_{ULT} - \text{Fracture}$
1	HSR1*	7047	21932	11777
2	HSR2	9673	80314	48054
3	HSR3	11454	80846	55917
4	HSR4	31485	111439	85974
AVERAGE (Tests 2-4)		17537	90866	63315
Standard Deviation		12112	17818	20013

* not included in average

Table 7-4 Dynamic test results for headed couplers at yield

Sample ID	Yield					
	Within the Bars			Coupler Region		
	Stress		Strain	Deformation		Strain
	ksi	MPa		in	mm	
HSR1*	70.8	488	0.00301	0.090	2.28	0.01498
HSR2	71.9	495	-	-	-	-
HSR3	71.9	495	-	-	-	-
HSR4	72.0	496	-	-	-	-
Average	71.9	495	-	-	-	-

* Not included in average

Table 7-5 Dynamic test results for headed couplers at ultimate and failure

Sample ID	Ultimate		Fracture			
	Reinforcing Bar		Reinforcing Bar	Coupler Region		
	Stress		Strain	Deformation		Strain
	ksi	MPa		in	mm	
HSR1*	96.9	667	0.15251	0.438	11.13	0.07331
HSR2	98.2	676	0.14236	0.516	13.11	0.08632
HSR3	98.1	676	0.16021	0.522	13.26	0.08723
HSR4	98.1	676	0.16204	0.547	13.88	0.09137
Average	98.1	676	0.15487	0.506	12.85	0.08831

Table 7-6 Measurements taken from cyclic test HCC-1

Percent of Yield	Stress		Coupler Region Strain at Peak Stress	Coupler Region Deformation at Peak Stress		Deformation During Return Cycle						Gap Length [(Pt. 1) - (Pt. 2)]	
	[ksi]	[MPa]		[in]	[mm]	Point 1		Point 2		Point 3		[in]	[mm]
						[in]	[mm]	[in]	[mm]	[in]	[mm]		
50%	34	234	0.0464	1.179	0.0384	0.975	0.0283	0.719	0.0322	0.818	0.0101	0.257	
70%	47.6	328	0.0810	2.057	0.0624	1.585	0.0334	0.848	0.0396	1.006	0.0290	0.737	
90%	61.2	422	0.0998	2.535	0.0790	2.007	0.0378	0.960	0.0658	1.671	0.0412	1.046	
110%	76.5	527	0.1840	4.674	0.1720	4.369	0.1210	3.073	0.1448	3.678	0.0510	1.295	
120%	81.6	562	0.2390	6.071	0.2280	5.791	0.1710	4.343	0.2031	5.159	0.0570	1.448	
130%	88.4	609	0.3250	8.255	0.3200	8.128	0.2550	6.477	0.2940	7.468	0.0650	1.651	

Table 7-7 Measurements taken from cyclic test HCC-2

Percent of Yield	Stress		Coupler Region Strain at Peak Stress	Coupler Region Deformation at Peak Stress		Deformation During Return Cycle						Gap Length [(Pt. 1) - (Pt. 2)]	
	[ksi]	[MPa]		[in]	[mm]	Point 1		Point 2		Point 3		[in]	[mm]
						[in]	[mm]	[in]	[mm]	[in]	[mm]		
50%	34	234	0.0315	0.800	0.0216	0.548	0.0175	0.445	0.0175	0.445	0.0041	0.103	
70%	47.6	328	0.0559	1.420	0.0443	1.125	0.0322	0.818	0.0294	0.747	0.0121	0.307	
90%	61.2	422	0.0749	1.902	0.0649	1.648	0.0368	0.935	0.0341	0.866	0.0281	0.714	
110%	76.5	527	0.1460	3.708	0.1460	3.708	0.1069	2.715	0.1306	3.318	0.0391	0.993	
120%	81.6	562	0.2078	5.278	0.2003	5.088	0.1495	3.797	0.1830	4.648	0.0508	1.290	
130%	88.4	609	0.2950	7.493	0.2980	7.569	0.2418	6.142	0.2812	7.142	0.0562	1.427	

Table 7-8 Summary of test results for cyclic tests on headed couplers

Sample ID	Stress in the Bars			Strain at Fracture	
	Yield		Ultimate	Within the Bar	Coupler Region
	[ksi]	[MPa]	[ksi]	[MPa]	[%]
HCC-1	68.5	472	93.3	643	7.8
HCC-2	67.7	466	94.6	652	8.5

Table 7-9 Results for single cycle slip tests on upset headed coupler

Sample	Initial		Stressed			Final			Slip		Pass/Fail
	Elongation	Average Stress	Elongation	Average Stress	Elongation	Average Stress	Elongation	Average Stress	[in]	[mm]	
	[in]	[ksi]	[mm]	[MPa]	[in]	[ksi]	[mm]	[MPa]	[in]	[mm]	
1	0.0015	3.16	0.033	29.8	0.0015	205	0.0381	20.0	0	0	Pass
2	0.0015	3.36	0.026	29.9	0.0085	206	0.2159	19.5	0.007	0.1778	Pass
3	0.0001	3.07	0.029	29.3	0.0016	202	0.04064	19.9	0.0006	0.0152	Pass

Table 7-10 Multi-cycle slip test results for HCS1

Cycle	Initial		Stressed			Final			Slip		Pass/Fail
	Elongation	Average Stress	Elongation	Average Stress	Elongation	Average Stress	Elongation	Average Stress	[in]	[mm]	
	[in]	[ksi]	[mm]	[MPa]	[in]	[ksi]	[mm]	[MPa]	[in]	[mm]	
1	0.0015	3.16	0.033	29.8	0.0015	205	0.0381	20.0	0	0	Pass
2	0.0015	2.91	0.034	30.6	0.0017	211	0.04318	3.33	0.0002	0.0051	Pass
3	0.0017	3.33	0.035	30.3	0.0017	209	0.04318	2.66	0	0	Pass
4	0.0017	2.66	0.035	30.3	0.0017	209	0.04318	2.66	0	0	Pass

Table 7-11 Multi-cycle slip test results for HCS2

Cycle	Initial			Stressed			Final			Slip		Pass/Fail		
	Elongation		Average Stress	Elongation		Average Stress	Elongation		Average Stress	Slip				
	[in]	[mm]	[MPa]	[in]	[mm]	[ksi]	[MPa]	[in]	[mm]	[ksi]	[MPa]		[in]	[mm]
1	0.0015	0.0381	3.36	0.026	0.6604	29.9	206	0.0085	0.2159	2.83	19.5	0.007	0.1778	Pass
2	0.0085	0.2159	2.83	0.026	0.6604	29.9	206	0.0085	0.2159	2.93	20.2	0	0	Pass
3	0.0085	0.2159	2.93	0.027	0.6731	30.4	210	0.0085	0.2159	2.50	17.2	0	0	Pass

Table 7-12 Multi-cycle slip test results for HCS3

Cycle	Initial			Stressed			Final			Slip		Pass/Fail		
	Elongation		Average Stress	Elongation		Average Stress	Elongation		Average Stress	Slip				
	[in]	[mm]	[MPa]	[in]	[mm]	[ksi]	[MPa]	[in]	[mm]	[ksi]	[MPa]		[in]	[mm]
1	0.001	0.0254	3.07	0.029	0.7366	29.3	202	0.0016	0.04064	2.89	19.9	0.0006	0.0152	Pass
2	0.0016	0.0406	2.89	0.031	0.7874	30.1	207	0.0018	0.04572	2.91	20.0	0.0002	0.0051	Pass
3	0.0018	0.0457	2.91	0.032	0.8128	30.3	209	0.0019	0.04699	2.97	20.4	5E-05	0.0013	Pass

Table 7-13 Summary of multi-cycle slip tests on headed couplers

Sample	Total No. of Cycles	Cumulative Slip		Pass/Fail
		[in]	[mm]	
HCS1	4	0.0002	0.00508	Pass
HCS2	3	0.007	0.1778	Pass
HCS3	3	0.00085	0.02159	Pass

Table 7-14 Static test results for grouted couplers at yield

Sample ID	Yield						
	Within the Bars			Coupler Region			Sleeve
	Stress		Strain	Deformation		Strain	Strain
	[ksi]	[MPa]		[in]	[mm]		
GS1	66.0	455	-	-	0.000	-	-
GS2	66.4	458	-	0.060	1.51	0.00331	0.00167
GS3	66.3	457	0.00299	0.047	1.20	0.00262	0.00169
Average	66.2	457	0.00299	0.053	0.90	0.00297	0.00168

Table 7-15 Static test results for grouted couplers at ultimate and failure

Sample ID	Ultimate		Fracture				
	Reinforcing Bars		Reinforcing Bars	Coupler Region		Sleeve	
			Strain	Deformation		Strain	Strain
	[ksi]	[MPa]		[in]	[mm]		
GS1*	108.5	747	-	-	-	-	-
GS2	108.7	749	0.15108	1.054	26.78	0.05856	0.00633
GS3	108.5	747	0.16789	0.964	24.49	0.05357	0.00723
Average	108.5	748.1	0.15949	1.009	25.64	0.05607	0.00678

* Not included in average

Table 7-16 Measured strain rates for grouted coupler dynamic tensile tests

Test	Sample ID	Average Strain Rate		
		$\sigma_0 - \sigma_Y$	$\sigma_Y - \sigma_{ULT}$	$\sigma_{ULT} - \text{Fracture}$
1	GSR1*	100933	133666	92723
2	GSR2	84636	95555	74576
3	GSR3	70200	87784	50412
4	GSR4	79490	94006	193919
Average		78109	92448	106302
Standard Deviation		7316	4113	76834

* Not included in average

Table 7-17 Dynamic test results for grouted couplers at yield

Sample ID	Yield						
	Within the Bars			Coupler Region			Sleeve
	Stress		Strain	Deformation		Strain	Strain
	[ksi]	[MPa]		[in]	[mm]		
GSR2*	-	-	-	-	-	-	-
GSR3	70.4	485	0.00318	0.018	0.45	0.00099	0.00166
GSR4*	-	-	-	-	-	-	-
Average	70.4	485	0.00318	0.018	0.45	0.00099	0.00166

Table 7-18 Dynamic test results for grouted couplers at ultimate and failure

Sample ID	Ultimate		Fracture				
	Reinforcing Bars		Reinforcing Bars	Coupler Region			Sleeve
			Strain	Deformation		Strain	Strain
	[ksi]	[MPa]		[in]	[mm]		
GSR2	110.8	763	0.14978	1.020	25.91	0.05365	0.00565
GSR3	110.7	763	0.13397	1.119	28.42	0.05852	0.00680
GSR4	111.0	765	0.20285	1.021	25.93	0.05371	0.00611
Average	110.8	764	0.16220	1.053	26.75	0.05529	0.00618

Table 7-19 Summary of results for GCC-1

Sample ID	Stress in the Bars				Strain at Fracture		
	Yield		Ultimate		Within the Bar	Coupler Region	Sleeve
	[ksi]	[MPa]	[ksi]	[MPa]	[%]	[%]	[%]
GCC-1	66.1	455	98.7	680	5.59	2.69	0.46

Table 7-20 Results for single cycle slip tests on grouted couplers

Sample	Initial		Stressed		Final		Slip		Pass/Fail		
	Elongation		Elongation		Elongation		Average Stress				
	[in]	[mm]	[in]	[mm]	[in]	[mm]	[ksi]	[MPa]		[in]	[mm]
1	0.005	0.127	0.0135	0.3429	0.004	0.1016	2.94	20.2	-0.001	-0.0254	Pass
2	0.001	0.0254	0.015	0.381	0.001	0.0254	2.64	18.2	0	0	Pass
3	0.0015	0.0381	0.01875	0.47625	0.00325	0.08255	2.75	18.9	0.00175	0.04445	Pass

Table 7-21 Multi-cycle slip test results for GCS1

Cycle	Initial		Stressed		Final		Slip		Pass/Fail		
	Elongation		Elongation		Elongation		Average Stress				
	[in]	[mm]	[in]	[mm]	[in]	[mm]	[ksi]	[MPa]		[in]	[mm]
1	0.005	0.127	0.0135	0.3429	0.004	0.1016	2.94	20.2	-0.001	-0.0254	Pass
2	0.004	0.1016	0.014	0.3556	0.004	0.1016	3.35	23.1	0	0	Pass
3	0.004	0.1016	0.0145	0.3683	0.0045	0.1143	3.23	22.2	0.0005	0.0127	Pass
4	0.0045	0.1143	0.015	0.381	0.0045	0.1143	3.19	22.0	0	0	Pass
5	0.0045	0.1143	0.015	0.381	0.0045	0.1143	3.09	21.3	0	0	Pass

Table 7-22 Multi-cycle slip test results for GCS2

Cycle	Initial		Stressed		Final		Slip		Pass/Fail		
	Elongation		Elongation		Elongation		Average Stress				
	[in]	[mm]	[in]	[mm]	[in]	[mm]	[ksi]	[MPa]		[in]	[mm]
1	0.001	0.0254	0.015	0.381	0.001	0.0254	2.64	18.2	0	0	Pass
2	0.001	0.0254	0.0155	0.3937	0.00125	0.03175	3.32	22.9	0.00025	0.00635	Pass
3	0.00125	0.03175	0.015	0.381	0.00125	0.03175	3.33	22.9	0	0	Pass

Table 7-23 Multi-cycle slip test results for GCS3

Cycle	Initial			Stressed			Final			Slip		Pass/Fail			
	Elongation [in]	Elongation [mm]	Average Stress [ksi]	Average Stress [MPa]	Elongation [in]	Elongation [mm]	Average Stress [ksi]	Average Stress [MPa]	Elongation [in]	Elongation [mm]	Average Stress [ksi]		Average Stress [MPa]		
1	0.0015	0.0381	3.19	22.0	0.01875	0.47625	29.4	202	0.00325	0.08255	2.75	18.9	0.00175	0.04445	Pass
2	0.00325	0.08255	2.75	18.9	0.019	0.4826	30.0	207	0.0035	0.0889	3.24	22.3	0.00025	0.00635	Pass
3	0.0035	0.0889	3.24	22.3	0.01925	0.48895	29.7	204	0.0035	0.0889	3.16	21.8	0	0	Pass
4	0.0035	0.0889	3.16	21.8	0.01925	0.48895	29.7	205	0.0035	0.0889	3.12	21.5	0	0	Pass

Table 7-24 Summary of multi-cycle slip tests on headed couplers

Sample	Total No. of Cycles	Cumulative Slip		Pass/Fail
		[in]	[mm]	
GCS1	5	-0.0005	-0.0127	Pass
GCS2	3	0.00025	0.00635	Pass
GCS3	4	0.002	0.0508	Pass

Table 7-25 Comparison of dynamic yield stress for headed couplers with available models

Sample ID	Measured			Calculated		
	Yield Stress [ksi]	Yield Stress [MPa]	Zadeh & Saïdi (2007) [ksi]	Difference [%]	Malvar (1998) [ksi]	Difference [%]
HSR1	71.25	491	71.37	0.2	76.11	6.8
HSR2	71.90	495	74.31	3.4	76.81	6.8
HSR3	71.85	495	76.79	6.9	77.19	7.4
HSR4	71.97	496	75.89	5.4	79.51	10.5
Average*	71.91	495	75.66	5.2	77.84	8.2

*Does not include HSR1

Table 7-26 Comparison of dynamic yield stress for grouted couplers with available models

Sample ID	Measured Yield Stress		Zadeh & Saiidi (2007)		Difference	Malvar (1998)		Difference
	[ksi]	[MPa]	[ksi]	[MPa]	[%]	[ksi]	[MPa]	[%]
GSR3	70.43	485	73.36-79.78	505-550	4.2-13.3	80.54	555	14.4

Table 7-27 Comparison of dynamic ultimate stress for headed couplers with available models

Sample ID	Measured		Calculated					
	Ultimate Stress		Zadeh & Saiidi (2007)		Difference	Malvar (1998)		Difference
	[ksi]	[MPa]	[ksi]	[MPa]	[%]	[ksi]	[MPa]	[%]
HSR1	96.87	667	100.4	692	3.7	99.76	674	3.0
HSR2	98.16	676	101.7	701	3.6	100.9	681	2.8
HSR3	98.08	676	101.8	701	3.8	100.9	682	2.9
HSR4	98.15	676	102.1	703	4.0	101.2	683	3.1
Average*	98.13	676	101.9	702	3.8	101.0	682	2.9

*Does not include HSR1

Table 7-28 Comparison of dynamic ultimate stress for grouted couplers with available models

Sample ID	Measured Ultimate Stress		Zadeh & Saiidi (2007)		Difference	Malvar (1998)		Difference
	[ksi]	[MPa]	[ksi]	[MPa]	[%]	[ksi]	[MPa]	[%]
GSR2	110.8	763	118.9	819	7.3	115.5	796	4.2
GSR3	110.7	763	118.8	818	7.3	115.4	795	4.3
GSR4	111.0	765	118.8	819	7.1	115.5	796	4.0
Average	110.8	764	118.8	819	7.2	115.5	796	4.2

Chapter 8 Tables

Table 8-1 Measured axial load data

Model	Maximum		Minimum		Average			
					Min/Max		All Data	
	[kips]	[kN]	[kips]	[kN]	[kips]	[kN]	[kips]	[kN]
CIP	223	991	187	832	205	911	208	925
HCNP	222	987	188	836	205	911	206	916
GCNP	221	981	196	872	208	926	209	930
HCPP	225	1000	190	845	207	923	207	921
GCPP	218	968	198	881	208	924	208	925

Table 8-2 Low-cycle fatigue-life parameters based on plastic strain amplitude

Study	ϵ'_{fp}	c_p	Steel Type	Bar Size Tested	
				US	Metric
Mander et al. (1994)	0.078	-0.486	A615 Gr. 40	#5	16
Brown & Kunnath (2000)	0.124	-0.536	A615 Gr. 60	#6	19
	0.105	-0.478		#7	22
	0.088	-0.432		#8	25
Hawileh et al. (2010)	0.128	-0.57		#6	19
Zhou et al. (2008)*	0.183	-0.472	A706 Gr. 60	#8	25
Hawileh et al. (2010)	0.103	-0.54		#6	19

* Values determined from reported data.

Table 8-3 Low-cycle fatigue-life parameters based on total strain amplitude

Study	ϵ'_{fa}	c_a	Steel Type	Bar Size Tested	
				US	Metric
Mander et al. (1994)	0.079	-0.448	A615 Gr. 40	#5	16
Brown & Kunnath (2000)	0.142	-0.503	A615 Gr. 60	#6	19
	0.115	-0.437		#7	22
	0.091	-0.377		#8	25
Hawileh et al. (2010)	0.101	-0.428		#6	19
Zhou et al. (2008)*	0.197	-0.482	A706 Gr. 60	#8	25
Hawileh et al. (2010)	0.09	-0.409		#6	19

* Values determined from reported data.

Table 8-4 Longitudinal reinforcing steel properties for CIP

Parameter	US		SI	
f_y	66.8	[ksi]	460	[MPa]
f_u	111.3	[ksi]	767	[MPa]
E_s	29000	[ksi]	200	[GPa]
E_{sh}	1247	[ksi]	8.59	[GPa]
ϵ_y	0.002303	[in/in]	0.002303	[mm/mm]
ϵ_{sh}	0.005	[in/in]	0.005	[mm/mm]
ϵ_{ult}	0.09	[in/in]	0.09	[mm/mm]

Table 8-5 Description of material properties for cementitious materials for CIP

Material Description	Material Definition in Opensees	Parameter	US		SI	
Unconfined concrete	Concrete01	f'_c	4.446	[ksi]	31	[MPa]
		f'_{cu}	0	[ksi]	0	[MPa]
		ϵ_{cc}	0.002	[in/in]	0.002	[mm/mm]
		ϵ_{cu}	0.005	[in/in]	0.005	[mm/mm]
Confined concrete	Concrete04	f'_c	4.446	[ksi]	31	[MPa]
		f'_{cc}	6.944	[ksi]	48	[MPa]
		f'_{cu}	5.544	[ksi]	38	[MPa]
		E_c	3801	[ksi]	26	[GPa]
		ϵ_{cc}	0.0076	[in/in]	0.0076	[mm/mm]
		ϵ_{cu}	0.0318	[in/in]	0.0318	[mm/mm]

Table 8-6 Rotational spring properties for modeling bond-slip in CIP

Source of Bond-Slip	Push			Pull		
	Moment		Rotation	Moment		Rotation
	[kip-in]	[kN-m]	[rad]	[kip-in]	[kN-m]	[rad]
Footing	0	0	0	0	0	0
	6746	762	0.00277	-6471.49	-731	-0.00293
	7859	887	0.04517	-7540.99	-851	-0.04904

Table 8-7 Longitudinal reinforcing steel properties for HCNP

Parameter	US		SI	
f_y	68	[ksi]	469	[MPa]
f_u	95	[ksi]	655	[MPa]
E_s	29000	[ksi]	200	[GPa]
E_{sh}	692	[ksi]	4.77	[GPa]
ϵ_y	0.002345	[in/in]	0.002345	[mm/mm]
ϵ_{sh}	0.011	[in/in]	0.005	[mm/mm]
ϵ_{ult}	0.1	[in/in]	0.09	[mm/mm]

Table 8-8 Description of material properties for cementitious materials in HCNP

Material Description	Material Definition in Opensees	Parameter	US		SI	
Unconfined concrete in the precast shell	Concrete01	f_c	3.860	[ksi]	27	[MPa]
		f_{cu}	0	[ksi]	0	[MPa]
		ϵ_{cc}	0.002	[in/in]	0.002	[mm/mm]
		ϵ_{cu}	0.005	[in/in]	0.005	[mm/mm]
Unconfined grout in the coupler region	Concrete01	f_c	4.228	[ksi]	29	[MPa]
		f_{cu}	0	[ksi]	0	[MPa]
		ϵ_{cc}	0.003	[in/in]	0.003	[mm/mm]
		ϵ_{cu}	0.005	[in/in]	0.005	[mm/mm]
Confined concrete in the precast shell	Concrete04	f_c	3.860	[ksi]	27	[MPa]
		f_{cc}	6.246	[ksi]	43	[MPa]
		f_{cu}	5.137	[ksi]	35	[MPa]
		E_c	3541	[ksi]	24	[GPa]
		ϵ_{cc}	0.00818	[in/in]	0.00818	[mm/mm]
		ϵ_{cu}	0.03412	[in/in]	0.03412	[mm/mm]
Confined SCC in the core of the precast shell	Concrete04	f_c	5.835	[ksi]	40	[MPa]
		f_{cc}	8.385	[ksi]	58	[MPa]
		f_{cu}	6.136	[ksi]	42	[MPa]
		E_c	4354	[ksi]	30	[GPa]
		ϵ_{cc}	0.00637	[in/in]	0.00637	[mm/mm]
		ϵ_{cu}	0.02643	[in/in]	0.02643	[mm/mm]
Confined grout in the coupler region	Concrete04	f_c	8.303	[ksi]	57	[MPa]
		f_{cc}	10.964	[ksi]	76	[MPa]
		f_{cu}	6.257	[ksi]	43	[MPa]
		E_c	5194	[ksi]	36	[GPa]
		ϵ_{cc}	0.00521	[in/in]	0.00521	[mm/mm]
		ϵ_{cu}	0.02316	[in/in]	0.02316	[mm/mm]

Table 8-9 Rotational spring properties for modeling bond-slip in HCNP

Source of Bond-Slip	Push			Pull		
	Moment		Rotation	Moment		Rotation
	[kip-in]	[kN-m]	[rad]	[kip-in]	[kN-m]	[rad]
Footing	0	0	0	0	0	0
	7123	804	0.00241	-7200	-813	-0.00243
	7662	865	0.02898	-7612	-859	-0.02599

Table 8-10 Properties for bi-linear ductile cast iron material

Property	US		SI	
Elastic Modulus	24500	[ksi]	169	[GPa]
$\sigma_{y,eff}$	60	[ksi]	413	[MPa]
σ_u	85	[ksi]	586	[MPa]
$\varepsilon_{y,eff}$	0.00245			
$0.5\varepsilon_u$	0.06			
ε_u	0.12			

Table 8-11 Longitudinal reinforcing steel properties for GCNP

Parameter	US		SI	
f_y	66.8	[ksi]	460	[MPa]
f_u	111.3	[ksi]	767	[MPa]
E_s	29000	[ksi]	200	[GPa]
E_{sh}	1247	[ksi]	8.59	[GPa]
ε_{sh}	0.005	[in/in]	0.005	[mm/mm]
ε_{ult}	0.09	[in/in]	0.09	[mm/mm]

Table 8-12 Description of material properties for cementitious materials in GCNP

Material Description	Material Definition in Opensees	Parameter	US		SI	
Unconfined concrete in the precast shell	Concrete01	f'_c	4.228	[ksi]	29	[MPa]
		f'_{cu}	0	[ksi]	0	[MPa]
		ϵ_{cc}	0.003	[in/in]	0.003	[mm/mm]
		ϵ_{cu}	0.005	[in/in]	0.005	[mm/mm]
Confined concrete in the precast shell	Concrete04	f'_c	4.228	[ksi]	29	[MPa]
		f'_{cc}	6.704	[ksi]	46	[MPa]
		f'_{cu}	5.418	[ksi]	37	[MPa]
		E_c	3706	[ksi]	26	[GPa]
		ϵ_{cc}	0.0079	[in/in]	0.0079	[mm/mm]
		ϵ_{cu}	0.0328	[in/in]	0.0328	[mm/mm]
Confined SCC in the core of the precast shell	Concrete04	f'_c	4.997	[ksi]	34	[MPa]
		f'_{cc}	7.543	[ksi]	52	[MPa]
		f'_{cu}	5.818	[ksi]	40	[MPa]
		E_c	4029	[ksi]	28	[GPa]
		ϵ_{cc}	0.0071	[in/in]	0.0071	[mm/mm]
		ϵ_{cu}	0.296	[in/in]	0.296	[mm/mm]

Table 8-13 Rotational spring properties for GCNP

Source of Bond-Slip	Push			Pull		
	Moment		Rotation	Moment		Rotation
	[kip-in]	[kN-m]	[rad]	[kip-in]	[kN-m]	[rad]
Footing	0	0	0	0	0	0
	7389	834	0.00270	-7416	-837	-0.00287
	8880	1003	0.05991	-8911	-1006	-0.05391
Base of grouted coupler	0	0	0	0	0	0
	7309	825	0.00061	-7225	-816	-0.00063
	8880	1003	0.01435	-8911	-1006	-0.01287
Top of grout coupler	0	0	0	0	0	0
	6342	716	0.00053	-6262	-707	-0.00055
	7706	870	0.01032	-7586	-856	-0.01070

Table 8-14 Results from moment-curvature analysis of the pedestal

Model ID	Description	Push						Pull					
		Moment			Curvature			Moment			Curvature		
		Capacity		% Difference relative to V1	Capacity		% Difference relative to V1	Capacity		% Difference relative to V1	Capacity		% Difference relative to V1
		[kip-in]	[kN-m]		[1/in]	[1/mm]		[kip-in]	[kN-m]		[1/in]	[1/mm]	
V1	CIP pedestal	7644	863	-	0.00523	0.133	-	7544	852	-	0.00530	0.135	-
V2	Precast pedestal without ducts or grout	7631	862	-0.17	0.00507	0.129	-3.18	7562	854	0.24	0.00522	0.133	-1.57
V3	Precast pedestal with ducts (compression only) and grout	8125	917	6.29	0.00530	0.135	1.27	7940	896	5.25	0.00540	0.137	1.89
V4	Precast pedestal with grout	8068	911	5.55	0.00530	0.135	1.27	7889	891	4.57	0.00538	0.137	1.57
V5	Precast pedestal with ducts (compression only)	7700	869	0.73	0.00513	0.130	-1.91	7614	860	0.92	0.00525	0.133	-0.94
V6	Precast pedestal with ducts (tension/compression) and grout	8336	941	9.05	0.00530	0.135	1.27	8150	920	8.03	0.00535	0.136	0.94

Table 8-15 Longitudinal reinforcing steel properties for HCPP

Parameter	US		SI	
f_y	68	[ksi]	469	[MPa]
f_u	95	[ksi]	655	[MPa]
E_s	29000	[ksi]	200	[GPa]
E_{sh}	692	[ksi]	4.77	[GPa]
ϵ_{sh}	0.011	[in/in]	0.005	[mm/mm]
ϵ_{ult}	0.1	[in/in]	0.09	[mm/mm]

Table 8-16 Description of material properties for cementitious materials in HCPP

Material Description	Material Definition in Opensees	Parameter	US		SI	
Unconfined concrete in the precast shell	Concrete01	f'_c	4.300	[ksi]	30	[MPa]
		f'_{cu}	0	[ksi]	0	[MPa]
		ϵ_{cc}	0.002	[in/in]	0.002	[mm/mm]
		ϵ_{cu}	0.005	[in/in]	0.005	[mm/mm]
Unconfined concrete in the pedestal	Concrete01	f'_c	4.300	[ksi]	30	[MPa]
		f'_{cu}	0	[ksi]	0	[MPa]
		ϵ_{cc}	0.002	[in/in]	0.002	[mm/mm]
		ϵ_{cu}	0.005	[in/in]	0.005	[mm/mm]
Unconfined concrete in the pedestal	Concrete01	f'_c	7.058	[ksi]	49	[MPa]
		f'_{cu}	0	[ksi]	0	[MPa]
		ϵ_{cc}	0.002	[in/in]	0.002	[mm/mm]
		ϵ_{cu}	0.006	[in/in]	0.006	[mm/mm]
Confined concrete in the precast shell	Concrete04	f'_c	4.300	[ksi]	30	[MPa]
		f'_{cc}	6.733	[ksi]	46	[MPa]
		f'_{cu}	5.414	[ksi]	37	[MPa]
		E_c	3738	[ksi]	26	[GPa]
		ϵ_{cc}	0.00766	[in/in]	0.00766	[mm/mm]
		ϵ_{cu}	0.03194	[in/in]	0.03194	[mm/mm]
Confined SCC in the core of the precast shell	Concrete04	f'_c	5.240	[ksi]	36	[MPa]
		f'_{cc}	7.751	[ksi]	53	[MPa]
		f'_{cu}	5.883	[ksi]	41	[MPa]
		E_c	4126	[ksi]	28	[GPa]
		ϵ_{cc}	0.00679	[in/in]	0.00679	[mm/mm]
		ϵ_{cu}	0.02827	[in/in]	0.02827	[mm/mm]
Confined concrete in the pedestal	Concrete04	f'_c	4.300	[ksi]	30	[MPa]
		f'_{cc}	6.638	[ksi]	46	[MPa]
		f'_{cu}	5.295	[ksi]	36	[MPa]
		E_c	3738	[ksi]	26	[GPa]
		ϵ_{cc}	0.00744	[in/in]	0.00744	[mm/mm]
		ϵ_{cu}	0.03103	[in/in]	0.03103	[mm/mm]
Confined grout in the coupler region	Concrete04	f'_c	7.186	[ksi]	50	[MPa]
		f'_{cc}	9.805	[ksi]	68	[MPa]
		f'_{cu}	6.234	[ksi]	43	[MPa]
		E_c	4832	[ksi]	33	[GPa]
		ϵ_{cc}	0.00564	[in/in]	0.00564	[mm/mm]
		ϵ_{cu}	0.02519	[in/in]	0.02519	[mm/mm]
Confined grout in the pedestal ducts	Concrete01	f'_c	7.058	[ksi]	49	[MPa]
		f'_{cu}	9.563	[ksi]	66	[MPa]
		ϵ_{cc}	0.00555	[in/in]	0.00555	[mm/mm]
		ϵ_{cu}	0.02476	[in/in]	0.02476	[mm/mm]

Table 8-17 Rotational spring properties for HCPP

Source of Bond-Slip	Push			Pull		
	Moment		Rotation	Moment		Rotation
	[kip-in]	[kN-m]	[rad]	[kip-in]	[kN-m]	[rad]
Footing	0	0	0	0	0	0
	6775	765	0.00269	-6839	-772	-0.00270
	7426	838	0.03134	-7244	-818	-0.02736
Base of the pedestal	0	0	0	0	0	0
	6775	765	0.00071	-6914	-781	-0.00072
	7426	838	0.00823	-7244	-818	-0.00718
Top of the pedestal	0	0	0	0	0	0
	6585	744	0.00071	-6579	-743	-0.00070
	7310	825	0.00472	-7300	-824	-0.00451
	7560	854	0.00944	-7550	-852	-0.00903

Table 8-18 Longitudinal reinforcing steel properties for GCPP

Parameter	US		SI	
f_v	66.8	[ksi]	460	[MPa]
f_u	111.3	[ksi]	767	[MPa]
E_s	29000	[ksi]	200	[GPa]
E_{sh}	1247	[ksi]	8.59	[GPa]
ϵ_{sh}	0.005	[in/in]	0.005	[mm/mm]
ϵ_{ult}	0.09	[in/in]	0.09	[mm/mm]

Table 8-19 Description of material properties for cementitious materials in GCPP

Material Description	Material Definition in Opensees	Parameter	US		SI	
Unconfined concrete in the precast shell	Concrete01	f'_c	4.203	[ksi]	29	[MPa]
		f'_{cu}	0	[ksi]	0	[MPa]
		ϵ_{cc}	0.002	[in/in]	0.002	[mm/mm]
		ϵ_{cu}	0.005	[in/in]	0.005	[mm/mm]
Unconfined concrete in the pedestal	Concrete01	f'_c	4.203	[ksi]	29	[MPa]
		f'_{cu}	0	[ksi]	0	[MPa]
		ϵ_{cc}	0.002	[in/in]	0.002	[mm/mm]
		ϵ_{cu}	0.005	[in/in]	0.005	[mm/mm]
Confined concrete in the precast shell	Concrete04	f'_c	4.203	[ksi]	29	[MPa]
		f'_{cc}	6.677	[ksi]	46	[MPa]
		f'_{cu}	5.409	[ksi]	37	[MPa]
		E_c	3695	[ksi]	25	[GPa]
		ϵ_{cc}	0.0079	[in/in]	0.0079	[mm/mm]
		ϵ_{cu}	0.0329	[in/in]	0.0329	[mm/mm]
Confined concrete in the pedestal	Concrete04	f'_c	4.997	[ksi]	34	[MPa]
		f'_{cc}	7.543	[ksi]	52	[MPa]
		f'_{cu}	5.818	[ksi]	40	[MPa]
		E_c	4029	[ksi]	28	[GPa]
		ϵ_{cc}	0.0071	[in/in]	0.0071	[mm/mm]
		ϵ_{cu}	0.0296	[in/in]	0.0296	[mm/mm]
Confined SCC in the core of the precast shell	Concrete04	f'_c	4.203	[ksi]	29	[MPa]
		f'_{cc}	6.532	[ksi]	45	[MPa]
		f'_{cu}	5.259	[ksi]	36	[MPa]
		E_c	3695	[ksi]	25	[GPa]
		ϵ_{cc}	0.0075	[in/in]	0.0075	[mm/mm]
		ϵ_{cu}	0.0315	[in/in]	0.0315	[mm/mm]
Confined grout in the pedestal ducts	Concrete01	f'_c	7.303	[ksi]	50	[MPa]
		f'_{cu}	9.518	[ksi]	66	[MPa]
		ϵ_{cc}	0.0056	[in/in]	0.0056	[mm/mm]
		ϵ_{cu}	0.0249	[in/in]	0.0249	[mm/mm]

Table 8-20 Rotational spring properties for GCPP

Source of Bond-Slip	Push			Pull		
	Moment		Rotation	Moment		Rotation
	[kip-in]	[kN-m]	[rad]	[kip-in]	[kN-m]	[rad]
Footing	0	0	0	0	0	0
	6423	725	0.00264	-6458	-729	-0.00262
	7666	865	0.04122	-7601	-858	-0.04214
Base of pedestal	0	0	0	0	0	0
	6415	724	0.00083	-6447	-728	-0.00082
	7666	865	0.01345	-7601	-858	-0.01375
Top of pedestal	0	0	0	0	0	0
	6595	745	0.000801	-6509	-735	-0.00079
	8117	916	0.008813	-8119	-917	-0.00824
	8716	984	0.017626	-8718	-984	-0.01647
Base of grouted coupler	0	0	0	0	0	0
	6618	747	0.000614	-6614	-747	-0.00061
	8117	916	0.00689	-8119	-917	-0.00643
	8716	984	0.01378	-8718	-984	-0.01287

Chapter 9 Tables

Table 9-1 Conventional column design details

Column Details	Half-Scale Model	Prototype
Aspect Ratio	4.5	
Diameter	24 in [610 mm]	48 in [1220 mm]
Cantilever Length	108 in [2743 mm]	216 in [5486 mm]
Axial Load (ALI = 0.1)	226 kip [1005 kN]	905 kip [4025 kN]
Longitudinal Steel (Ratio)	11 - #8 Bar [D25] (1.92%)	16 - #14 Bars [D43] (1.98%)
Trans	#3 at 2-in Pitch [D9.5 at 51-mm Pitch] (1.05%)	#6 at 3.75-in Pitch [D19 at 95-mm Pitch] (1.08%)
Clear Cover	1.75 in [44.5 mm]	2.875 in [73 mm]

Table 9-2 Typical material properties used for parametric study

Material Type	OpenSEES Material Model	Properties				
		[US]			[SI]	
Unconfined Concrete	<i>Concrete01</i>	f'_c	5	ksi	34	MPa
		f'_{cu}	0	ksi	0	MPa
		ϵ_{co}	0.002			
		ϵ_{cu}	0.005			
Confined Concrete	<i>Concrete04</i>	Properties determined using Mander's model and transverse steel details				
Unconfined Grout	<i>Concrete01</i>	f'_g	7	ksi	48	MPa
		f'_{gu}	0	ksi	0	MPa
		ϵ_{go}	0.002			
		ϵ_{gu}	0.006			
Confined Grout	<i>Concrete04</i>	Properties determined using Mander's model and transverse steel details				
Longitudinal Reinforcement (ASTM A706)	<i>ReinforcingSteel</i>	f_v	68	ksi	469	MPa
		f_u	95	ksi	655	MPa
		ϵ_v	0.00234			
		ϵ_{sh}	0.0075			
		ϵ_{ult}	0.07			
		E	29000	ksi	200	GPa
E_{sh}	1247	ksi	8.59	GPa		
Ductile Cast-Iron	<i>Hysteretic</i>	$f_{y,eff}$	60	ksi	413	MPa
		f_u	85	ksi	586	MPa
		$\epsilon_{y,eff}$	0.00245			
		ϵ_u	0.06			
		E_{Sleeve}	24500	ksi	169	GPa
Materials Not Directly Used in OpenSEES						
Footing Concrete		f'_c	5.5	ksi	38	MPa
Coupler Grout		f'_g	14	ksi	96	MPa
Transverse Steel (ASTM A706)		f_y	68	ksi	469	MPa
		f_u	95	ksi	655	MPa
		ϵ_y	0.00234			
		ϵ_{sh}	0.015			
		ϵ_{ult}	0.12			
		E	29000	ksi	200	GPa
		E_{sh}	1247	ksi	8.59	GPa

Table 9-3 Parametric study matrix

Study	Variable	Description	Nomenclature	
			Precast	Conventional
GC Column Studies	Target Design Displacement Ductility (DD)	$\mu_D = 7.0$. Confining steel varied.	GN-DD7	C-DD7
		$\mu_D = 6.0$. Confining steel varied.	GN-DD6	C-DD6
		$\mu_D = 5.0$. Confining steel varied.	GN-DD5	C-DD5
	Aspect Ratio (AR)	AR = 4.5. Models C-DD7 and GN-DD7 were used	GN-DD7	C-DD7
		AR = 6.0. Height of the column varied.	GN-AR6	C-AR6
	Longitudinal Steel Reinforcement Ratio (RR)	RR = 2%. Models C-DD7 and GN-DD7 were used	GN-DD7	C-DD7
RR = 1%. Bar size and number varied.		GN-RR1	C-RR1	
Pedestal Details	Pedestal Height / Detailing	Height: 0.5D. Detailing: Precast	XP-PC-05D	C-DD7
		Height: 0.5D. Detailing: Cast-in-place.	XP-CIP-05D	C-DD7
		Height: 1.0D. Detailing: Precast	XP-PC-1D	C-DD7
		Height: 1.0D. Detailing: Cast-in-place.	XP-CIP-1D	C-DD7

Table 9-4 Model details used in parameter study of target design displacement ductility for GC columns

Column Details	DD = 7.0 (Prototype)	DD = 6.0	DD = 5.0
Target Design Displacement Ductility	7.0	6.0	5.0
Calculated Displacement Ductility (M- ϕ analysis)	7.3	6.17	5.16
Calculated Moment Capacity	58,940 kip-in [6654 kN-m]	56,270 kip-in [6353 kN-m]	53,935 kip-in [6089 kN-m]
Transverse Steel (Ratio)	#6 at 3.75-in Pitch [D19 at 95-mm Pitch] (1.08%)	#6 at 5.25-in Pitch [D19 at 133-mm Pitch] (0.78%)	#5 at 5.25-in Pitch [D17 at 133-mm Pitch] (0.54%)
Clear Cover Outside Coupler Region	2.875 in [73 mm]	2.875 in [73 mm]	3.0 in [76 mm]
Clear Cover Inside Coupler Region	2.0 in [51 mm]	2.0 in [51 mm]	2.125 in [54 mm]

Table 9-5 Summary of results for ductility study

Performance Measure	Model								% Difference Relative to C-type
	C-DD7				GN-DD7				
	[US]		[SI]		[US]		[SI]		
μ_b	6.52				7.23				10.9
Maximum Moment	61604	kip-in	6955	kN-m	68296	kip-in	7711	kN-m	10.9
Maximum Base Shear	285	kip	1269	kN	316	kip	1406	kN	10.9
Effective Yield Displacement	2.44	in	61.8	mm	2.92	in	74.0	mm	19.7
Ultimate Displacement	15.9	in	403	mm	21.1	in	536	mm	32.9
V_p	264	kip	1174	kN-m	295	kip	1310	kN-m	11.6
M_p	57016	kip-in	6437	kN-m	63639	kip-in	7185	kN-m	11.6
Effective Stiffness	108	kip/in	19.0	kN/mm	101	kip/in	17.7	kN/mm	-6.8
Performance Measure	Model								% Difference Relative to C-type
	C-DD6				GN-DD6				
	[US]		[SI]		[US]		[SI]		
μ_b	5.06				5.42				7.1
Maximum Moment	58593	kip-in	6615	kN-m	65354	kip-in	7378	kN-m	11.5
Maximum Base Shear	271	kip	1207	kN	303	kip	1346	kN	11.5
Effective Yield Displacement	2.39	in	60.7	mm	2.84	in	72.1	mm	18.8
Ultimate Displacement	12.1	in	307	mm	15.4	in	391	mm	27.3
V_p	256	kip	1140	kN-m	287	kip	1276	kN-m	12.0
M_p	55344	kip-in	6248	kN-m	61988	kip-in	6998	kN-m	12.0
Effective Stiffness	107	kip/in	18.8	kN/mm	101	kip/in	17.7	kN/mm	-5.7
Performance Measure	Model								% Difference Relative to C-type
	C-DD5				GN-DD5				
	[US]		[SI]		[US]		[SI]		
μ_b	3.94				3.12				-20.8
Maximum Moment	55284	kip-in	6242	kN-m	62360	kip-in	7040	kN-m	12.8
Maximum Base Shear	256	kip	1138	kN	289	kip	1284	kN	12.8
Effective Yield Displacement	2.36	in	59.9	mm	2.73	in	69.2	mm	15.6
Ultimate Displacement	9.3	in	236	mm	8.5	in	216	mm	-8.6
V_p	249	kip	1109	kN-m	275	kip	1223	kN-m	10.3
M_p	53843	kip-in	6079	kN-m	59377	kip-in	6704	kN-m	10.3
Effective Stiffness	106	kip/in	18.5	kN/mm	101	kip/in	17.7	kN/mm	-4.6

Table 9-6 Model details for aspect ratio study

Column Details	AR = 4.5	AR = 6
Cantilever Height	216 in [5486 mm]	288 in [7315 mm]
Diameter	48 in [1220 mm]	48 in [1220 mm]
Calculated Displacement Ductility (M- ϕ analysis)	7.3	7.09
Calculated Moment Capacity	58,940 kip-in [6654 kN-m]	60,886 kip-in [6874 kN-m]
Longitudinal Steel (Ratio)	16 - #14 Bars [D43] (1.98%)	16 - #14 Bars [D43] (1.98%)
Transverse Steel (Ratio)	#6 at 3.75-in Pitch [D19 at 95-mm Pitch] (1.08%)	#6 at 3-in Pitch [D19 at 76-mm Pitch] (1.36%)
Clear Cover Outside Coupler Region	2.875 in [73 mm]	2.875 in [73 mm]
Clear Cover Inside Coupler Region	2.0 in [51 mm]	2.0 in [51 mm]

Table 9-7 Summary of results for aspect ratio study

Performance Measure	Model								% Difference Relative to C-type
	C-AR6				GN-AR6				
	[US]		[SI]		[US]		[SI]		
μ_b	7.78				7.75952892				-0.3
Maximum Moment	63709	kip-in	7193	kN-m	68083	kip-in	7687	kN-m	6.9
Maximum Base Shear	221	kip	984	kN	236	kip	1051	kN	6.9
Effective Yield Displacement	4.18	in	106.2	mm	4.57	in	116.1	mm	9.3
Ultimate Displacement	32.6	in	827	mm	35.5	in	902	mm	9.1
V_p	206	kip	917	kN-m	219	kip	976	kN-m	6.4
M_p	59395	kip-in	6706	kN-m	63199	kip-in	7135	kN-m	6.4
Effective Stiffness	49	kip/in	8.6	kN/mm	48	kip/in	8.4	kN/mm	-2.8

Table 9-8 Model details for reinforcement ratio study

Column Details	RR = 2%	RR = 1%	RR = 1% Modified
Cantilever Height	216 in [5486 mm]	216 in [5486 mm]	217 in [5486 mm]
Diameter	48 in [1220 mm]	48 in [1220 mm]	49 in [1220 mm]
Calculated Displacement Ductility (M-φ analysis)	7.3	7.04	7.01
Calculated Moment Capacity of the Conventional Section	58,940 kip-in [6654 kN-m]	37,563 kip-in [4240 kN-m]	36,633 kip-in [4135 kN-m]
Longitudinal Steel Above Coupler (Ratio)	16 - #14 Bars [D43] (1.98%)	12 - #11 Bars [D39] (1.03%)	12 - #11 Bars [D39] (1.03%)
Longitudinal Steel Below Coupler (Ratio)	16 - #14 Bars [D43] (1.98%)	12 - #11 Bars [D39] (1.03%)	12 - #14 Bars [D43] (1.49%)
Transverse Steel (Ratio)	#6 at 3.75-in Pitch [D19 at 95-mm Pitch] (1.08%)	#6 at 5.25-in Pitch [D19 at 133-mm Pitch] (0.78%)	#6 at 5.25-in Pitch [D19 at 133-mm Pitch] (0.78%)
Clear Cover Outside Coupler Region	2.875 in [73 mm]	2.81 in [71 mm]	3.15 in [80 mm]
Clear Cover Inside Coupler Region	2.0 in [51 mm]	2.0 in [51 mm]	2.0 in [51 mm]
Sleeve Length	24.41 in [620 mm]	19.5 in [495 mm]	24.41 in [620 mm]

Table 9-9 Summary of results for reinforcement ratio study

Performance Measure	Model								% Difference Relative to C-type
	C-RR1				GN-RR1				
	[US]		[SI]		[US]		[SI]		
μ_b	6.62				5.40				-18.5
Maximum Moment	39002	kip-in	4403	kN-m	42383	kip-in	4785	kN-m	8.7
Maximum Base Shear	181	kip	803	kN	196	kip	873	kN	8.7
Effective Yield Displacement	1.80	in	45.6	mm	1.95	in	49.4	mm	8.4
Ultimate Displacement	11.9	in	302	mm	10.5	in	267	mm	-11.6
V_p	173	kip	770	kN-m	186	kip	829	kN-m	7.7
M_p	37397	kip-in	4222	kN-m	40264	kip-in	4546	kN-m	7.7
Effective Stiffness	96	kip/in	16.9	kN/mm	96	kip/in	16.8	kN/mm	-0.6
Performance Measure	Model								% Difference Relative to C-type
	C-RR1				GN-RR1-M				
	[US]		[SI]		[US]		[SI]		
μ_b	6.62				2.37				-64.2
Maximum Moment	39002	kip-in	4403	kN-m	42017	kip-in	4744	kN-m	7.7
Maximum Base Shear	181	kip	803	kN	195	kip	865	kN	7.7
Effective Yield Displacement	1.80	in	45.6	mm	2.06	in	52.2	mm	14.5
Ultimate Displacement	11.9	in	302	mm	4.9	in	123.8	mm	-58.9
V_p	173	kip	770	kN-m	186	kip	828	kN-m	7.5
M_p	37397	kip-in	4222	kN-m	40188	kip-in	4537	kN-m	7.5
Effective Stiffness	96	kip/in	16.9	kN/mm	91	kip/in	15.8	kN/mm	-6.1

Table 9-10 Summary of results for HP columns with pedestals of height 0.5D

Performance Measure	C-DD7				HP-PC-05D				% Difference Relative to C-type	HP-CIP-05D				% Difference Relative to C-type
	[US]		[SI]		[US]		[SI]			[US]		[SI]		
μ_b	6.52				6.27				-3.8	6.43				-1.3
Maximum Moment	61604	kip-in	6955	kN-m	65326	kip-in	7375	kN-m	6.0	61673	kip-in	6963	kN-m	0.1
Maximum Base Shear	285	kip	1269	kN	302	kip	1345	kN	6.0	286	kip	1270	kN	0.1
Effective Yield	2.44	in	61.8	mm	2.73	in	69.3	mm	12.1	2.44	in	62.0	mm	0.2
Ultimate Displacement	15.9	in	403	mm	17	in	435	mm	7.8	16	in	399	mm	-1.1
Vp	264	kip	1174	kN-m	281	kip	1250	kN-m	6.4	267	kip	1186	kN-m	1.1
Mp	57016	kip-in	6437	kN-m	60688	kip-in	6852	kN-m	6.4	57615	kip-in	6505	kN-m	1.1
Effective Stiffness	108	kip/in	19.0	kN/mm	103	kip/in	18.0	kN/mm	-5.1	109	kip/in	19.1	kN/mm	0.8

Table 9-11 Summary of results for HP columns with pedestals of height 1.0D

Performance Measure	C-DD7				HP-PC-1D				% Difference Relative to C-type	HP-CIP-1D				% Difference Relative to C-type
	[US]		[SI]		[US]		[SI]			[US]		[SI]		
μ_D	6.52				5.97				-8.5	6.60				1.3
Maximum Moment	61604	kip-in	6955	kN-m	65398	kip-in	7383	kN-m	6.2	61490	kip-in	6942	kN-m	-0.2
Maximum Base Shear	285	kip	1269	kN	303	kip	1347	kN	6.2	285	kip	1266	kN	-0.2
Effective Yield	2.44	in	61.8	mm	2.66	in	67.6	mm	9.2	2.48	in	63.0	mm	1.8
Ultimate Displacement	15.9	in	403	mm	16	in	403	mm	0.0	16	in	416	mm	3.1
Vp	264	kip	1174	kN-m	281	kip	1250	kN-m	6.4	267	kip	1190	kN-m	1.3
Mp	57016	kip-in	6437	kN-m	60686	kip-in	6851	kN-m	6.4	57767	kip-in	6522	kN-m	1.3
Effective Stiffness	108	kip/in	19.0	kN/mm	106	kip/in	18.5	kN/mm	-2.6	108	kip/in	18.9	kN/mm	-0.5

Table 9-12 Summary of results for GP columns with pedestals of height 0.5D

Performance Measure	C-DD7				GP-PC-05D				% Difference Relative to C-type	GP-CIP-05D				% Difference Relative to C-type
	[US]		[SI]		[US]		[SI]			[US]		[SI]		
μ_b	6.52				5.64				-13.5	6.18				-5.3
Maximum Moment	61604	kip-in	6955	kN-m	64866	kip-in	7323	kN-m	5.3	61635	kip-in	6959	kN-m	0.0
Maximum Base Shear	285	kip	1269	kN	300	kip	1336	kN	5.3	285	kip	1269	kN	0.0
Effective Yield Displacement	2.44	in	61.8	mm	2.79	in	70.9	mm	14.6	2.55	in	64.8	mm	4.7
Ultimate Displacement	15.9	in	403	mm	16	in	400	mm	-0.8	16	in	400	mm	-0.8
V_p	264	kip	1174	kN-m	279	kip	1240	kN-m	5.6	267	kip	1186	kN-m	1.0
M_p	57016	kip-in	6437	kN-m	60195	kip-in	6796	kN-m	5.6	57604	kip-in	6503	kN-m	1.0
Effective Stiffness	108	kip/in	19.0	kN/mm	100	kip/in	17.5	kN/mm	-7.9	105	kip/in	18.3	kN/mm	-3.5

Table 9-13 Summary of results for GP columns with pedestals of height 1.0D

Performance Measure	C-DD7				GP-PC-1D				% Difference Relative to C-type	GP-CIP-1D				% Difference Relative to C-type
	[US]		[SI]		[US]		[SI]			[US]		[SI]		
μ_D	6.52				5.58				-14.4	6.46				-0.9
Maximum Moment	61604	kip-in	6955	kN-m	65026	kip-in	7341	kN-m	5.6	61499	kip-in	6943	kN-m	-0.2
Maximum Base Shear	285	kip	1269	kN	301	kip	1339	kN	5.6	285	kip	1266	kN	-0.2
Effective Yield Displacement	2.44	in	61.8	mm	2.76	in	70.1	mm	13.3	2.55	in	64.8	mm	4.7
Ultimate Displacement	15.9	in	403	mm	15	in	391	mm	-3.0	16	in	419	mm	3.8
V_p	264	kip	1174	kN-m	280	kip	1245	kN-m	6.0	266	kip	1185	kN-m	1.0
M_p	57016	kip-in	6437	kN-m	60459	kip-in	6826	kN-m	6.0	57559	kip-in	6498	kN-m	1.0
Effective Stiffness	108	kip/in	19.0	kN/mm	101	kip/in	17.7	kN/mm	-6.4	105	kip/in	18.3	kN/mm	-3.6

Figures

Chapter 1 Figures

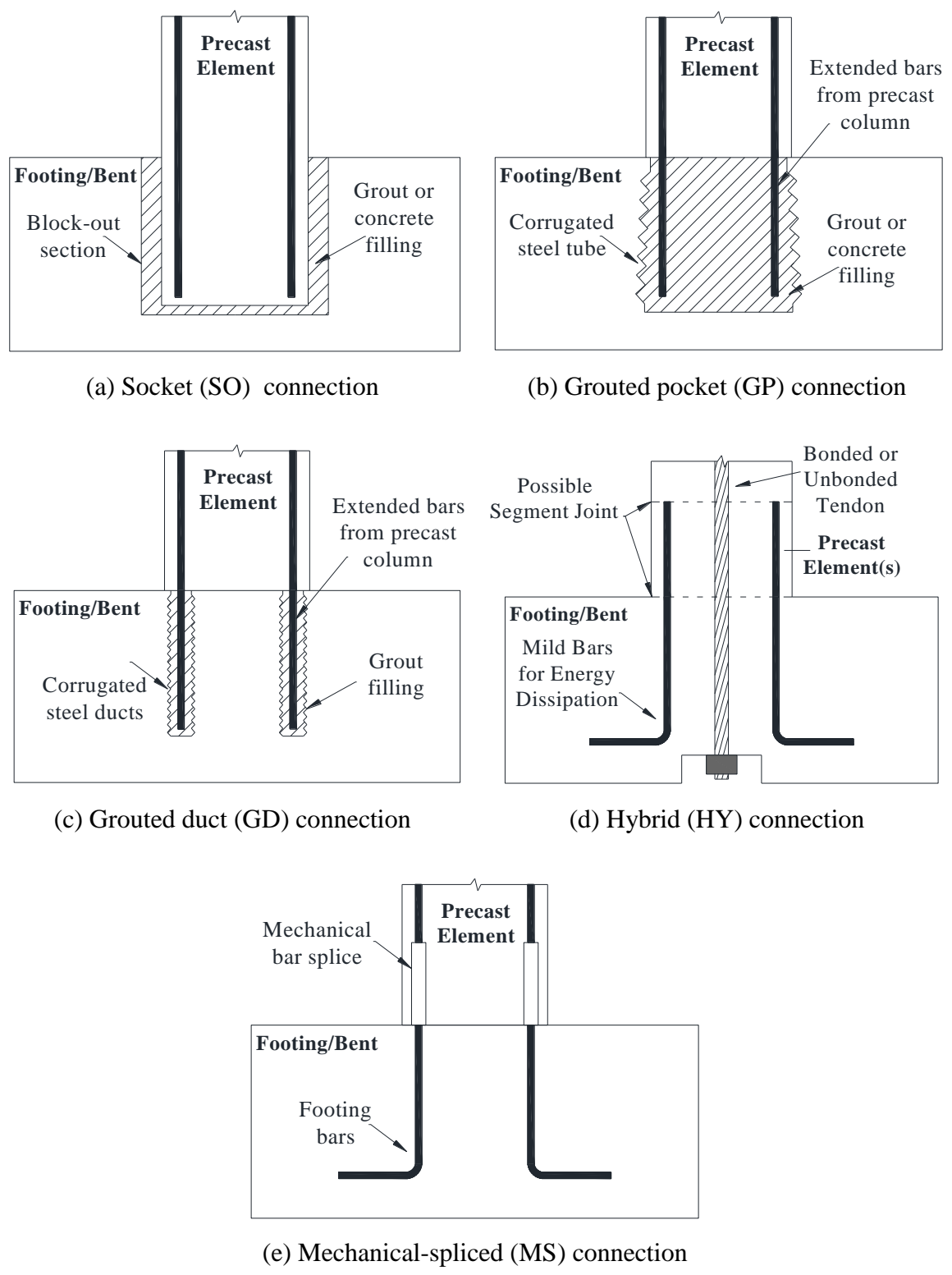


Figure 1-1 Precast columns connection types for ABC (adapted from Marsh et al., 2011)

Chapter 2 Figures

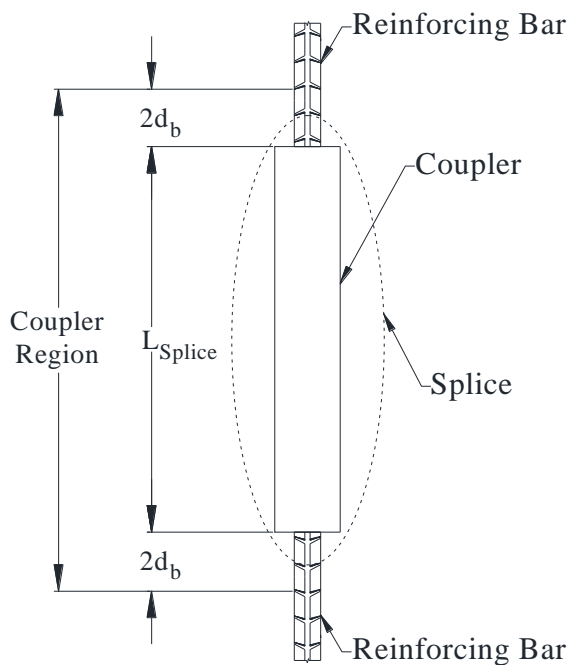
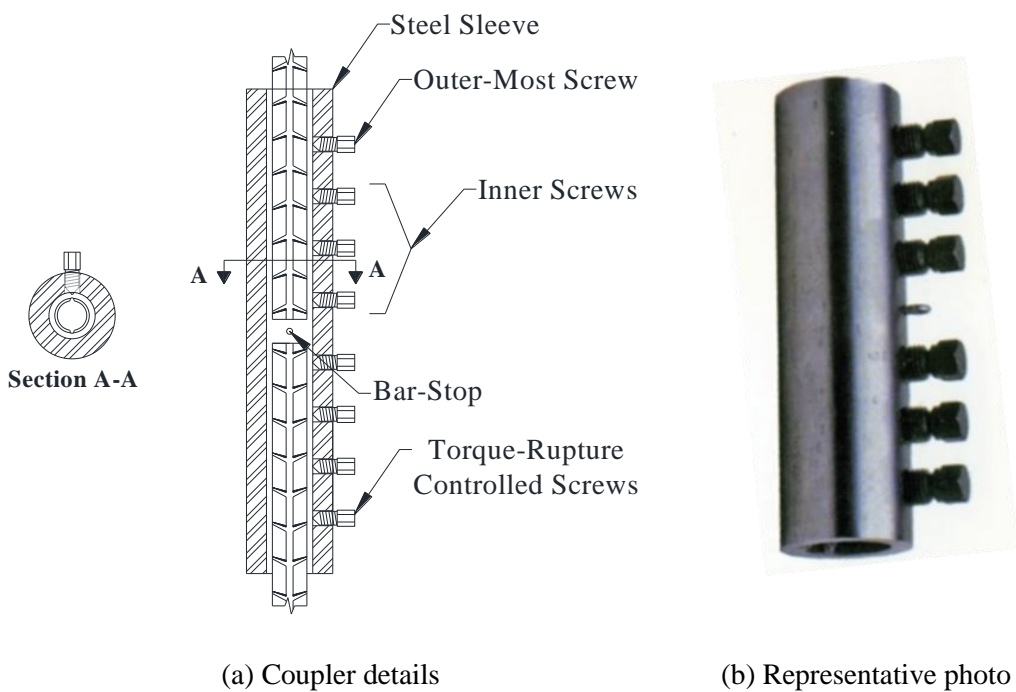


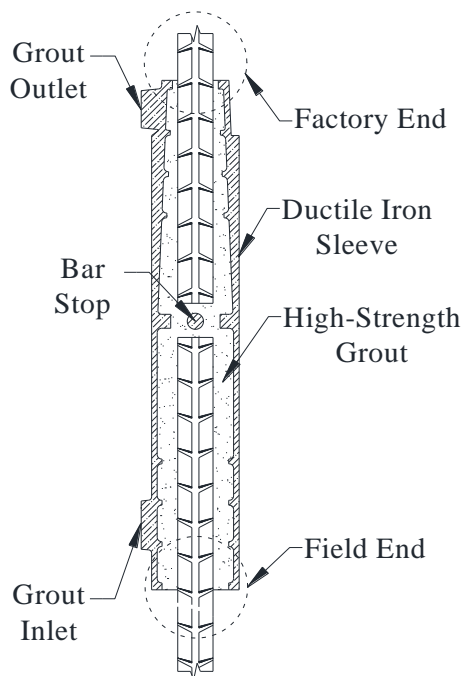
Figure 2-1 Schematic for commonly used terms



(a) Coupler details

(b) Representative photo

Figure 2-2 Shear-screw coupler

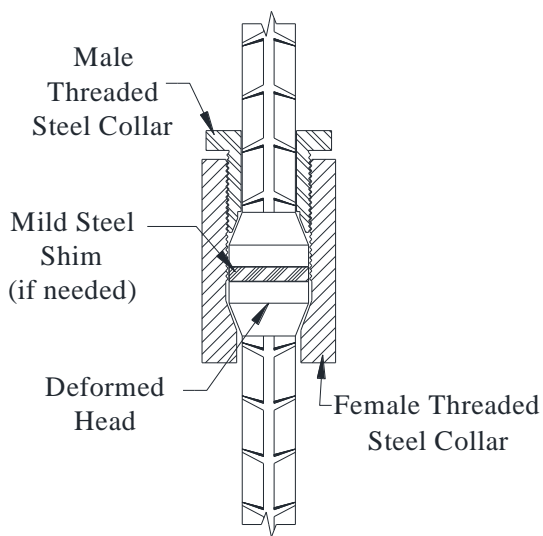


(a) Coupler details



(b) Representative photo

Figure 2-3 Grout-filled sleeve coupler

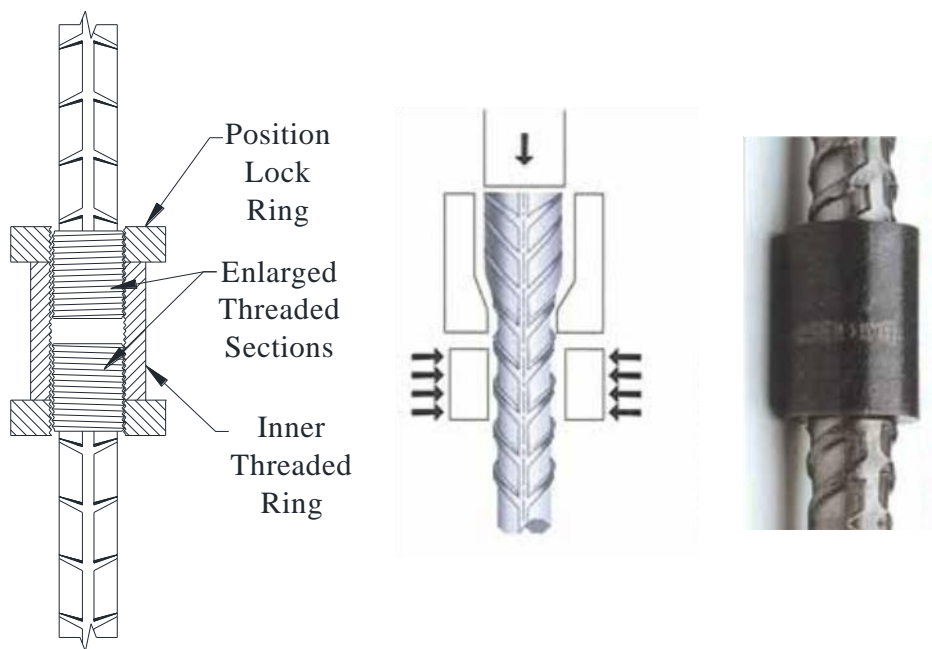


(a) Coupler details



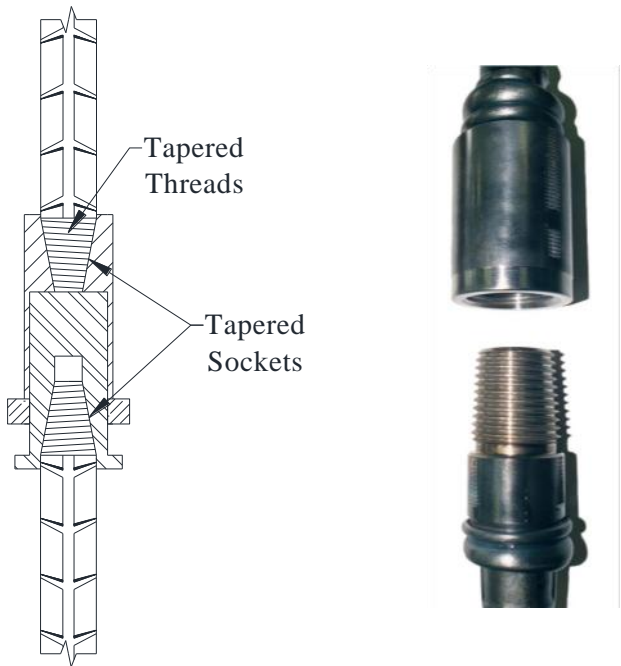
(b) Representative photo

Figure 2-4 Upset headed coupler



(a) Coupler details (b) Deformation of cut bar end prior to threading (c) Representative Photo (shown without position ring)

Figure 2-5 Straight threaded coupler



(a) Coupler details (b) Representative photo

Figure 2-6 Tapered threaded coupler



(a) Fracture at the first screw

(b) Bar pull-out

Figure 2-7 Failure of shear screw splices other than bar rupture



(a) Bar pull-out

(b) Sleeve rupture

Figure 2-8 Failure of grouted sleeve splices other than bar rupture



Figure 2-9 Failure of upset headed splices other than bar rupture



(a) Stripping of the threads (b) Fracture at the threads
Figure 2-10 Failure of tapered thread splices other than bar rupture

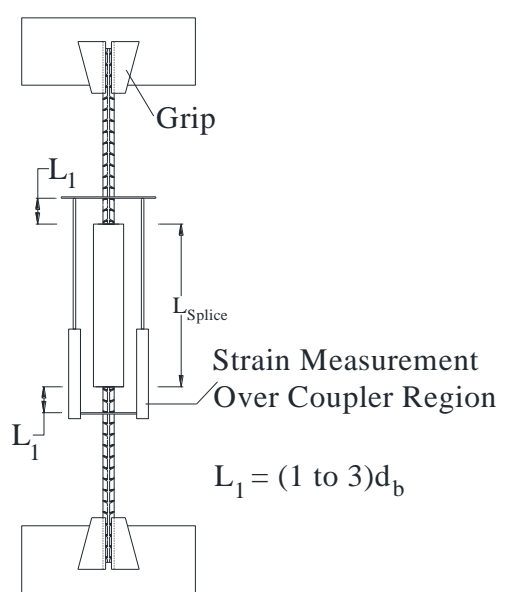


Figure 2-11 Strain measurement region defined by ASTM A1034

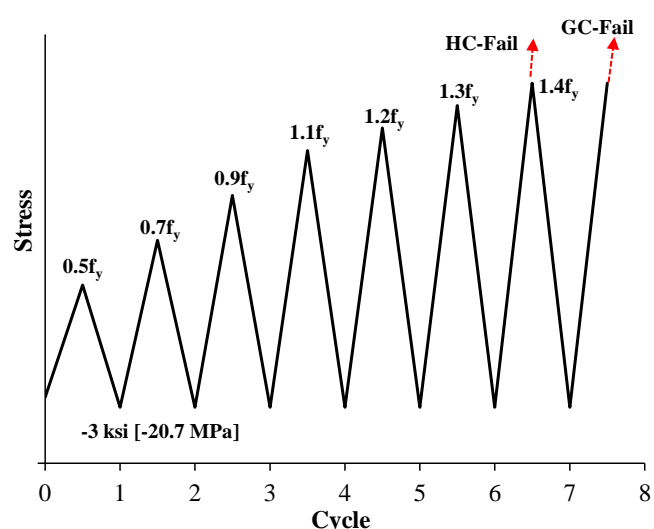


Figure 2-12 Cyclic loading protocol



Figure 2-13 Support frame for construction of grouted coupler specimens



Figure 2-14 Grouted coupler test specimens ready for grouting



Figure 2-15 Grouted coupler test specimens after grouting and bar insertion

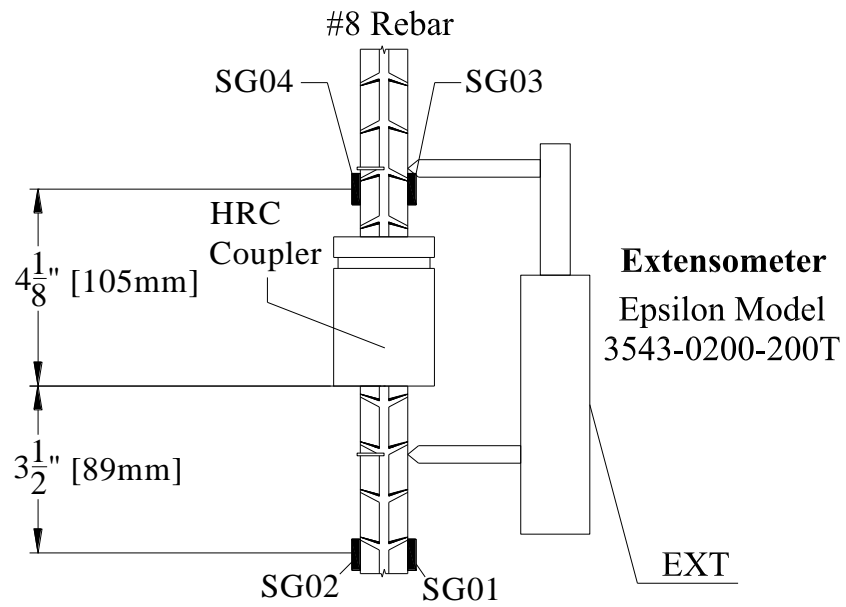


Figure 2-16 Instrumentation plan for HC couplers (Static and High Rate Tests)



Figure 2-17 HC tensile test specimen set-up

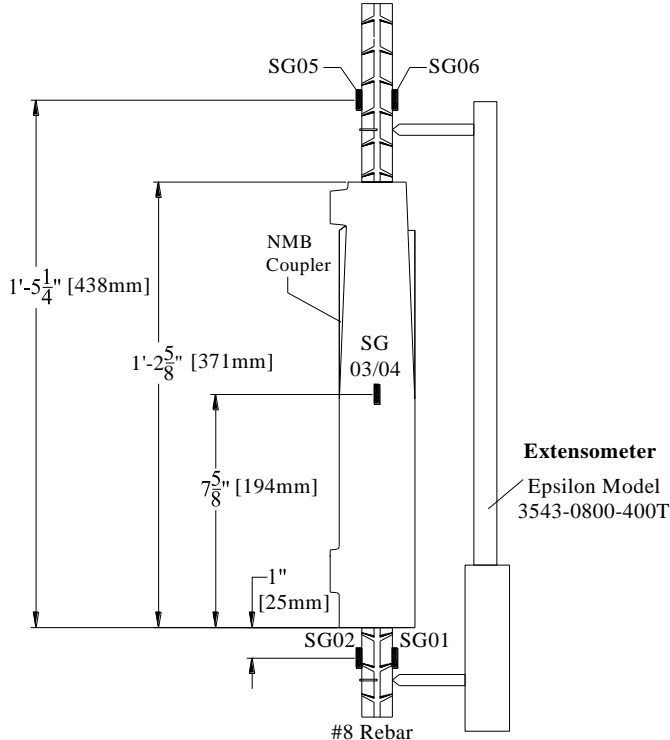


Figure 2-18 Instrumentation plan for GC couplers (Static and High Rate Tests)



Figure 2-19 GC tensile test specimen set-up

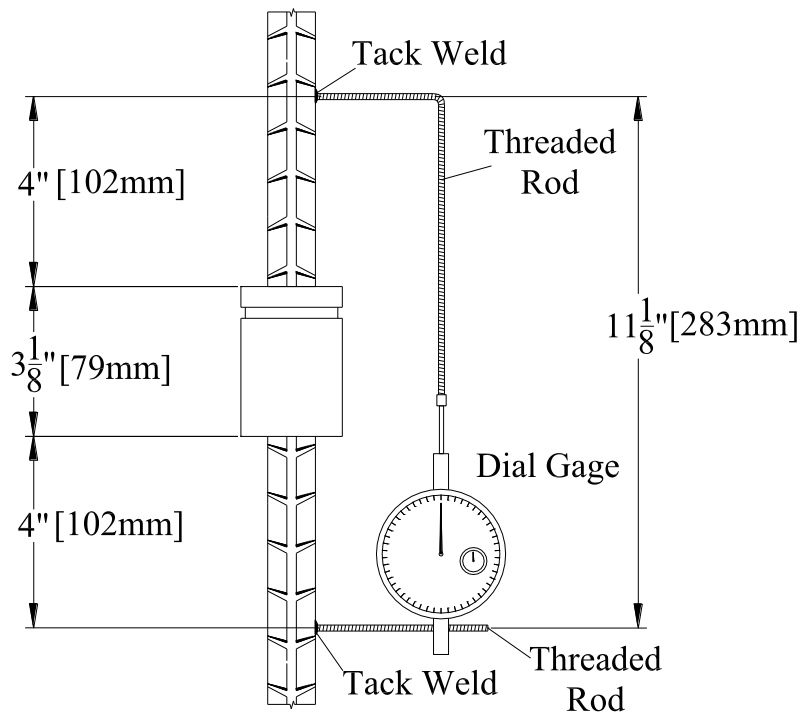


Figure 2-20 Instrumentation for HC slip test



Figure 2-21 HC slip test set-up

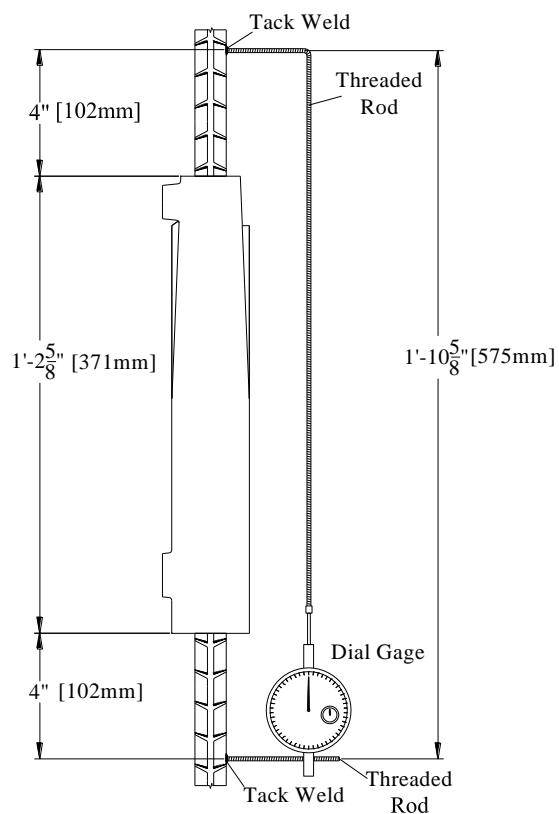


Figure 2-22 Instrumentation for GC slip test



Figure 2-23 GC slip test set-up

Chapter 3 Figures

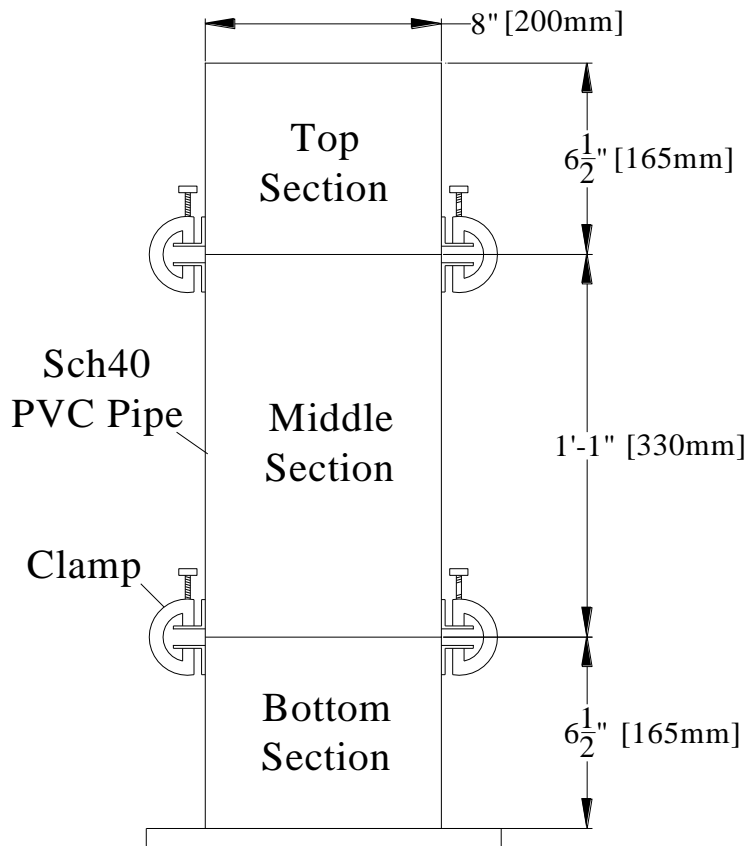


Figure 3-1 Static segregation column

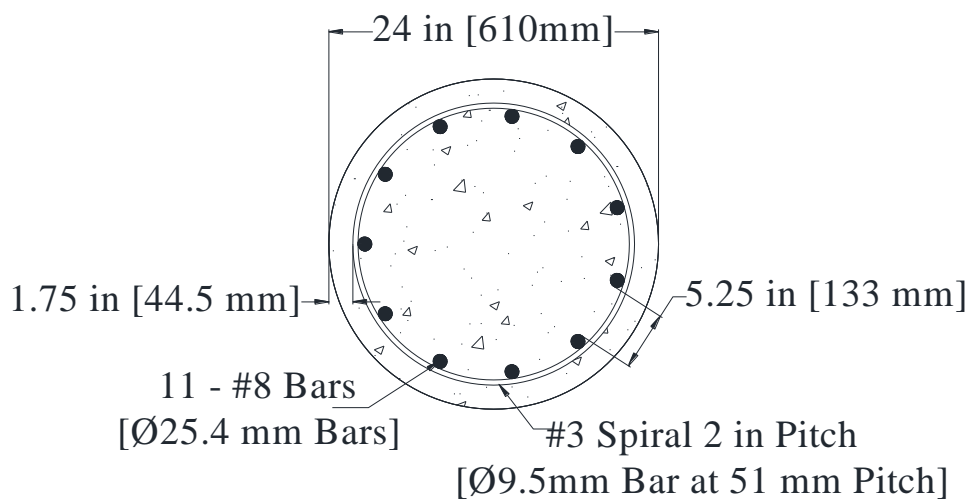


Figure 3-2 Benchmark column cross-section details

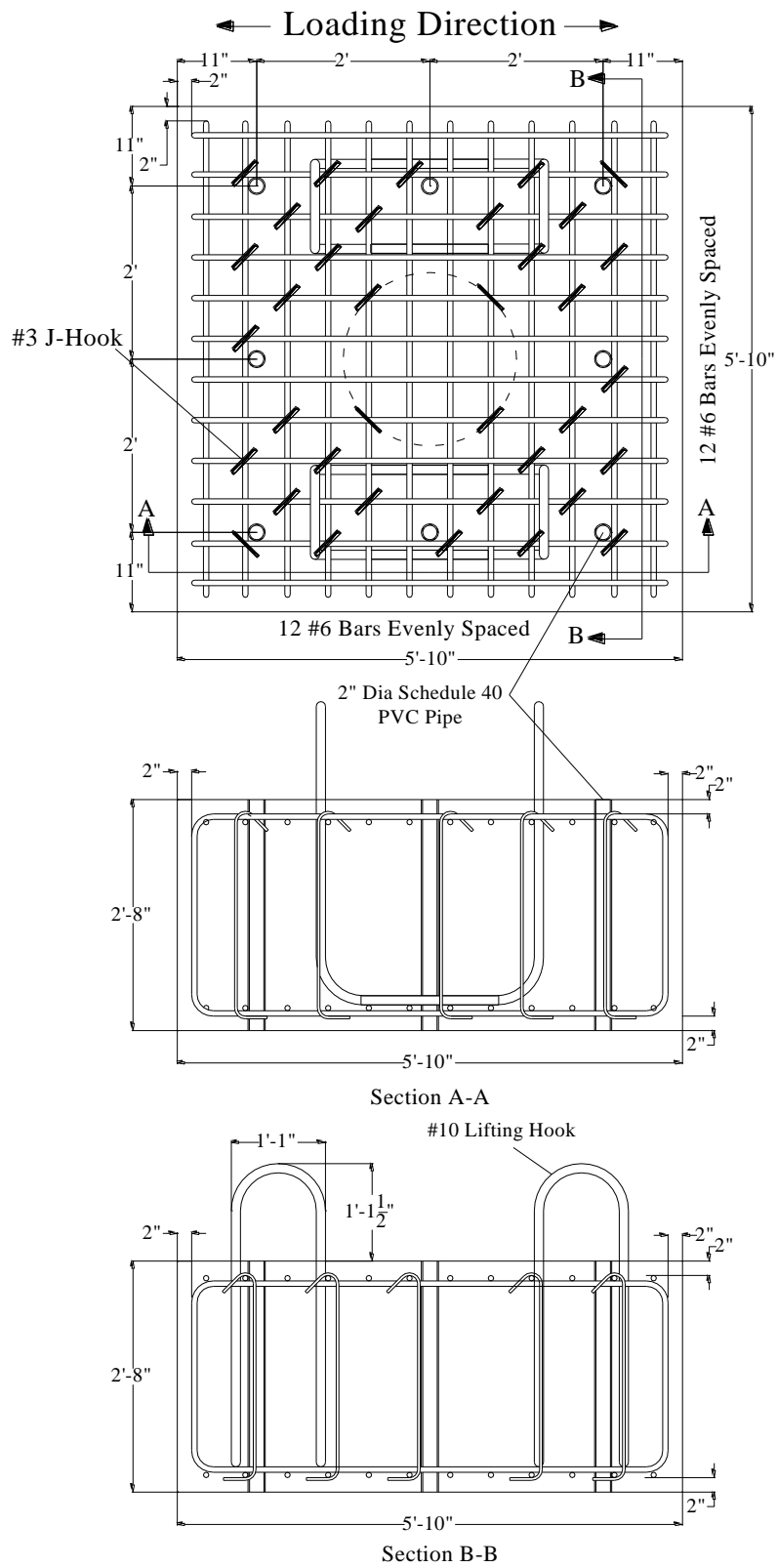


Figure 3-3 Footing dimensions and reinforcement details

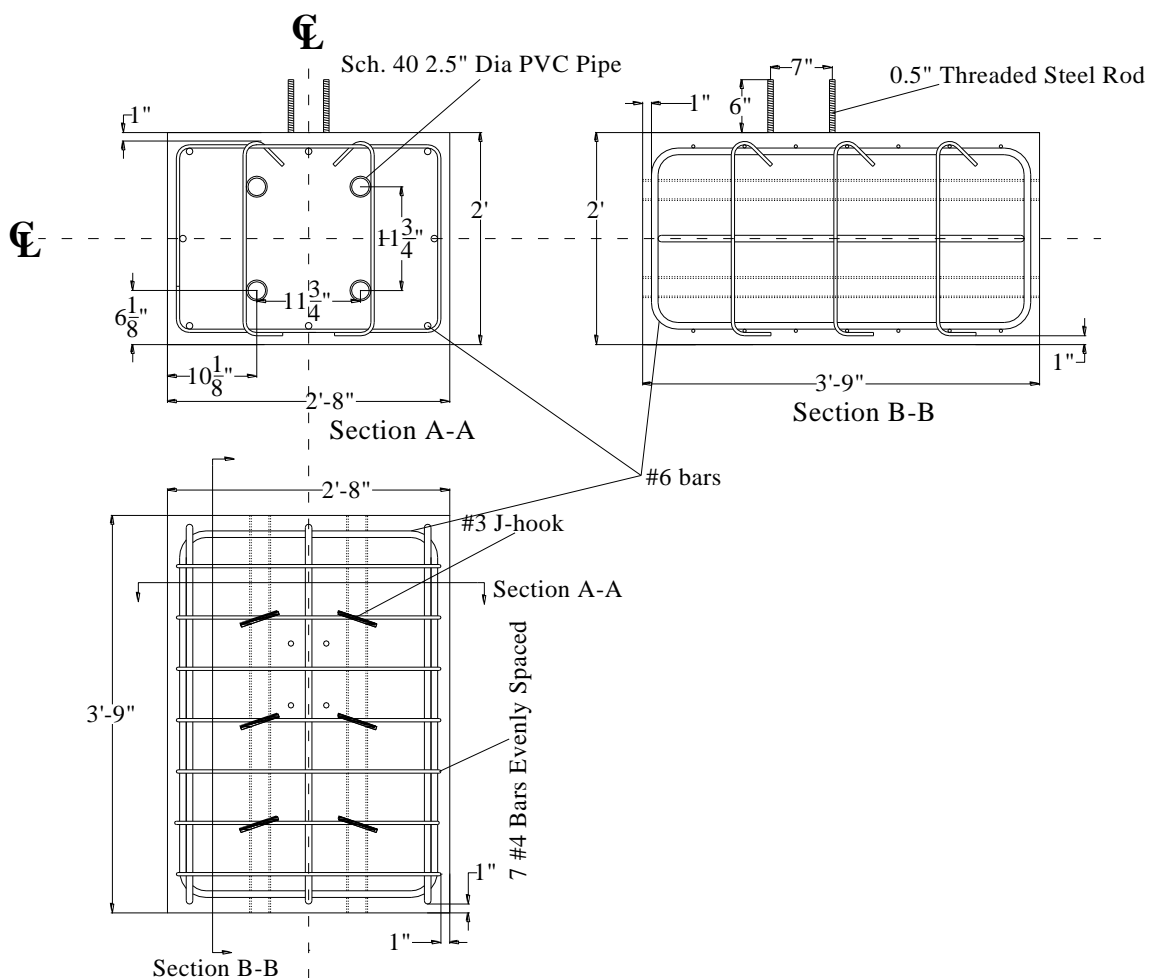


Figure 3-4 Loading head dimensions and reinforcement details

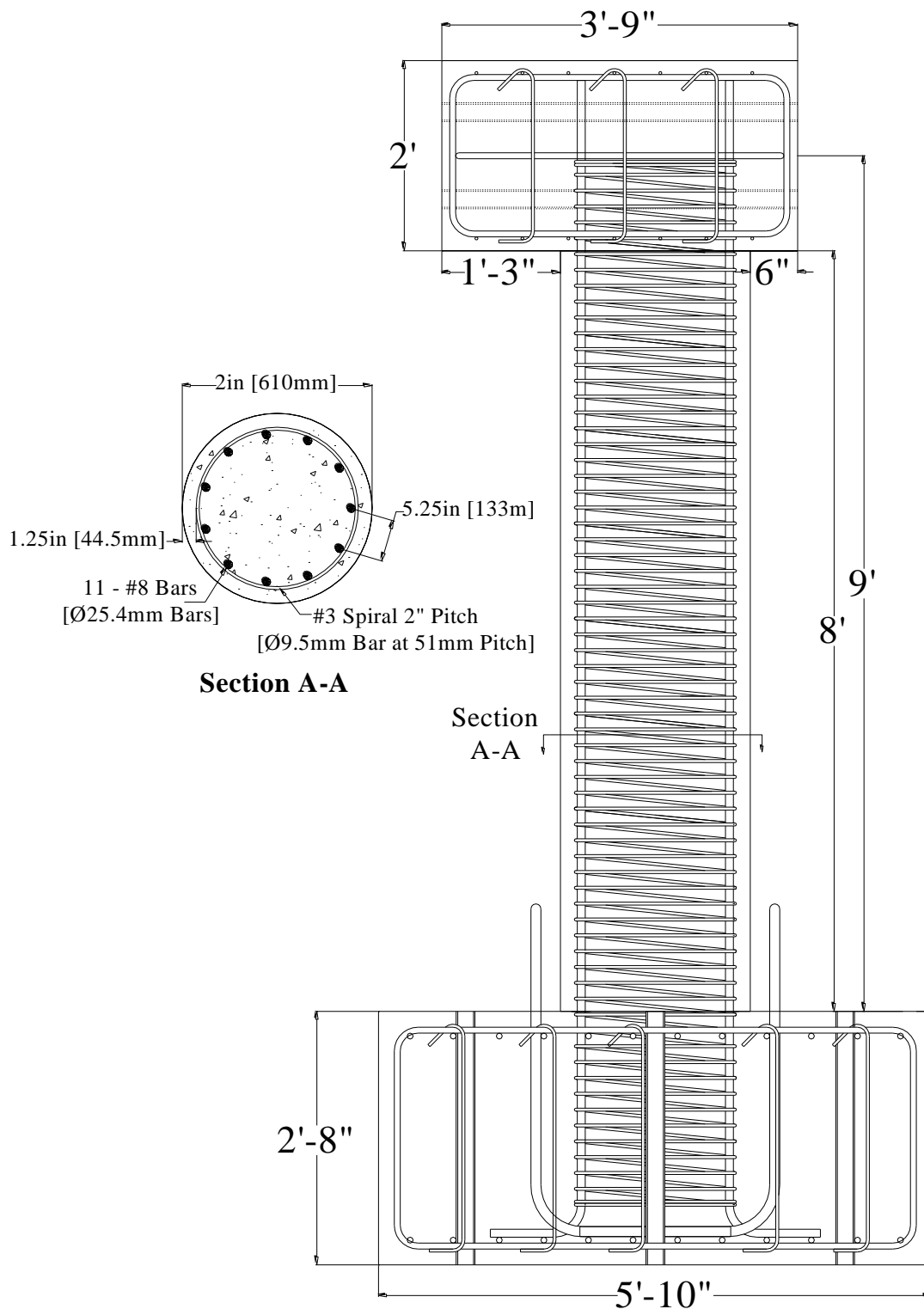


Figure 3-5 CIP full column model details



Figure 3-6 Bottom steel in footing form

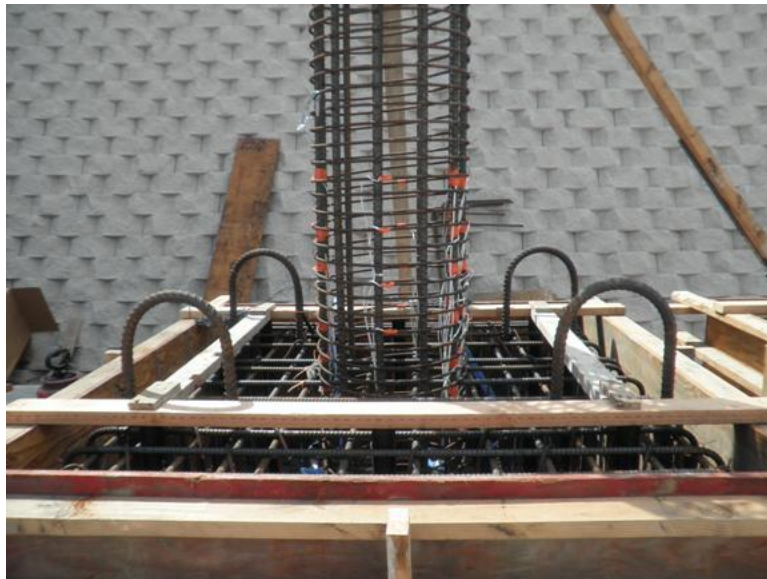


Figure 3-7 CIP footing ready for casting concrete



Figure 3-8 Form-work for column ready for head construction



Figure 3-9 CIP column head formwork and reinforcement



Figure 3-10 Completed CIP column model

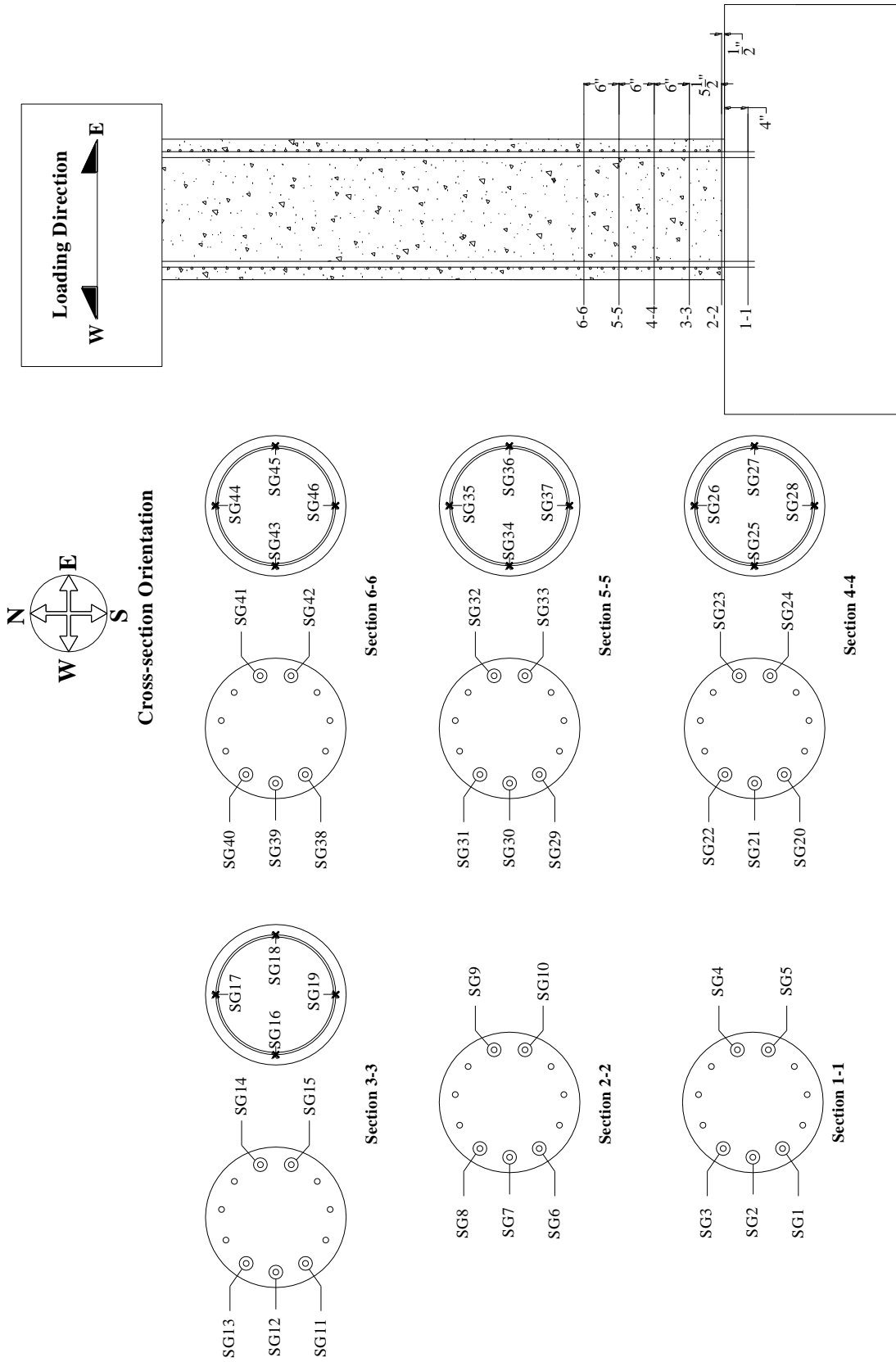


Figure 3-11 CIP strain gage schematic



Figure 3-12 Instrumented cast-in-place column cage

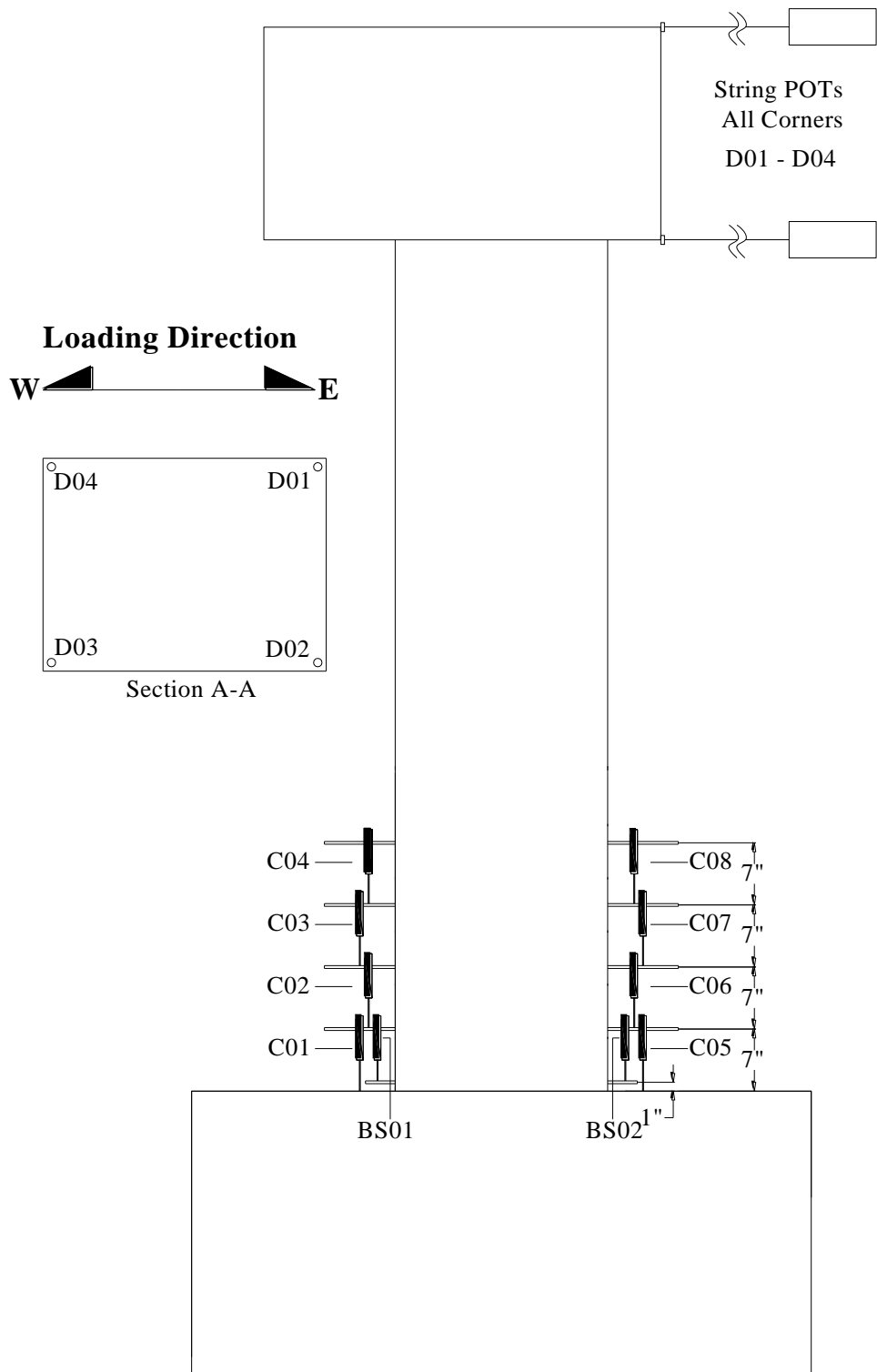


Figure 3-13 CIP displacement and curvature instrumentation

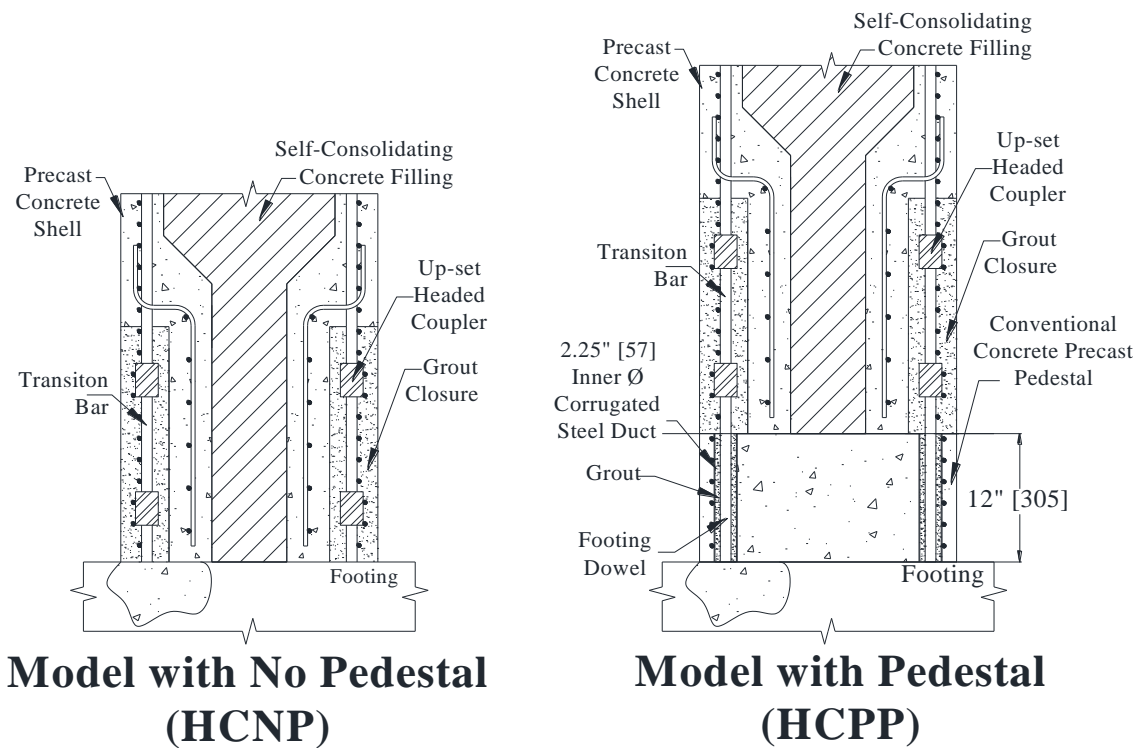


Figure 3-14 General details of headed coupler connection

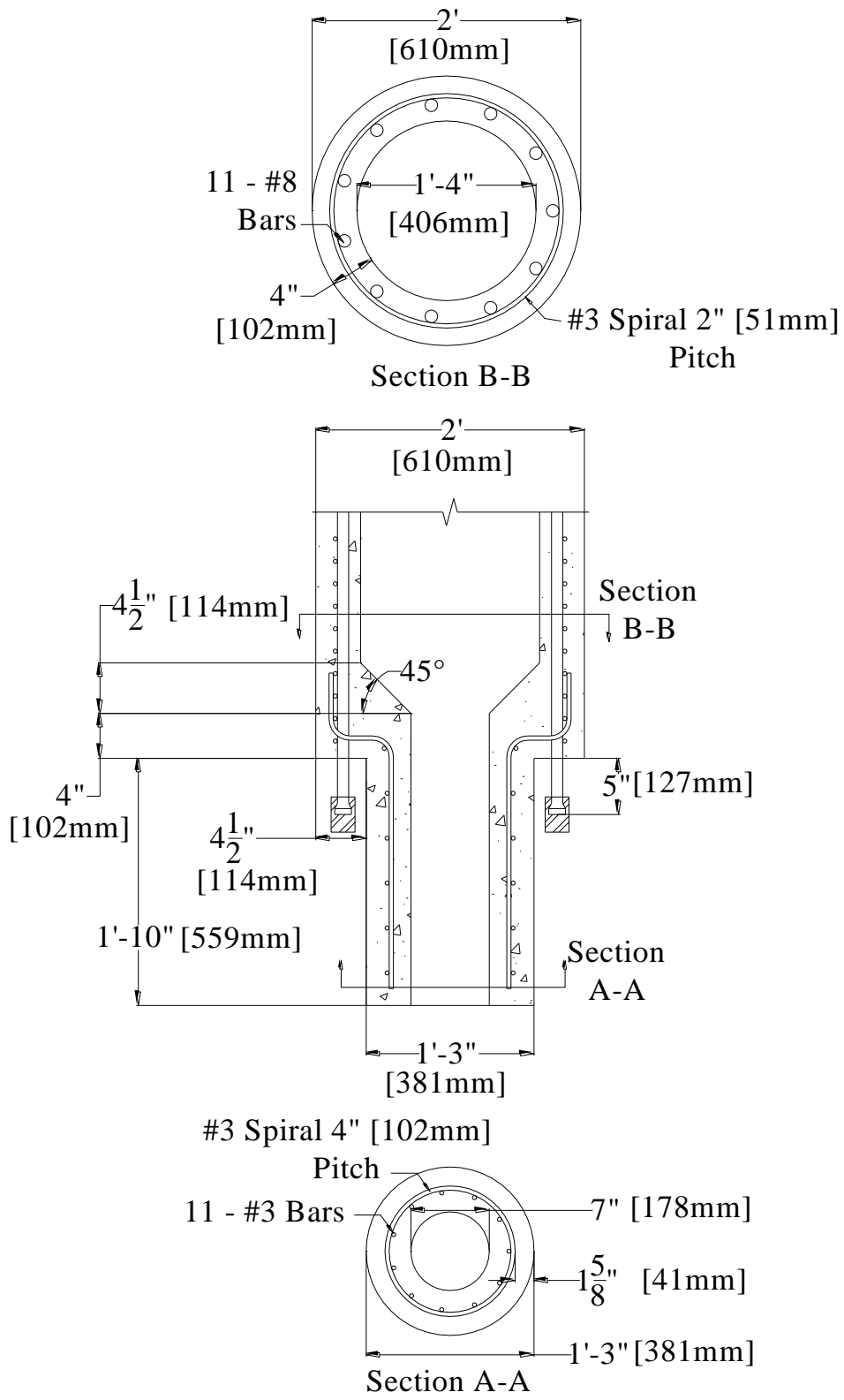


Figure 3-15 Column shell connection details for HC models

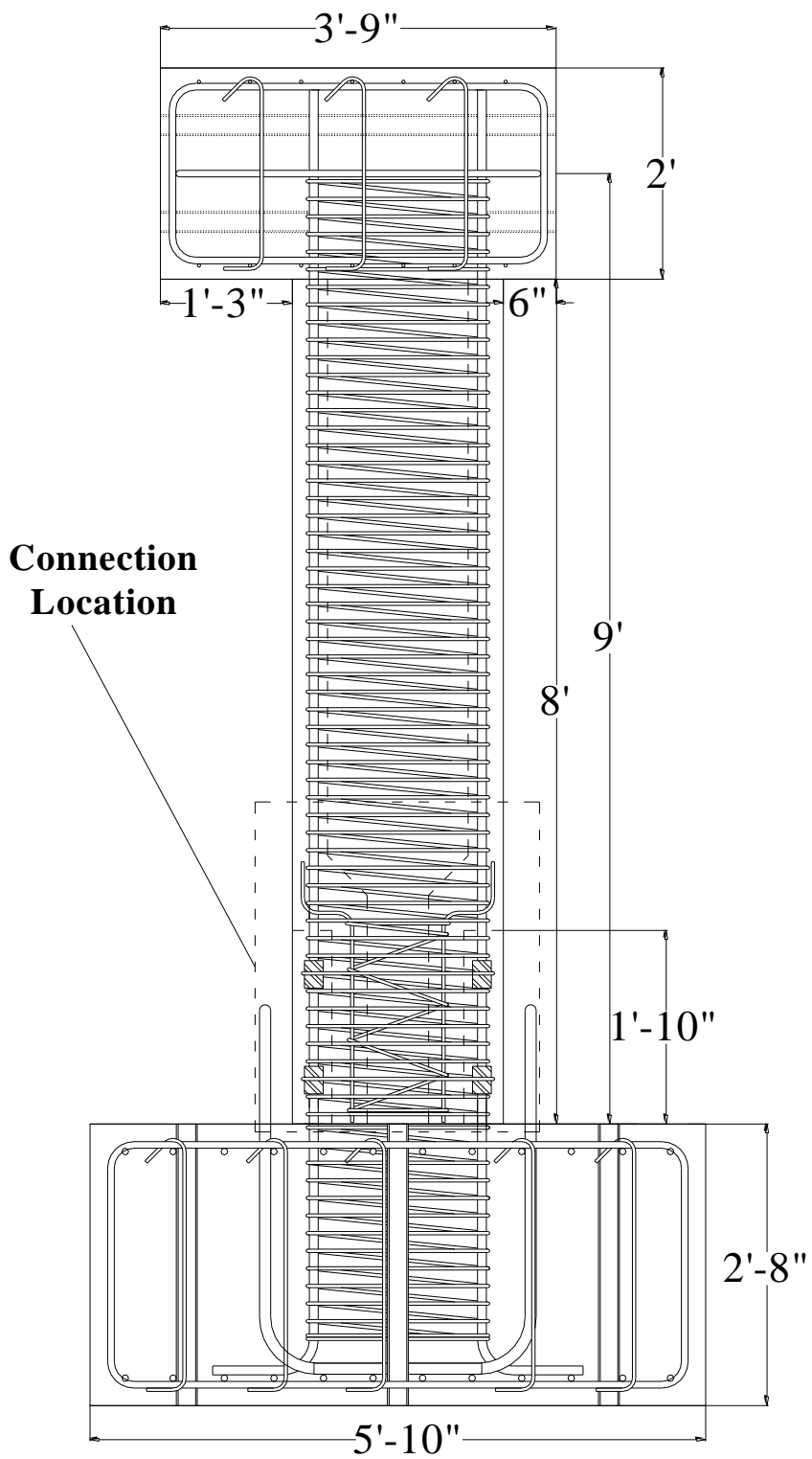


Figure 3-16 HCNP full column reinforcement drawing

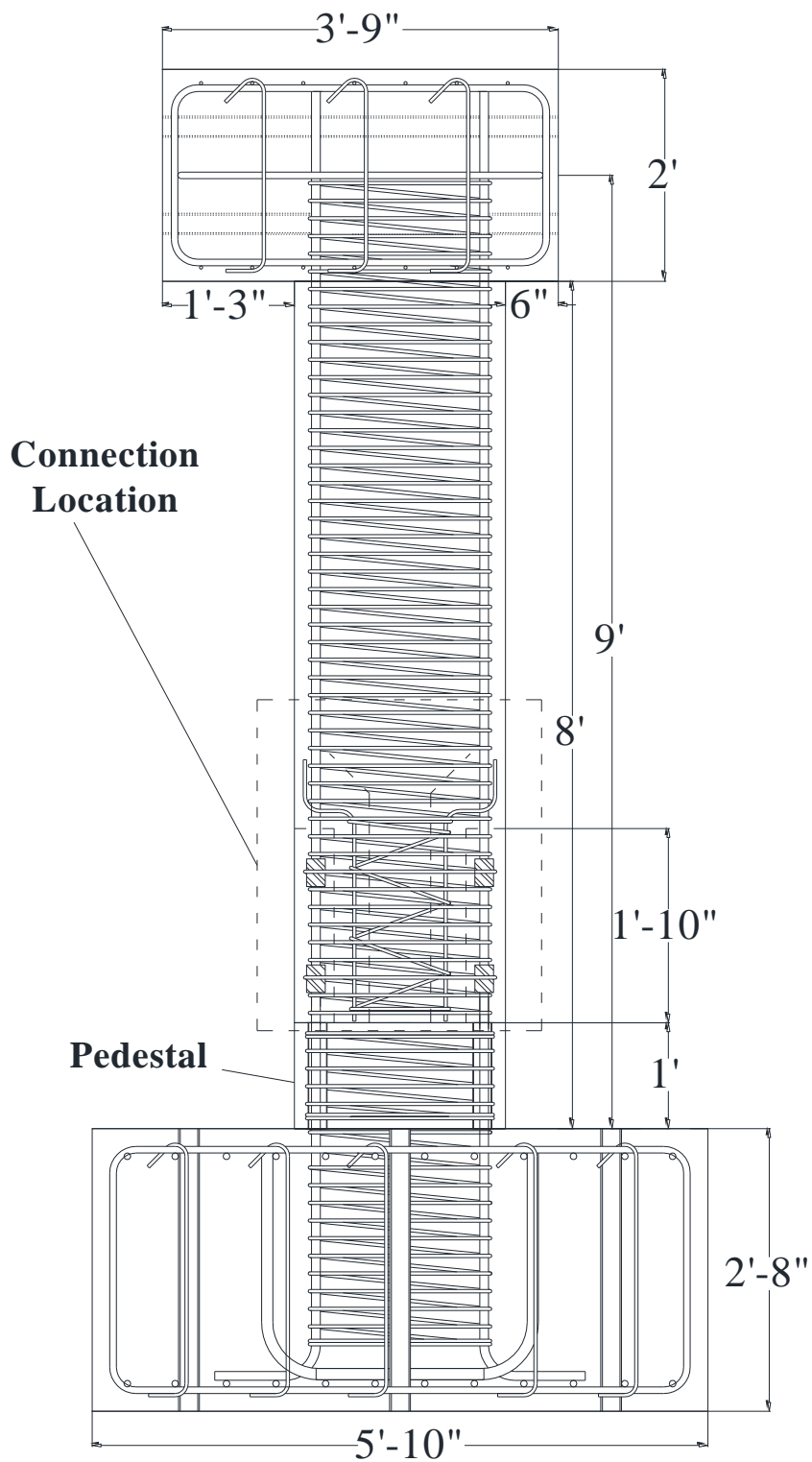


Figure 3-17 HCPP full column reinforcement drawing

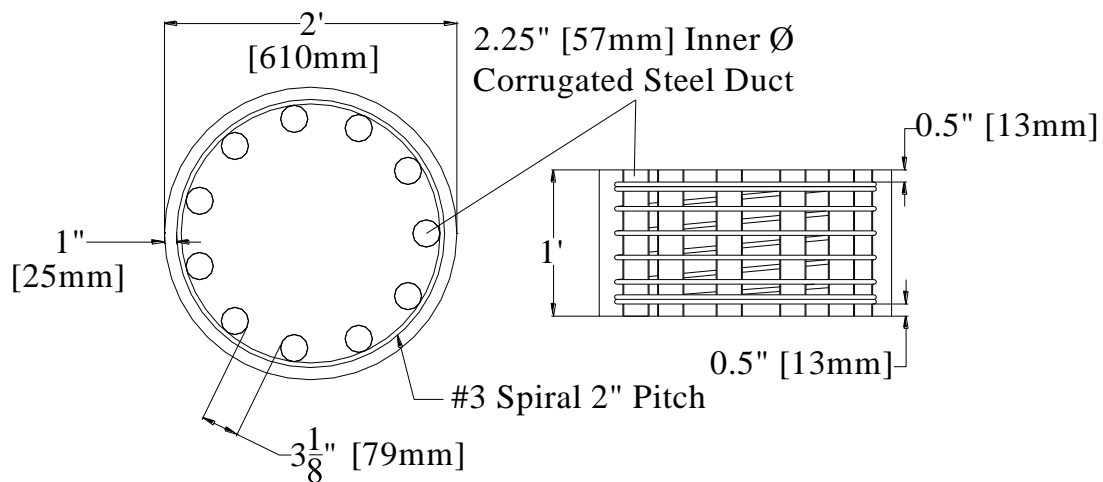


Figure 3-18 HCPP pedestal reinforcement details

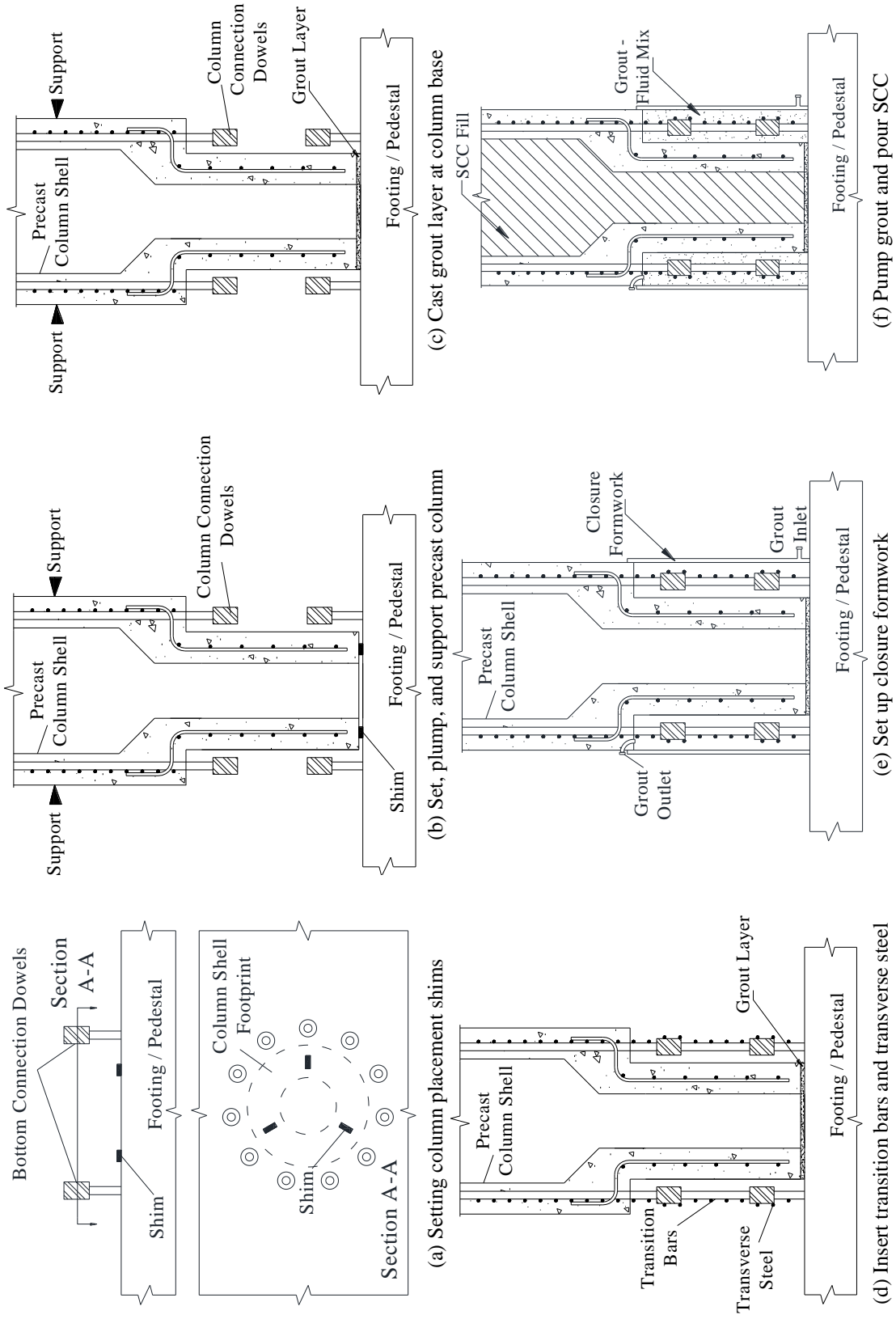


Figure 3-19 HC connection construction procedure



Figure 3-20 Longitudinal reinforcing bar template



Figure 3-21 Placement of HCNP footing column cage



Figure 3-22 HCNP footing reinforcement and form-work prior to casting concrete



Figure 3-23 Footing after casting showing HRC headed dowels



Figure 3-24 Prepared form-work for HC column base segment



Figure 3-25 Construction of column cage base segment



Figure 3-26 Column cages and internal PVC form



Figure 3-27 HCNP column sell ready for casting concrete



Figure 3-28 HCNP column shell after removal of formwork



Figure 3-29 Transition bar with male threaded ends



Figure 3-30 Initial setting of HCNP column shell



Figure 3-31 Steel spacers for HRC couplers



Figure 3-32 Spacer inserted between upper heads



Figure 3-33 Torqueing HRC couplers



Figure 3-34 Connection region after tightening of couplers and tying spiral



Figure 3-35 Connection region ready for closure grouting



Figure 3-36 Grout ready for pumping



(a) Sample before testing



(b) Sample after testing

Figure 3-37 Flow table test for grout (ASTM C1437)



Figure 3-38 Casting of grout cubes



Figure 3-39 Void left from bleed material



Figure 3-40 Void region prepared for epoxy injection



Figure 3-41 Final slump-flow test of SCC



Figure 3-42 Filling SCC segregation column



Figure 3-43 Collection of segregation column top and bottom contents



Figure 3-44 Sieving segregation column contents



Figure 3-45 Segregation column contents after sieving



Figure 3-46 Cast SCC in column core



Figure 3-47 HCPP footing reinforcement and form-work



Figure 3-48 HCPP footing dowels and placement of corrugated ducts for pedestal



Figure 3-49 Pedestal reinforcement and form-work



Figure 3-50 HCPP pedestal after casting concrete



Figure 3-51 Voids found in HCPP coupling region



Figure 3-52 Repair form-work and casting of new concrete



Figure 3-53 Completed repair

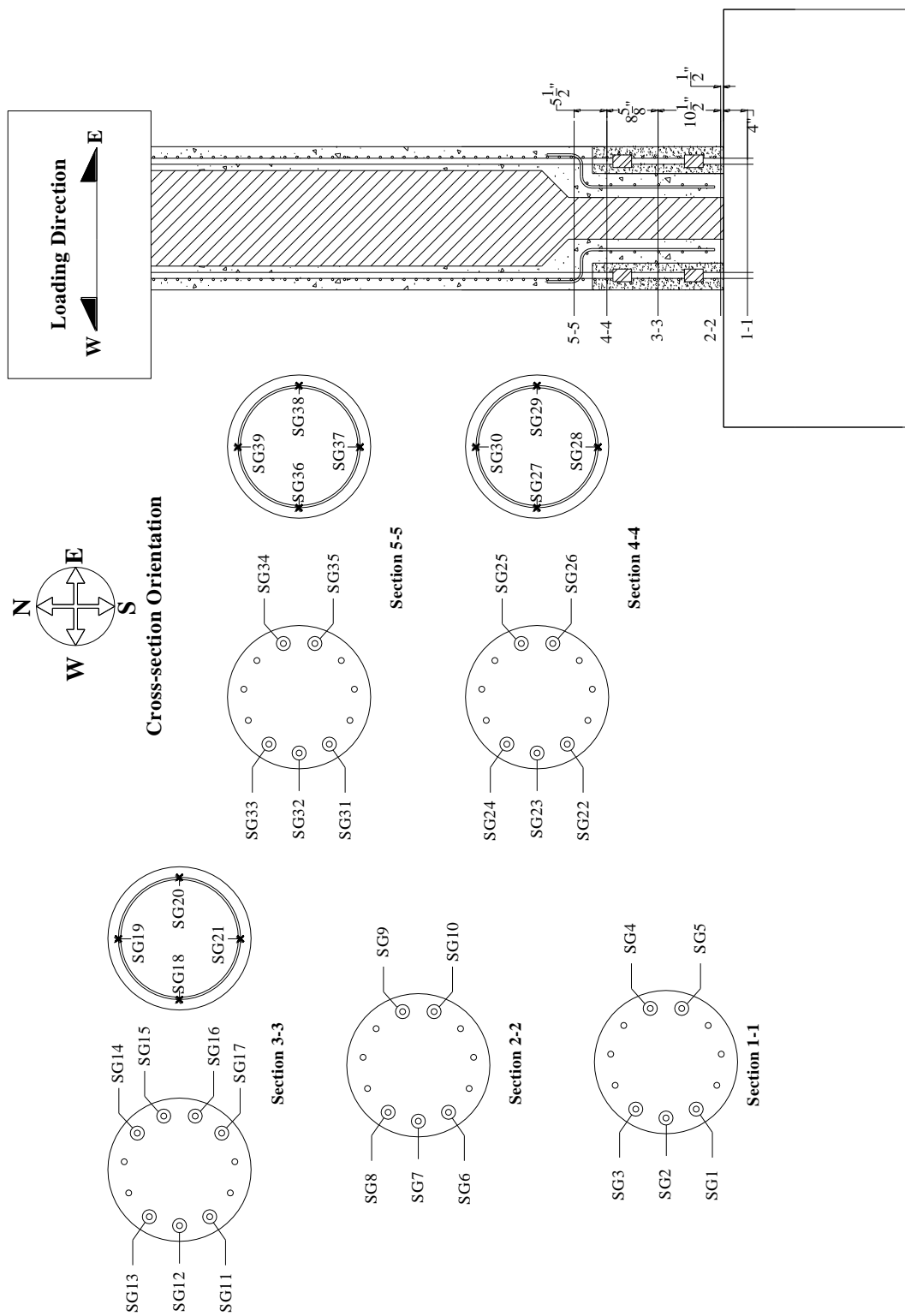


Figure 3-54 HCNP strain gage instrumentation plan



Figure 3-55 HCNP instrumented footing dowel cage

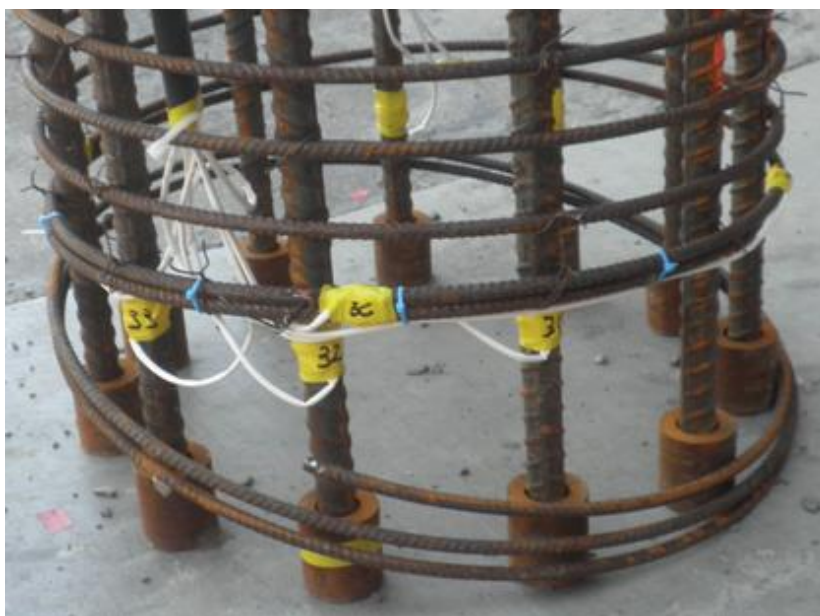


Figure 3-56 HCNP instrumented column cage



Figure 3-57 Instrumentation of closure region

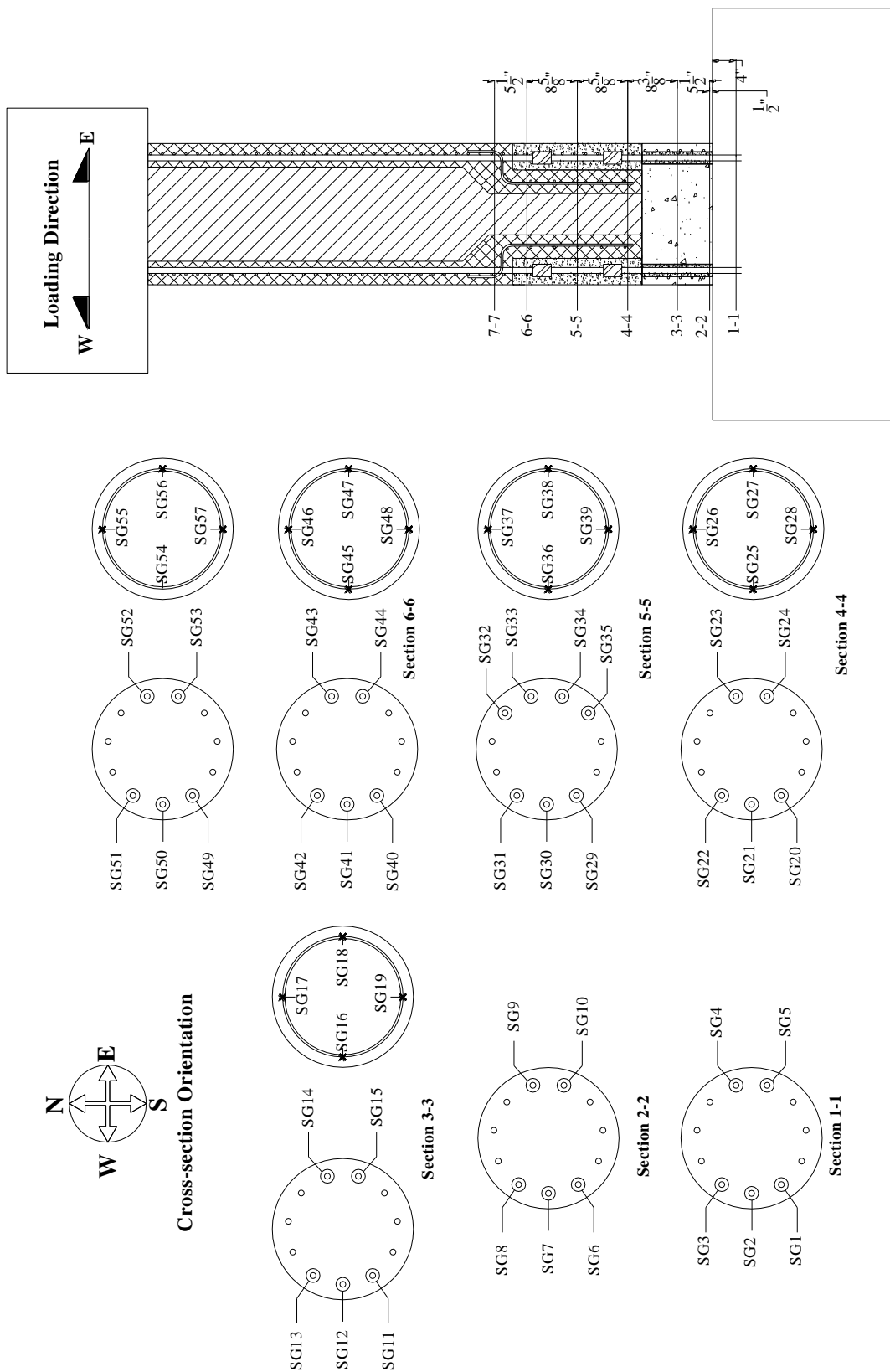


Figure 3-59 HCPP strain gage instrumentation plan

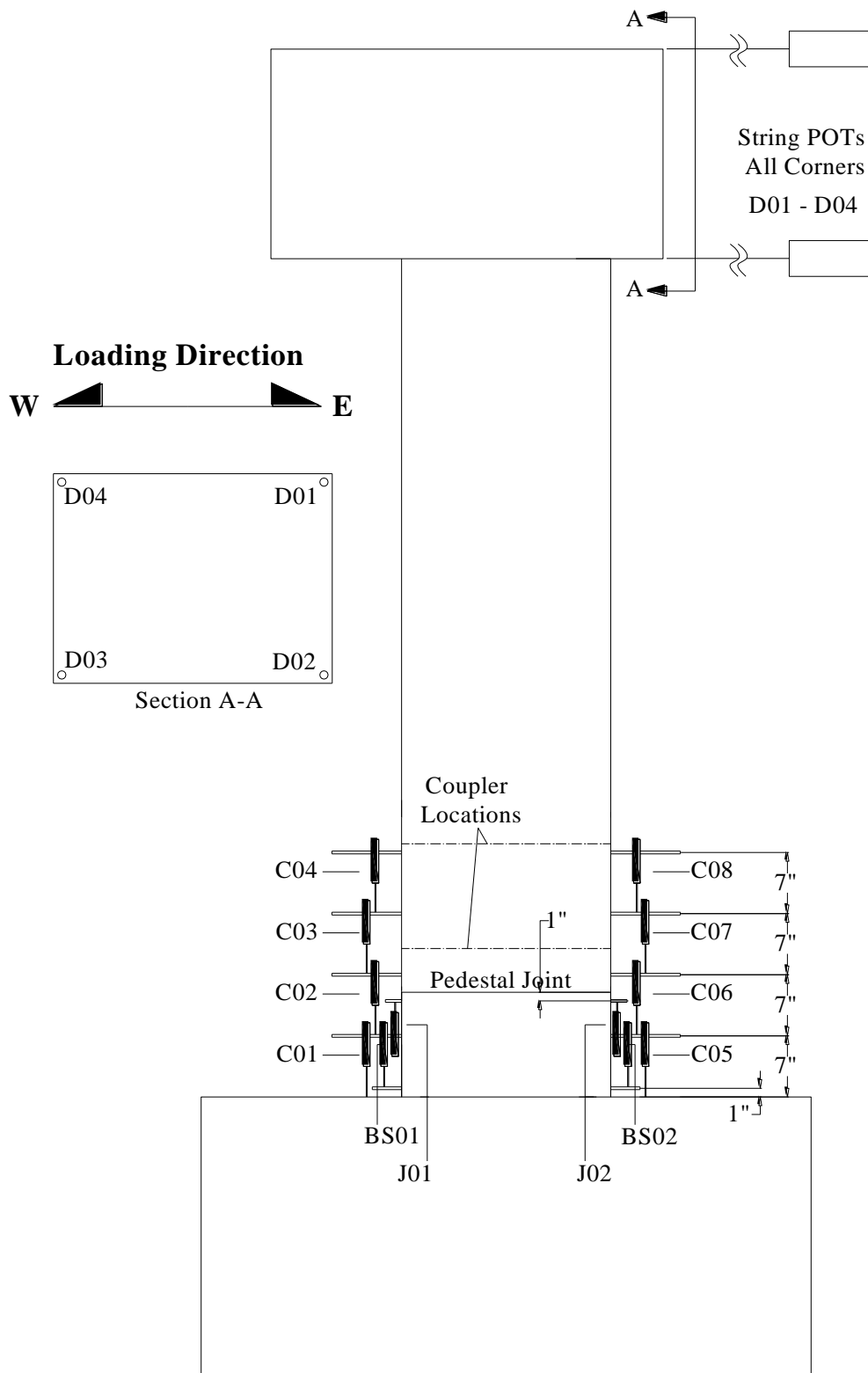


Figure 3-60 HCPP displacement and curvature gage instrumentation plan

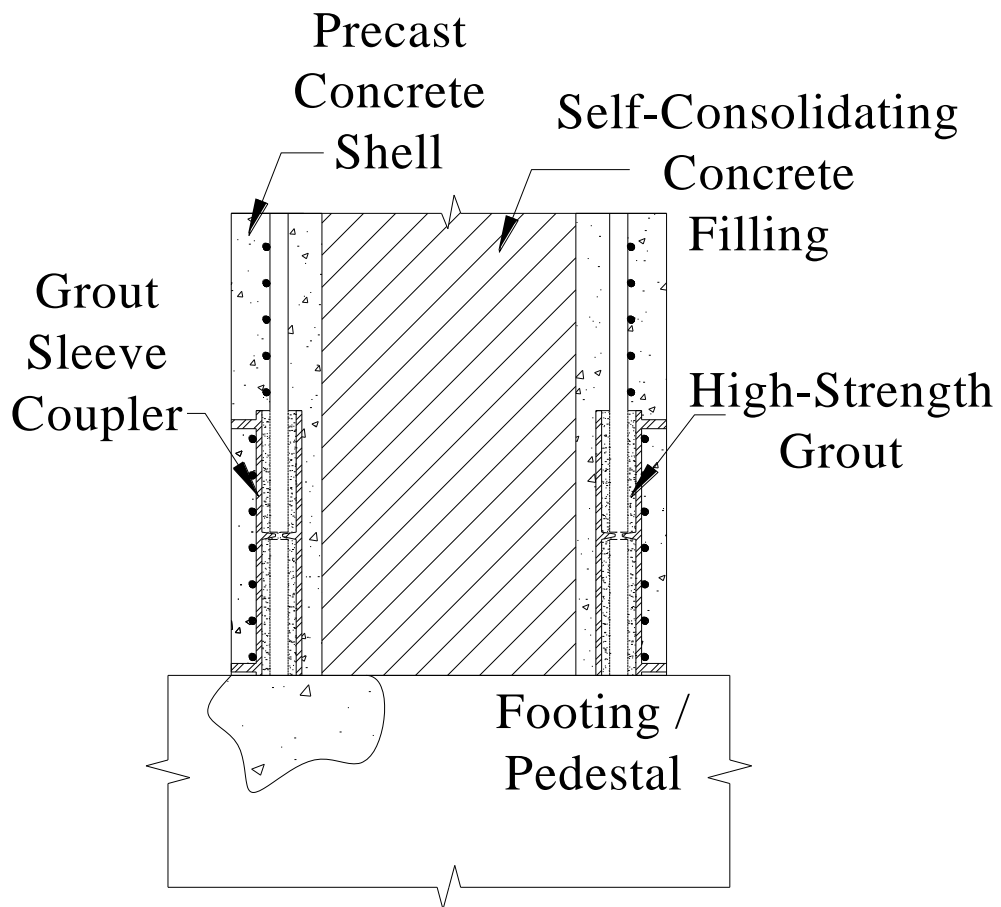


Figure 3-61 General GC connection detail

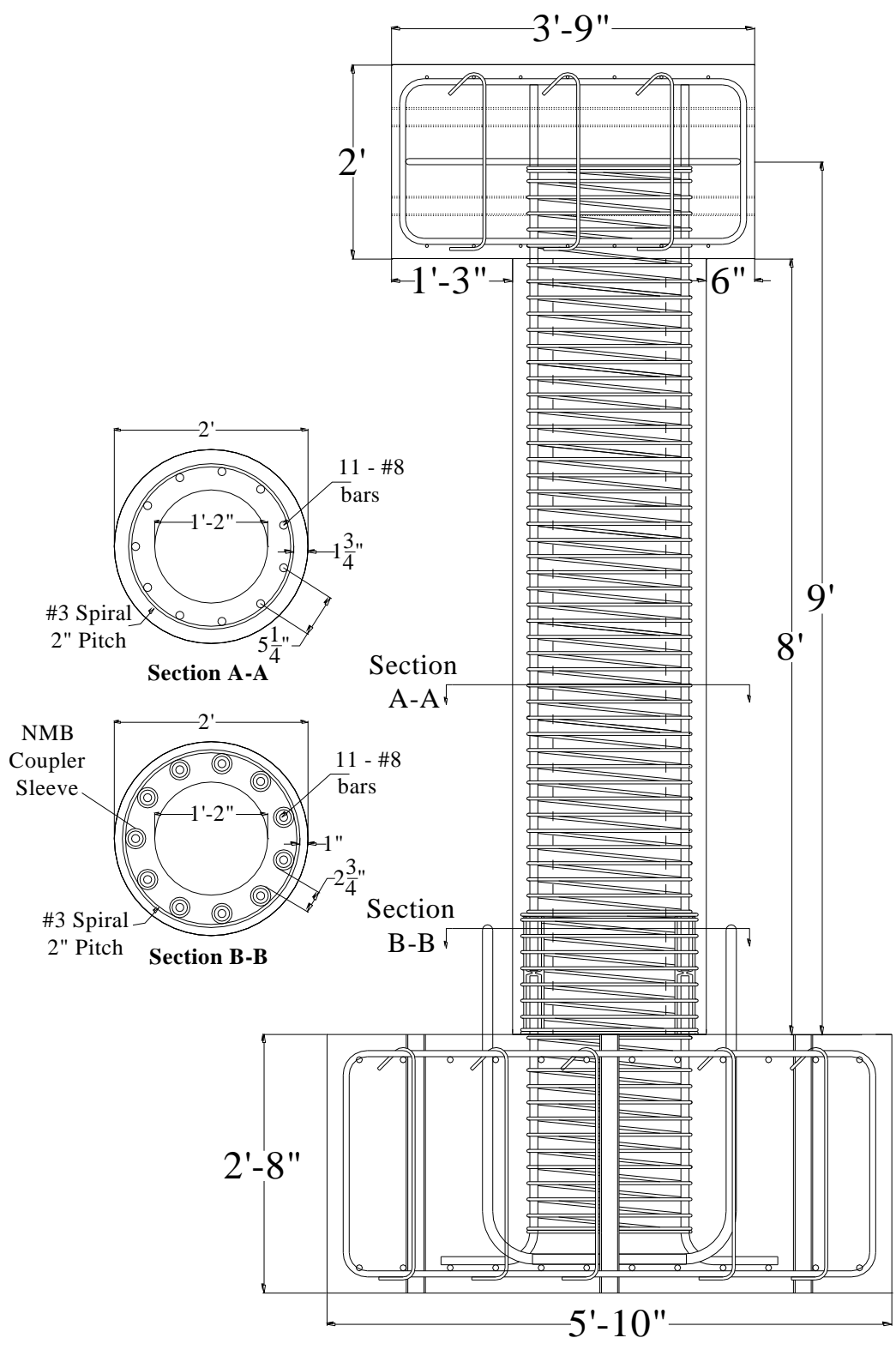


Figure 3-62 GCNP column model geometry and reinforcement details

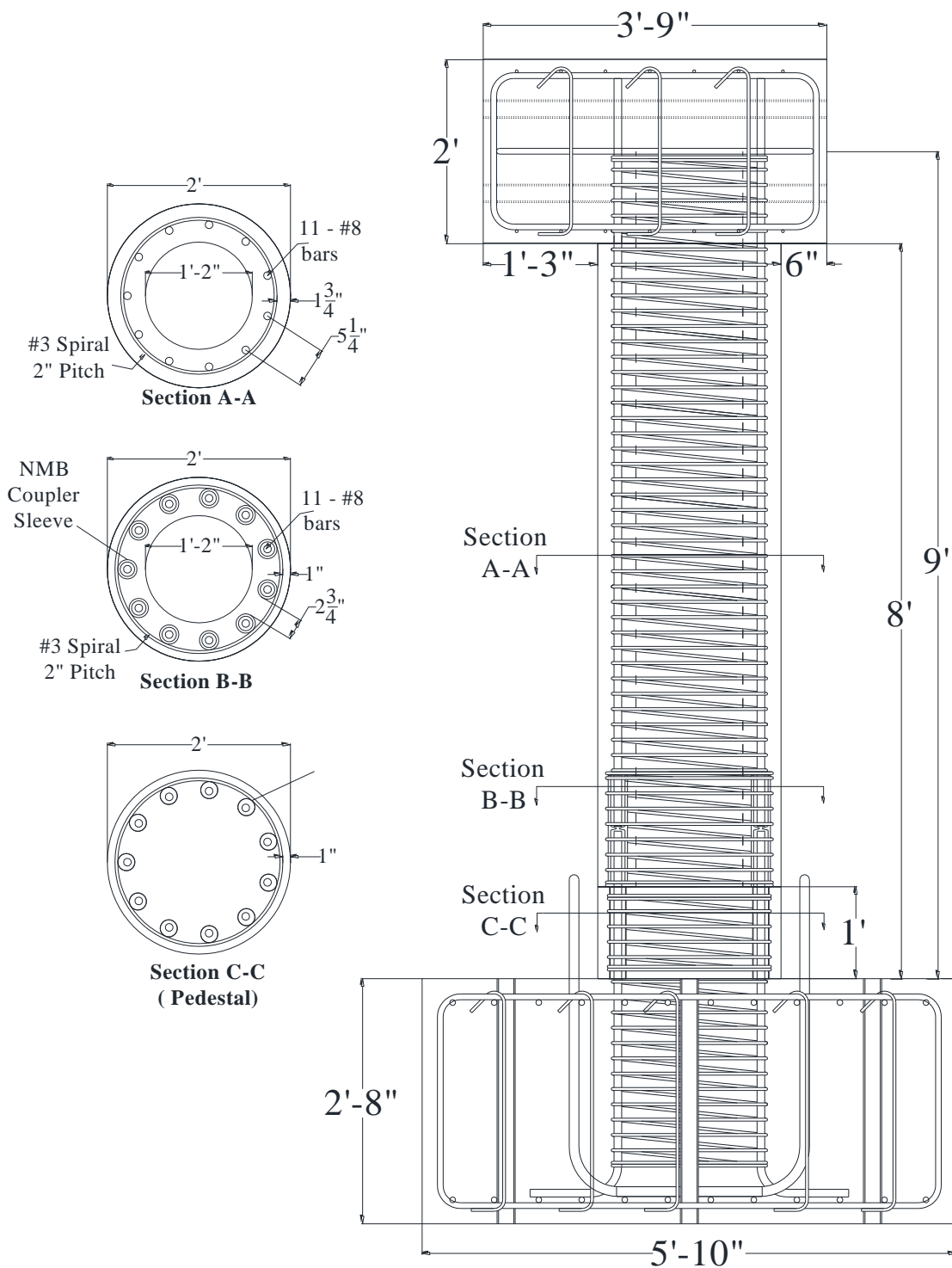


Figure 3-63 GCPP column model geometry and reinforcement details

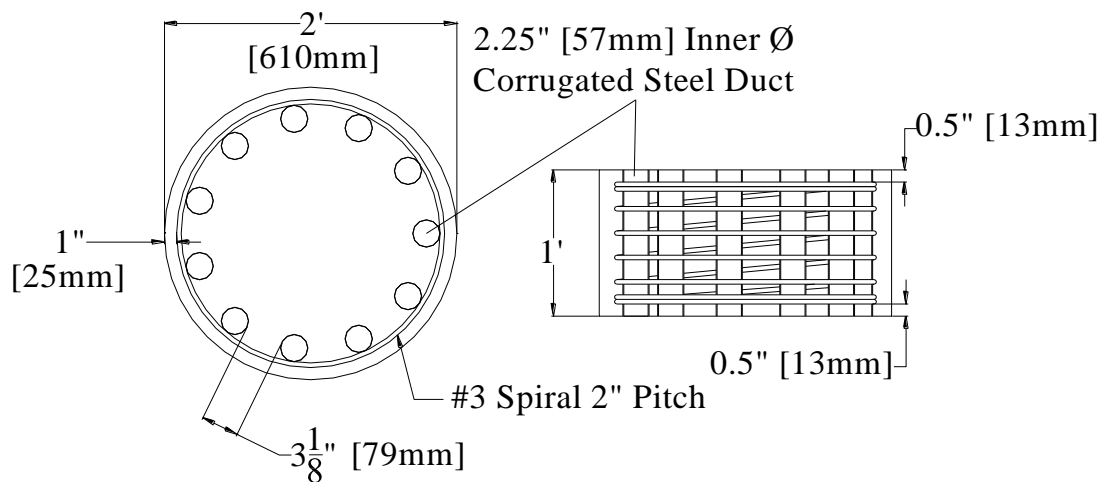


Figure 3-64 GCPP pedestal details

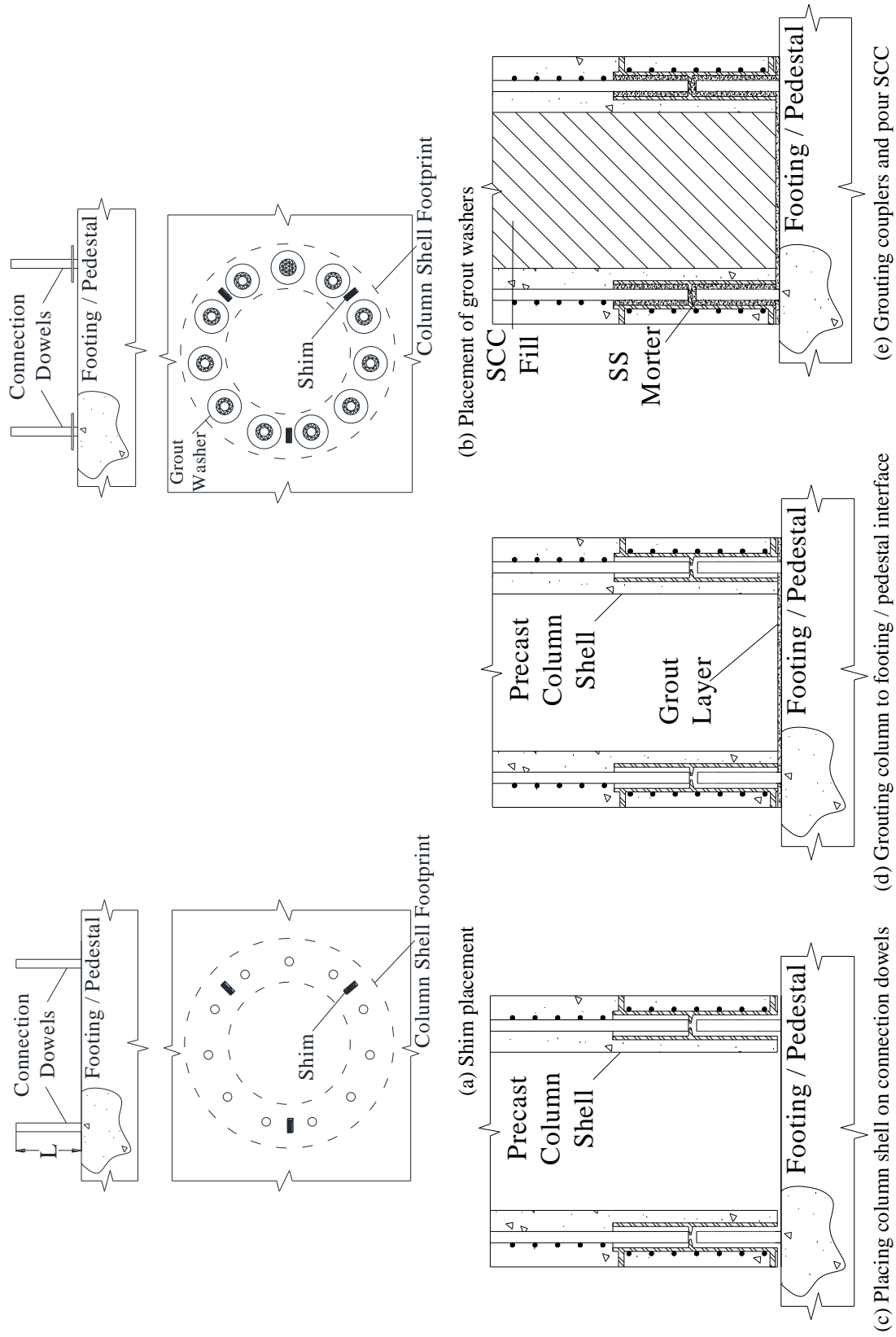


Figure 3-65 Construction sequence of GC column connection



Figure 3-66 GCNP footing dowel reinforcement cage



Figure 3-67 GCNP completed footing form and reinforcement



Figure 3-68 GCNP footing casting concrete



Figure 3-69 Measurement of GCNP footing dowel



Figure 3-70 GCNP footing after removal of formwork



Figure 3-71 Installation of NMB couplers on GCNP column cage



Figure 3-72 Tying spiral around GCNP coupler region



Figure 3-73 GCNP column shell platform with NMB Sleeve Setters

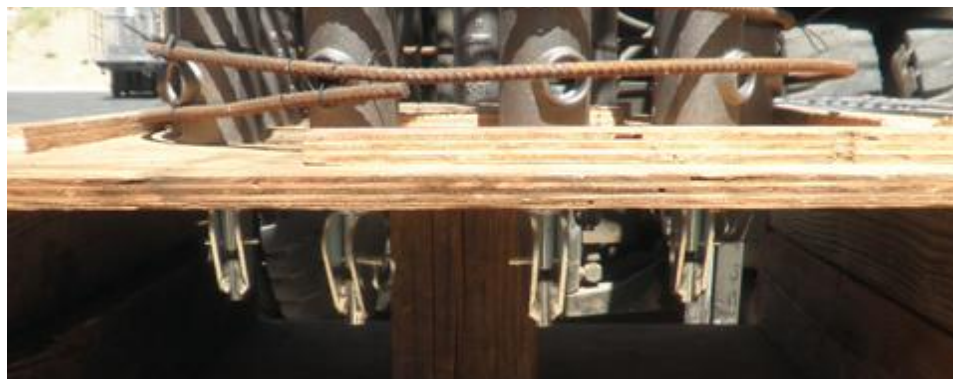


Figure 3-74 NMB Sleeve Setters



Figure 3-75 GCNP column cage on platform with PVC form in the center



Figure 3-76 Grout ports protruding through form



Figure 3-77 Complete GCNP column shell

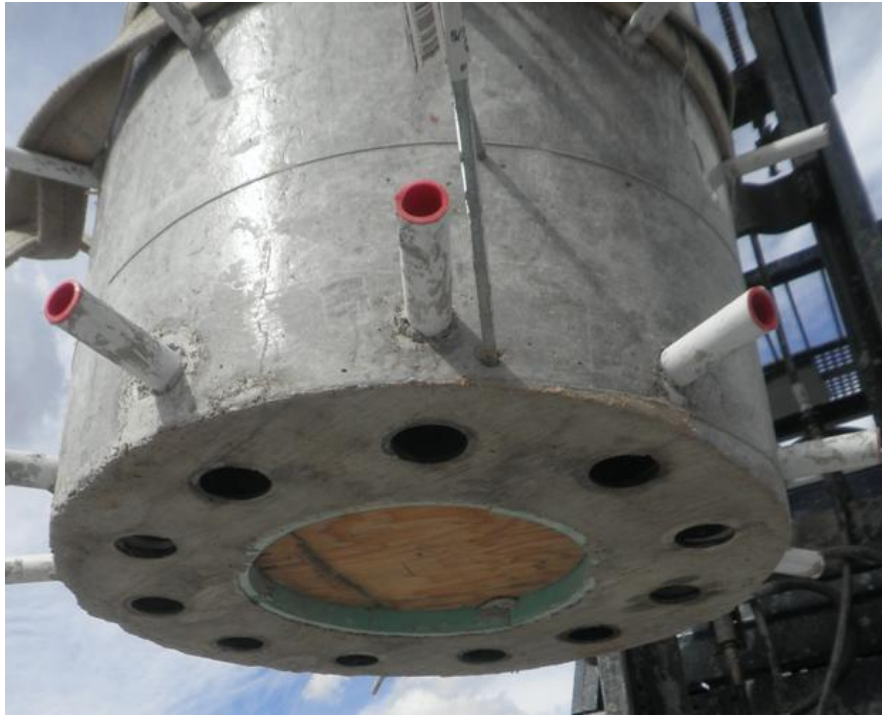


Figure 3-78 Grout sleeve ports below GCNP column shell



Figure 3-79 GCNP footing dowel bars after cleaning



Figure 3-80 GCNP column shell after placement on footing dowels



Figure 3-81 Steel shim between column shell and footing



Figure 3-82 Temporary formwork for grouting column shell-to-footing interface



Figure 3-83 Grout after placement



Figure 3-84 GCPP footing formwork and reinforcement



Figure 3-85 GCPP pedestal formwork and reinforcement



Figure 3-86 GCPP pedestal ducts after grouting and cleaning dowels



Figure 3-87 Temporary grout form and grout washers



Figure 3-88 Placement of the GCPP column shell

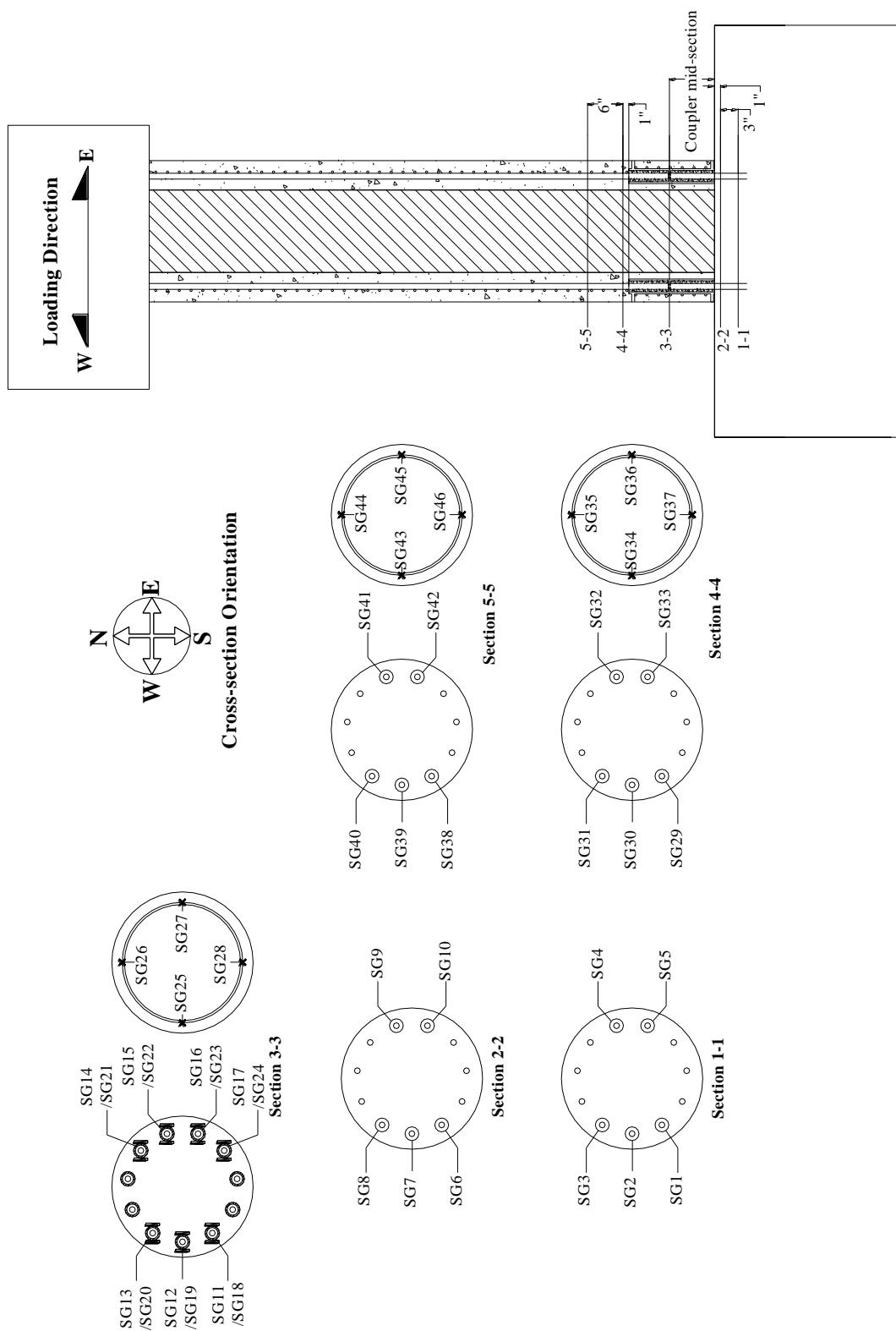


Figure 3-89 GCNP strain gage instrumentation plan



Figure 3-90 Wiring of GCNP footing cage



Figure 3-91 Strain gage installation on NMB couplers



Figure 3-92 Instrumented couplers



Figure 3-93 GCNP column cage instrumentation

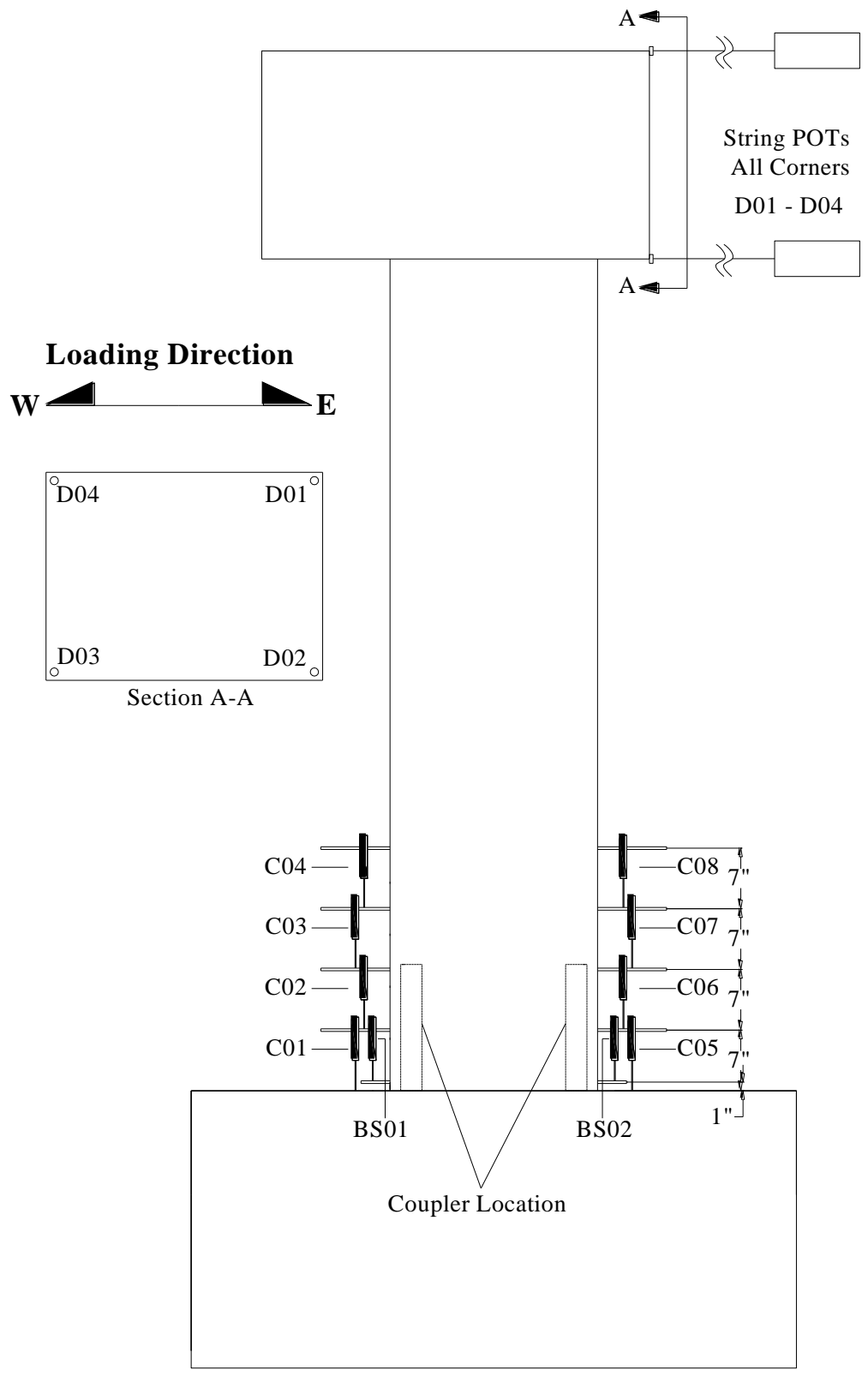


Figure 3-94 GCNP Displacement and curvature instrumentation

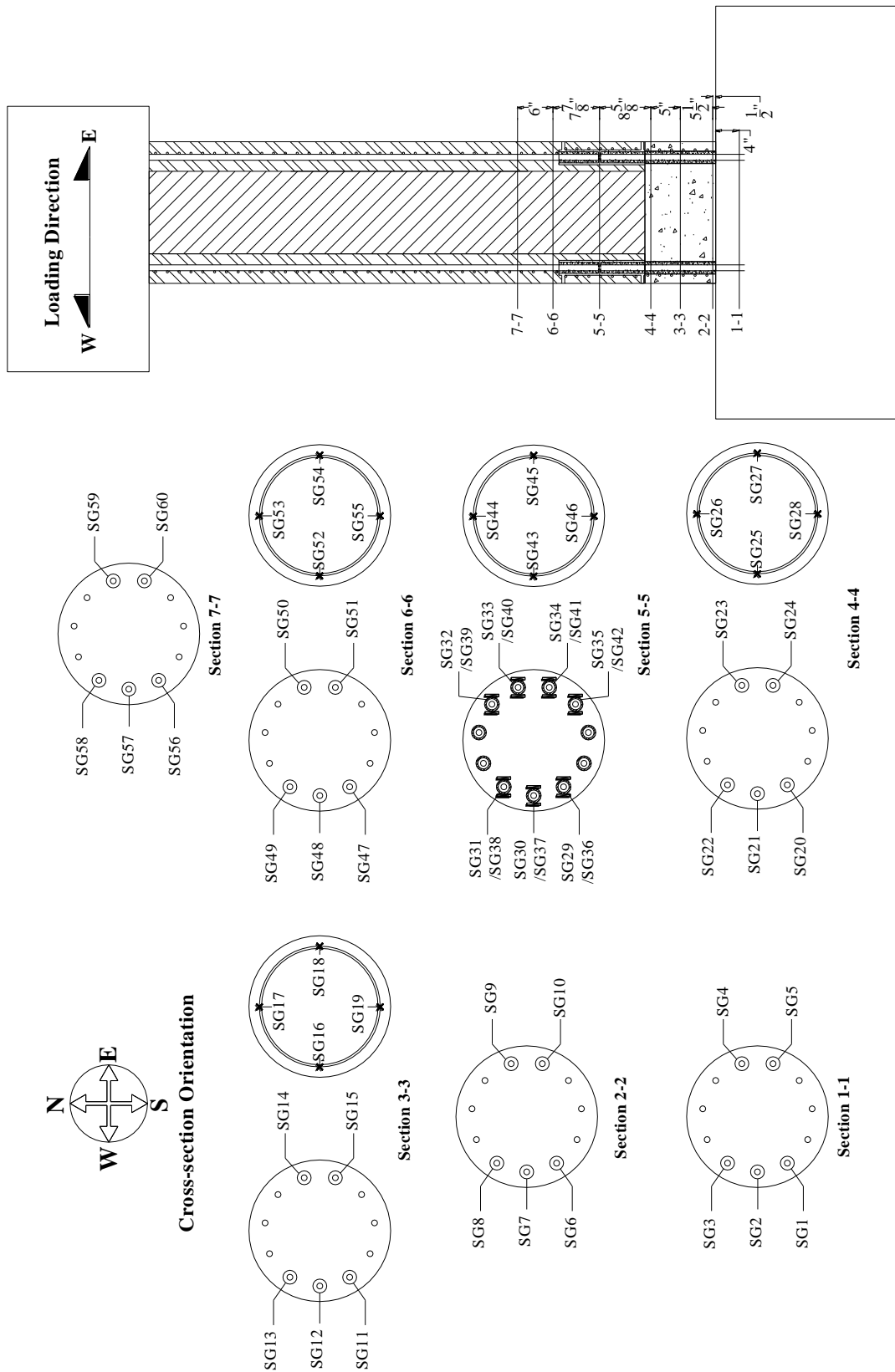


Figure 3-95 GCPP strain gage instrumentation plan

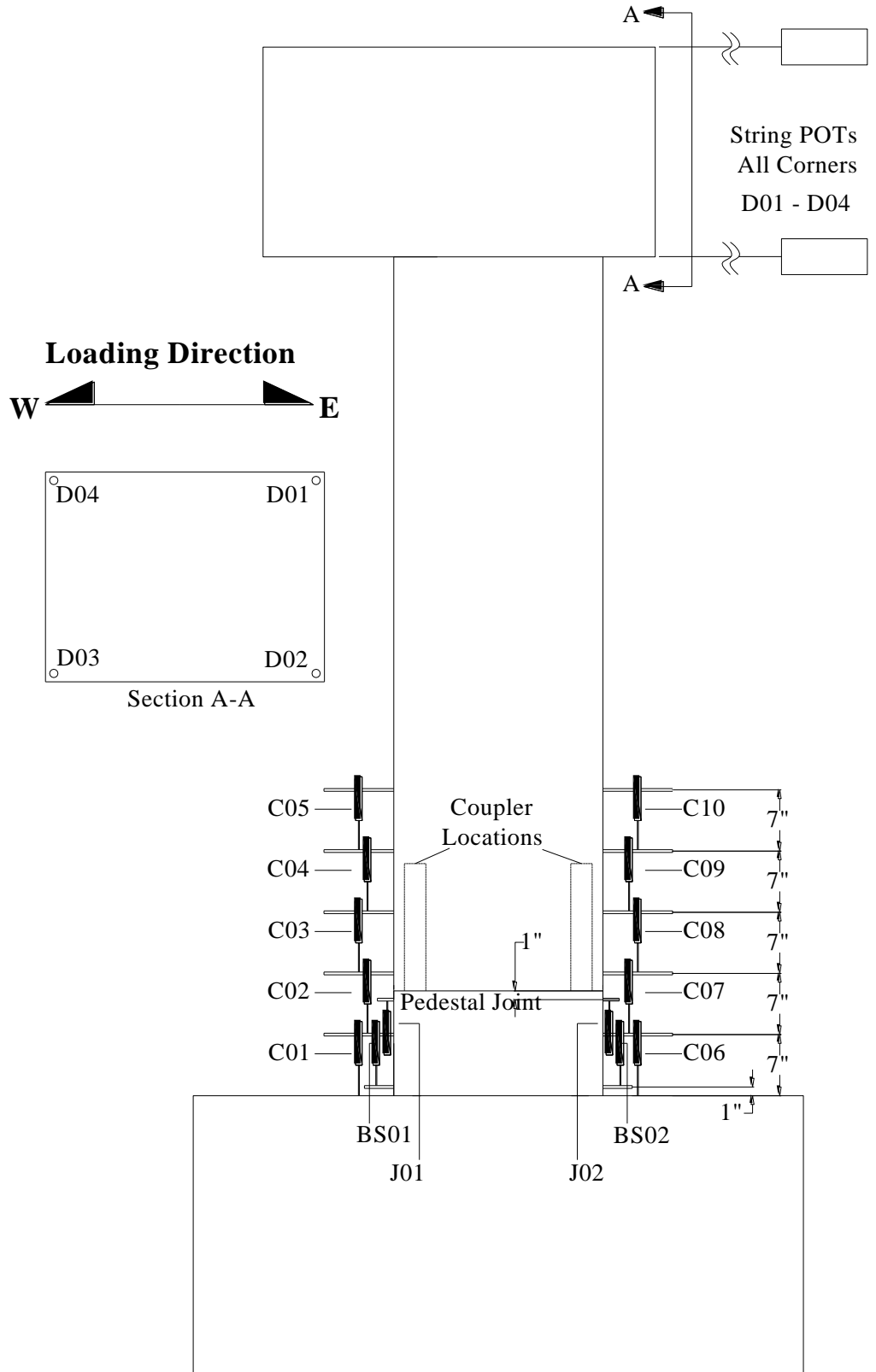


Figure 3-96 GCPP displacement and curvature instrumentation plan

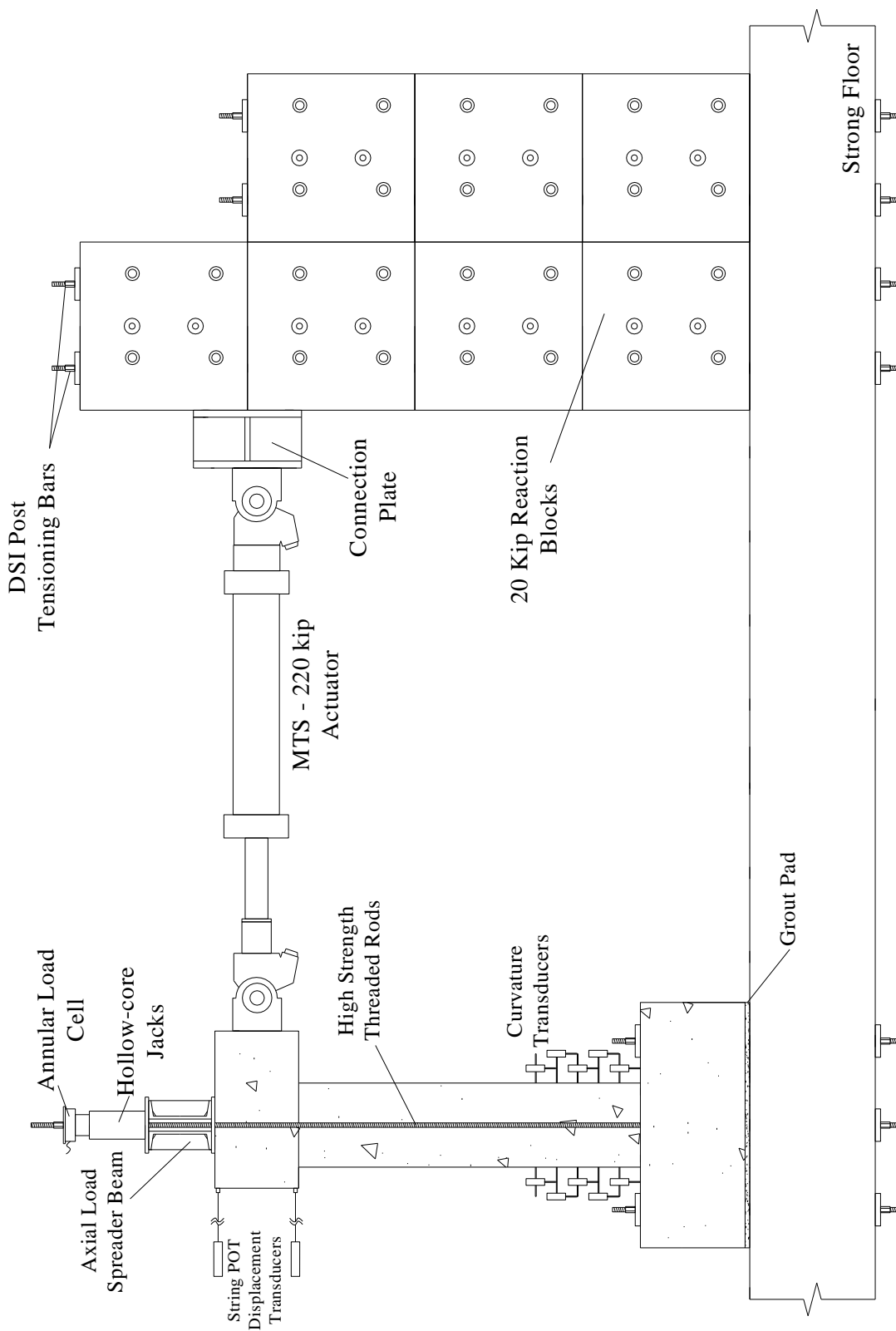


Figure 3-97 Schematic of experimental set-up



Figure 3-98 Photo of test set-up



Figure 3-99 Placement of column model



Figure 3-100 Construction of reaction pylon



Figure 3-101 Spreader beam and loading rams



Figure 3-102 Nitrogen accumulator

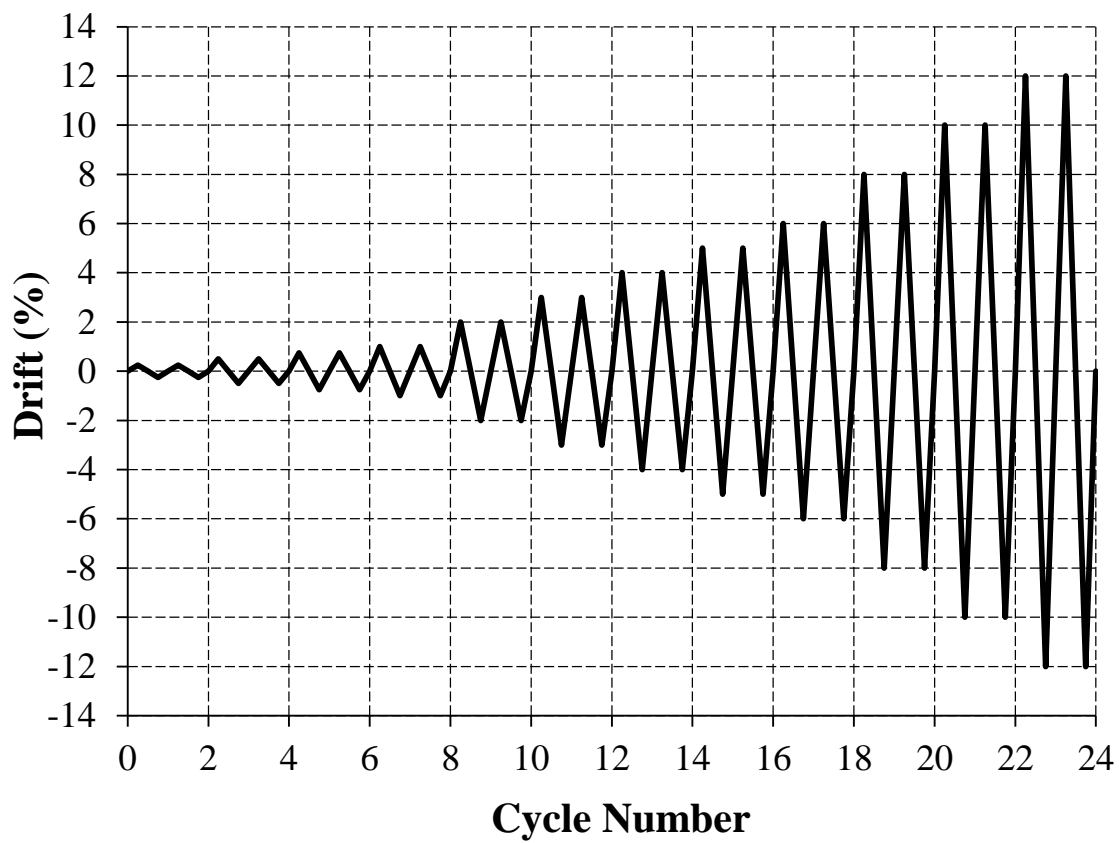


Figure 3-103 Loading protocol

Chapter 4 Figures

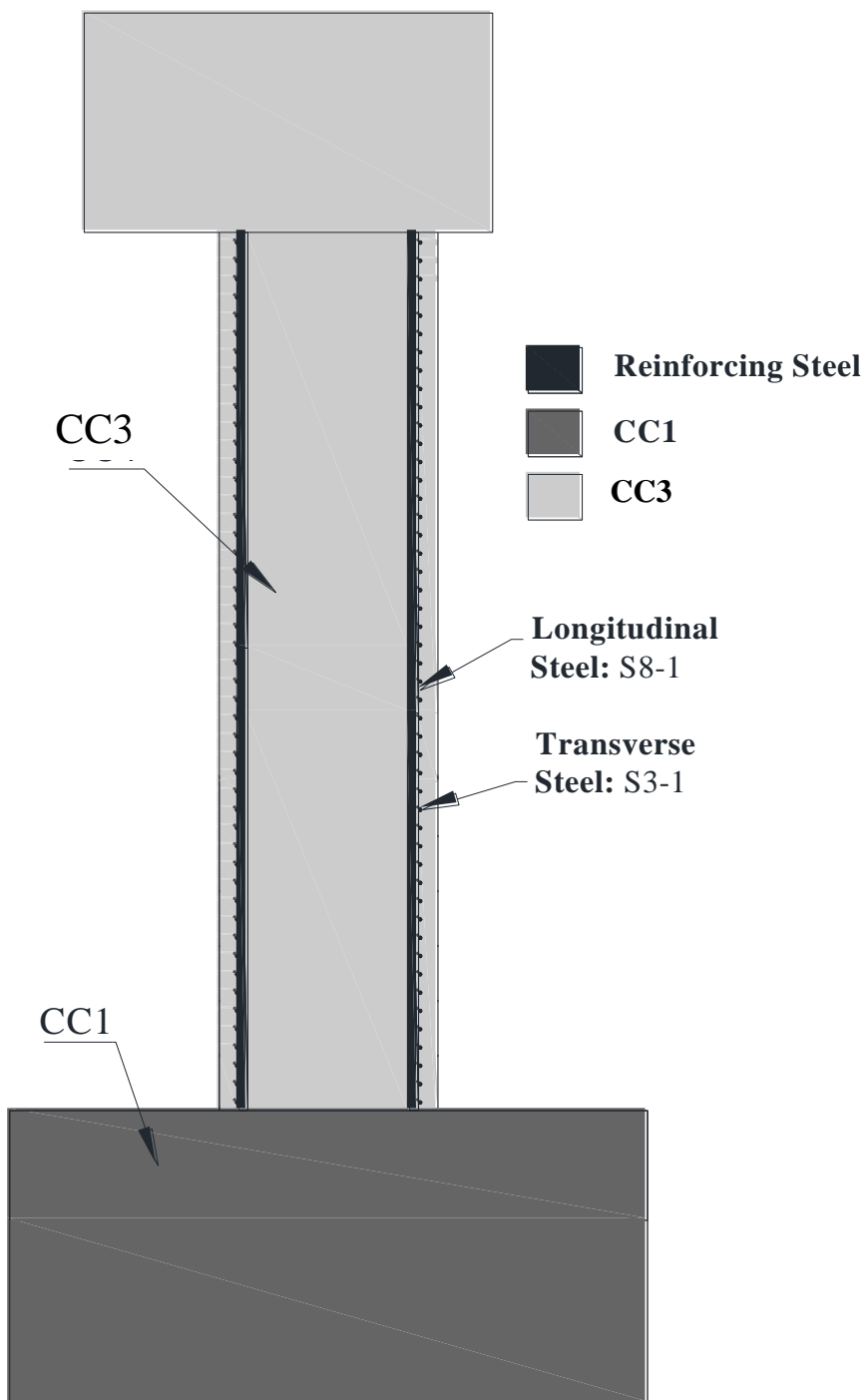


Figure 4-1 CIP material schematic

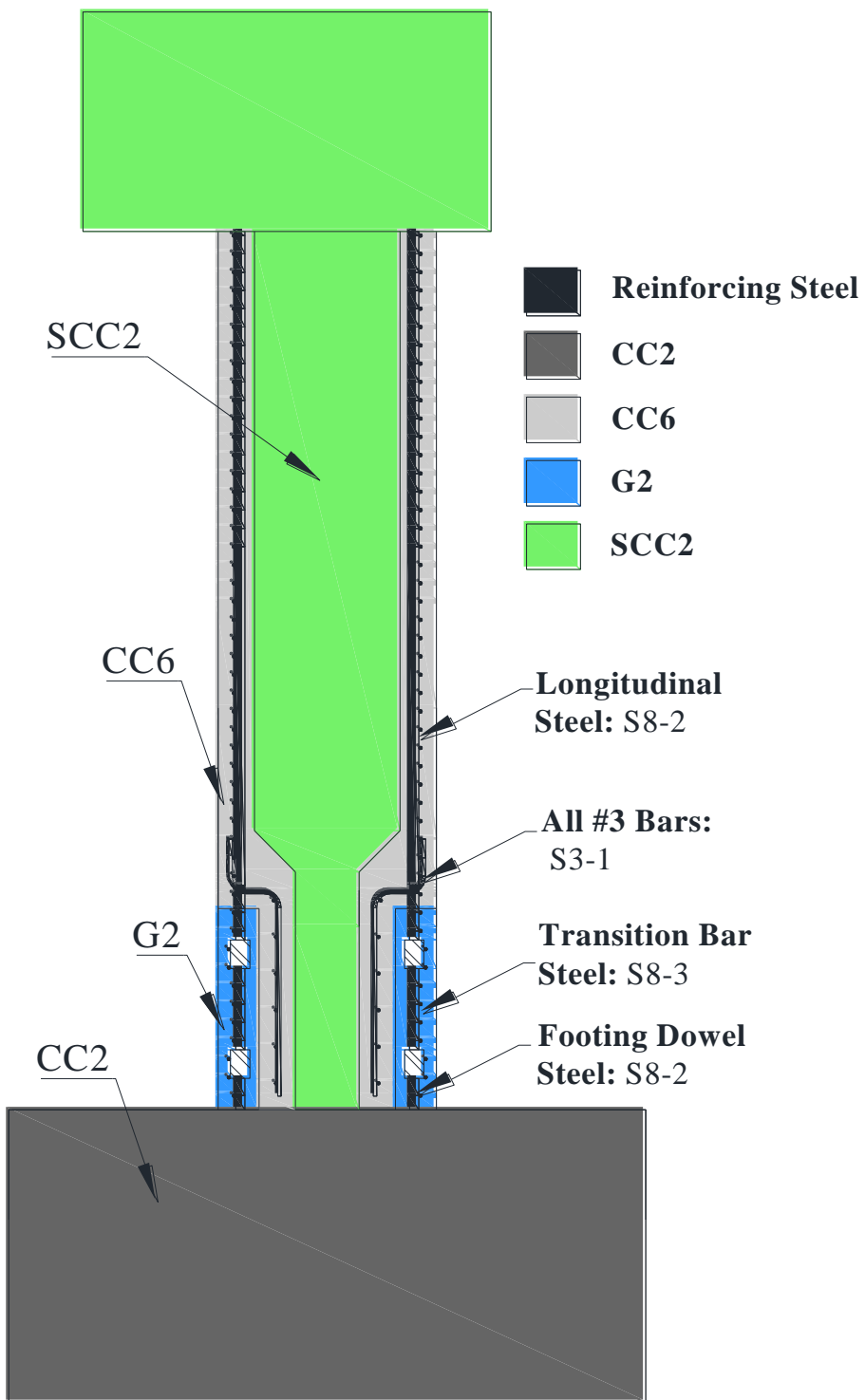


Figure 4-2 HCNP material schematic

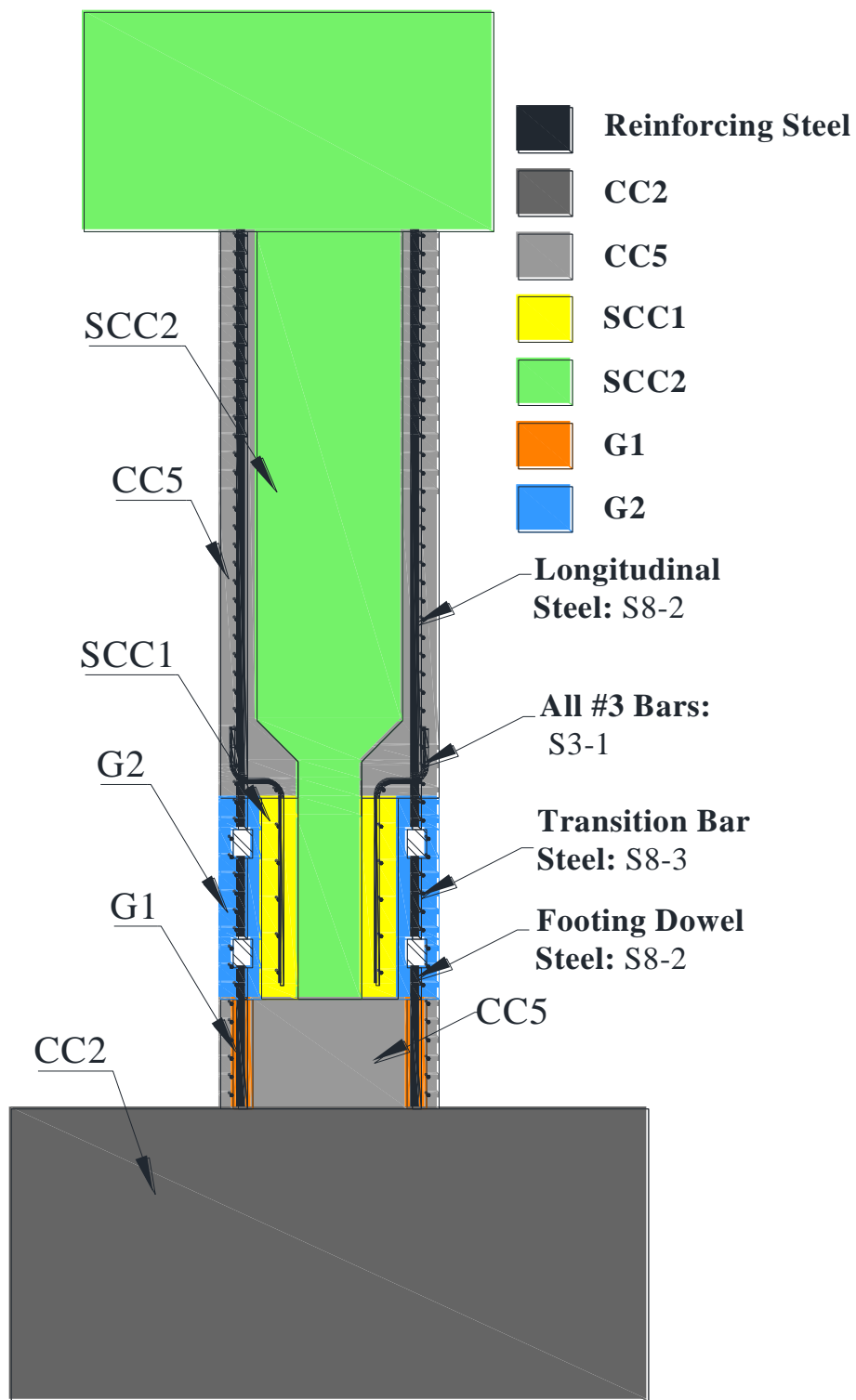


Figure 4-3 HCPP material schematic

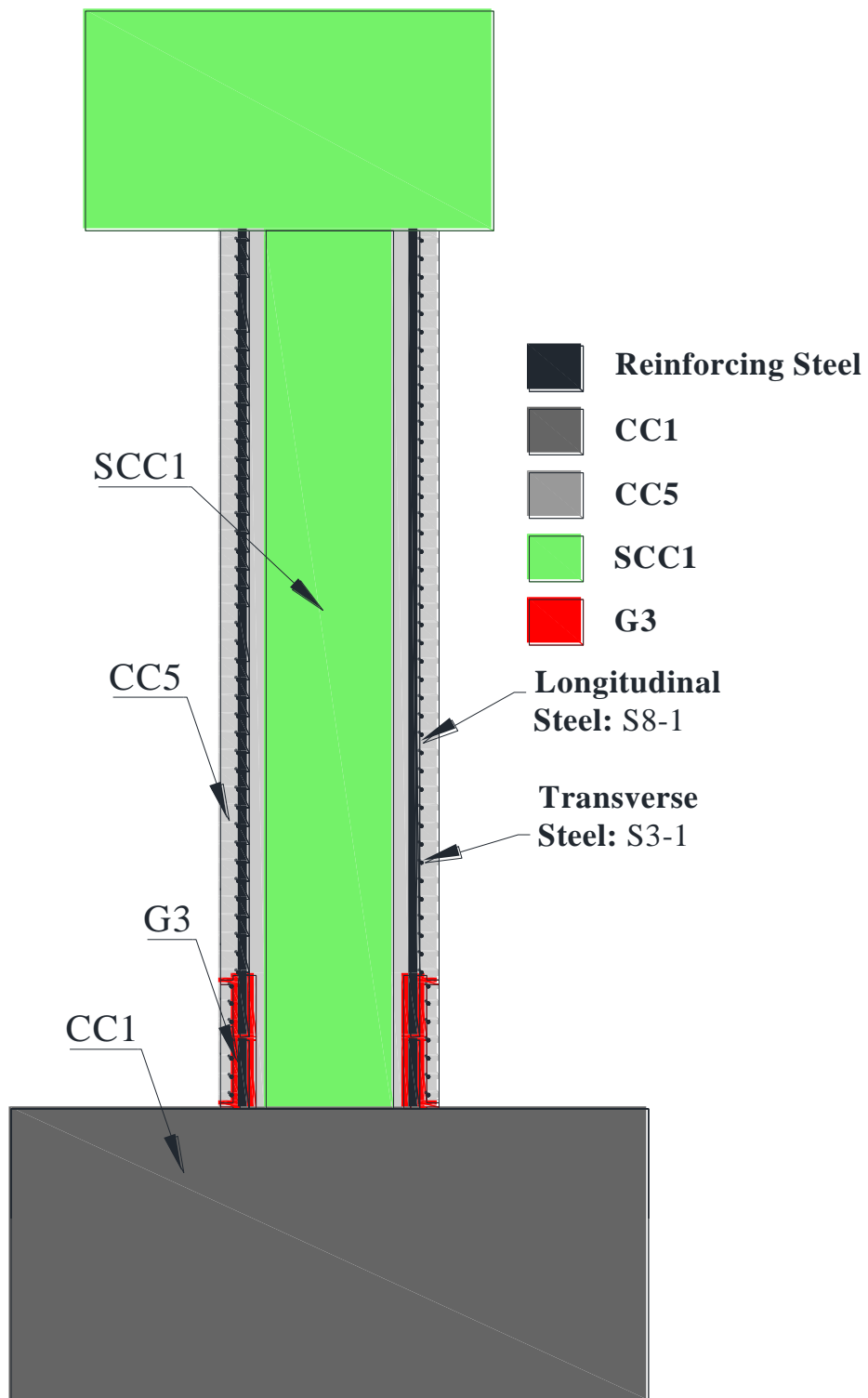


Figure 4-4 GCNP material schematic

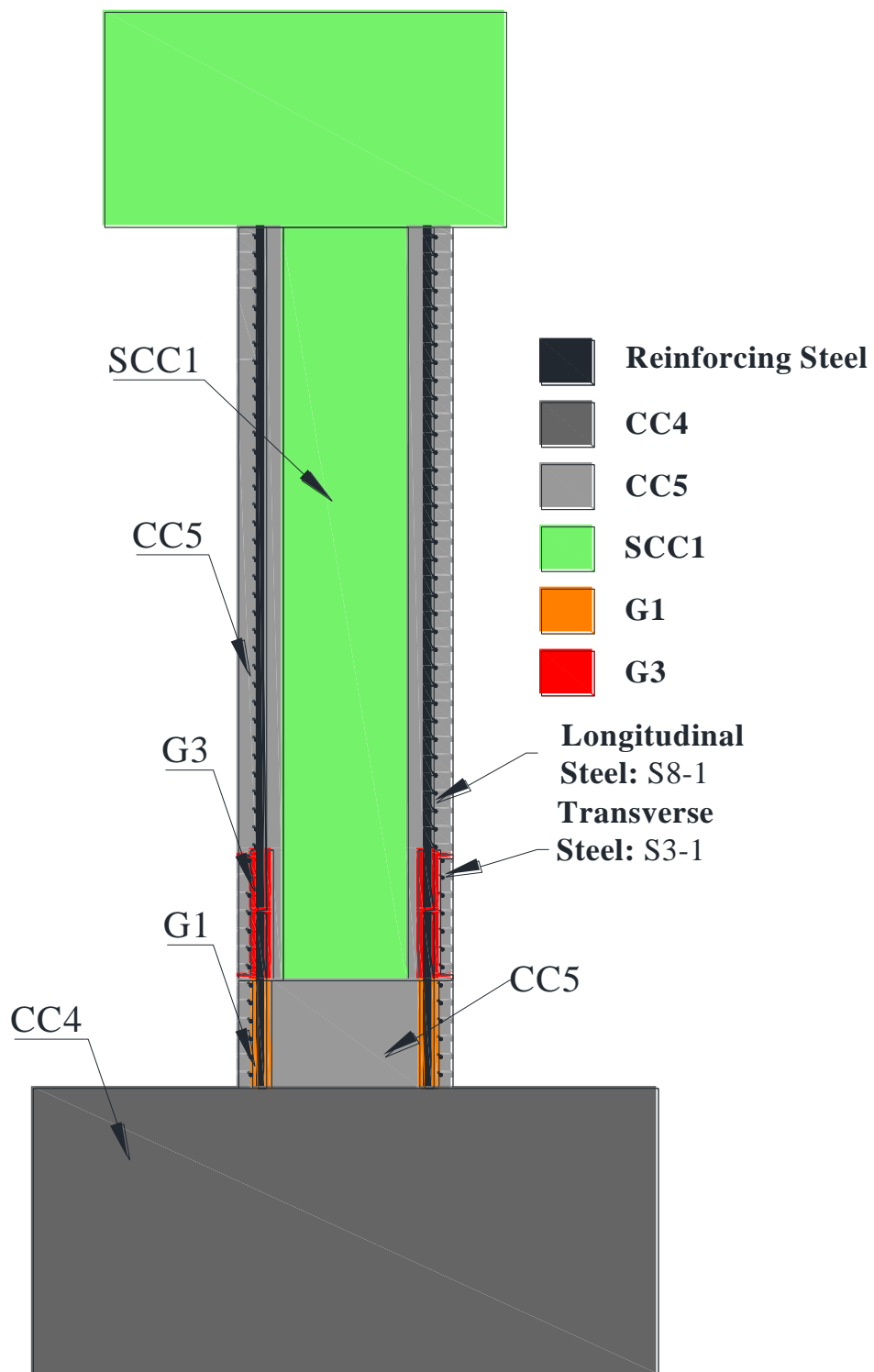


Figure 4-5 GCPP material schematic



(a) Slump flow test 1:
 $d_{\text{avg}} = 17.3\text{in}$ [439mm] and VSI = 1.0



(b) Slump flow test 2:
 $d_{\text{avg}} = 20.3\text{in}$ [516mm] and VSI = 0.0

Figure 4-6 SCC1 slump flow test results



(a) Slump flow test 1:
 $d_{\text{avg}} = 16.5\text{in}$ [419mm] and VSI = 1.0



(b) Slump flow test 3:
 $d_{\text{avg}} = 25.3\text{in}$ [643mm] and VSI = 0.0

Figure 4-7 SCC2 slump flow test results

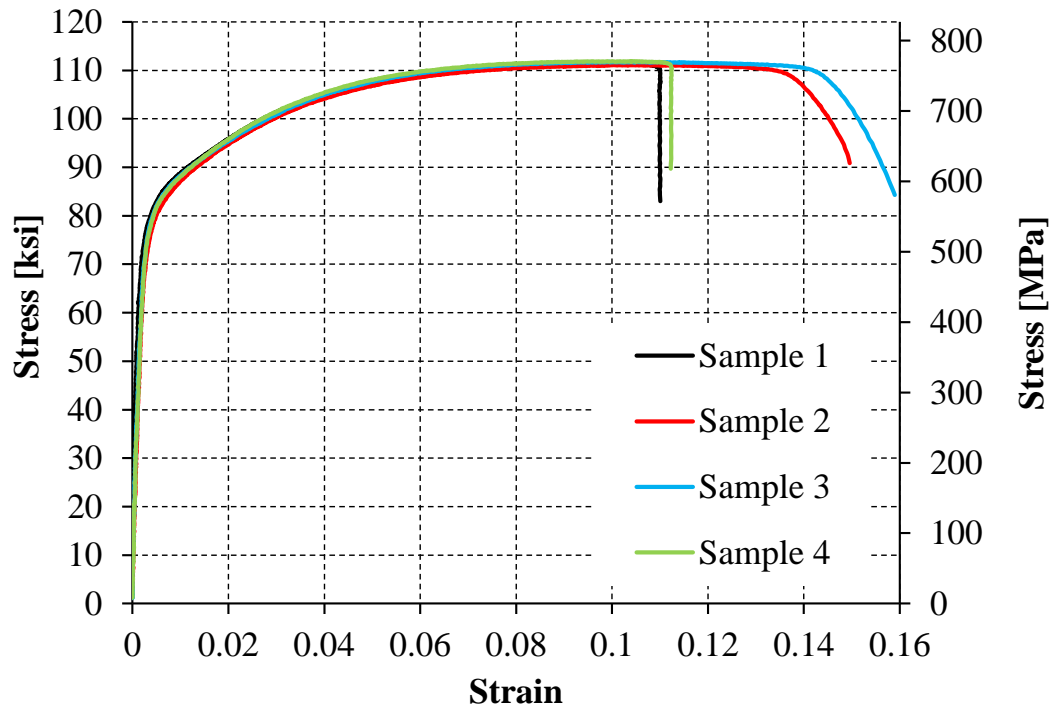
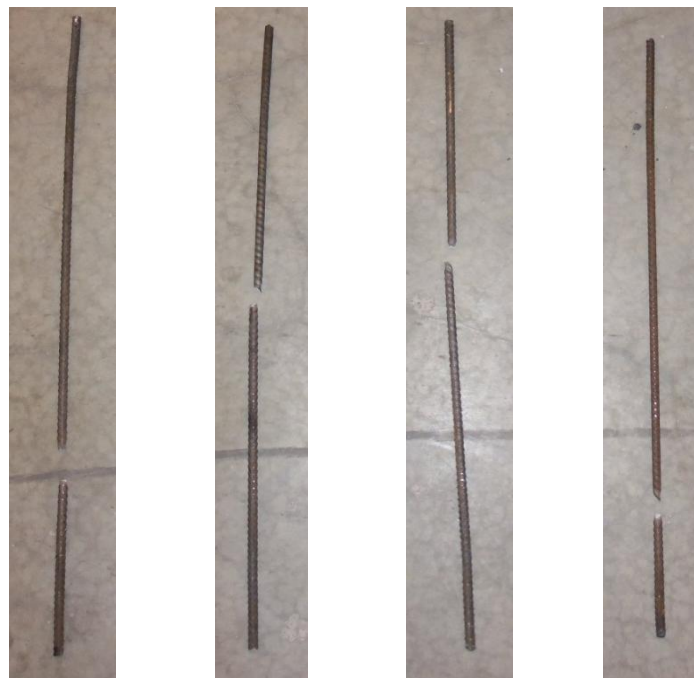


Figure 4-8 Stress-strain behavior of #3 reinforcing steel 1 (S3-1)



(a) Sample 1 (b) Sample 2 (c) Sample 3 (d) Sample 4

Figure 4-9 S3-1 reinforcing bars after testing

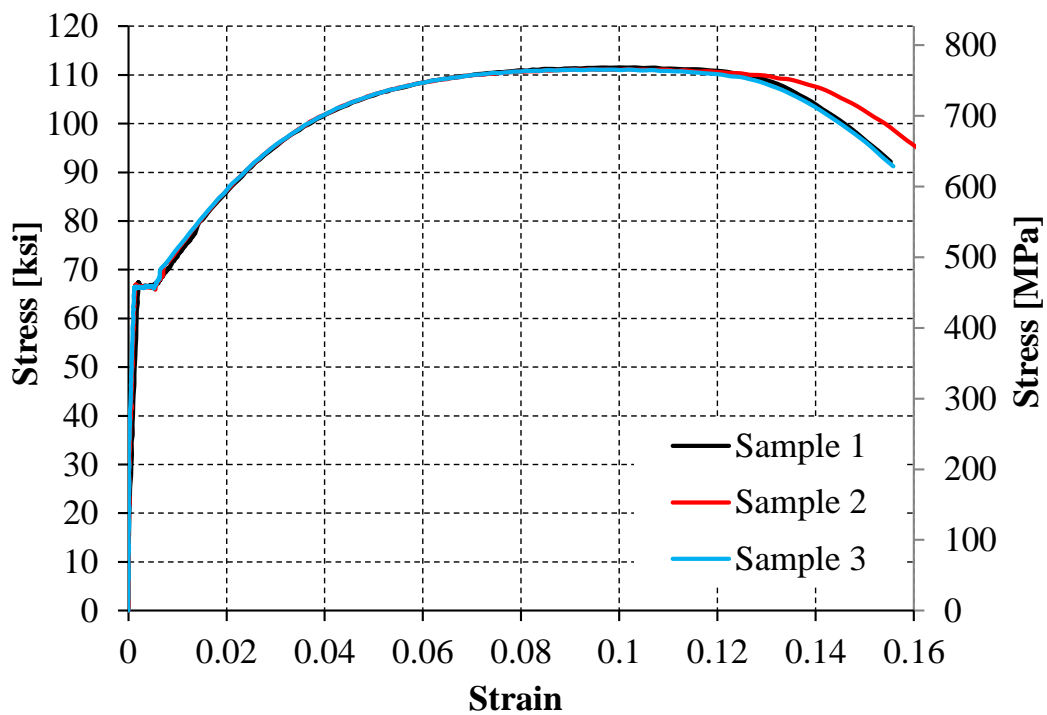
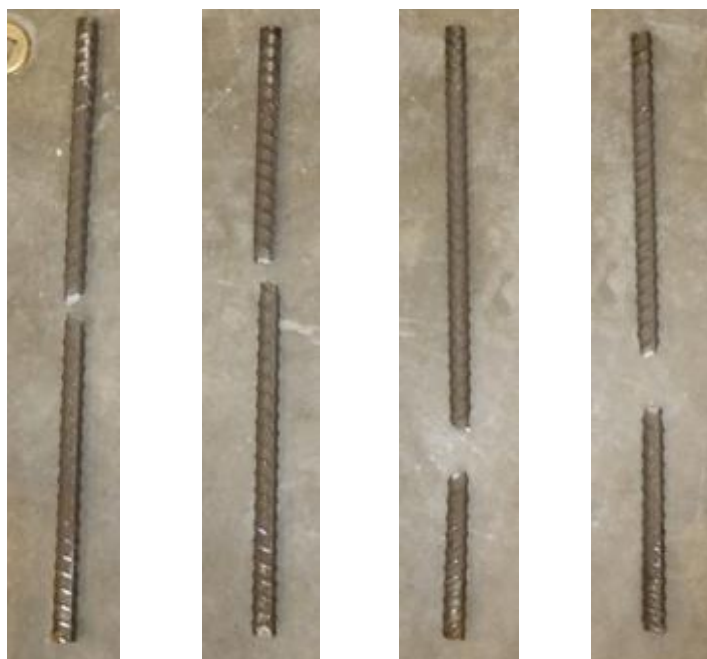


Figure 4-10 Stress-strain behavior of #8 reinforcing steel 1 (S8-1)



(a) Sample 1 (b) Sample 2 (c) Sample 3 (d) Sample 4

Figure 4-11 S8-1 samples after testing

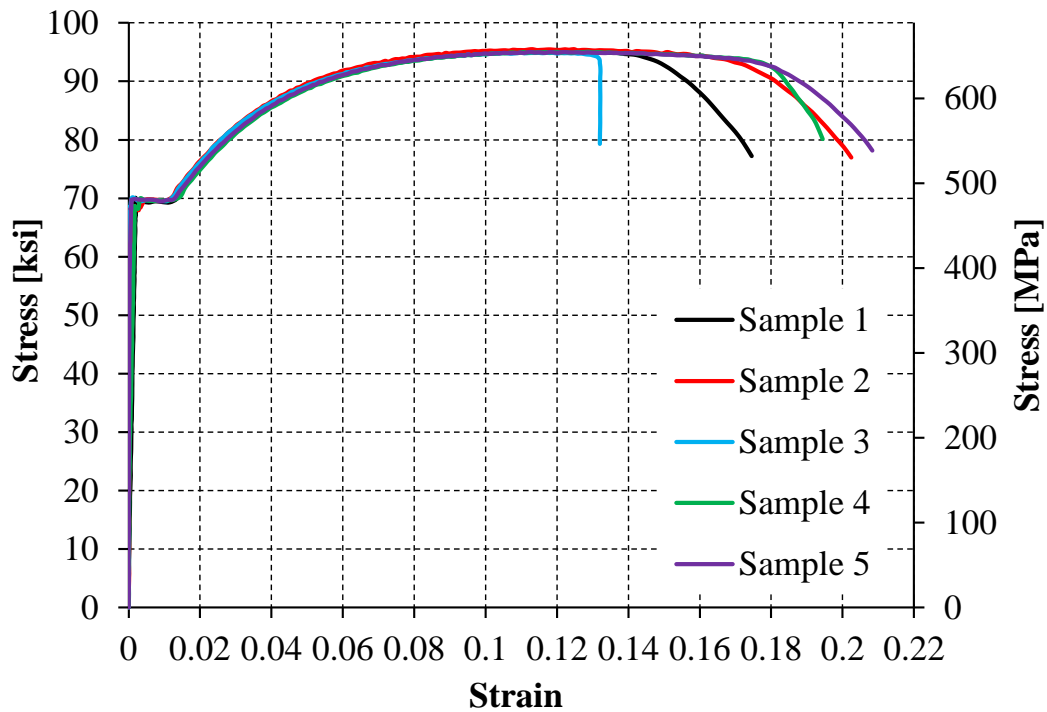


Figure 4-12 Stress-strain behavior of #8 reinforcing steel 2 (S8-2)



(a) Sample 1 (b) Sample 2 (c) Sample 3 (d) Sample 4 (e) Sample 5
Figure 4-13 S8-2 samples after testing

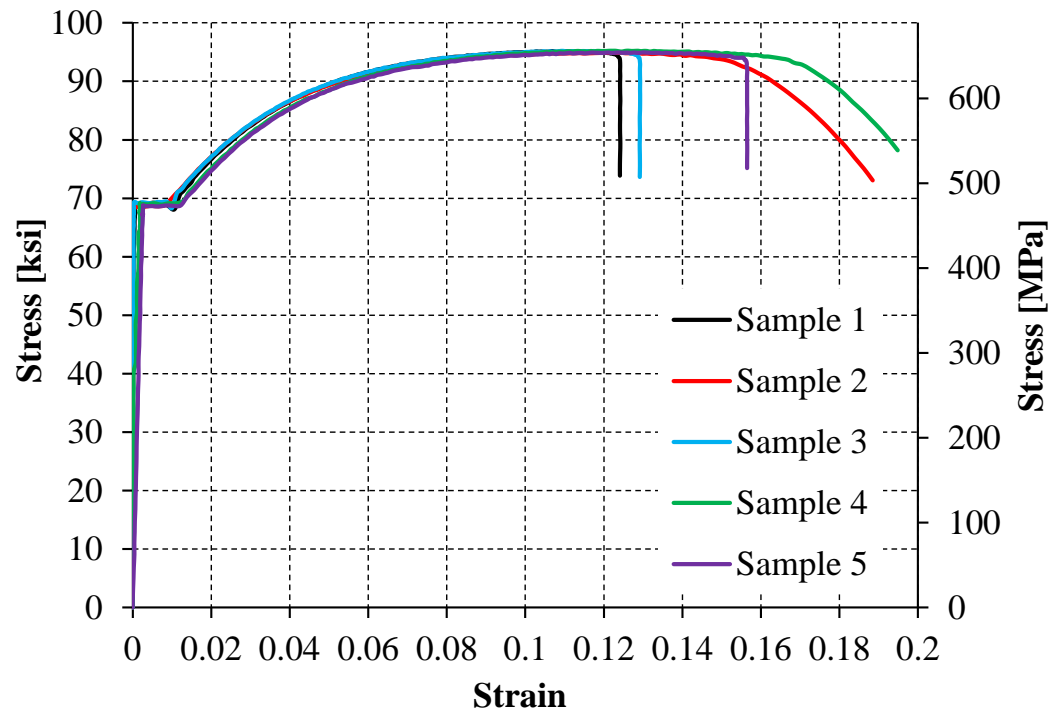
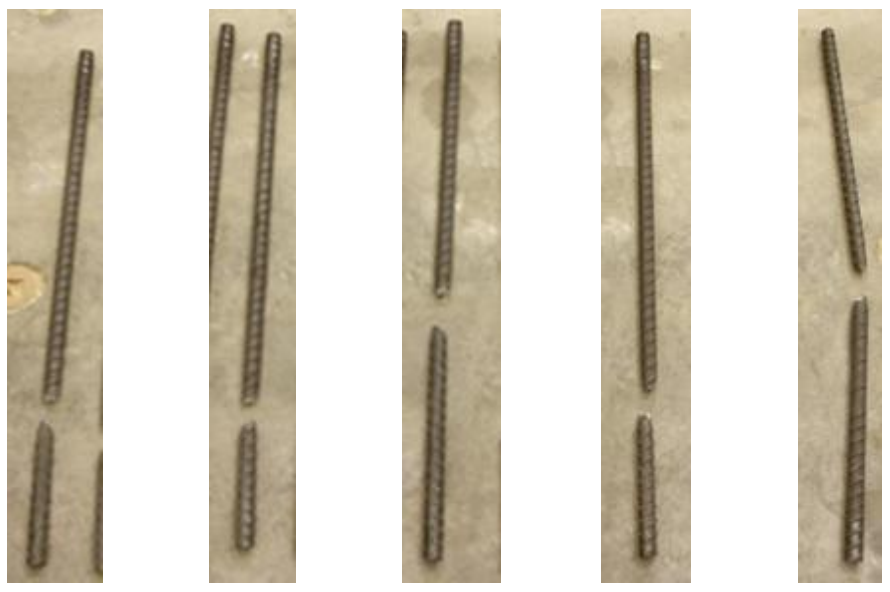
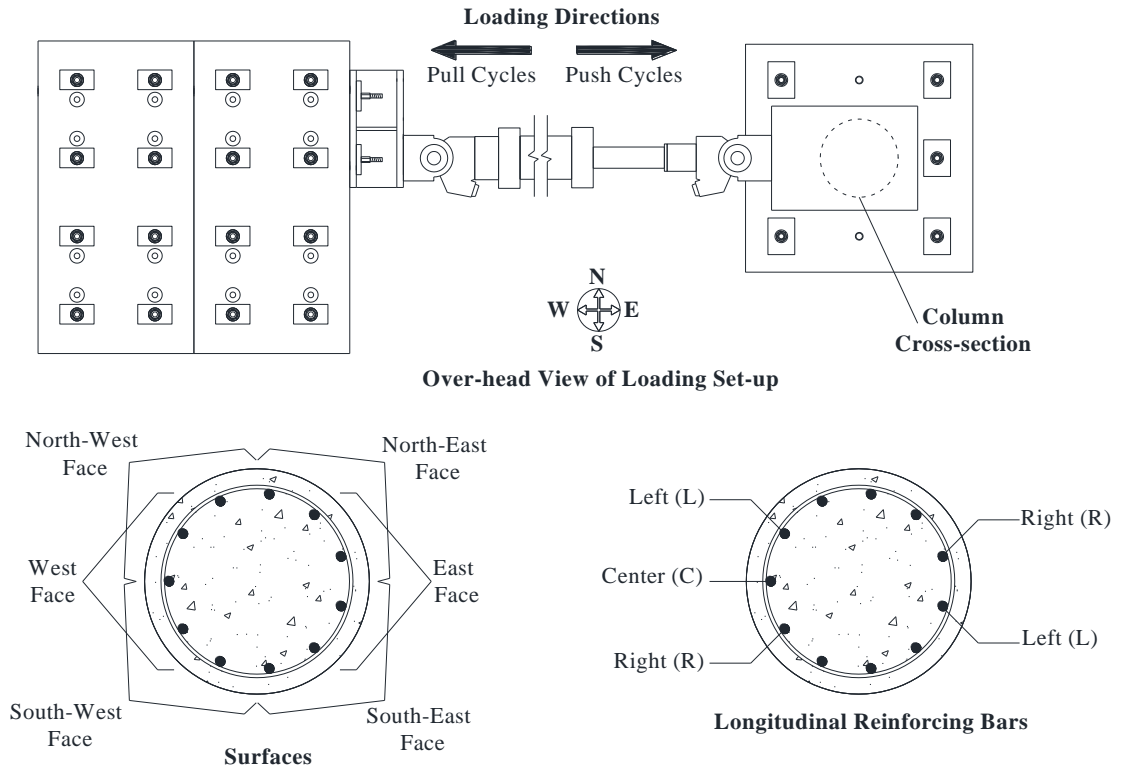


Figure 4-14 Stress-strain behavior of #8 reinforcing steel 3 (S8-3)



(a) Sample 1 (b) Sample 2 (c) Sample 3 (d) Sample 4 (e) Sample 5
Figure 4-15 S8-3 samples after testing



Nomenclature used to refer to specific locations on or within the column cross-section

Figure 4-16 Reference orientation of the test set-up

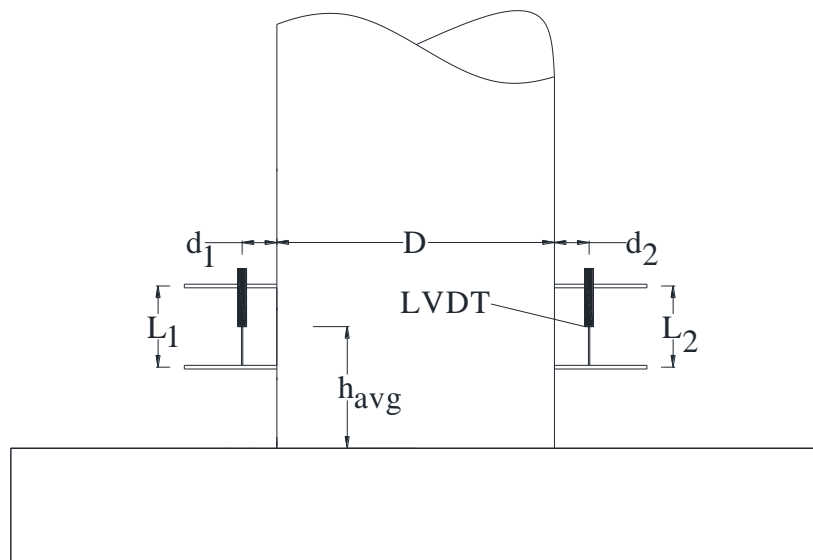
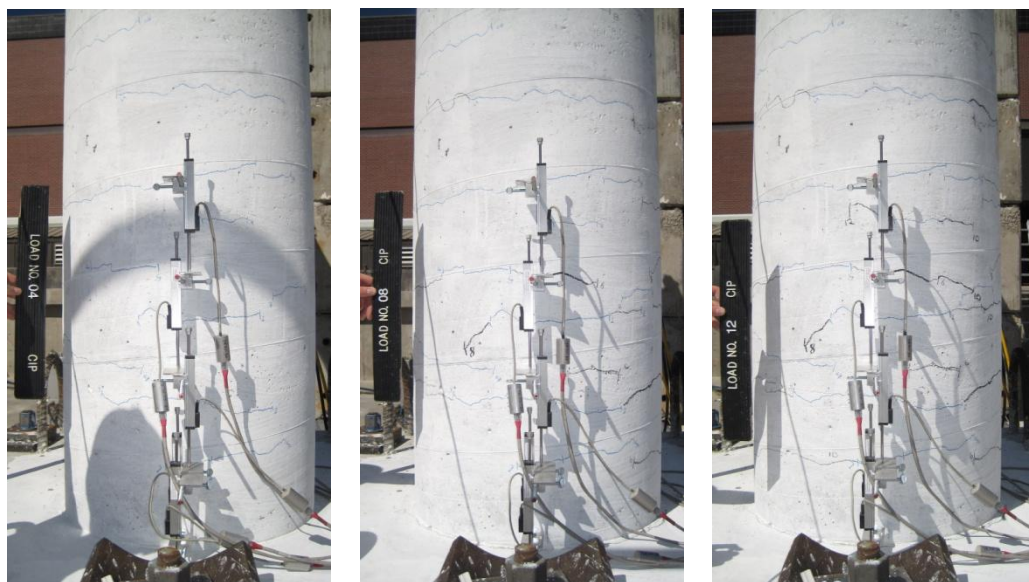


Figure 4-17 Variables used in the determination of section curvature



(a) Second cycle of
0.25% - East face

(b) Second cycle of
0.5% - East face

(c) Second cycle of
0.75% - East face

Figure 4-18 Observed damage for CIP at drift levels less than 1%



(a) West face push cycle 2

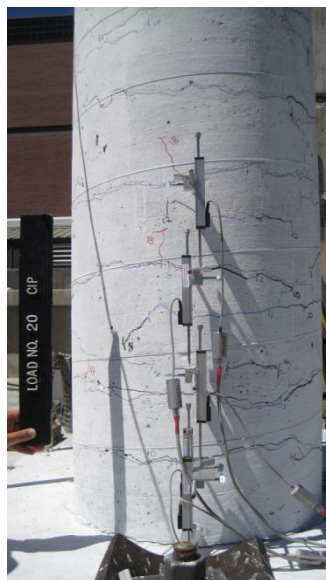
(b) East face pull cycle 2

(c) South-east face pull
cycle 2

Figure 4-19 CIP damage at 1% drift



(a) West face push cycle 2



(b) East face pull cycle 2

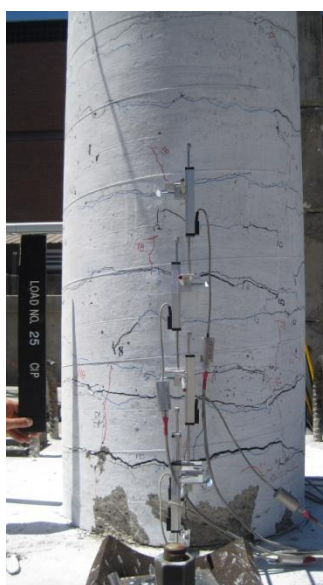


(c) South-east face pull cycle 2

Figure 4-20 CIP damage at 2% drift



(a) south-west face push cycle 2



(b) East face pull cycle 2



(c) North face pull cycle 2

Figure 4-21 CIP damage at 3% drift

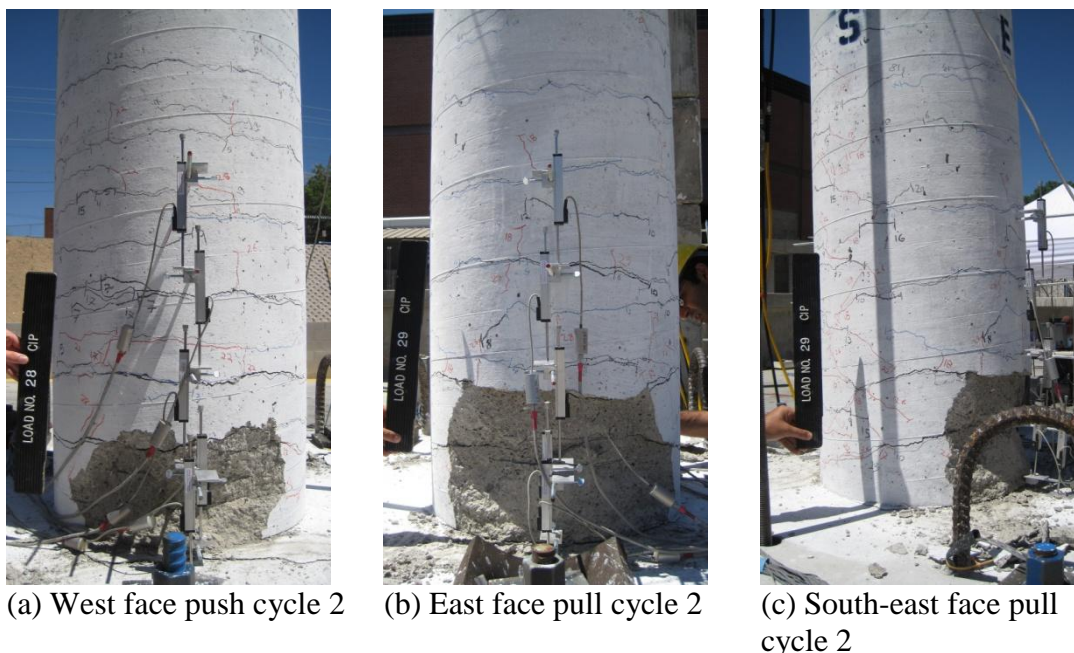


Figure 4-22 CIP damage at 4% drift

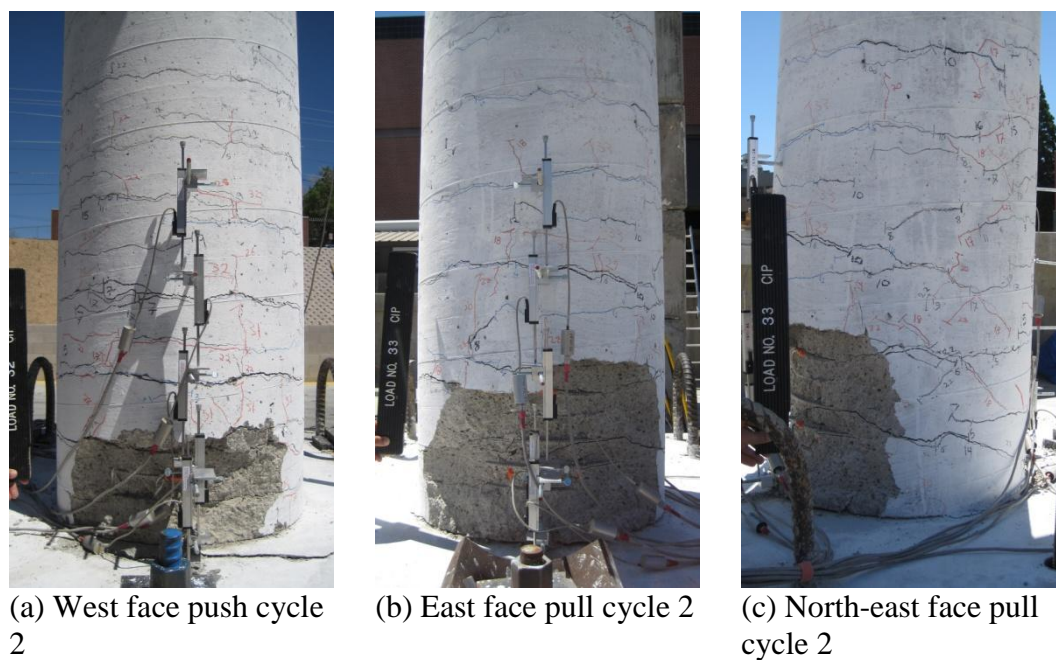


Figure 4-23 CIP damage at 5% drift

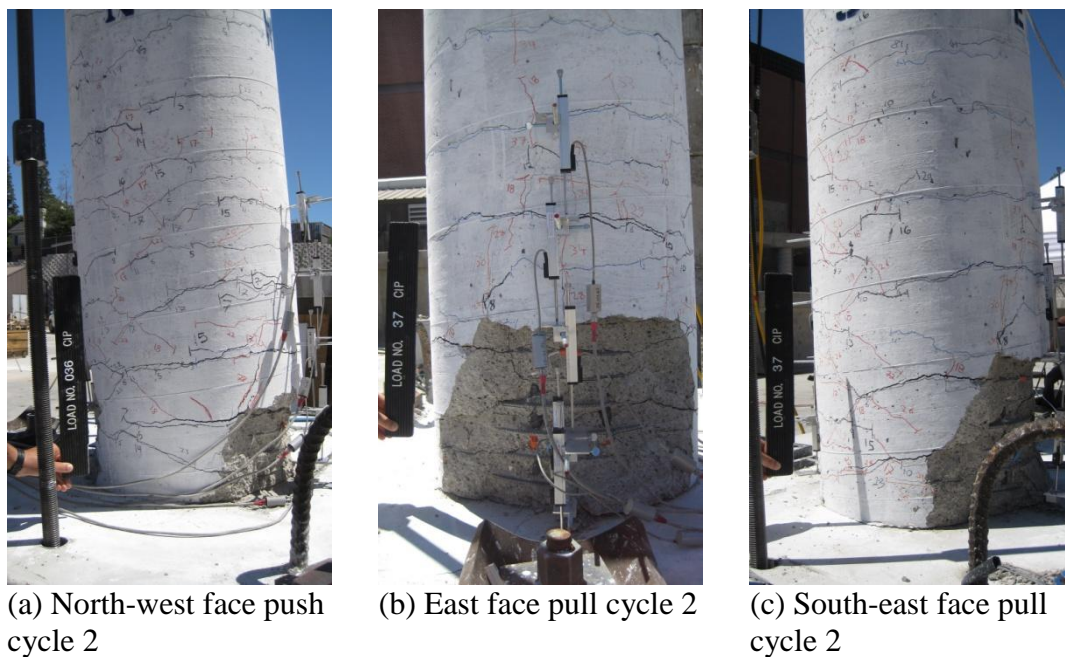


Figure 4-24 CIP damage at 6% drift

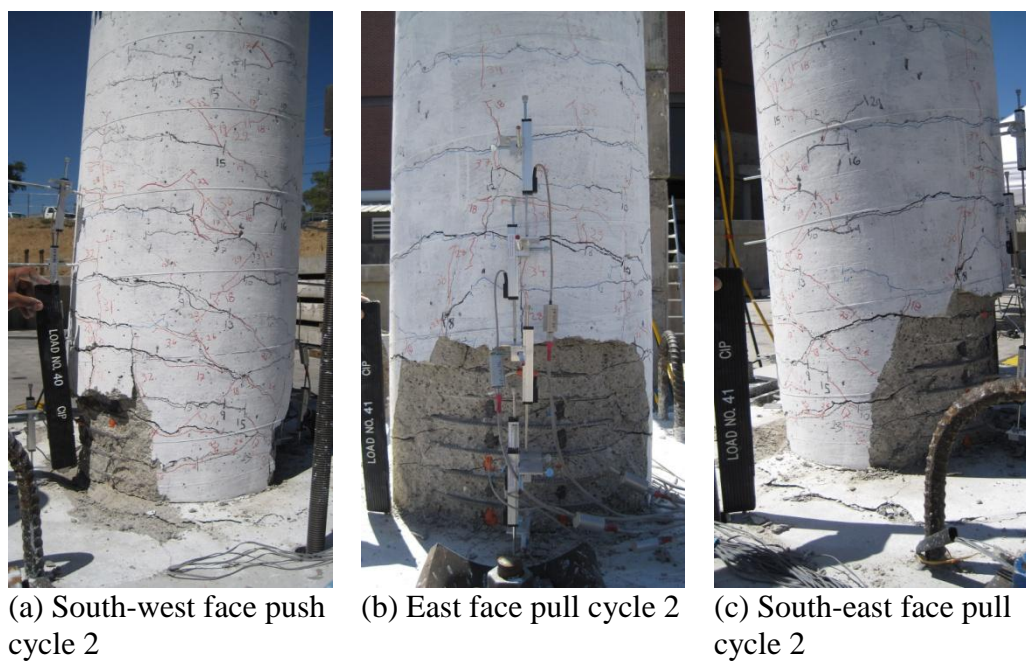


Figure 4-25 CIP damage at 8% drift



(a) West face push cycle 1 (b) South-west face push cycle 1 (c) East face pull cycle 2

Figure 4-26 CIP damage at 10% drift



(a) Bar buckling on East face

(b) Fracture of transverse bar of East face



(c) Fractured longitudinal bar on East face



(d) Fractured longitudinal bar on East face

Figure 4-27 Failure mechanisms of CIP

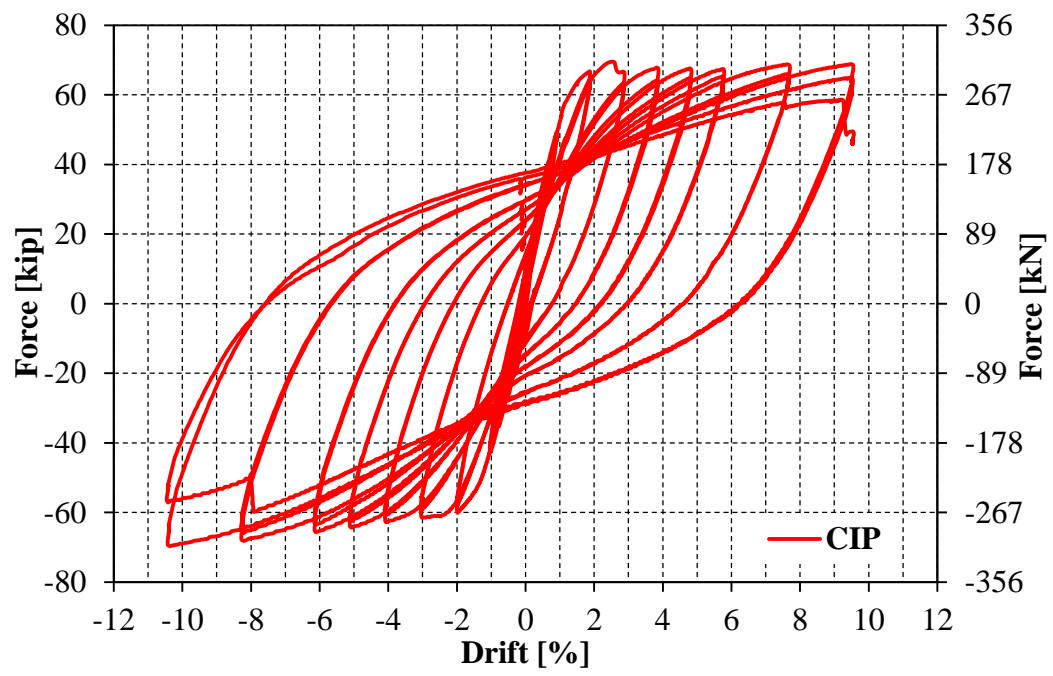


Figure 4-28 CIP hysteretic force-displacement response

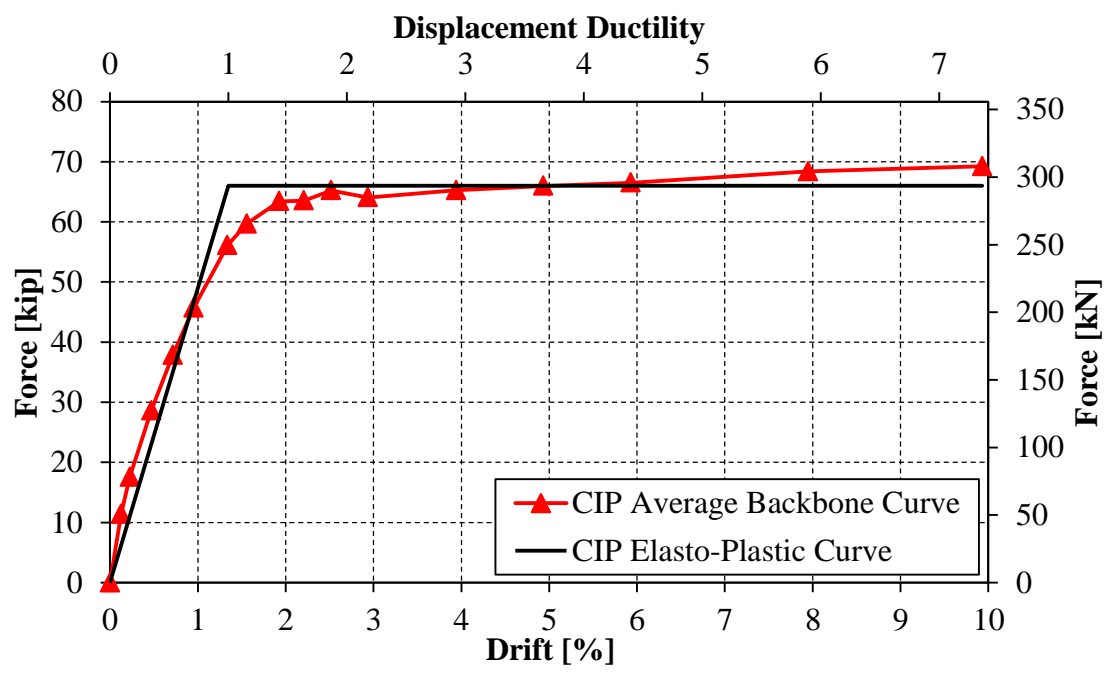
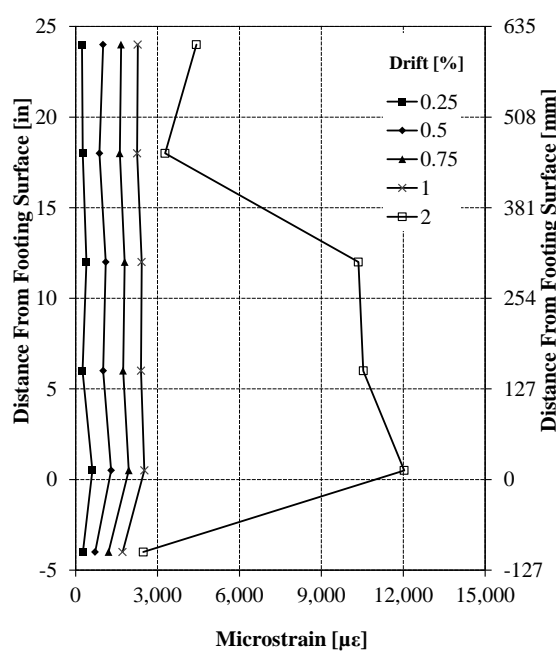
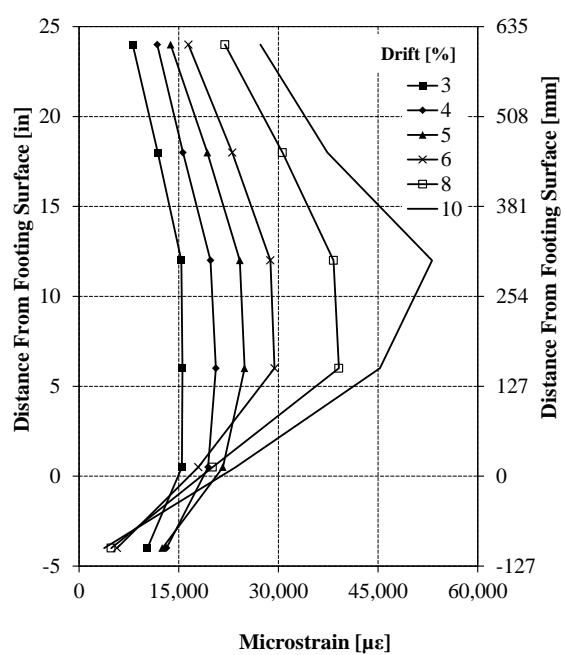


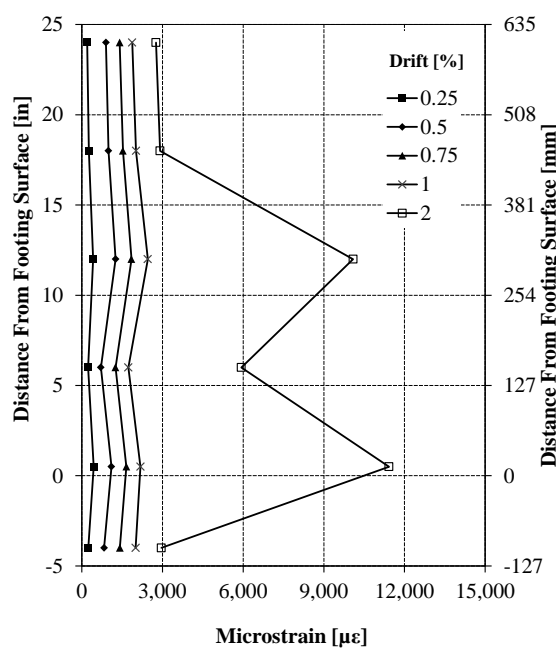
Figure 4-29 CIP average force-displacement backbone curve



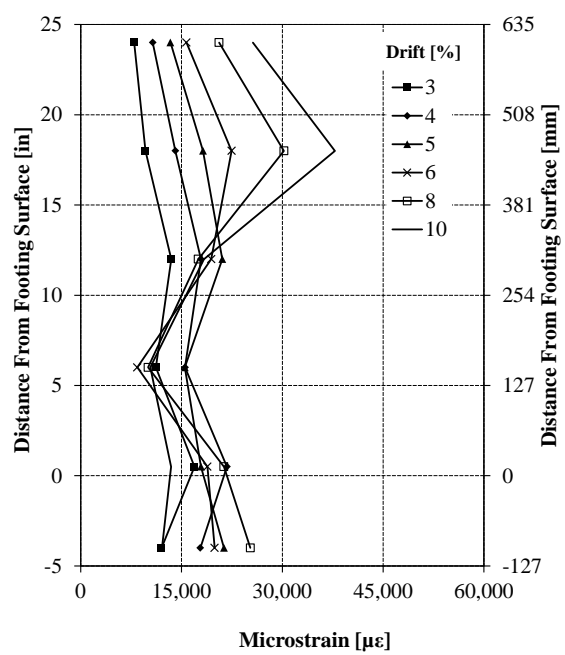
(a) Push cycle low drift levels



(b) Push cycle high drift levels



(c) Pull cycle low drift levels



(d) Pull cycle high drift levels

Figure 4-30 CIP Measured longitudinal tensile strain profiles

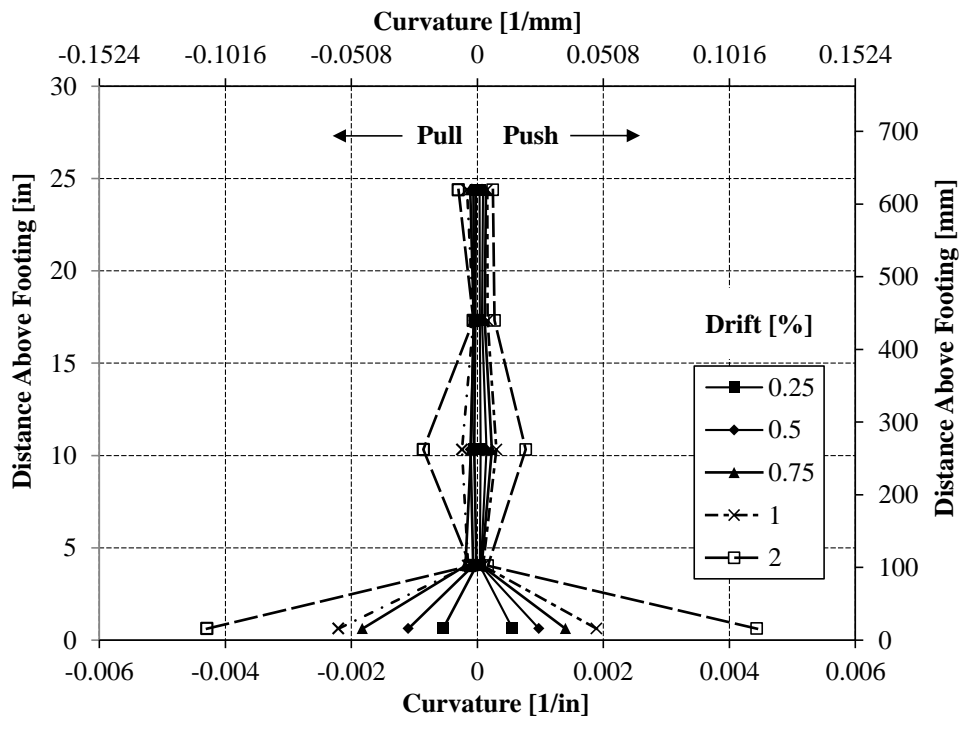


Figure 4-31 CIP plastic hinge curvatures for lower drift levels

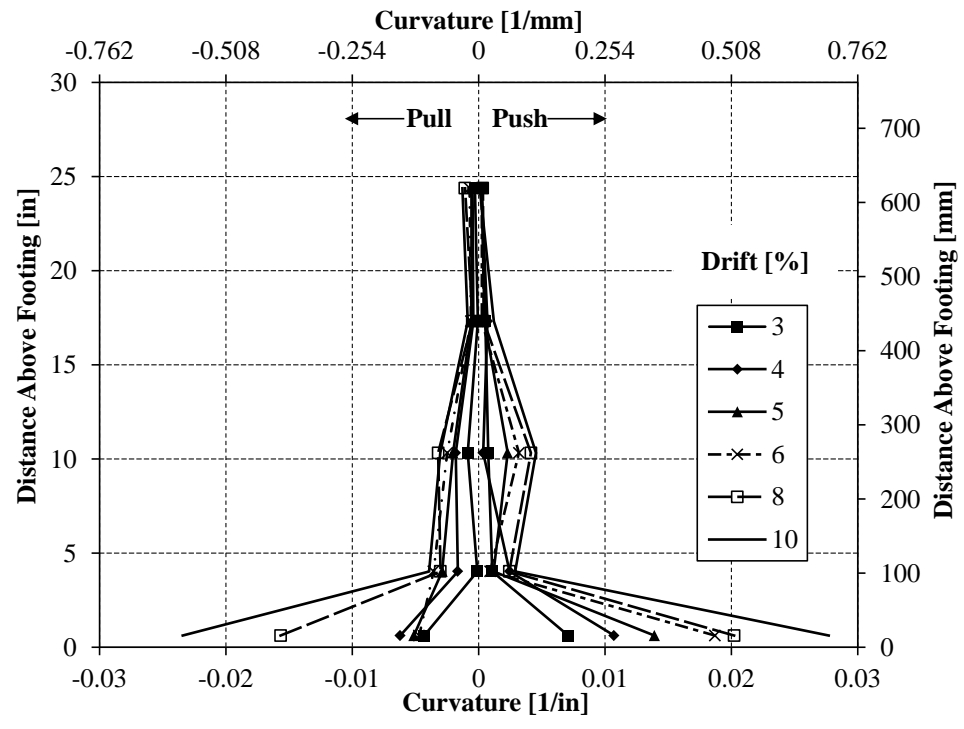


Figure 4-32 CIP plastic hinge curvatures for higher drift levels

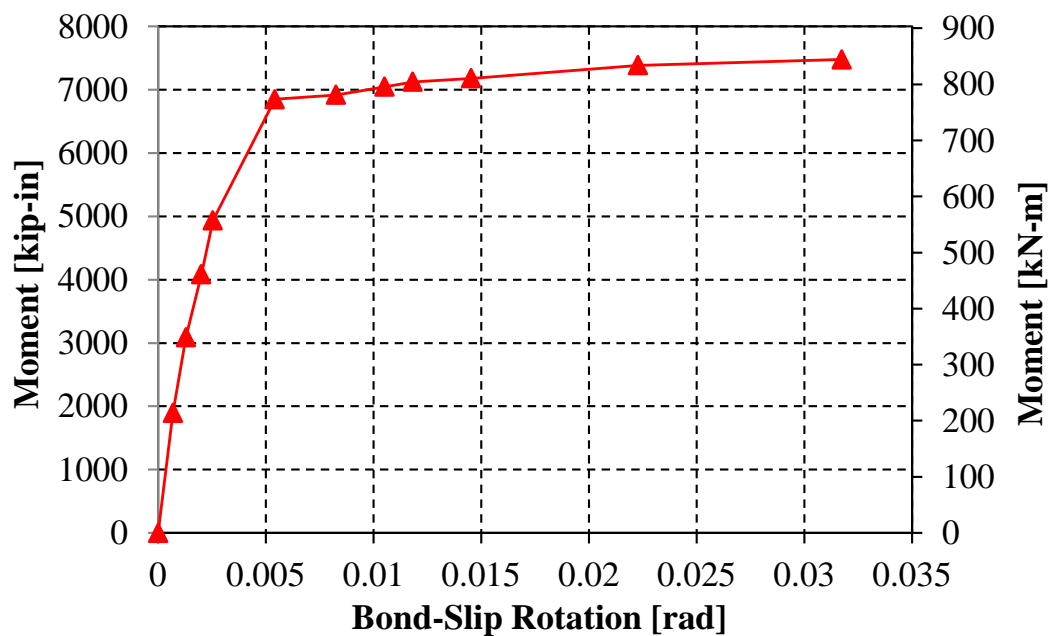


Figure 4-33 CIP moment vs. bond-slip rotation relationship

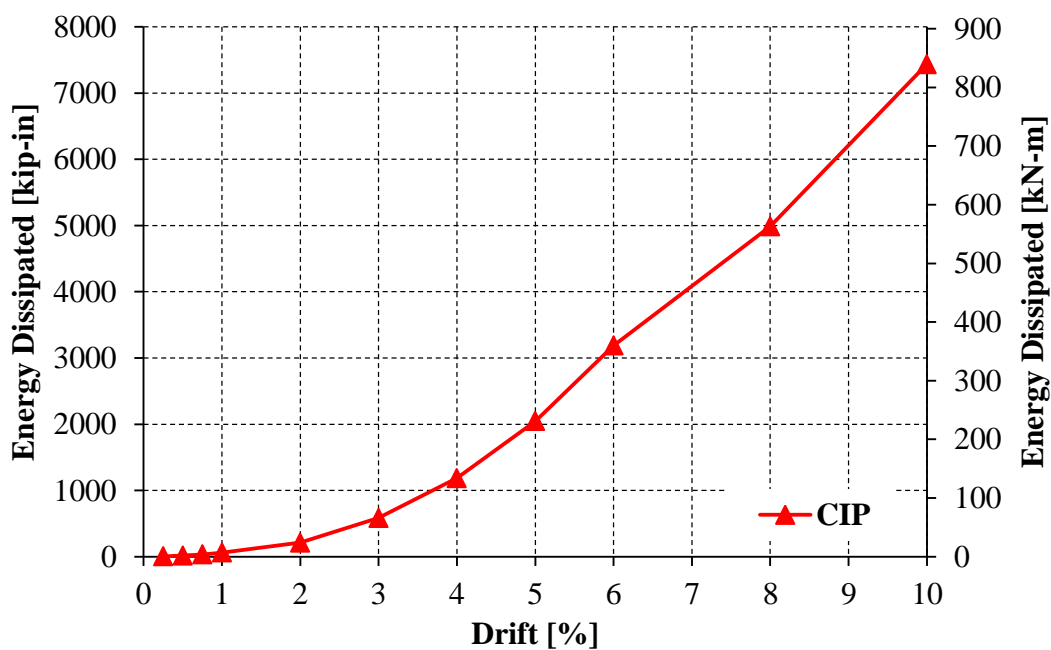


Figure 4-34 CIP cumulative energy dissipation

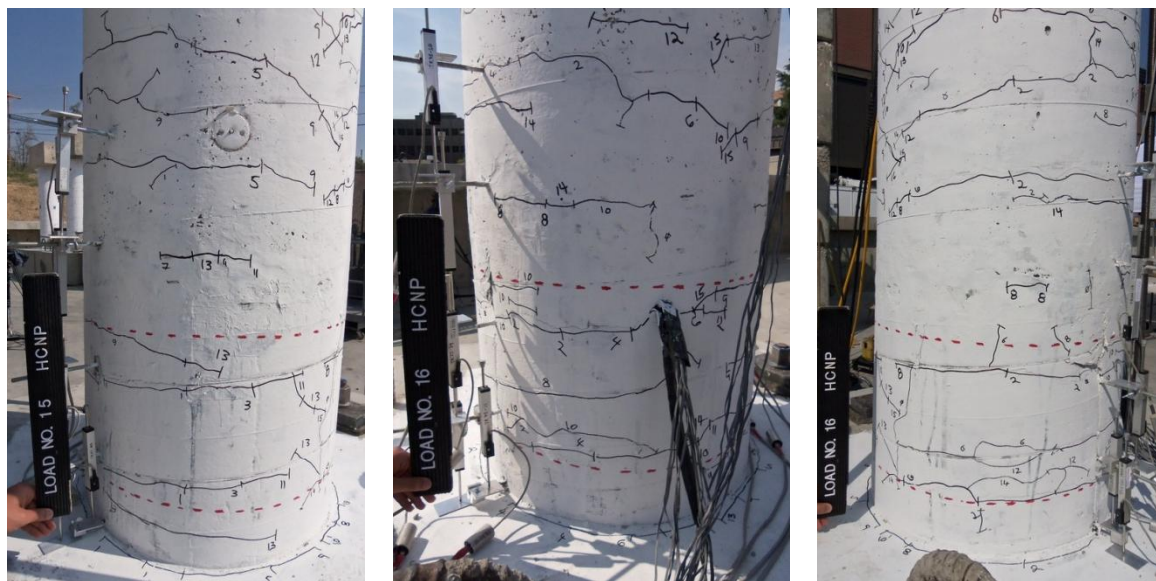


(a) Second cycle of 0.25%
North-east face

(b) Second cycle of 0.5%
North-east face

(c) Second cycle of 0.75%
North-east face

Figure 4-35 Damage observed for HCNP at drift levels less than 1%



(a) North-west face second
push cycle

(b) North-east face second pull
cycle

(c) South-east face second
pull cycle

Figure 4-36 HCNP observed damage at 1% drift



(a) North-west face second push cycle

(b) North-east face second pull cycle

(c) South-east face second pull cycle

Figure 4-37HCNP observed damage at 2% drift



(a) North-west face second push cycle

(b) East face second push cycle

(c) North-west face second pull cycle

Figure 4-38HCNP observed damage at 3% drift



(a) South-west face second push cycle (b) North-east face second pull cycle (c) South-east face second pull cycle

Figure 4-39 HCNP observed damage at 4% drift



(a) West face first push cycle (b) South-west face second push cycle (c) East face second pull cycle

Figure 4-40 HCNP observed damage at 5% drift



(a) South-west face second push cycle

(b) North-east face second pull cycle

(c) East face second pull cycle

Figure 4-41 HCNP observed damage at 6% drift



(a) South-west face second push cycle

(b) North-east face second pull cycle

(c) South-east face second pull cycle

Figure 4-42 HCNP observed damage at 8% drift



(a) South-west face second push cycle (b) North-east face second pull cycle (c) South-east face second pull cycle

Figure 4-43 HCNP observed damage at 10% drift



(a) South-west face (b) East face (c) Close-up on east face

Figure 4-44 HCNP observed damage at 12% drift



Figure 4-45 Removal of concrete from plastic hinge and footing



Figure 4-46 Fractured bar located on the east face of HCNP (left bar)

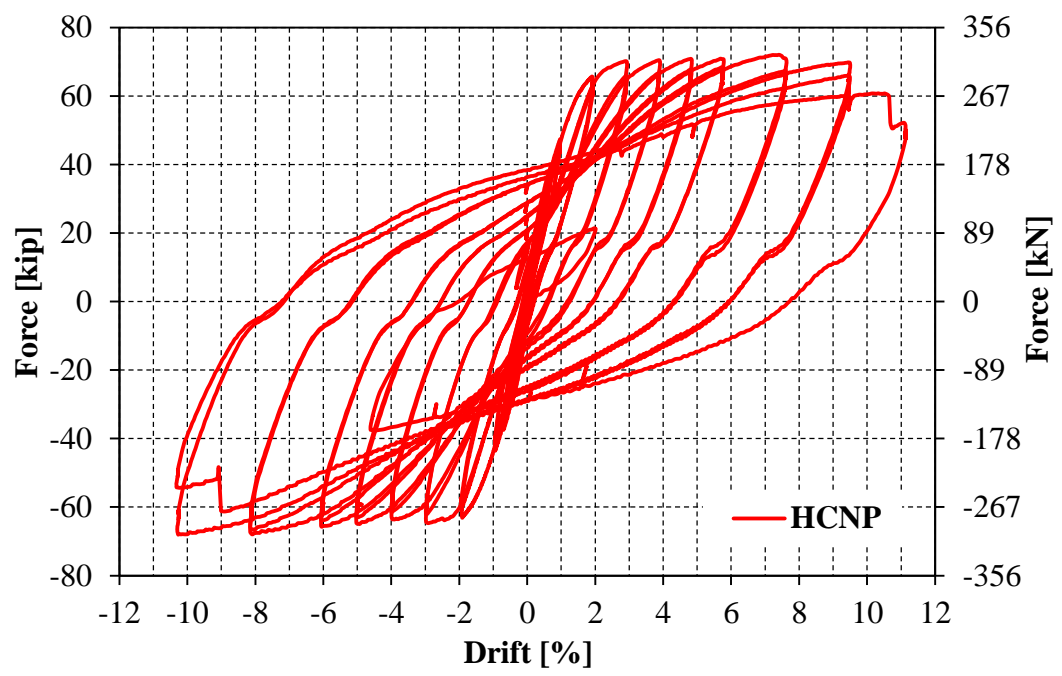


Figure 4-47 HCNP hysteretic force-displacement response

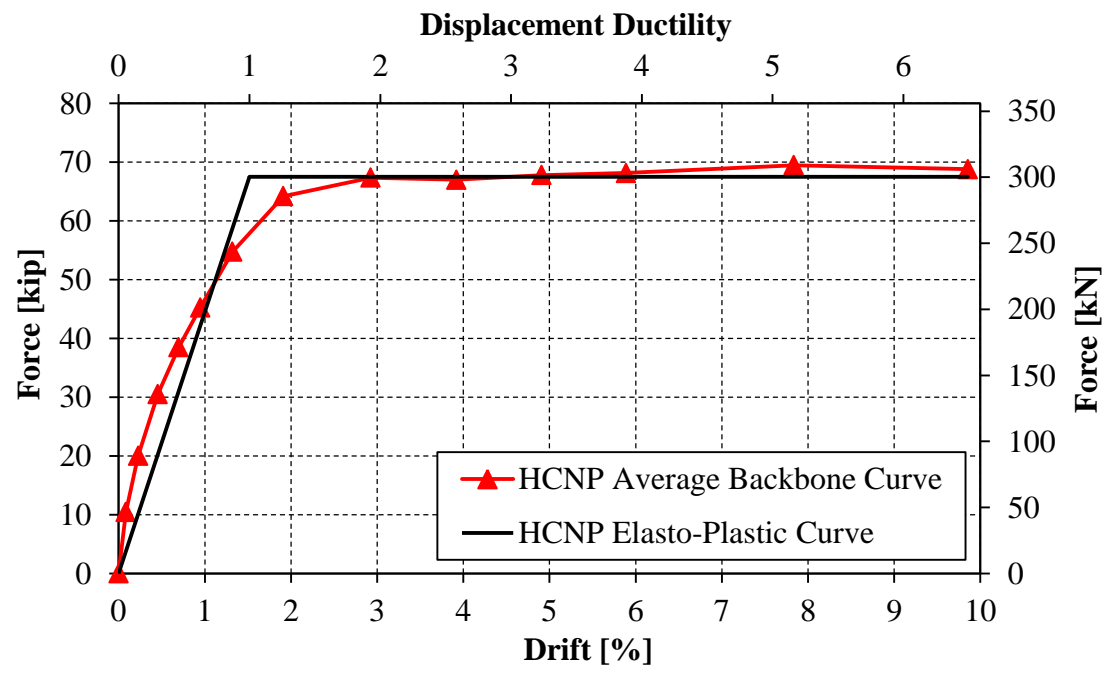
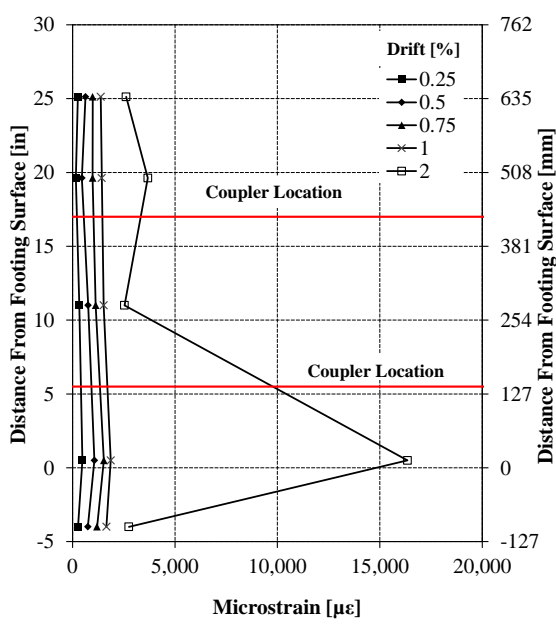
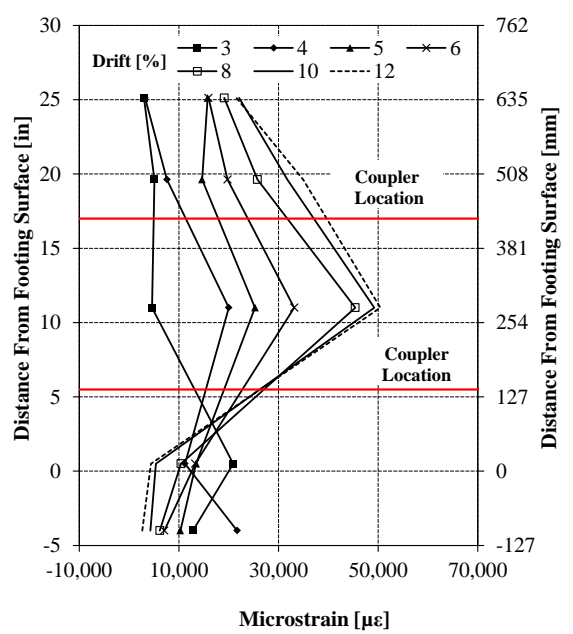


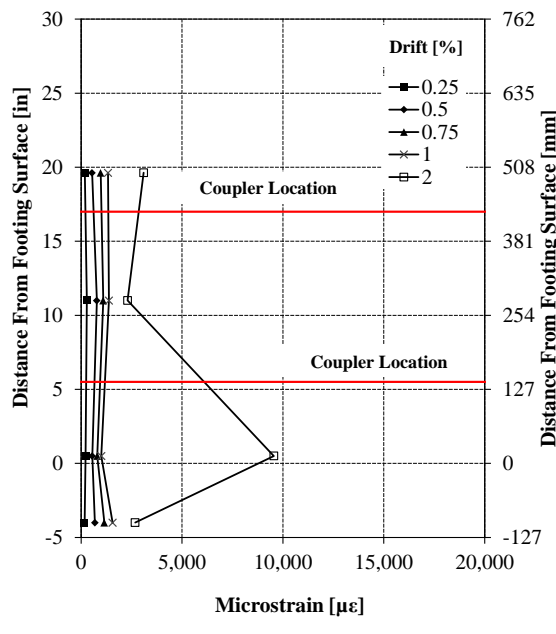
Figure 4-48 HCNP average force-displacement backbone curve



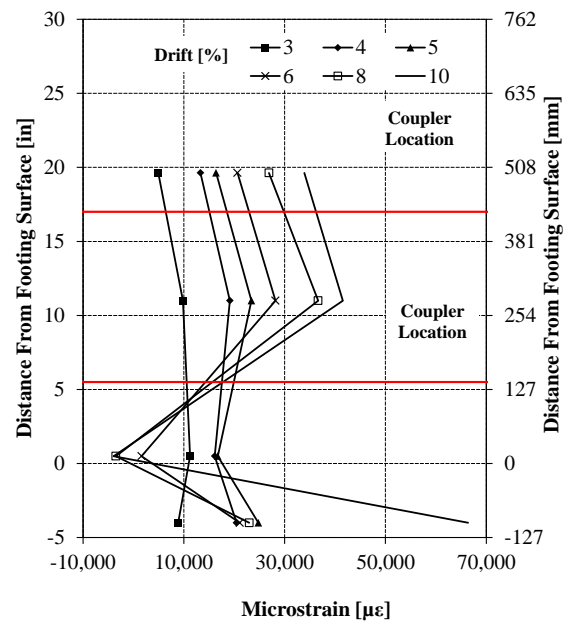
(a) Push cycle low drift levels



(b) Push cycle high drift levels



(c) Pull cycle low drift levels



(d) Pull cycle high drift levels

Figure 4-49 HCNP Measured longitudinal strain profiles

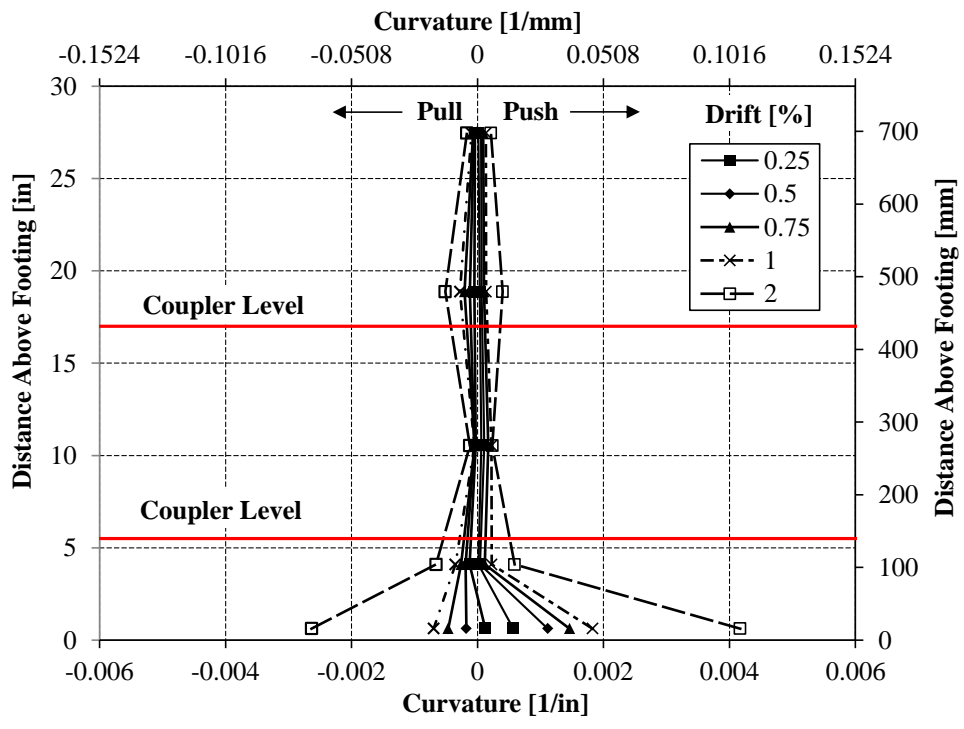


Figure 4-50 HCNP plastic hinge curvatures for lower drift levels

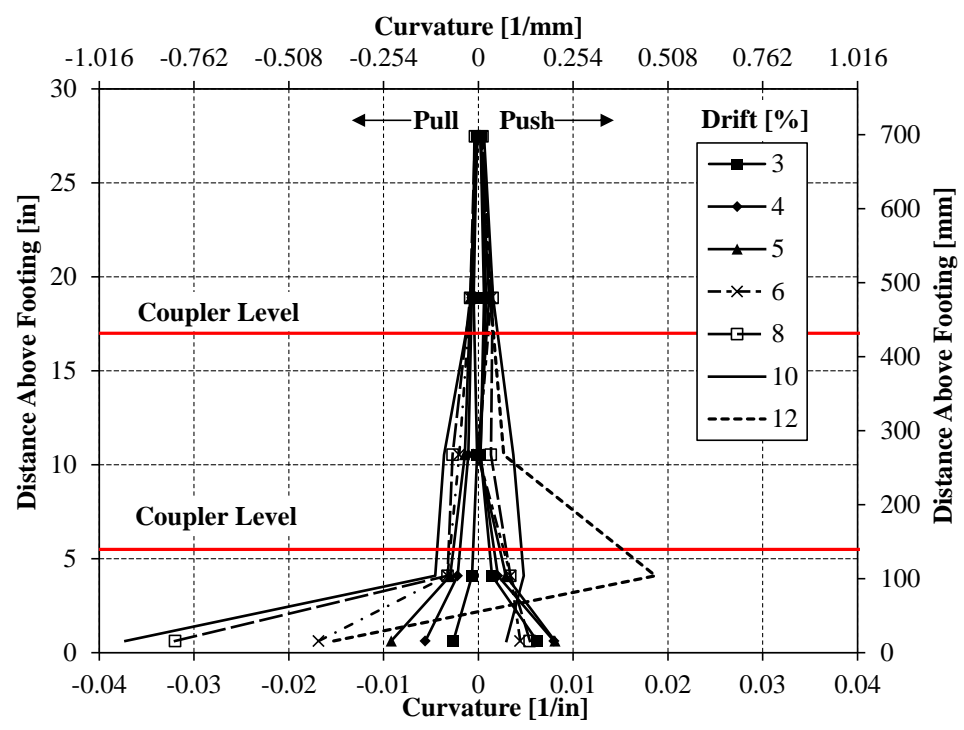


Figure 4-51 HCNP plastic hinge curvatures for higher drift levels

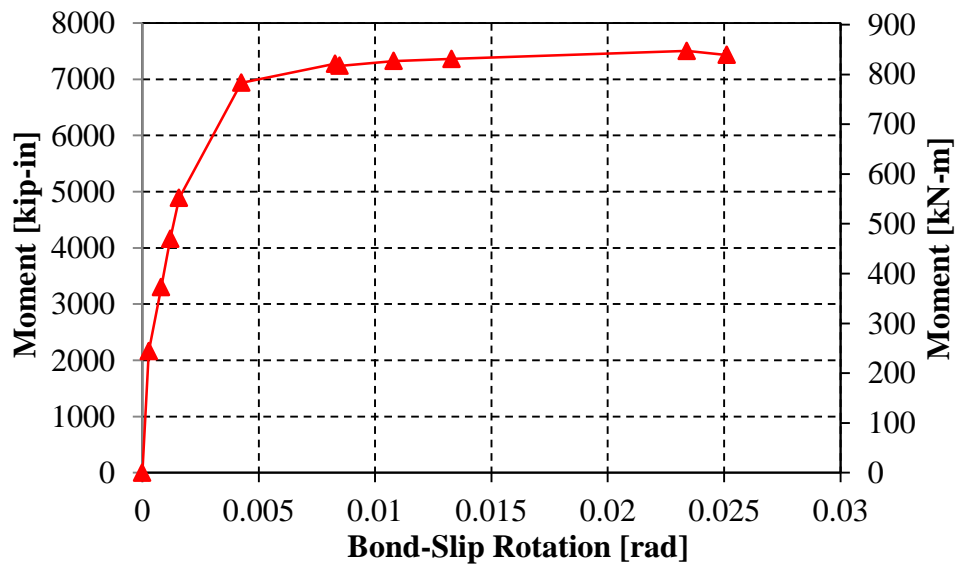


Figure 4-52 HCNP moment vs. bond-slip rotation relationship

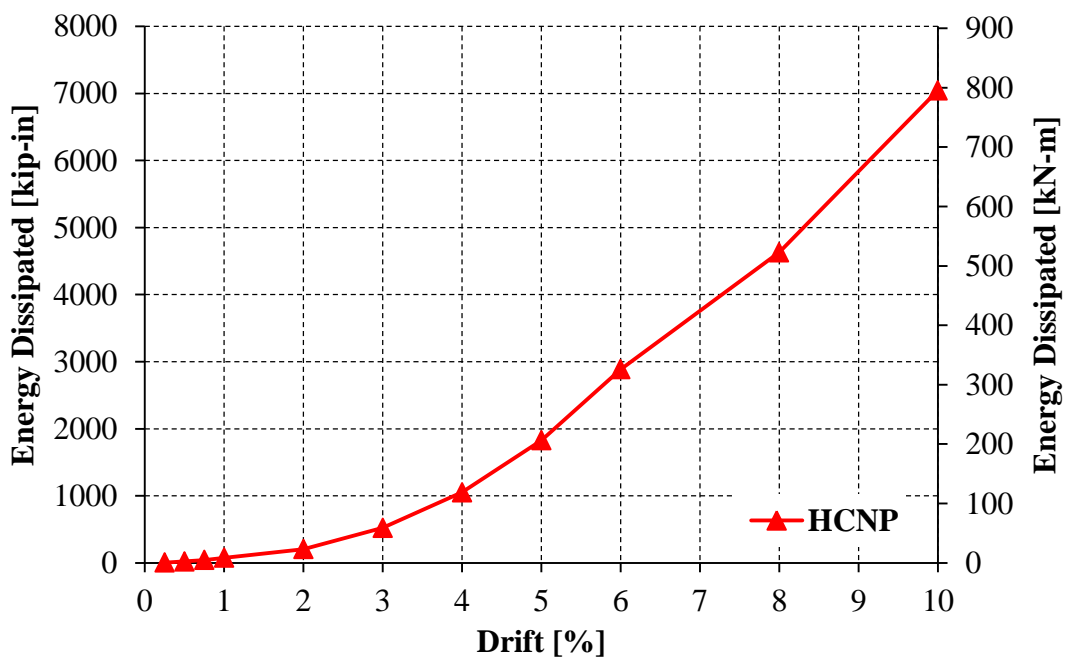


Figure 4-53 HCNP cumulative energy dissipation

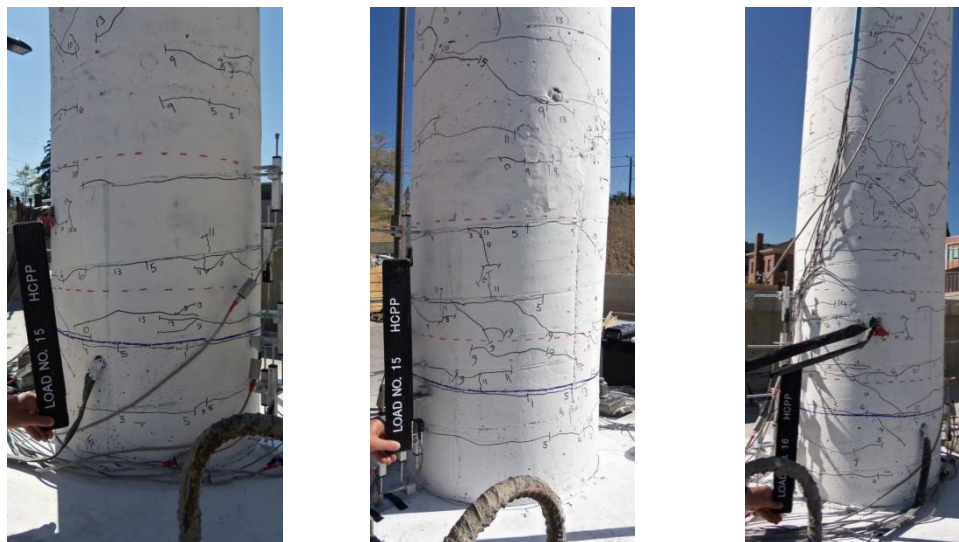


(a) North-east face second cycle of -0.25% drift

(b) North-east face second cycle of -0.5% drift

(c) South-west face first cycle of +0.75% drift

Figure 4-54. HCPP damage at drift levels less than 1%



(a) North-west face second push cycle

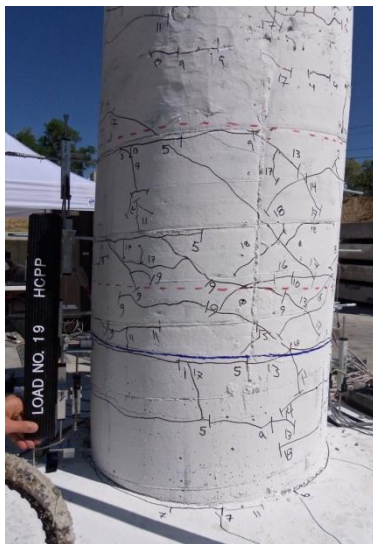
(b) South-west face second push cycle

(c) North-east face second pull cycle

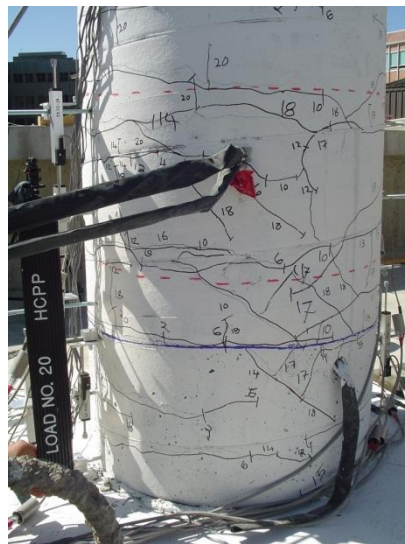
Figure 4-55 HCPP observed damage at 1.0% drift



(a) North-west face second push cycle



(b) South-west face second push cycle

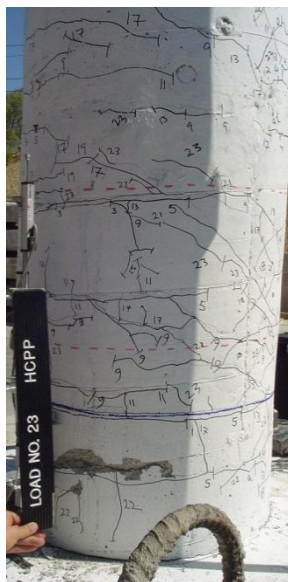


(c) North-east face second pull cycle

Figure 4-56 HCPP observed damage at 2.0% drift



(a) Pedestal-footing joint during first cycle (West face)



(b) South-west face second push cycle

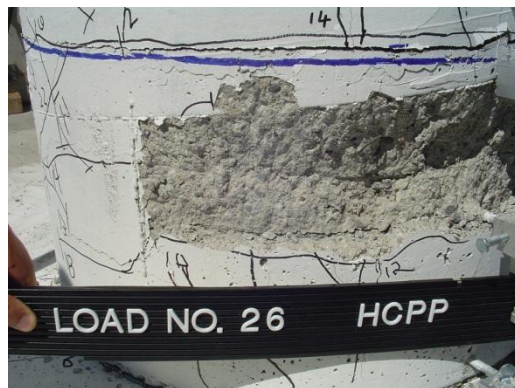


(c) East face second pull cycle

Figure 4-57 HCPP observed damage at 3.0% drift



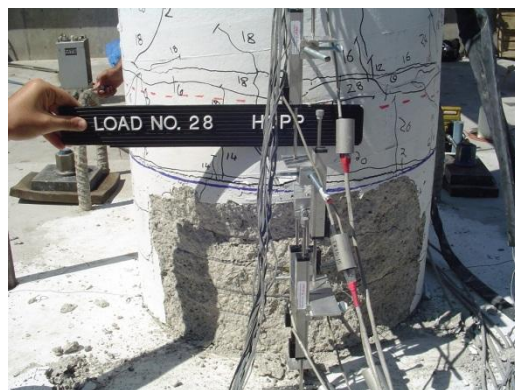
(a) Pedestal-footing joint during first push cycle (West face)



(b) Pedestal after first pull cycle (East face)



(c) West face second pull cycle

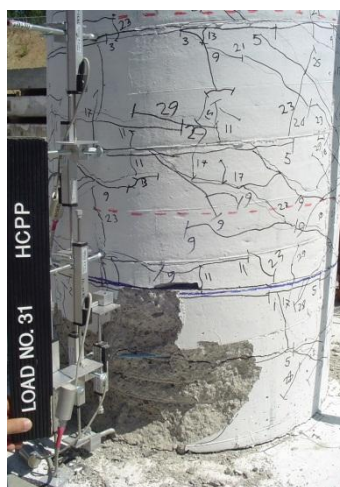


(d) East face second pull cycle

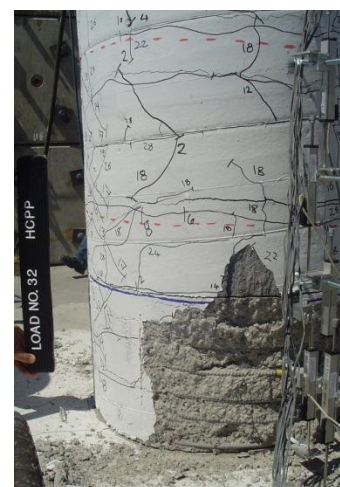
Figure 4-58 LCPP observed damage at 4.0% drift



(a) East face first pull cycle



(b) South-west face second push cycle



(c) South-east face second pull cycle

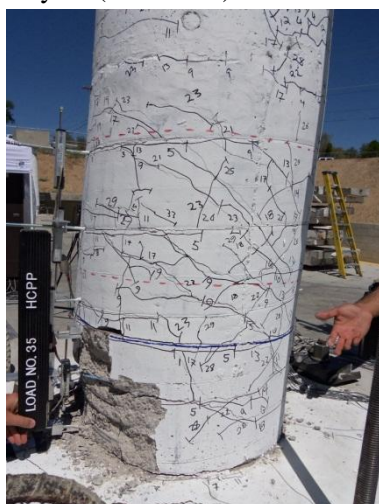
Figure 4-59 LCPP observed damage at 5.0% drift



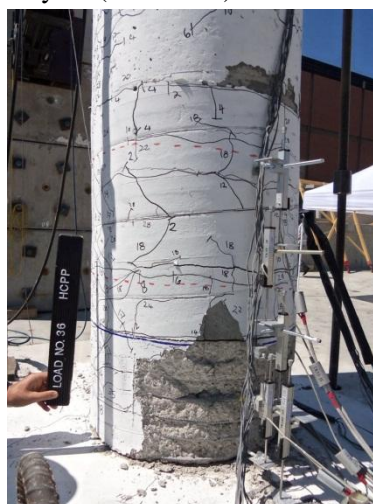
(a) Pedestal-footing joint during first push cycle (West face)



(b) Damage to footing after second push cycle (West face)



(c) South-west face second push cycle

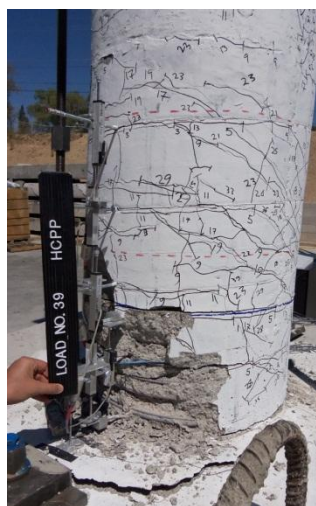


(d) South-east face second pull cycle

Figure 4-60 HCPP observed damage at 6.0% drift



(a) Pedestal-footing joint during second push cycle (West face)



(b) South-west face second push cycle



(c) North-east face second pull cycle

Figure 4-61 HCPP observed damage at 8.0% drift

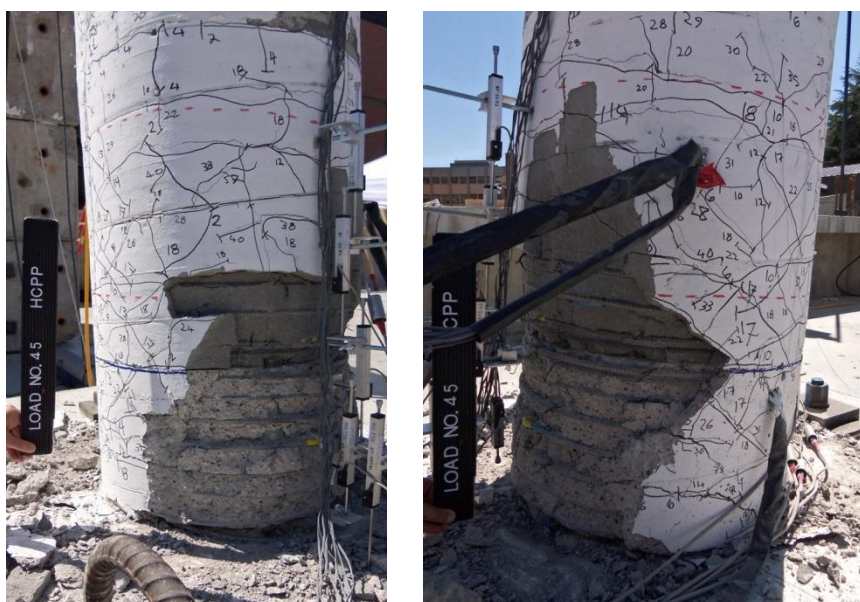


(a) West face first push cycle

(b) North-east face first pull cycle

(c) South-west face second push cycle

Figure 4-62 HCPP observed damage at 10.0% drift



(a) South-east face first pull cycle (b) North-east face first pull cycle

Figure 4-63 HCPP observed damage at 12.0% drift



Figure 4-64 Locations of fractured bar on the west face of HCPP



Figure 4-65 Location of fractured bar on the east face of HCPP



(a) Left bar from west face



(b) Center bar from west face



(c) Right bar from west face



(d) Right bar from east face

Figure 4-66 Bars and pedestal ducts removed from HCPP

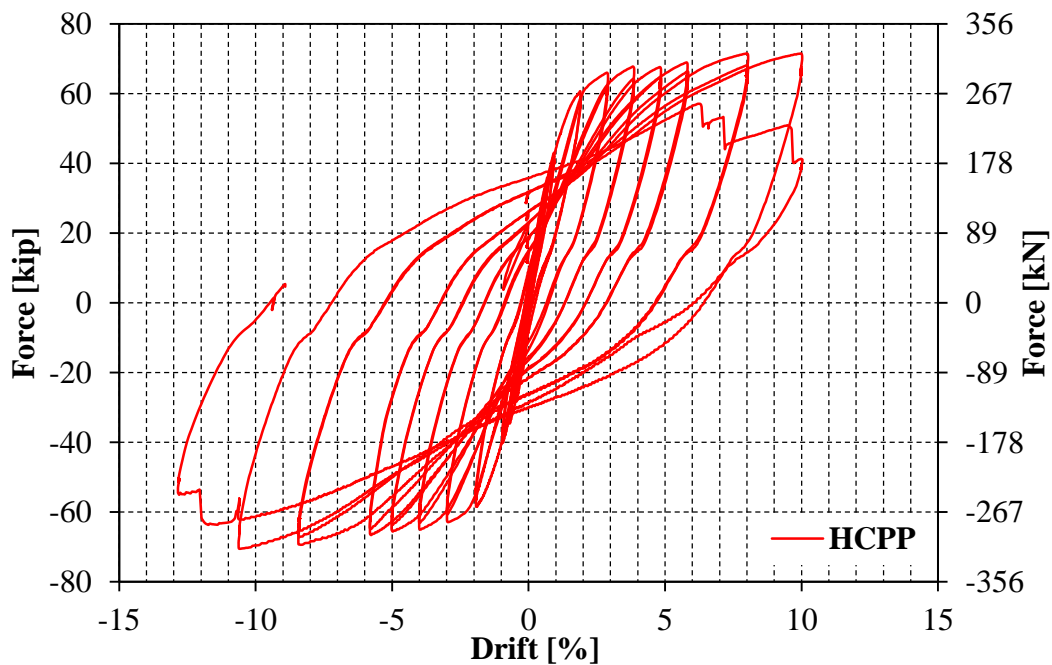


Figure 4-67 HCPP hysteretic force-displacement response

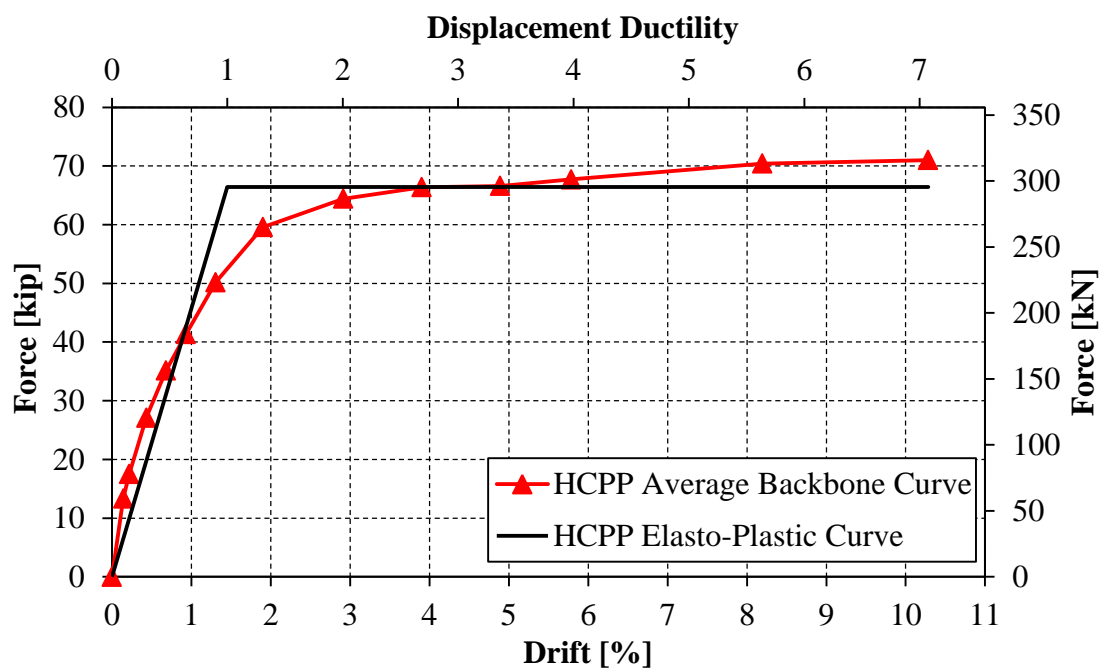
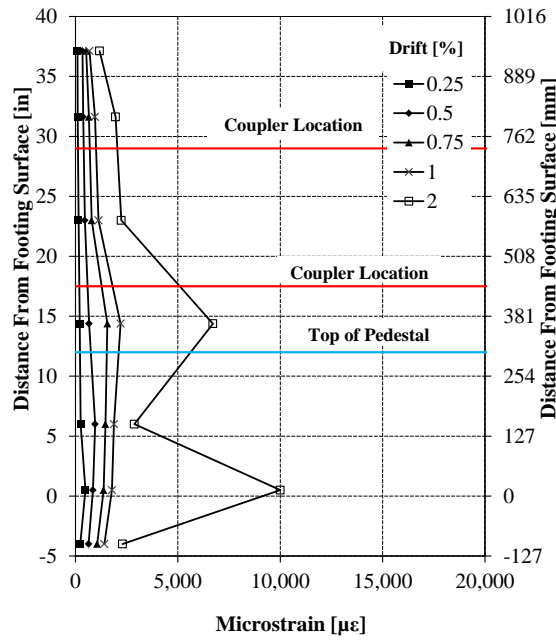
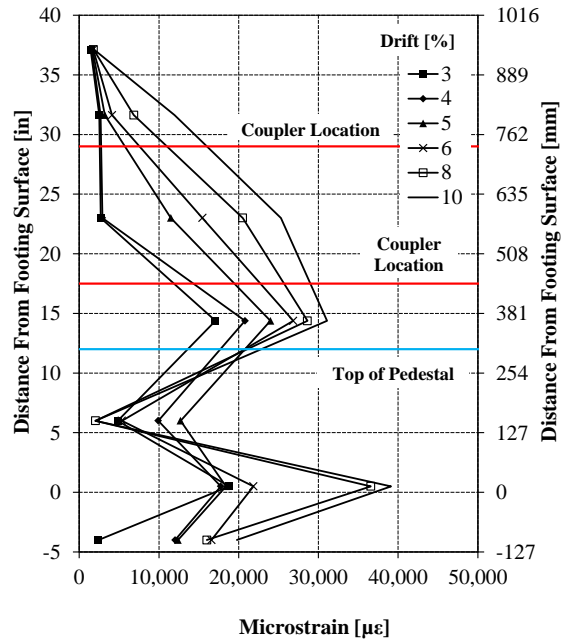


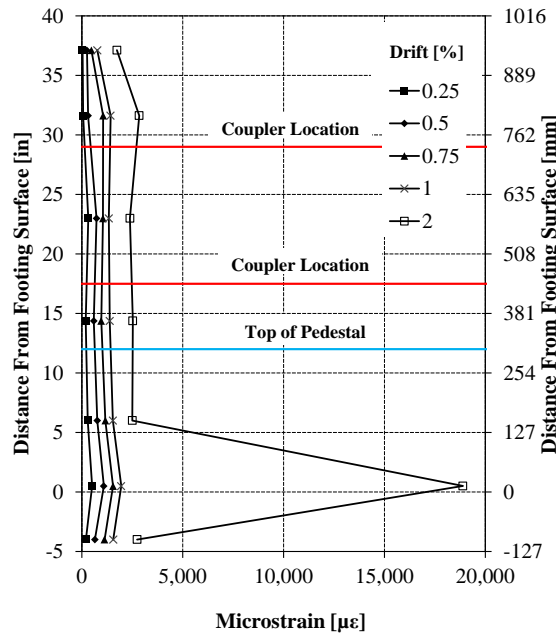
Figure 4-68 HCPP average force-displacement backbone curve



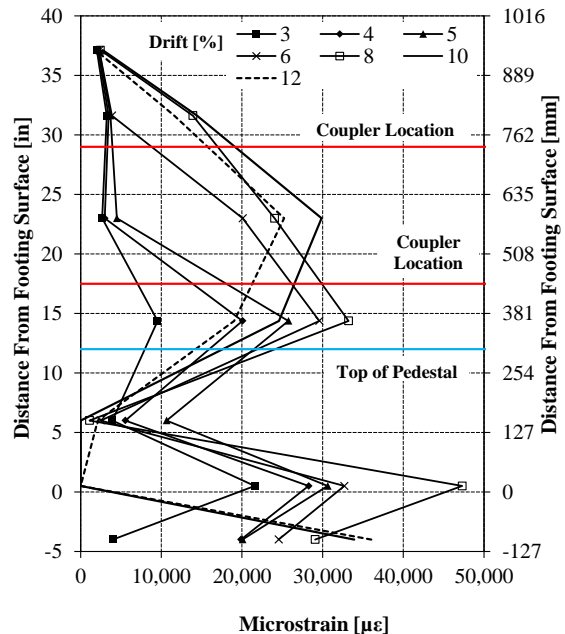
(a) Push cycle low drift levels



(b) Push cycle high drift levels



(c) Pull cycle low drift levels



(d) Pull cycle high drift levels

Figure 4-69 Measured longitudinal tensile strain profiles for HCPP

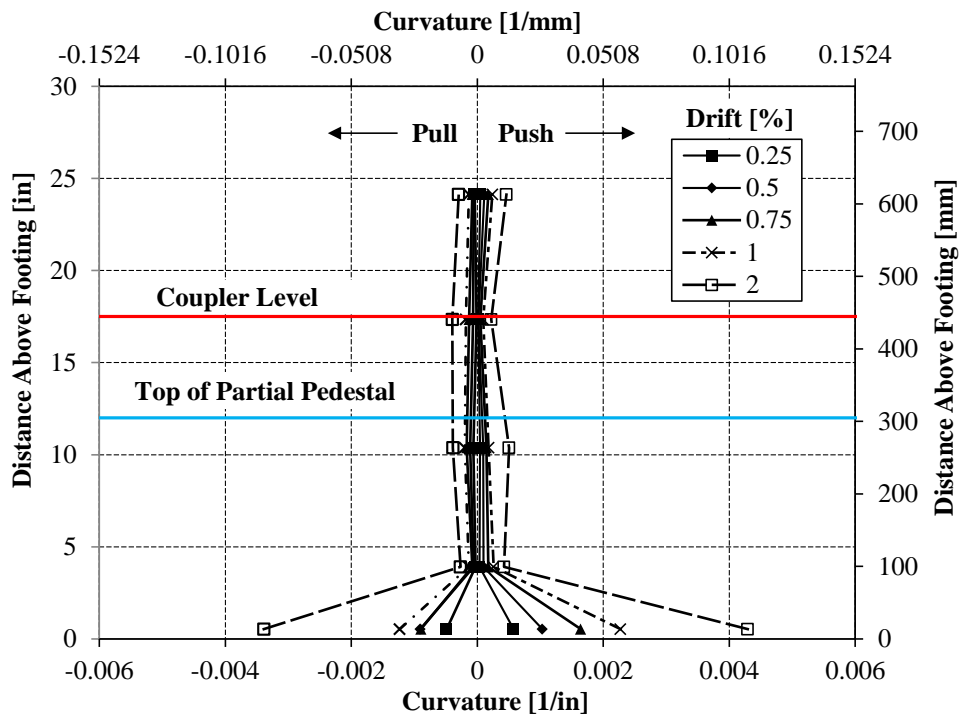


Figure 4-70 HCPP plastic hinge curvatures for lower drift levels

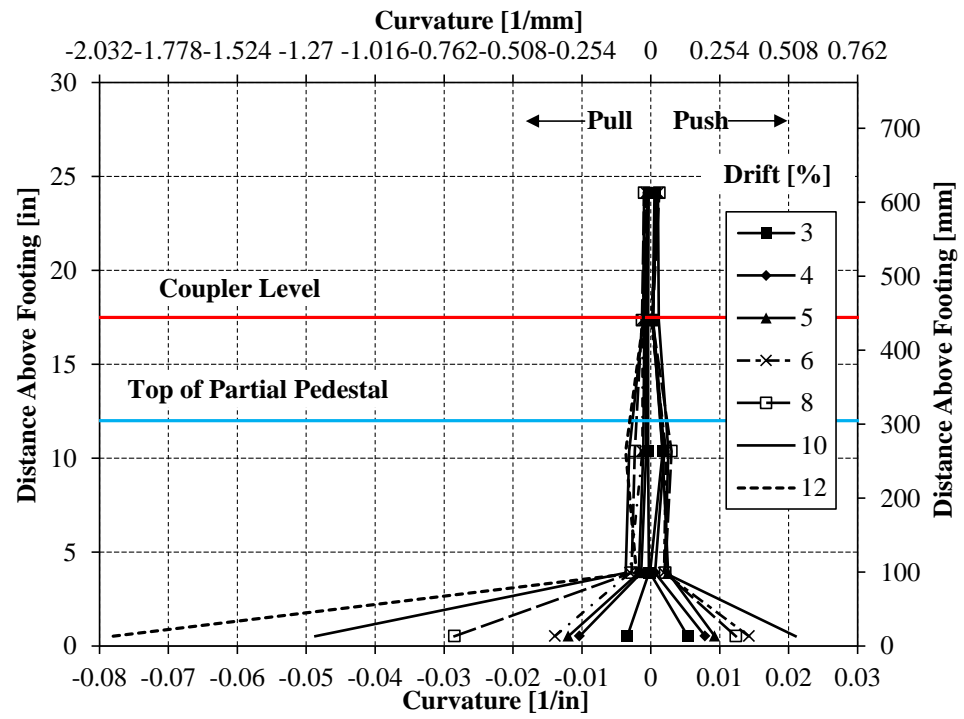


Figure 4-71 HCPP plastic hinge curvatures for higher drift levels

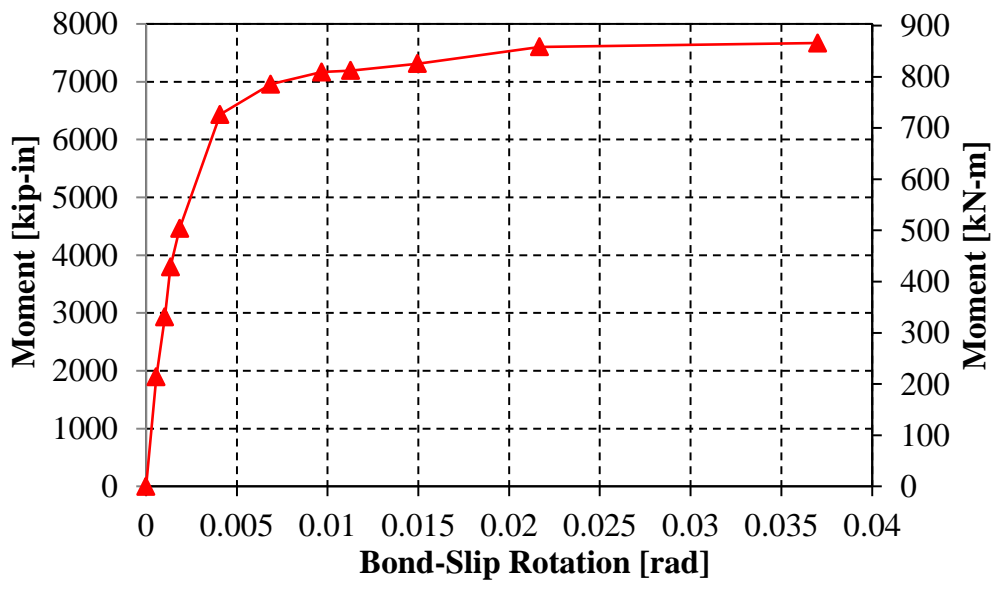


Figure 4-72 HCPP moment vs. bond-slip rotation relationship

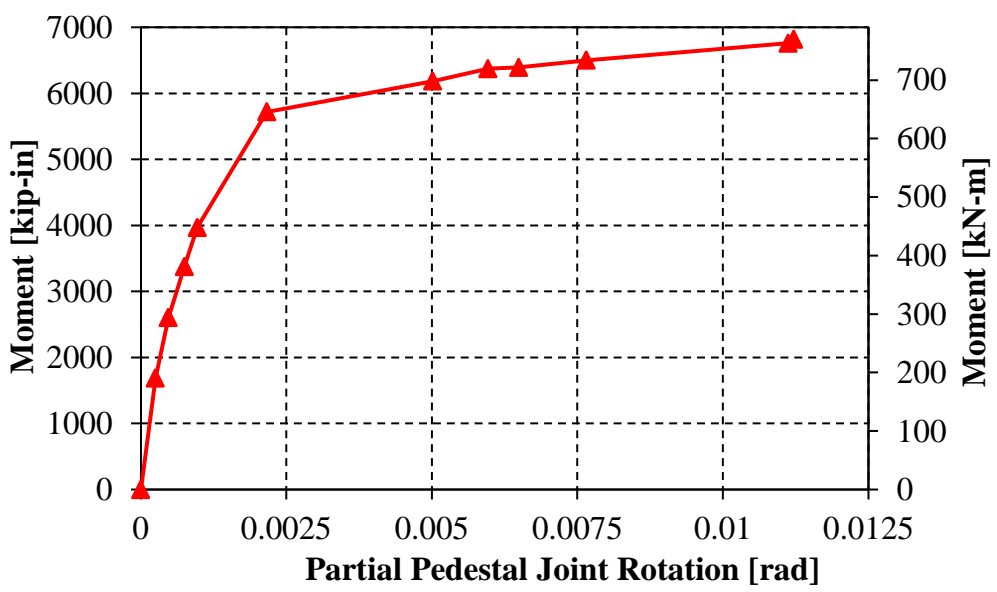


Figure 4-73 HCPP moment vs. pedestal joint rotation

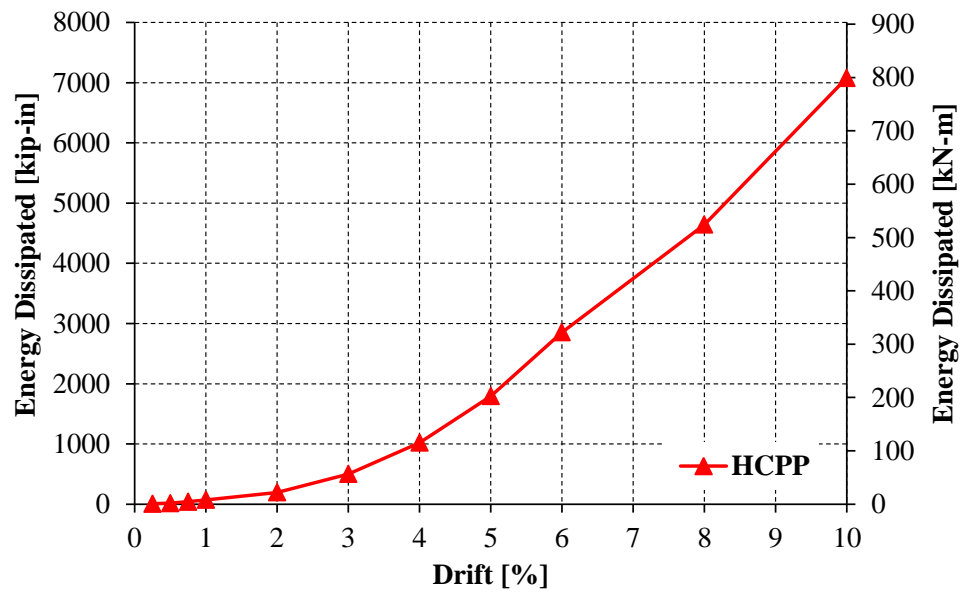
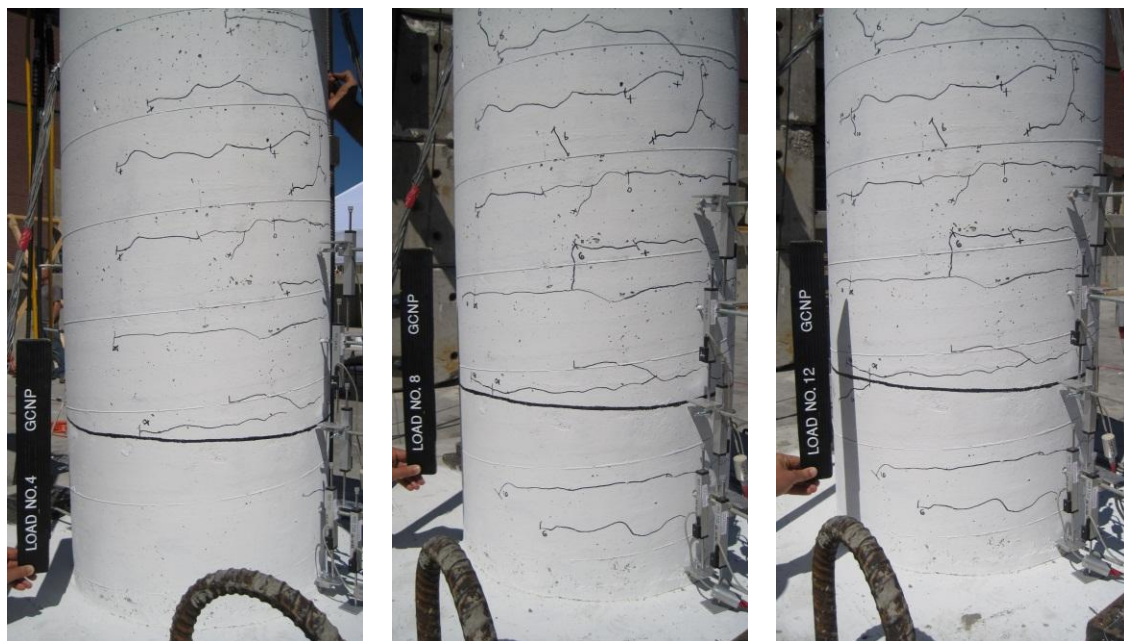


Figure 4-74 HCPP cumulative energy dissipation



(a) South-east face second cycle of 0.25% drift

(b) South-east face second cycle of 0.5% drift

(c) South-east face second cycle of 0.75% drift

Figure 4-75 Damage observed for GCNP at drift levels less than 1%

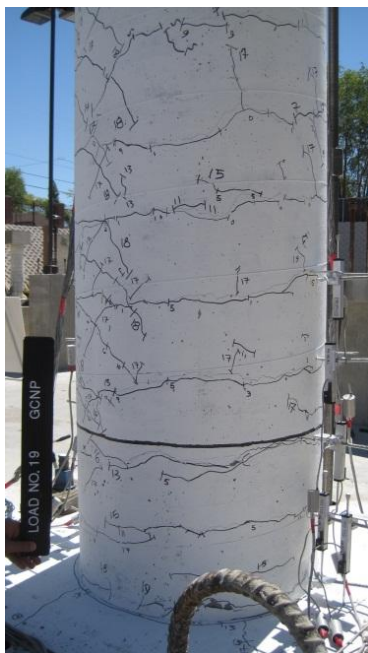


(a) South-west face second push cycle

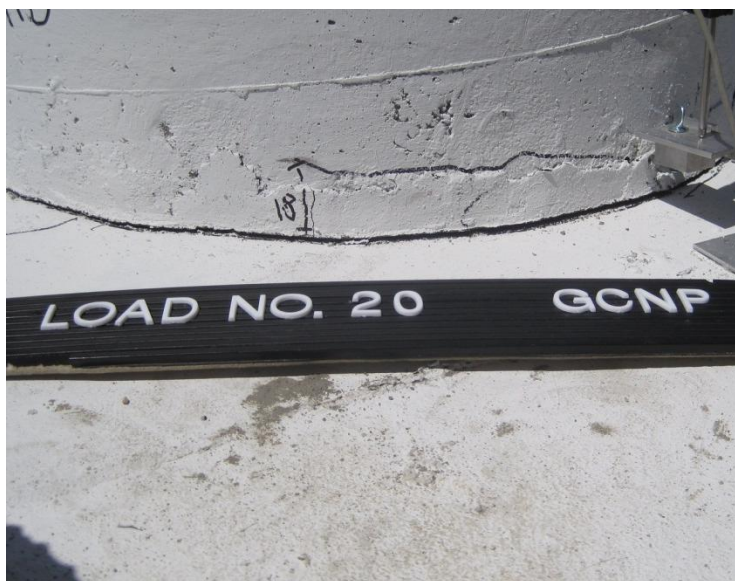
(b) North-west face second push cycle

(c) North-east face second pull cycle

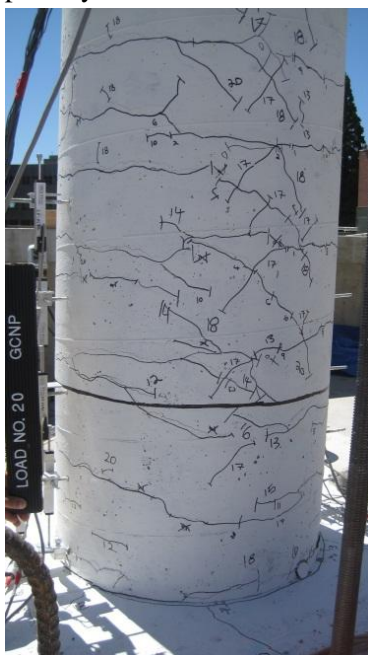
Figure 4-76 GCNP observed damage at 1.0% drift



(a) North-west face second push cycle



(b) Column-footing joint (east face) during second pull cycle



(c) North-east face second pull cycle

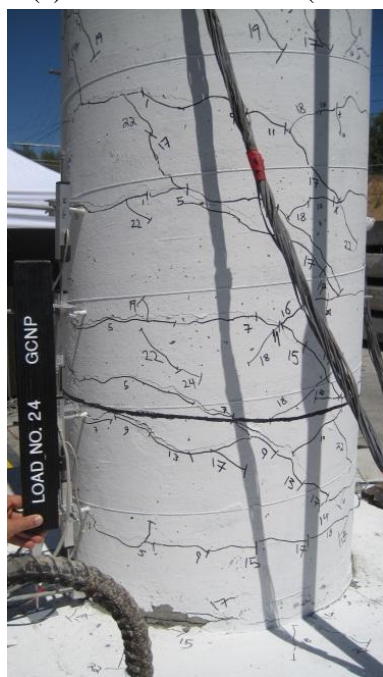


(d) South-east face second pull cycle

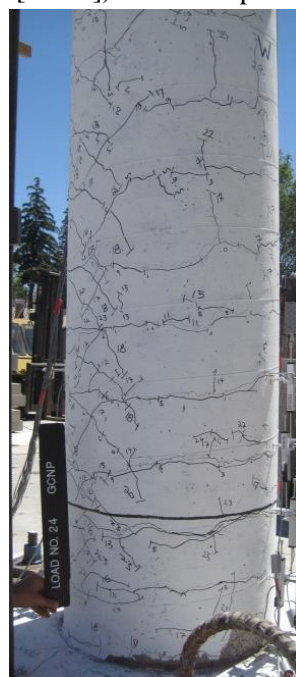
Figure 4-77 GCNP observed damage at 2.0% drift



(a) Concentrated crack (≈ 0.12 in [3 mm]) above coupler region during second push cycle



(b) South-west face second push cycle

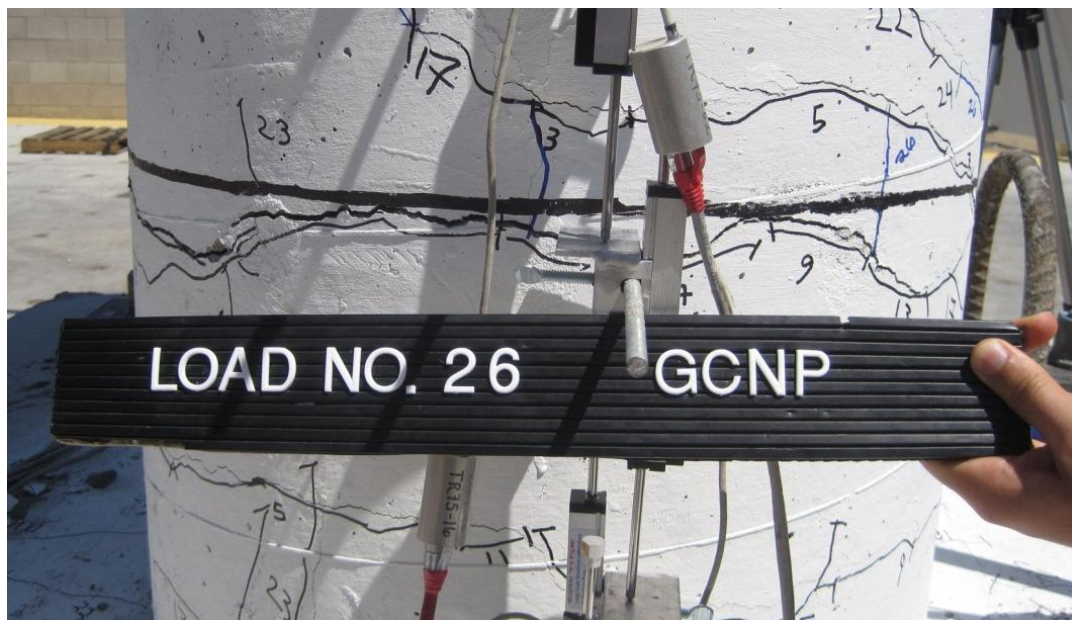


(c) North-west face second push cycle

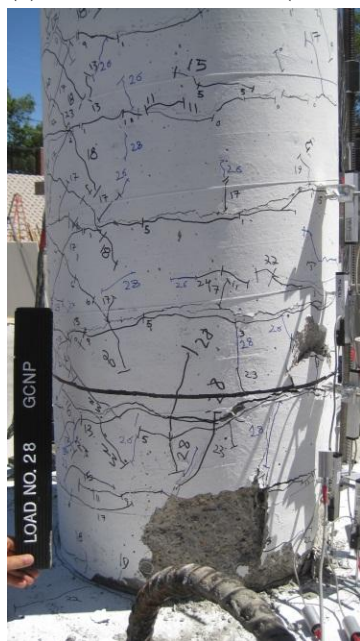


(d) South-east face second pull cycle

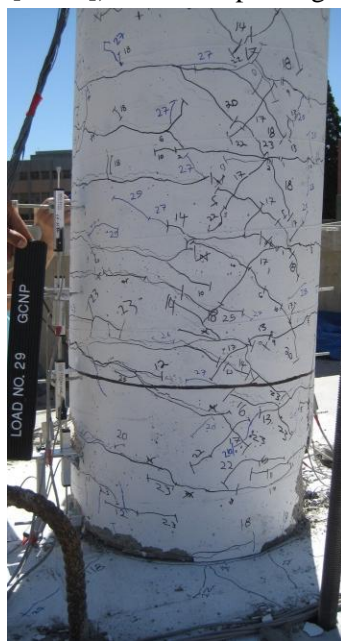
Figure 4-78 GCNP observed damage at 3.0% drift



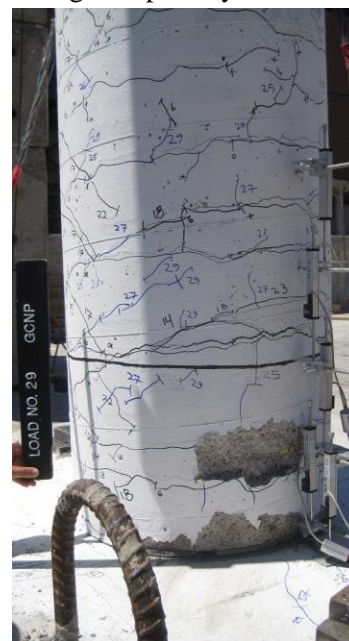
(a) Concentrated crack (≈ 0.19 in [5 mm]) above coupler region during first push cycle



(b) North-west face second push cycle



(c) North-east face second pull cycle

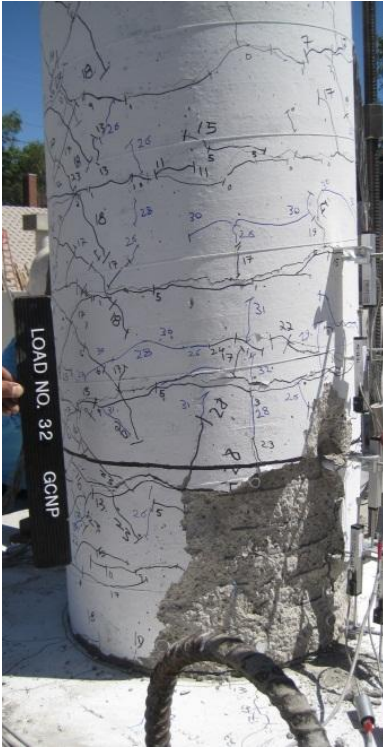


(d) South-east face second pull cycle

Figure 4-79 GCNP observed damage at 4.0% drift



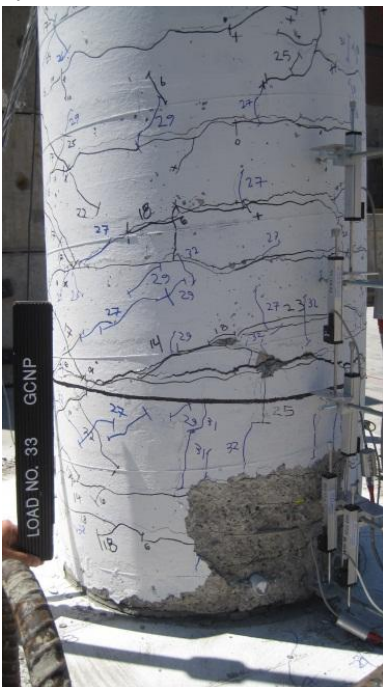
(a) Column-footing joint during first pull cycle (east face)



(b) North-west face second push cycle



(c) Concentrated cracking above coupler region during second push cycle (east face)



(d) South-east face second pull cycle

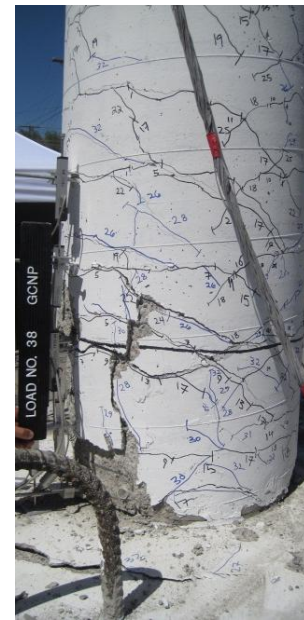
Figure 4-80 GCNP observed damage at 5.0% drift



(a) Column-footing joint during first push cycle (west face)



(b) South-east face second pull cycle



(c) South-west face third push cycle

Figure 4-81 GCNP observed damage at 6.0% drift



(a) Footing damage on west face during first push cycle



(b) South-west face first push cycle

Figure 4-82 GCNP observed damage at 8.0% drift



Figure 4-83 Location of removed grouted coupler (center bar west face)



(a) Center bar from west face



(b) Left side bar from east face

Figure 4-84 Couplers removed from GCNP



Figure 4-85 Grout cone due to strain penetration

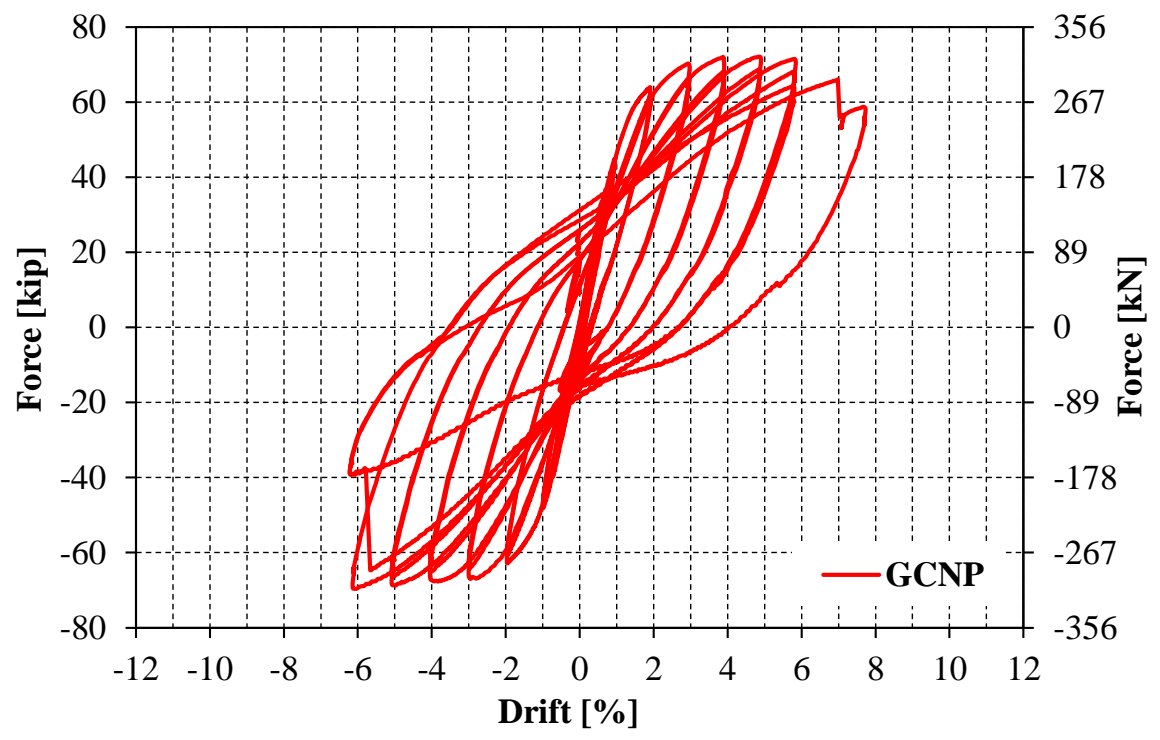


Figure 4-86 GCNP hysteretic force-displacement response

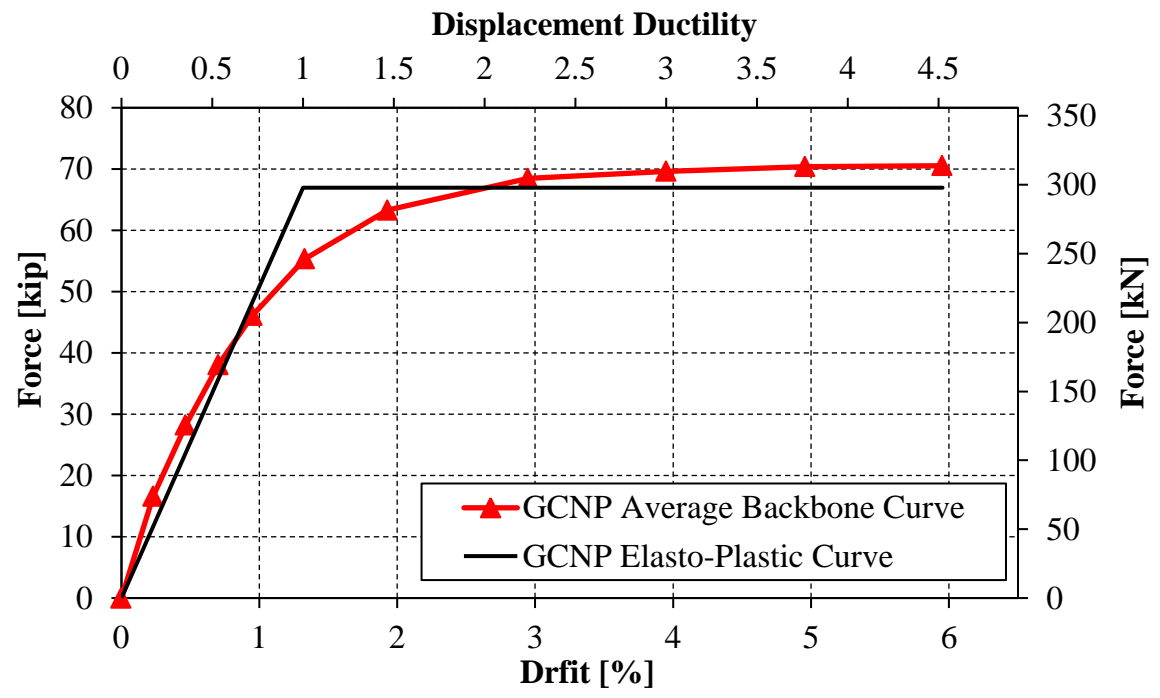
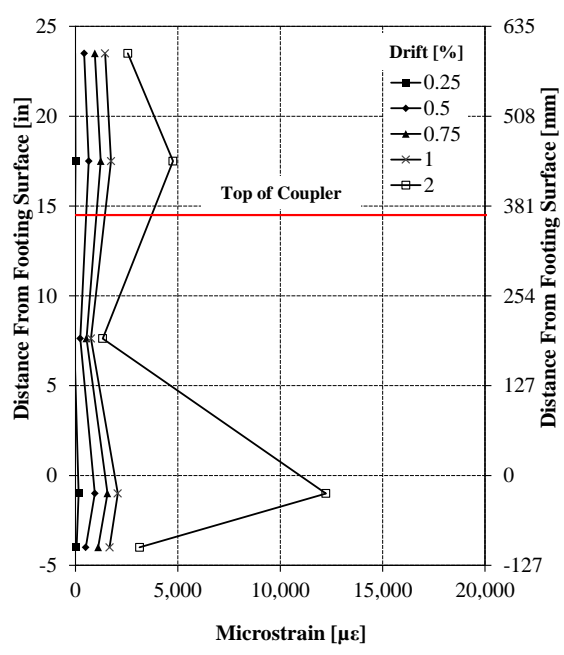
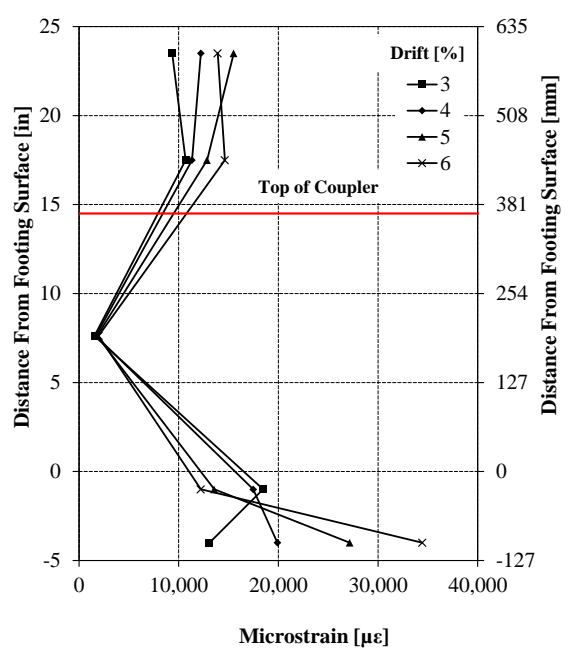


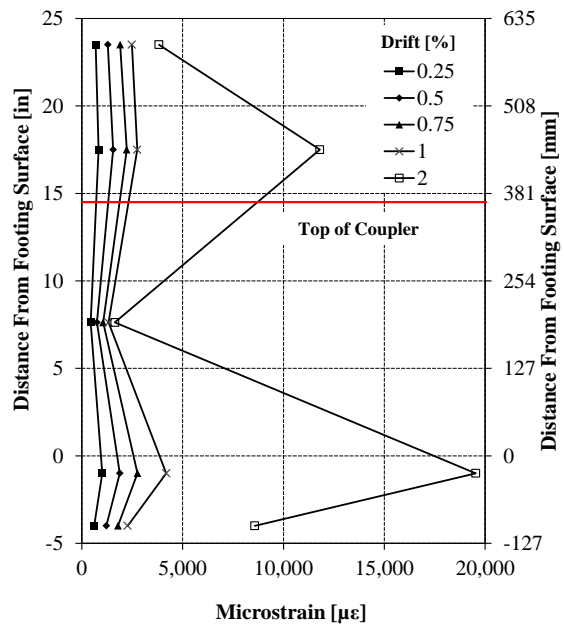
Figure 4-87 GCNP average force-displacement backbone curve



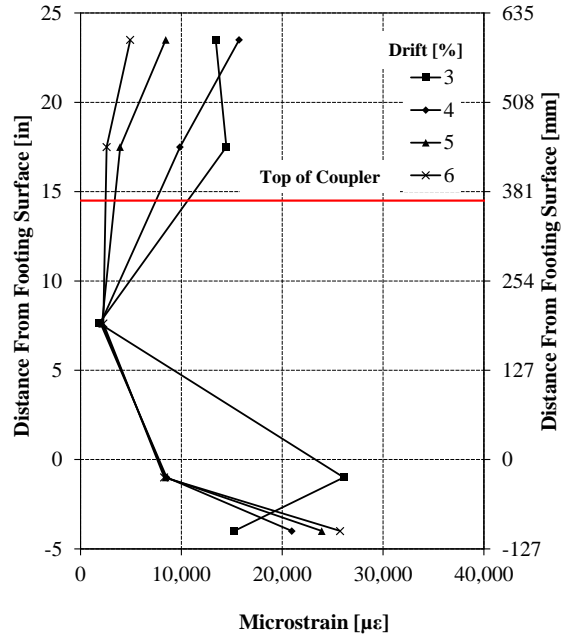
(a) Push cycle low drift levels



(b) Push cycle high drift levels



(c) Pull cycle low drift levels



(d) Pull cycle high drift levels

Figure 4-88 Measured average longitudinal tensile strain profiles for GCNP

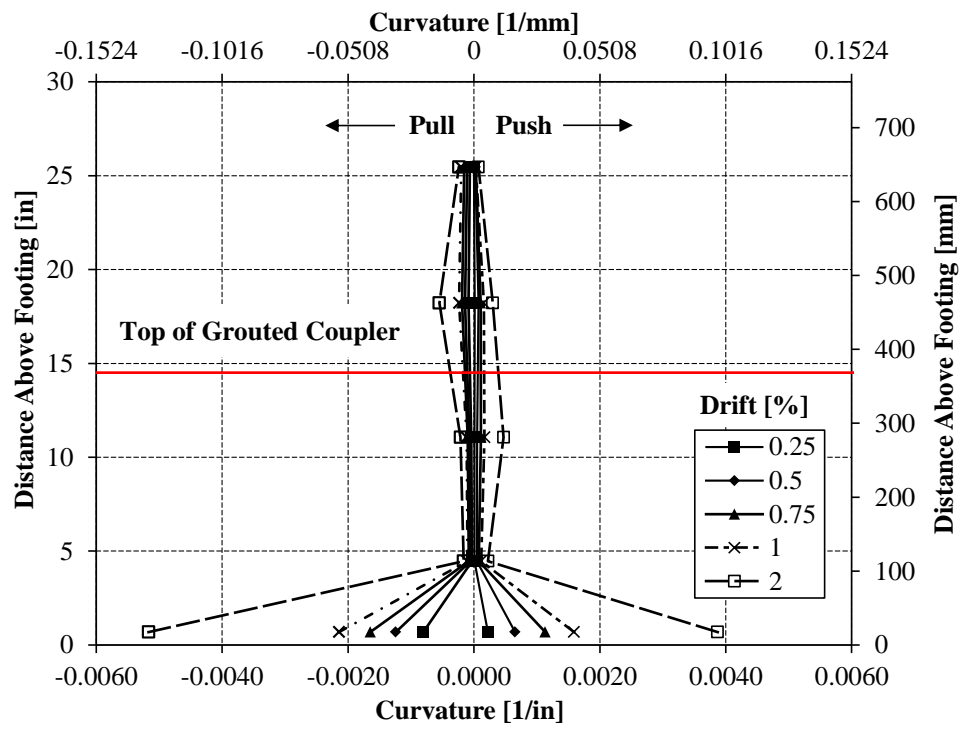


Figure 4-89 GCNP plastic hinge curvatures for lower drift levels

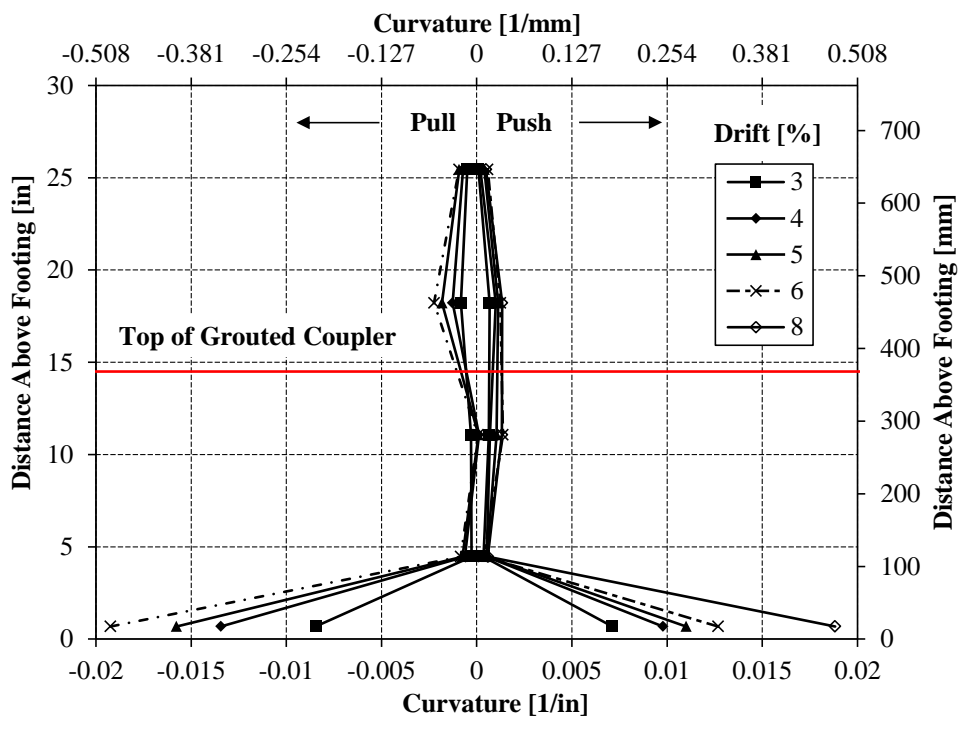


Figure 4-90 GCNP plastic hinge curvatures for higher drift levels

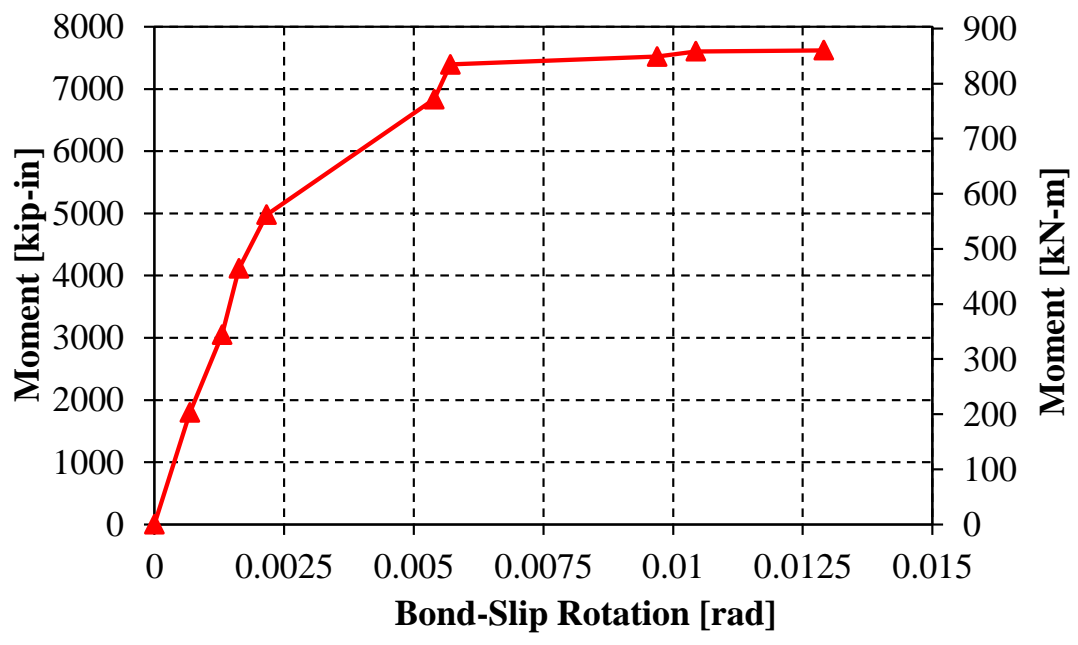


Figure 4-91 GCNP moment vs. bond-slip rotation relationship

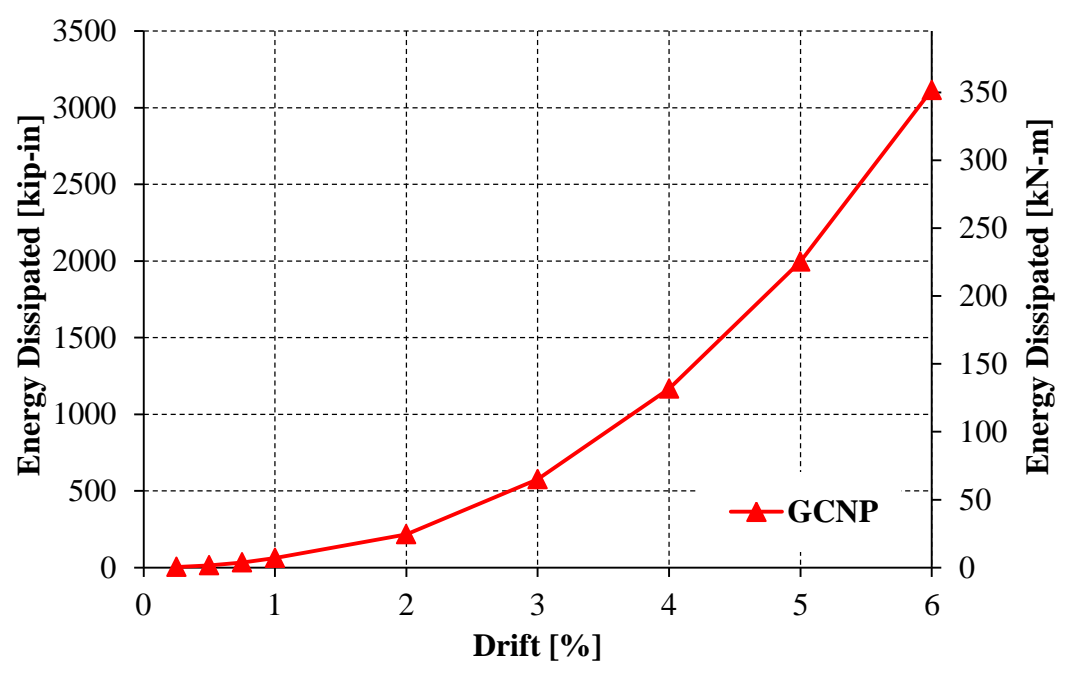


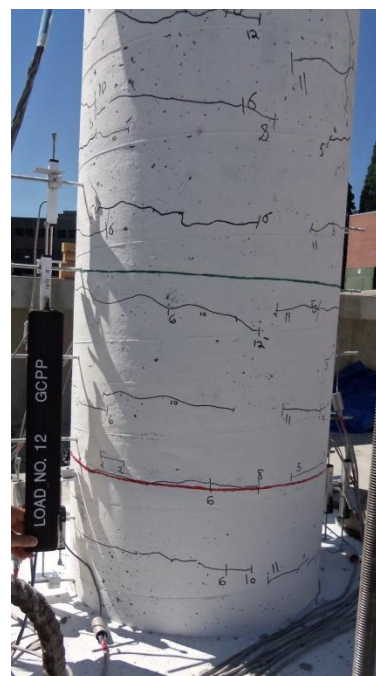
Figure 4-92 GCNP cumulative energy dissipation



(a) South-east face second pull cycle of 0.25% drift

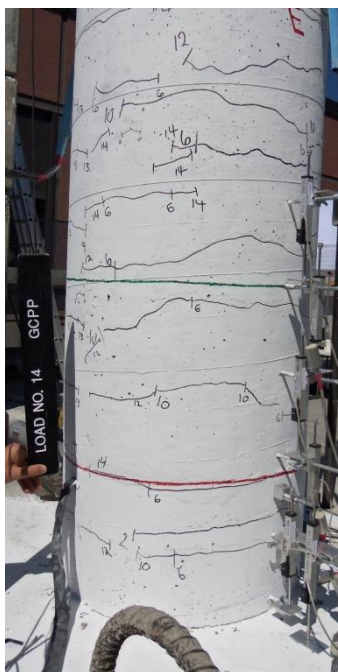


(b) South-east face second pull cycle of 0.5% drift

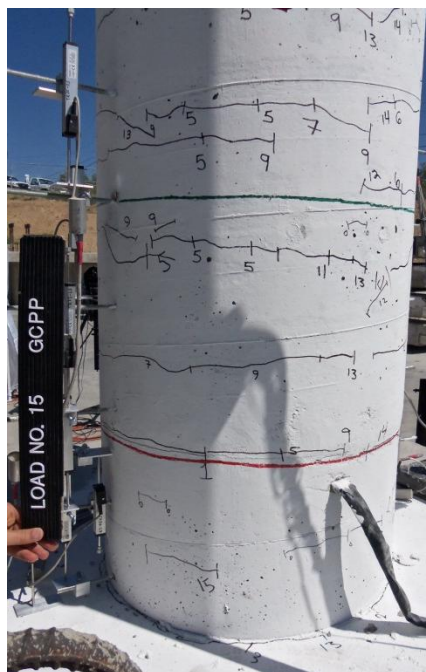


(c) North-east face second pull cycle of 0.75% drift

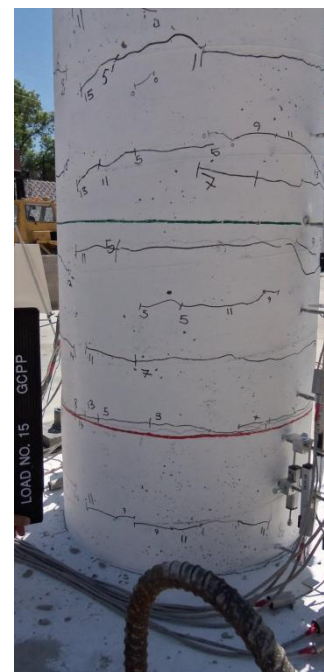
Figure 4-93 Damage observed for GCPP at drift levels less than 1%



(a) South-east face first pull cycle



(b) South-west face second push cycle

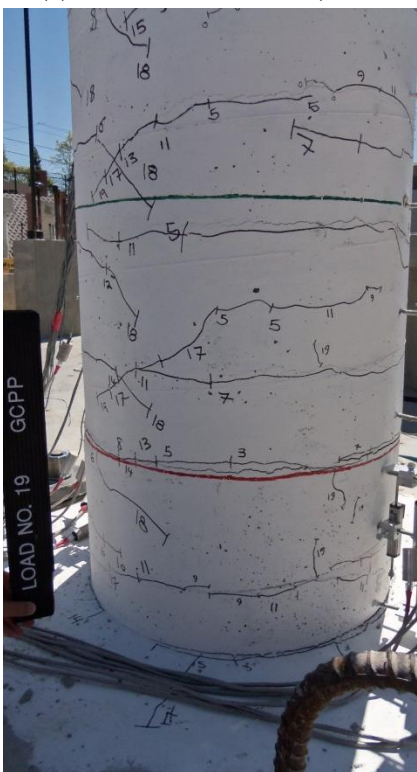


(c) North-west face second push cycle

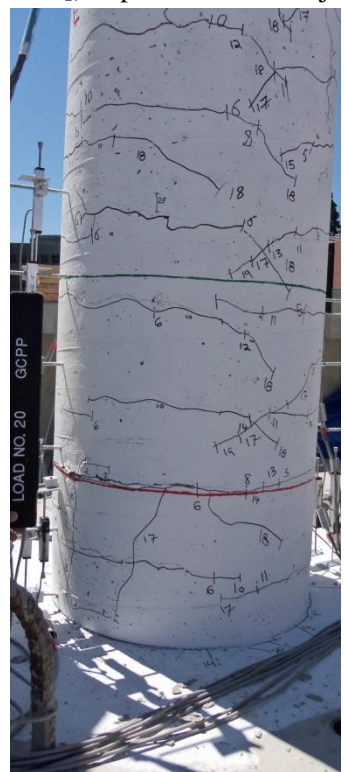
Figure 4-94 GCPP observed damage at 1.0% drift



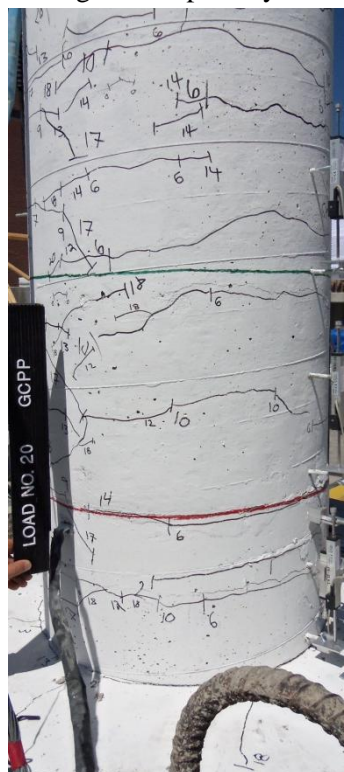
(a) Concentrated crack (≈ 0.08 in [2 mm]) at pedestal-column joint during second push cycle



(a) North-west face second push cycle



(b) North-east face second pull cycle

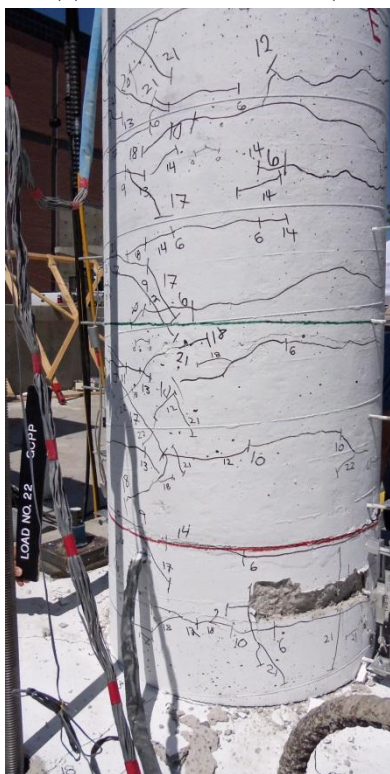


(c) South-east face second pull cycle

Figure 4-95 GCPP observed damage at 2.0% drift



(a) Concentrated crack (≈ 0.14 in [3.5 mm]) at pedestal-column joint during first pull cycle



(a) South-east face first pull cycle

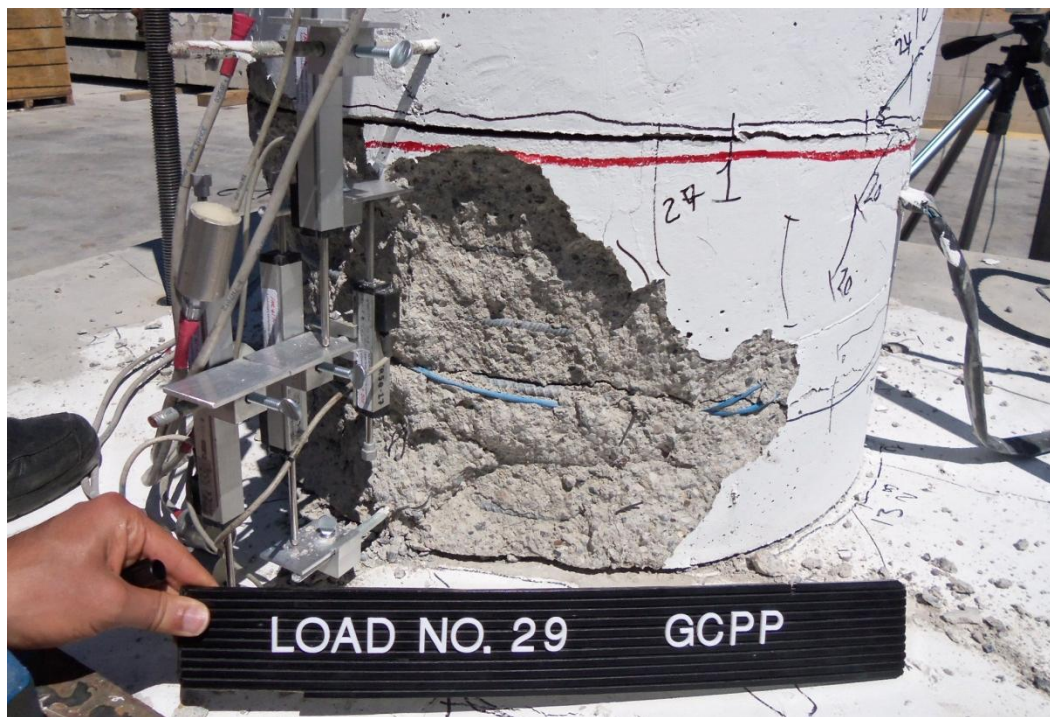


(b) North-east face first pull cycle

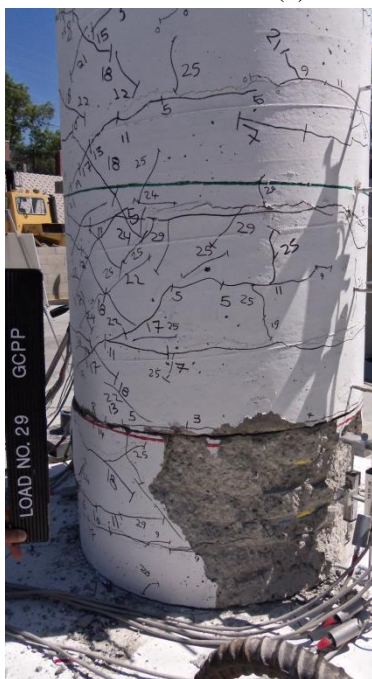


(c) North-west face second push cycle

Figure 4-96 GCPP observed damage at 3.0% drift



(a) Joint opening during first push cycle (west face)



(b) North-west face first push cycle



(c) North-east face first pull cycle

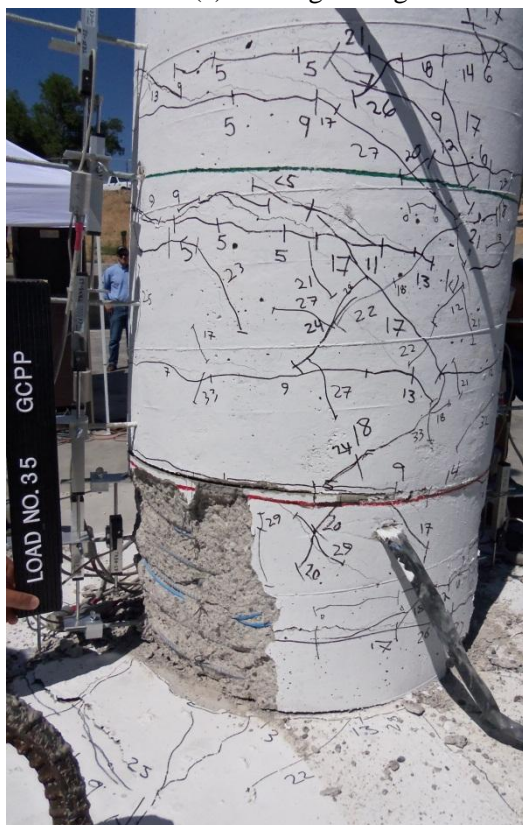


(d) South-east face second pull cycle

Figure 4-98 GCPP observed damage at 5.0% drift



(a) Footing damage on west face during first push cycle



(b) South-west face second push cycle



(c) East face second pull cycle

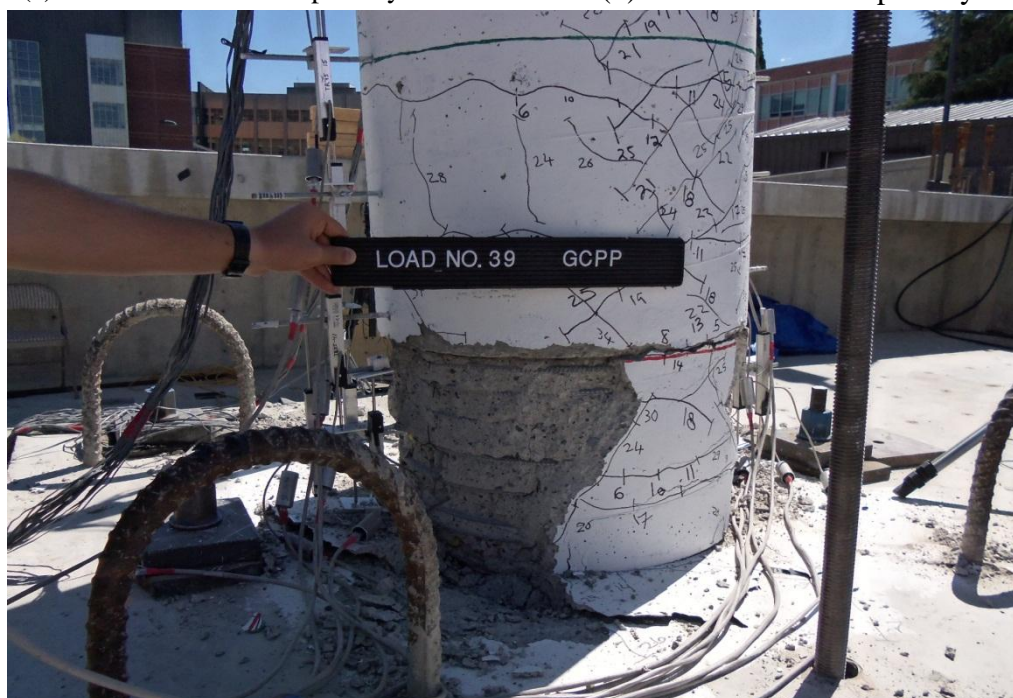
Figure 4-99 GCPP observed damage at 6.0% drift



(a) South-west face first push cycle



(b) West face second push cycle



(c) North-east face second push cycle

Figure 4-100 GCPP observed damage at 8.0% drift



Figure 4-101 Bar fracture location of west face of GCPP



Figure 4-102 Bar fracture location of east face of GCPP

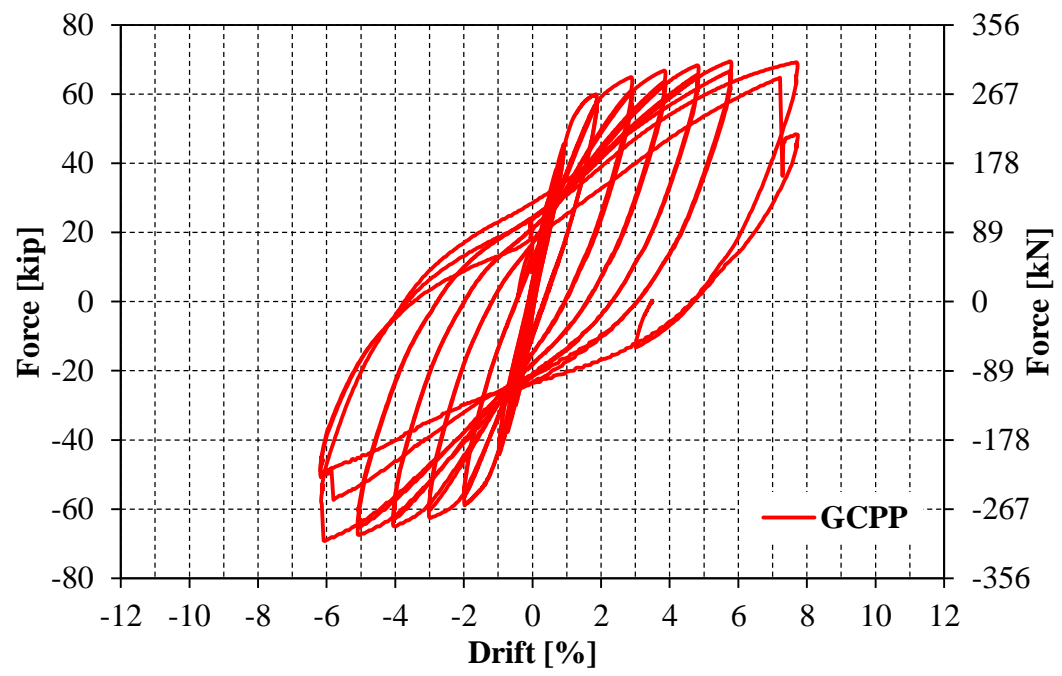


Figure 4-103 GCPP hysteretic force-displacement response

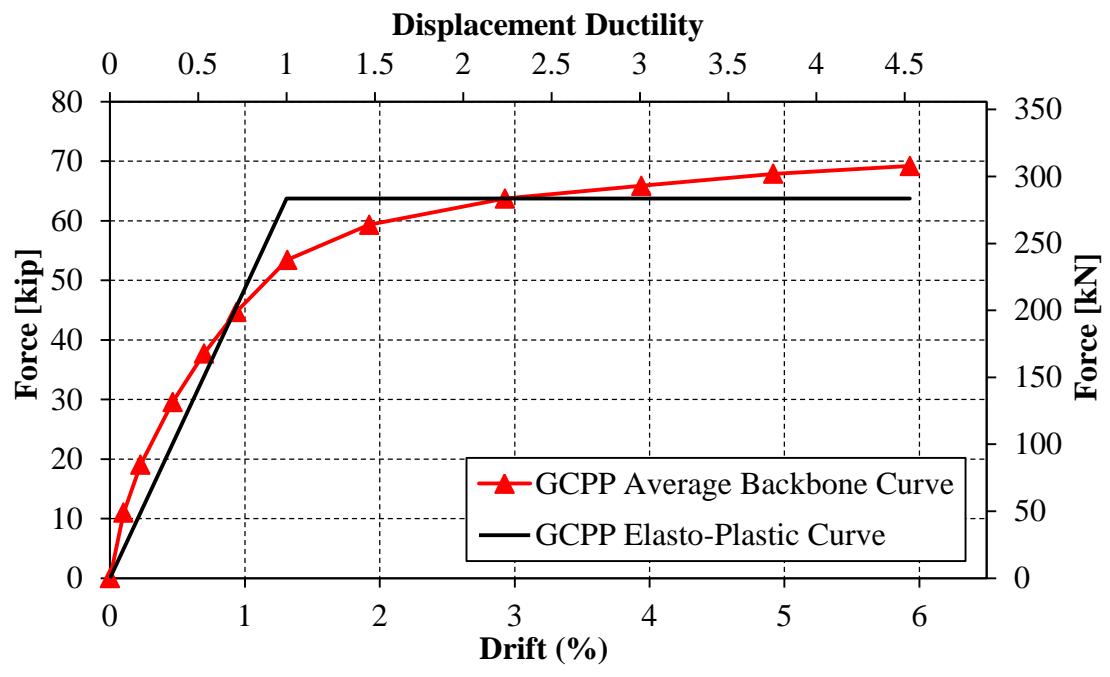
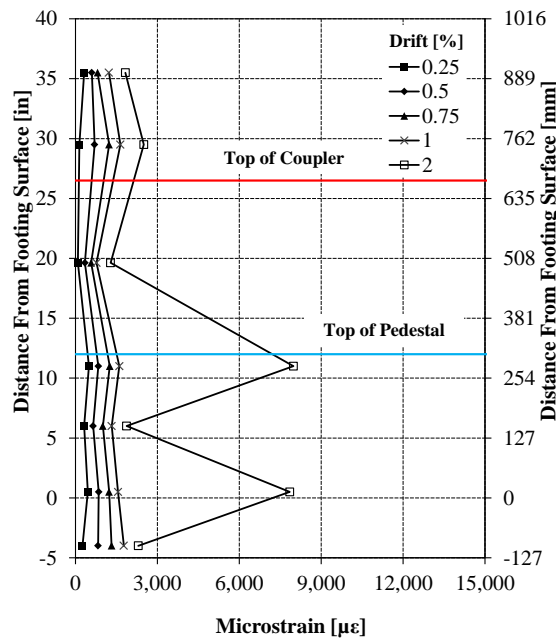
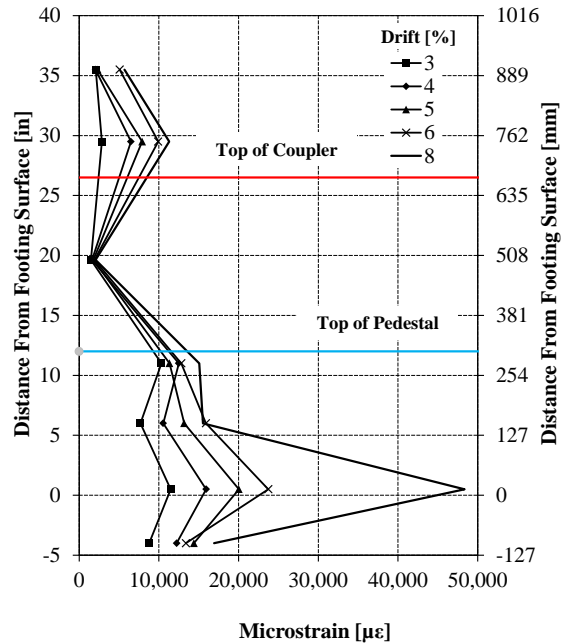


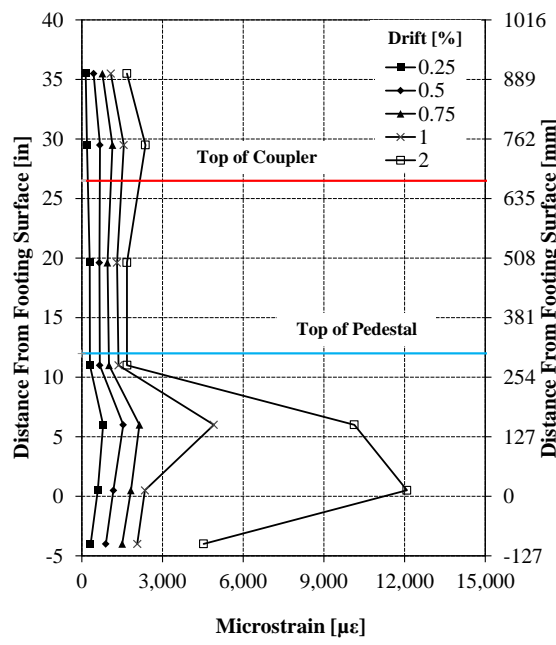
Figure 4-104 GCPP average force-displacement backbone curve



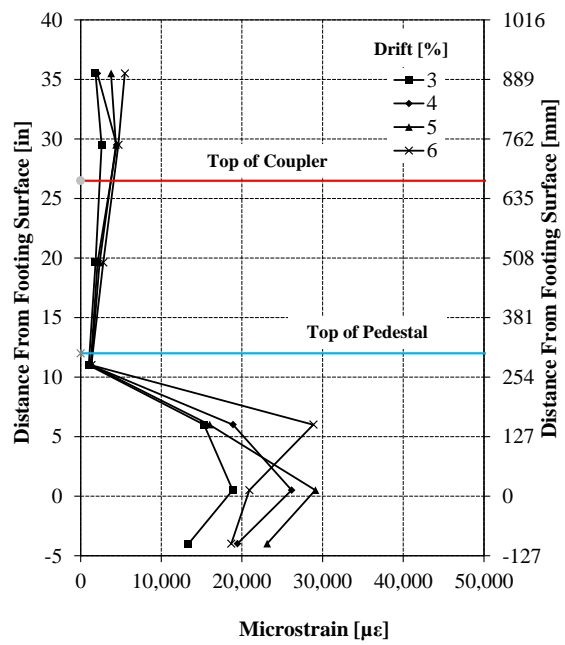
(a) Push cycle low drift levels



(b) Push cycle high drift levels



(c) Pull cycle low drift levels



(d) Pull cycle high drift levels

Figure 4-105 GCPP measured longitudinal strain profiles

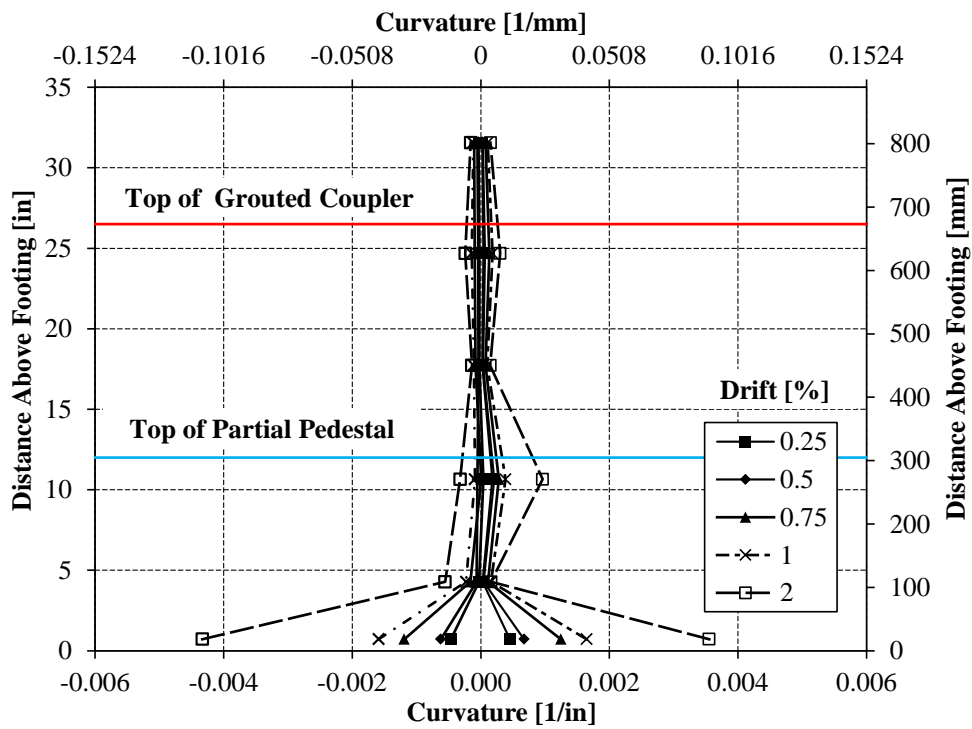


Figure 4-106 GCPP plastic hinge curvatures for lower drift levels

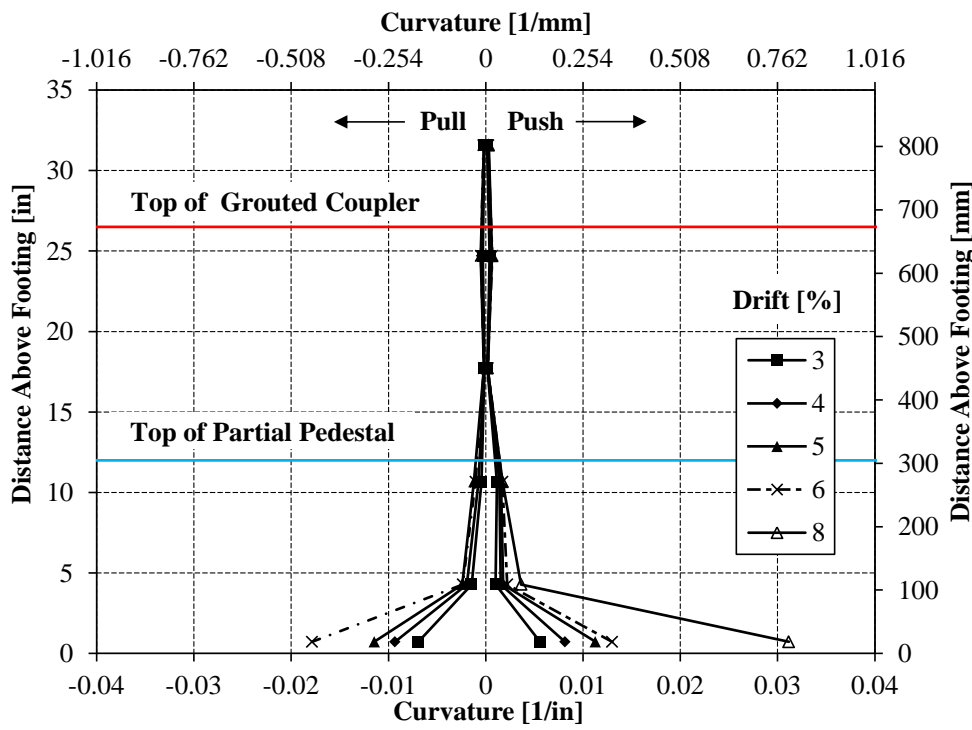


Figure 4-107 GCPP plastic hinge curvatures for higher drift levels

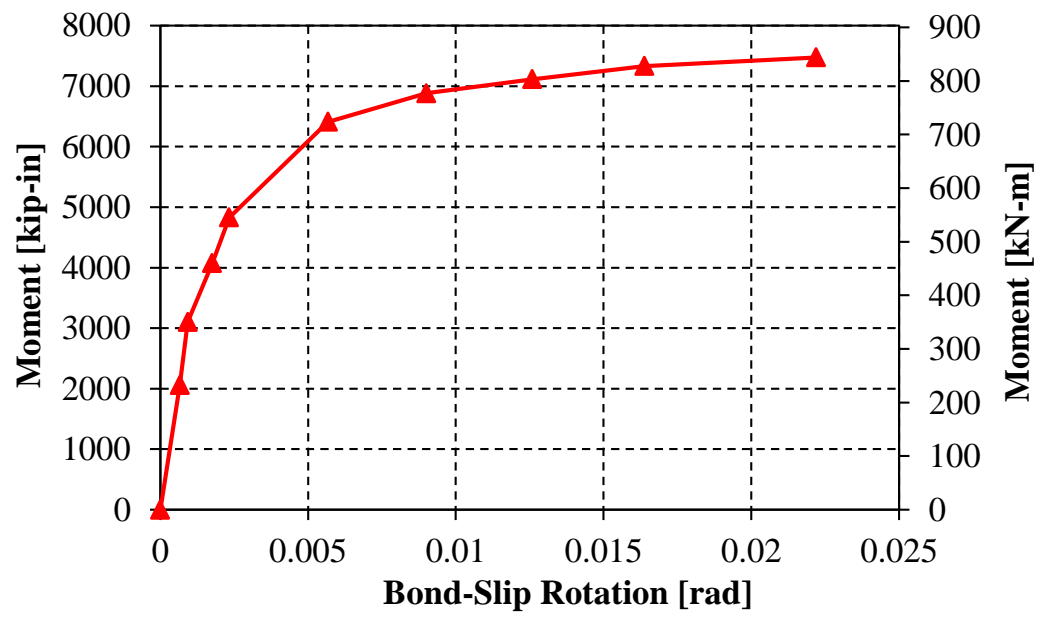


Figure 4-108 GCPP moment vs. bond-slip rotation relationship

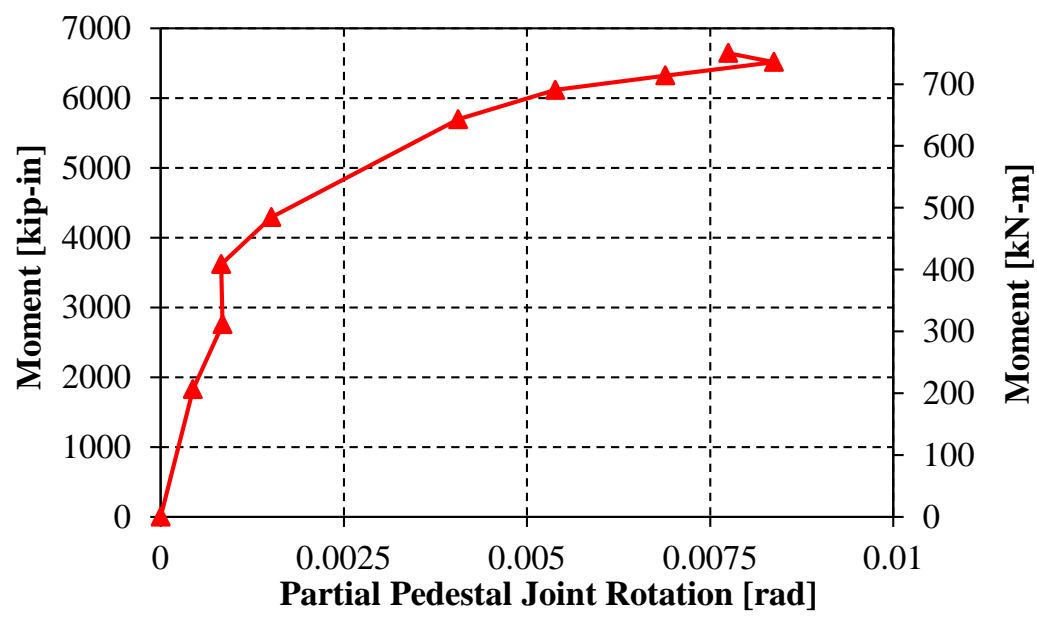


Figure 4-109 GCPP moment vs. pedestal joint rotation relationship

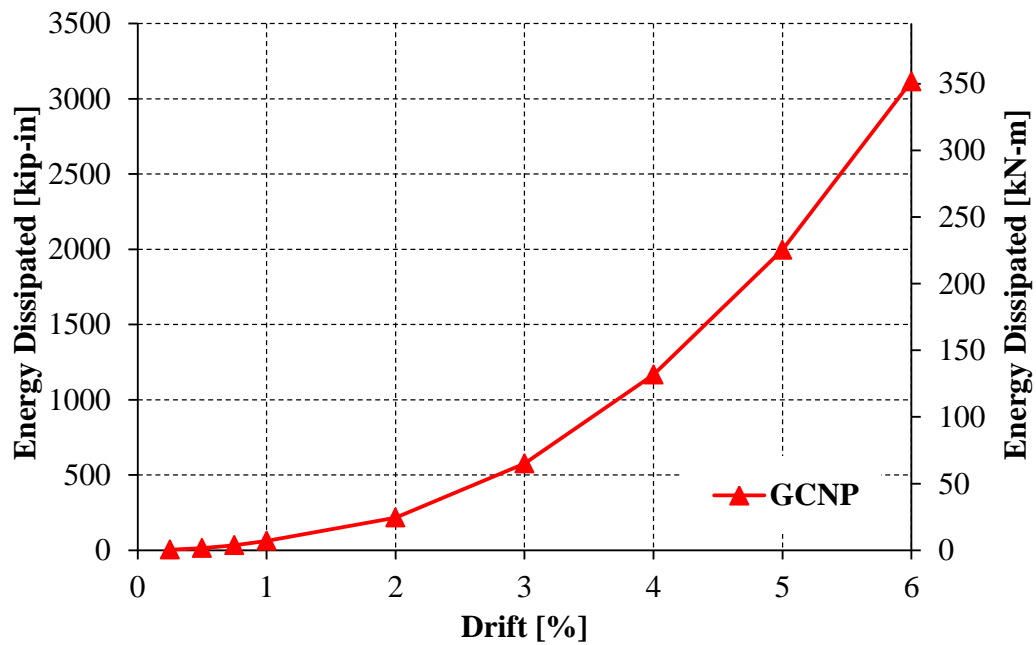


Figure 4-110 GCNP cumulative energy dissipation

Chapter 5 Figures

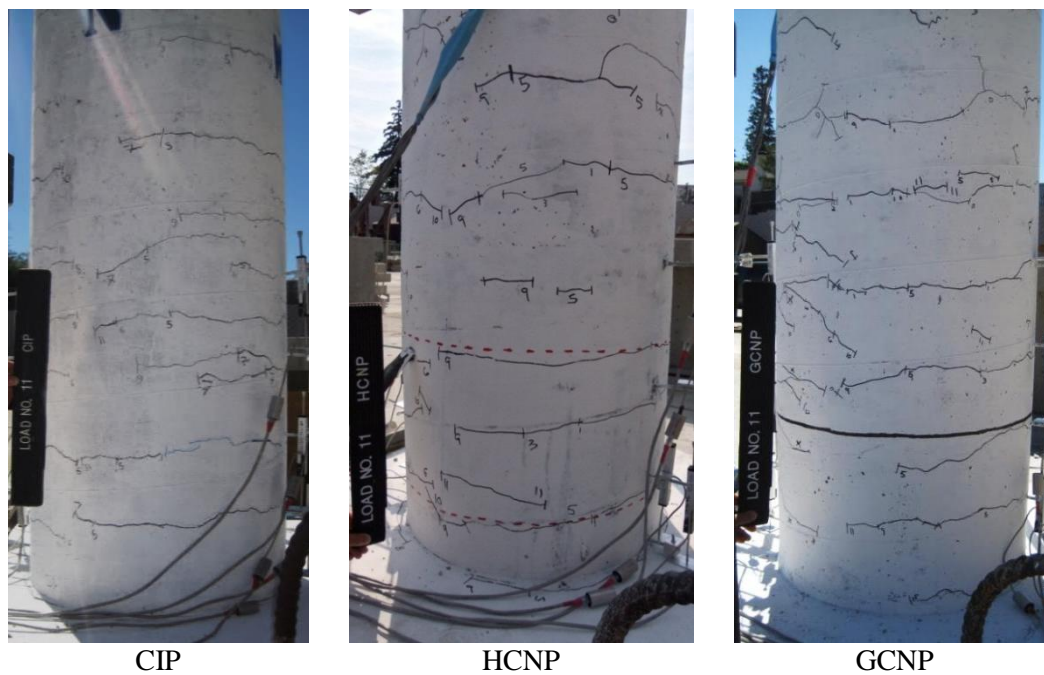


Figure 5-1 Comparison of damage in models without pedestal after second push cycle of 0.75% drift

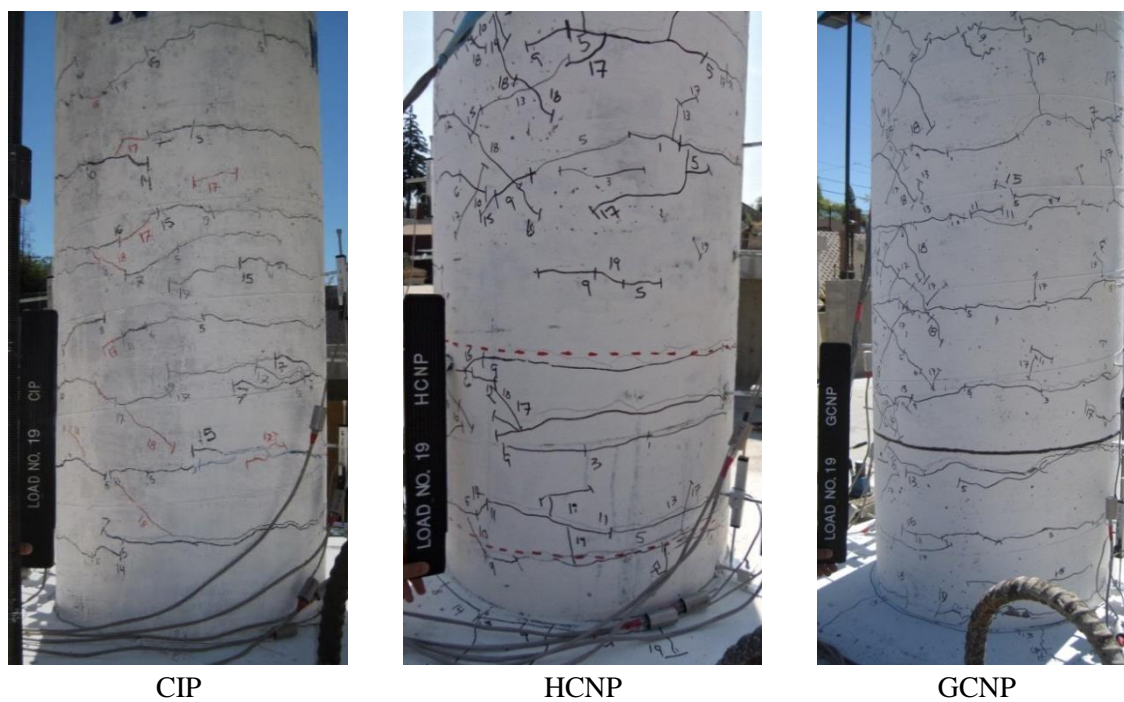


Figure 5-2 Comparison of damage in models without pedestal after second push cycle of 2.0% drift

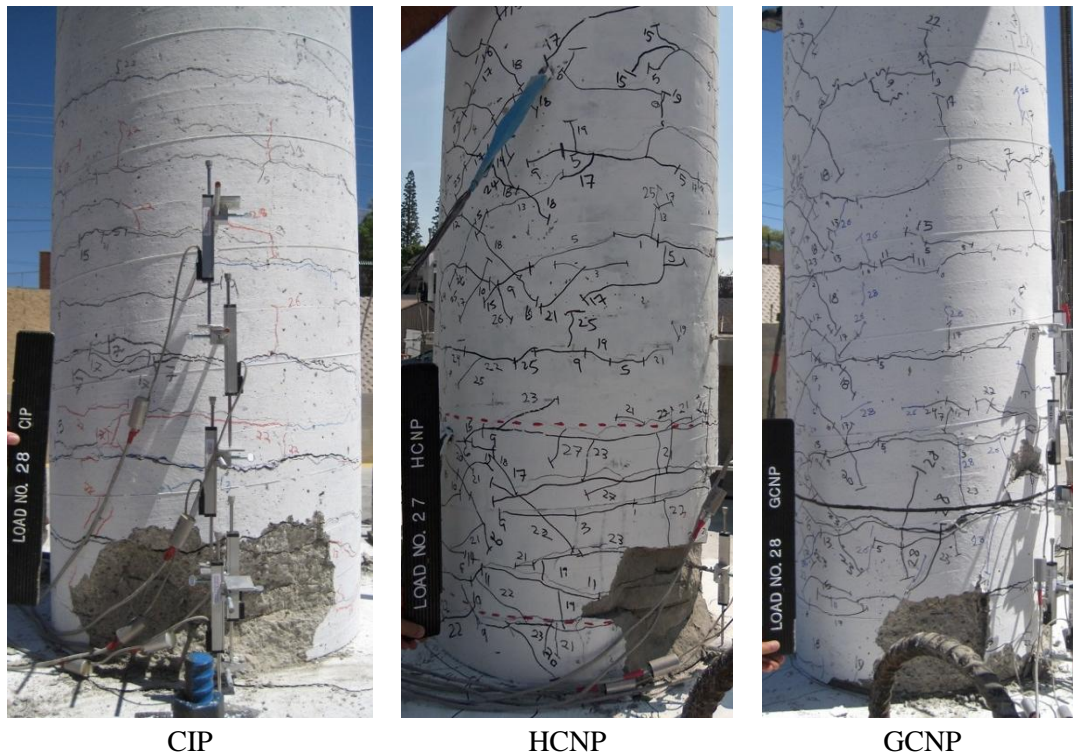


Figure 5-3 Comparison of damage in models without pedestal after second push cycle of 4.0% drift

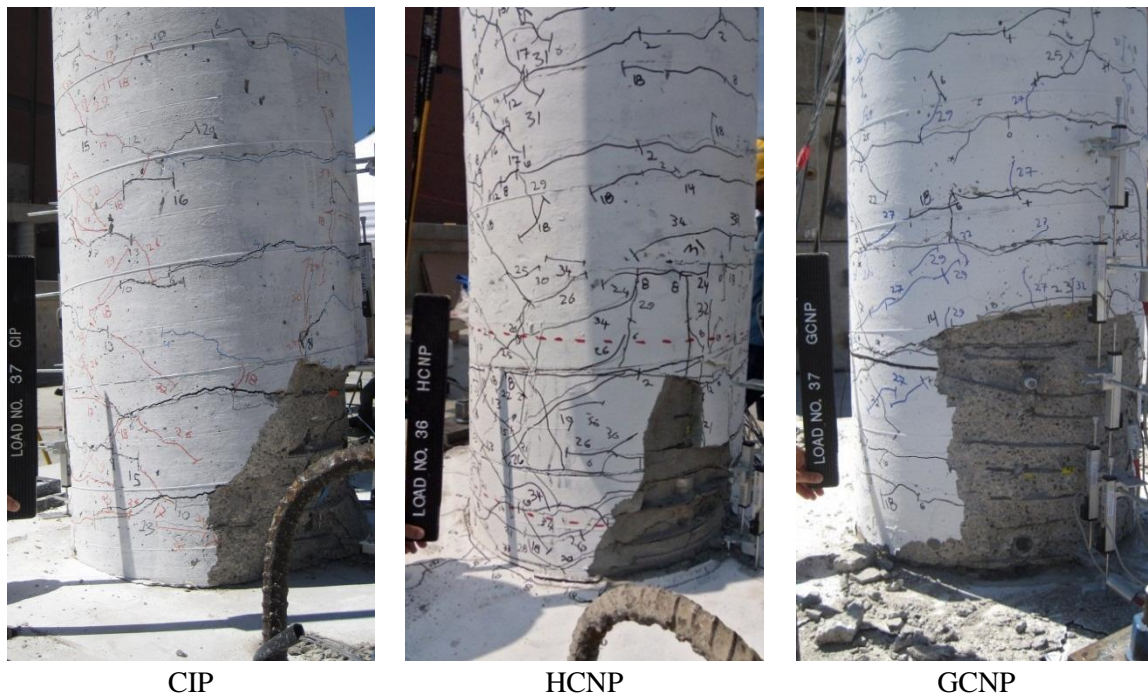
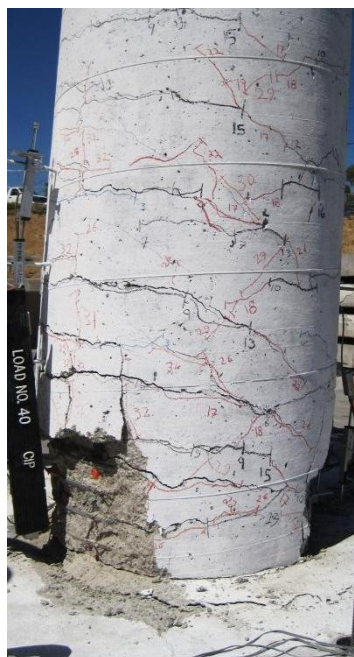
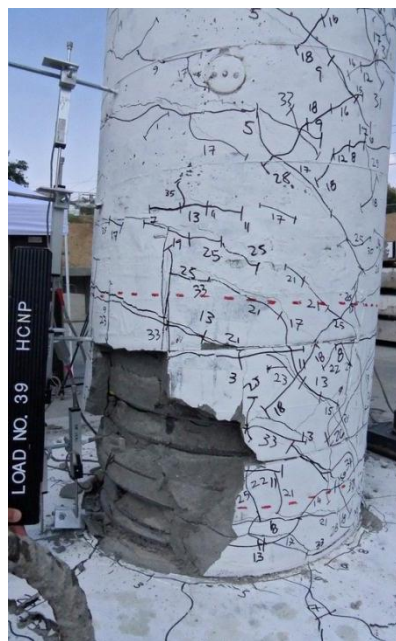


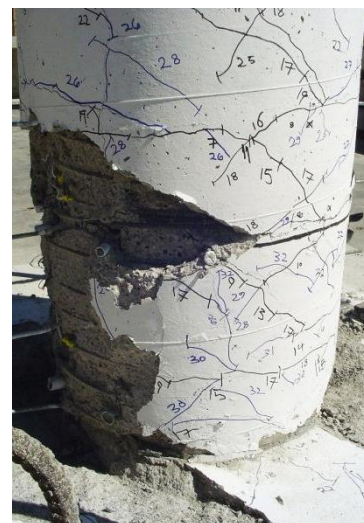
Figure 5-4 Comparison of damage in models without pedestal after second push cycle of 6.0% drift



CIP



HCNP



GCNP

Figure 5-5 Comparison of damage in models without pedestal after second push cycle of 8.0% drift

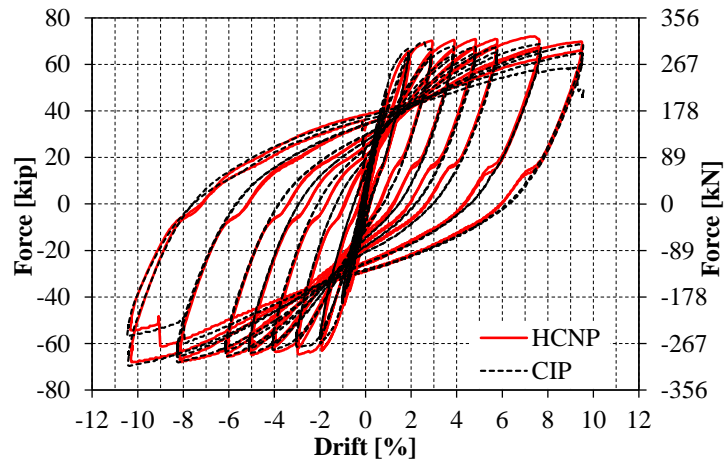


Figure 5-7 Comparison of the hysteretic force-displacement response of CIP and HCNP

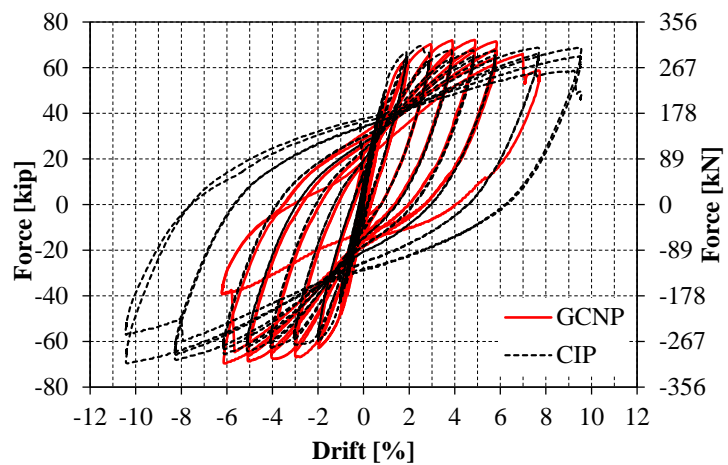


Figure 5-8 Comparison of the hysteretic force-displacement response of CIP and GCNP

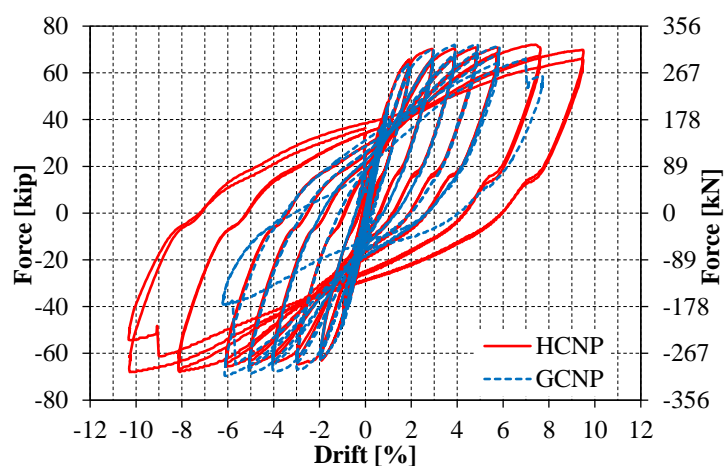


Figure 5-9 Comparison of the hysteretic force-displacement response of HCNP and GCNP

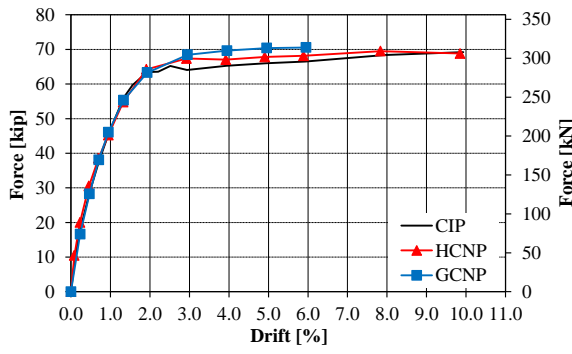


Figure 5-10 Average pushover response for models without pedestal

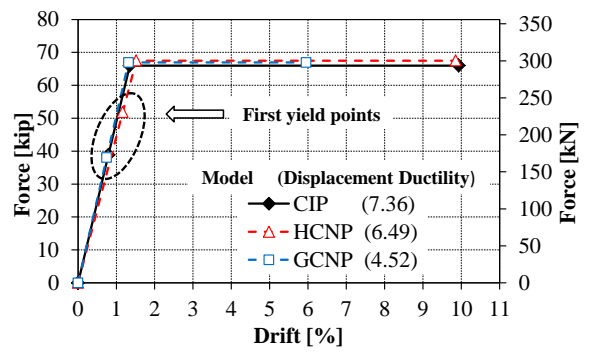


Figure 5-11 Elasto-plastic response of models without pedestal

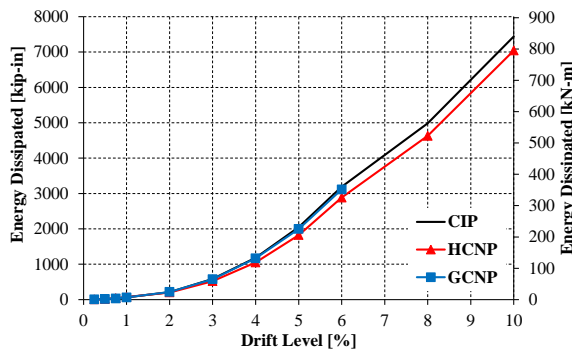


Figure 5-12 Energy dissipation capacity of models without pedestal

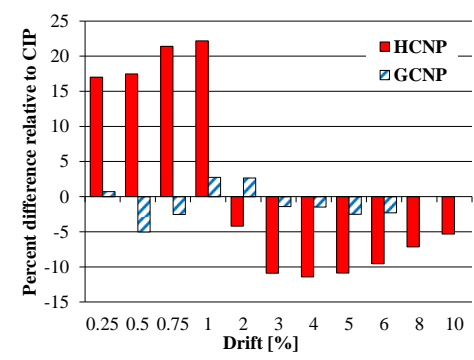


Figure 5-13 Comparison of energy dissipation for models without pedestals

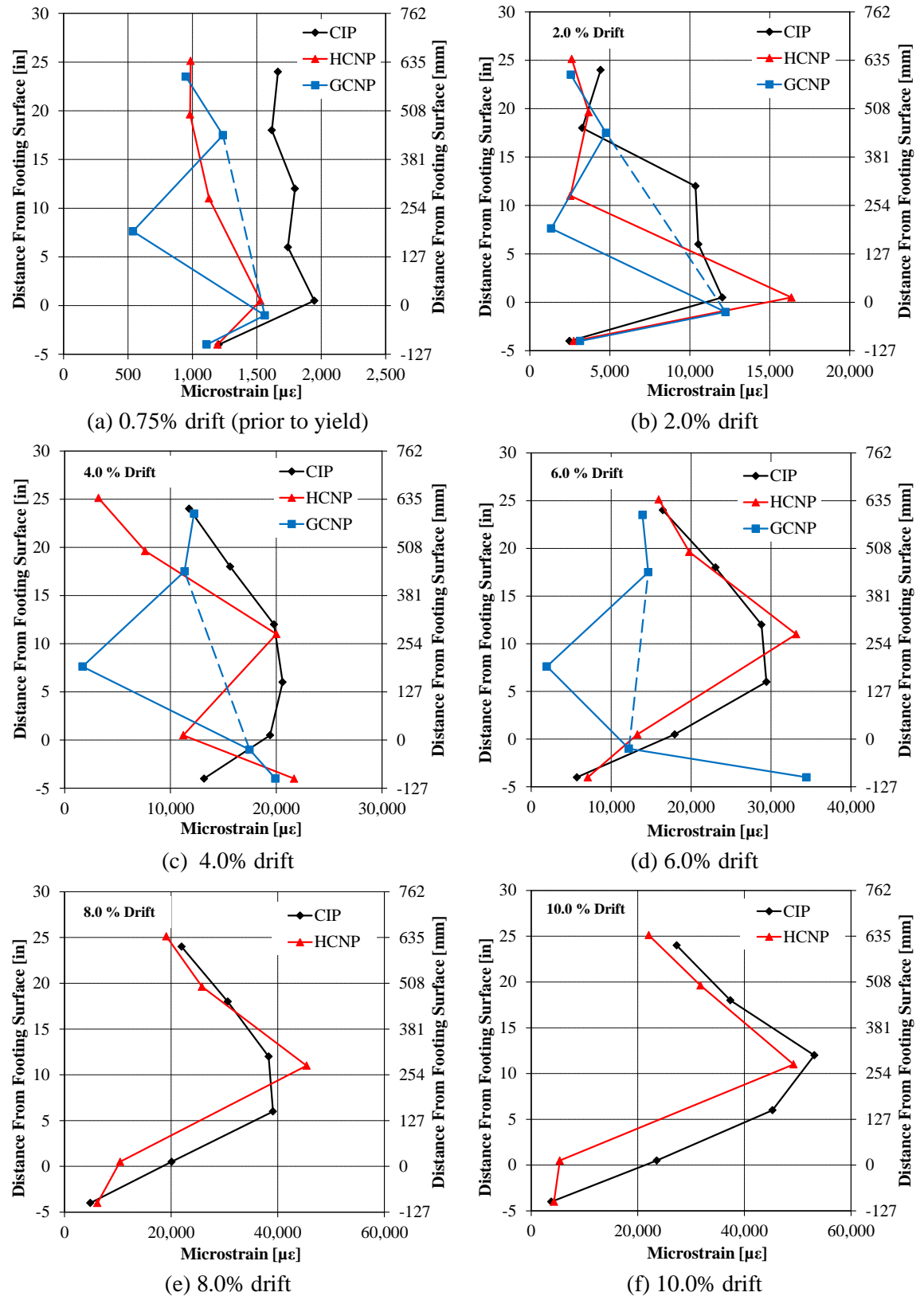


Figure 5-14 Comparison of plastic hinge longitudinal strain profiles for models without pedestal

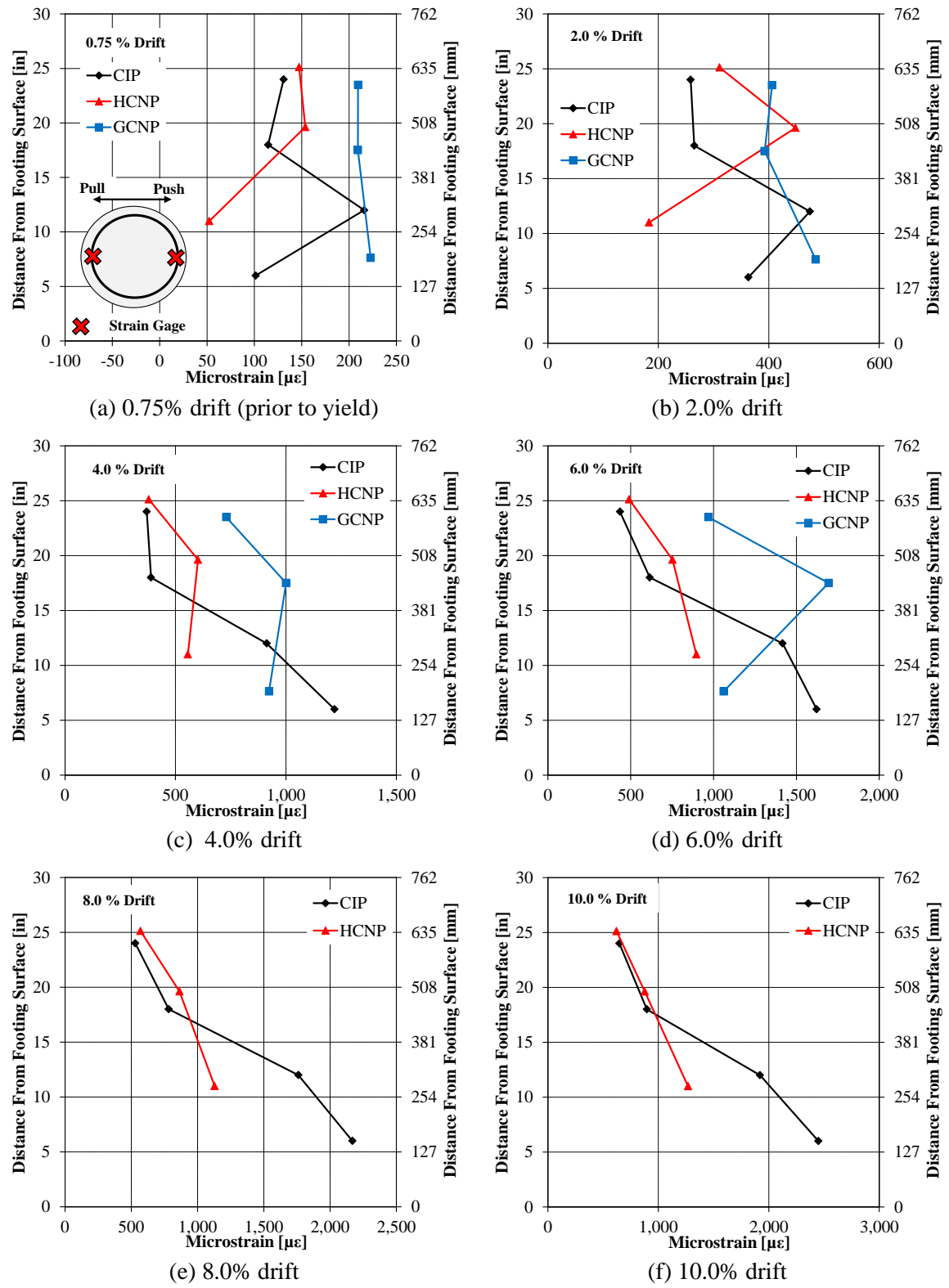


Figure 5-15 Average transverse strain profiles due to compression zone dilation

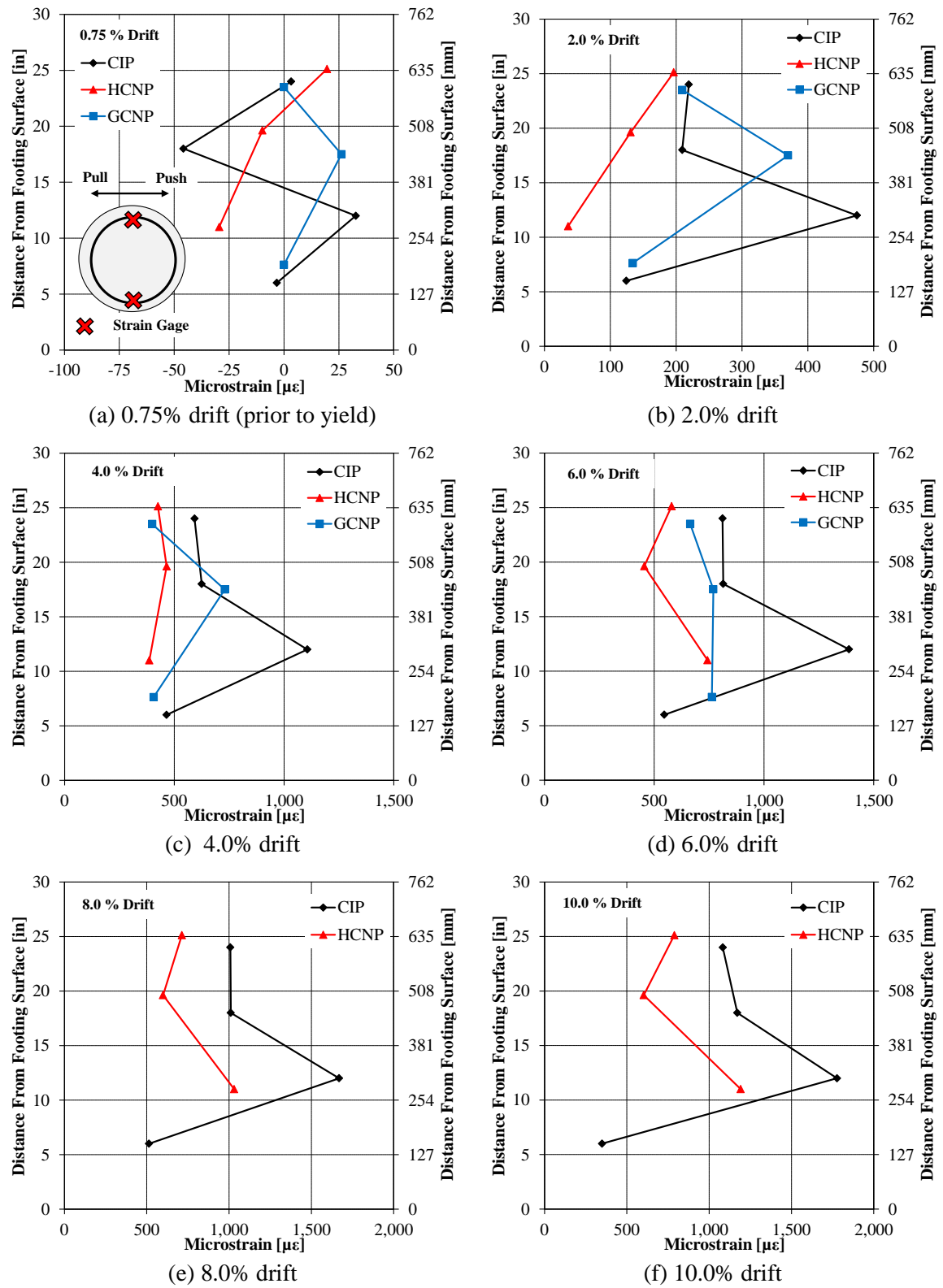


Figure 5-16 Average transverse strain profiles due to shear deformation

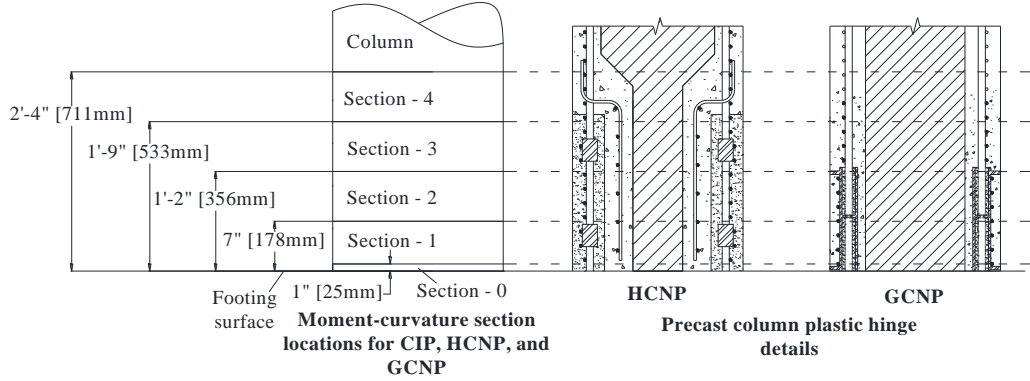


Figure 5-17 Nomenclature for curvature measurement locations for models without pedestals

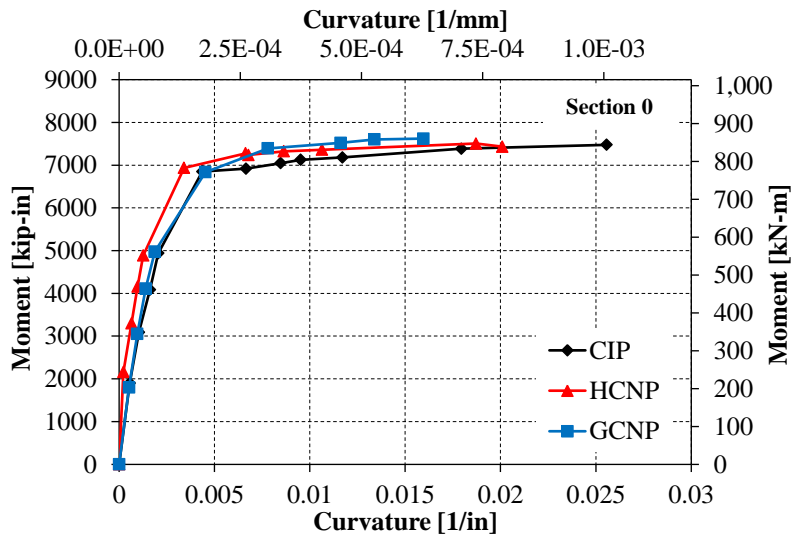


Figure 5-18 Average moment-curvature response of models without pedestal at Section 0

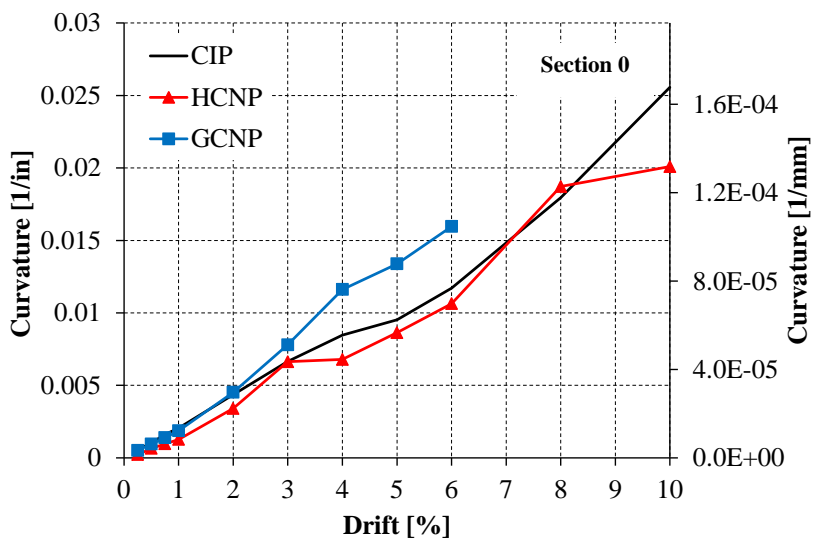
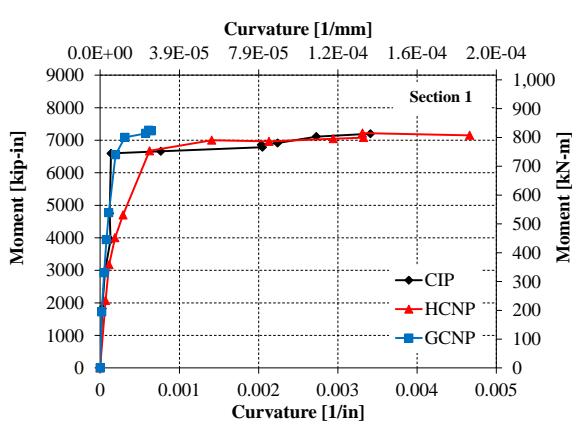
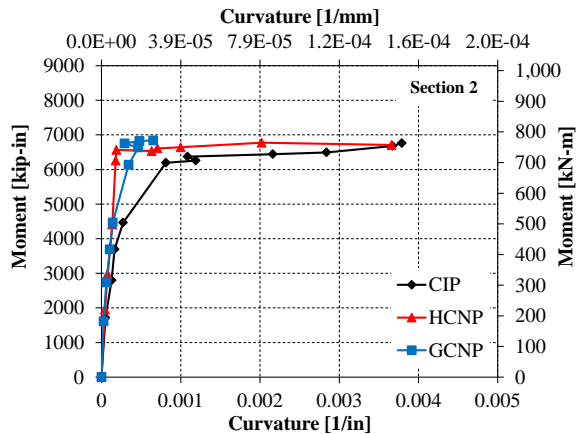


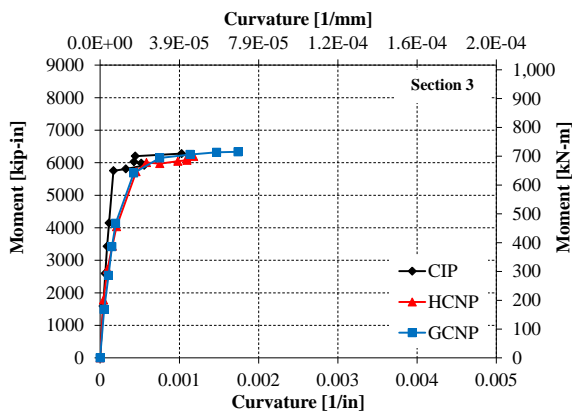
Figure 5-19 Average curvature per drift level for models without pedestals



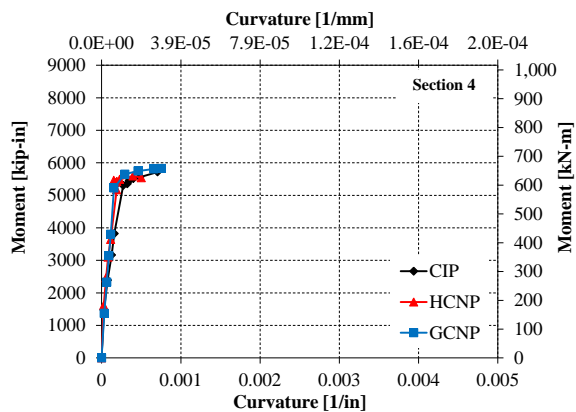
(a) Section 1: 1-7 in [25-178 mm] above the footing



(b) Section 2: 7-14 in [178-356 mm] above the footing

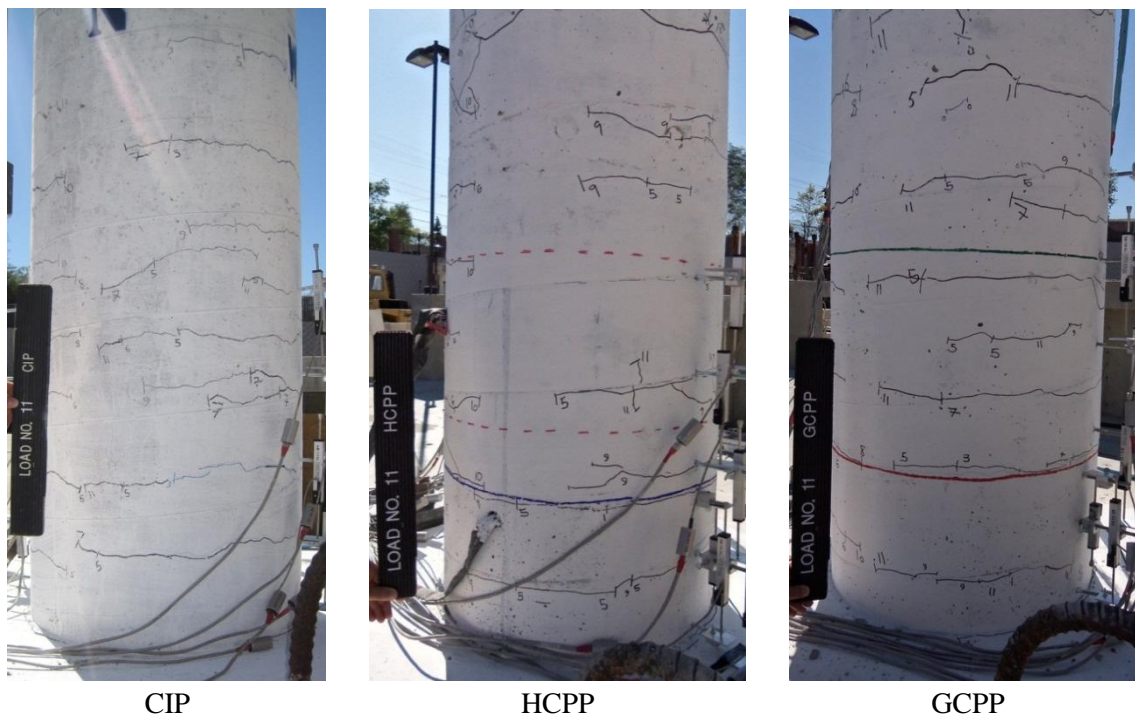


(c) Section 3: 14-21 in [356-533 mm] above the footing

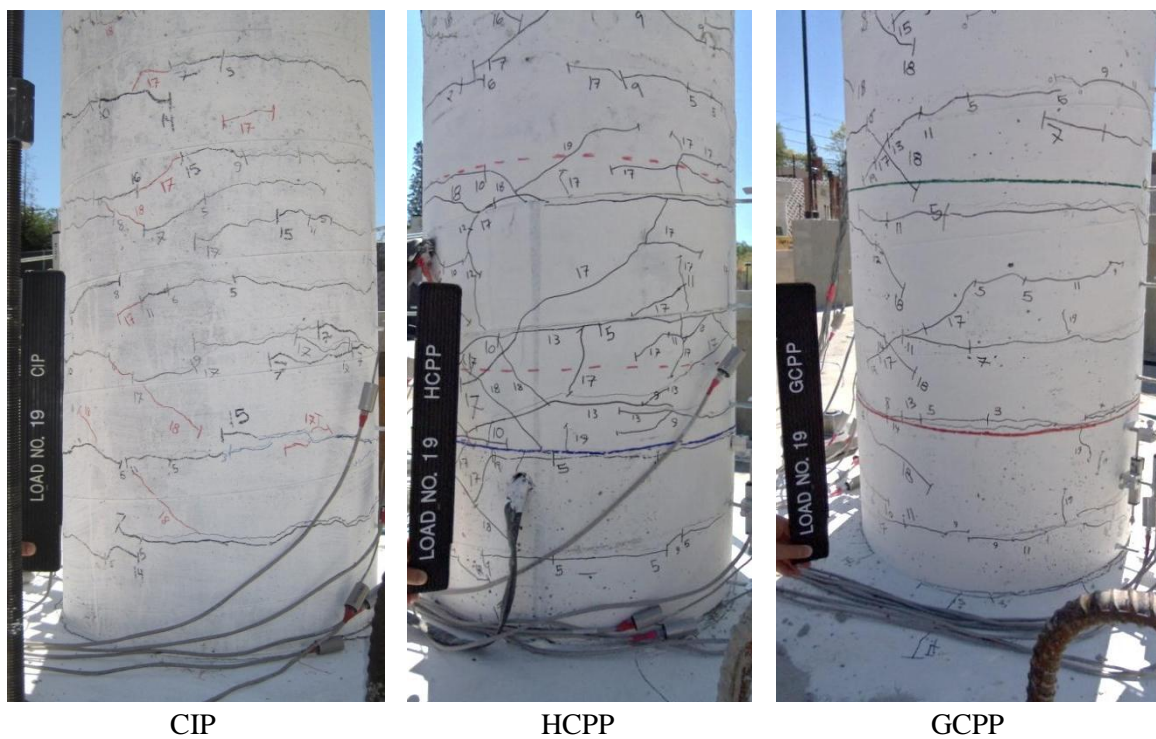


(d) Section 4: 21-28 in [533-711 mm] above the footing

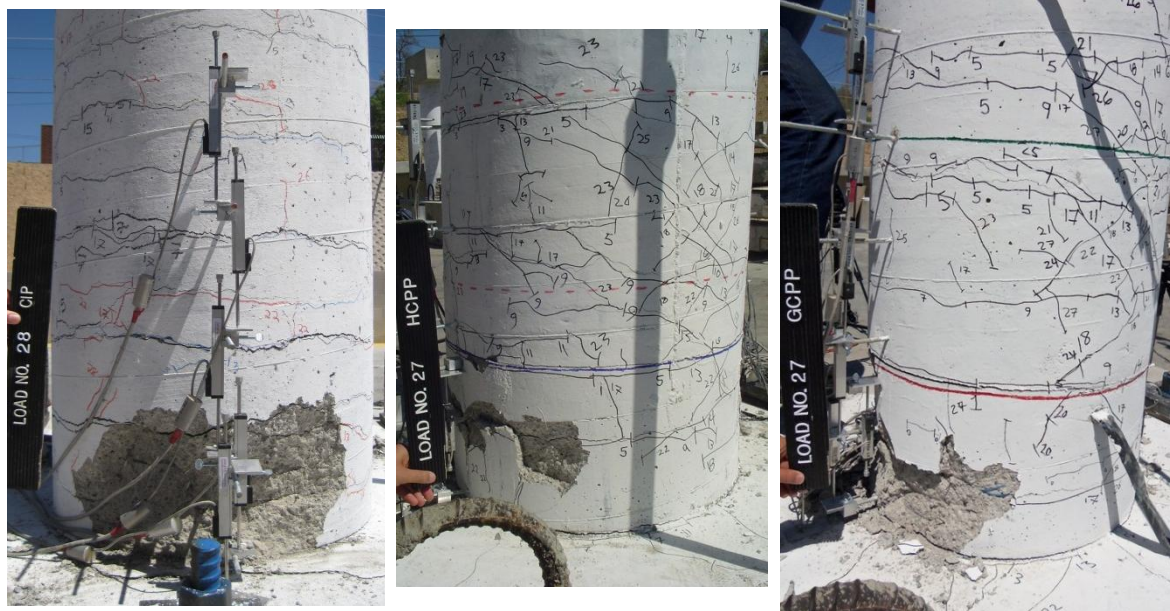
Figure 5-20 Moment-curvature response of models without pedestal Sections 1 - 4



CIP HCPP GCPP
 Figure 5-21 Comparison of damage in models with pedestal after second push cycle of 0.75% drift



CIP HCPP GCPP
 Figure 5-22 Comparison of damage in models with pedestal after second push cycle of 2.0% drift



CIP

HCPP

GCPP

Figure 5-23 Comparison of damage in models with pedestal after second push cycle of 4.0% drift

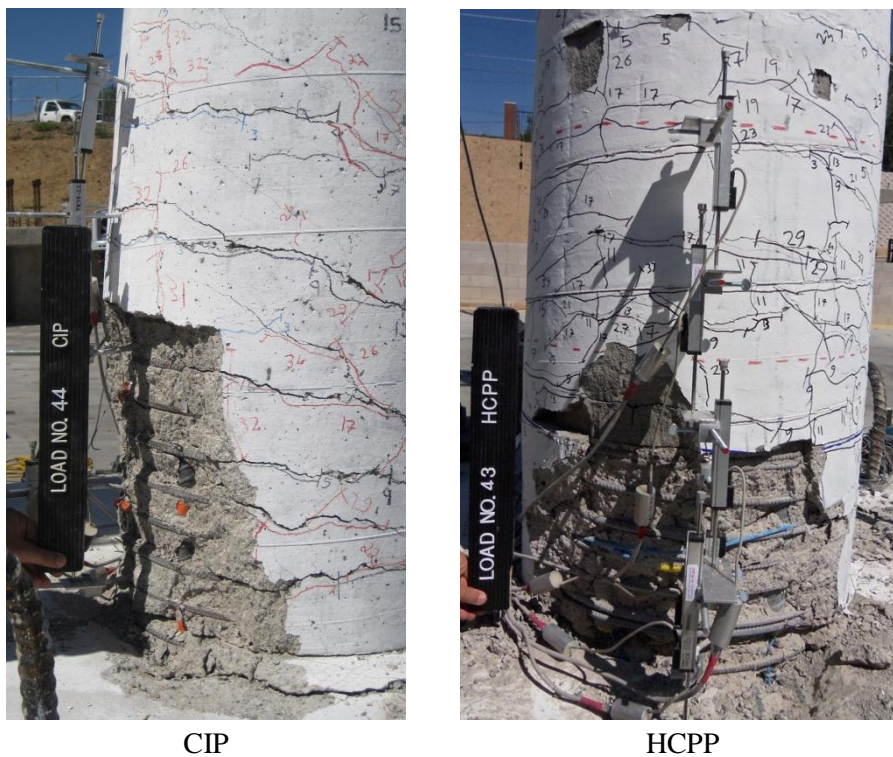


CIP

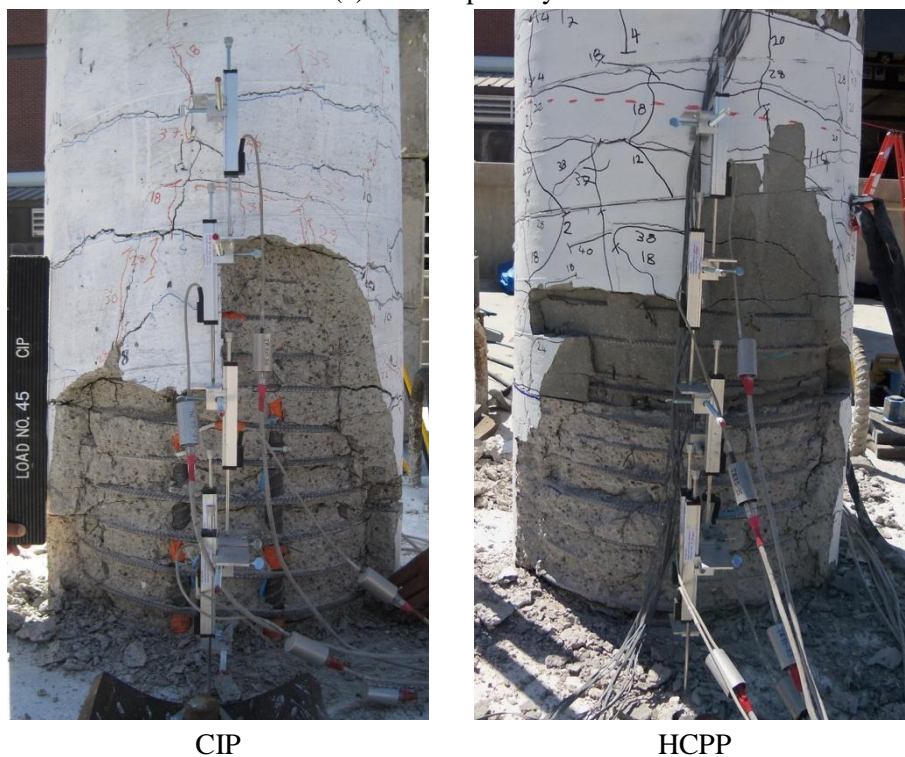
HCPP

GCPP

Figure 5-24 Comparison of damage in models with pedestal after second push cycle of 6.0% drift



(a) Second push cycle



(b) Second pull cycle

Figure 5-26 Comparison of damage in models with pedestal after 10.0% drift

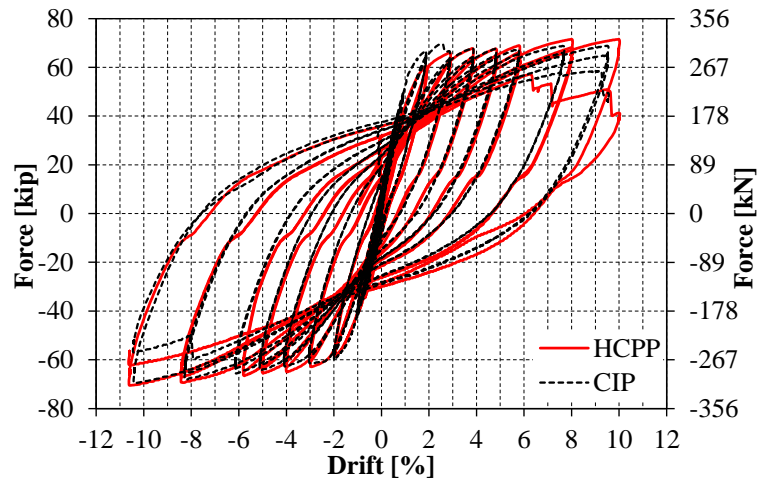


Figure 5-27 Comparison of the hysteretic force-displacement response of CIP and HCPP

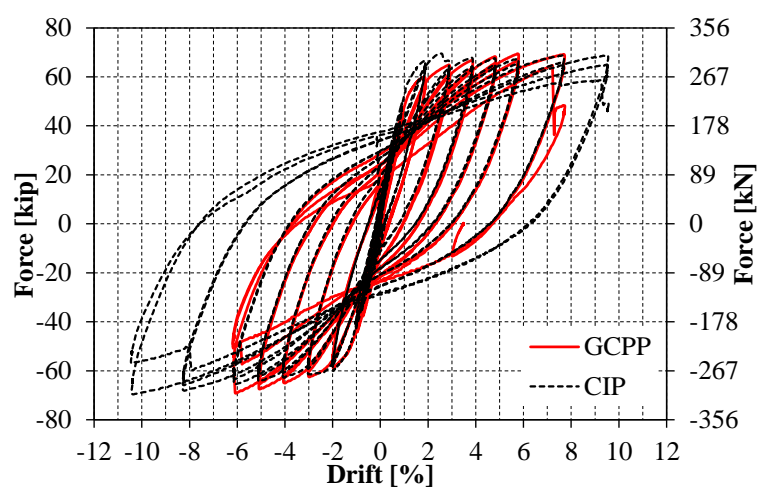


Figure 5-28 Comparison of the hysteretic force-displacement response of CIP and GCPP

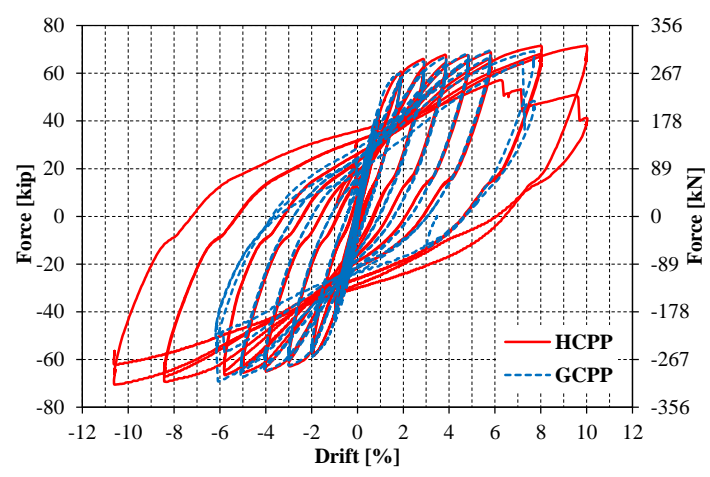


Figure 5-29 Comparison of the hysteretic force-displacement response of HCPP and GCPP

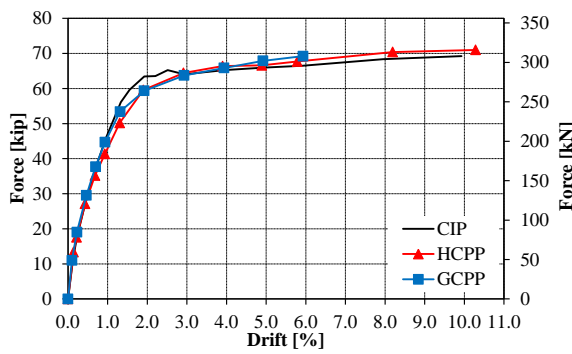


Figure 5-30 Average pushover response of models with pedestals

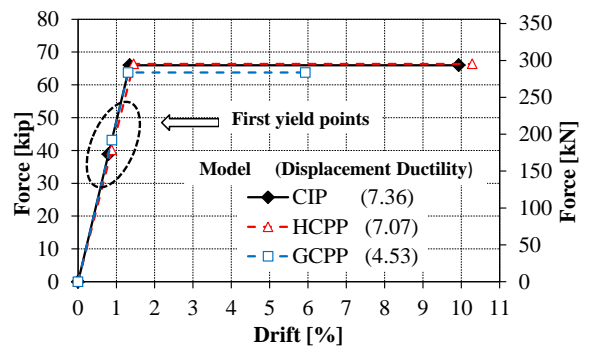


Figure 5-31 Elasto-plastic response of models with pedestals

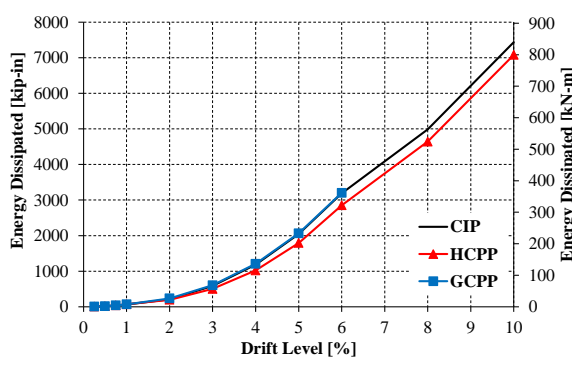


Figure 5-32 Energy dissipation capacity of models with pedestals

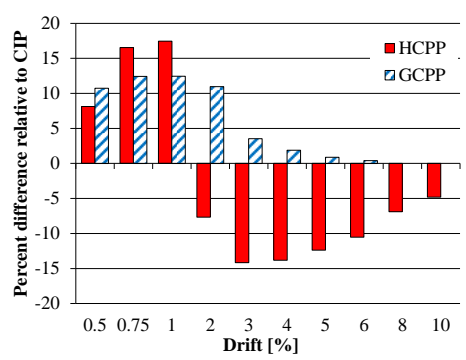


Figure 5-33 Comparison of energy dissipation for models with pedestals

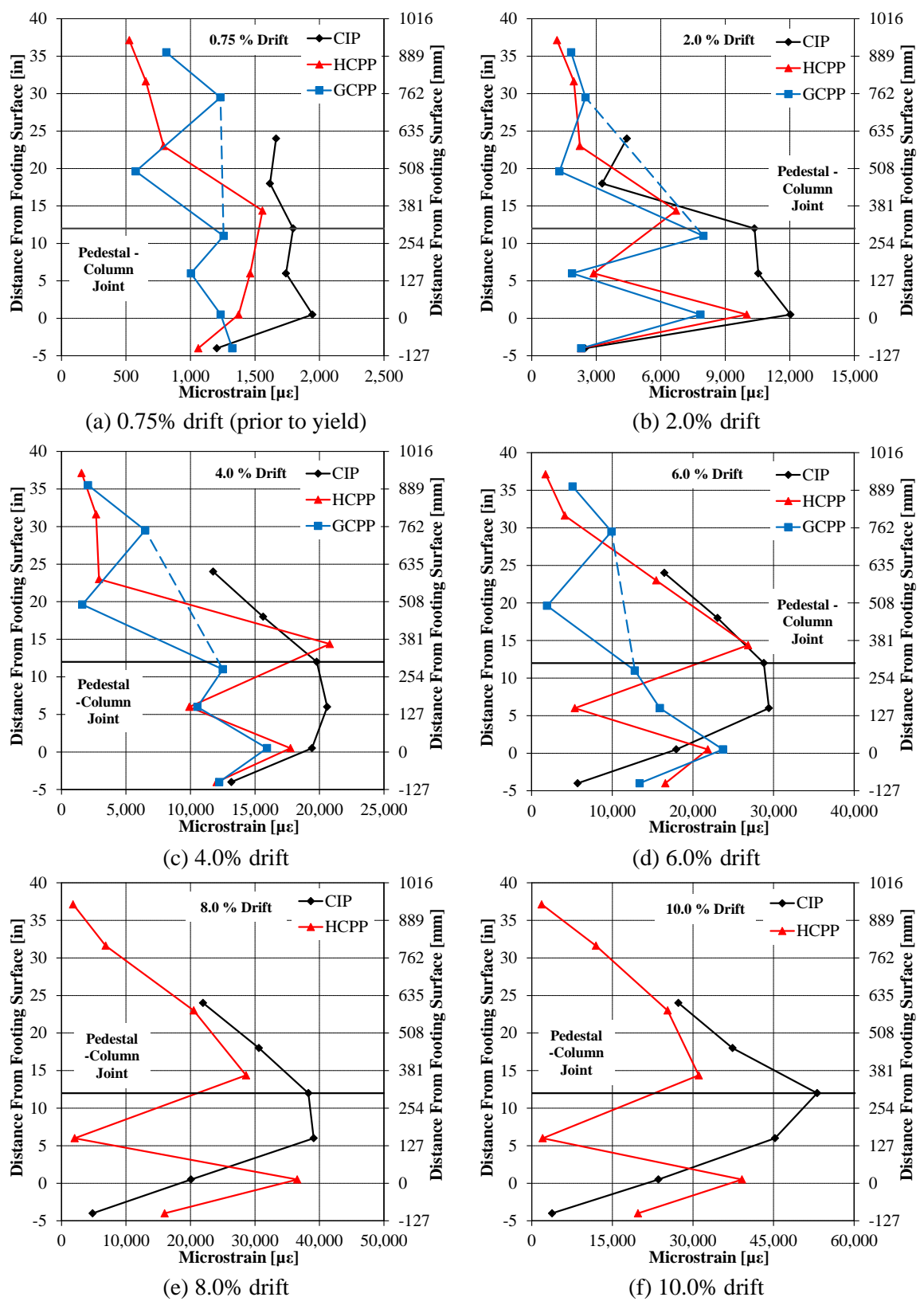


Figure 5-34 Comparison of plastic hinge strain profiles for models with pedestal

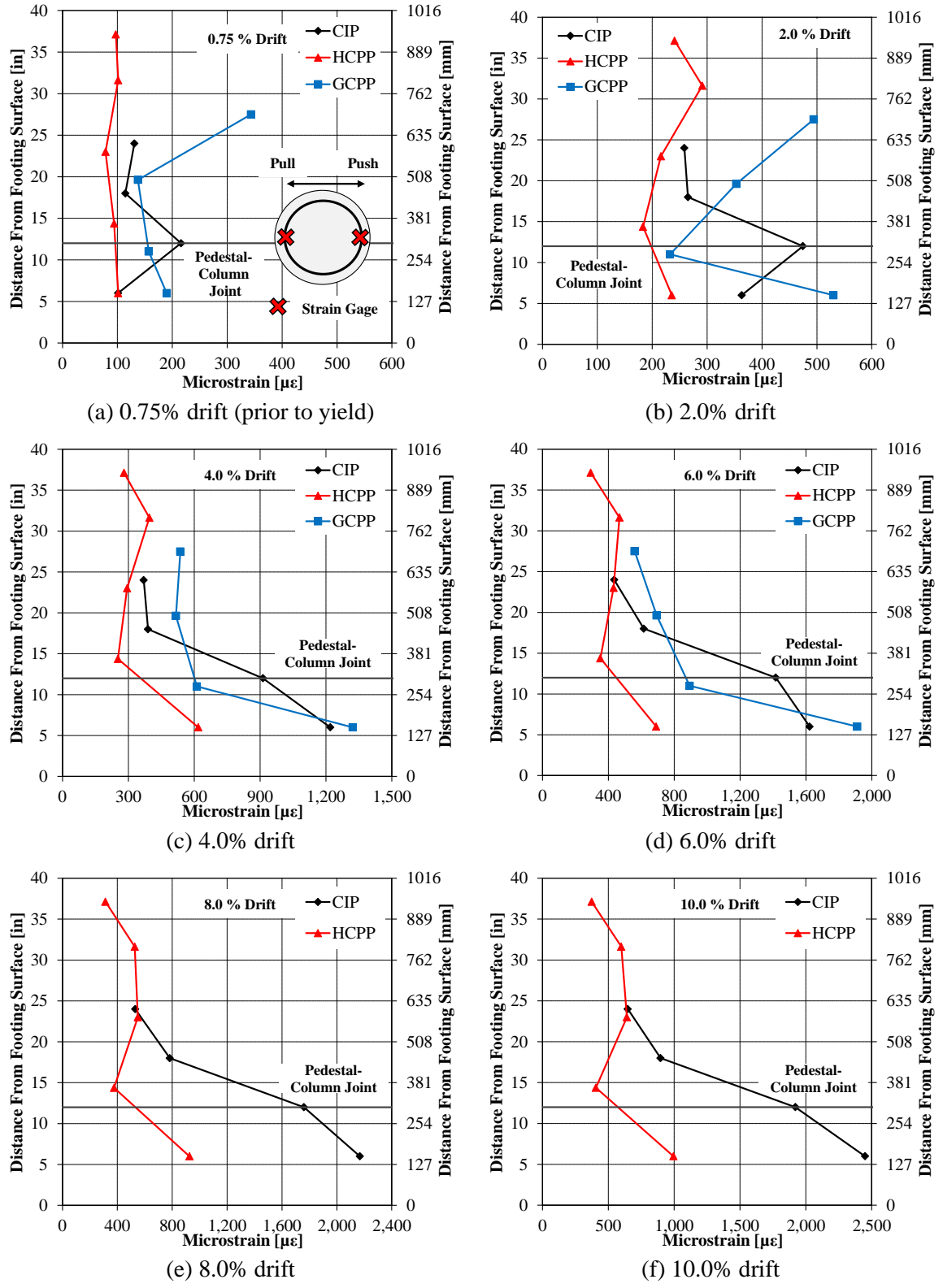
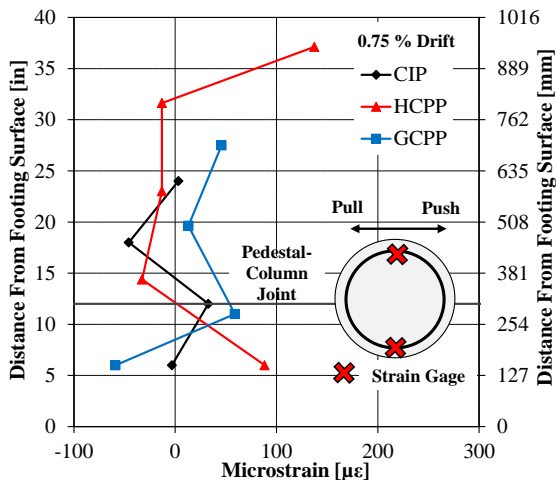
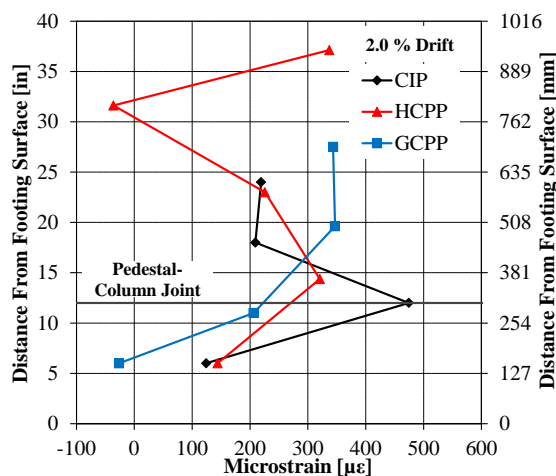


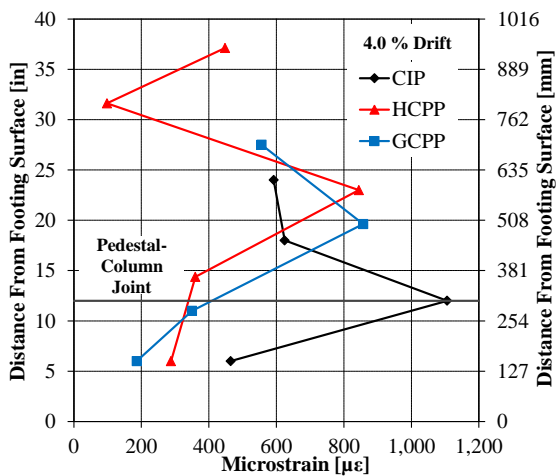
Figure 5-35 Average transverse strain profiles due to compression zone dilation



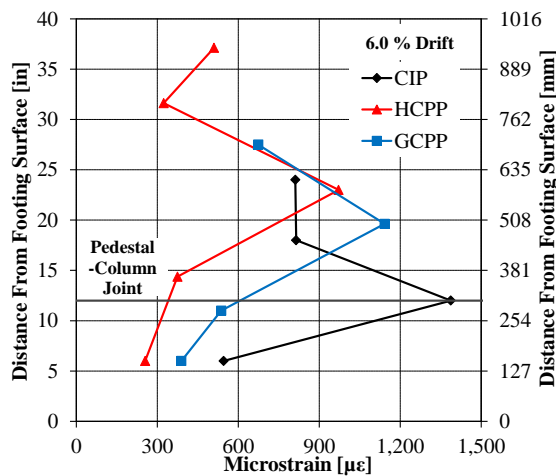
(a) 0.75% drift (prior to yield)



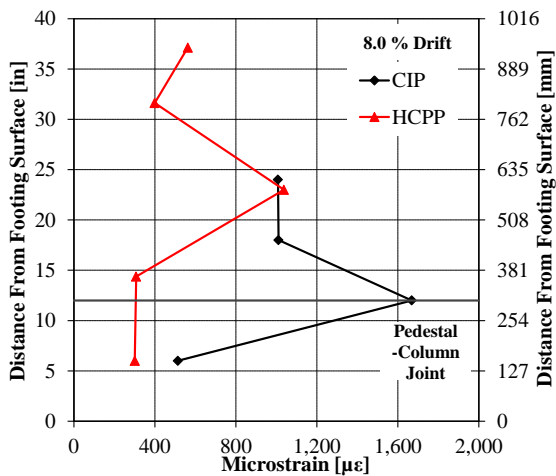
(b) 2.0% drift



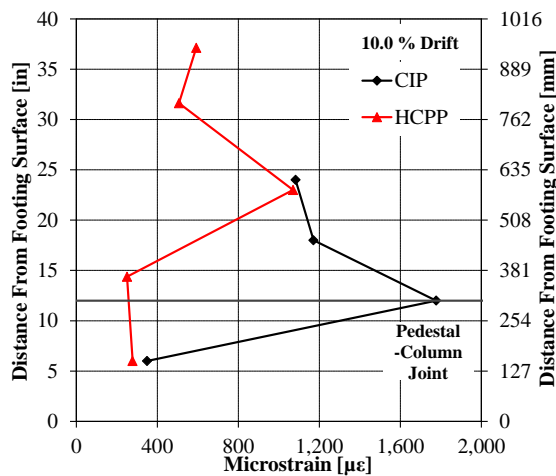
(c) 4.0% drift



(d) 6.0% drift

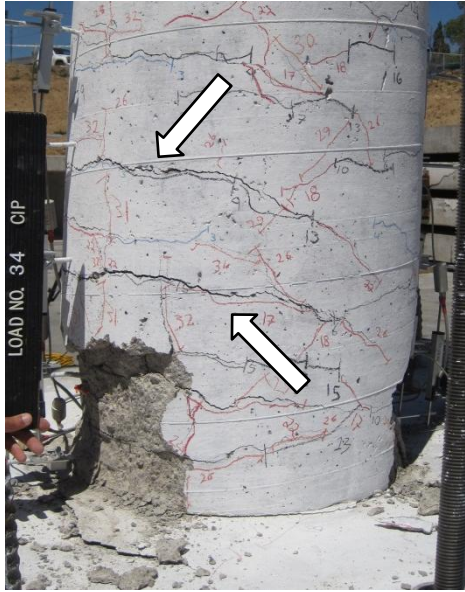
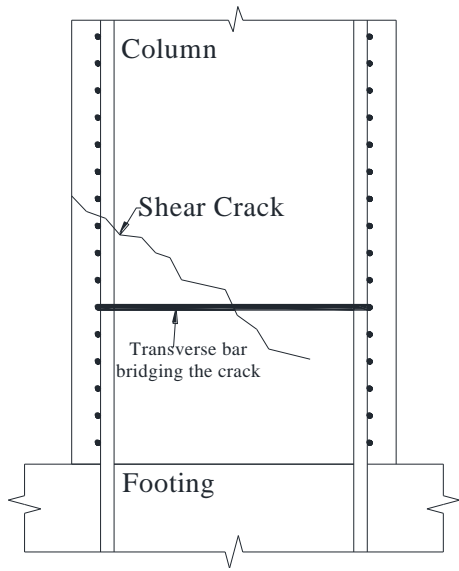


(e) 8.0% drift



(f) 10.0% drift

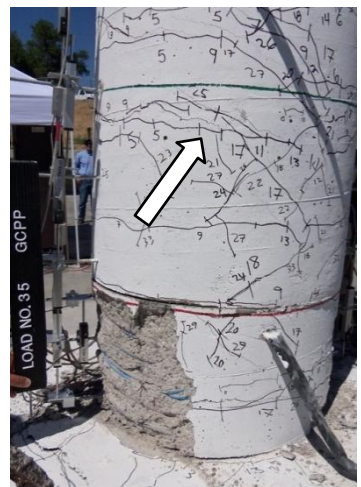
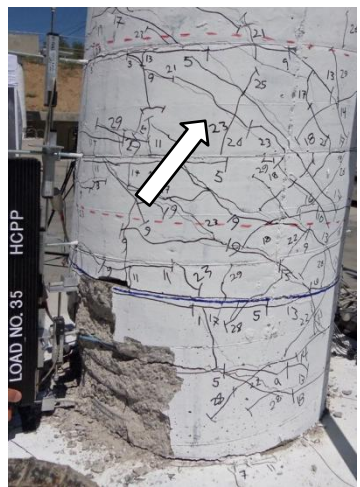
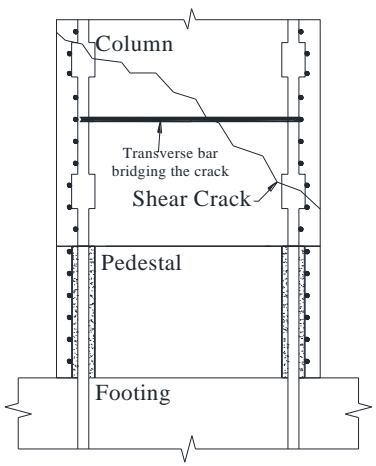
Figure 5-36 Average transverse strain profiles due to shear deformation



(a) Theoretical model

(b) Representative photo

Figure 5-37 Shear cracking mechanism in CIP



(a) Proposed Model

(b) Representative photo of HCPP

(c) Representative photo of GCPP

Figure 5-38 Shear cracking mechanism in models with precast pedestal

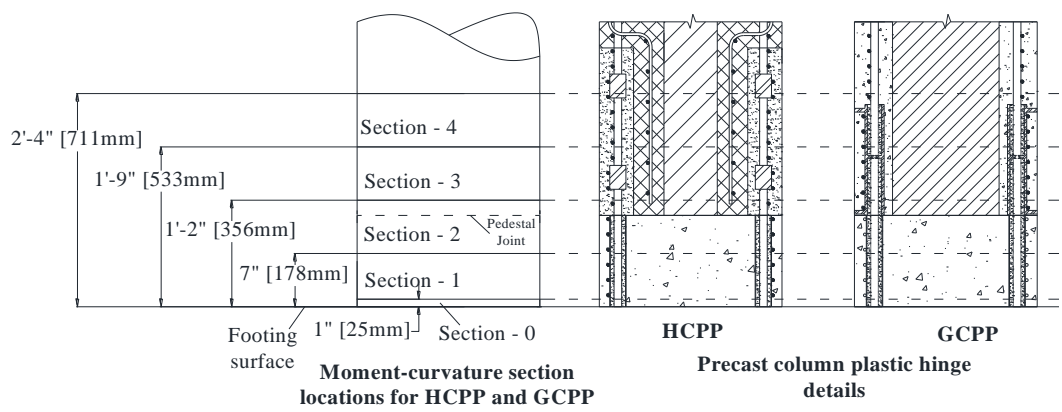


Figure 5-39 Nomenclature for curvature measurement locations for models with pedestals

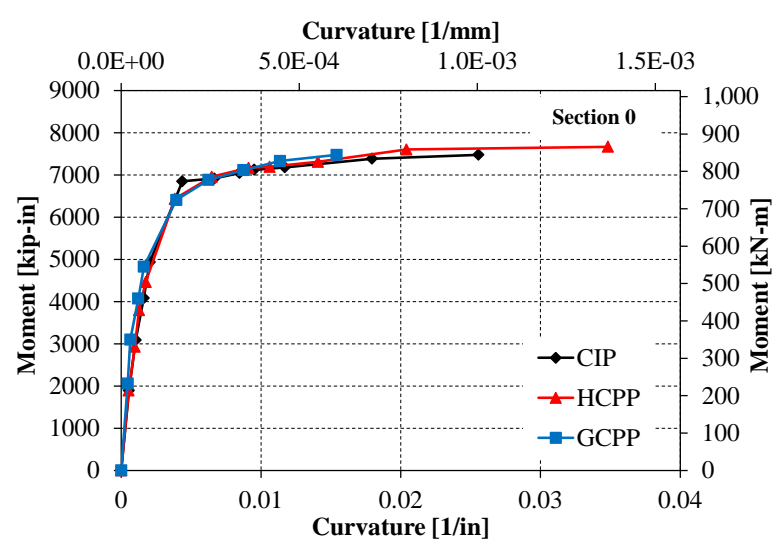


Figure 5-40 Average moment-curvature response of models with pedestal at Section 0

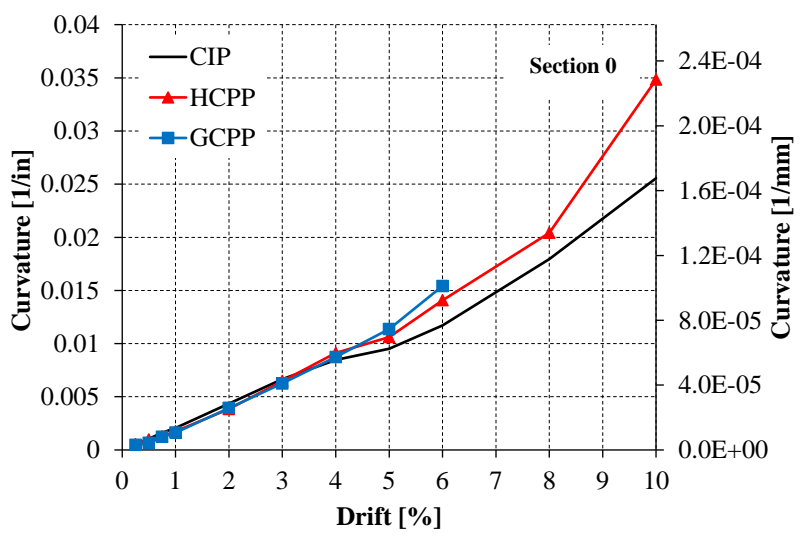
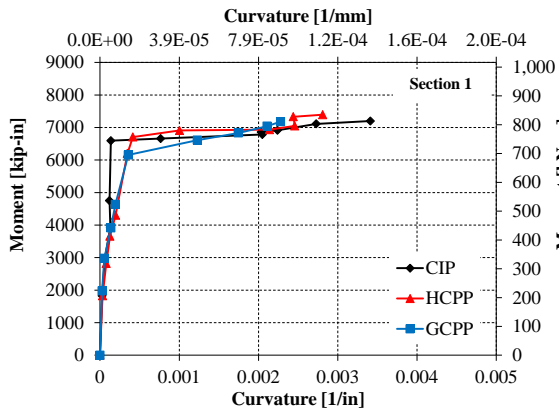
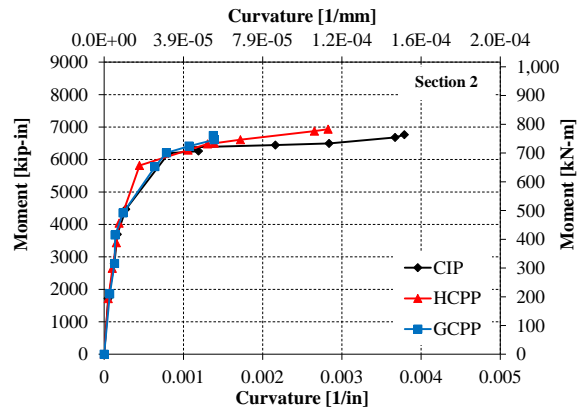


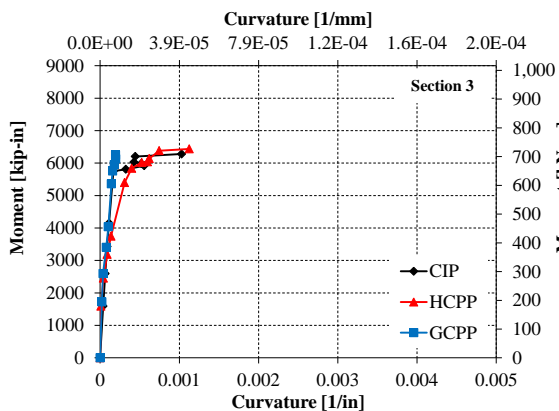
Figure 5-41 Average curvature per drift level for models with pedestals



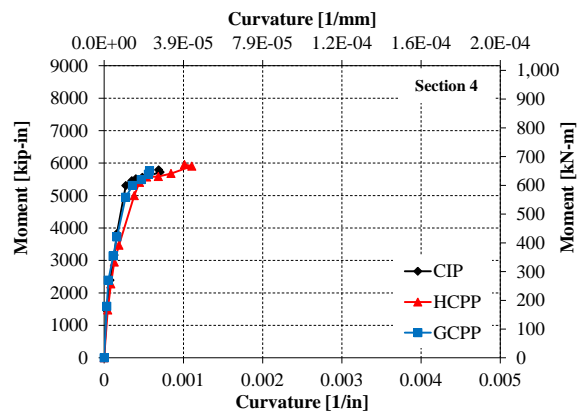
(a) Section 1: 1-7 in [25-178 mm] above the footing



(b) Section 2: 7-14 in [178-356 mm] above the footing

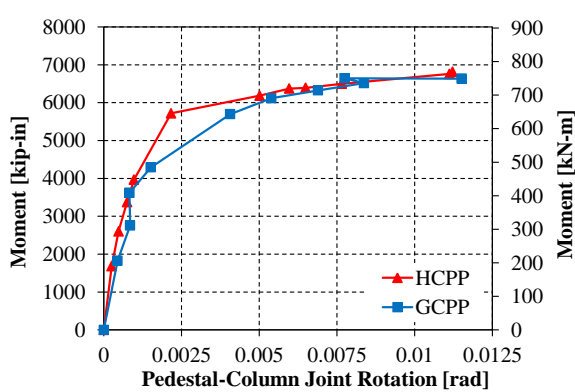


(c) Section 3: 14-21 in [356-533 mm] above the footing

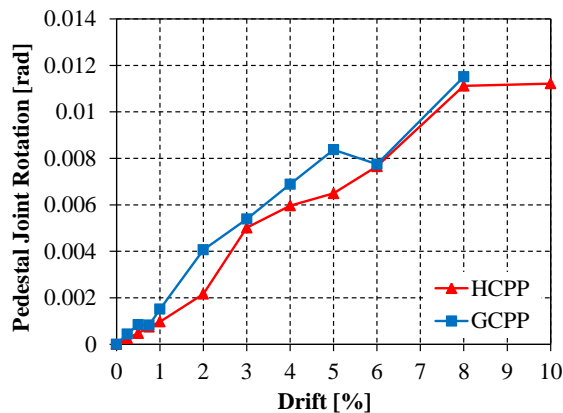


(d) Section 4: 21-28 in [533-711 mm] above the footing

Figure 5-42 Moment-curvature response of models with pedestal Sections 1 – 4



(a) Moment-rotation relationship

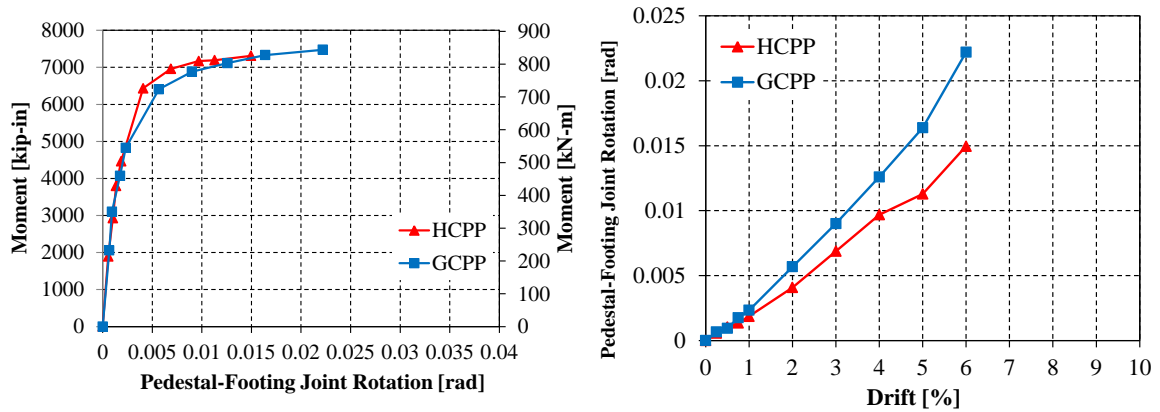


(b) Rotation-drift relationship

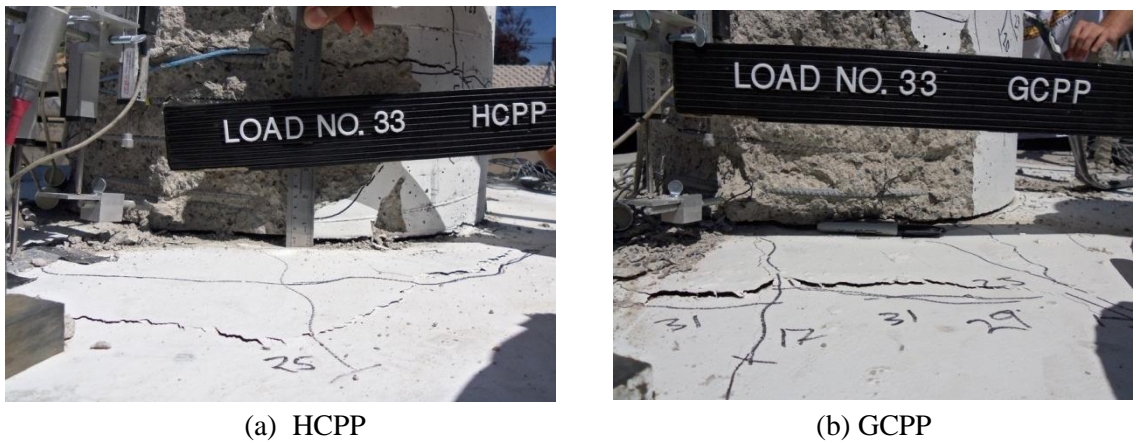
Figure 5-43 Rotation behavior of the pedestal-column joint



(a) HCPP (b) GCPP
 Figure 5-44 Pedestal-column joints at 4.0% drift



(a) Moment-rotation relationship (b) Rotation-drift relationship
 Figure 5-45 Rotation behavior of the pedestal-footing joints



(a) HCPP (b) GCPP
 Figure 5-46 Pedestal-footing joints at 6.0% drift.

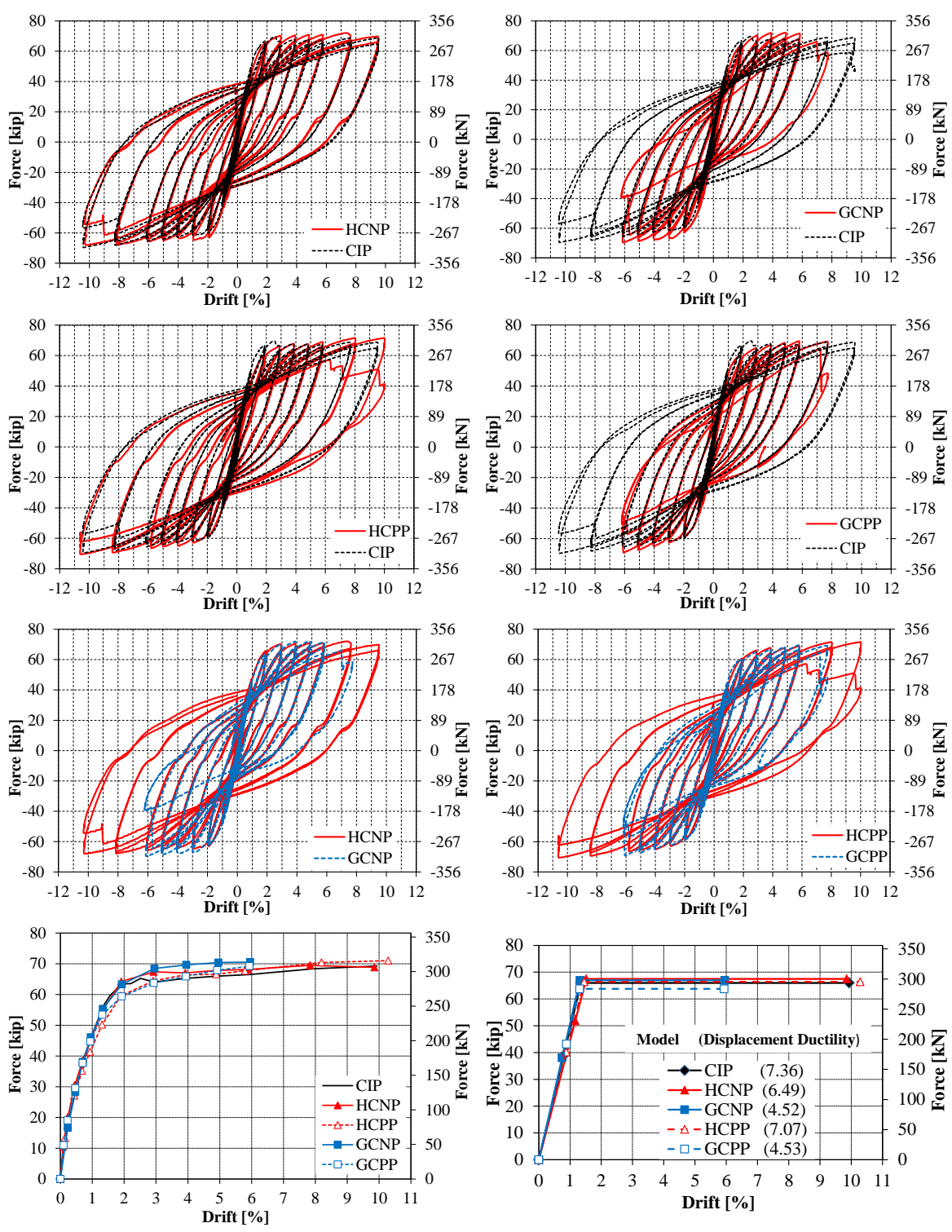
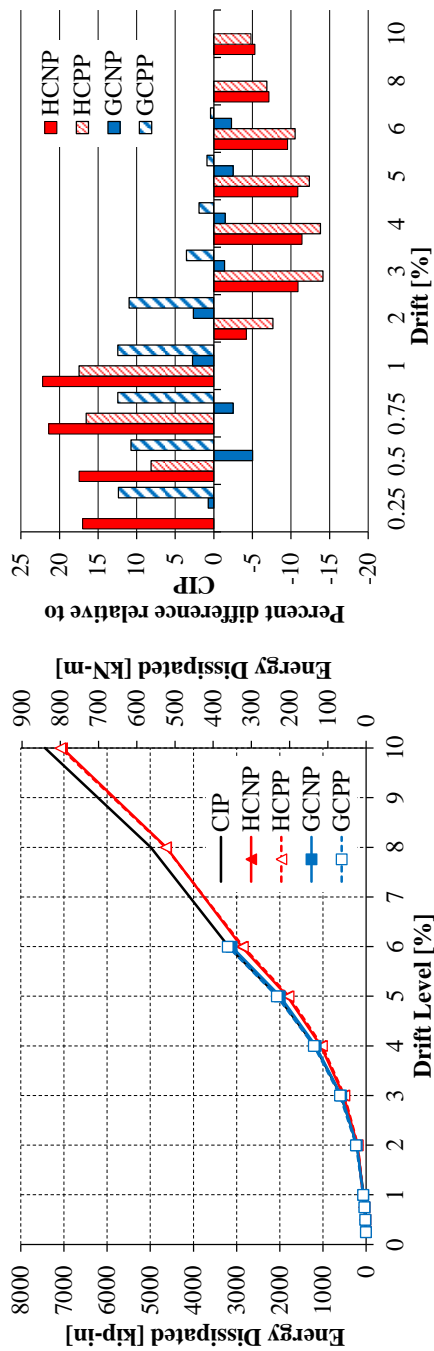


Figure 5-47 Summary of force-displacement relationships:

(a) – (d) Hysteresis comparison between precast and CIP models; (e) – (f) Hysteresis comparison between precast models; (g) Pushover envelopes; (h) Elasto-plastic curves and displacement ductilities



(a) Cumulative energy dissipated per drift level (b) Percent difference relative to CIP per drift level
 Figure 5-48 Summary of energy dissipation behavior

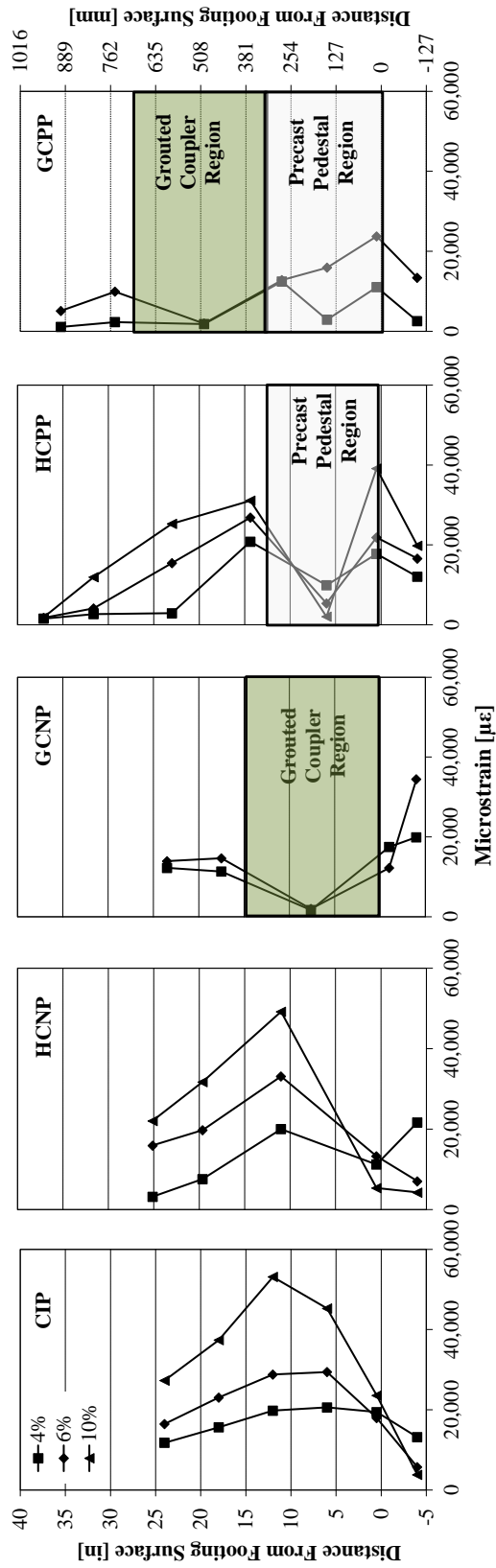


Figure 5-49 Summary of longitudinal strain profiles

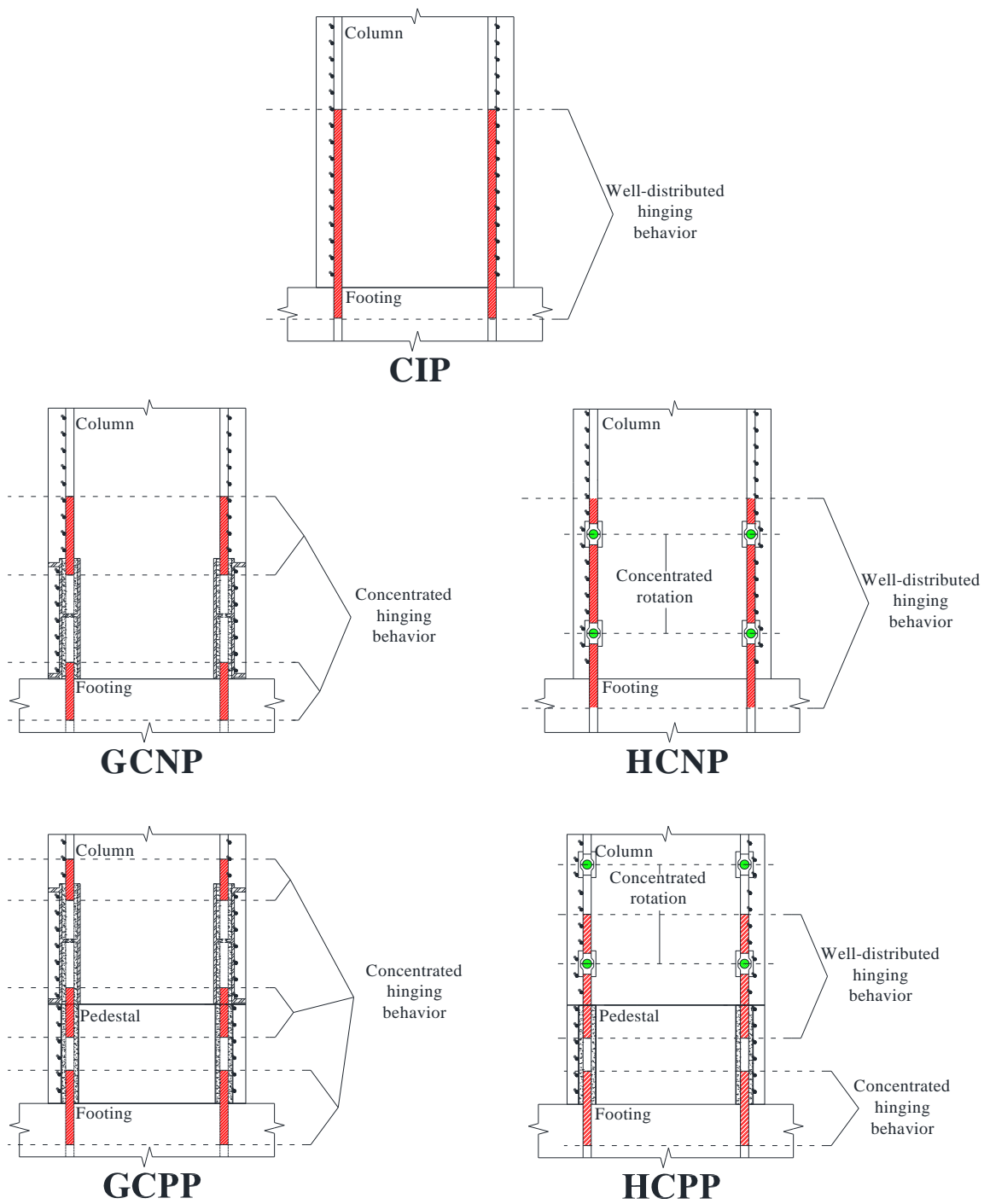


Figure 5-50 Observed hinge mechanisms

Chapter 6 Figures

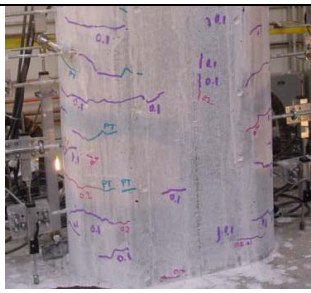
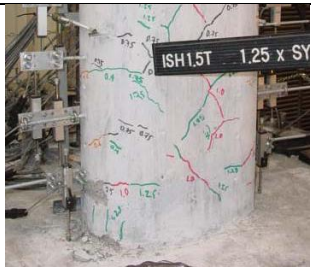
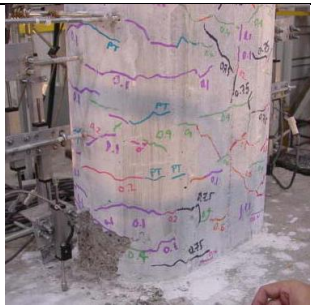


<p>DS-1</p>	<p>Flexural cracks</p>	
<p>DS-2</p>	<p>Development of shear crack and minor spalling</p>	
<p>DS-3</p>	<p>Extensive cracking and spalling</p>	
<p>DS-4</p>	<p>Visible transverse and longitudinal reinforcing bars</p>	
<p>DS-5</p>	<p>Damage to confined concrete core (Failure imitate)</p>	

Figure 6-1 Damage states as defined by Vosooghi and Saiidi (2010)

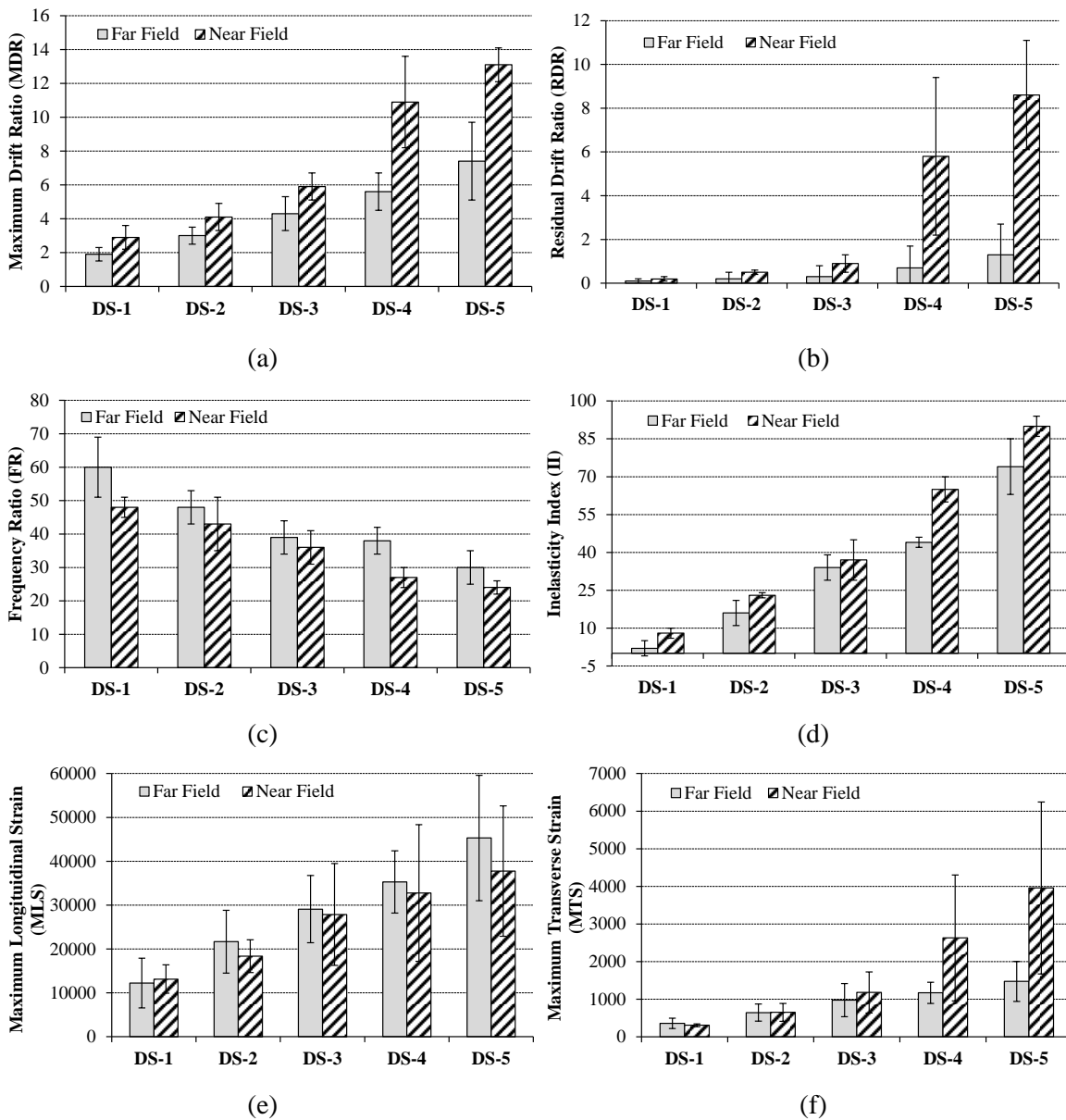


Figure 6-2 Response parameters for standard columns under near- and far-field motions

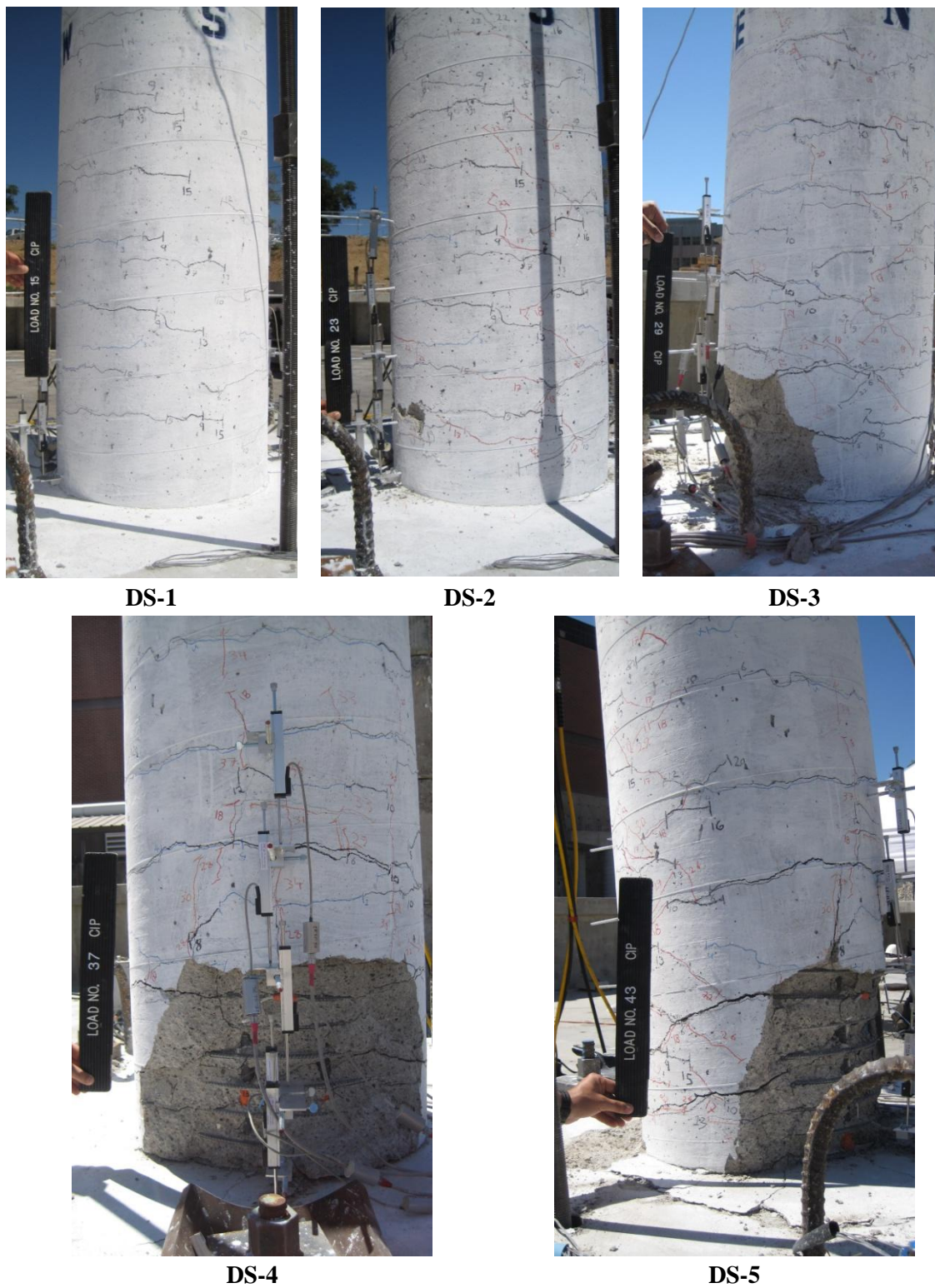
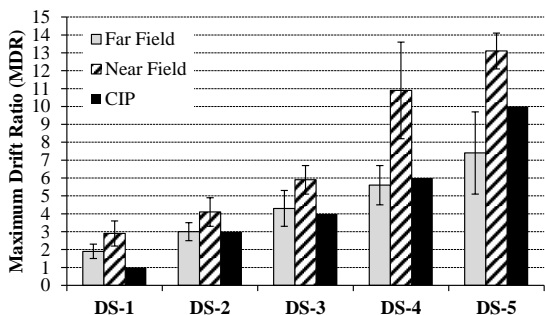
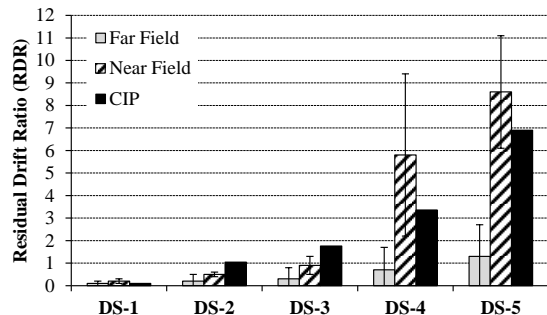


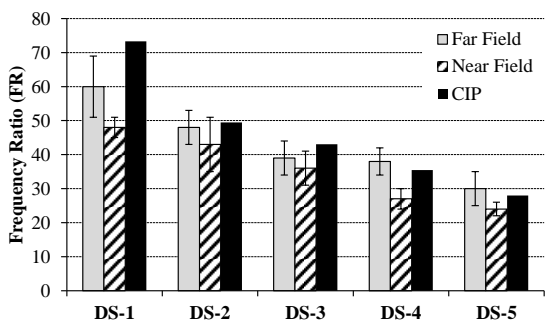
Figure 6-3 Damage states for CIP



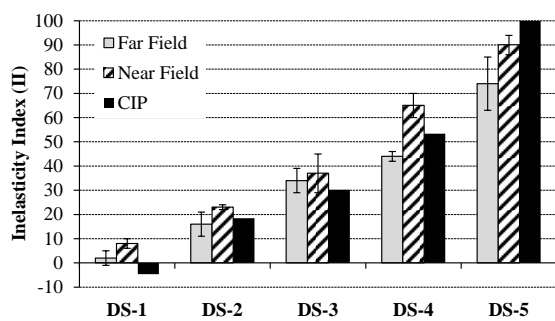
(a) Maximum drift ratio (MDR)



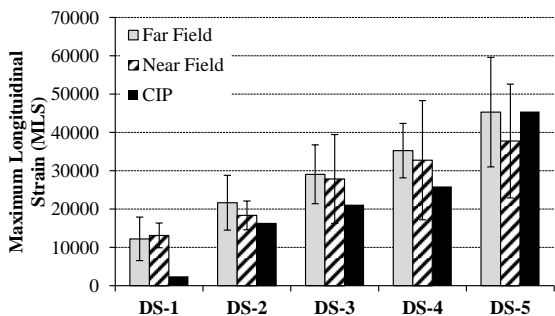
(b) Residual drift ratio (RDR)



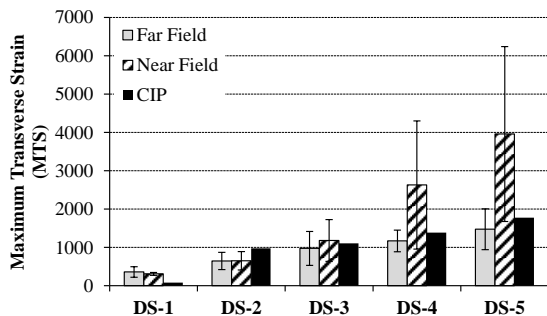
(c) Frequency ratio (FR)



(d) Inelasticity index (II)

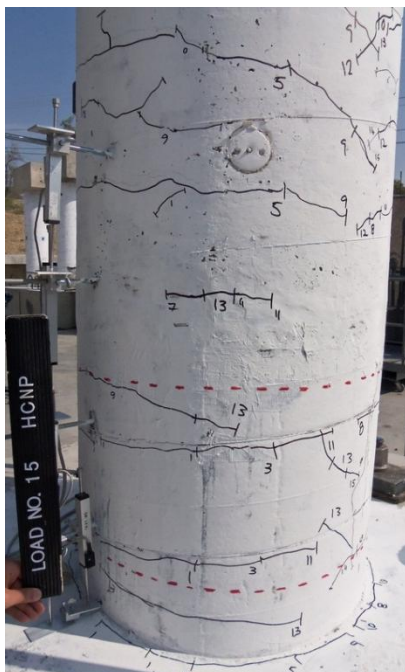


(e) Maximum longitudinal strain (MLS)



(f) Maximum transverse strain (MTS)

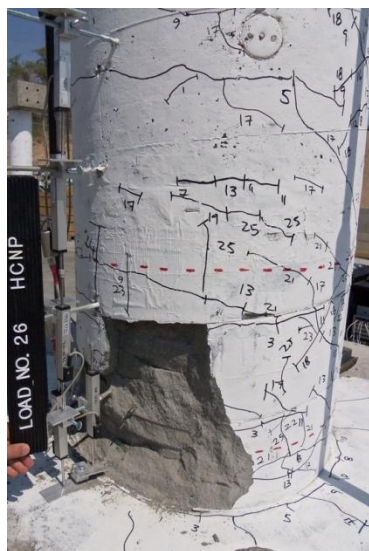
Figure 6-4 Response parameters for CIP



DS-1



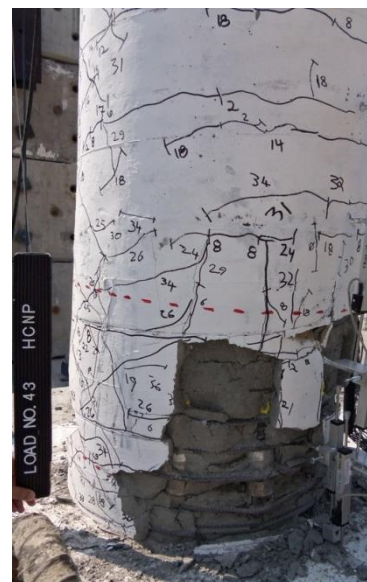
DS-2



DS-3

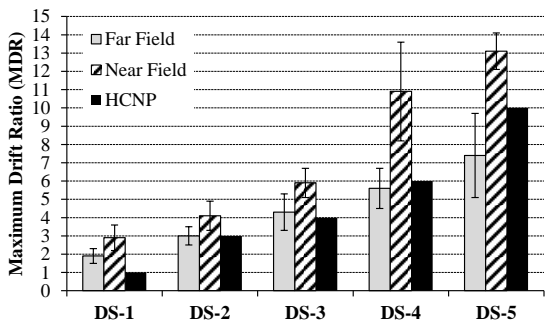


DS-4

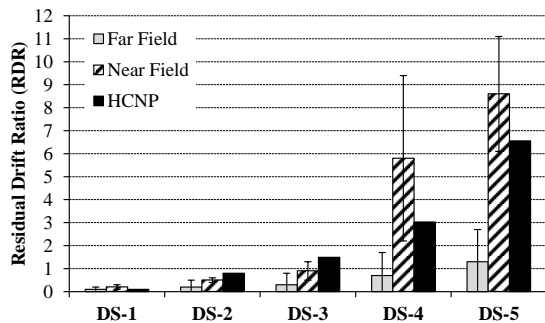


DS-5

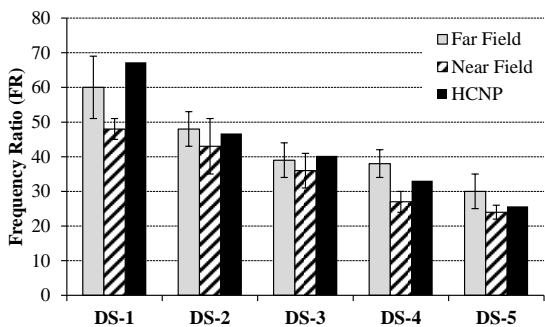
Figure 6-5 Damage states for HCNP



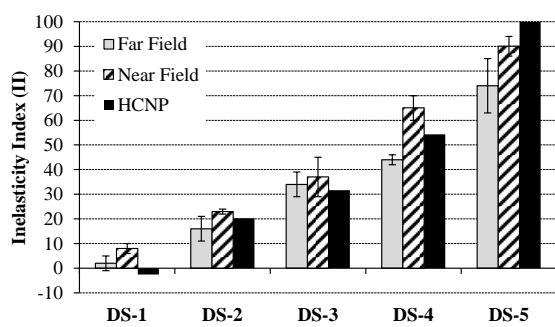
(a) Maximum drift ratio (MDR)



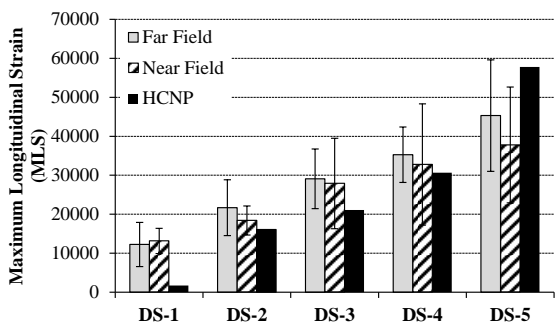
(b) Residual drift ratio (RDR)



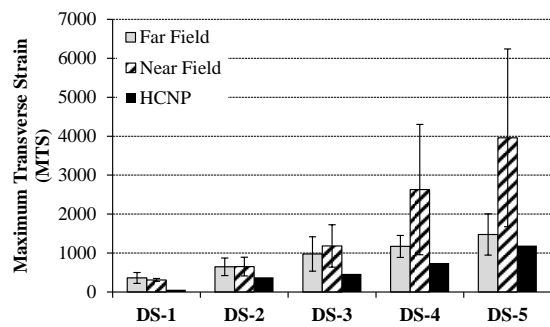
(c) Frequency ratio (FR)



(d) Inelasticity index (II)

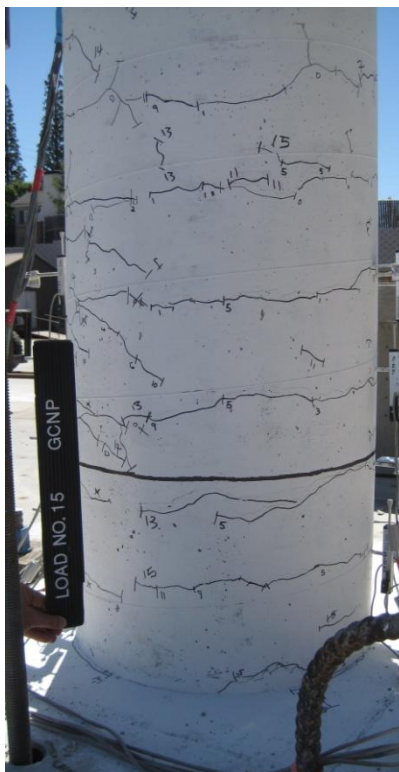


(e) Maximum longitudinal strain (MLS)

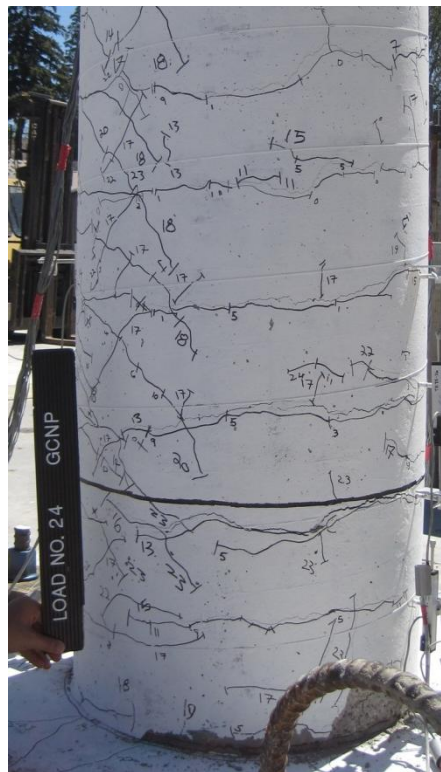


(f) Maximum transverse strain (MTS)

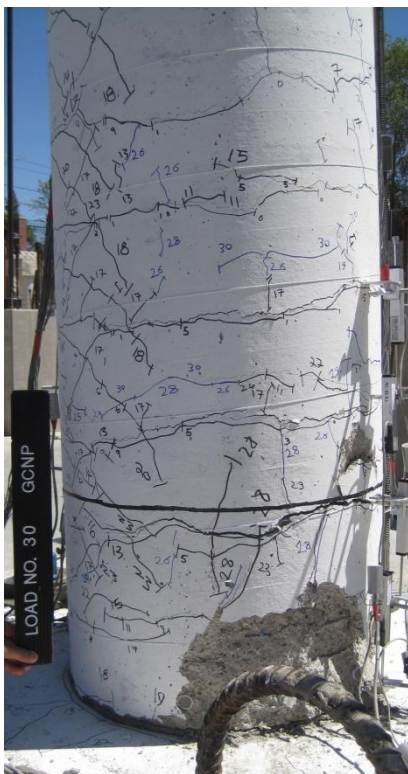
Figure 6-6 Response parameters for HCNP



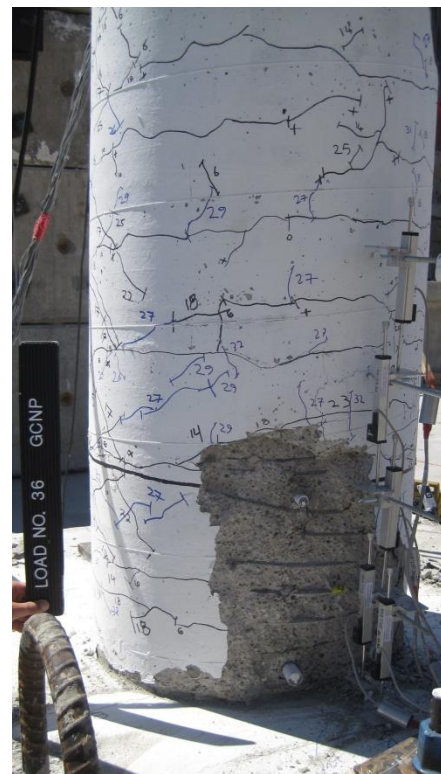
DS-1



DS-2

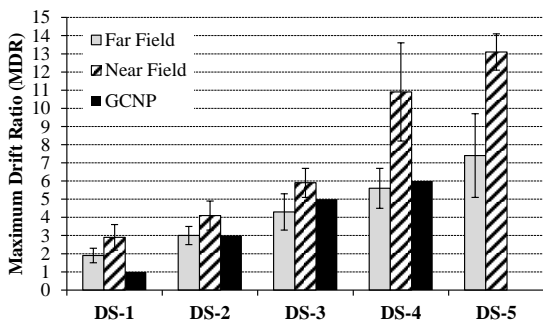


DS-3

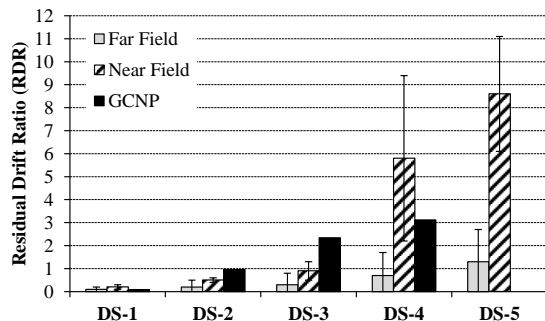


DS-4

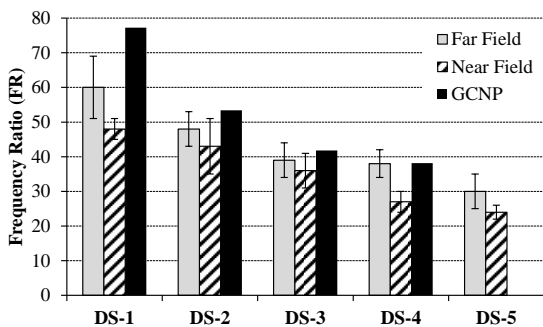
Figure 6-7 Damage states for GCNP



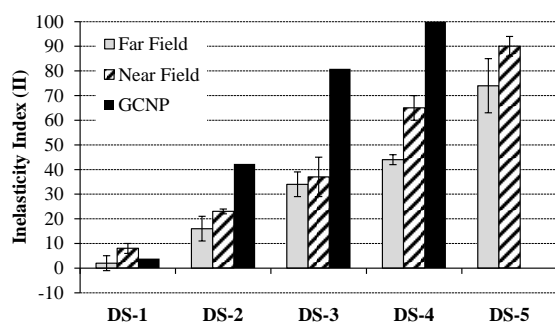
(a) Maximum drift ratio (MDR)



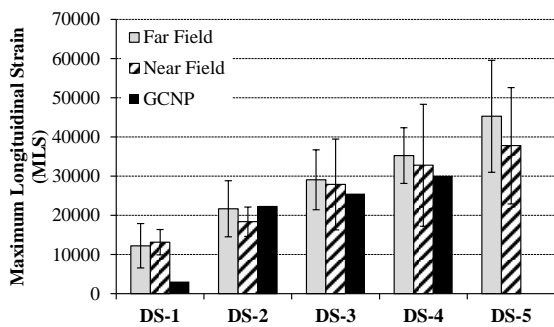
(b) Residual drift ratio (RDR)



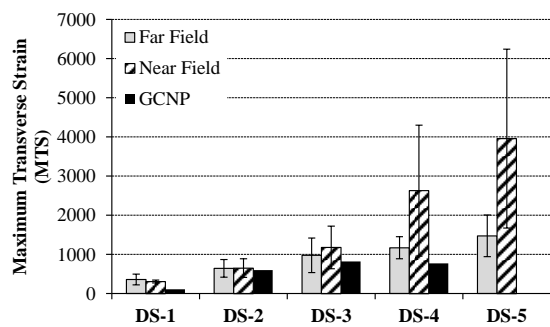
(c) Frequency ratio (FR)



(d) Inelasticity index (II)



(e) Maximum longitudinal strain (MLS)



(f) Maximum transverse strain (MTS)

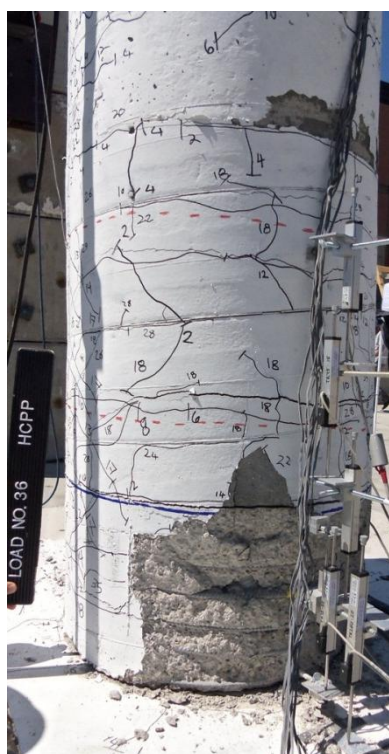
Figure 6-8 Response parameters for GCNP



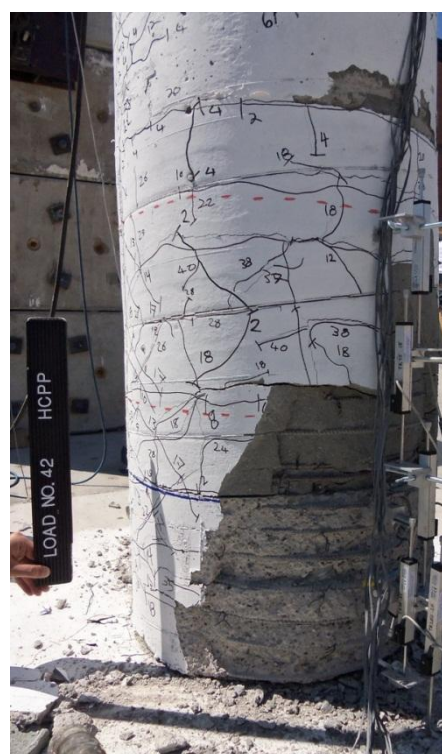
DS-1

DS-2

DS-3

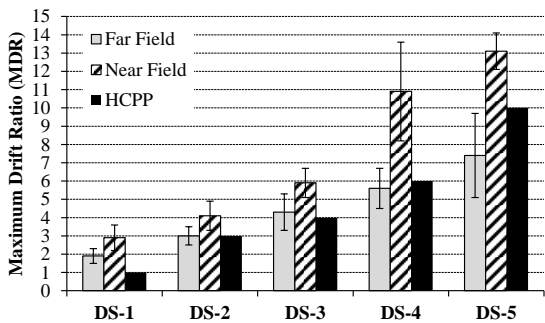


DS-4

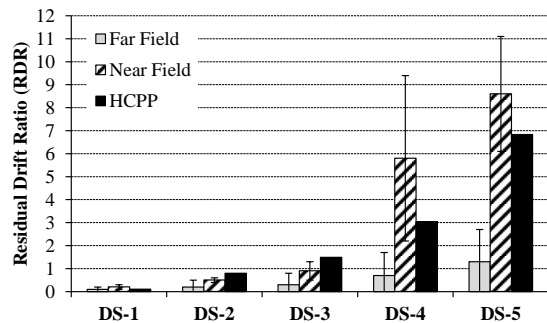


DS-5

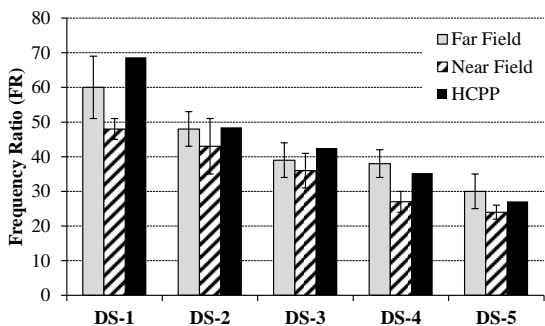
Figure 6-9 Damage states for HCPP



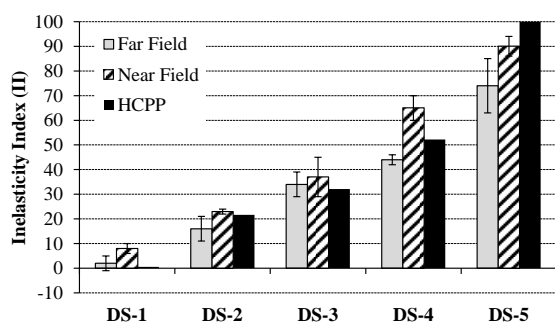
(a) Maximum drift ratio (MDR)



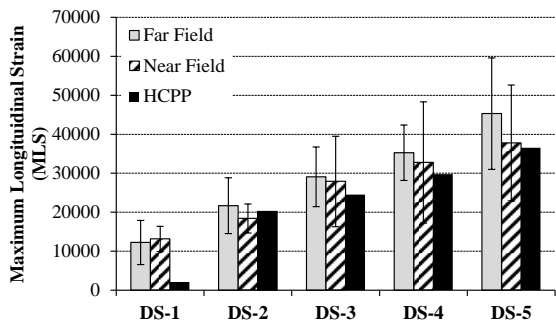
(b) Residual drift ratio (RDR)



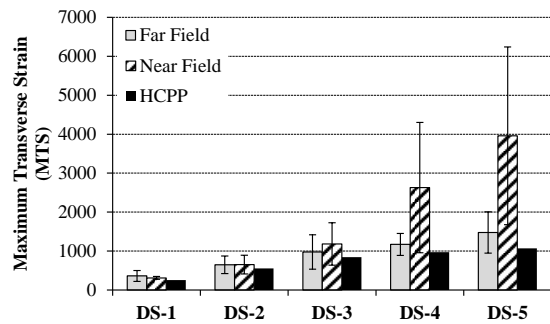
(c) Frequency ratio (FR)



(d) Inelasticity index (II)

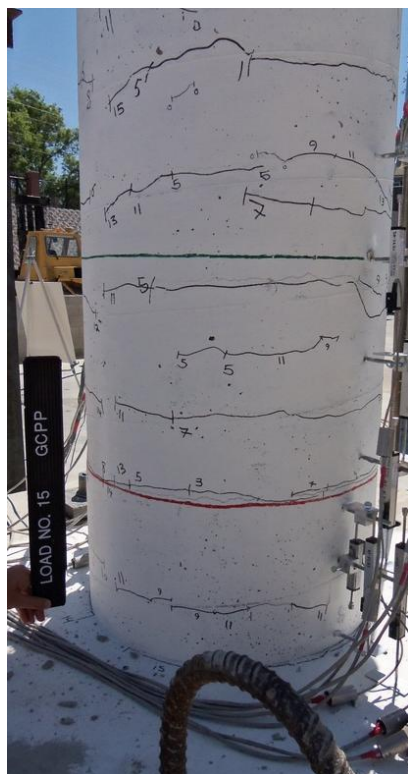


(e) Maximum longitudinal strain (MLS)

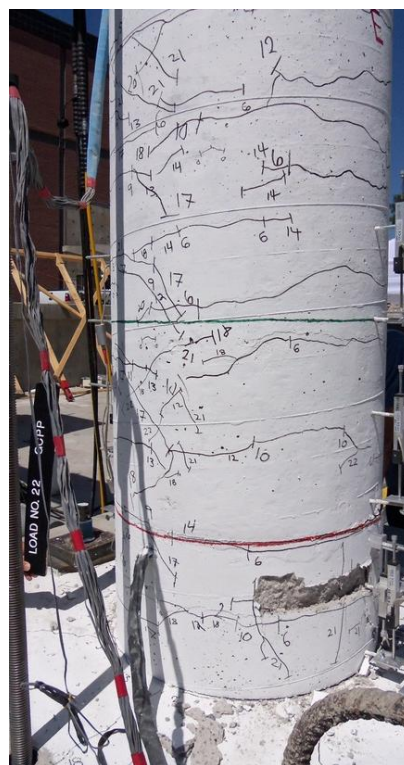


(f) Maximum transverse strain (MTS)

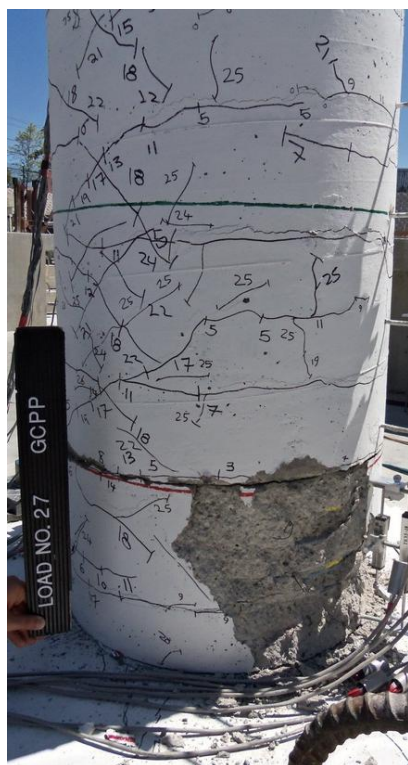
Figure 6-10 Response parameters for HCPP



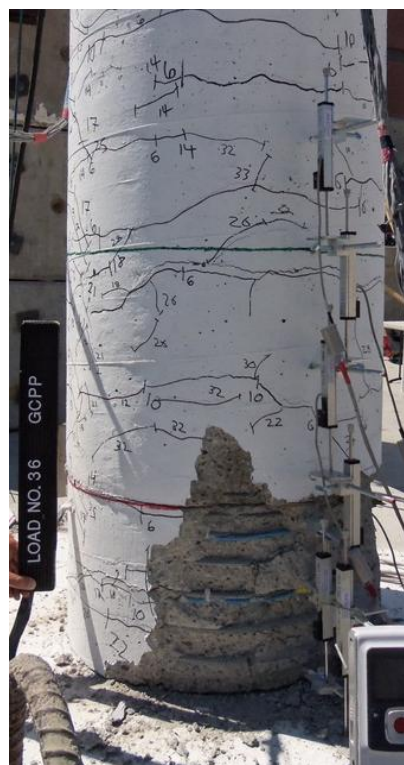
DS-1



DS-2

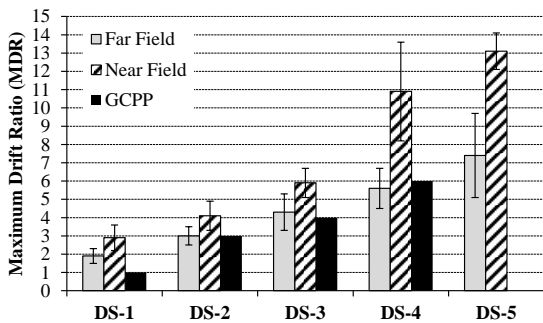


DS-3

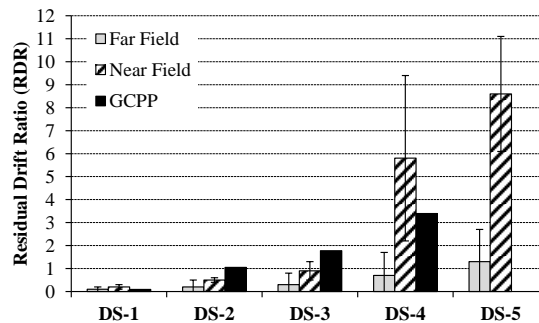


DS-4

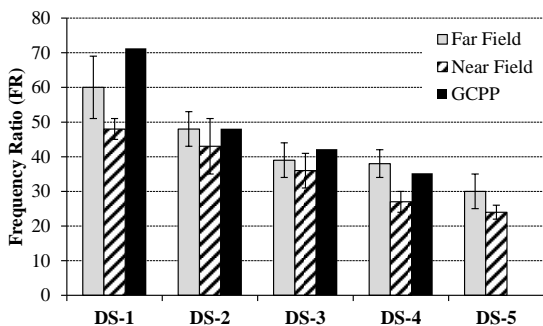
Figure 6-11 Damage states for GCPP



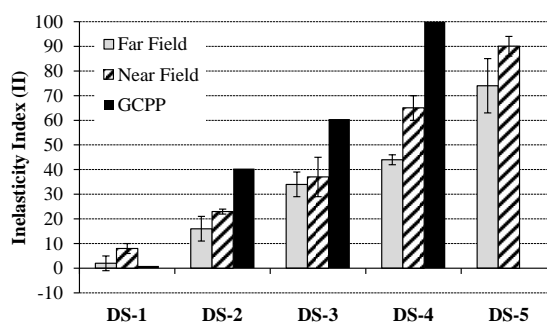
(a) Maximum drift ratio (MDR)



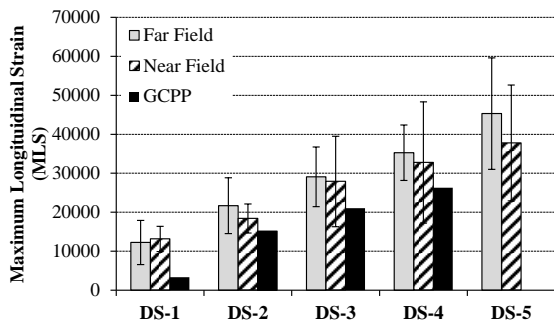
(b) Residual drift ratio (RDR)



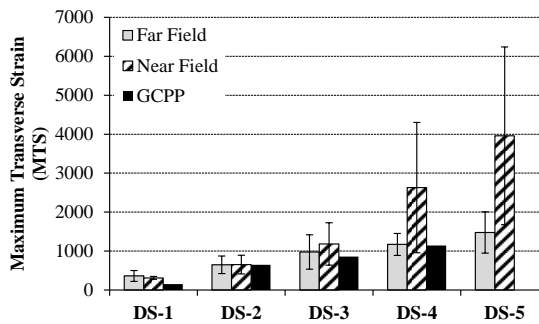
(c) Frequency ratio (FR)



(d) Inelasticity index (II)

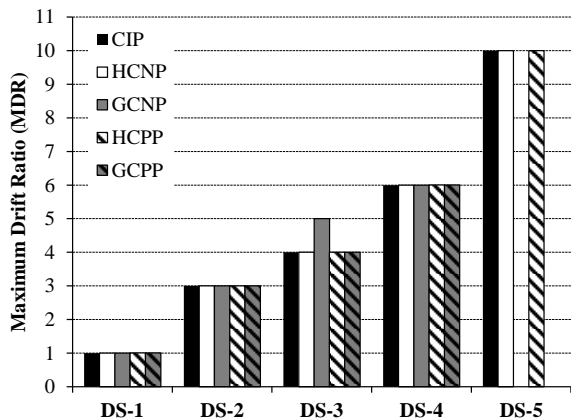


(e) Maximum longitudinal strain (MLS)

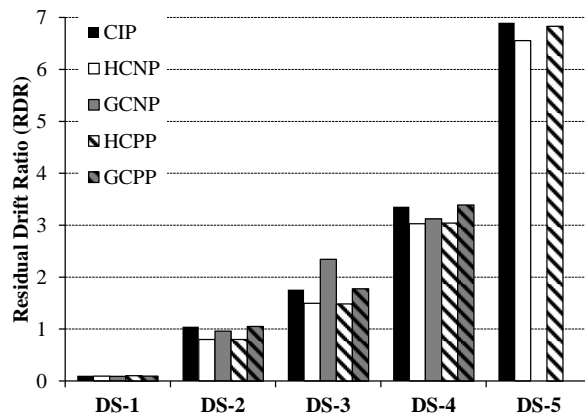


(f) Maximum transverse strain (MTS)

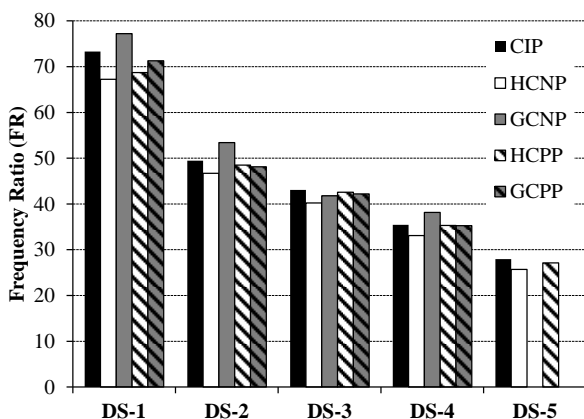
Figure 6-12 Response parameters for GCPP



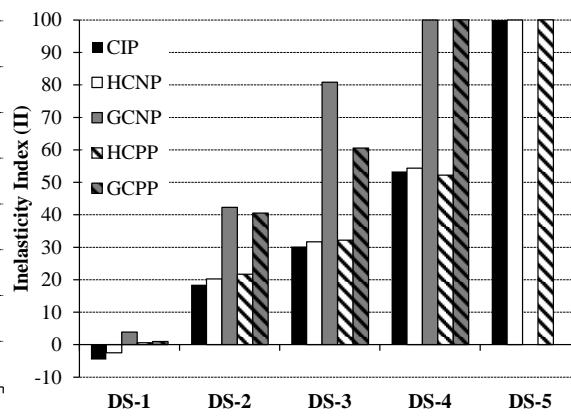
(a) Maximum drift ratio



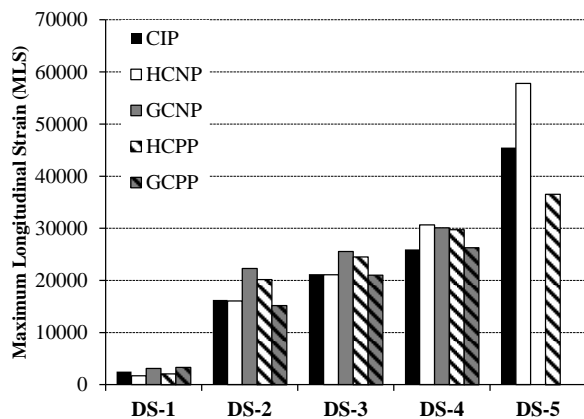
(b) Residual drift ratio



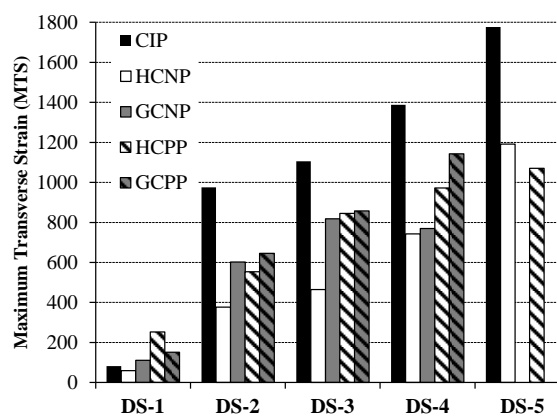
(c) Frequency ratio



(d) Inelasticity index



(e) Maximum longitudinal strain



(f) Maximum transverse strain

Figure 6-13 Comparison of damage states for all columns

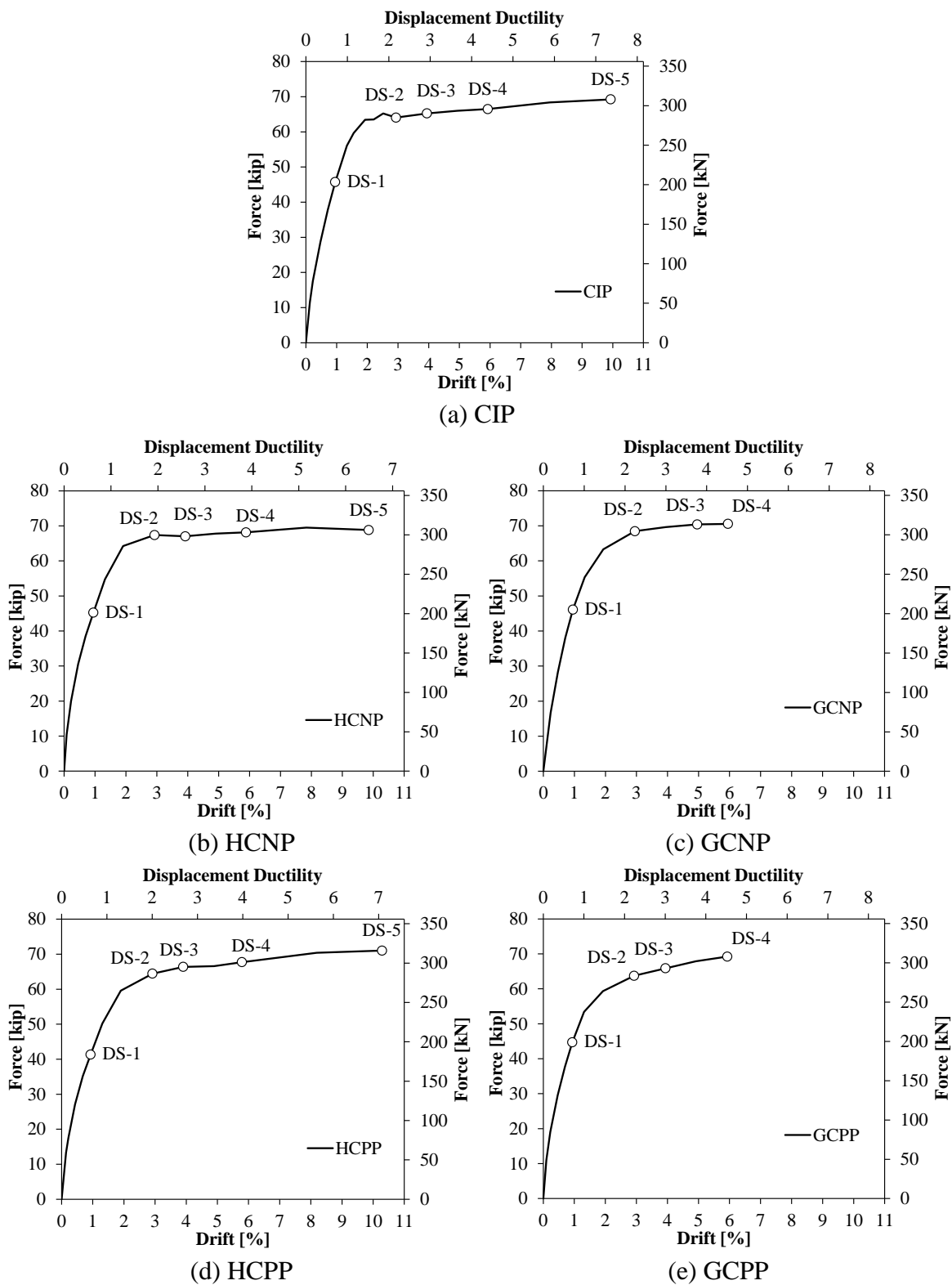
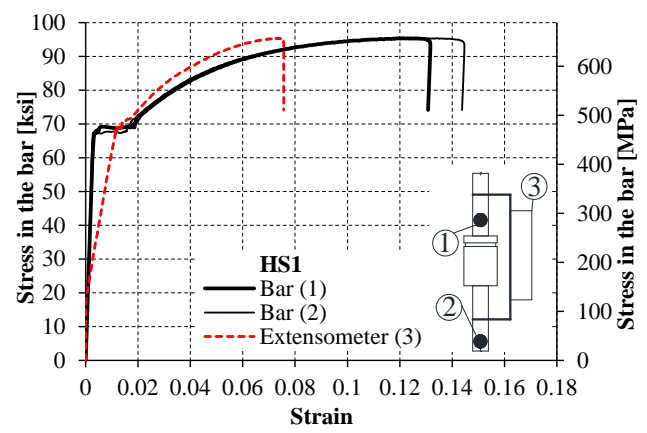
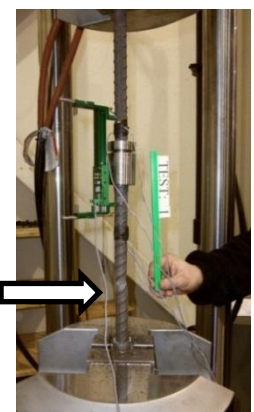


Figure 6-14 Correlation between average push-over response and apparent damage states

Chapter 7 Figures

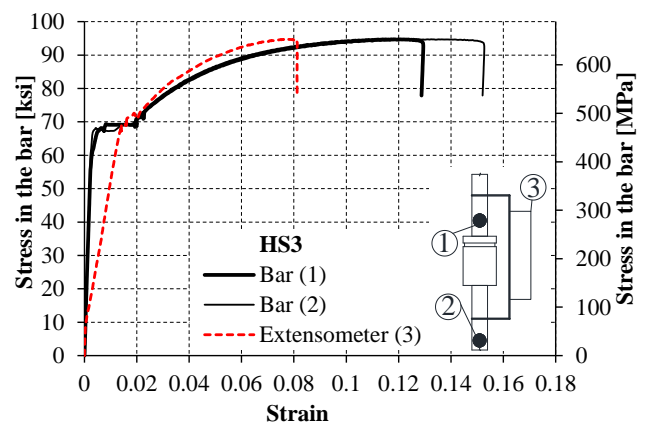


(a) Stress-strain behavior

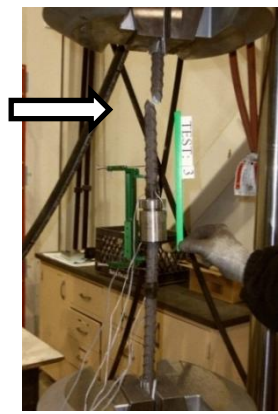


(b) Location of rupture

Figure 7-1 Static test result for sample HS1

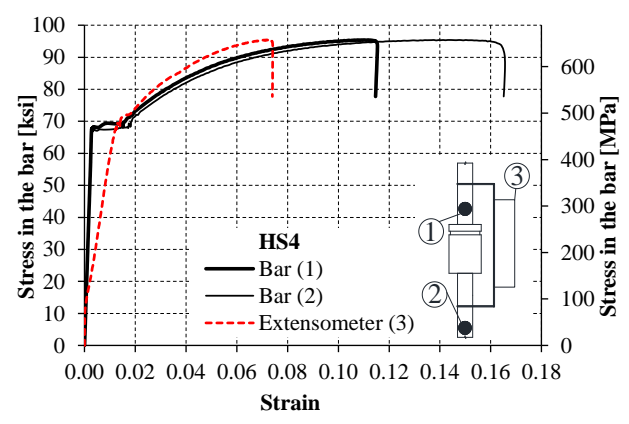


(a) Stress-strain behavior



(b) Location of rupture

Figure 7-2 Static test result for sample HS3



(a) Stress-strain behavior



(b) Location of rupture

Figure 7-3 Static test result for sample HS4

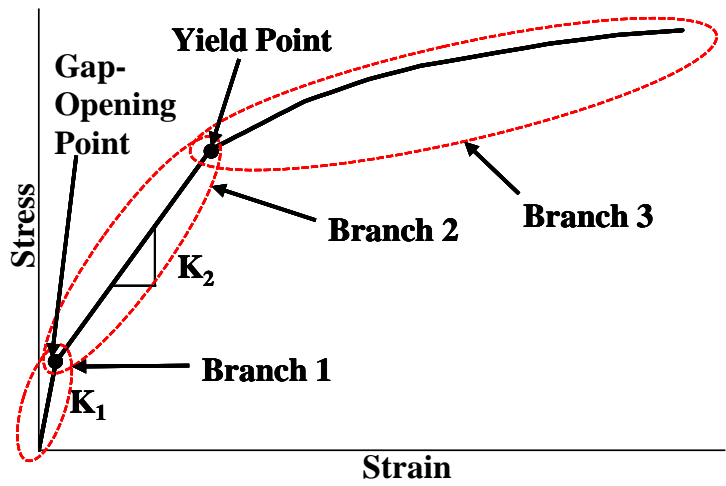
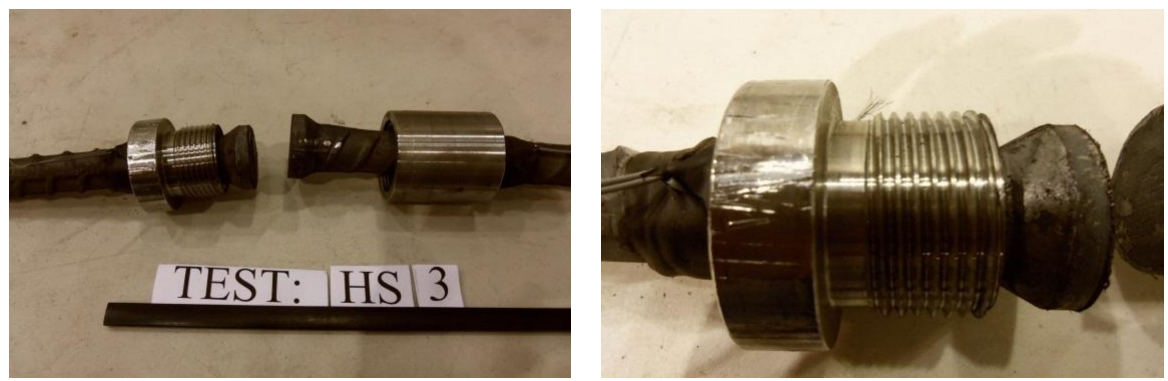
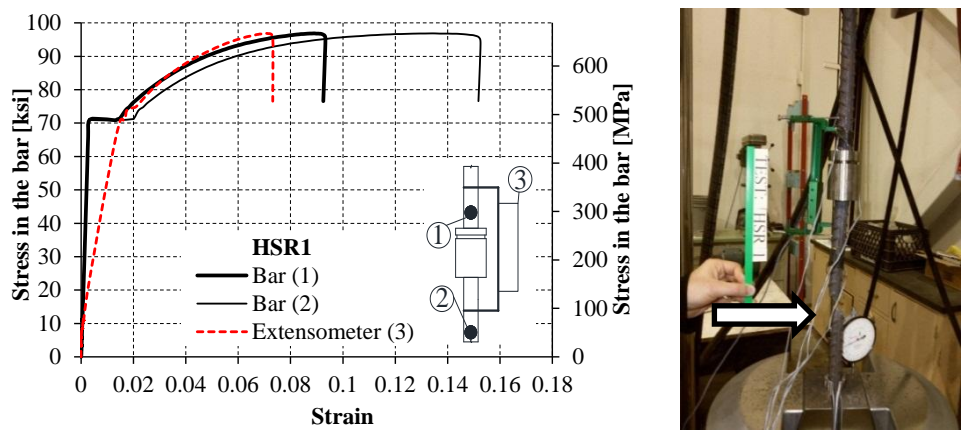


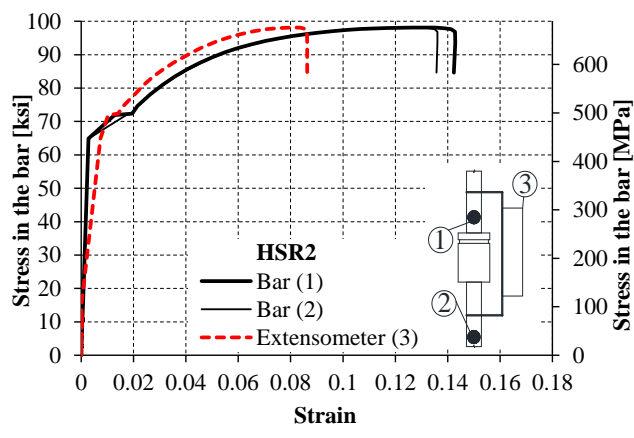
Figure 7-4 Monotonic stress-strain behavior of the headed coupler region



(a) View of both sleeves and deformed heads (b) Close-up view
Figure 7-5 Sample HS3 disassembled after testing



(a) Stress-strain behavior (b) Location of rupture
Figure 7-6 Dynamic test result for sample HSR1

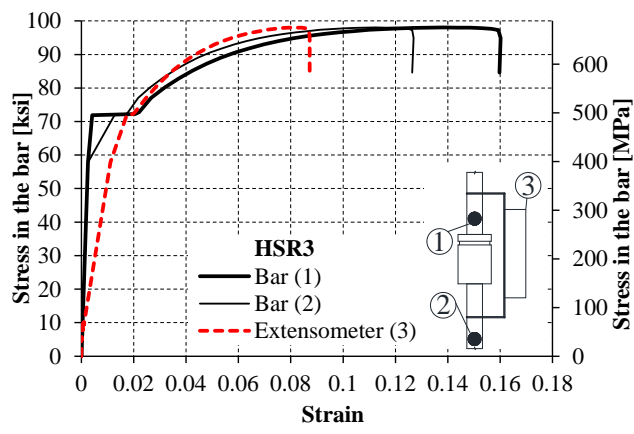


(a) Stress-strain behavior

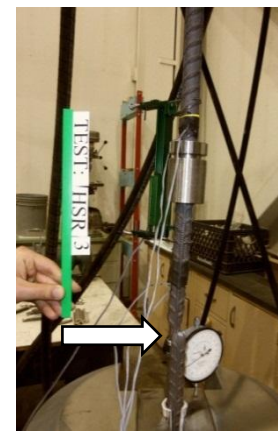


(b) Location of rupture

Figure 7-7 Dynamic test result for sample HSR2

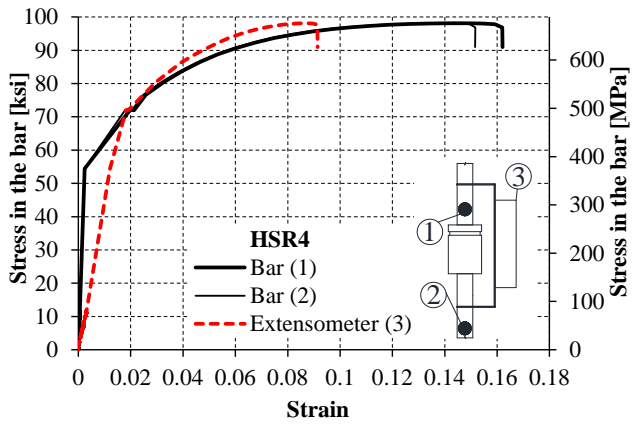


(a) Stress-strain behavior

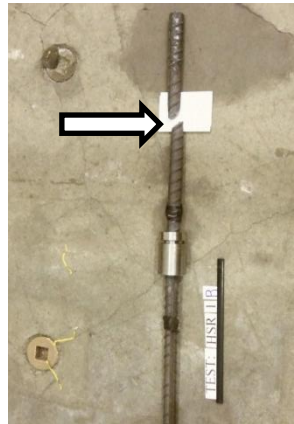


(b) Location of rupture

Figure 7-8 Dynamic test result for sample HSR3

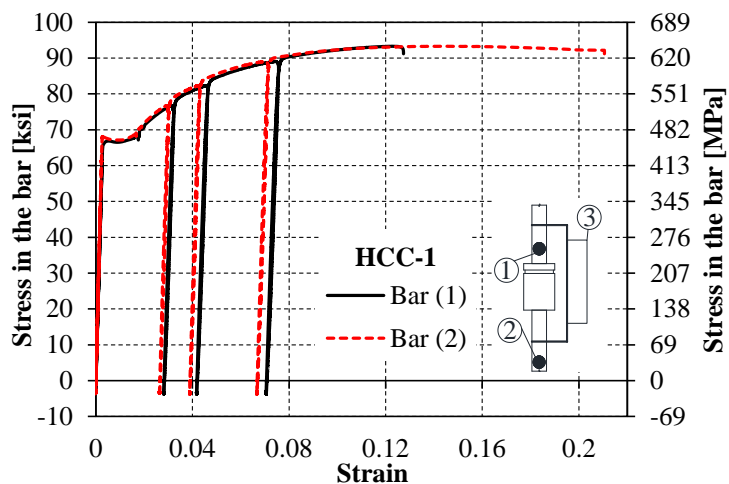


(a) Stress-strain behavior

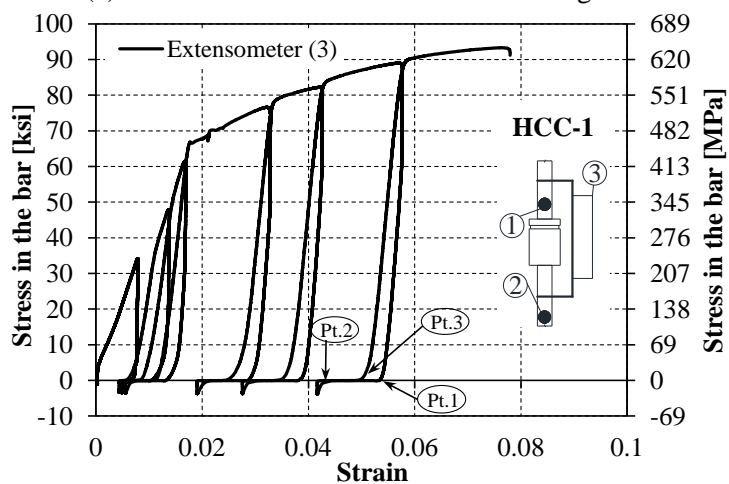


(b) Location of rupture

Figure 7-9 Dynamic test result for sample HSR4



(a) Stress-strain behavior of the reinforcing bars



(b) Stress-strain behavior of the coupler region



(c) Location of rupture

Figure 7-10 Cyclic test results for headed coupler sample HCC-1

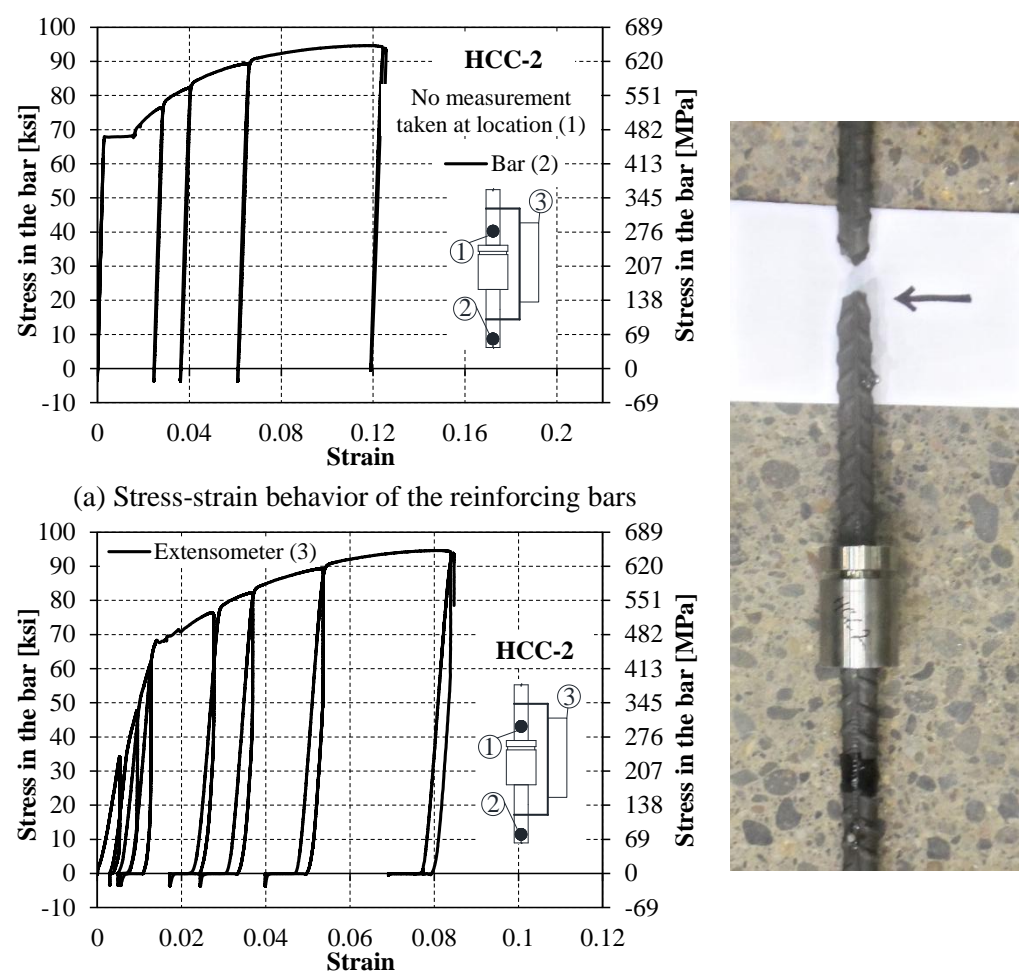


Figure 7-11 Cyclic test results for headed coupler sample HCC-2

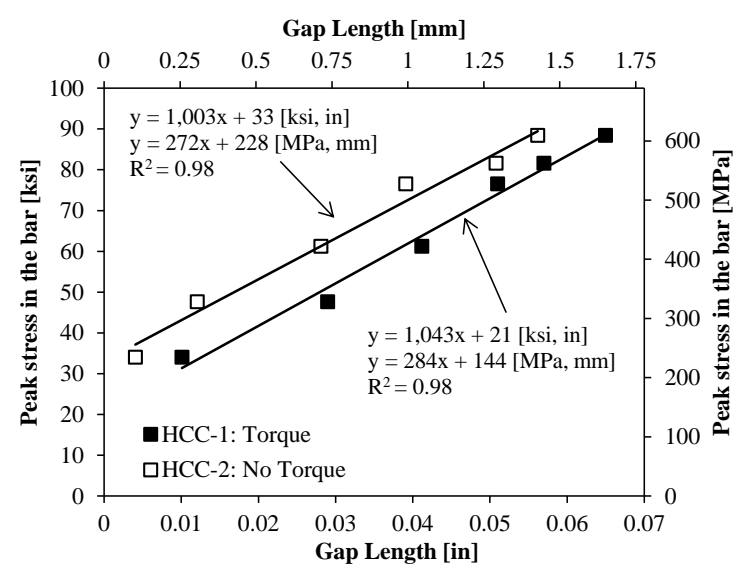
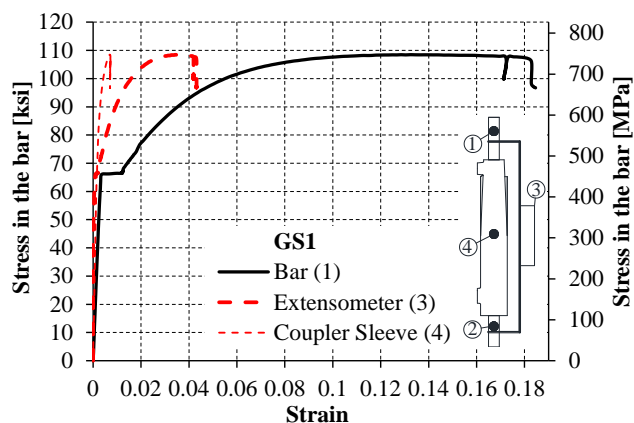


Figure 7-12 Measured relationship between peak stress in the bars and gap length

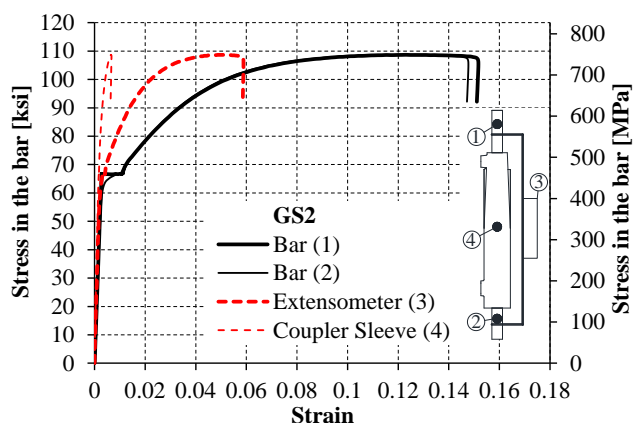


(a) Stress-strain behavior



(b) Location of rupture

Figure 7-13 Static test result for sample GS1

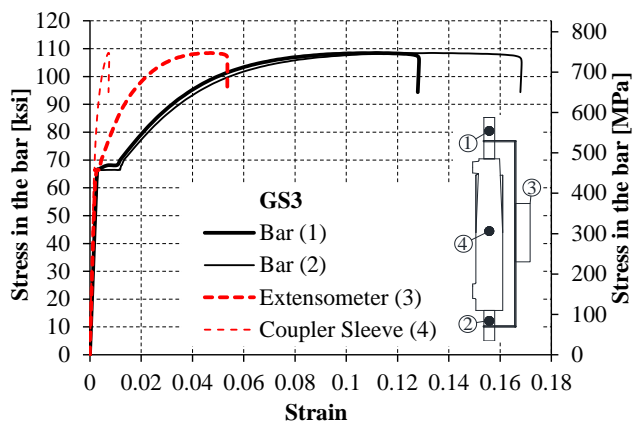


(a) Stress-strain behavior

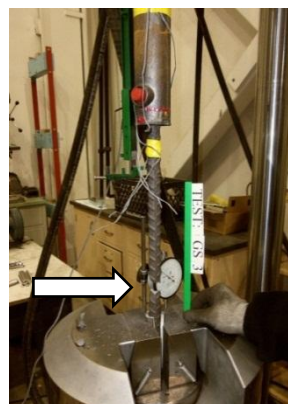


(b) Location of rupture

Figure 7-14 Static test result for sample GS2



(a) Stress-strain behavior



(b) Location of rupture

Figure 7-15 Static test result for sample GS3

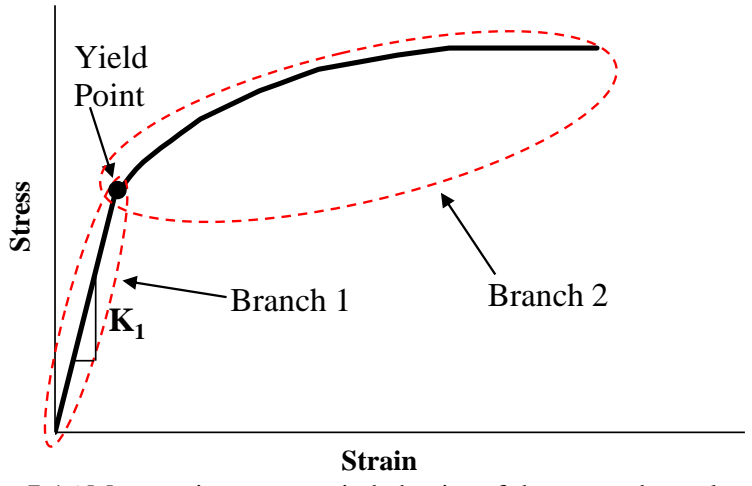


Figure 7-16 Monotonic stress-strain behavior of the grouted coupler region

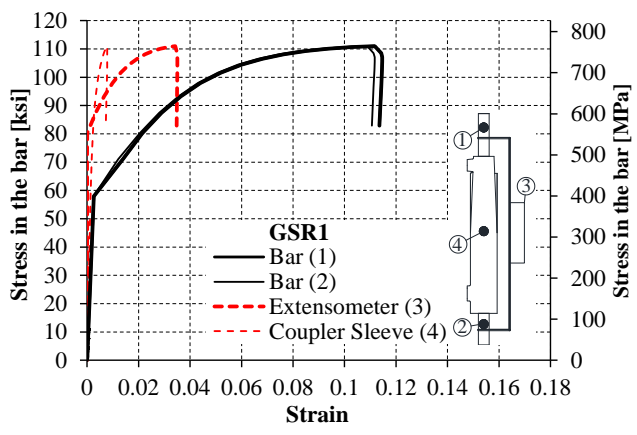


(a) Factory end



(b) Field end

Figure 7-17 Evidence of strain penetration into the grouted sleeve

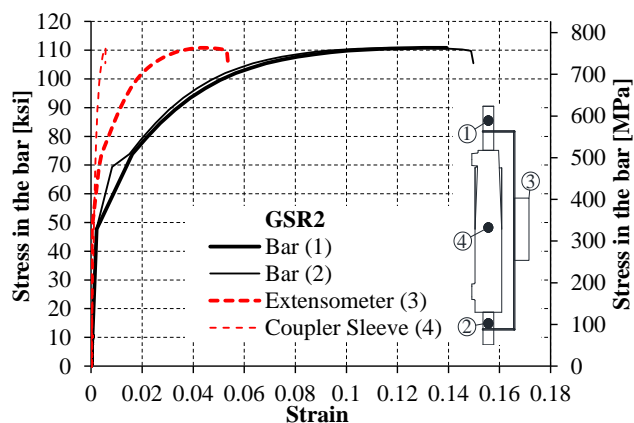


(a) Stress-strain behavior

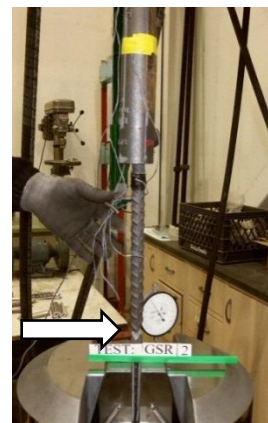


(b) Location of rupture

Figure 7-18 Dynamic test result for sample GSR1

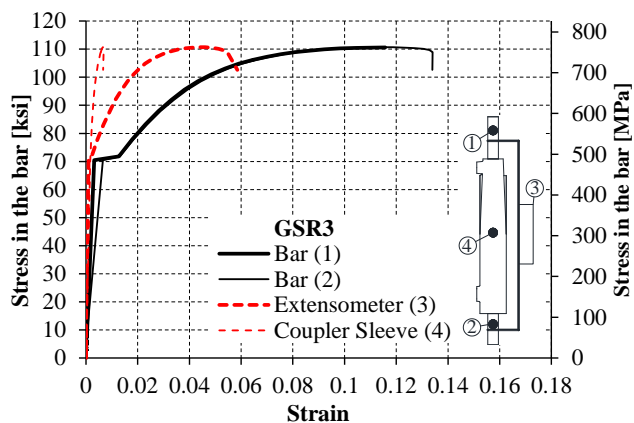


(a) Stress-strain behavior



(b) Location of rupture

Figure 7-19 Dynamic test result for sample GSR2

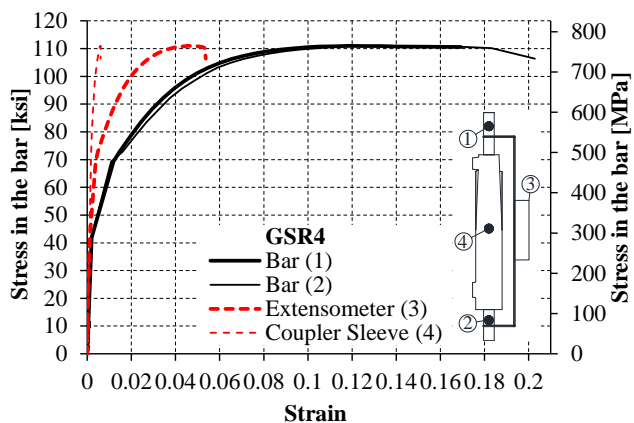


(a) Stress-strain behavior



(b) Location of rupture

Figure 7-20 Dynamic test result for sample GSR3

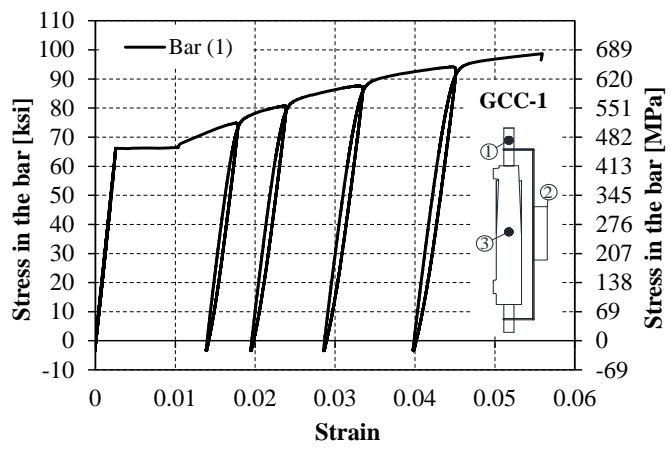


(a) Stress-strain behavior

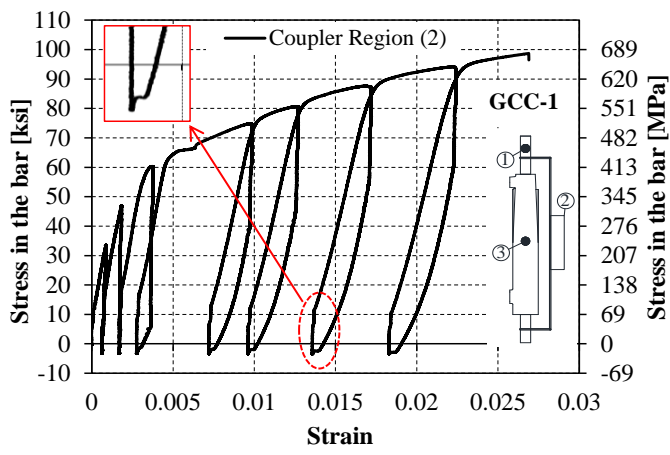


(b) Location of rupture

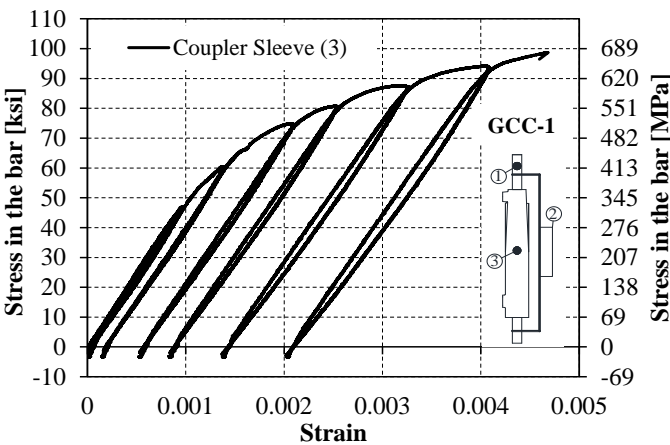
Figure 7-21 Dynamic test result for sample GSR4



(a) Behavior of the reinforcing bar



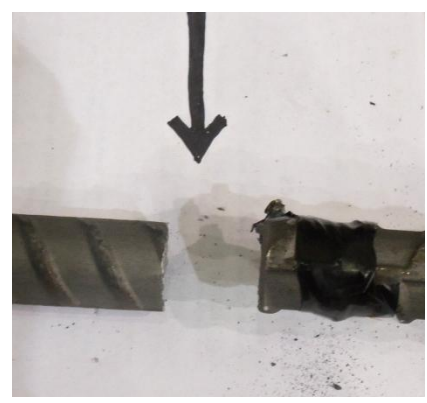
(b) Behavior of the coupler region



(c) Behavior of the ductile iron sleeve



(d) Bar failure



(e) Close-up on failure location

Figure 7-22 Cyclic test results for grouted coupler sample GCC-1

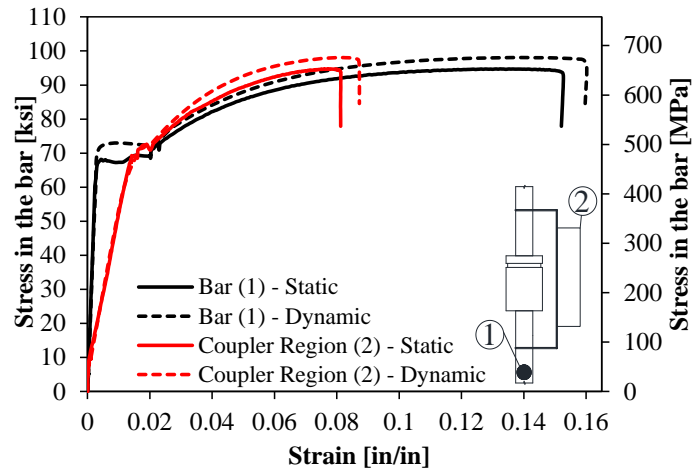


Figure 7-23 Comparison of static and dynamic stress-strain behavior for headed coupler tests

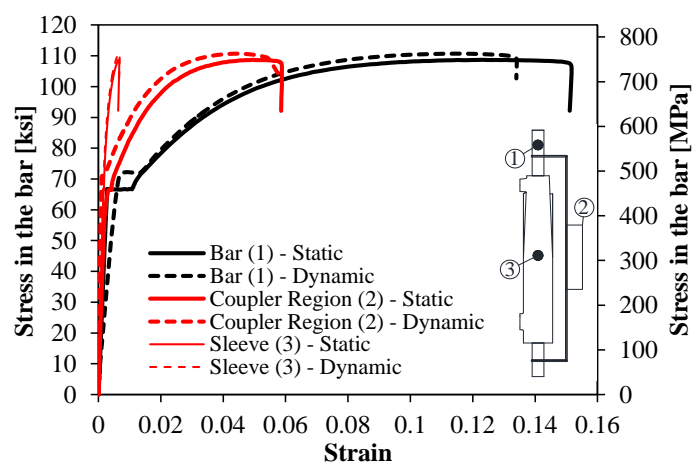


Figure 7-24 Comparison of static and dynamic stress-strain behavior for grouted coupler tests

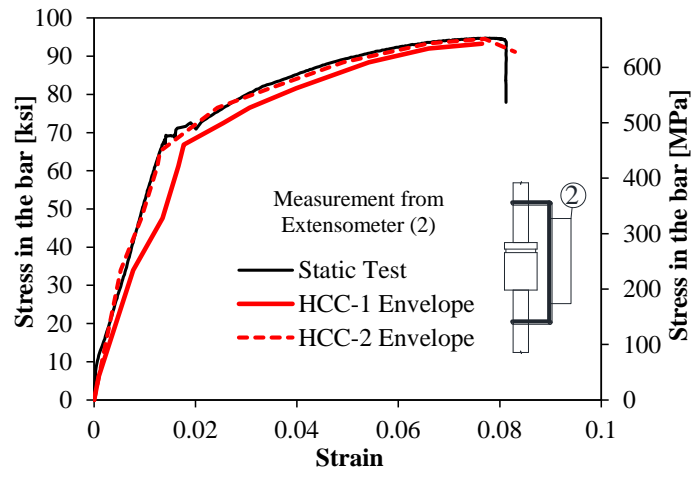


Figure 7-25 Comparison of static and cyclic stress-strain behavior for headed coupler tests

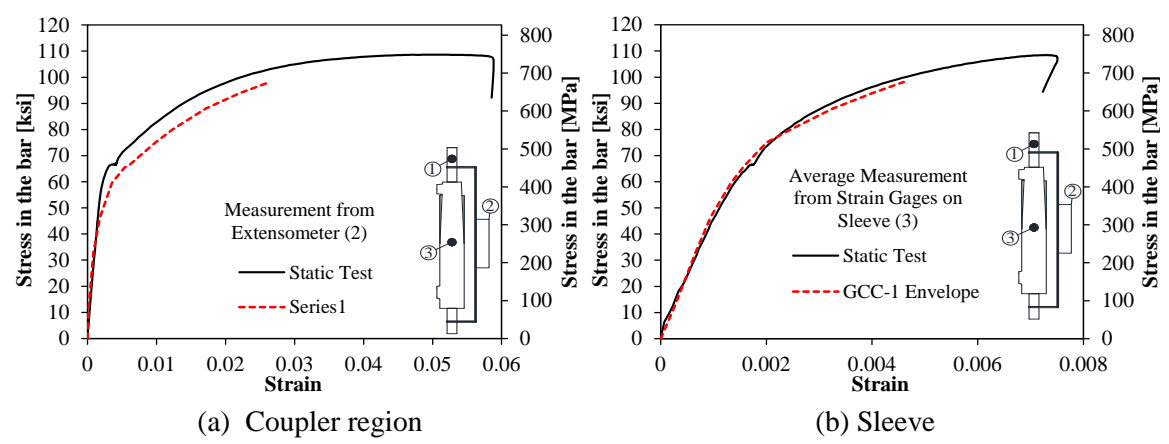


Figure 7-26 Comparison of static and cyclic stress-strain behavior for grouted coupler tests

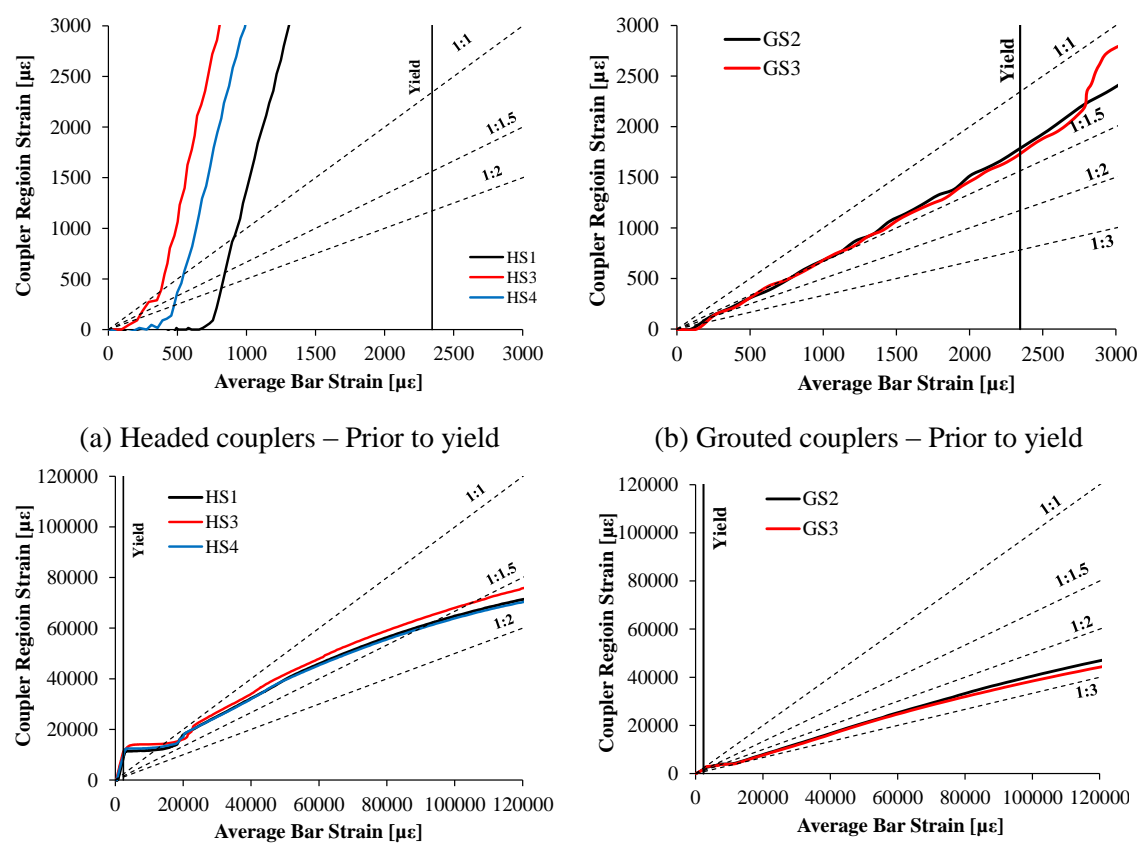


Figure 7-27 Comparison of the bar-to-coupler region strain ratio for static loading

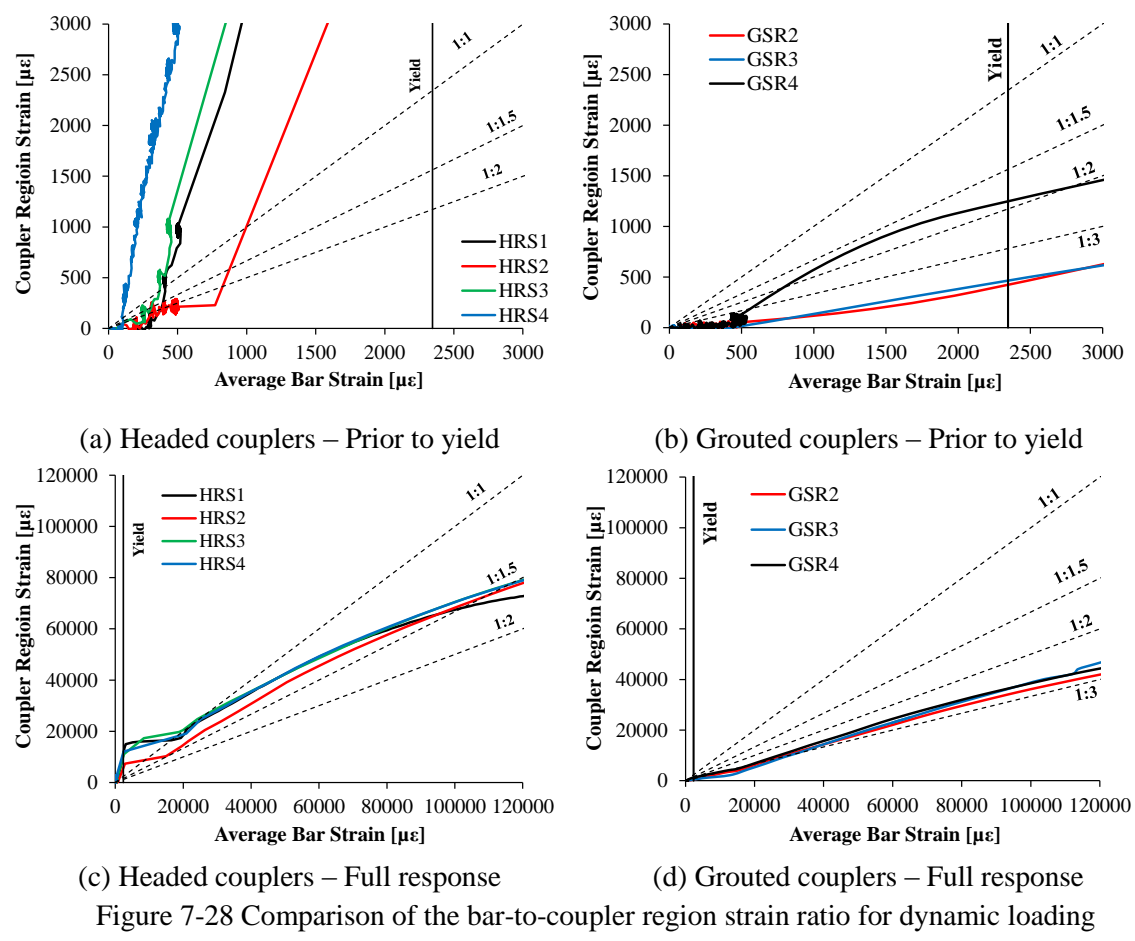


Figure 7-28 Comparison of the bar-to-coupler region strain ratio for dynamic loading

Chapter 8 Figures

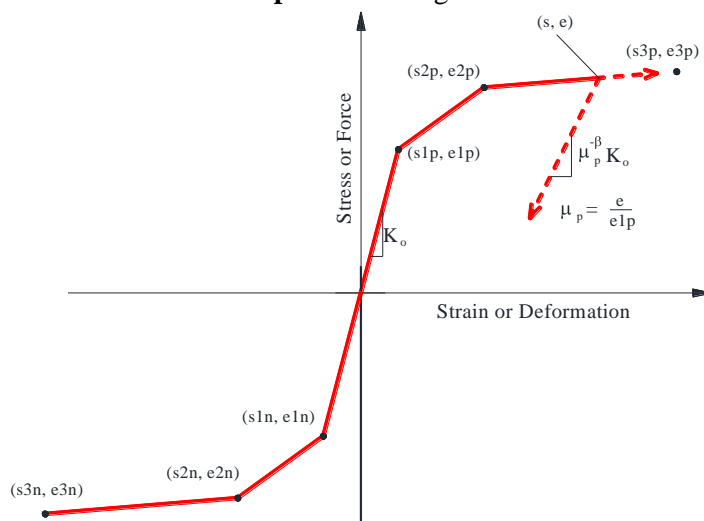


Figure 8-1 Constitutive behavior for “Hysteretic” material

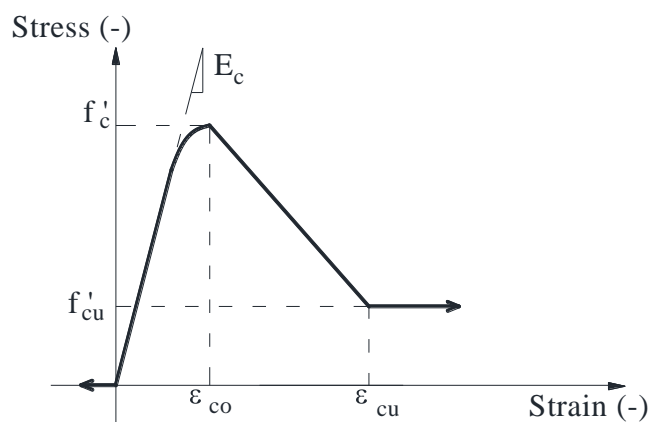


Figure 8-2 Constitutive model for unconfined concrete

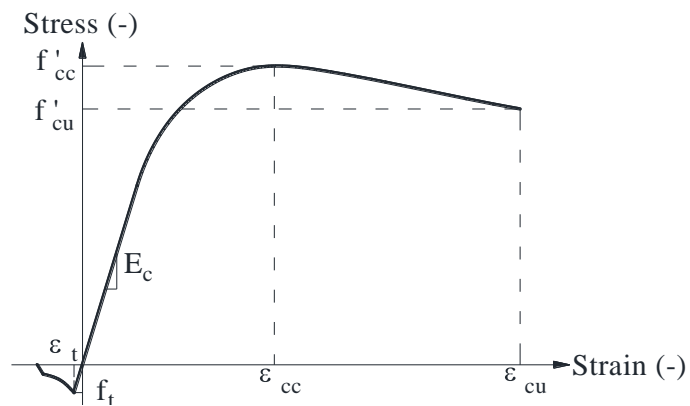


Figure 8-3 Constitutive model for confined concrete

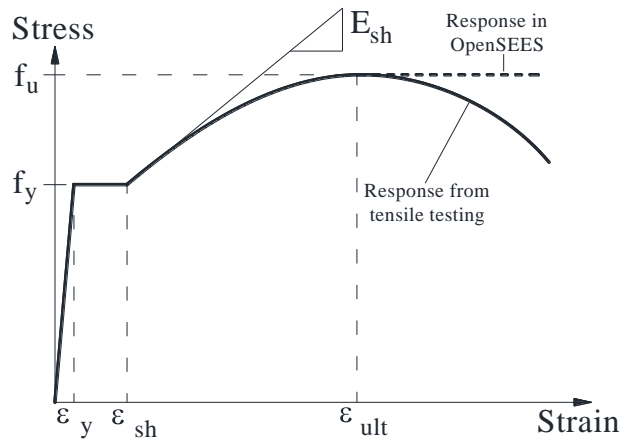


Figure 8-4 Constitutive model for reinforcing steel

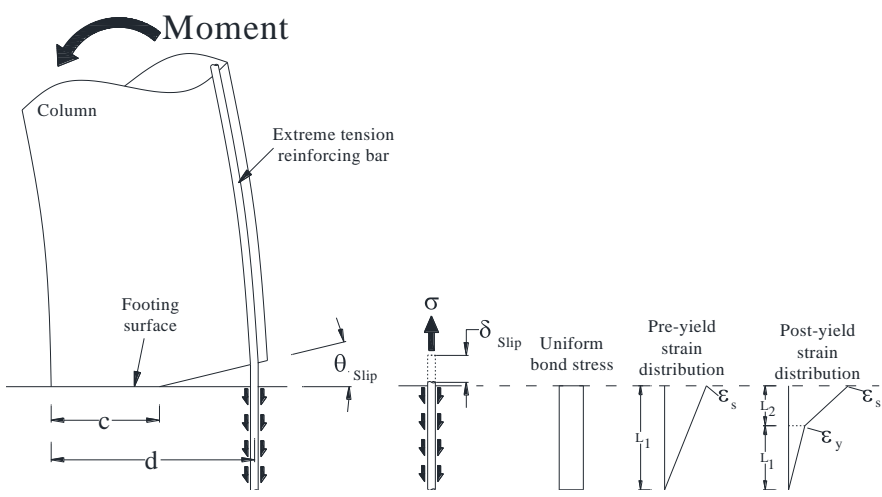


Figure 8-5 Wehbe's method for calculating bond-slip rotation

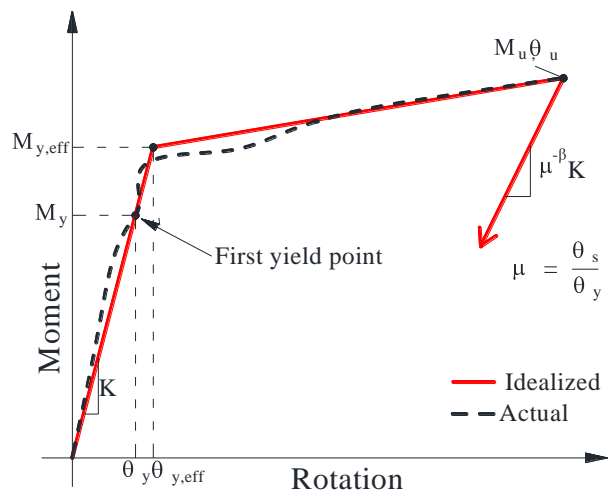


Figure 8-6 Moment-rotation relationship for bond-slip

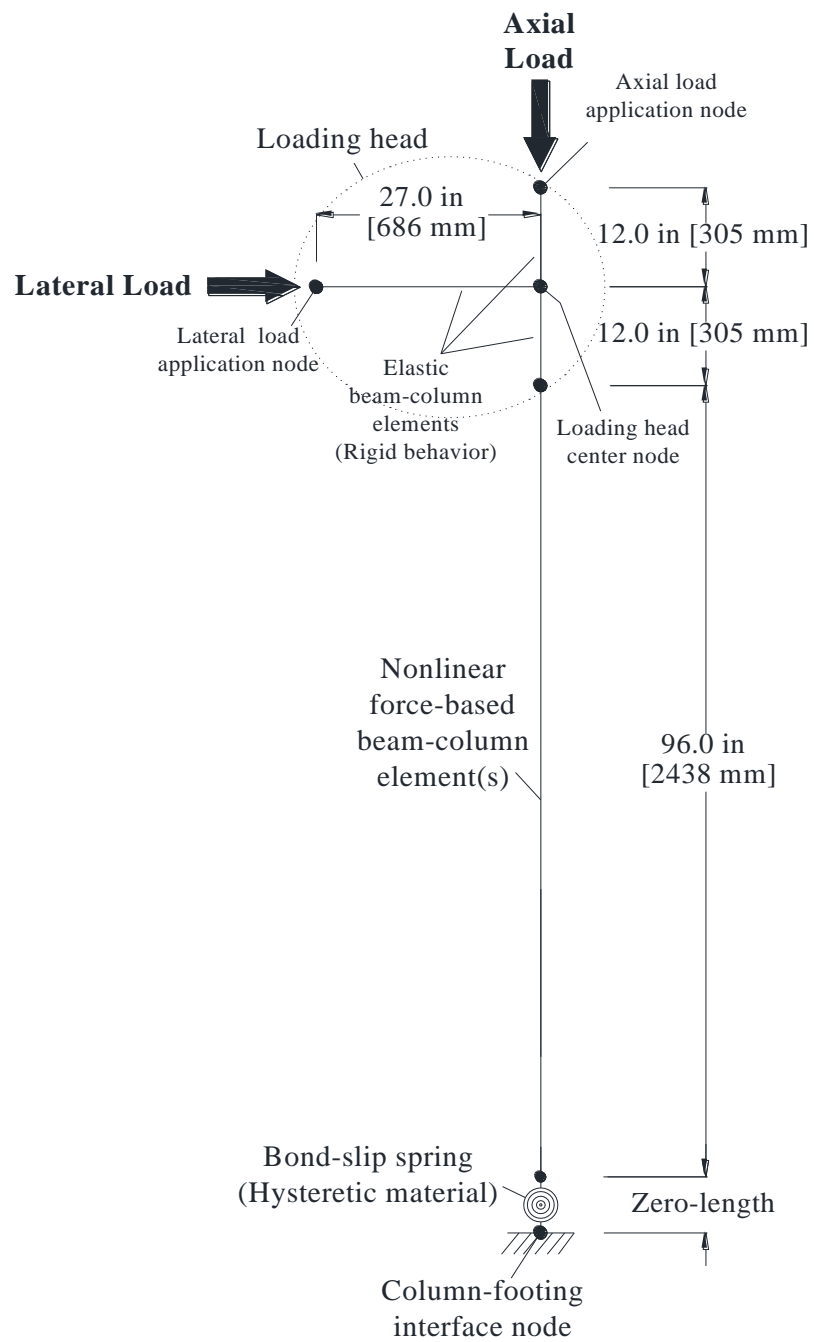


Figure 8-7 General details of analytical column models

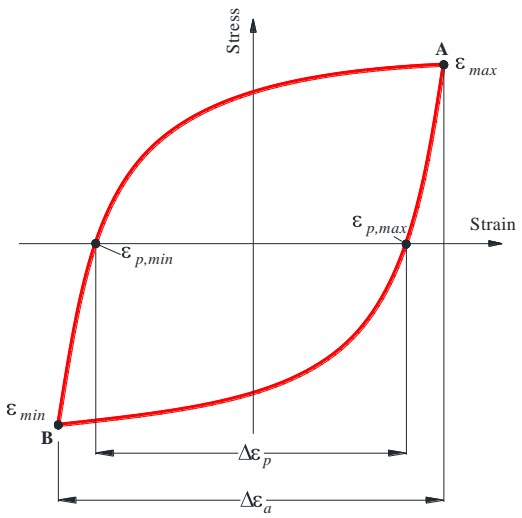


Figure 8-8 Parameters that define a stable hysteresis loop

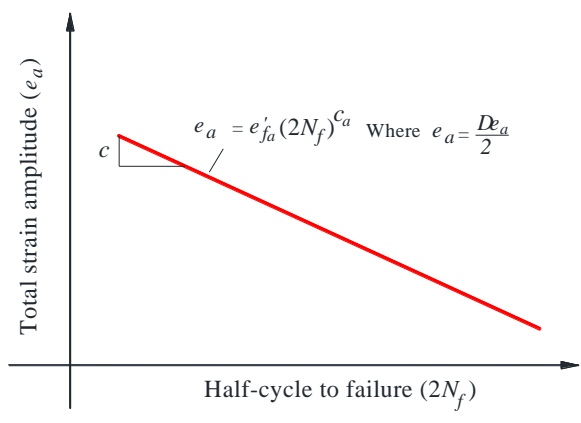


Figure 8-9 Total strain amplitude – fatigue-life relationship

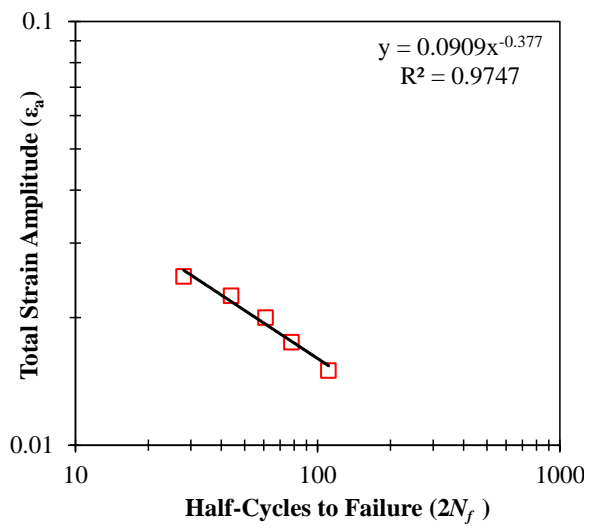


Figure 8-10 Data reported by Brown and Kunnath (2000) for No. 8 A615 Gr. 60 bars

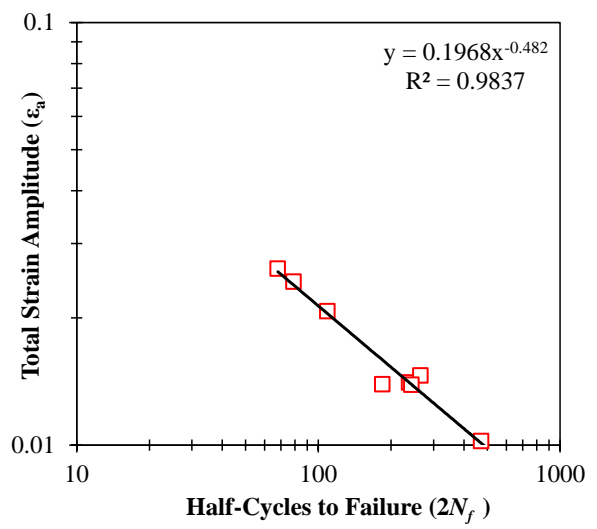


Figure 8-11 Data reported by Zhou et al. (2010) for No. 8 A706 Gr. 60 bars

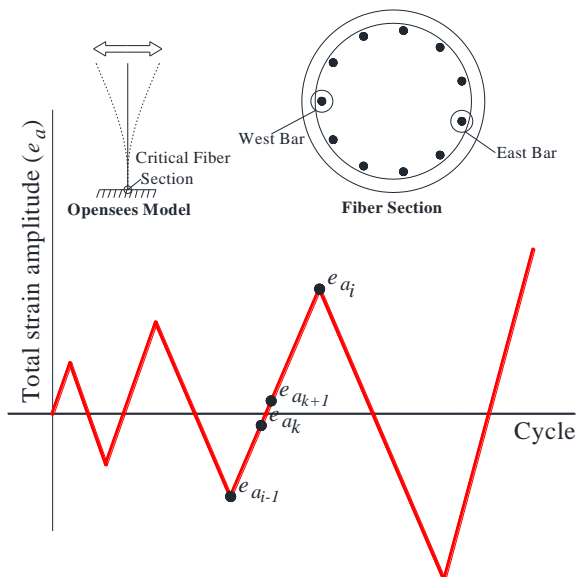


Figure 8-12 Schematic for description of low-cycle fatigue determination

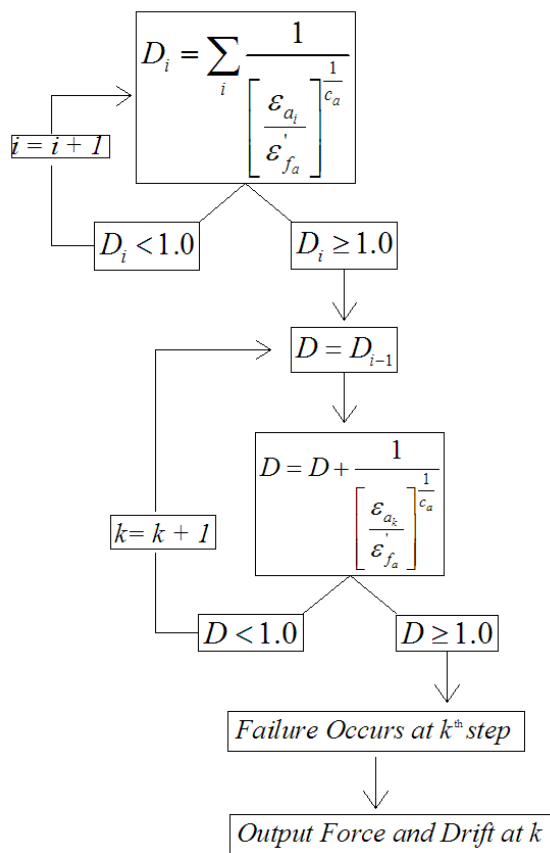
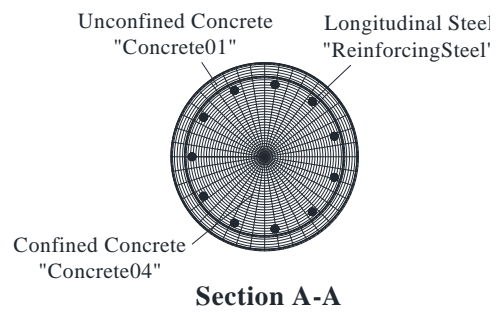
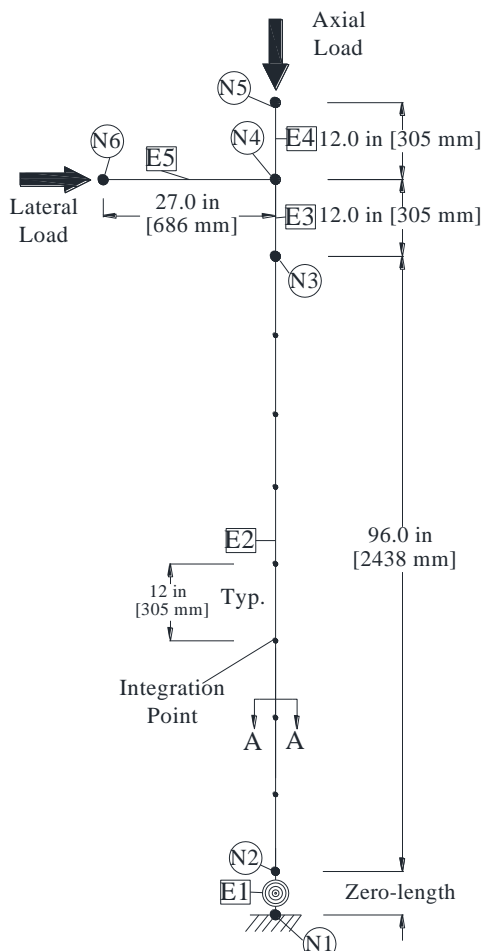


Figure 8-13 Algorithm for determining fatigue fracture



(a) Full model schematic

(b) Fiber section A-A

Figure 8-14 Analytical model of CIP

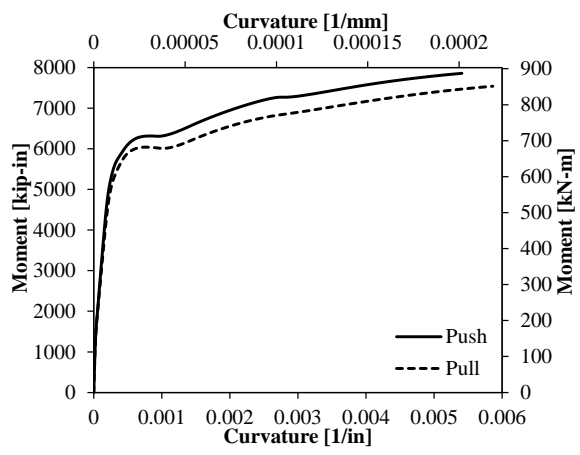


Figure 8-15 Moment-curvature response for CIP (Section A-A shown in Fig. 8-14)

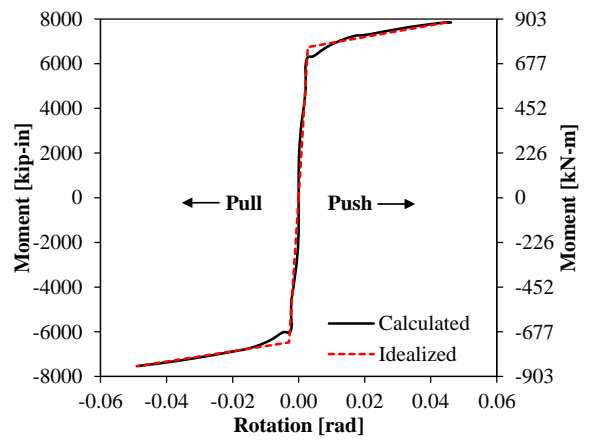


Figure 8-16 Calculated bond-slip behavior for CIP

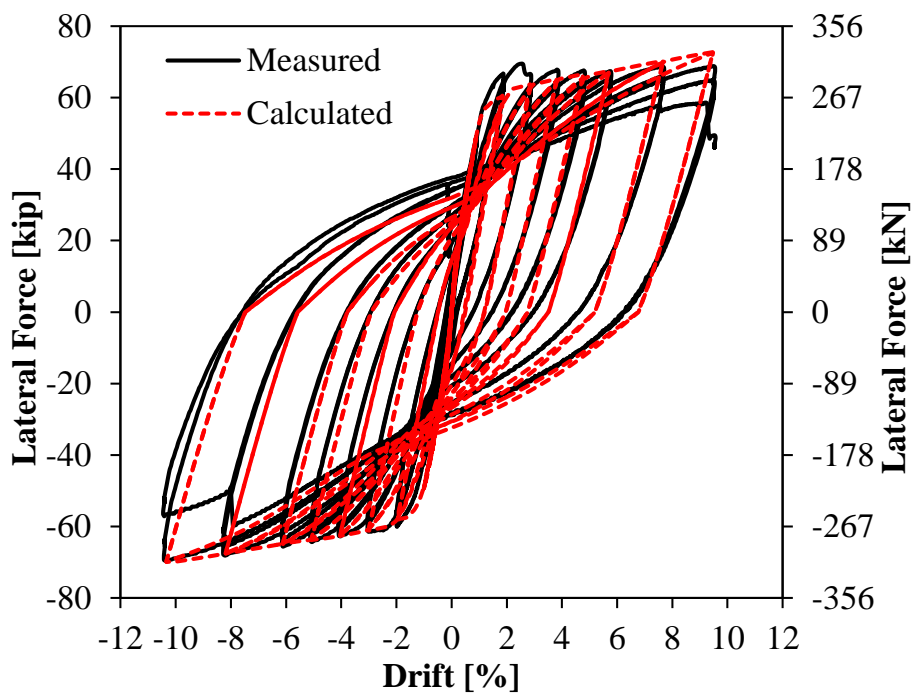


Figure 8-17 Hysteresis curves for CIP

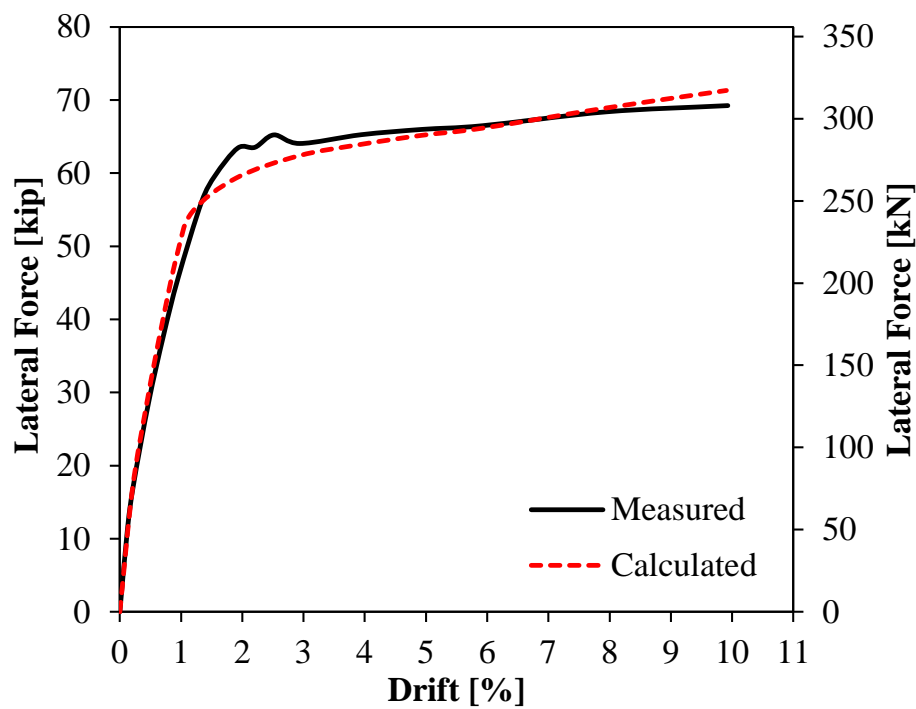


Figure 8-18 Average envelope curves for CIP

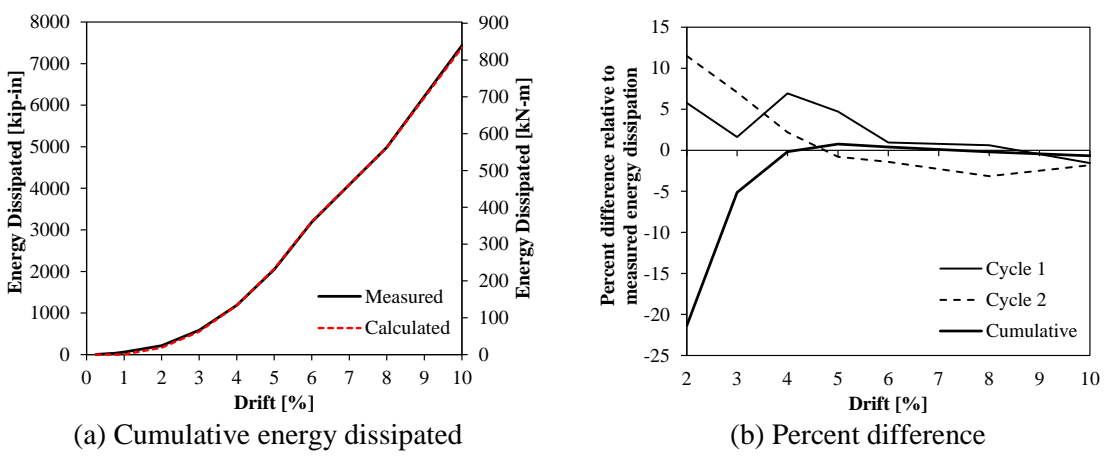


Figure 8-19 Energy dissipation for CIP

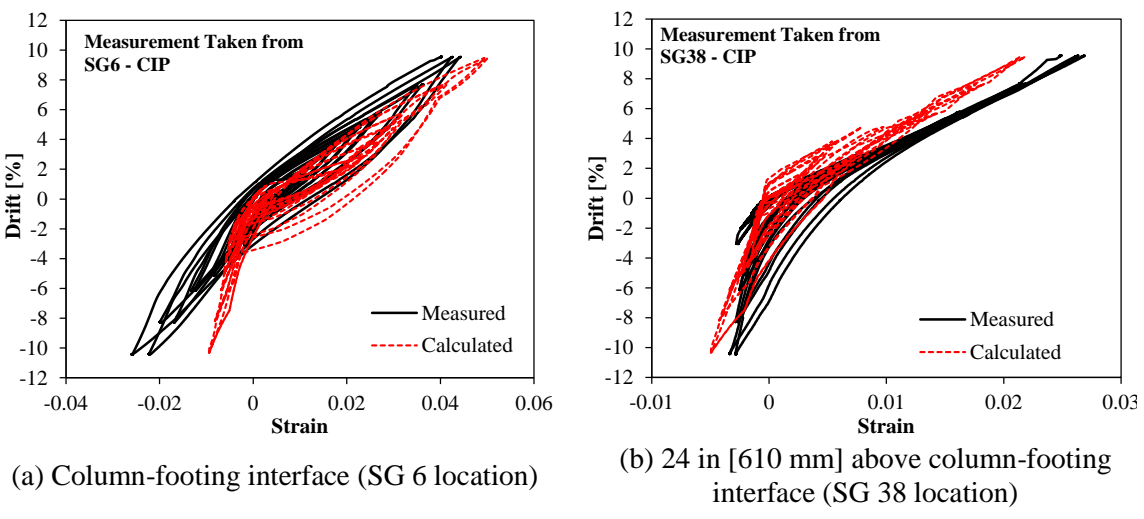


Figure 8-20 Comparison between measured and calculated strains

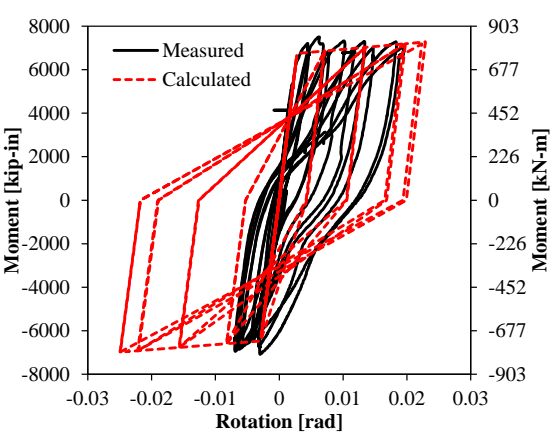


Figure 8-21 Bond-slip rotation hysteresis for CIP up to 6% Drift

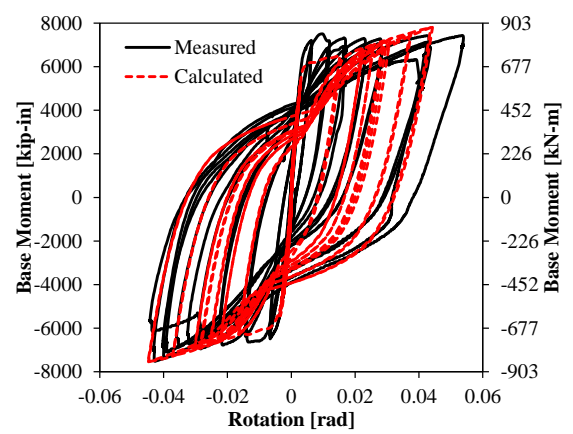


Figure 8-22 Moment-rotation of the 14-in [356-mm] section above the footing for CIP

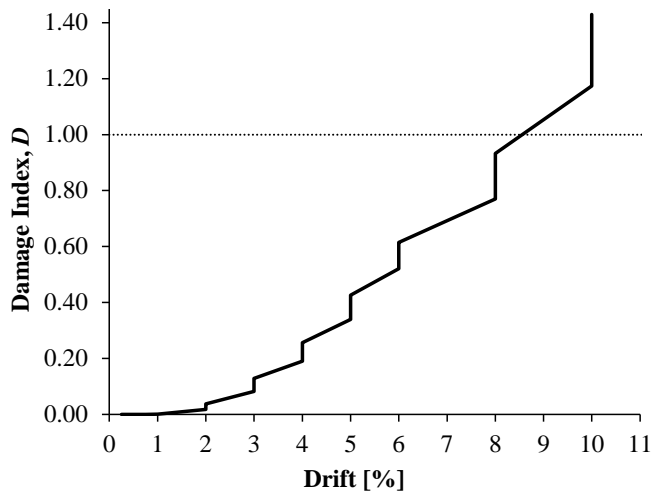


Figure 8-23 Cumulative damage as a function of drift for CIP

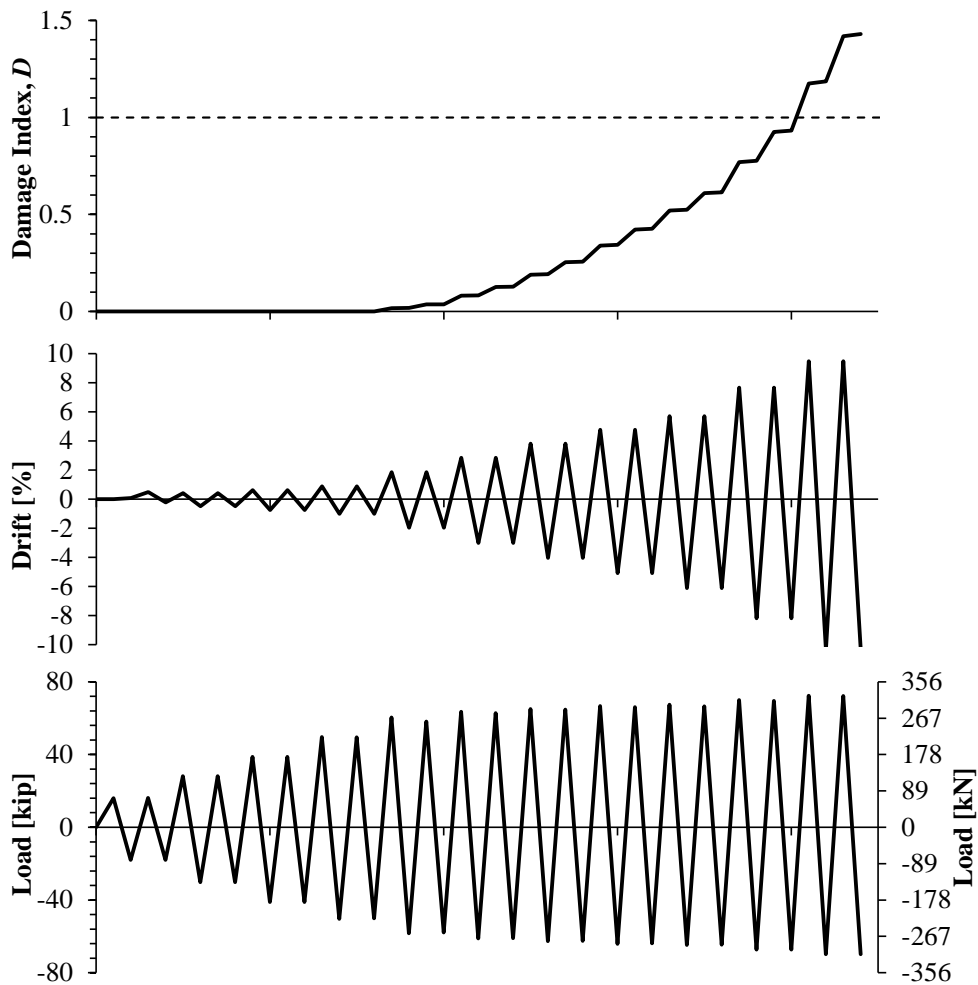


Figure 8-24 Cumulative damage plotted with drift and load for CIP

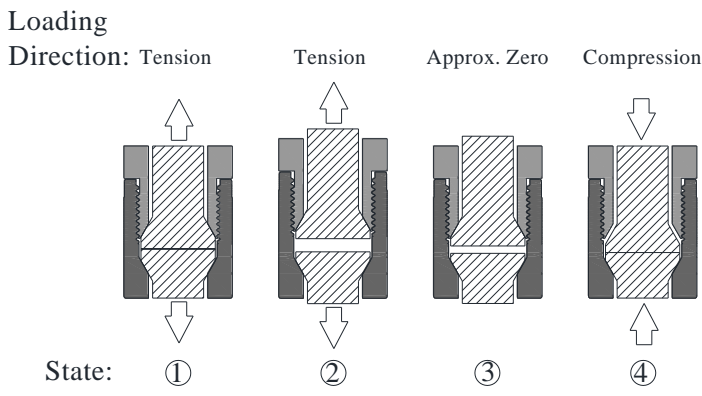
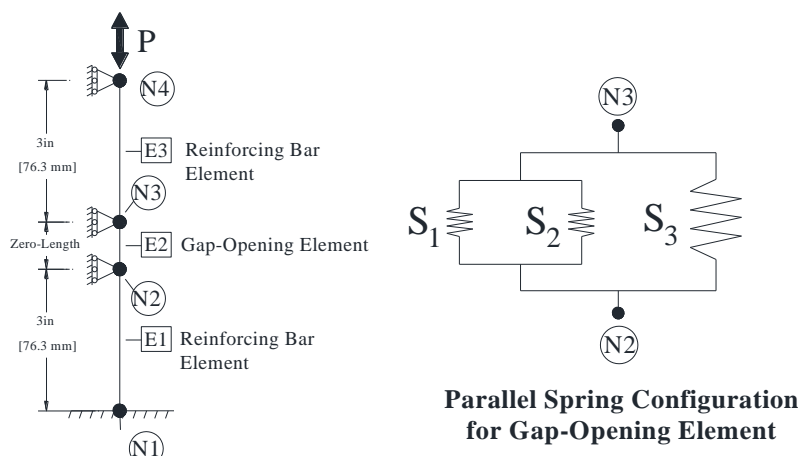


Figure 8-25 HC gap opening/closing mechanism



Uni-axial HC Component Model

Figure 8-26 Analytical model for HC uni-axial test

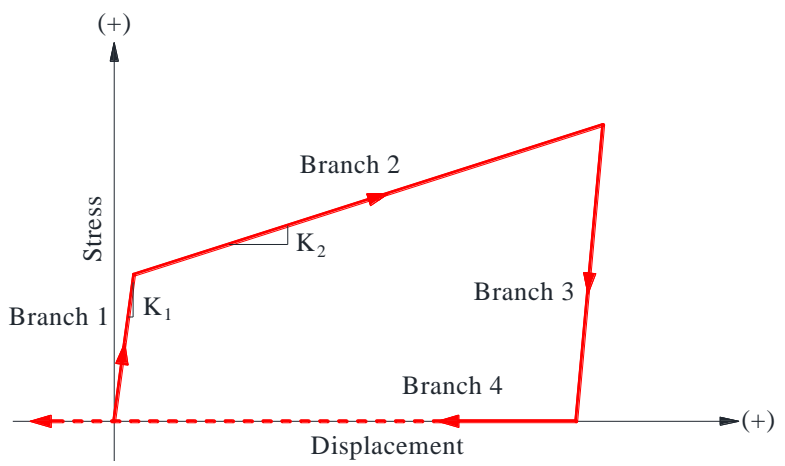


Figure 8-27 Constitutive behavior for spring 1 (S_1)

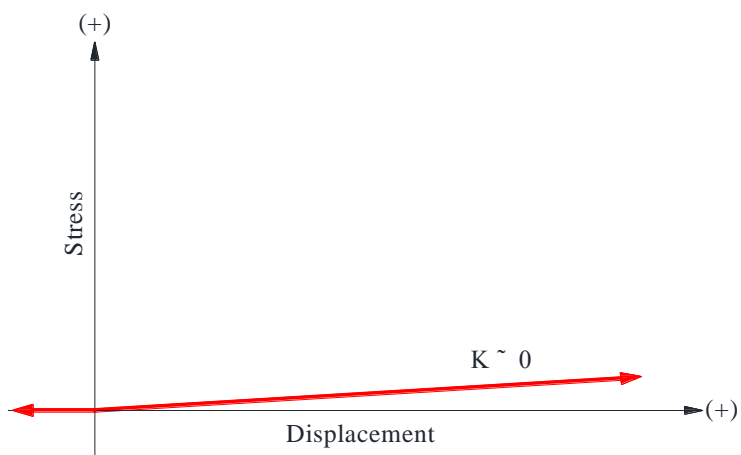
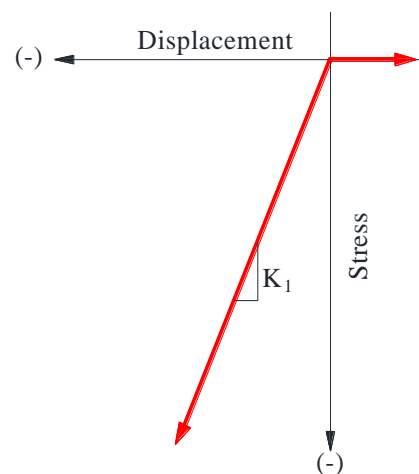
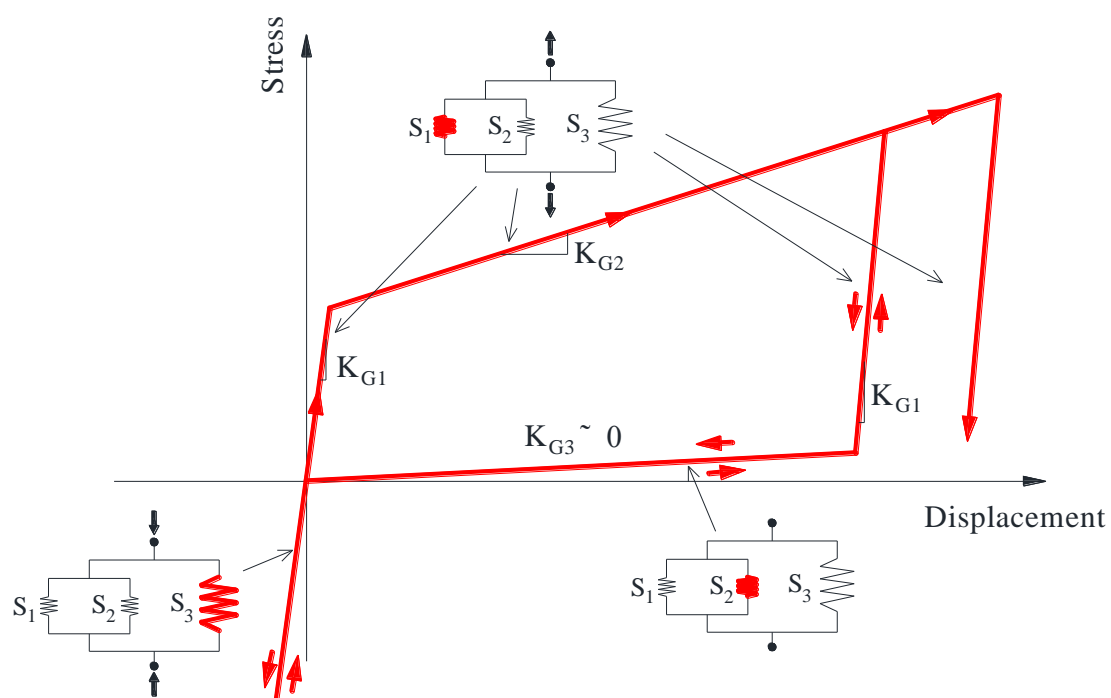
Figure 8-28 Constitutive behavior for spring 2 (S_2)Figure 8-29 Constitutive behavior for spring 3 (S_3)

Figure 8-30 Combine behavior of the gap spring system

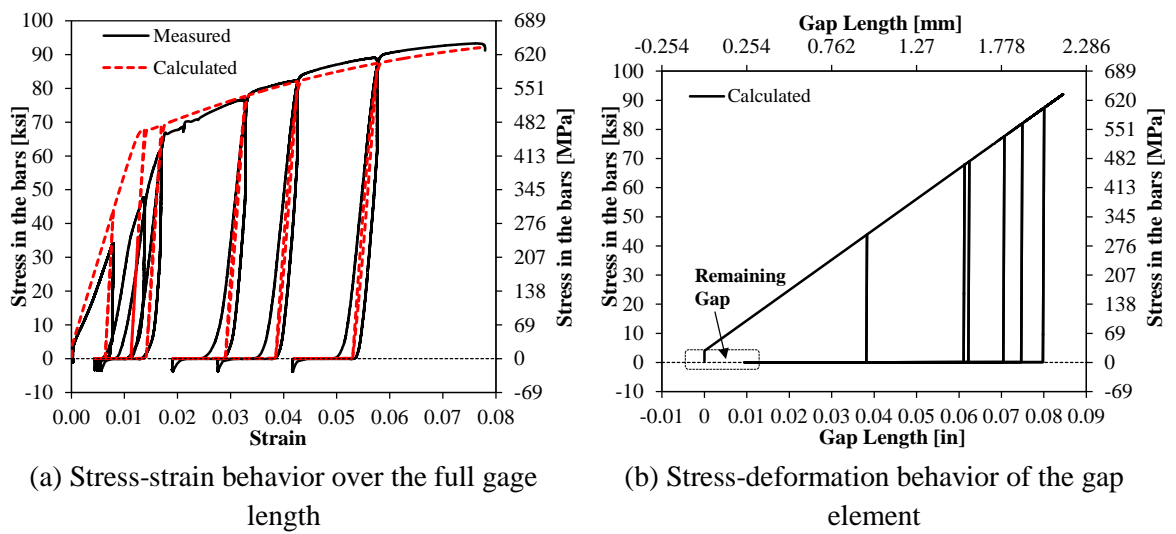


Figure 8-31 Results using displacement history from HCC1 test

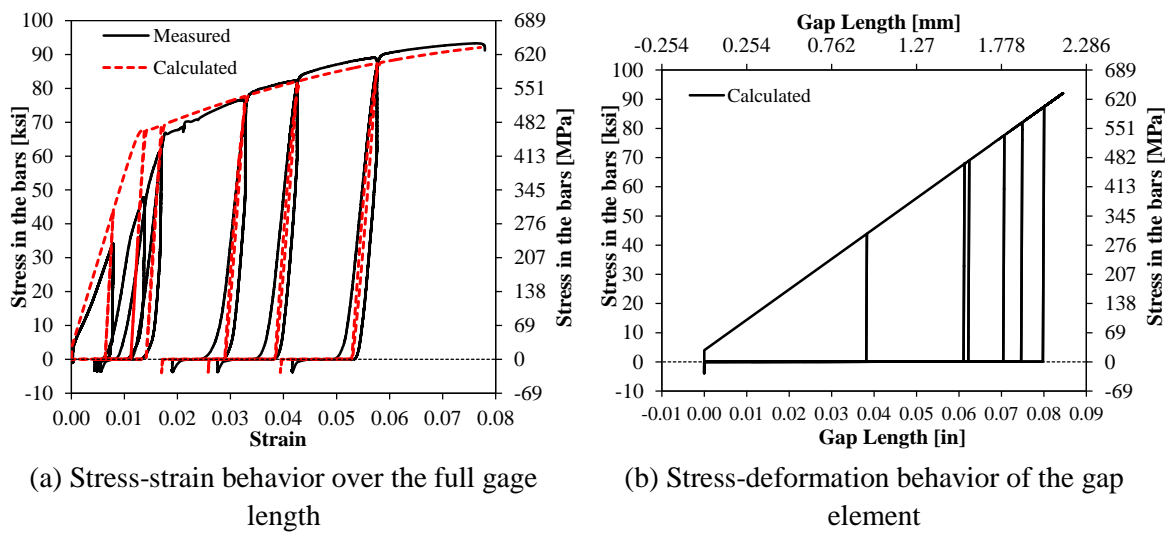
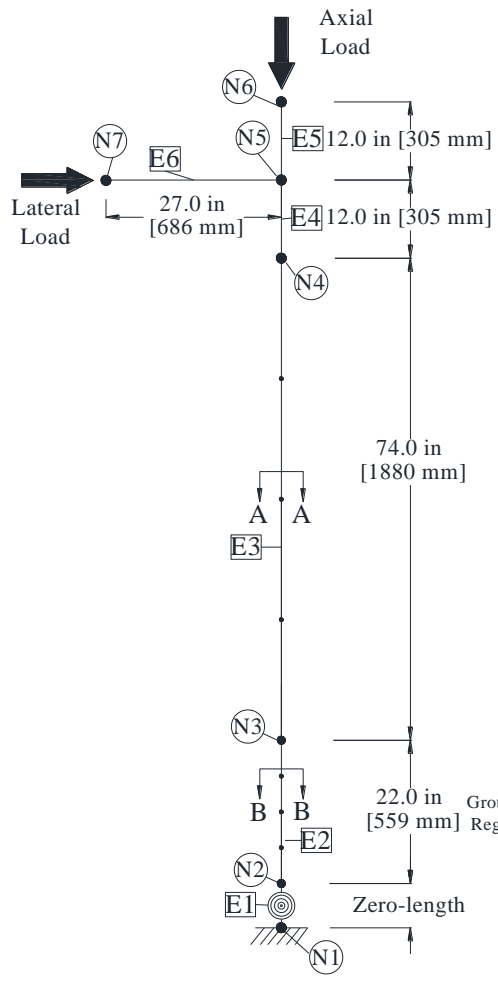
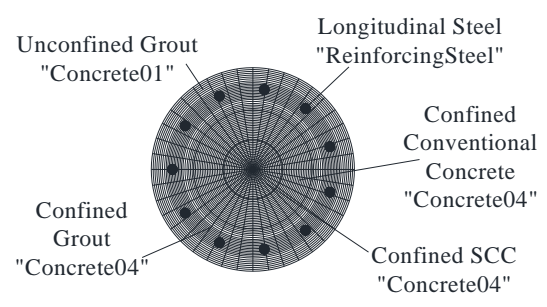
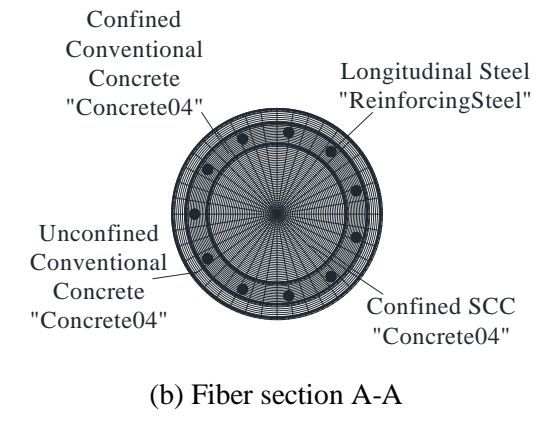


Figure 8-32 Results using modified displacement history compared to data from HCC1 test



(a) Full model schematic



(c) Fiber section B-B

Figure 8-33 Analytical model of HCNP

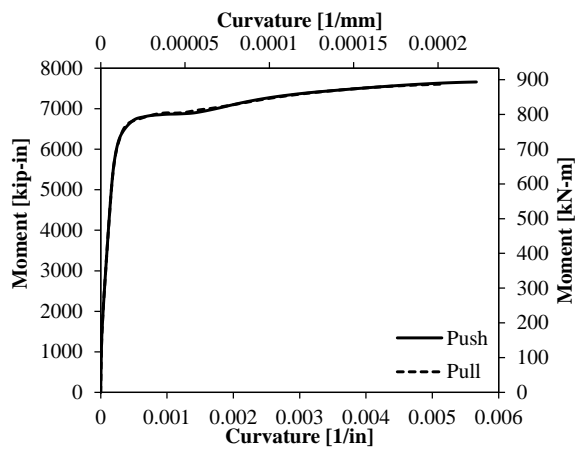


Figure 8-34 Moment-curvature response from HCNP grouted region

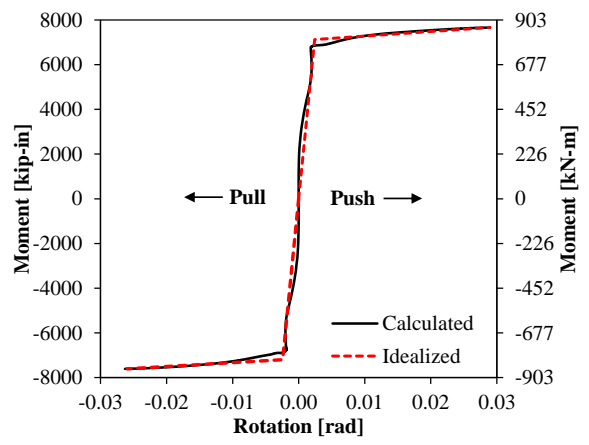


Figure 8-35 Calculated bond-slip behavior for HCNP

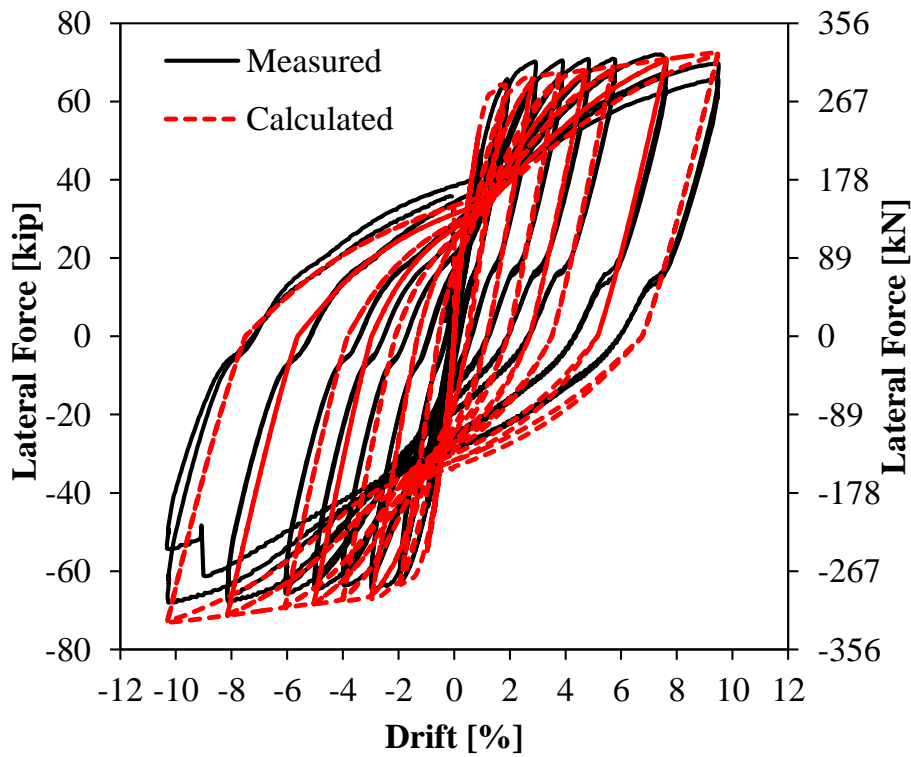


Figure 8-36 Hysteresis curves for HCNP

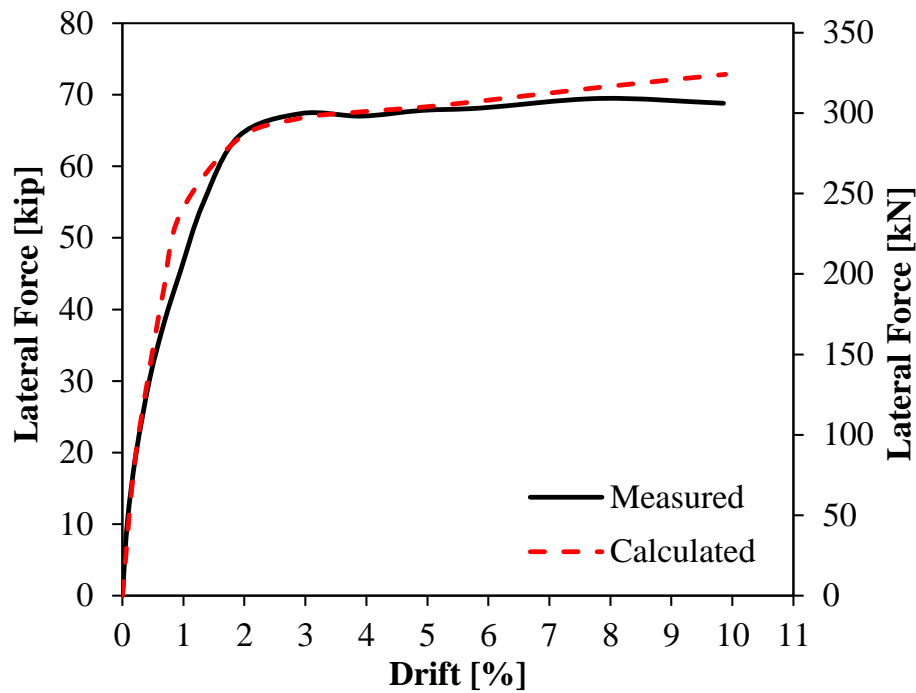


Figure 8-37 Average envelopes for HCNP

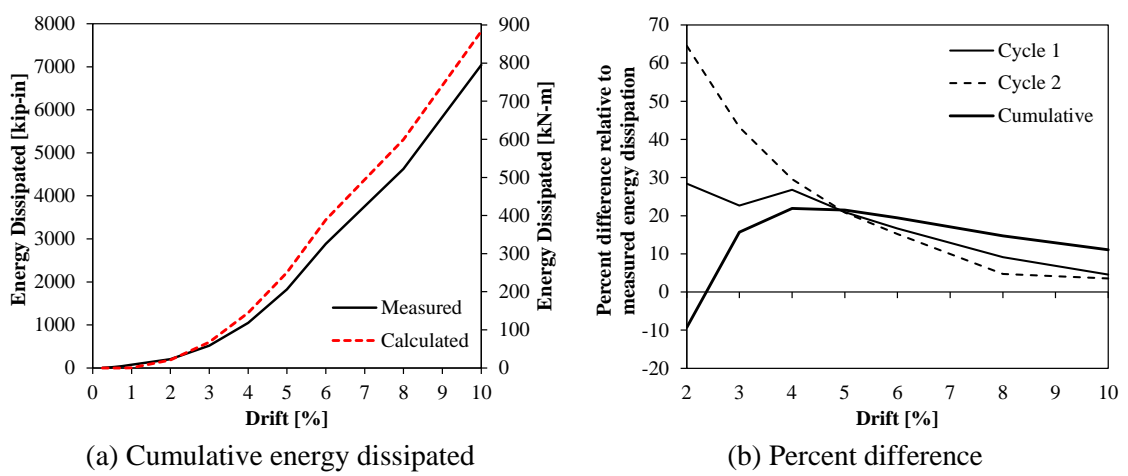


Figure 8-38 Energy dissipation for HCNP

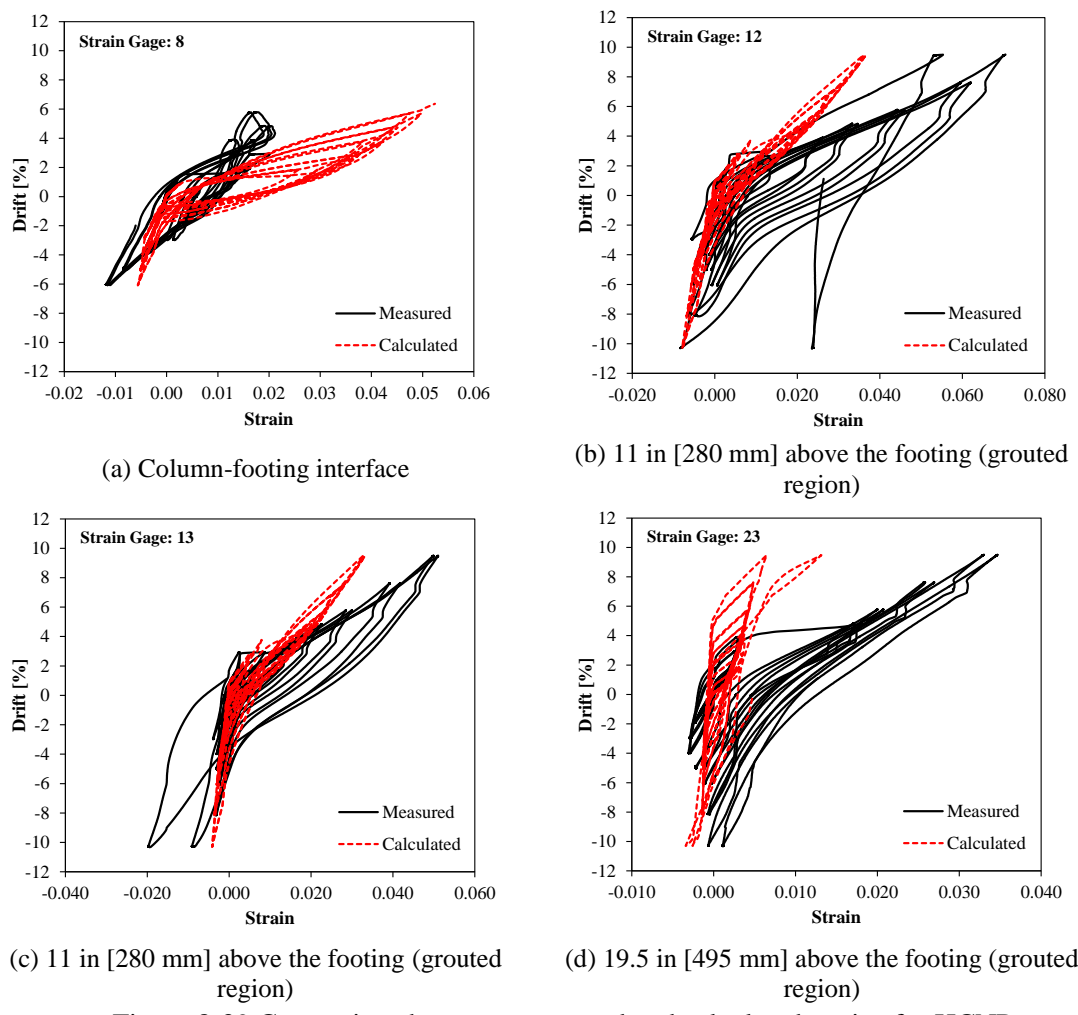
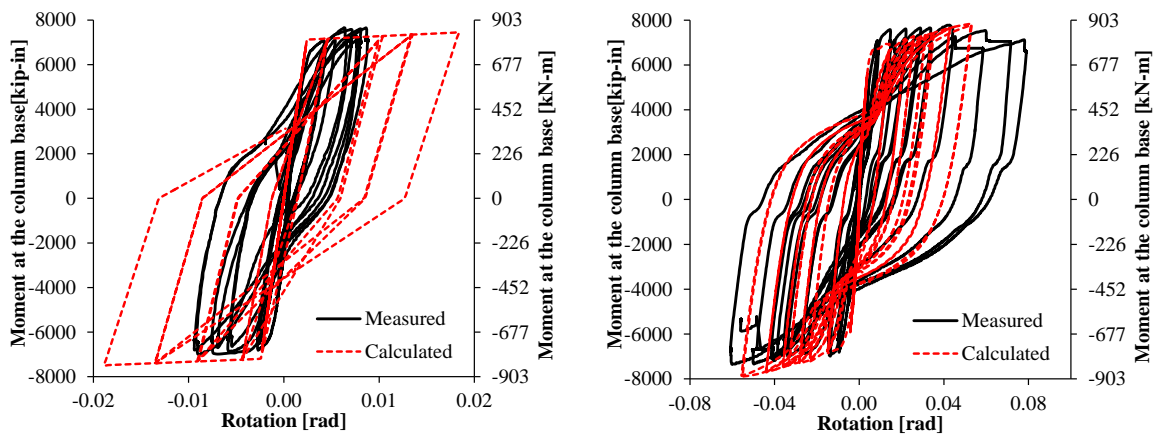


Figure 8-39 Comparison between measured and calculated strains for HCNP



(a) Bond-slip rotation hysteresis up to 6% drift (b) Grouted region rotation up to 10% drift
 Figure 8-40 Comparison between measured and calculated moment-rotation relationships for HCNP

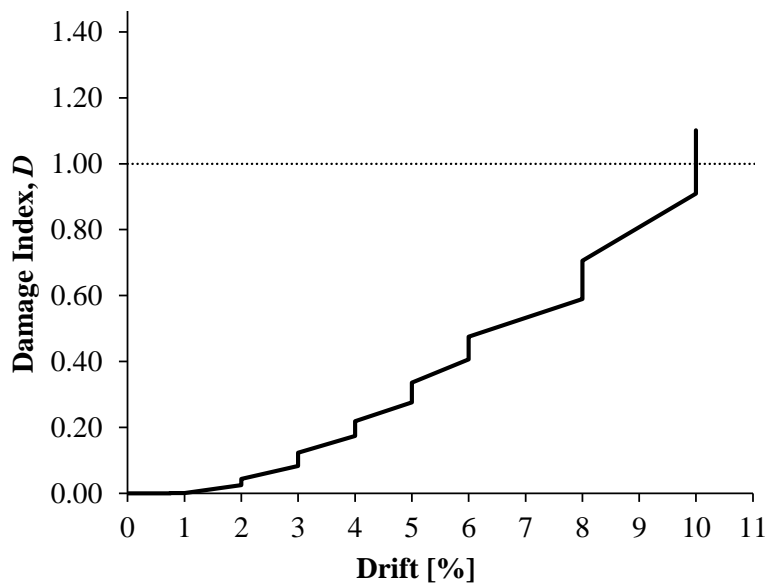


Figure 8-41 Cumulative damage as a function of drift for HCNP

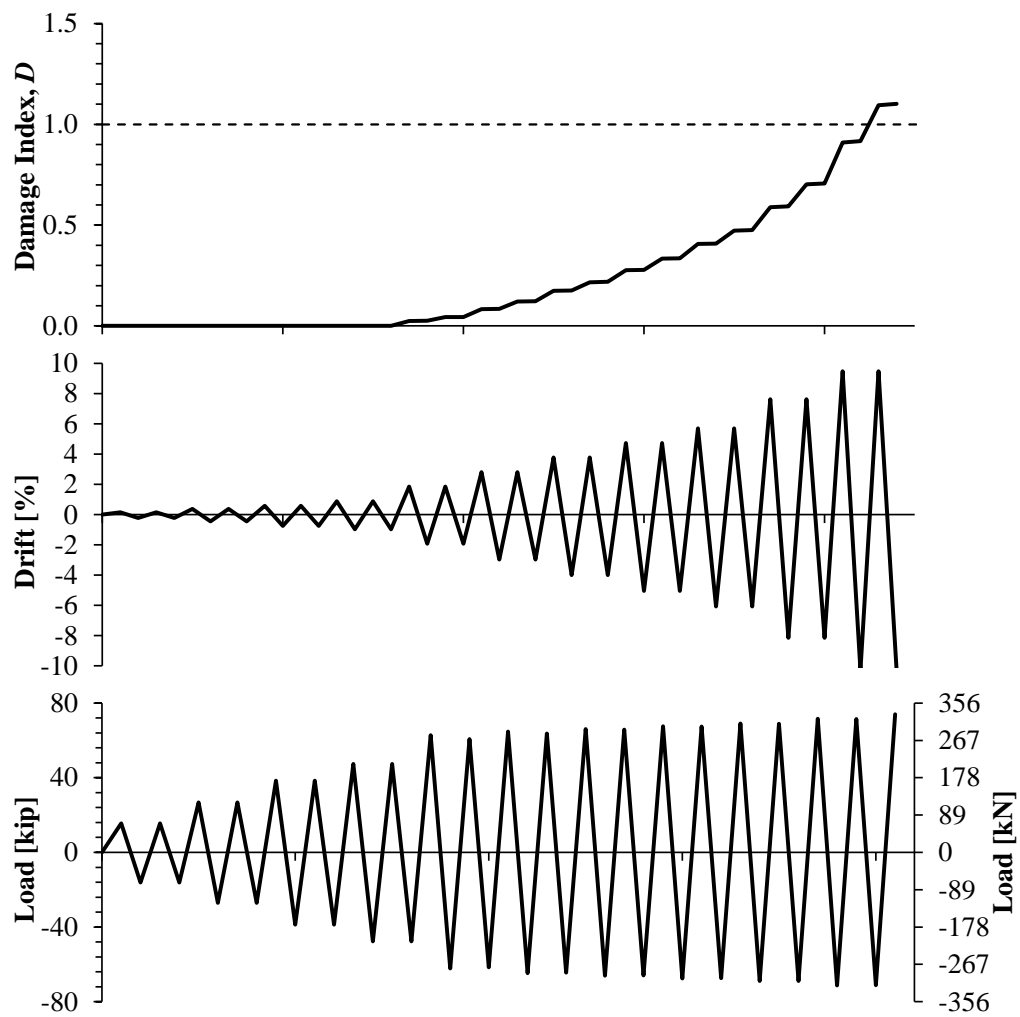


Figure 8-42 Cumulative damage plotted with drift and load for HCNP

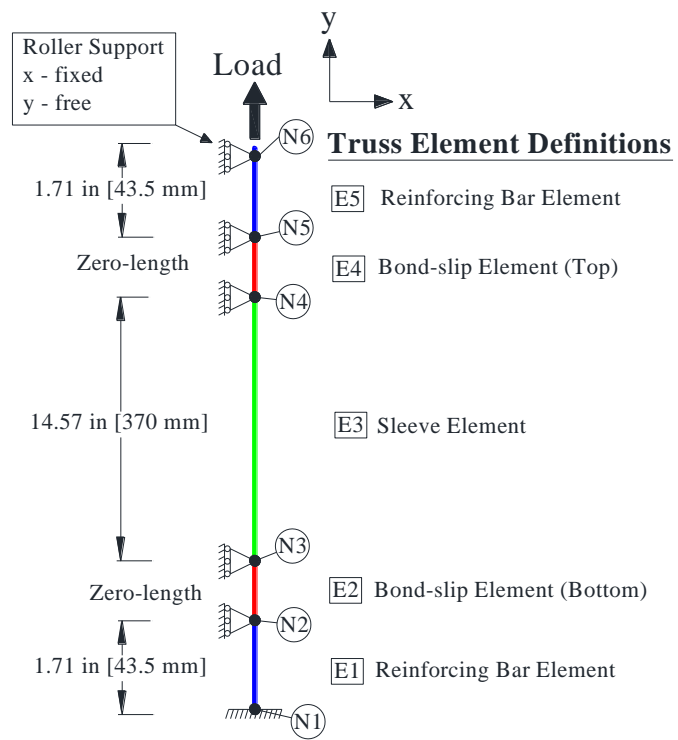


Figure 8-43 Component model details for individual grouted coupler

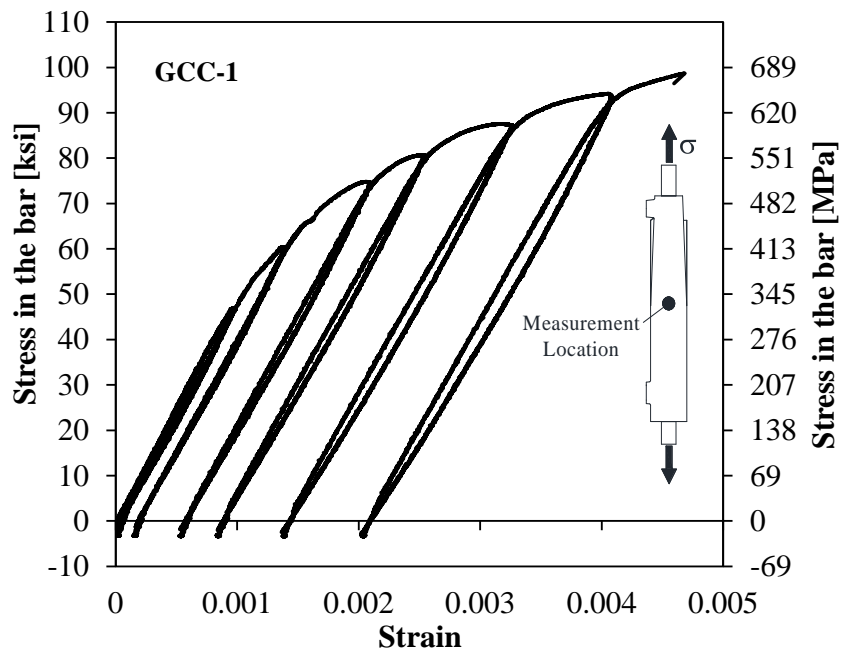


Figure 8-44 Observed cyclic strain behavior from GCC1

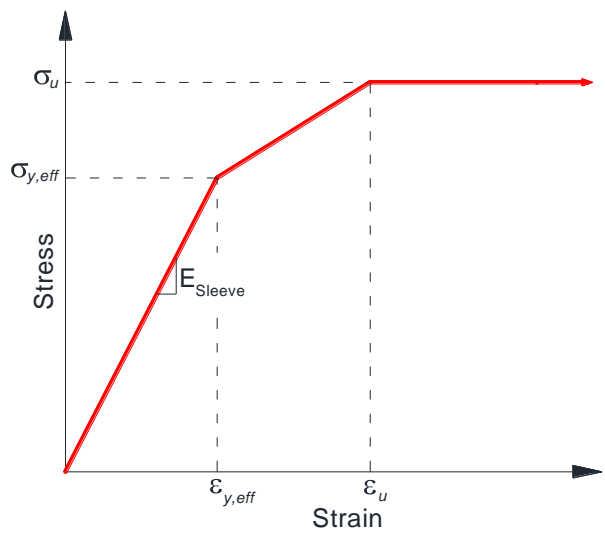


Figure 8-45 Proposed stress-strain model for ductile cast iron

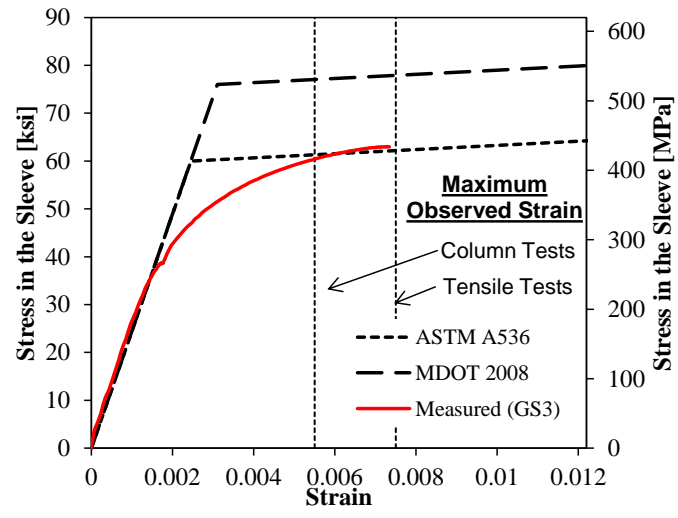


Figure 8-46 Comparison between bi-linear models and measured data

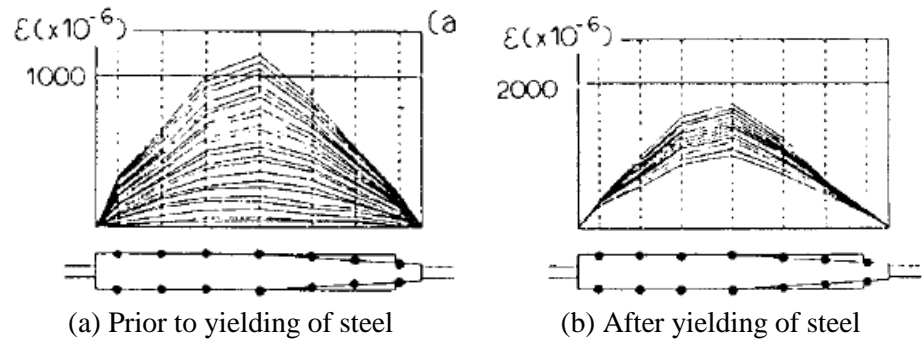


Figure 8-47 Strain distribution along the grout-filled sleeve (Matsuzaki et al., 1987)

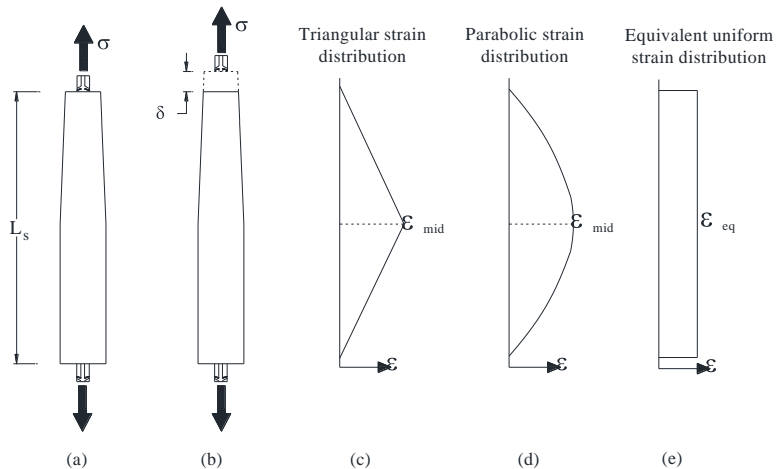


Figure 8-48 Determination of equivalent strain for the grouted sleeve

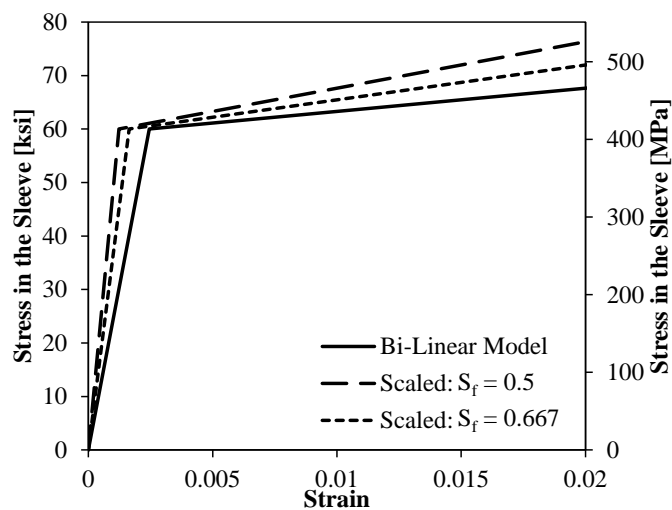


Figure 8-49 Stress-strain behavior for the grouted sleeve

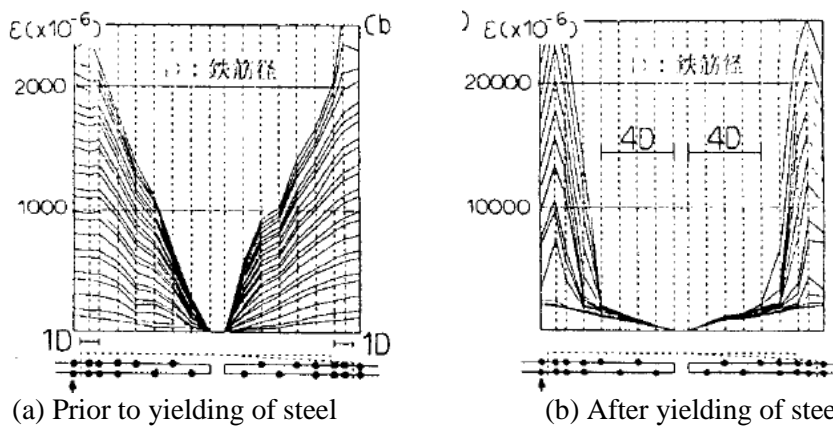


Figure 8-50 Strain distribution along the reinforcing bar within the grout-filled sleeve (Matsuzaki et al., 1987)

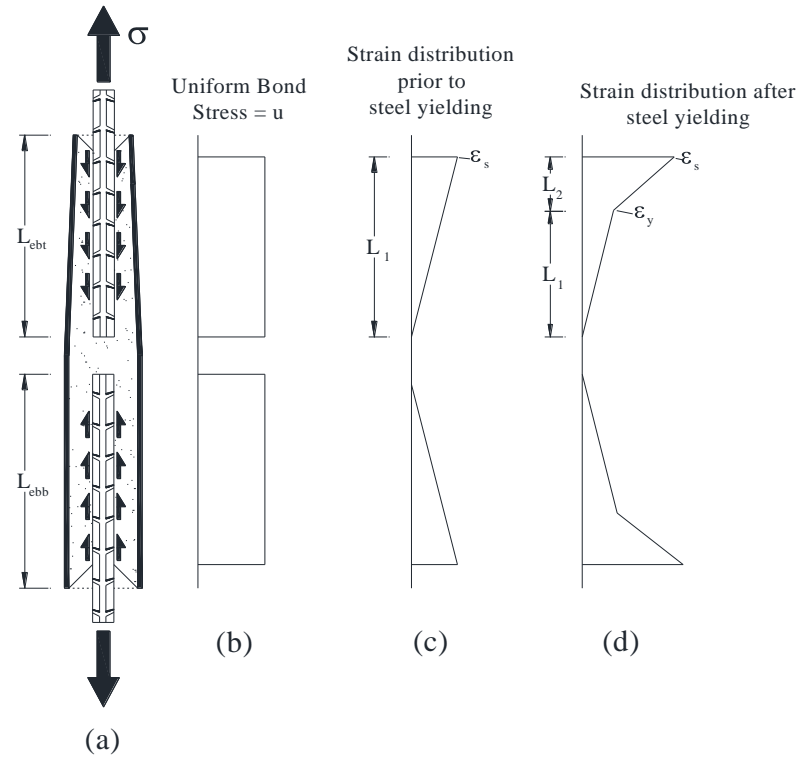
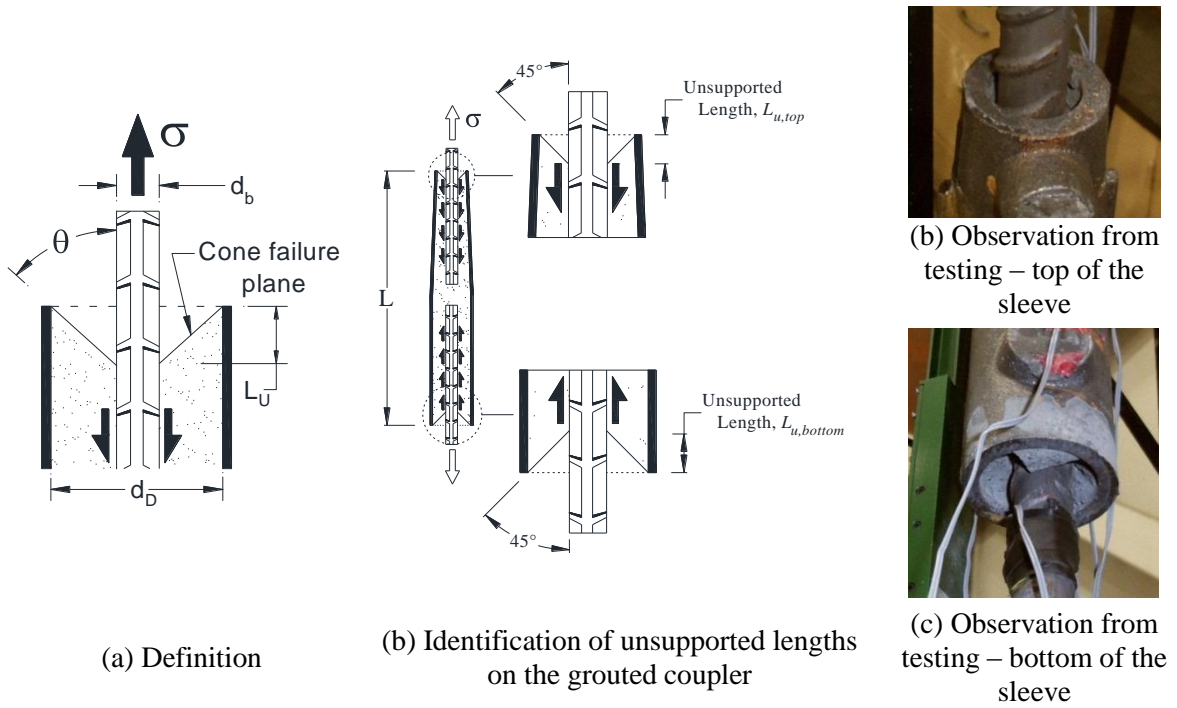


Figure 8-51 Calculation of bond-slip behavior of reinforcing bar embedded in the grouted sleeve



(a) Definition

(b) Identification of unsupported lengths on the grouted coupler

(c) Observation from testing – bottom of the sleeve

Figure 8-52 Identification of the unsupported length for the grouted coupler

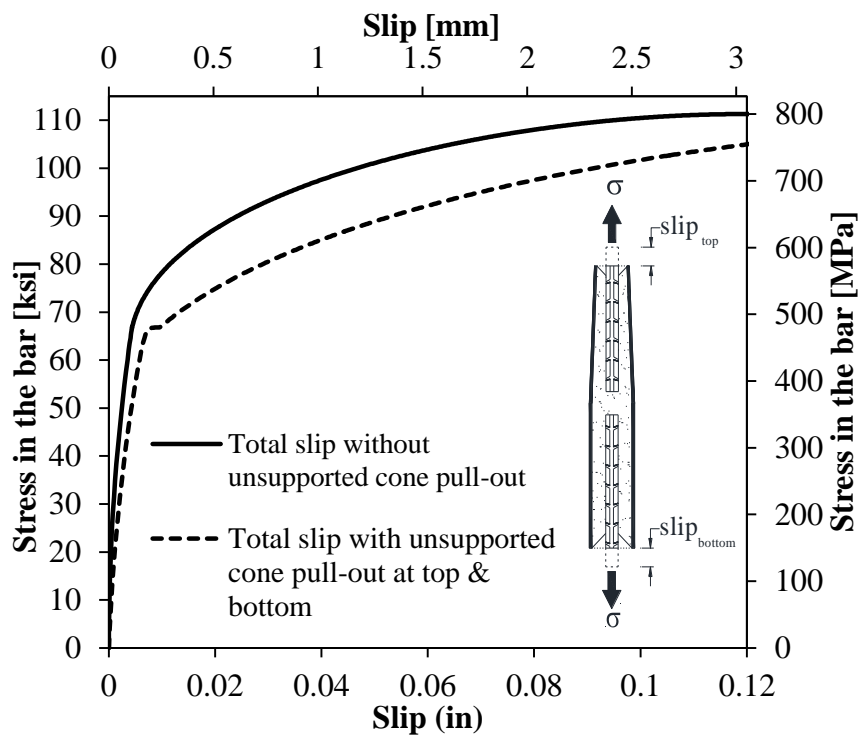


Figure 8-53 Calculated stress-slip response for the

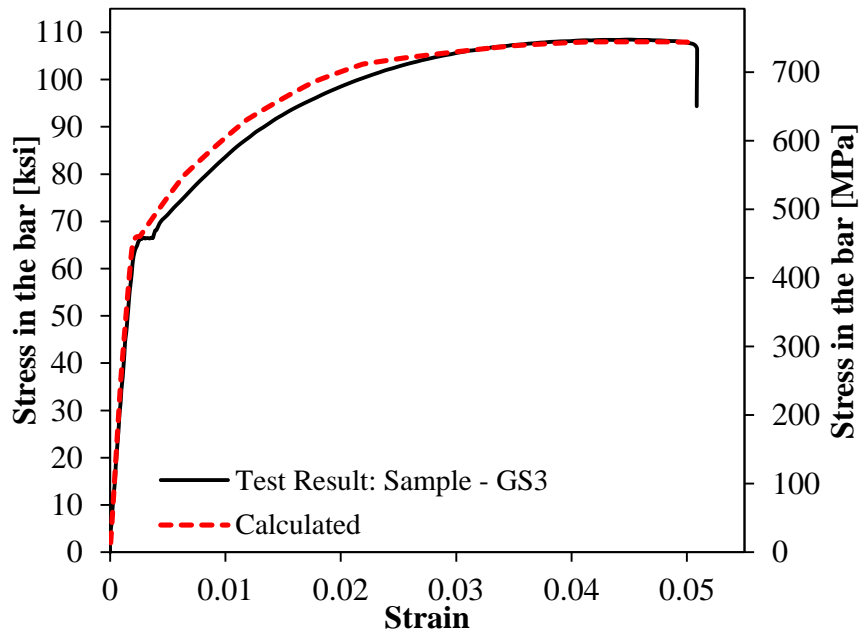
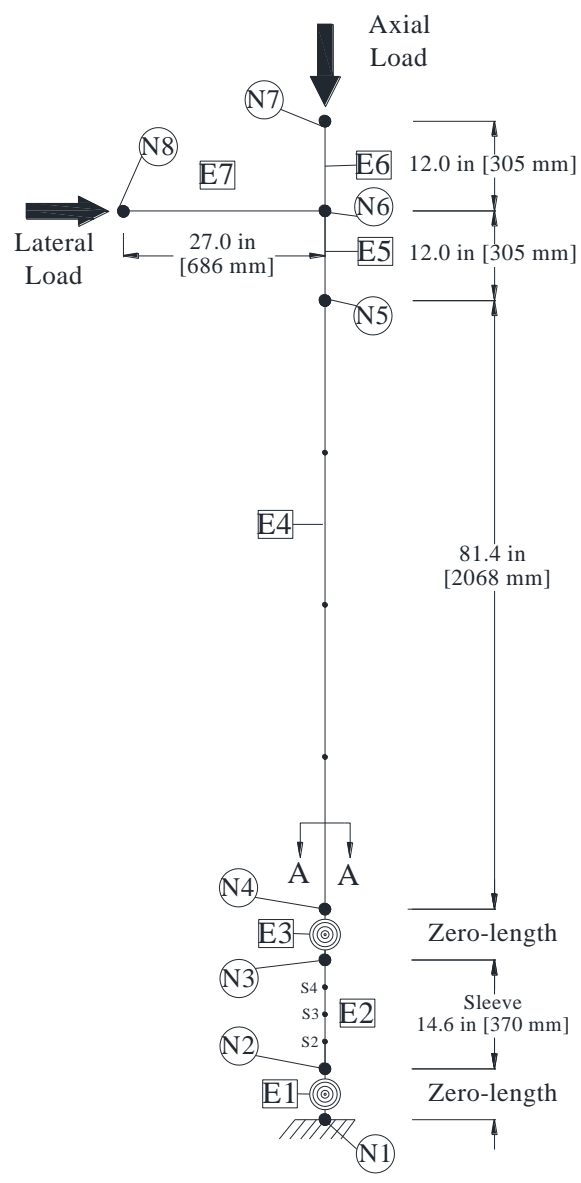
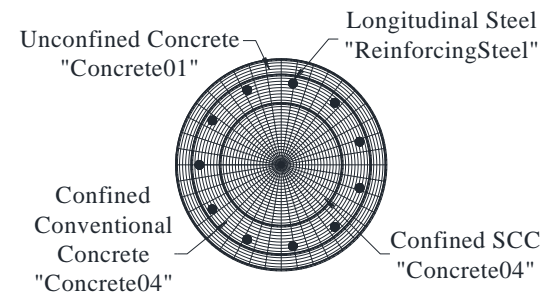


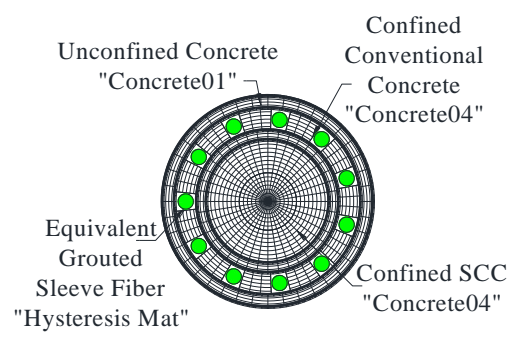
Figure 8-54 Calculated coupler region response compared to test result



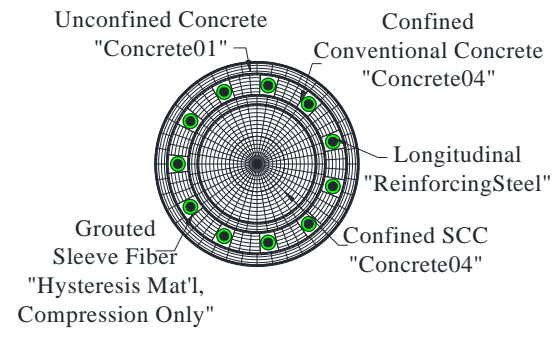
(a) Full model schematic



(b) Fiber section A-A



(c) Fiber section of element 2: sections 2-4



(d) Fiber section of element 2 at nodes 2 and 3

Figure 8-55 Analytical model of GCNP

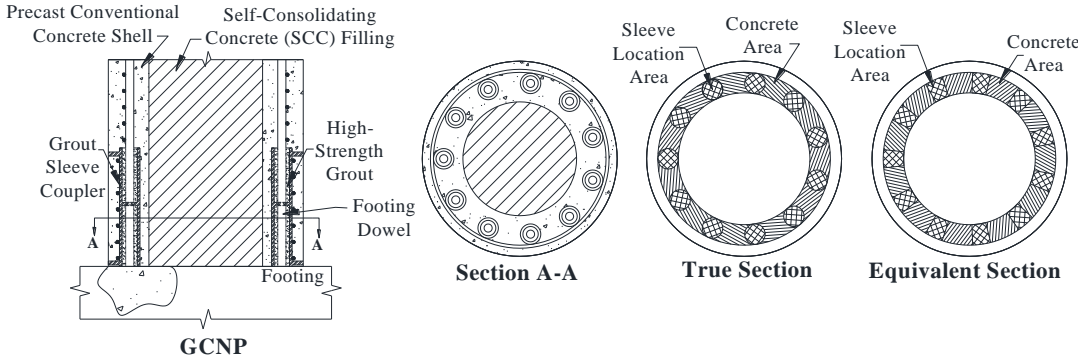


Figure 8-56 Determination of an equivalent section for the grouted coupler region

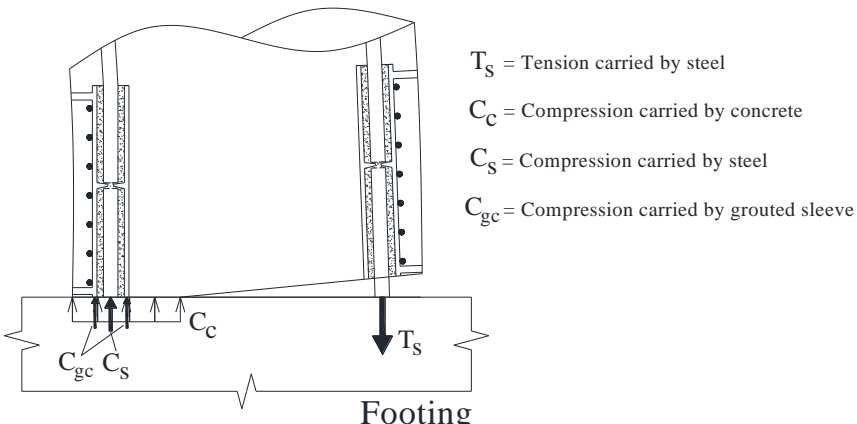


Figure 8-57 Forces at the column-footing interface for GCNP

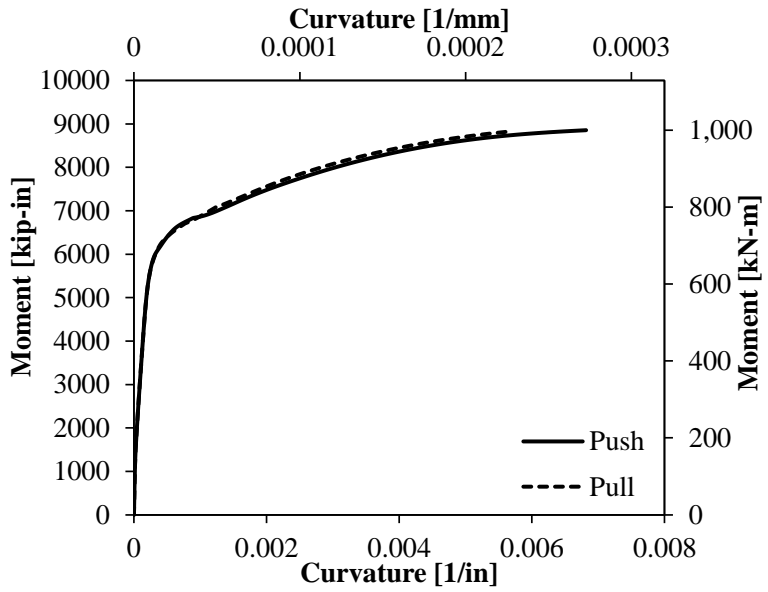


Figure 8-58 Moment-curvature response from GCNP fiber section shown in Figure 8-55d

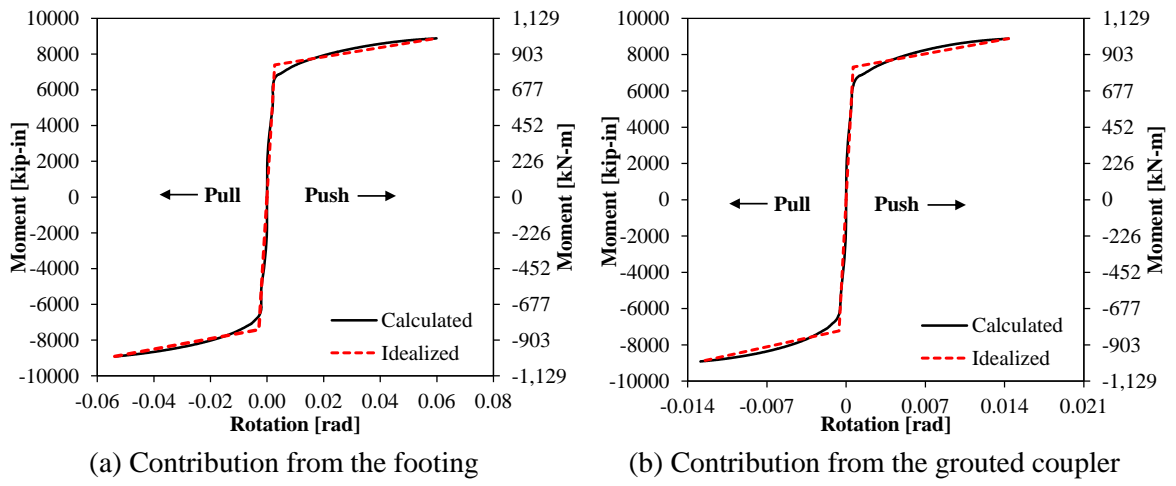


Figure 8-59 Calculated bond-slip behavior at the column-footing interface for GCNP

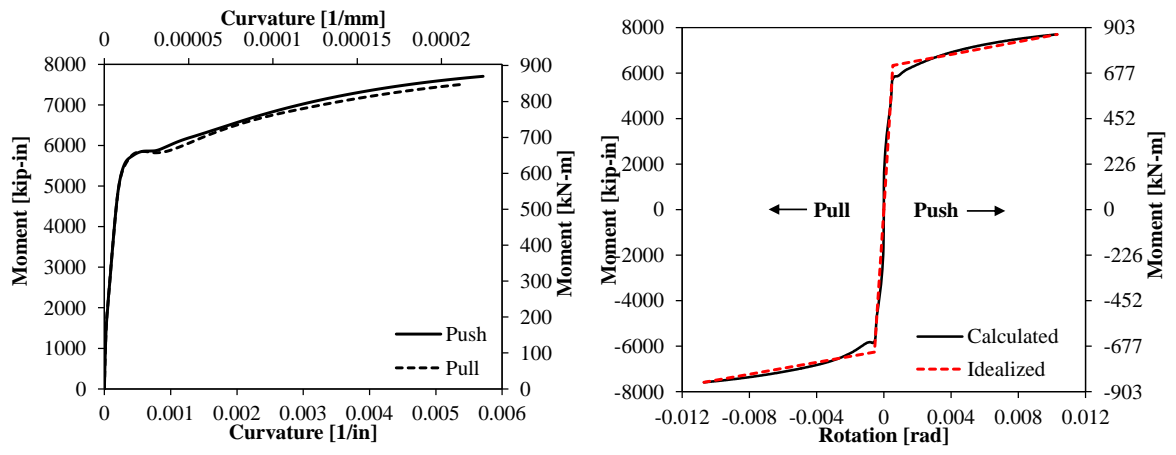


Figure 8-60 Moment-curvature response from GCNP fiber section shown in Figure 8-55a

8-61 Calculated bond-slip behavior at the top of the grouted coupler for GCNP

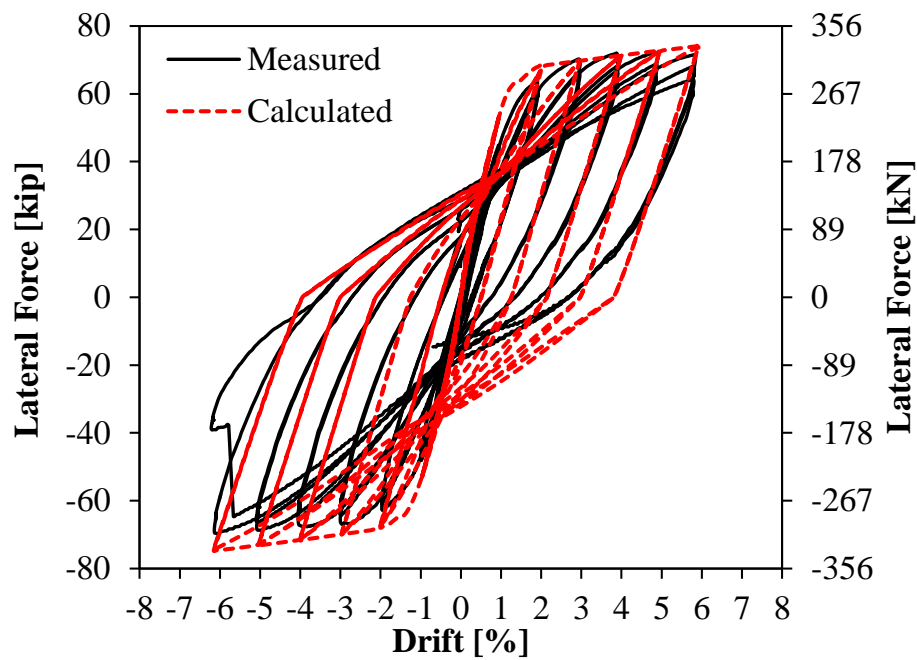


Figure 8-62 Hysteresis curves for GCNP

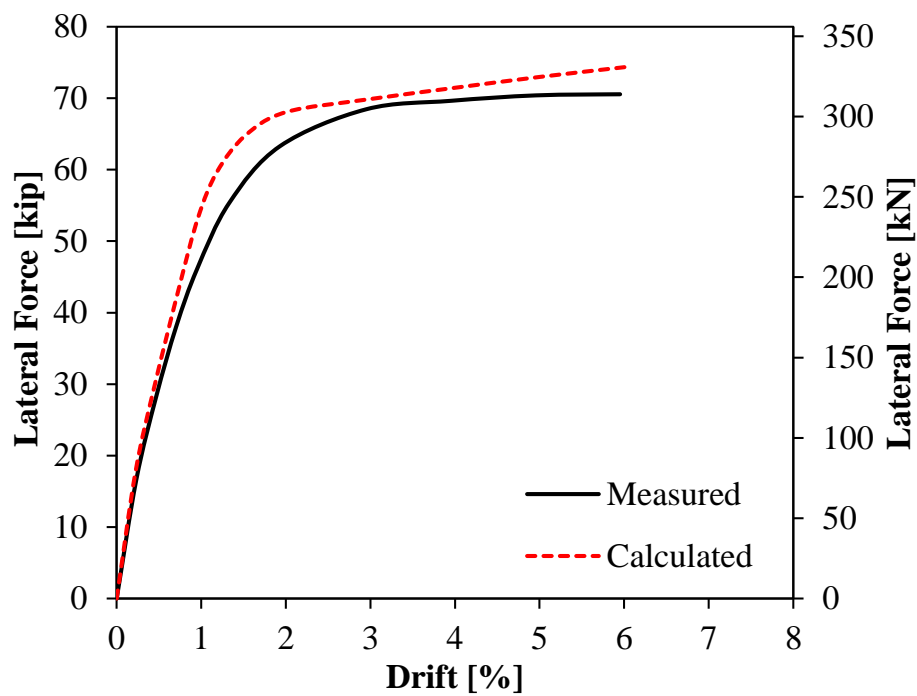


Figure 8-63 Average envelope curves for GCNP

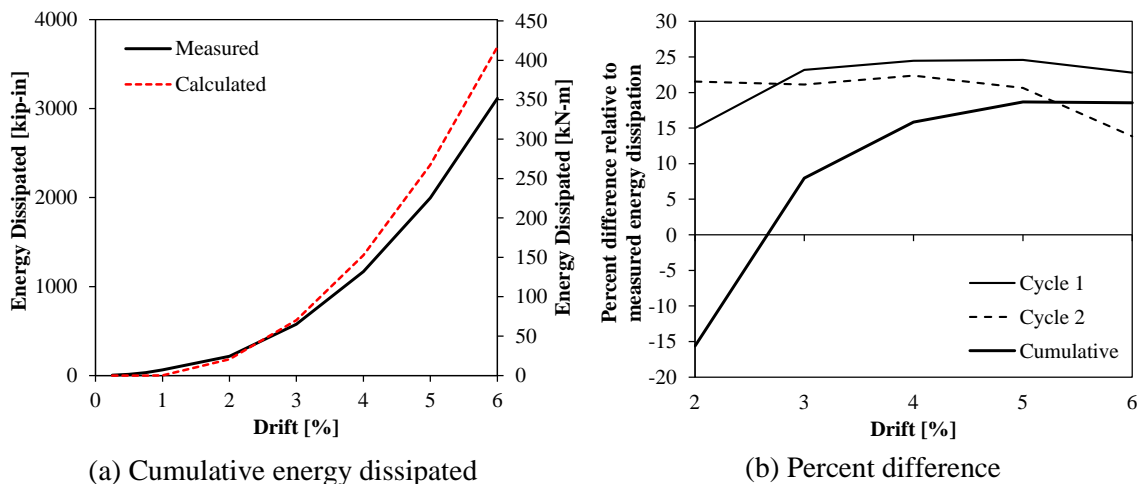


Figure 8-64 Energy dissipation for GCNP

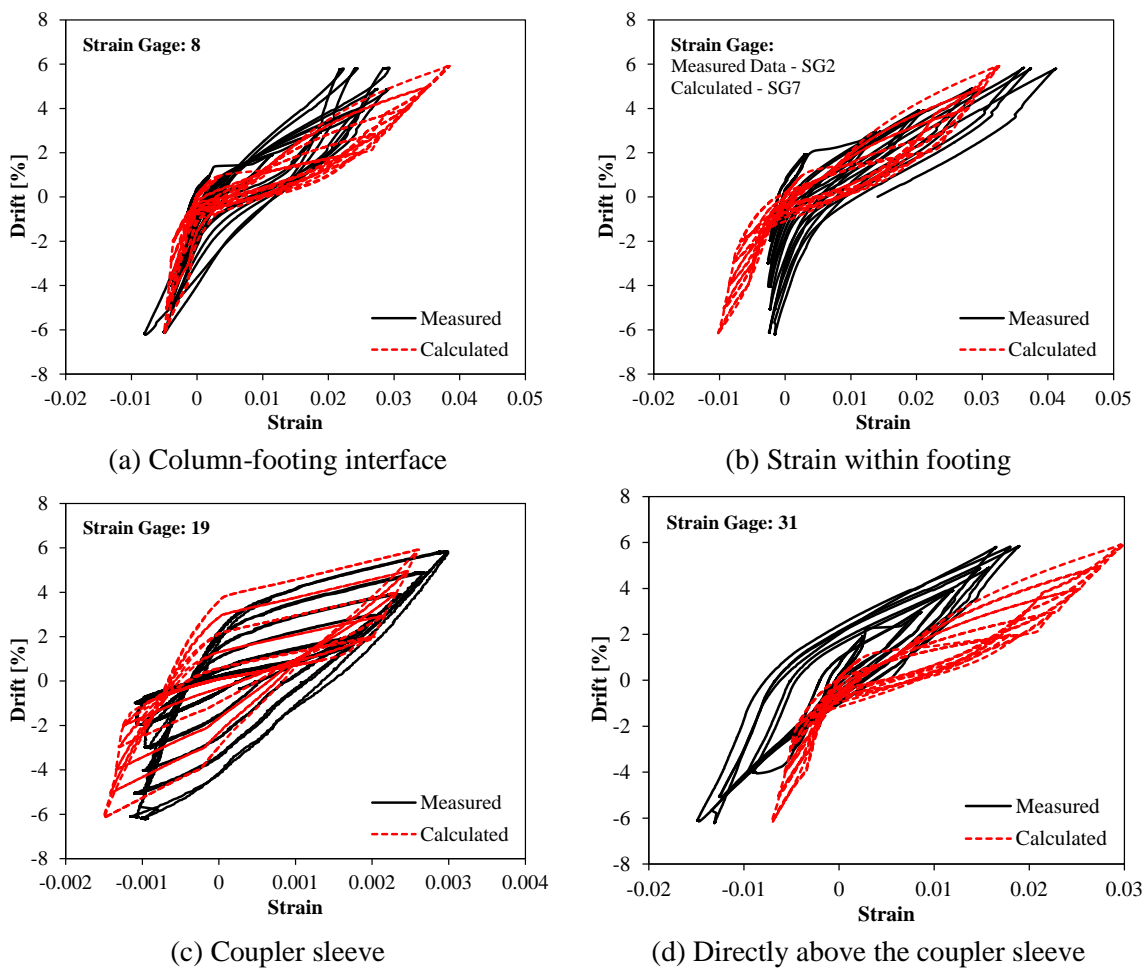


Figure 8-65 Comparison between measured and calculated strains for GCNP

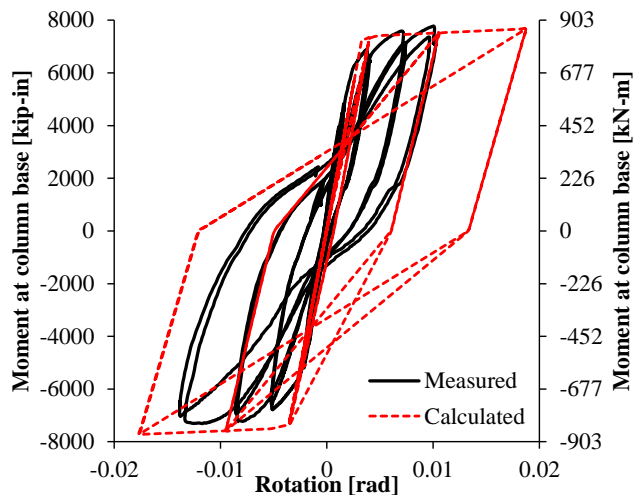
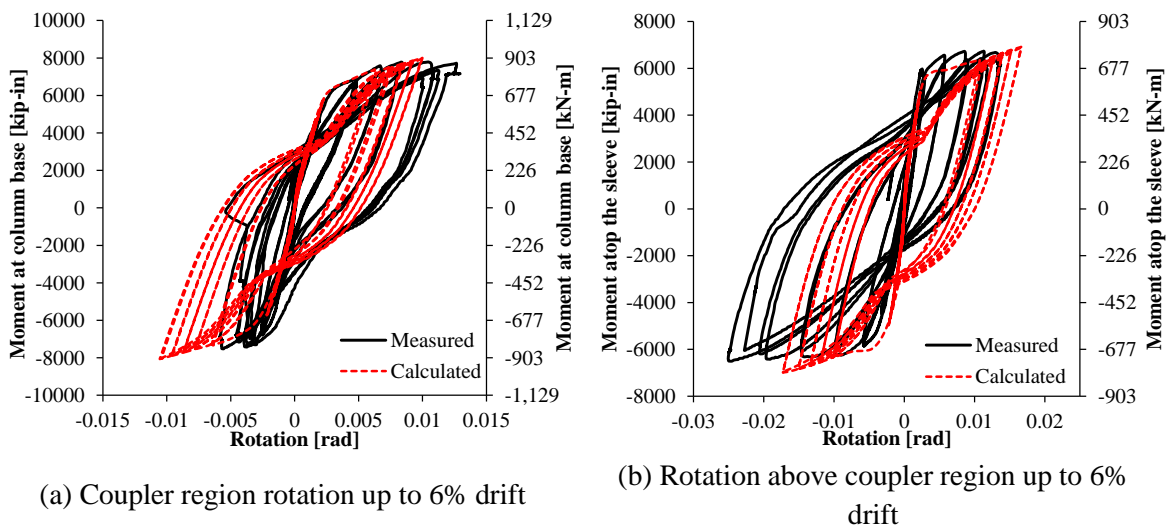


Figure 8-66 Hysteretic bond-slip rotation for GCNP up to 4% drift



(a) Coupler region rotation up to 6% drift

(b) Rotation above coupler region up to 6% drift

Figure 8-67 Moment-rotation relationships for GCNP

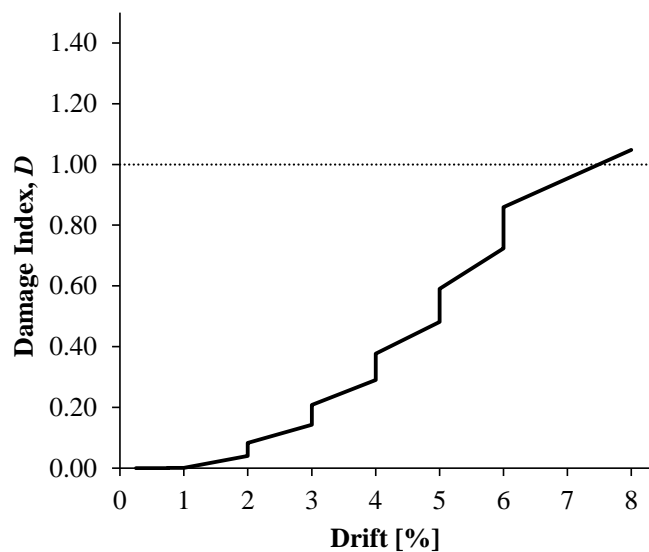


Figure 8-68 Cumulative damage as a function of drift for GCNP

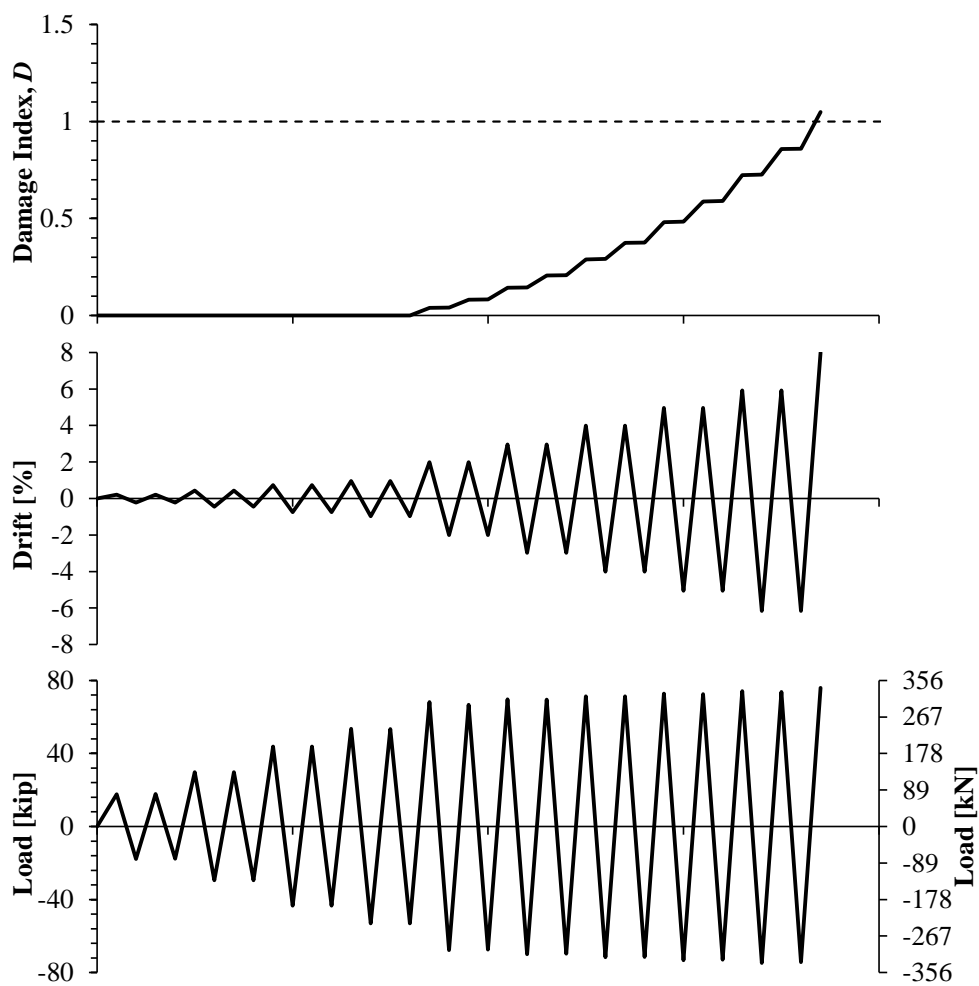


Figure 8-69 Cumulative damage plotted with drift and load for GCNP

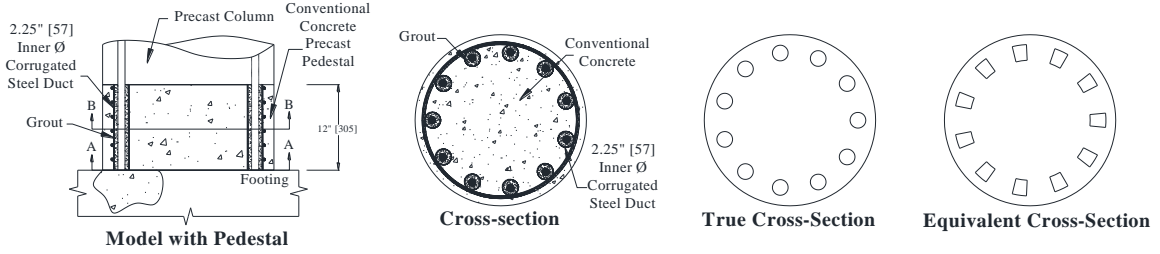


Figure 8-70 Pedestal geometry, details and equivalent cross-section

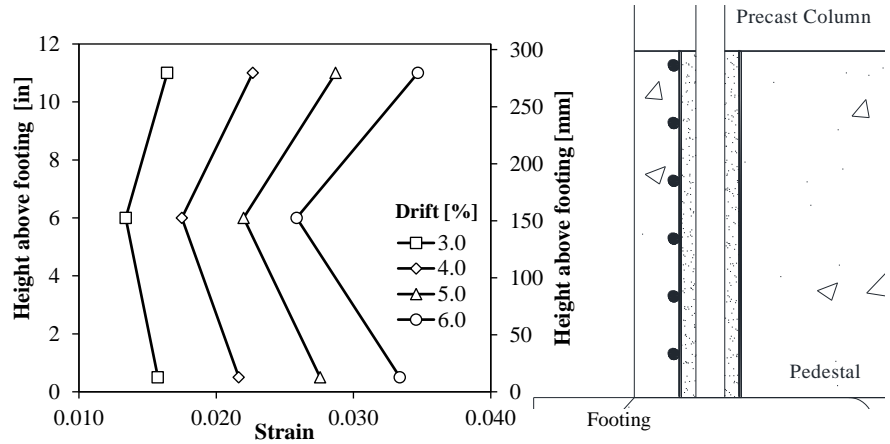


Figure 8-71 Measured strain within the pedestal for GCPP

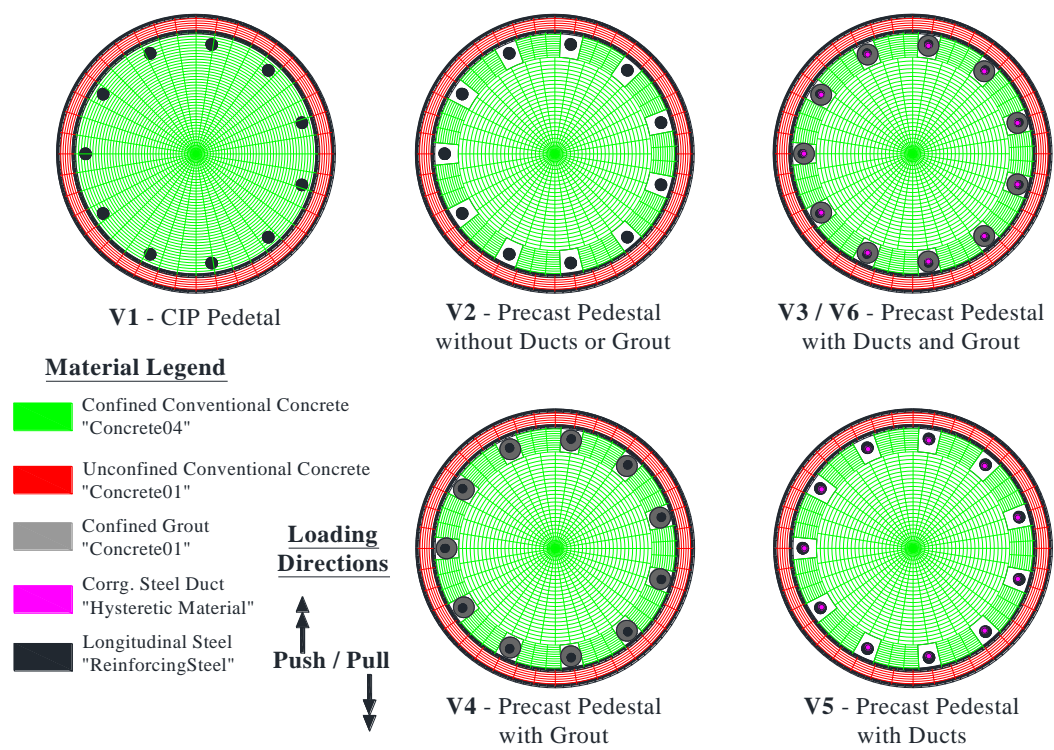


Figure 8-72 Pedestal sections investigated using moment-curvature analysis.

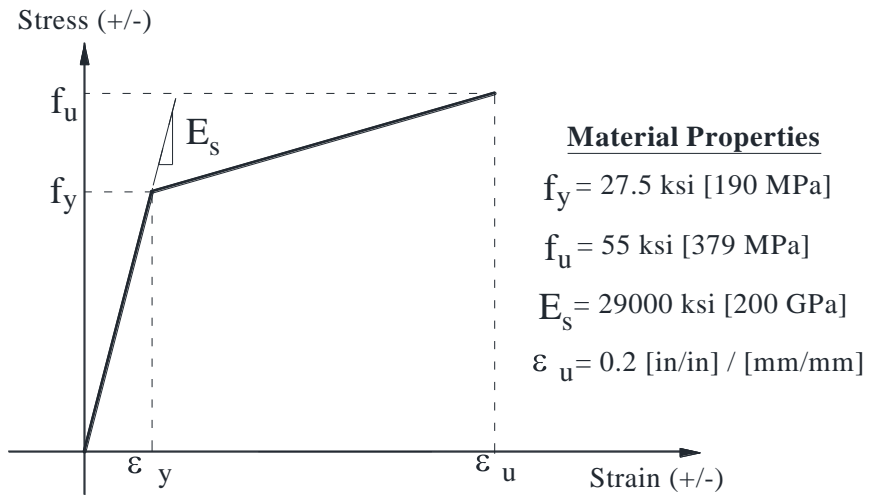


Figure 8-73 Constitutive model for corrugated steel ducts

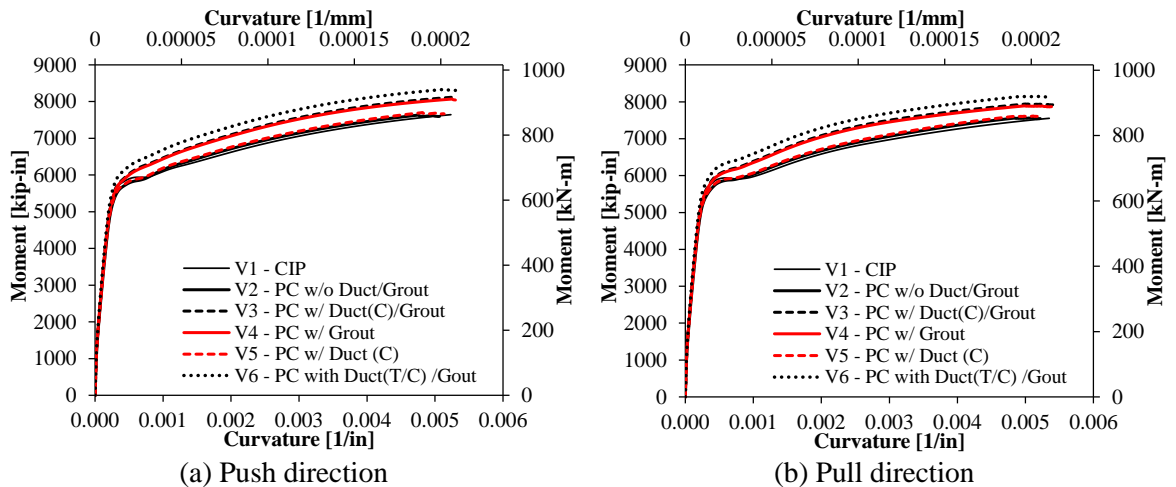


Figure 8-74 Moment-curvature response of different pedestal section configurations

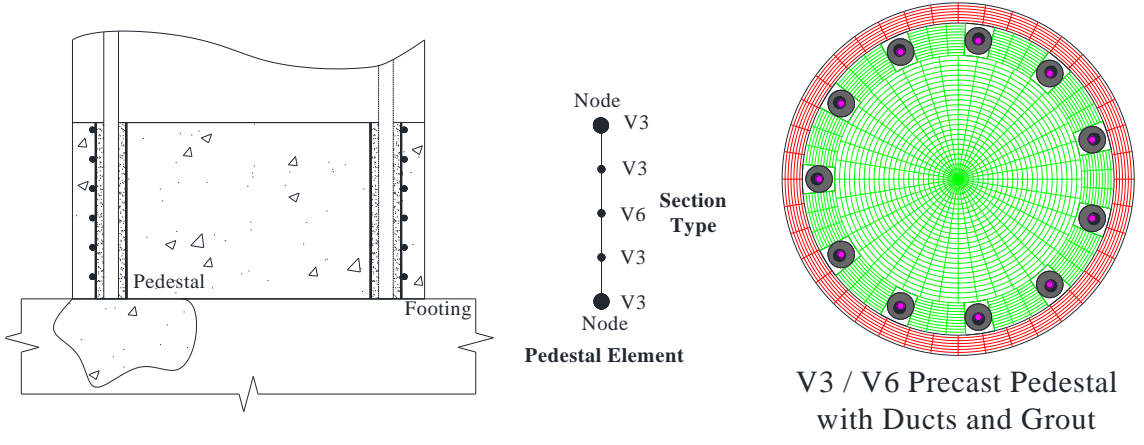
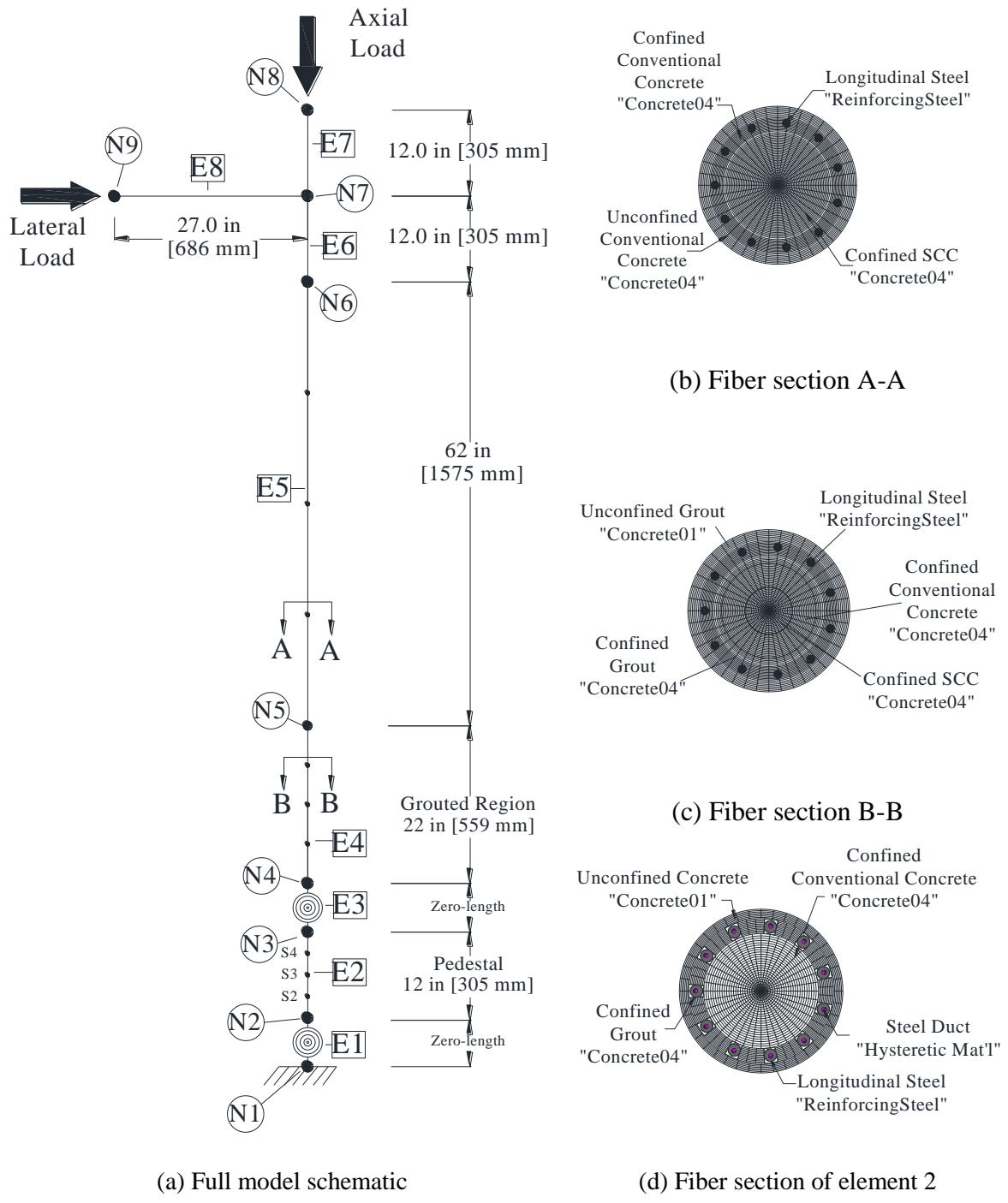


Figure 8-75 Definition of pedestal element



(a) Full model schematic

(d) Fiber section of element 2

Figure 8-76 Analytical model of HCPP

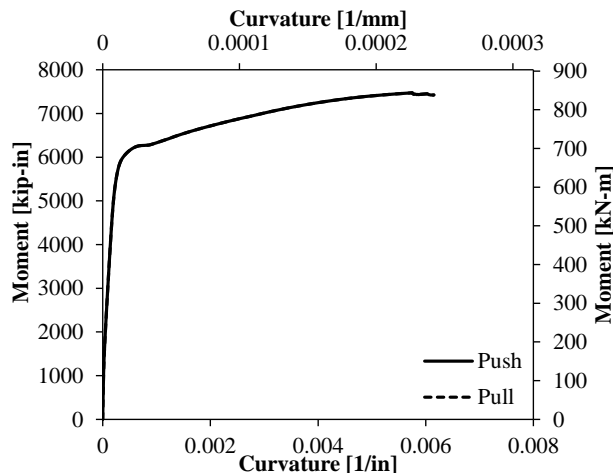
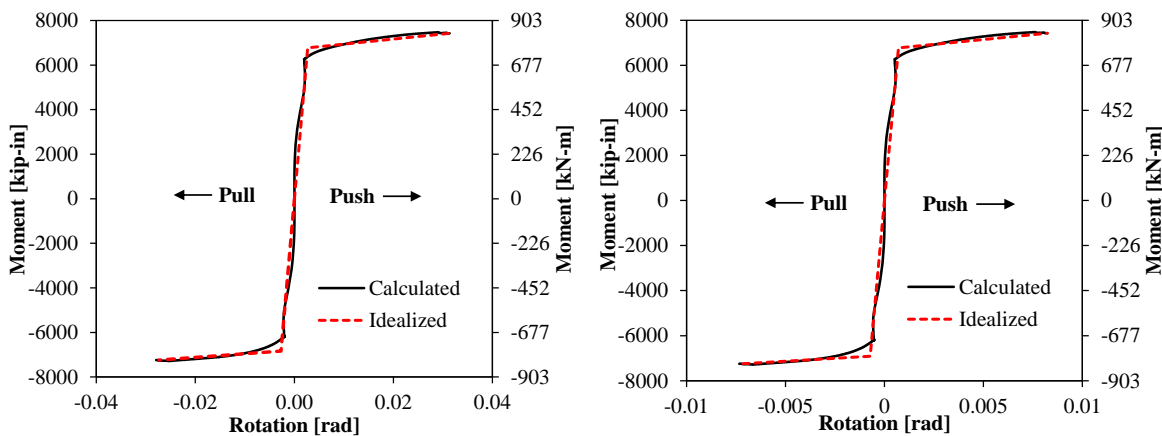


Figure 8-77 Moment-curvature response from HCPP fiber section shown in Figure 8-76d



(a) Contribution from the footing

(b) Contribution from the pedestal duct

Figure 8-78 Moment-rotation relationships for bond-slip at the pedestal-footing interface for HCPP

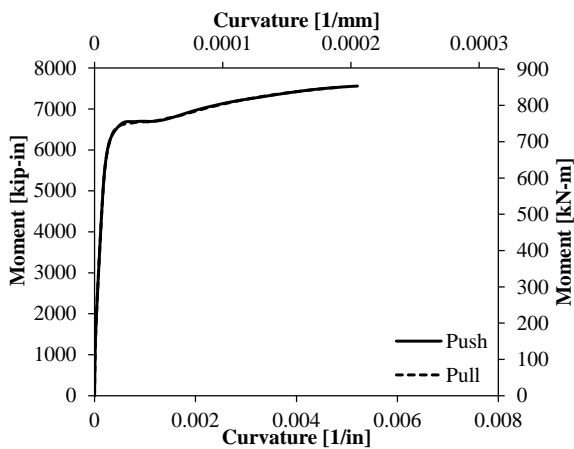


Figure 8-79 Moment-curvature response from section shown in Figure 8-76b

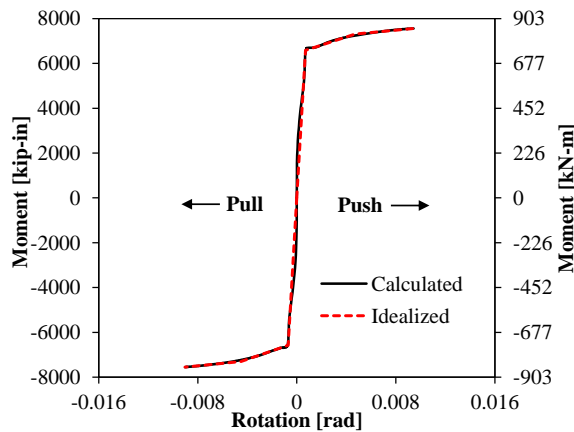


Figure 8-80 Bond-slip rotation at the pedestal-column interface

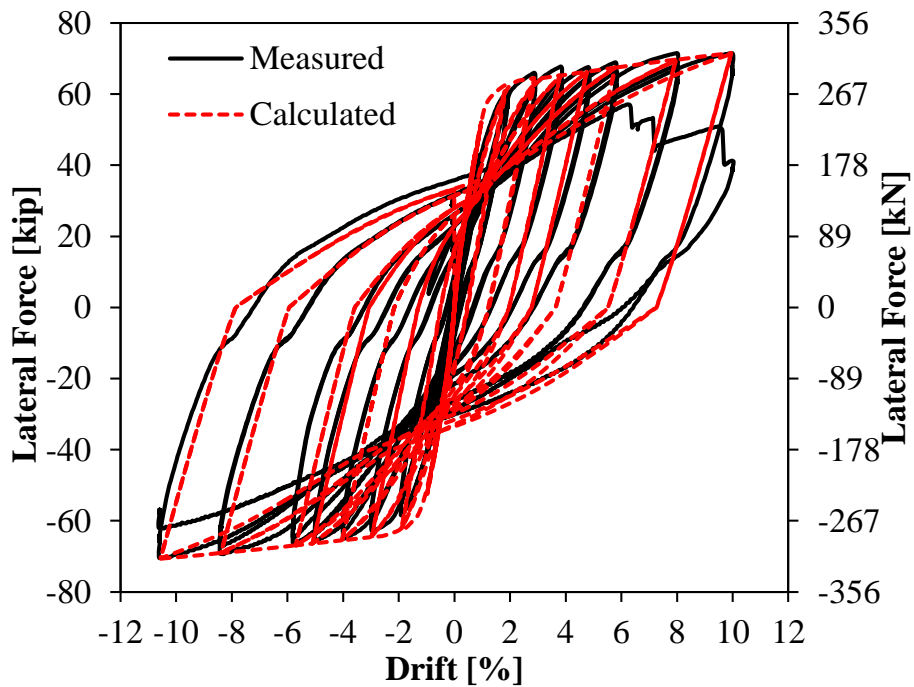


Figure 8-81 Hysteresis curves for HCPP

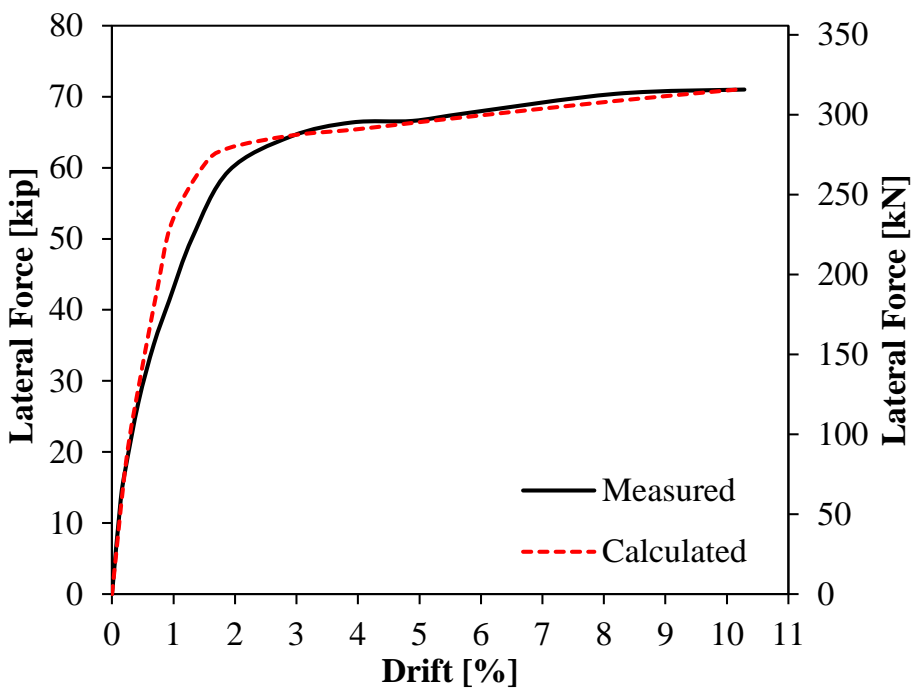


Figure 8-82 Average envelope curves for HCPP

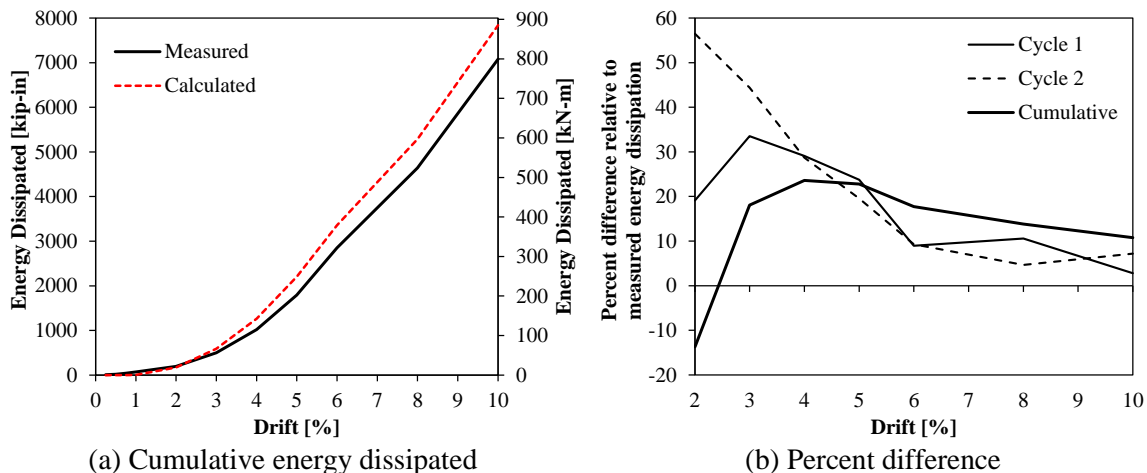


Figure 8-83 Energy dissipation for HCPP

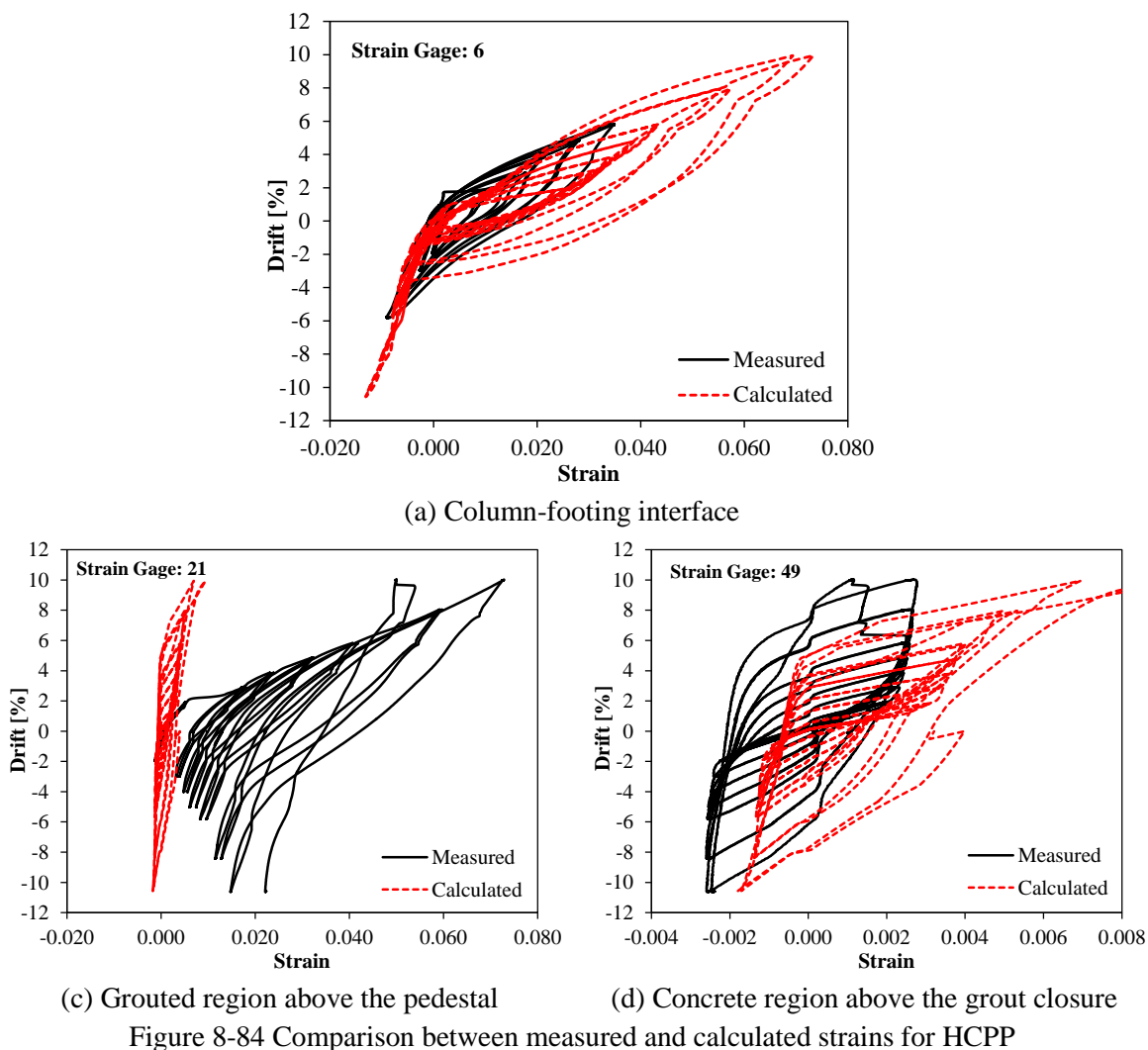


Figure 8-84 Comparison between measured and calculated strains for HCPP

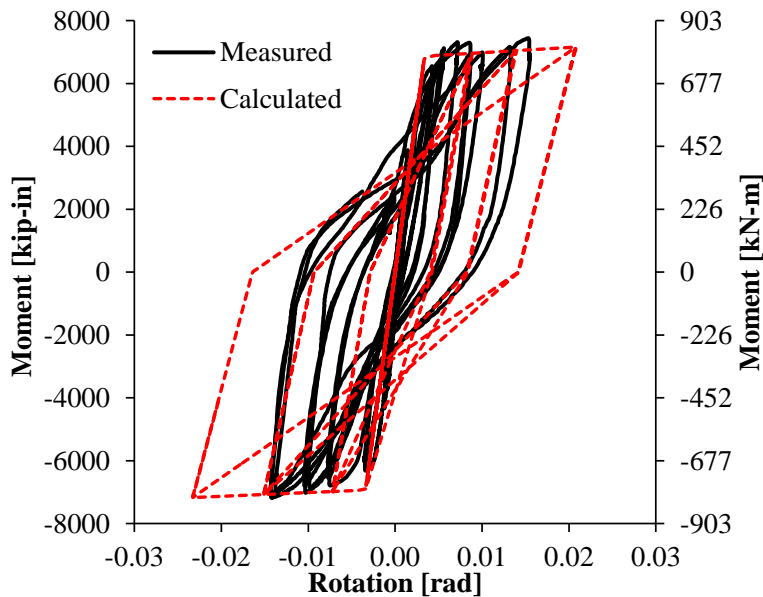
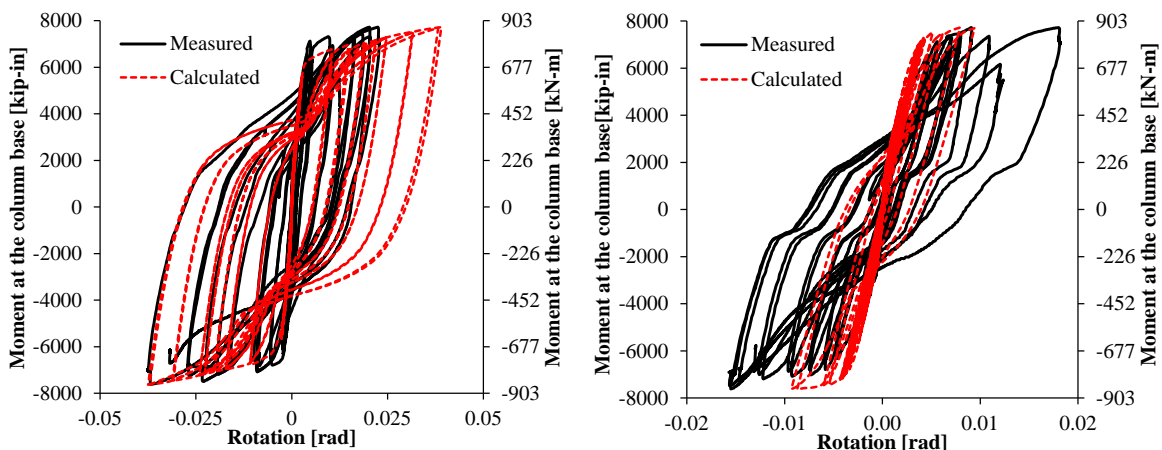


Figure 8-85 Moment-rotation relationship for bond-slip at the pedestal-footing interface up to 5% drift



(a) Pedestal rotation up to 10% drift

(b) Rotation within the grouted region up to 10% drift

Figure 8-86 Comparison between measured and calculated moment-rotation relationships for HCPP

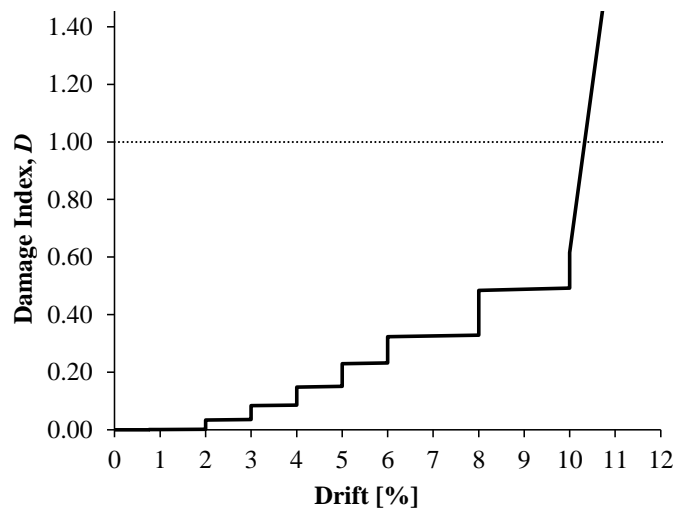


Figure 8-87 Cumulative damage as a function of drift for HCPP

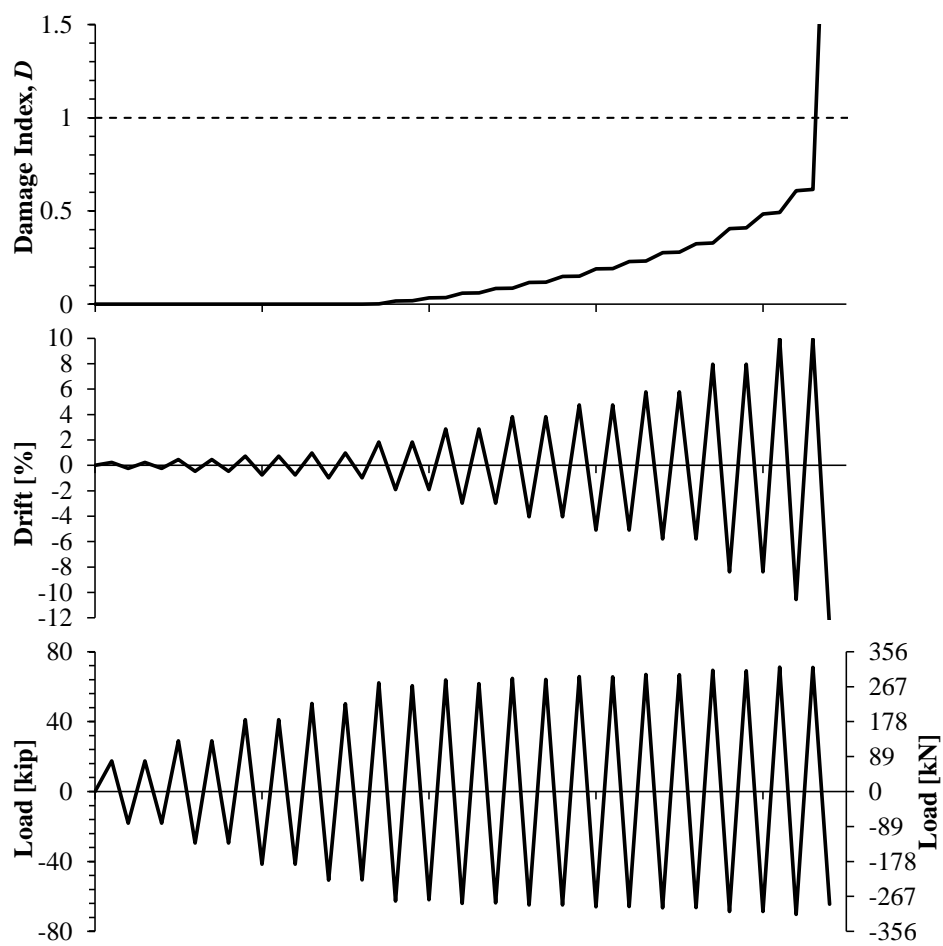
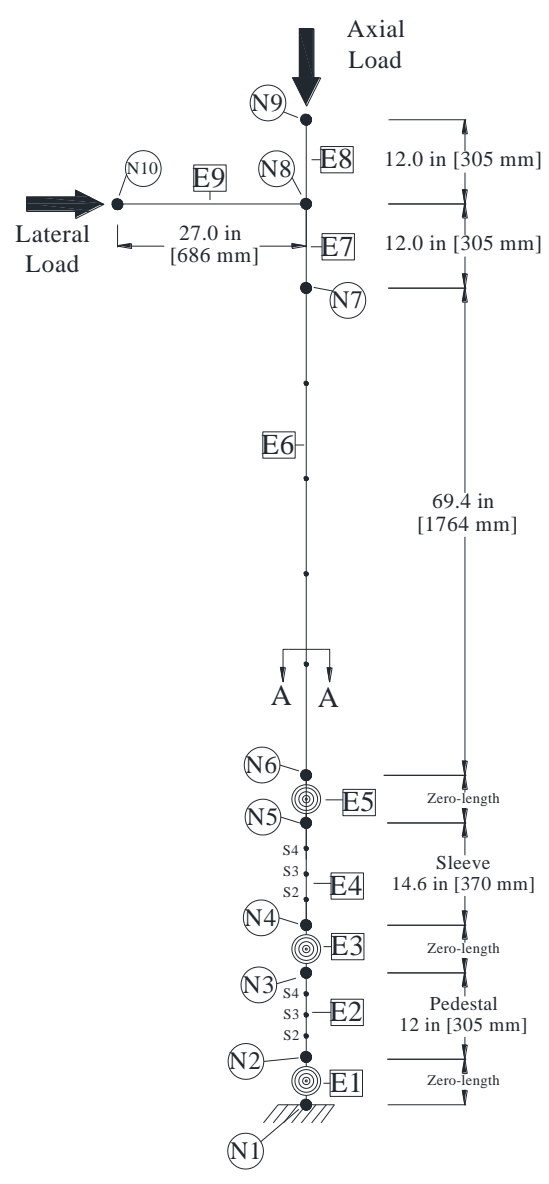
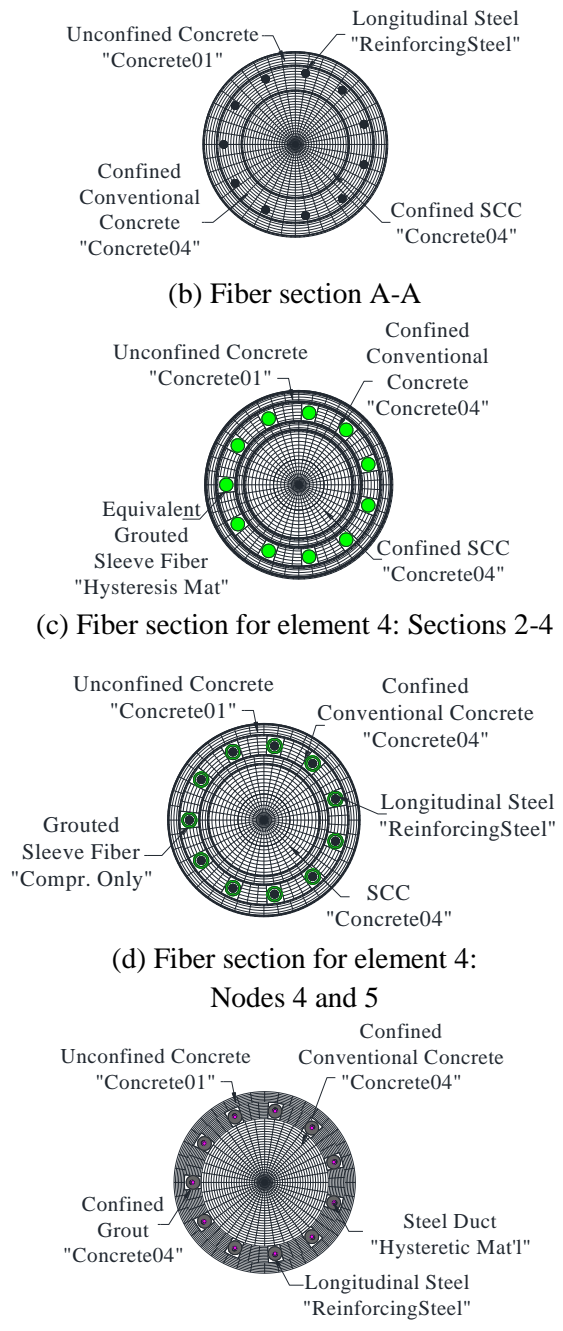


Figure 8-88 Cumulative damage plotted with drift and load for HCPP



(a) Full model schematic



(e) Fiber section for element 2

Figure 8-89 Analytical model for GCPP

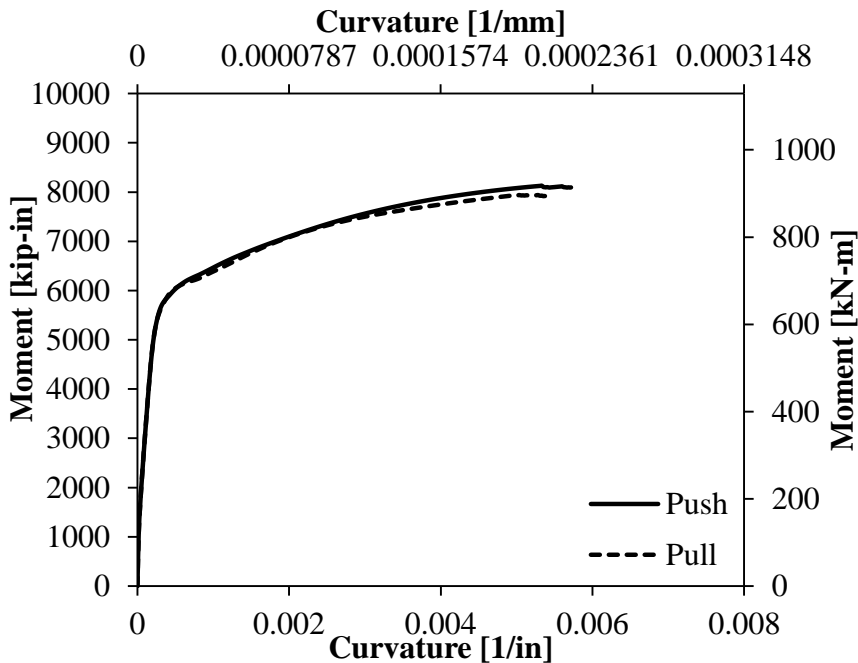
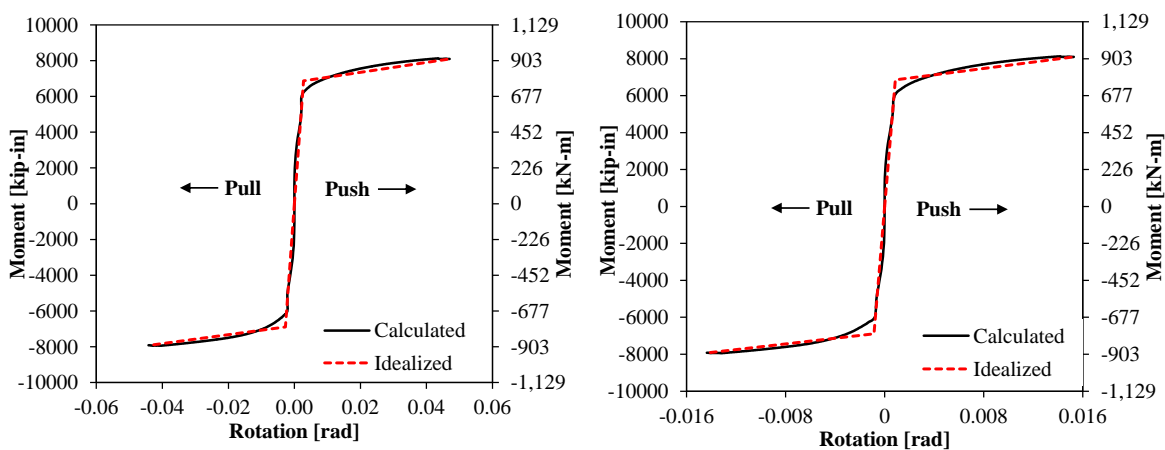


Figure 8-90 Moment-curvature response for the GCPP fiber-section shown in Figure 8-89e



(a) Bond-slip component from the footing

(b) Bond-slip component from the base of the pedestal

Figure 8-91 Moment-rotation relationships for bond-slip at the pedestal-footing interface

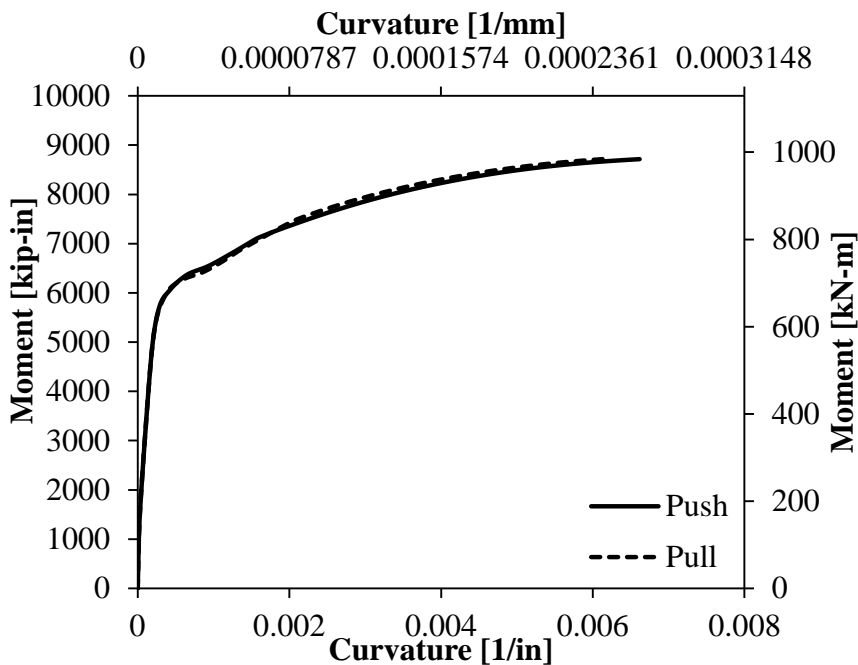
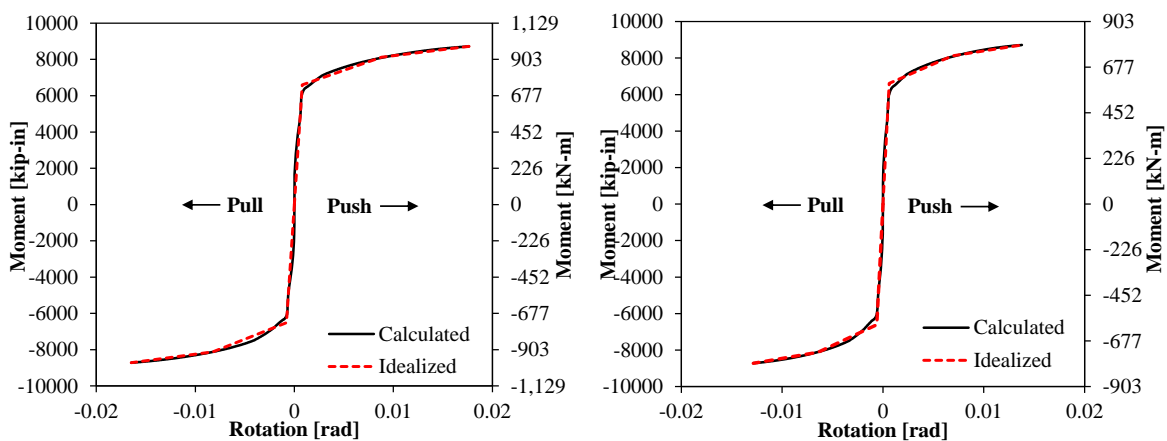


Figure 8-92 Moment-curvature response for the GCPP fiber-section shown in Figure 8-89d



(a) Bond-slip component from the top of the pedestal

(b) Bond-slip component from the bottom of the grouted coupler

Figure 8-93 Moment-rotation relationships for bond-slip at the column-pedestal interface

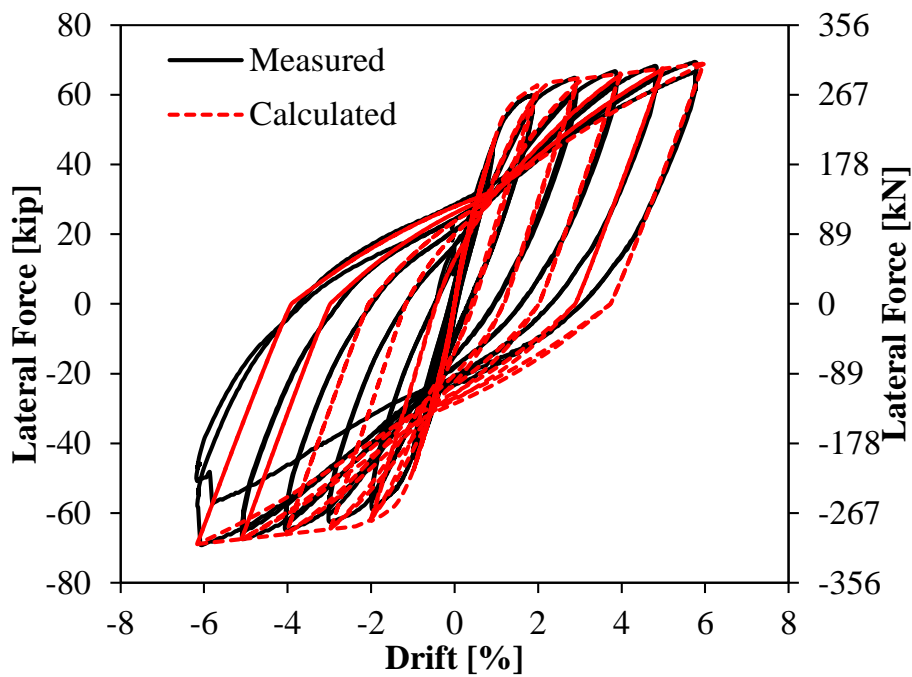


Figure 8-94 Hysteresis curves for GCPP

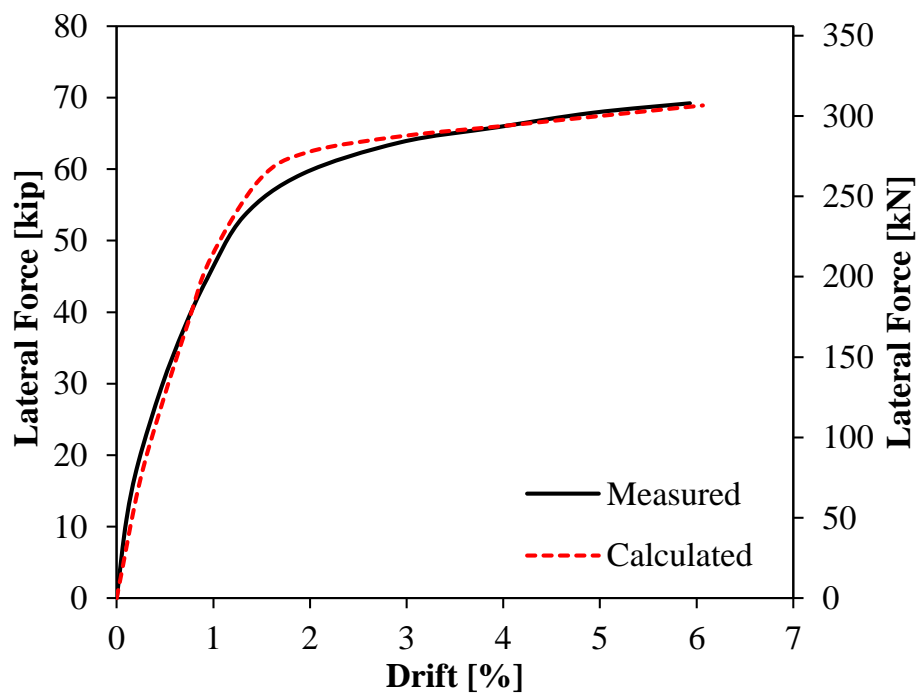


Figure 8-95 Average envelope curves for GCPP

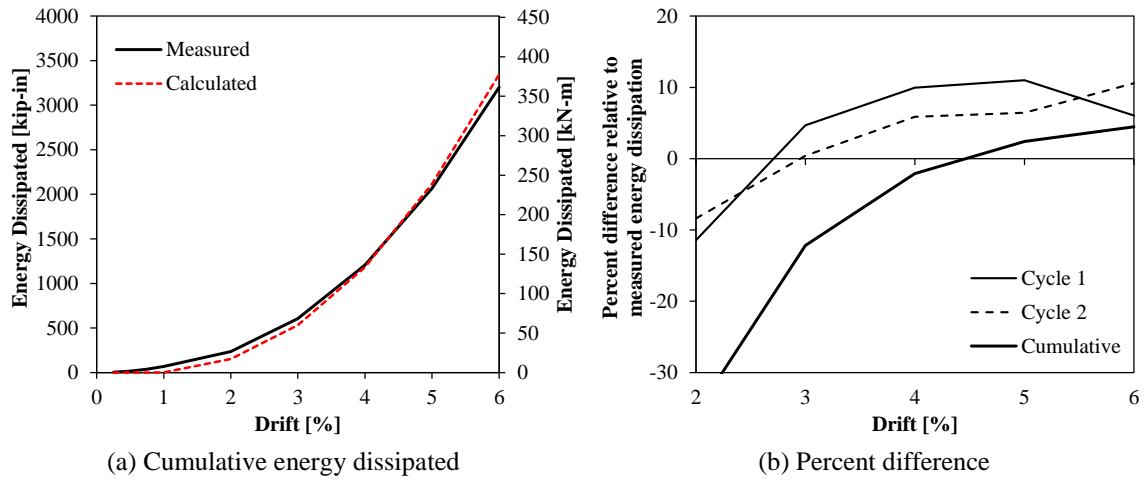


Figure 8-96 Energy dissipation for GCPP

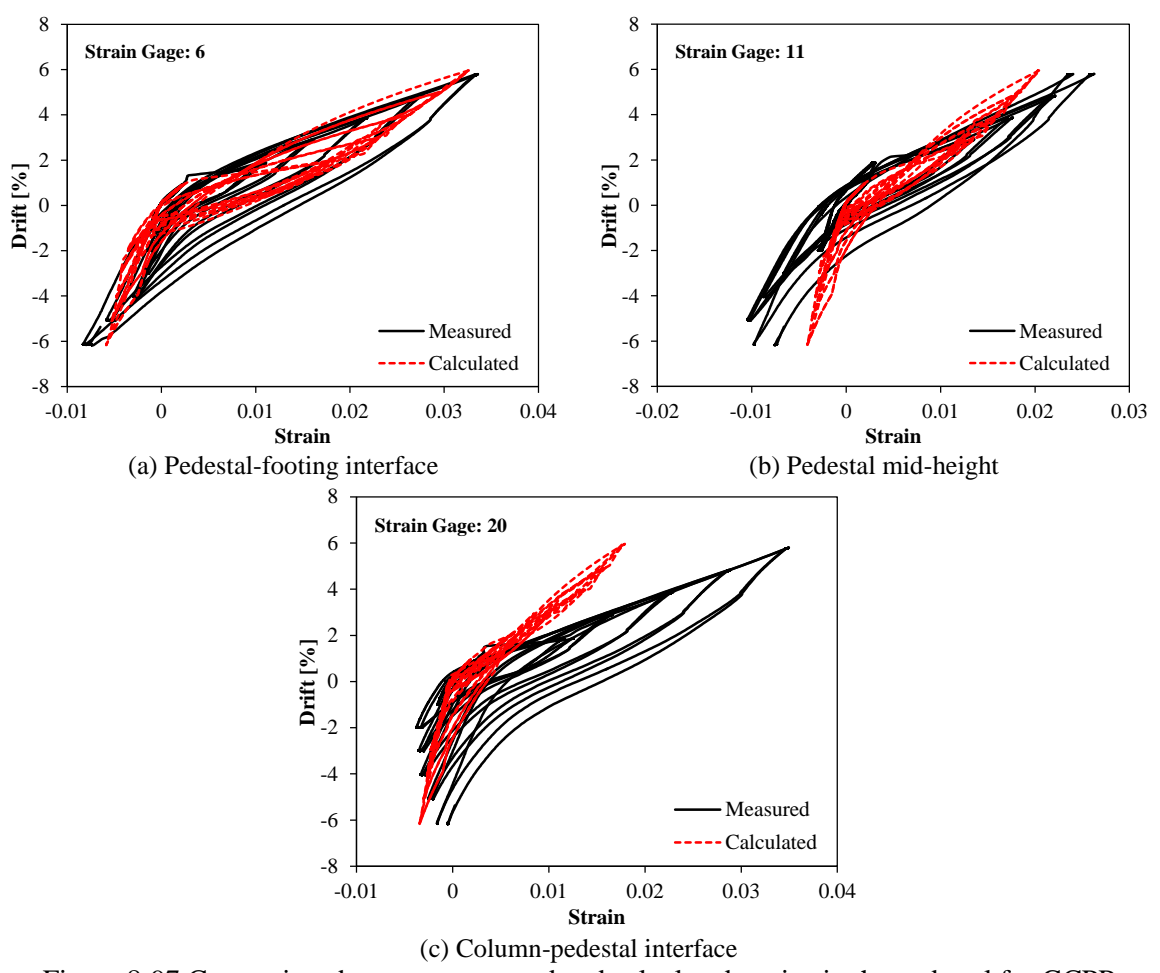
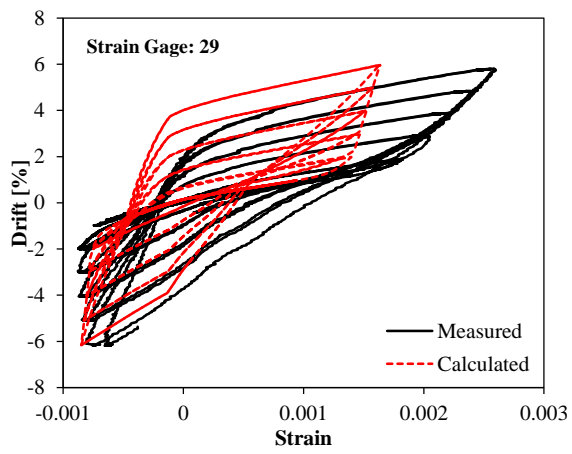
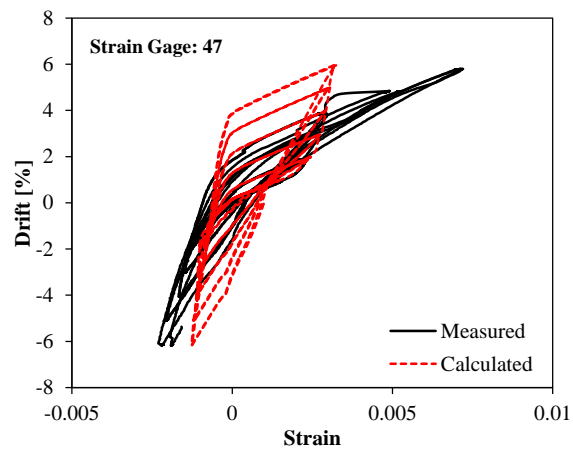


Figure 8-97 Comparison between measured and calculated strains in the pedestal for GCPP

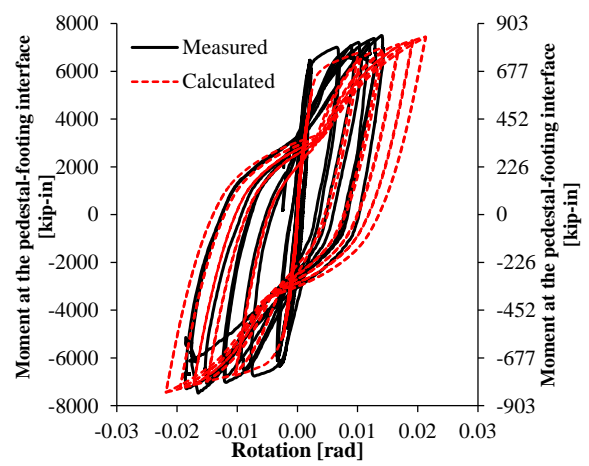


(a) Mid-height of the grouted coupler

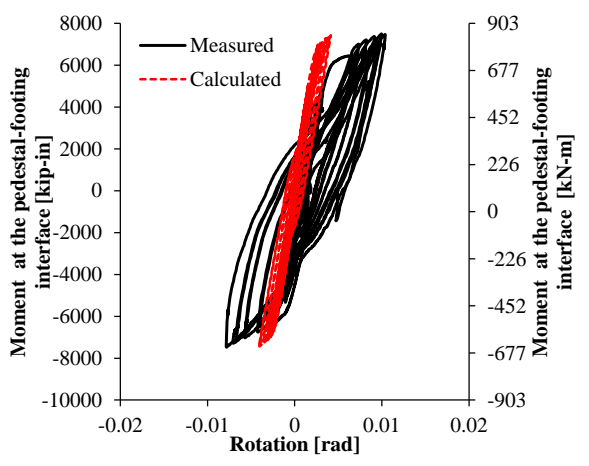


(b) Directly above the grouted coupler

Figure 8-98 Comparison between measured and calculated strains within the precast column for GCPP



(a) Rotation of the pedestal up to 6% drift



(b) Rotation of the coupler region up to 6% drift

Figure 8-99 Comparison between measured and calculated moment-rotation relationships for HCPP

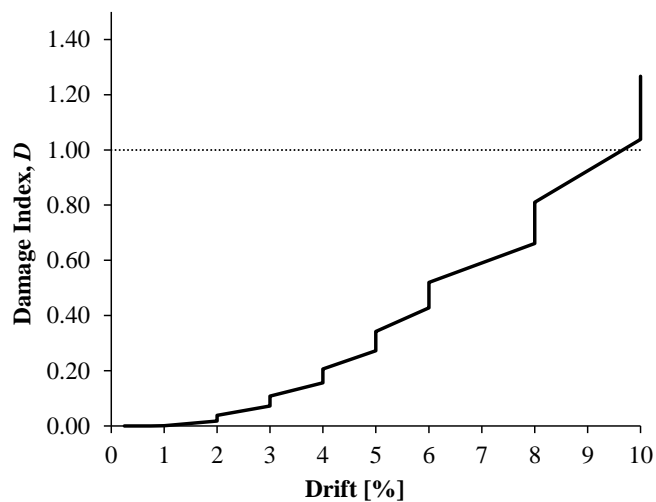


Figure 8-100 Cumulative damage as a function of drift for GCPP

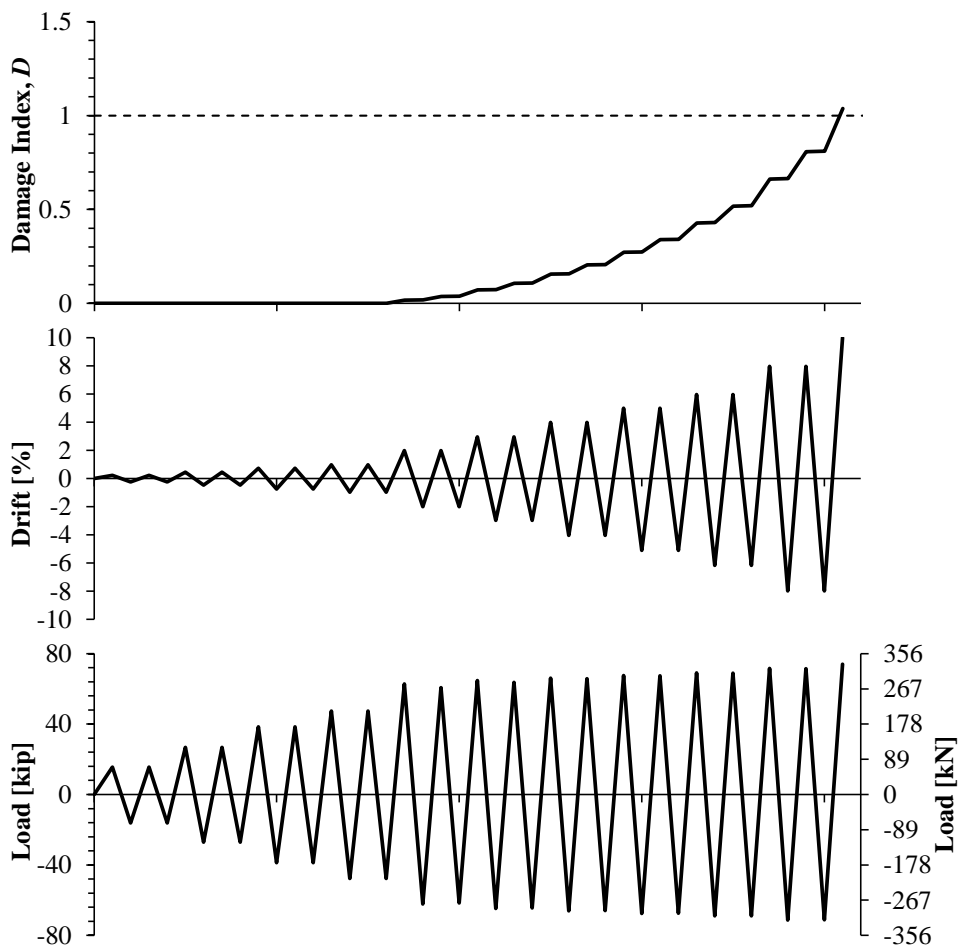
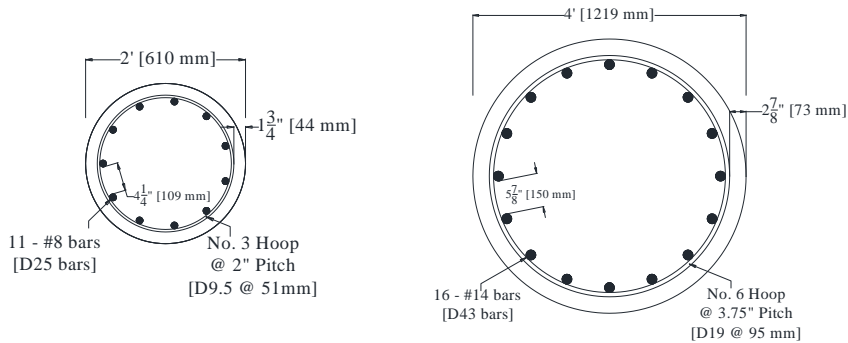


Figure 8-101 Cumulative damage plotted with drift and load for GCPP

Chapter 9 Figures



(a) Half-scale model (b) Full-scale prototype
Figure 9-1 Cross-sections for the conventional columns

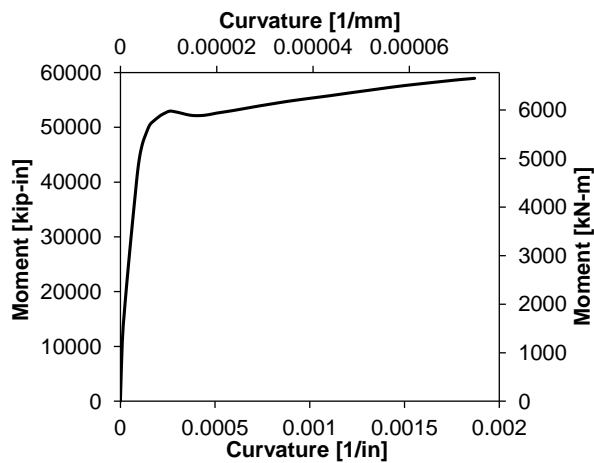


Figure 9-2 Moment-curvature response of the prototype column

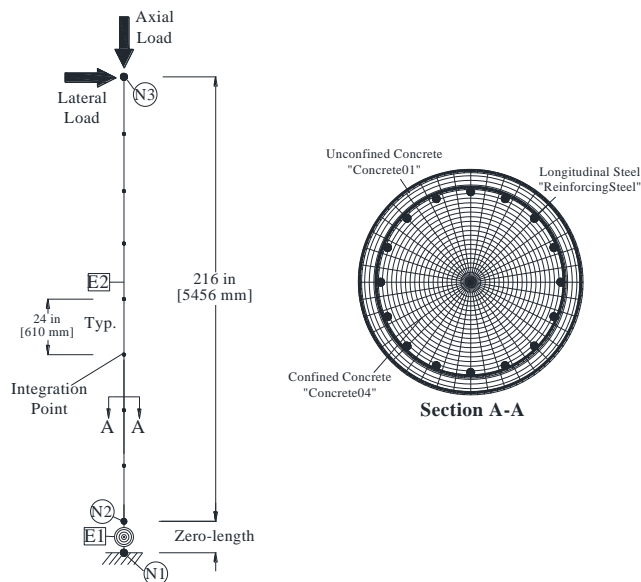


Figure 9-3 General details of the prototype OpenSEES models

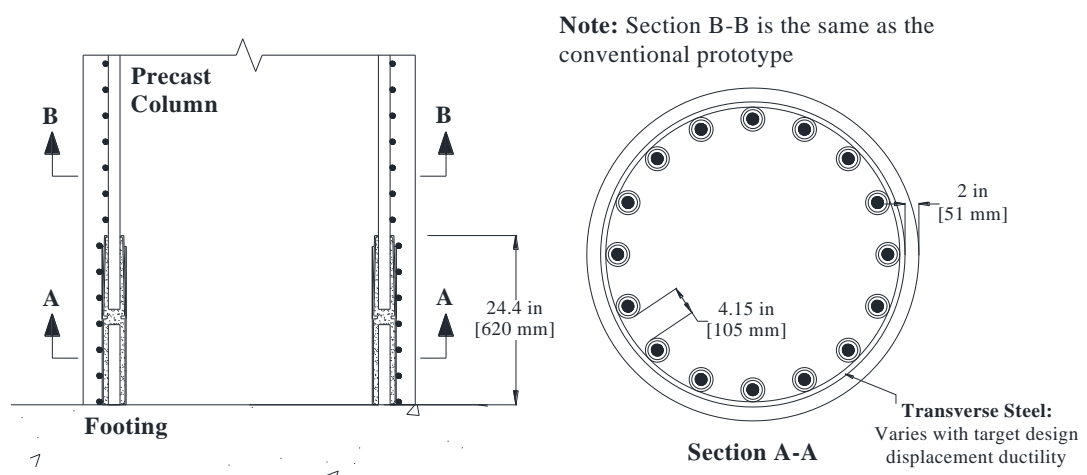


Figure 9-4 General Connection details for parameter study of target design ductility of GC columns

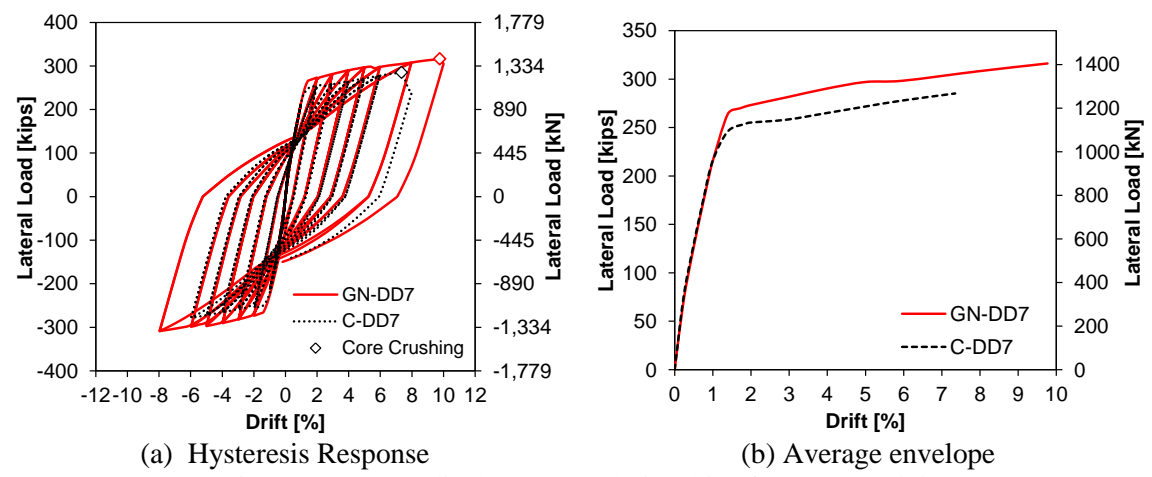


Figure 9-5 Force-displacement relationships for DD7 models

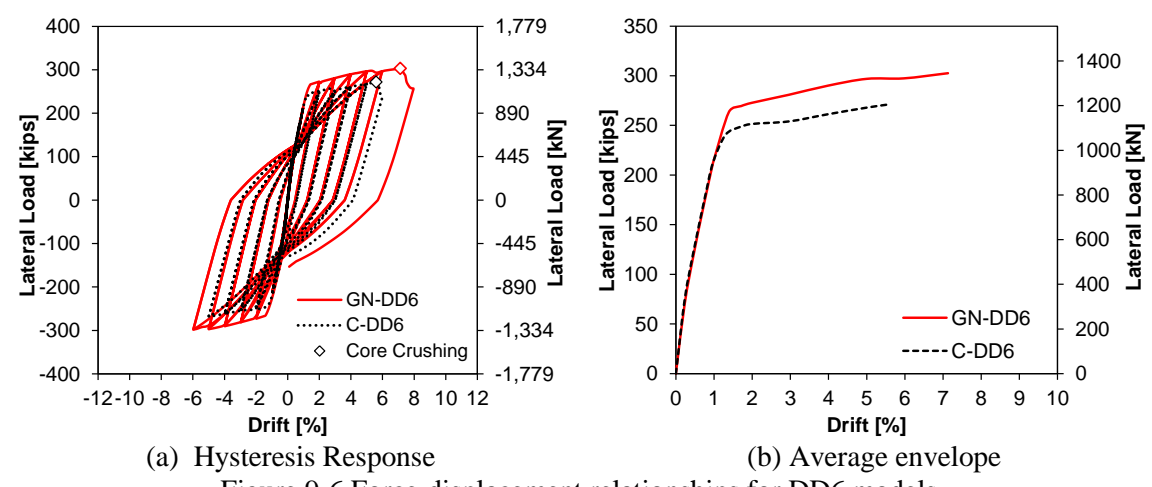
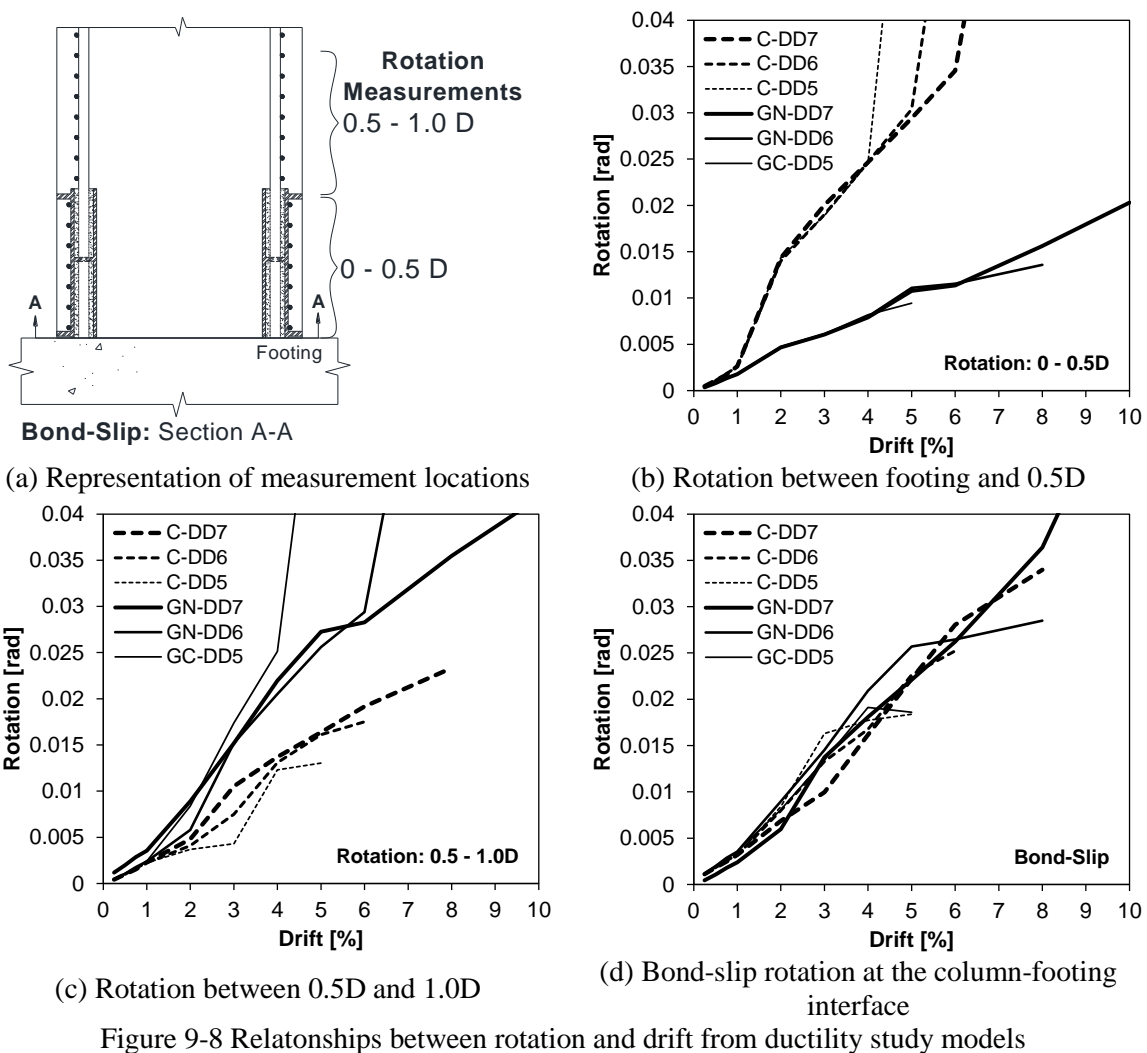
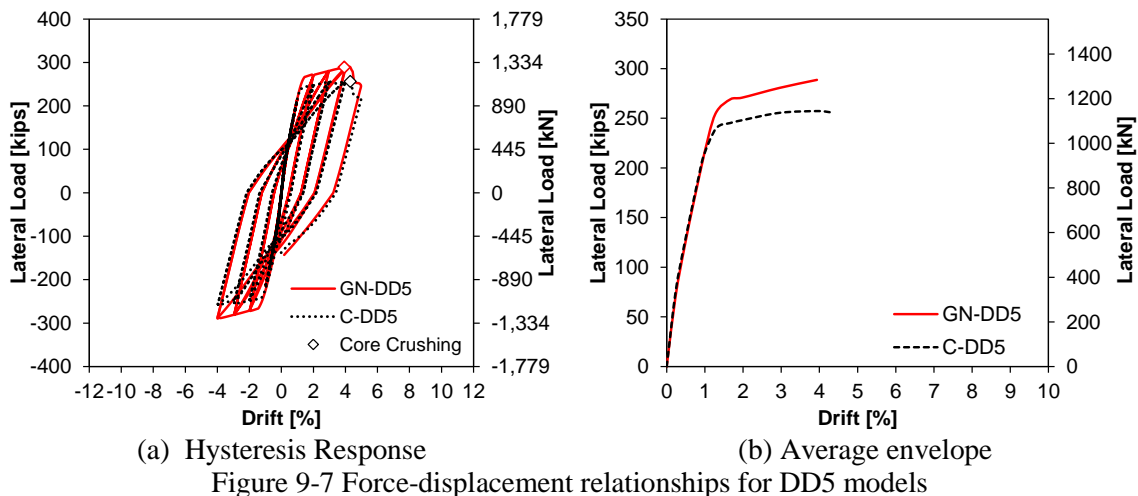


Figure 9-6 Force-displacement relationships for DD6 models



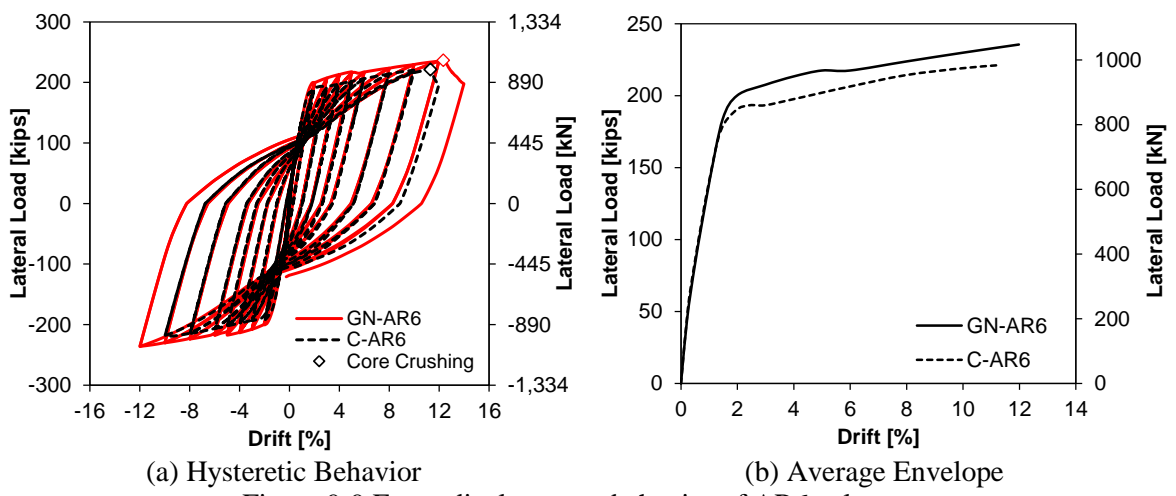
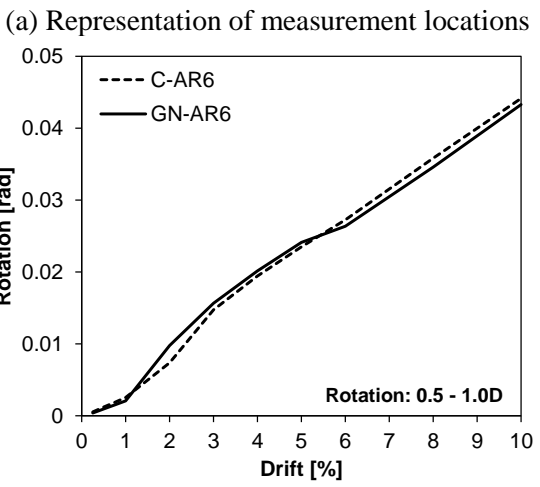
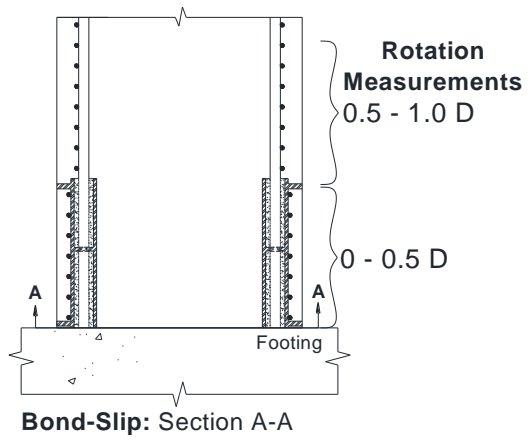
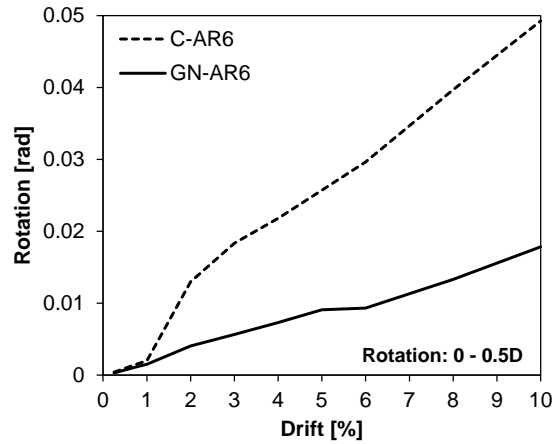


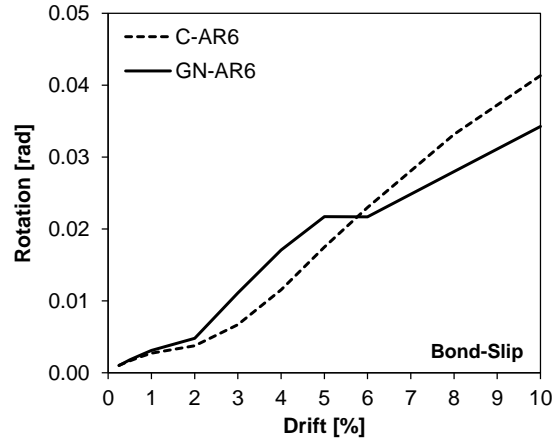
Figure 9-9 Force-displacement behavior of AR6 columns



(a) Rotation between 0.5D and 1.0D



(b) Rotation between footing and 0.5D



(d) Bond-slip rotation at the column-footing interface

Figure 9-10 Relationships between rotation and drift from aspect ratio study models

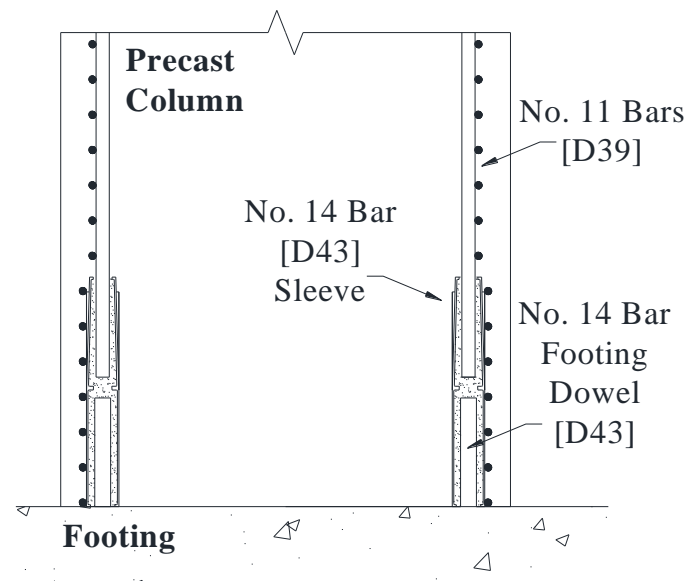
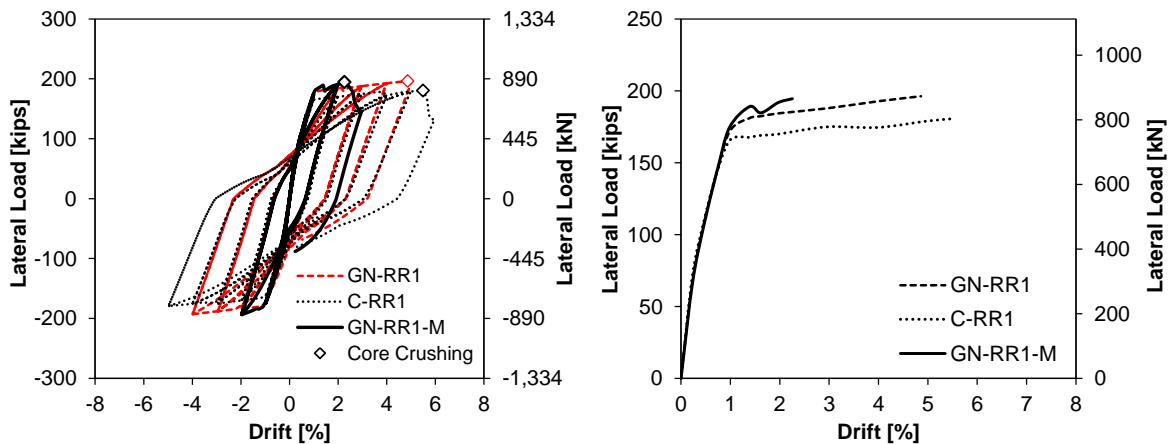


Figure 9-11 Proposed GC column detail to reduce strain concentrations within the footing



(a) Hysteretic Behavior

(b) Average Envelope

Figure 9-12 Force-displacement behavior of RR1 columns

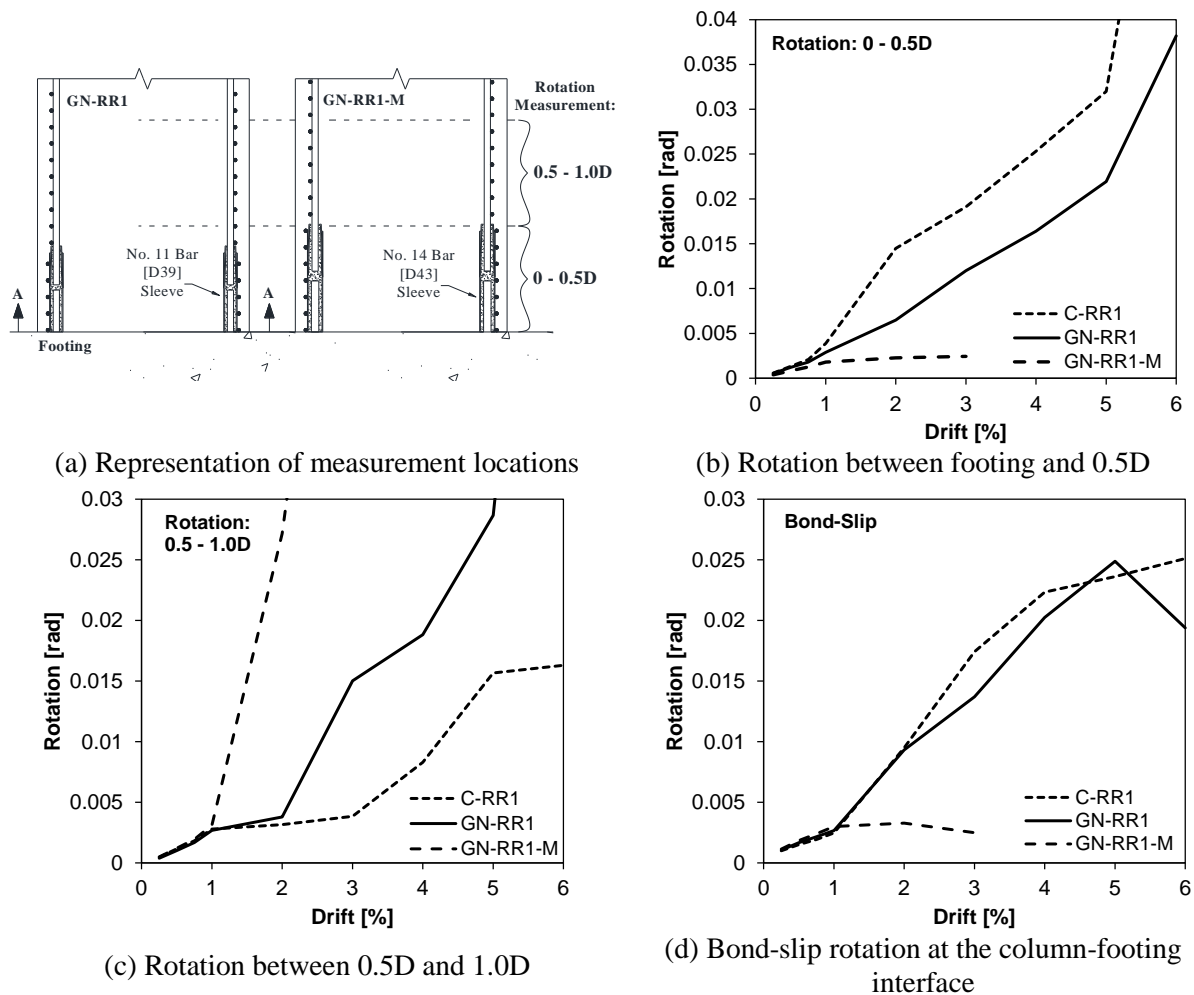


Figure 9-13 Relationships between rotation and drift from reinforcement ratio study models

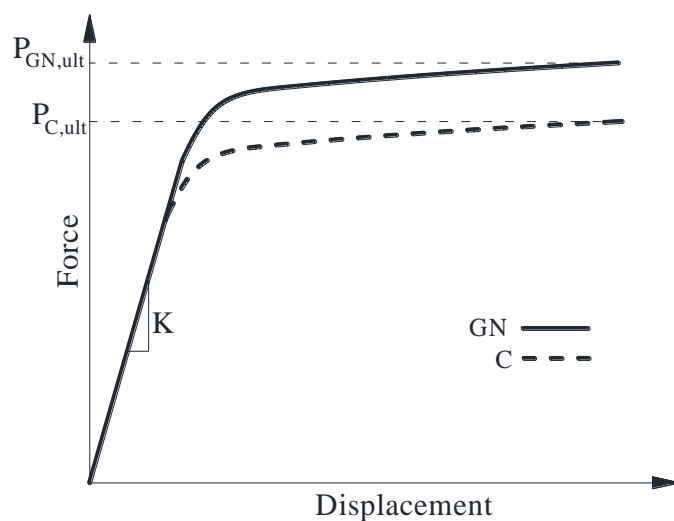
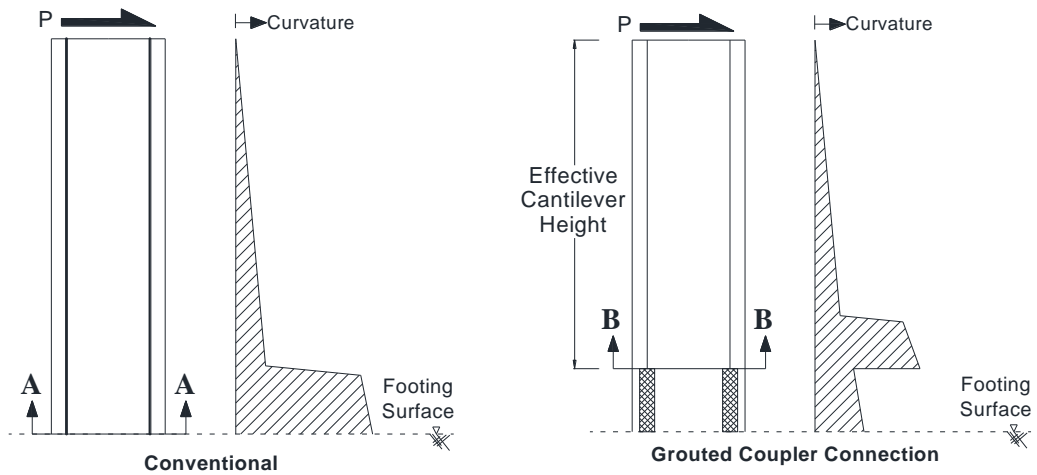
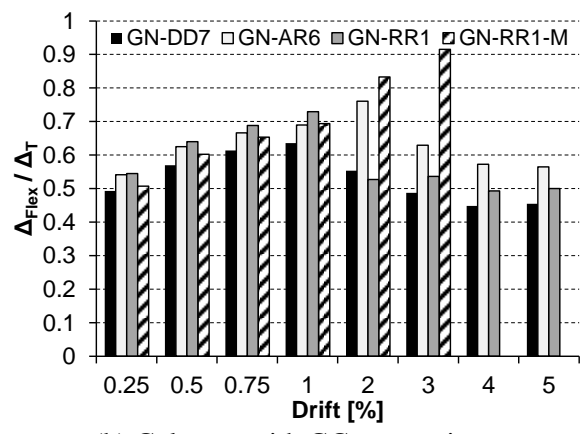
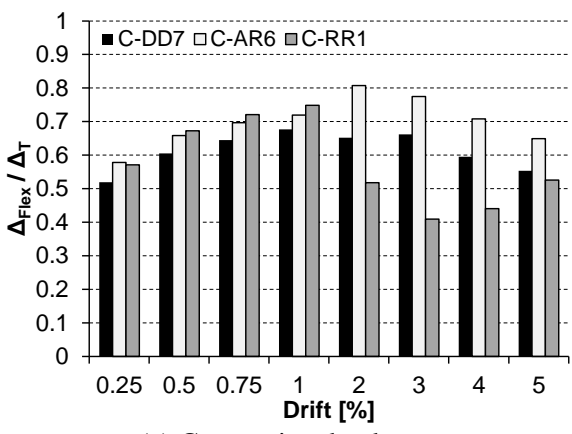


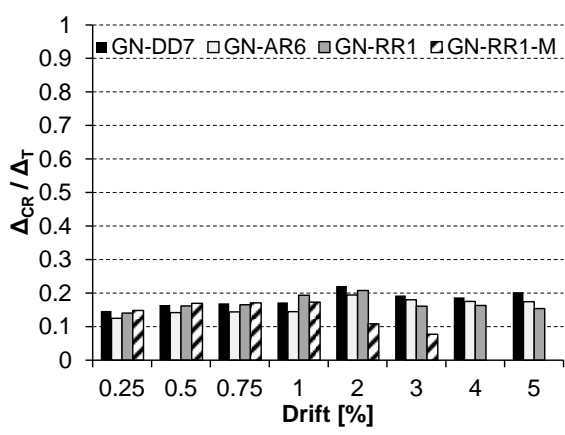
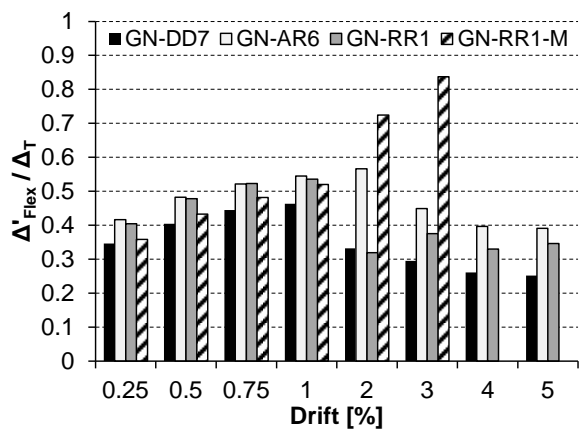
Figure 9-14 Generalized force-displacement relationships



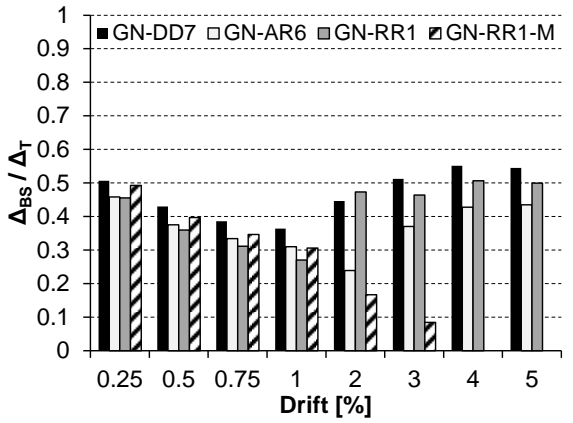
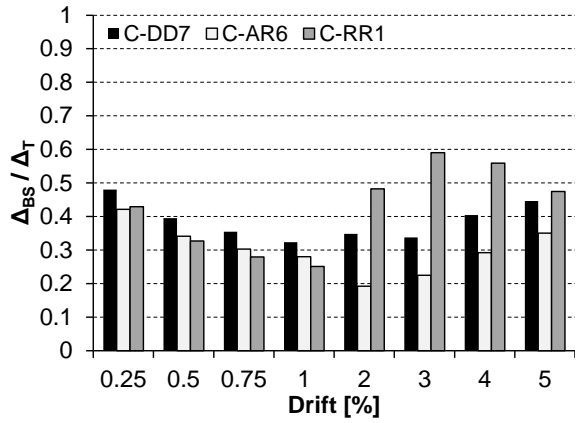
(a) Conventional columns (b) Columns with GC connections
 Figure 9-15 Critical sections and generalized curvature distributions



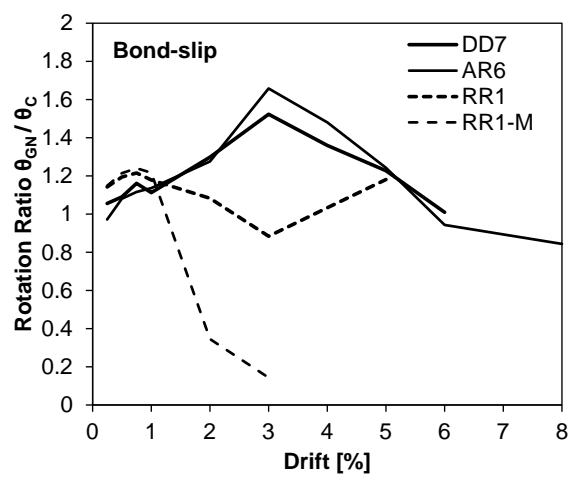
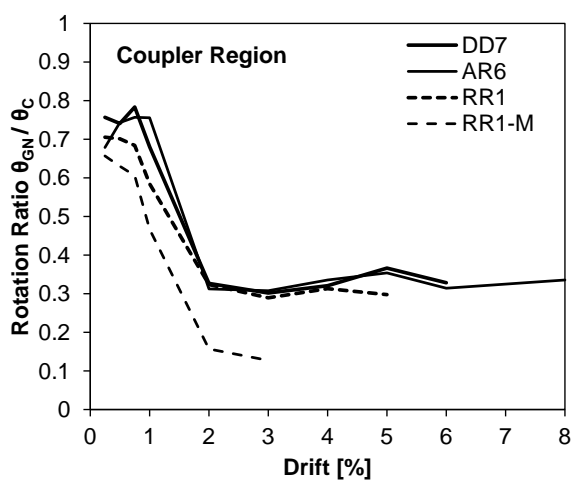
(a) Conventional columns (b) Columns with GC connections
 Figure 9-16 Flexural contribution to tip displacement



(a) Flexure above the coupler region (b) Coupler region
 Figure 9-17 Flexure components from GN columns



(a) Conventional columns (b) Columns with GC connections
 Figure 9-18 Bond-slip rotation contribution to tip displacement



(a) Over coupler region (b) Bond-slip
 Figure 9-19 GN-to-C rotation ratios

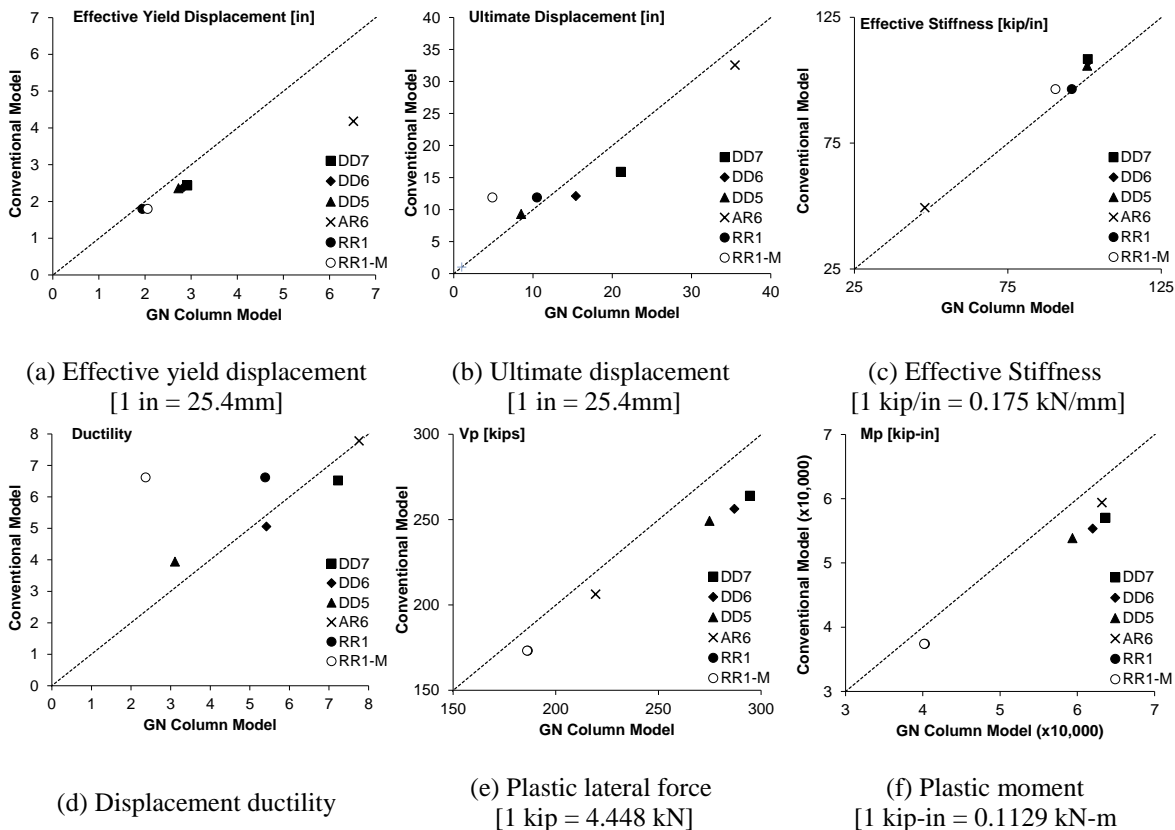


Figure 9-20 Comparison of key calculated results for all models

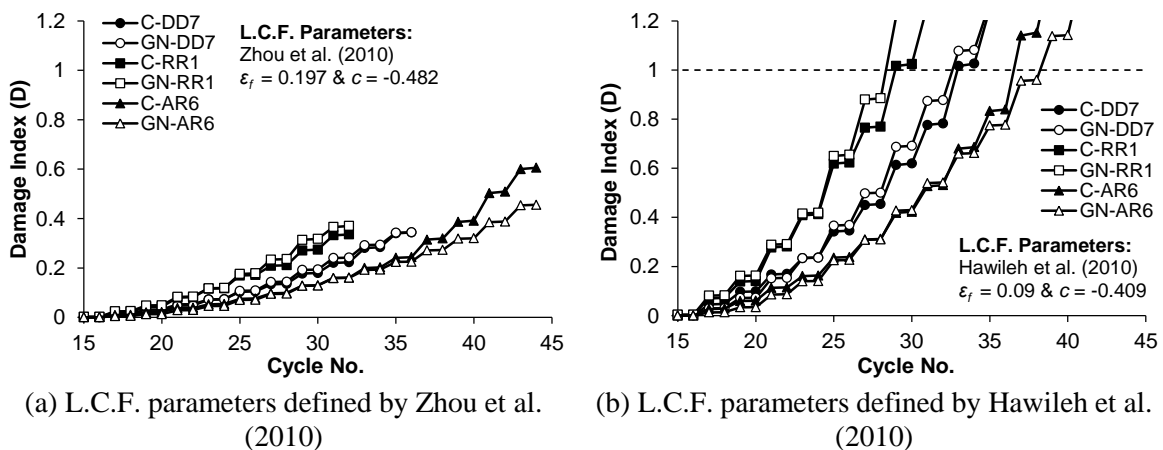


Figure 9-21 Damage index (DI) in extreme reinforcing bar as a function of cycle

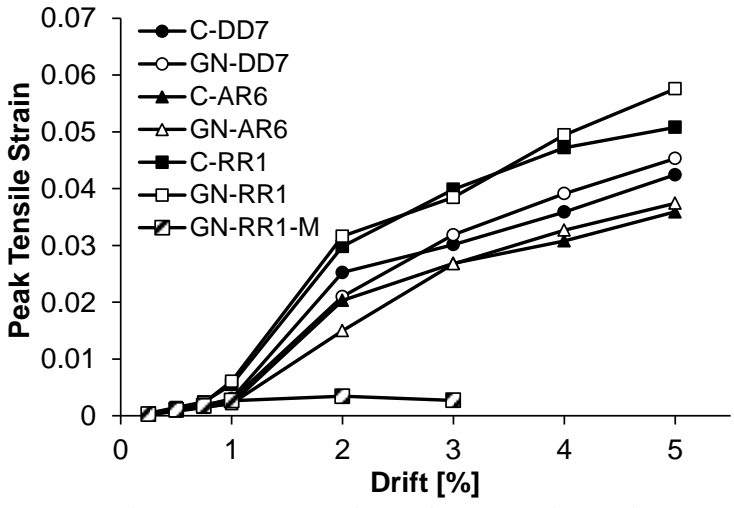


Figure 9-22 Comparison of peak tensile strain

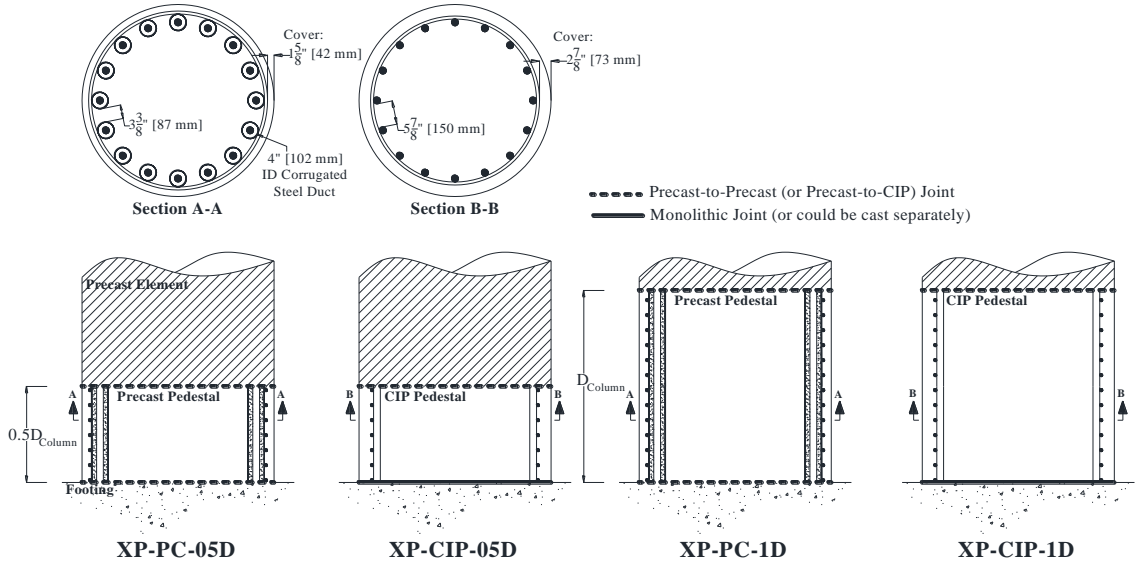
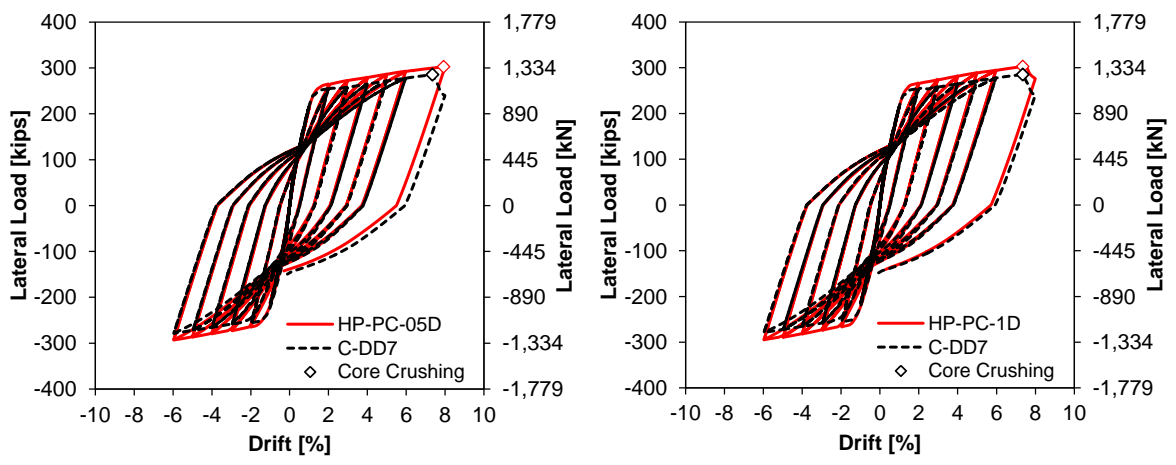
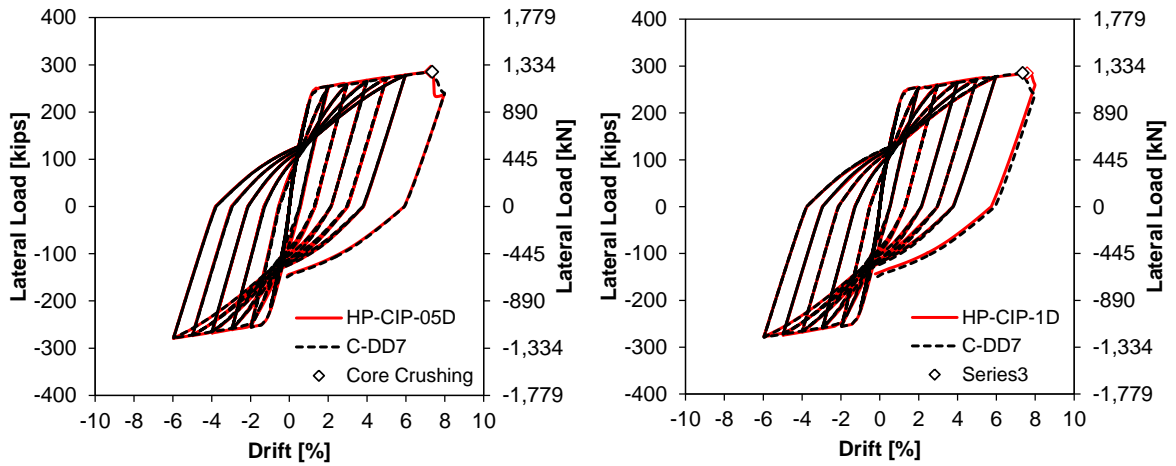


Figure 9-23 Pedestal detail configurations investigated



(a) Precast pedestal – 0.5D

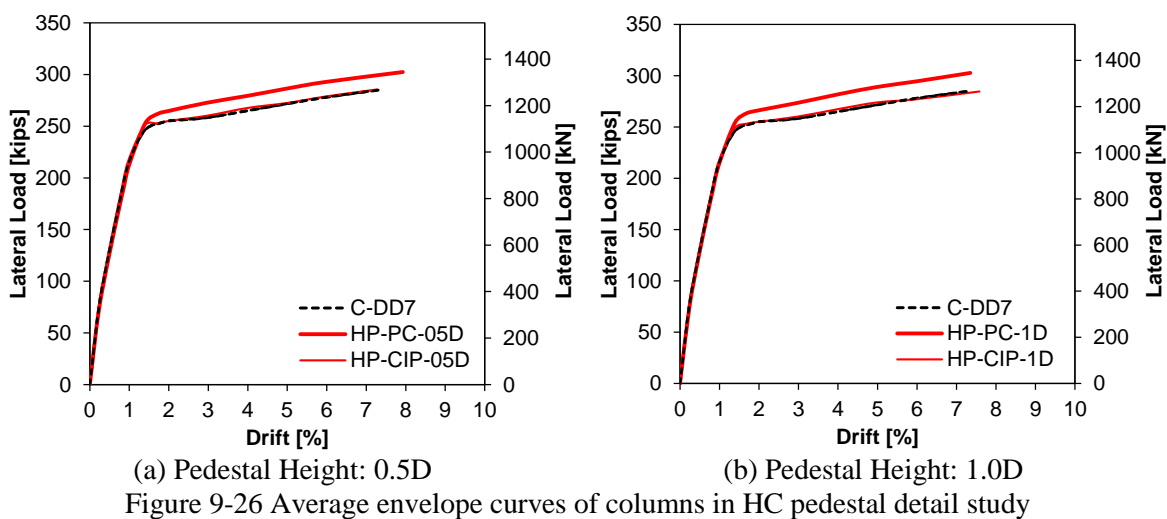
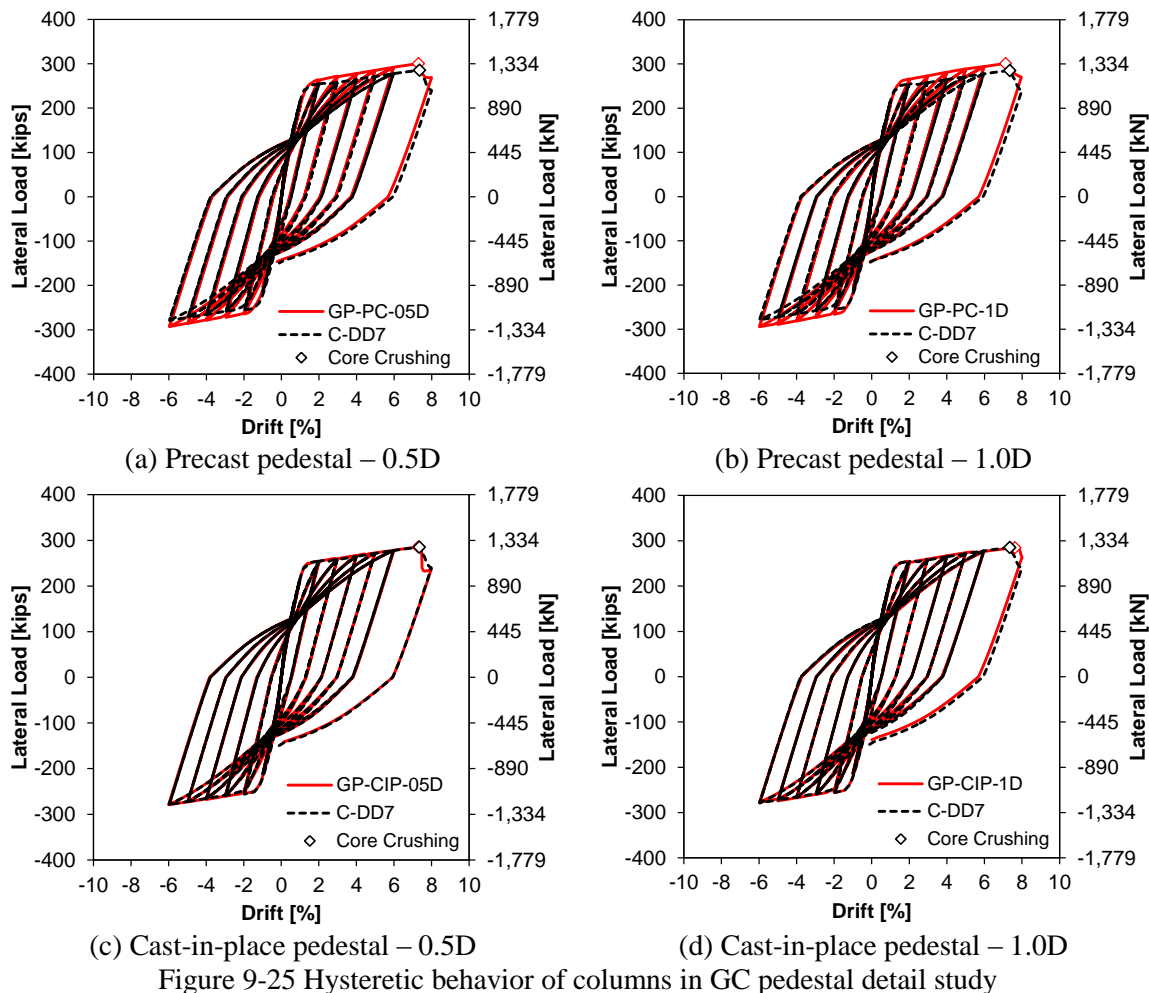
(b) Precast pedestal – 1.0D

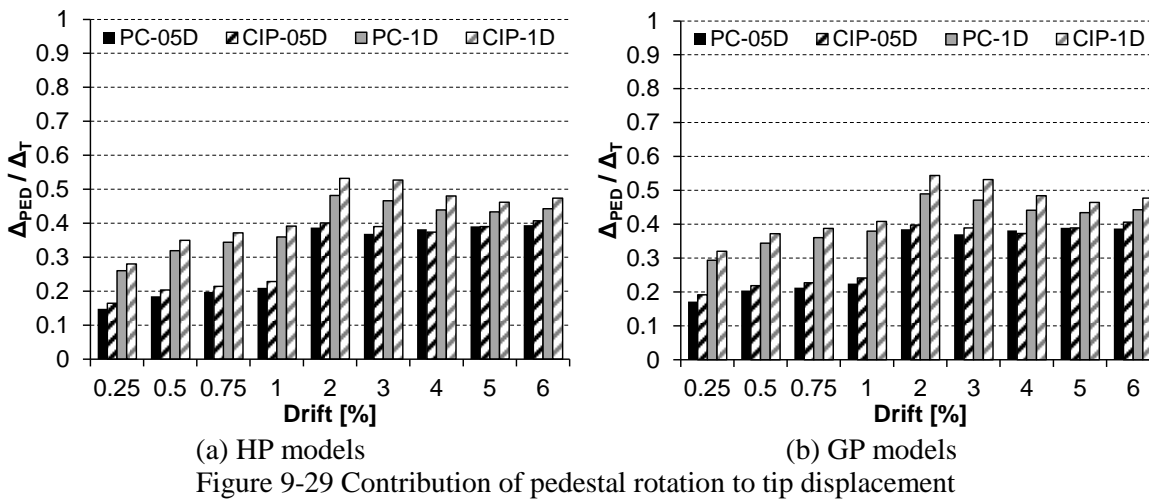
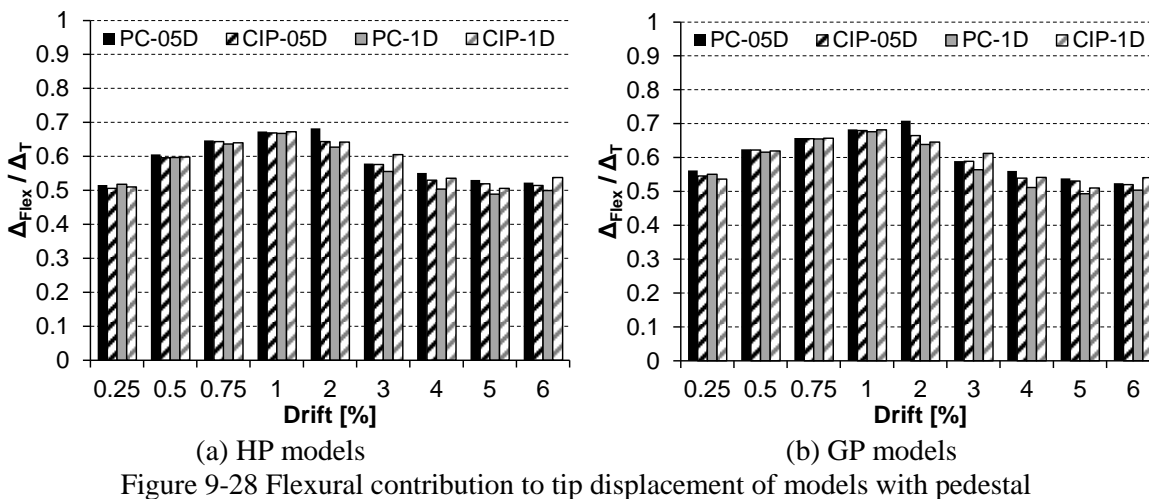
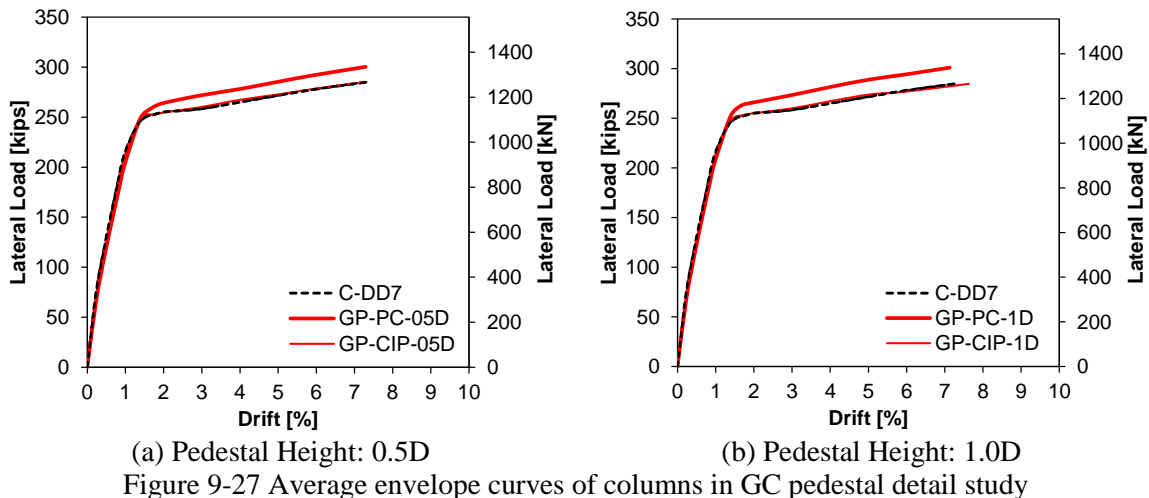


(c) Cast-in-place pedestal – 0.5D

(d) Cast-in-place pedestal – 1.0D

Figure 9-24 Hysteretic behavior of columns in HC pedestal detail study





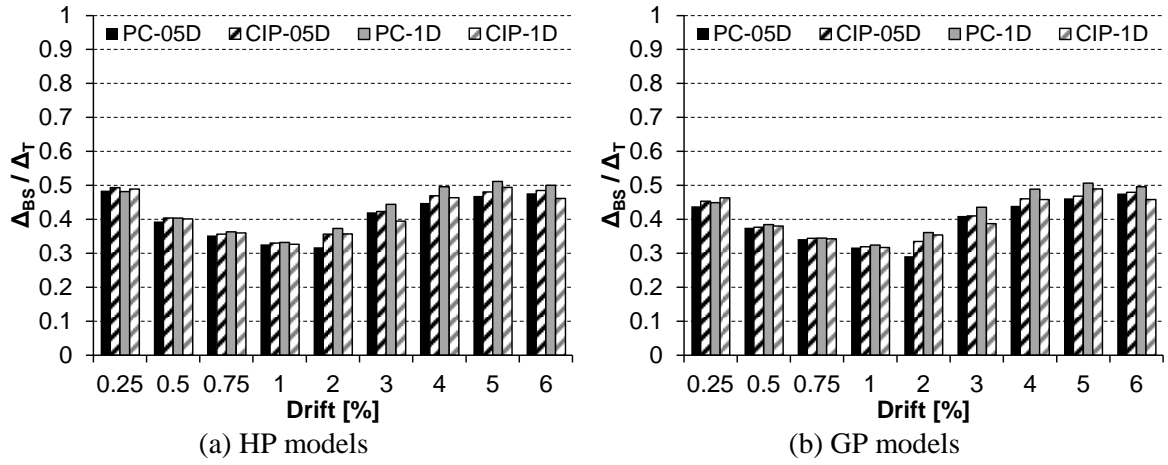


Figure 9-30 Contribution of bond-slip rotation to tip displacement of models with pedestal

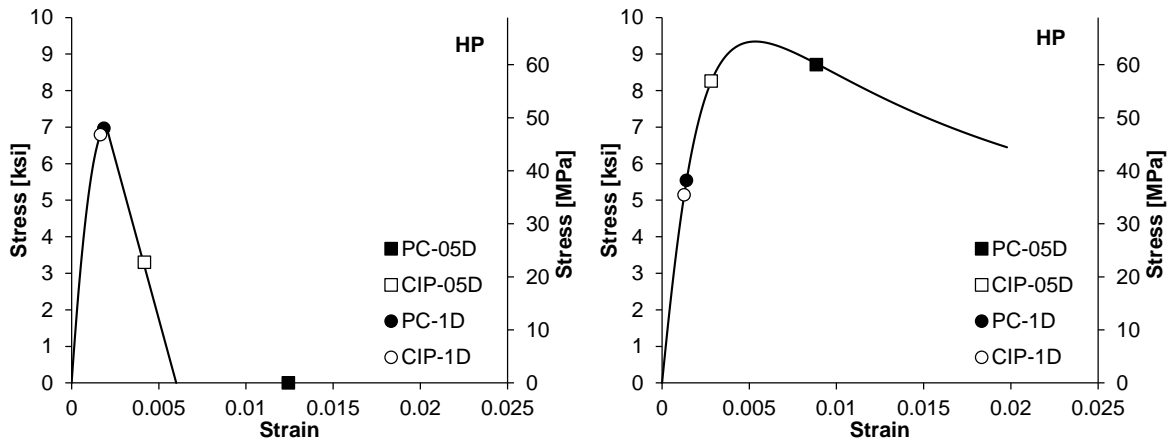


Figure 9-31 Maximum stress-strain occurring in grout above the pedestal region in HP models

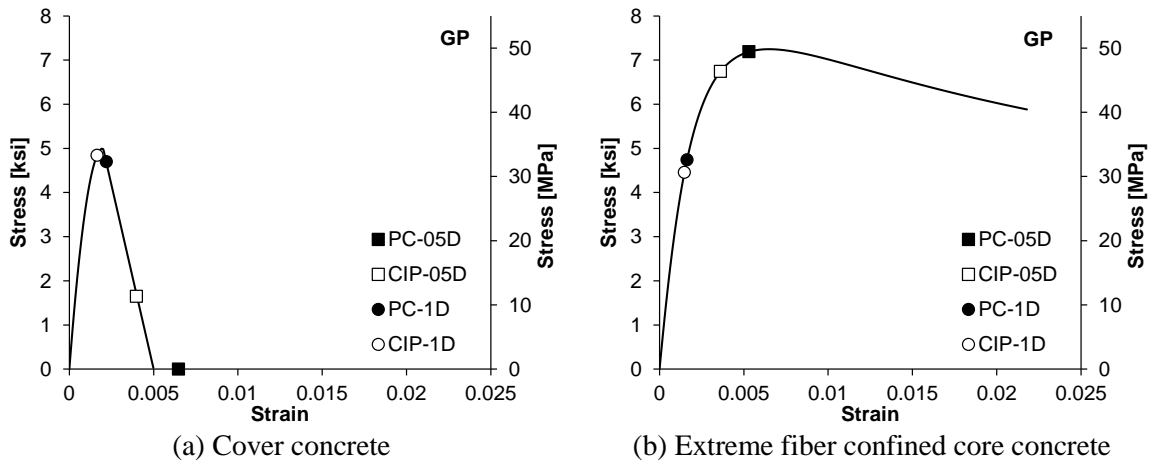
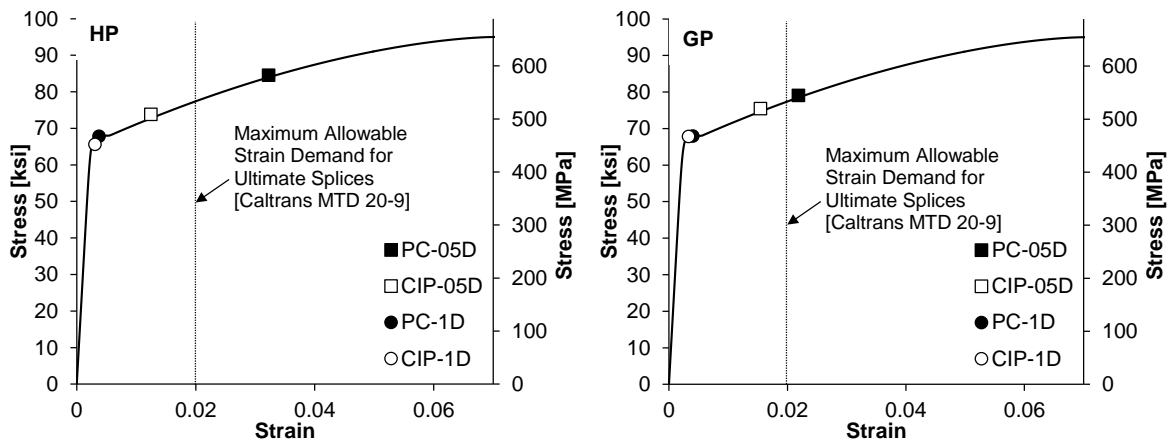


Figure 9-32 Maximum stress-strain occurring in concrete above the pedestal region in HP models



(a) HP column models (b) GP column models
 Figure 9-33 Maximum steel stress-strain occurring above the pedestal region

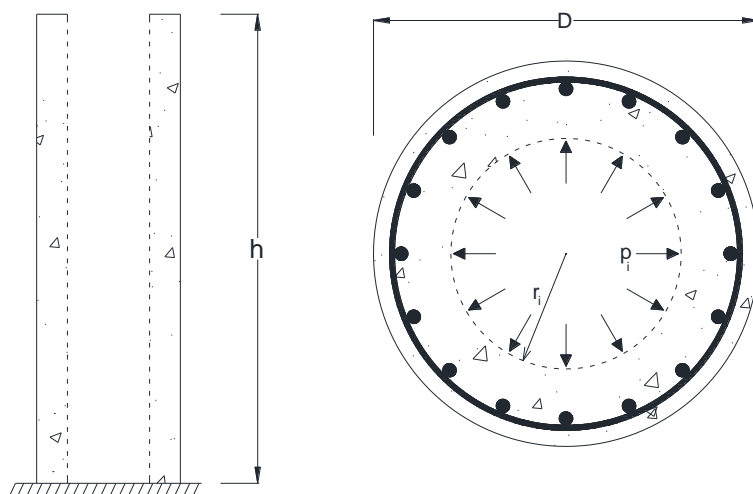


Figure 9-34 Determination of circumferential stress due to concrete fluid head

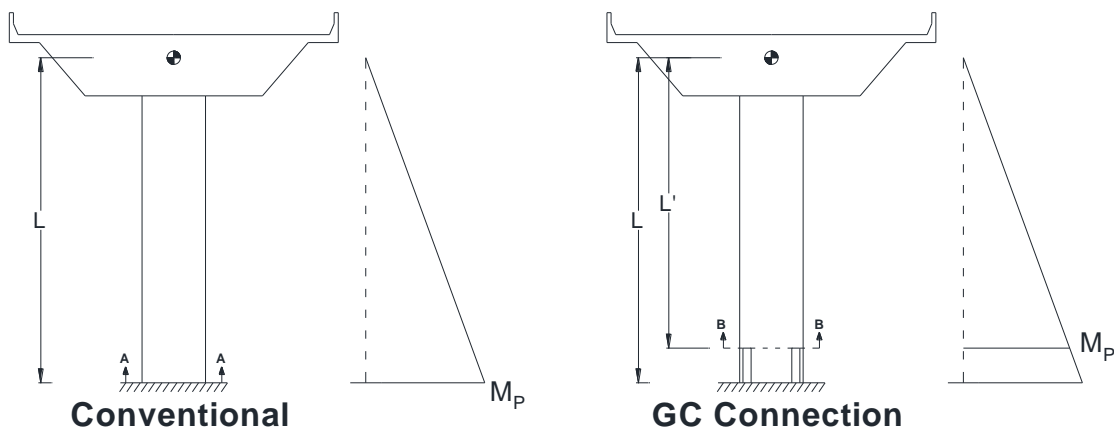


Figure 9-35 Plastic hinge formation in conventional and GC columns

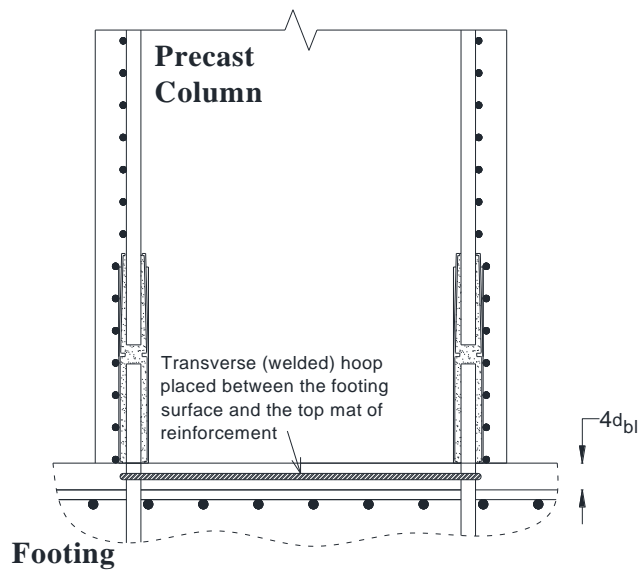


Figure 9-36 Suggested detailing near the footing surface

Appendix A: Strain Gage Measurement Tables

Appendix A Tables
Table A-1 CIP longitudinal bar strain gages1-5

Strain Gage	Cycle	Loading Action	Drift [%]											+10 3rd Cycle
			0.25	0.5	0.75	1	2	3	4	5	6	8	10	
1	1st	Push	242	766	1315	1911	2847	11322	13907	9863	5713	5563	5445	4385
		Pull	-373	-524	-648	-792	-1643	-916	-327	3685	4620	4555	3469	
	2nd	Push	262	759	1309	1872	3004	11034	13940	7264	5589	5366	5007	
		Pull	-373	-510	-648	-818	-1754	-478	982	4411	4594	4398	2677	
2	1st	Push	DEAD											
		Pull												
	2nd	Push												
		Pull												
3	1st	Push	292	664	1095	1526	2110	9233	12443	15222	-	4102	2115	451
		Pull	-302	-436	-565	-684	-1298	-698	-550	1481	-	862	-3091	
	2nd	Push	287	654	1085	1496	2393	9308	13171	8030	-	3165	897	
		Pull	-307	-451	-580	-703	-1461	-510	-372	-	-	168	-4052	
4	1st	Push	-648	-838	-1060	-1276	-2075	-3187	-1904	-1492	2349	4044	4980	5739
		Pull	281	916	1544	2127	2991	13304	19606	20712	11190	7513	6629	
	2nd	Push	-654	-838	-1067	-1302	-2493	-2048	-1656	1544	3756	4830	5360	
		Pull	281	870	1512	2094	5229	13507	20221	15104	8462	6871	6086	
5	1st	Push	-504	-720	-922	-1105	-1818	-2211	-2132	-1949	-1374	-726	16902	15058
		Pull	203	739	1289	1877	2924	10754	16000	21926	28657	42955	17537	
	2nd	Push	-536	-720	-929	-1125	-2080	-2034	-1871	-1491	-739	1583	13730	
		Pull	203	706	1276	1884	2983	10819	16529	22770	29618	37422	15365	

Table A-2 CIP longitudinal bar strain gages 6-10

Strain Gage	Cycle	Loading Action	Drift [%]											+10 3rd Cycle
			0.25	0.5	0.75	1	2	3	4	5	6	8	10	
6	1st	Push	550	1211	1807	2317	10748	14316	18414	22655	26995	36166	44015	40028
		Pull	-517	-700	-910	-1119	-576	-1427	-5178	-7960	-12123	-19252	-21713	
	2nd	Push	524	1159	1741	2271	10343	13969	17956	22250	26419	34733	42208	
		Pull	-484	-687	-910	-1126	-406	-1754	-5630	-8798	-12778	-16692	-25686	
7	1st	Push	707	1460	2166	2795	13705	17337	22043	24602	23202	-	-	-
		Pull	-628	-923	-1217	-1538	-2121	-5184	-12972	-17357	-18352	-	-	
	2nd	Push	681	1414	2107	2729	12730	16696	20642	21840	21650	-	-	
		Pull	-602	-903	-1211	-1558	-2068	-5832	-13070	-14588	-	-	-	
8	1st	Push	576	1230	1865	2441	11648	14756	17806	17675	3638	4011	3115	2794
		Pull	-465	-667	-851	-1086	-229	-1414	-4921	-1263	-6694	-3265	2716	
	2nd	Push	563	1211	1819	2389	11157	14128	16432	4731	3881	3154	2938	
		Pull	-425	-641	-864	-1086	-65	-1675	-4875	-3259	-4522	1237	2591	
9	1st	Push	-713	-943	-1185	-1427	-2383	-2140	-2049	-5819	-9197	-16050	11952	10434
		Pull	419	1047	1597	2088	10113	15755	20992	25738	30300	33848	13432	
	2nd	Push	-727	-949	-1191	-1420	-1322	-1296	-3947	-6376	-9400	818	11599	
		Pull	380	975	1519	2036	9792	15284	20102	25031	29351	15513	11540	
10	1st	Push	-752	-988	-1256	-1518	-2577	-2198	-2231	157	4743	4579	-	-
		Pull	458	1158	1721	2277	12730	18101	22543	10042	7392	8772	-	
	2nd	Push	-759	-1001	-1250	-1492	-857	-1276	-3022	4913	4926	-	-	
		Pull	399	1066	1649	2198	11984	16976	16197	8432	7582	-	-	

Table A-3 CIP longitudinal bar strain gages 11-15

Strain Gage	Cycle	Loading Action	Drift [%]										+10 3rd Cycle	
			0.25	0.5	0.75	1	2	3	4	5	6	8		10
11	1st	Push	242	884	1577	2232	10100	15624	20297	24493	28787	36111	35803	24755
		Pull	-556	-897	-1165	-1420	-2926	-3783	-5714	-7658	-8823	-1996	-903	
	2nd	Push	236	903	1571	2206	9877	15532	19355	23806	28387	31156	26758	
		Pull	-563	-877	-1172	-1414	-2808	-4097	-5865	-7455	-8208	-26	-1519	
12	1st	Push	288	1152	1958	2658	11616	17129	22393	27062	31711	42992	51013	11111
		Pull	-589	-982	-1342	-1663	-4060	-5939	-8558	-10974	-12958	-15387	-3667	
	2nd	Push	334	1166	1945	2613	11039	16402	21470	26210	31206	41591	26983	
		Pull	-596	-956	-1316	-1657	-3772	-6273	-8532	-10614	-12342	-12087	9704	
13	1st	Push	222	988	1688	2296	9891	13947	19115	23197	27769	38223	48997	51333
		Pull	-563	-896	-1164	-1413	-3062	-4723	-6221	-7556	-8354	-9171	-13024	
	2nd	Push	229	988	1662	2263	9610	13659	18376	22824	27815	38256	49815	
		Pull	-536	-877	-1151	-1407	-2839	-4815	-6195	-7229	-7641	-8857	-17126	
14	1st	Push	-478	-733	-969	-1237	-2239	-4556	1139	1237	1466	1348	1473	27361
		Pull	255	746	1237	1722	5086	10034	3456	3685	4039	4719	-	
	2nd	Push	-452	-733	-995	-1237	-2952	943	1276	1414	1597	1695	-18216	
		Pull	236	713	1231	1715	5970	3423	3162	3463	3724	4202	-	
15	1st	Push	-465	-687	-916	-1126	-2029	-6669	-9110	-10589	-5098	-7167	-7599	127280
		Pull	209	668	1270	1734	6774	12343	15518	15492	8417	10033	10360	
	2nd	Push	-439	-694	-903	-1100	-2481	-5995	-8384	-8096	-4824	-4614	-14778	
		Pull	209	674	1237	1715	6905	11257	14379	7939	7677	9032	6211	

Table A-4 CIP longitudinal bar strain gages 20-24

Strain Gage	Cycle	Loading Action	Drift [%]										+10 3rd Cycle	
			0.25	0.5	0.75	1	2	3	4	5	6	8		10
20	1st	Push	328	950	1606	2163	9784	13748	17483	20910	24226	31330	-	-
		Pull	-544	-845	-1081	-1271	-1474	-1396	-1619	-1881	-2182	-2307	-	
	2nd	Push	328	957	1592	2136	9404	13447	16933	20458	23931	30943	-	
		Pull	-537	-826	-1055	-1265	-1298	-1311	-1579	-1861	-1789	-2457	-	
21	1st	Push	504	1329	2120	2827	14044	19286	24659	30576	36943	49725	62421	-
		Pull	-766	-1211	-1571	-1891	-3154	-2971	-4719	-4974	-4594	-3881	97204	
	2nd	Push	504	1329	2081	2781	12978	18750	24136	30883	37500	50137	83625	
		Pull	-772	-1191	-1571	-1885	-2893	-3390	-4365	-4247	-3691	-2965	89024	
22	1st	Push	366	1034	1662	2264	7244	13120	17229	21129	25219	33817	43829	45707
		Pull	-635	-949	-1198	-1407	-2519	-2087	-2343	-2447	-2951	-3377	-5222	
	2nd	Push	386	1021	1656	2218	7931	12871	16974	21077	25422	34524	45177	
		Pull	-648	-936	-1184	-1387	-2362	-1904	-2094	-2258	-2526	-2814	-5287	
23	1st	Push	-556	-949	-1289	-1564	-2460	-3978	-4730	-5718	-4684	-5345	-3448	3978
		Pull	425	1210	1793	2388	9061	12823	17062	18004	11462	10657	10494	
	2nd	Push	-615	-1001	-1289	-1544	-2434	-3337	-4645	-4305	-4089	-4082	92	
		Pull	451	1165	1753	2362	8564	12581	16670	11423	9526	9094	4246	
24	1st	Push	-648	-1060	-1367	-1655	-2820	-5463	-7111	-8439	-9048	-5908	-6235	14236
		Pull	412	1302	1904	2519	11115	14098	18717	24140	27353	24324	26169	
	2nd	Push	-667	-1047	-1361	-1636	-2695	-4933	-6941	-8034	-4979	-4920	10009	
		Pull	445	1250	1871	2480	10140	13706	18547	24154	21380	22825	15937	

Table A-5 CIP longitudinal bar strain gages 29-33

Strain Gage	Cycle	Loading Action	Drift [%]											+10 3rd Cycle
			0.25	0.5	0.75	1	2	3	4	5	6	8	10	
29	1st	Push	222	903	1734	2428	3985	12726	15867	18713	21664	28789	34639	31740
		Pull	-661	-1001	-1282	-1544	-2414	-2369	-2133	-2735	-3147	-3664	-5215	
	2nd	Push	242	923	1727	2421	4384	12386	15455	18432	21730	28475	33173	
		Pull	-674	-988	-1289	-1518	-2585	-1943	-2166	-2709	-2964	-3782	-5254	
30	1st	Push	295	923	1637	2265	2920	11888	16411	21085	25536	33548	41266	33149
		Pull	-628	-1008	-1316	-1610	-2213	-3011	-2920	-2965	-2736	-3208	-4720	
	2nd	Push	295	930	1637	2232	2939	11933	16574	21399	25686	34085	40723	
		Pull	-622	-1008	-1329	-1610	-2252	-2625	-2730	-2579	-2226	-2900	-3882	
31	1st	Push	255	799	1479	2062	2920	10938	14630	18159	21955	29509	36225	35302
		Pull	-517	-851	-1080	-1296	-1938	-2036	-2082	-2023	-1964	-2429	-3273	
	2nd	Push	255	812	1493	2049	2926	10866	14480	18289	22354	29712	35754	
		Pull	-537	-825	-1087	-1283	-1990	-1872	-1931	-1813	-1767	-2389	-3594	
32	1st	Push	-654	-988	-1309	-1603	-2513	-3148	-5242	-6112	-6393	-7080	-7702	209
		Pull	262	1041	1616	2107	3082	10536	14926	18918	23368	31626	39675	
	2nd	Push	-622	-1001	-1322	-1610	-2467	-3887	-5137	-5719	-5791	-6380	-5935	
		Pull	288	1021	1564	2074	3233	10457	14841	18957	23486	31698	26699	
33	1st	Push	-635	-955	-1283	-1564	-2467	-2670	-4548	-5012	-5726	-6838	-7957	-
		Pull	268	942	1446	1924	2735	8716	13237	17477	21528	28837	35995	
	2nd	Push	-602	-975	-1283	-1557	-2329	-3573	-4214	-4829	-5313	-6386	-1885	
		Pull	268	903	1420	1911	2729	8893	13434	17621	21456	29026	39417	

Table A-6 CIP longitudinal bar strain gages 38-42

Strain Gage	Cycle	Loading Action	Drift [%]											+10 3rd Cycle
			0.25	0.5	0.75	1	2	3	4	5	6	8	10	
38	1st	Push	255	981	1687	2387	5519	7395	12508	14274	16203	21486	26775	24781
		Pull	-647	-1000	-1262	-1484	-2354	-2785	-2066	-2177	-2511	-2838	-3335	
	2nd	Push	255	981	1707	2374	5525	7807	12129	13999	16137	21754	26259	
		Pull	-673	-981	-1255	-1484	-2308	-2602	-1877	-2158	-2511	-2661	-2857	
39	1st	Push	255	1014	1694	2303	4376	9440	12397	15347	18749	24800	30661	22595
		Pull	-635	-1034	-1354	-1616	-2578	-3264	-2839	-2833	-2532	-2499	-3363	
	2nd	Push	281	1007	1681	2270	4376	9499	12331	15511	18880	25173	30315	
		Pull	-648	-1014	-1335	-1603	-2571	-2859	-2669	-2591	-2126	-2375	-3264	
40	1st	Push	196	1021	1610	2140	3377	7369	10393	11734	14431	19581	24457	22709
		Pull	-504	-831	-1054	-1224	-1774	-2101	-1728	-1885	-1924	-2094	-2664	
	2nd	Push	249	1021	1577	2134	3344	8128	9823	11832	14529	19771	23881	
		Pull	-491	-825	-1041	-1204	-1787	-1787	-1617	-1832	-1813	-1970	-2513	
41	1st	Push	-530	-844	-1106	-1401	-2075	-2160	-2651	-1944	-1839	-2520	-3534	-1649
		Pull	183	870	1420	1878	2756	7029	10466	13038	15420	20231	25526	
	2nd	Push	-524	-799	-1113	-1414	-2049	-2435	-1734	-1617	-1656	-2428	-3331	
		Pull	209	857	1381	1865	2710	8149	10682	13038	15446	20427	15021	
42	1st	Push	-563	-883	-1191	-1459	-2153	-2257	-2159	-1597	-1413	-1904	-2958	-
		Pull	209	923	1400	1871	2761	8873	10973	13662	16050	20931	25695	
	2nd	Push	-550	-877	-1178	-1440	-2133	-2113	-1466	-1250	-1197	-1983	-2356	
		Pull	216	870	1361	1865	2715	8859	11202	13741	16096	20971	25885	

Table A-7 CIP transverse bar strain gages 16-19

Strain Gage	Cycle	Loading Action	Drift [%]											+10 3rd Cycle
			0.25	0.5	0.75	1	2	3	4	5	6	8	10	
16	1st	Push	-33	7	20	39	72	353	150	150	262	497	595	320
		Pull	39	85	105	137	386	948	1026	1138	1648	2216	2406	
	2nd	Push	-26	-13	26	39	131	366	177	216	510	726	523	
		Pull	46	85	105	150	386	909	948	1203	1706	2157	2288	
17	1st	Push	DEAD											
		Pull												
	2nd	Push												
		Pull												
18	1st	Push	33	65	98	137	340	982	1413	1597	1597	2120	2493	-
		Pull	13	39	39	33	72	229	523	942	1139	1570	1786	
	2nd	Push	39	72	111	157	327	929	1283	1512	1492	1852	1518	
		Pull	13	46	33	39	72	242	556	1021	1132	1413	-635	
19	1st	Push	-7	-33	0	-7	0	72	314	255	321	340	216	-491
		Pull	-20	-39	-7	13	249	576	615	674	772	687	484	
	2nd	Push	-13	-20	-26	-7	52	150	249	288	327	281	242	
		Pull	0	-26	-13	20	262	458	589	674	713	615	177	

Table A-8 CIP transverse bar strain gages 25-28

Strain Gage	Cycle	Loading Action	Drift [%]											+10 3rd Cycle
			0.25	0.5	0.75	1	2	3	4	5	6	8	10	
25	1st	Push	20	13	26	13	52	111	183	327	366	465	825	877
		Pull	177	242	301	366	622	759	1119	1492	1793	2205	2356	
	2nd	Push	39	20	7	26	79	151	262	347	399	772	1093	
		Pull	157	236	288	360	641	818	1217	1571	1702	2160	1747	
26	1st	Push	39	26	26	52	229	798	825	962	1100	1361	1414	1211
		Pull	26	26	39	111	720	1152	1387	1512	1675	1976	2140	
	2nd	Push	26	33	46	79	249	687	870	982	1119	1315	1446	
		Pull	33	46	52	177	707	1028	1270	1440	1590	1872	1525	
27	1st	Push	52	98	131	177	327	465	707	811	1040	1315	1485	1695
		Pull	-26	0	33	79	314	425	687	838	962	1139	1230	
	2nd	Push	72	118	131	177	321	510	661	877	975	1178	1047	
		Pull	-13	20	26	111	340	386	681	844	916	1034	1355	
28	1st	Push	DEAD											
		Pull												
	2nd	Push												
		Pull												

Table A-9 CIP transverse bar strain gages 34-37

Strain Gage	Cycle	Loading Action	Drift [%]											+10 3rd Cycle
			0.25	0.5	0.75	1	2	3	4	5	6	8	10	
34	1st	Push	-20	-13	-7	13	39	59	137	275	491	687	805	262
		Pull	105	151	183	209	393	576	615	753	916	1041	1113	
	2nd	Push	-20	-26	-7	7	46	98	203	373	602	772	903	
		Pull	85	151	170	216	393	550	635	766	916	982	1021	
35	1st	Push	DEAD											
		Pull												
	2nd	Push												
		Pull												
36	1st	Push	-20	7	46	52	137	144	164	236	314	524	681	87357
		Pull	0	26	13	7	20	20	-79	13	229	445	609	
	2nd	Push	0	0	20	52	124	92	151	183	268	484	-	
		Pull	13	13	0	0	26	-33	-65	92	249	504	-	
37	1st	Push	26	7	-78	-7	183	517	929	1191	1282	1485	1570	1478
		Pull	13	0	-13	33	235	307	321	307	347	536	772	
	2nd	Push	20	-13	-52	33	235	648	968	1158	1249	1406	1648	
		Pull	33	13	-7	46	268	307	307	307	334	530	850	

Table A-10 CIP transverse bar strain gages 43-46

Strain Gage	Cycle	Loading Action	Drift [%]											+10 3rd Cycle
			0.25	0.5	0.75	1	2	3	4	5	6	8	10	
43	1st	Push	-26	39	85	111	131	190	170	151	288	419	517	216
		Pull	72	105	124	138	249	334	380	439	478	563	648	
	2nd	Push	-13	39	92	118	164	177	105	177	347	445	537	
		Pull	92	98	105	131	249	321	354	432	485	576	596	
44	1st	Push	0	-7	-13	0	164	281	393	465	517	727	792	491
		Pull	0	-33	-20	-46	52	118	177	209	255	295	354	
	2nd	Push	0	7	-13	0	196	327	432	484	543	694	746	
		Pull	-7	-33	-39	-52	65	131	196	229	262	288	321	
45	1st	Push	72	111	137	177	268	288	360	393	393	497	648	83397
		Pull	-7	33	52	105	144	216	229	111	-39	26	524	
	2nd	Push	59	105	144	170	288	301	380	360	386	504	641	
		Pull	20	20	52	85	137	223	203	39	-72	196	654	
46	1st	Push	7	7	20	79	275	497	792	981	1106	1289	1374	1093
		Pull	13	13	39	33	249	425	550	621	700	883	1119	
	2nd	Push	-7	-7	26	111	360	576	824	981	1093	1263	1282	
		Pull	33	26	20	65	307	458	582	641	726	942	1034	

Table A-11 HCNP longitudinal bar strain gages 1-5

Strain Gage	Cycle	Loading Action	Drift [%]											
			0.25	0.5	0.75	1	2	3	4	5	6	8	10	12
1	1st	Push	222	647	1060	1465	2610	3165	19457	6383	5958	6030	5847	5716
		Pull	-301	-432	-523	-589	-1589	-2498	-327	5042	5042	5186	5324	
	2nd	Push	229	641	1053	1439	2655	12276	20189	5899	5932	5880	5814	
		Pull	-301	-432	-504	-569	-1648	-1230	4094	5003	5173	5239	5579	
2	1st	Push	301	831	1276	1734	2716	17413	24611	14540	7506	5641	5418	-
		Pull	-340	-537	-667	-785	-2166	-281	-733	2971	-1322	-4908	-3998	
	2nd	Push	301	805	1256	1695	2761	17243	25481	8219	5968	4581	5549	
		Pull	-340	-550	-654	-766	-2199	59	438	-366	-2735	-4561	-1649	
3	1st	Push	268	766	1250	1761	2920	17877	20987	9924	7764	6808	1584	-438.58
		Pull	-380	-563	-681	-838	-2134	-700	2874	6906	6382	-1866	-10519	
	2nd	Push	255	746	1218	1715	2998	16705	14892	7391	7639	3489	393	
		Pull	-373	-563	-681	-838	-2206	242	4334	7011	4478	-6814	-4982	
4	1st	Push	-471	-694	-844	-975	-1630	-2396	-2743	-3044	-2455	-6618	-19946	-41554
		Pull	196	694	1133	1525	2422	13943	19200	26885	12719	2841	-1126	
	2nd	Push	-484	-687	-805	-943	-2134	-2841	-3044	-2507	-1610	-12942	-45613	
		Pull	177	661	1093	1486	2442	14356	19442	22852	4137	432	-13668	
5	1st	Push	-458	-628	-805	-995	-1826	-2735	-3521	-2323	-3174	-3750	-2519	40762
		Pull	144	674	1165	1597	2938	3841	21739	22688	29454	43118	66395	
	2nd	Push	-458	-609	-792	-1001	-2323	-3036	-2133	-2866	-3547	-3854	5726	
		Pull	144	687	1152	1512	2958	4391	18716	23316	30600	46586	54472	

Table A-12 HCNP longitudinal bar strain gages 6-10

Strain Gage	Cycle	Loading Action	Drift [%]											
			0.25	0.5	0.75	1	2	3	4	5	6	8	10	12
6	1st	Push	445	1047	1518	1825	16595	21645	8831	7523	8536	7542	3591	-156.99
		Pull	-379	-569	-687	-824	6162	4128	5370	5325	1616	-6855	-14548	
	2nd	Push	438	1007	1452	1779	15562	15634	7765	8366	8778	5763	-98	
		Pull	-360	-556	-687	-798	6397	5030	5828	4697	-85	-6940	-3918	
7	1st	Push	DEAD											
		Pull												
	2nd	Push												
		Pull												
8	1st	Push	511	1093	1538	1911	16107	20133	13594	19367	18045	13306	7160	8907.8
		Pull	-452	-681	-870	-1080	3665	1754	-3849	-7697	-10819	-9517	-10675	
	2nd	Push	497	1067	1440	1806	14949	13234	17207	20695	16644	10682	5230	
		Pull	-452	-661	-890	-1080	3901	406	-4143	-7808	-11388	-5740	-3017	
9	1st	Push	DEAD											
		Pull												
	2nd	Push												
		Pull												
10	1st	Push	-602	-896	-1145	-1374	-2925	-3062	-8696	-11491	-18093	-29858	-10057	-4547.8
		Pull	438	1099	1603	2002	19107	22503	32253	33477	3206	-6943	-7852	
	2nd	Push	-628	-877	-1086	-1355	2408	-3684	-7394	-7296	-14435	-28085	-10548	
		Pull	380	1040	1505	1904	16045	21784	29734	18289	249	-9711	-6315	

Table A-13 HCNP longitudinal bar strain gages 11-17

Strain Gage	Cycle	Loading Action	Drift [%]											
			0.25	0.5	0.75	1	2	3	4	5	6	8	10	12
11	1st	Push	203	550	858	1172	2043	2384	17856	21510	27115	38103	27705	15604
		Pull	-314	-504	-635	-792	-1526	-2482	-1545	-792	-98	282	10110	
	2nd	Push	210	557	858	1152	2036	2914	16796	20724	27757	37251	16259	
		Pull	-295	-498	-622	-786	-1572	-3470	-720	-118	177	2023	12068	
12	1st	Push	432	884	1290	1774	3122	8863	25803	33003	43980	59159	70241	79765
		Pull	-334	-497	-622	-681	-1591	-5361	-2605	-2082	-622	-3220	-7973	
	2nd	Push	465	890	1276	1787	3122	16750	25777	34083	45420	61594	55199	
		Pull	-268	-465	-550	-583	-1676	-2108	-1132	-772	668	-6081	23551	
13	1st	Push	354	853	1240	1620	2440	2551	16382	21288	28345	38943	49705	55935
		Pull	-505	-794	-1030	-1266	-1961	-2754	-3004	-3004	-2741	-3089	-8224	
	2nd	Push	354	846	1200	1548	2368	5719	16559	22265	29623	41507	50846	
		Pull	-505	-794	-1030	-1240	-2013	-3863	-2518	-2676	-2348	-3266	-18947	
14	1st	Push	-459	-622	-727	-812	-891	-1022	-1821	2581	3001	2509	531	-6911.8
		Pull	256	806	1140	1422	2332	3630	17813	21561	25793	35496	46149	
	2nd	Push	-465	-629	-734	-825	-1048	-1893	2123	2706	2850	1317	701	
		Pull	256	799	1094	1356	2142	3643	16674	21338	25616	35306	48055	
15	1st	Push	-536	-837	-1151	-1399	-2125	-2785	-2138	-1811	-1314	-16303	-	-
		Pull	346	778	1085	1360	2203	14728	19755	24978	30626	33273	-	
	2nd	Push	-549	-863	-1137	-1406	-2301	-1726	-1379	-817	-588	-	-	-
		Pull	301	719	1020	1307	2203	13211	19081	24926	30815	-	-	
16	1st	Push	-550	-838	-1113	-1401	-2212	-2913	-3142	-3639	-4627	-14118	-32549	-
		Pull	301	746	1047	1342	2278	16009	20473	25277	30546	37818	36961	
	2nd	Push	-543	-825	-1119	-1394	-2409	-2415	-2343	-3220	-4117	-22810	-	
		Pull	281	707	988	1296	2258	13941	19243	24571	30180	33060	-	
17	1st	Push	-419	-602	-786	-936	-1355	-1807	-1264	-589	-131	-249	-	-
		Pull	164	543	838	1100	2115	4662	14758	19040	23113	32600	-	
	2nd	Push	-412	-609	-792	-936	-1532	-2187	-445	-157	242	249	-	
		Pull	144	537	792	1087	2004	8191	13835	18346	22667	31506	-	

Table A-14 HCNP longitudinal bar strain gages 22-26

Strain Gage	Cycle	Loading Action	Drift [%]											
			0.25	0.5	0.75	1	2	3	4	5	6	8	10	12
22	1st	Push	170	465	897	1309	2389	2847	3031	8123	17064	22156	26980	27674
		Pull	-425	-707	-929	-1132	-1735	-2402	-2651	-3194	-1172	-1296	-1021	
	2nd	Push	190	484	897	1296	2356	2821	3155	15283	16913	22045	26803	
		Pull	-439	-707	-943	-1093	-1767	-2455	-2664	-1394	-884	-1041	-52	
23	1st	Push	170	432	949	1283	2402	2756	2926	17883	19965	25758	32926	35217
		Pull	-399	-720	-988	-1244	-2226	-2802	-2887	-2134	-1008	-694	-655	
	2nd	Push	209	458	897	1244	2376	2651	3306	16947	20593	26818	34601	
		Pull	-399	-733	-1008	-1244	-2330	-2939	-3064	-1054	-196	-471	1132	
24	1st	Push	137	478	1100	1696	6232	9675	16857	17937	22290	29406	35402	41949
		Pull	-432	-740	-962	-975	209	-242	1538	2880	3515	4897	5296	
	2nd	Push	151	517	1054	1715	6559	9859	16176	18873	23547	30198	36646	
		Pull	-445	-766	-995	-956	295	-72	2082	3188	4327	5584	6435	
25	1st	Push	-451	-772	-1086	-1367	-2139	-2774	-3552	-2008	-1322	-1335	-1047	3604.7
		Pull	183	543	981	1374	2689	3821	14792	18056	23270	29858	38134	
	2nd	Push	-464	-798	-1073	-1367	-2329	-2754	-2139	-1021	98	-307	190	
		Pull	196	550	968	1335	2650	4135	13994	18606	23656	30761	39508	
26	1st	Push	-381	-614	-837	-1040	-1619	-2065	-2308	-495	-253	-371	-758	11717
		Pull	178	540	956	1298	3511	6012	11811	14762	18031	23904	29644	
	2nd	Push	-376	-614	-847	-1035	-1654	-1926	-817	-104	406	-129	-69	
		Pull	193	555	926	1283	3392	6349	11885	15307	18209	24246	23310	

Table A-15 HCNP longitudinal bar strain gages 31-35

Strain Gage	Cycle	Loading Action	Drift [%]											
			0.25	0.5	0.75	1	2	3	4	5	6	8	10	12
31	1st	Push	229	661	1021	1426	2787	3344	3232	18498	17215	19610	22463	22169
		Pull	-589	-916	-1191	-1440	-2199	-2787	-3134	-1296	-746	-1551	-1963	
	2nd	Push	262	635	975	1400	2715	3062	3259	15691	16554	18897	21213	
		Pull	-595	-929	-1197	-1433	-2185	-2801	-3167	-595	-726	-1466	-1145	
32	1st	Push	321	661	995	1375	2442	2573	2501	18035	16431	19835	23331	20647
		Pull	-628	-956	-1211	-1460	-2357	-2776	-3031	-2749	-2985	-3672	-3947	
	2nd	Push	334	609	936	1303	2317	2520	2599	14362	15979	19534	23056	
		Pull	-596	-923	-1172	-1414	-2304	-2828	-3070	-2475	-2828	-3384	-3149	
33	1st	Push	223	583	943	1336	2619	2973	3850	10778	14209	17849	20416	21804
		Pull	-602	-943	-1251	-1513	-2187	-2554	-2691	-3614	-2626	-2685	-2606	
	2nd	Push	229	550	917	1297	2495	2920	3614	12834	14248	17476	20128	
		Pull	-609	-969	-1257	-1506	-2194	-2528	-2658	-2600	-2357	-2397	-1945	
34	1st	Push	DEAD											
		Pull												
	2nd	Push												
		Pull												
35	1st	Push	DEAD											
		Pull												
	2nd	Push												
		Pull												

Table A-16 HCNP transverse bar strain gages 18-21

Strain Gage	Cycle	Loading Action	Drift [%]											
			0.25	0.5	0.75	1	2	3	4	5	6	8	10	12
18	1st	Push	-13	13	65	85	150	85	602	523	242	222	144	-85
		Pull	59	85	72	92	203	393	648	916	962	864	1269	
	2nd	Push	-13	26	65	65	105	726	563	393	222	203	124	
		Pull	39	85	85	98	183	458	661	936	759	850	1191	
19	1st	Push	0	0	0	0	33	144	615	778	746	1119	1276	1249
		Pull	7	-20	-13	-26	275	445	576	595	785	1060	1184	
	2nd	Push	0	-7	-13	7	98	255	615	720	811	1132	1060	
		Pull	-7	-26	-13	-20	268	432	510	602	791	981	1177	
20	1st	Push	13	26	33	59	164	275	465	596	831	1394	-	-
		Pull	20	72	46	7	-26	105	340	576	818	1165	-	
	2nd	Push	20	39	46	59	137	294	432	602	844	1158	-	
		Pull	13	59	26	-33	-72	98	445	635	877	1139	-	
21	1st	Push	-33	-46	-59	-33	39	144	157	361	741	944	1108	1134
		Pull	-33	-26	-33	7	79	151	125	603	721	767	708	
	2nd	Push	-26	-39	-59	-20	7	138	197	485	773	996	-	
		Pull	-33	-33	-26	-7	59	92	177	623	708	728	-	

Table A-17 HCNP transverse bar strain gages 27-30

Strain Gage	Cycle	Loading Action	Drift [%]											
			0.25	0.5	0.75	1	2	3	4	5	6	8	10	12
27	1st	Push	-7	13	52	124	183	262	366	242	262	380	412	360
		Pull	65	118	177	281	471	556	556	713	798	949	1086	
	2nd	Push	0	65	98	131	236	262	327	216	321	419	425	
		Pull	59	137	209	308	484	537	563	700	785	955	1034	
28	1st	Push	13	-7	0	13	144	353	366	386	334	399	340	236
		Pull	33	7	-13	-20	26	52	79	65	39	190	308	
	2nd	Push	0	0	26	13	216	399	386	340	268	308	262	
		Pull	26	0	-13	-20	26	39	46	46	46	249	222	
29	1st	Push	65	72	131	196	425	563	648	687	707	779	667	255
		Pull	-13	-13	-20	13	177	249	314	353	111	-301	-1034	
	2nd	Push	52	79	144	236	386	510	582	622	661	661	393	
		Pull	7	-20	-13	59	170	203	380	164	65	-635	-622	
30	1st	Push	13	0	-20	-20	118	400	563	603	577	799	865	793
		Pull	-13	-20	-20	13	157	321	472	478	616	681	898	
	2nd	Push	13	13	-13	-33	177	459	544	596	603	753	852	
		Pull	0	-7	-7	13	177	400	472	537	635	786	773	

Table A-18 HCNP transverse bar strain gages 36-39

Strain Gage	Cycle	Loading Action	Drift [%]											
			0.25	0.5	0.75	1	2	3	4	5	6	8	10	12
36	1st	Push	-20	0	7	59	137	183	203	190	262	393	406	550
		Pull	72	131	183	236	445	491	497	595	667	785	883	
	2nd	Push	-13	7	33	72	170	183	209	190	294	340	471	
		Pull	72	137	190	268	458	465	471	595	661	779	811	
37	1st	Push	DEAD											
		Pull												
	2nd	Push												
		Pull												
38	1st	Push	39	72	111	137	177	242	262	294	314	353	360	301
		Pull	-13	13	33	46	137	131	164	164	59	268	399	
	2nd	Push	52	72	118	144	190	229	268	288	327	360	340	
		Pull	0	26	26	39	157	151	164	151	118	301	412	
39	1st	Push	20	0	26	79	229	347	439	524	655	818	910	884
		Pull	-26	-26	13	39	164	301	412	491	504	609	668	
	2nd	Push	33	20	46	98	268	373	445	537	655	825	943	
		Pull	-13	-7	7	52	203	327	399	458	498	609	622	

Table A-19 HCPP longitudinal bar strain gages 1-5

Strain Gage	Cycle	Loading Action	Drift [%]											
			0.25	0.5	0.75	1	2	3	4	5	6	8	10	12
1	1st	Push	295	668	1087	1454	2364	2501	12532	17017	23591	32876	46881	
		Pull	-255	-386	-537	-674	-1388	-1846	-1067	-393	-668	-2148	1598	-
	2nd	Push	288	701	1094	1441	2344	2704	12729	18288	24017	35023	-	
		Pull	-268	-386	-550	-694	-1427	-2194	-602	-242	-930	-1840	-	
2	1st	Push	223	668	1074	1421	2108	2200	8040	4308	4367	3739	2835	
		Pull	-386	-570	-825	-1041	-1827	-2161	2953	3149	1945	-1113	-766	3385
	2nd	Push	236	707	1041	1375	2128	9454	4924	4217	3837	2920	7117	
		Pull	-393	-589	-825	-1061	-1860	-2351	3248	3084	1310	-1421	3555	
3	1st	Push	190	589	1021	1361	2421	2558	15519	15839	21793	11404	9631	
		Pull	-393	-543	-694	-831	-1544	-2022	-589	-419	-726	5051	5443	-
	2nd	Push	196	608	988	1335	2434	2643	13687	16533	21145	9245	-	
		Pull	-386	-563	-707	-844	-1577	-2179	39	-451	2807	5195	-	
4	1st	Push	-537	-831	-1080	-1296	-2035	-2539	-3377	-3456	-5766	-3423	3613	
		Pull	209	668	1165	1617	2768	3894	20956	20484	24032	19326	11826	9123
	2nd	Push	-563	-851	-1073	-1283	-2310	-3194	-2899	-4490	-4385	2644	3933	
		Pull	209	687	1165	1571	2788	3946	17474	21479	20648	13240	9562	
5	1st	Push	-471	-707	-949	-1191	-1800	-2206	-3535	-1944	-3194	-4255	-3960	
		Pull	190	628	1087	1499	2716	4078	18785	19643	25075	38827	56035	62966
	2nd	Push	-471	-740	-975	-1198	-1983	-2743	-1728	-2363	-3626	-4084	1748	
		Pull	203	635	1054	1453	2736	7638	16782	20297	25854	41183	56212	

Table A-20 HCPP longitudinal bar strain gages 6-10

Strain Gage	Cycle	Loading Action	Drift [%]											
			0.25	0.5	0.75	1	2	3	4	5	6	8	10	12
6	1st	Push	-355	267	804	1216	9756	17667	21168	27842	34530	48278	62098	
		Pull	-1297	-1532	-1748	-1951	176	-2043	-4320	-6054	-8351	-10406	-5531	-31555
	2nd	Push	-355	280	712	1118	10168	15992	20611	27057	33705	47480	30911	
		Pull	-1310	-1532	-1748	-1964	418	-2115	-4379	-6329	-7474	-7716	-18625	
7	1st	Push	622	1342	1957	2454	16655	21877	13003	1904	1505	-6106	-18638	
		Pull	-602	-864	-1158	-1453	-262	-3475	-5491	-17840	-26111	-44893	-48781	-
	2nd	Push	628	1348	1859	2369	15706	20261	3266	779	-1152	-14600	-23199	
		Pull	-596	-870	-1158	-1440	543	-3377	-12081	-17251	-31687	-44036	110270	
8	1st	Push	360	949	1361	1682	3592	16848	19099	25485	29522	24857	16142	
		Pull	-510	-687	-896	-1086	-1669	-2408	-3834	-6249	-8454	-2146	-4868	8643
	2nd	Push	386	949	1263	1616	4829	14682	18687	24432	26224	15167	-	
		Pull	-491	-694	-903	-1093	-1538	-2257	-4279	-7819	-7093	1106	10802	
9	1st	Push	-766	-1067	-1355	-1604	-2632	-818	-2822	-5447	-6756	-9028	-11496	
		Pull	478	1093	1552	1958	19758	22083	29769	40126	50810	73456	-	-
	2nd	Push	-779	-1080	-1323	-1578	2278	-903	-1971	-5251	-3764	-	-	
		Pull	452	1041	1480	1846	16537	21408	29081	38698	50044	71799	-	
10	1st	Push	-844	-1152	-1506	-1892	-2926	-2645	-4969	-6671	-7221	1244	-3980	
		Pull	550	1087	1545	1951	18028	21105	26761	21118	14552	21151	-	-
	2nd	Push	-877	-1185	-1538	-1912	52	-2874	-2128	-15135	-13	-2946	-	
		Pull	543	1061	1460	1833	14559	20228	20968	14042	19907	22853	-	

Table A-21 HCPP longitudinal bar strain gages 11-15

Strain Gage	Cycle	Loading Action	Drift [%]											
			0.25	0.5	0.75	1	2	3	4	5	6	8	10	12
11	1st	Push	DEAD											
		Pull												
	2nd	Push												
		Pull												
12	1st	Push	282	1054	1631	2096	2908	6509	10635	10733	524	616	-4964	
		Pull	-674	-1048	-1408	-1729	-7622	-12160	-13529	-11525	-16816	-29645	-51608	-19698
	2nd	Push	308	1094	1565	2037	4787	6647	10386	1408	-504	-3746	-15048	
		Pull	-655	-1054	-1395	-1709	-8042	-11152	-12927	-11813	-16810	-33862	-19875	
13	1st	Push	229	864	1296	1669	2847	3135	9183	14680	10197	3462	2036	
		Pull	-615	-877	-1145	-1335	-2350	-12390	-10747	-12462	-8679	-13561	-23071	-15479
	2nd	Push	268	910	1231	1623	2814	7586	9137	12383	5118	1394	-1453	
		Pull	-596	-877	-1119	-1322	-2337	-10681	-10950	-11140	-7442	-13889	-14262	
14	1st	Push	-648	-1021	-1355	-1597	-2723	-1047	-4411	-10446	-14026	-20603	-27691	
		Pull	288	740	1126	1492	2376	929	988	20	-785	-1191	0	2134
	2nd	Push	-648	-1028	-1289	-1505	-2409	-1512	-6394	-8842	-11552	-18286	-21618	
		Pull	288	720	1093	1433	2258	969	772	-216	-1008	-1368	2173	
15	1st	Push	-635	-1008	-1362	-1728	-2697	-11528	-10690	-12758	-9944	-16431	-24810	
		Pull	288	792	1205	1591	2632	6978	10075	10657	2488	1106	-3129	-6566
	2nd	Push	-622	-1021	-1362	-1715	-2638	-8844	-10644	-7247	-11043	-19318	-23363	
		Pull	295	779	1172	1545	2651	5996	9256	4144	1840	517	-6330	

Table A-22 HCPP longitudinal bar strain gages 20-24

Strain Gage	Cycle	Loading Action	Drift [%]											
			0.25	0.5	0.75	1	2	3	4	5	6	8	10	12
20	1st	Push	209	609	1243	1643	2369	15123	19252	25822	31313	18474	11949	
		Pull	-288	-465	-609	-681	-1963	2402	3560	4738	6675	10706	10660	10536
	2nd	Push	288	661	1217	1571	2245	14645	19252	25705	27341	12990	10935	
		Pull	-308	-465	-596	-681	-2029	2932	3979	5235	7918	10706	10601	
21	1st	Push	256	780	1828	2483	5254	17427	22747	31499	40193	58753	72662	
		Pull	-472	-635	-740	-937	-1304	3178	4756	6067	8281	11511	14760	22236
	2nd	Push	282	825	1795	2457	5261	17152	23710	32023	41379	59245	50007	
		Pull	-459	-570	-701	-871	-1232	3918	5634	7469	9670	12815	22118	
22	1st	Push	151	602	1603	2494	12520	18718	20406	14634	9045	8639	8645	
		Pull	-170	-72	-20	46	6937	9064	9581	9313	8292	8011	7912	8109
	2nd	Push	177	654	1597	2435	12415	18475	19883	9896	8652	8659	8462	
		Pull	-144	-20	-13	39	7068	9306	10203	8757	8076	7991	7991	
23	1st	Push	-622	-170	-327	-798	-2329	-4920	-406	-1740	-1956	-5195	11188	
		Pull	72	445	981	1577	2990	13433	20244	26492	30830	29090	13976	13629
	2nd	Push	-537	-196	-425	-909	-2355	-1420	379	-366	-1727	10279	11627	
		Pull	360	661	1106	1426	3003	14761	18889	25583	30163	13936	13550	
24	1st	Push	-537	-838	-1074	-1342	-2075	-2579	-3666	-2736	-2010	-4530	-5106	
		Pull	308	740	943	1191	2062	5642	19879	25010	28342	37362	35182	24434
	2nd	Push	-550	-805	-1087	-1362	-2278	-2978	-1820	-1290	-943	-3502	6912	
		Pull	314	655	903	1113	2029	7436	17778	23826	28257	36354	24238	

Table A-23 HCPP longitudinal bar strain gages 29-35

Strain Gage	Cycle	Loading Action	Drift [%]											
			0.25	0.5	0.75	1	2	3	4	5	6	8	10	12
29	1st	Push	157	510	890	1308	2525	3035	3244	13775	14278	19871	24861	
		Pull	-307	-491	-680	-863	-1472	-1916	-2315	-890	-281	-137	661	2289
	2nd	Push	183	523	903	1308	2584	3107	3283	12918	14592	20440	14573	
		Pull	-301	-491	-687	-850	-1524	-1884	-2381	-131	-131	438	2407	
30	1st	Push	177	523	890	1237	2342	2709	2833	17378	19773	25151	30458	
		Pull	-399	-615	-896	-1171	-1983	-2218	-2473	-124	1073	1662	2166	4096
	2nd	Push	164	543	864	1230	2460	2722	3121	16246	19544	25223	18059	
		Pull	-399	-615	-883	-1165	-1983	-2179	-2853	576	1623	1989	4142	
31	1st	Push	118	347	595	844	1845	2356	2650	3337	12315	16510	20560	
		Pull	-373	-530	-707	-864	-1368	-1767	-2074	-2434	-1492	-1106	-982	681
	2nd	Push	111	353	589	825	1839	2434	2775	7754	11864	16654	11144	
		Pull	-380	-537	-700	-857	-1413	-1806	-2107	-2388	-1054	-674	746	
32	1st	Push	-366	-510	-621	-693	-929	-935	-1217	-1406	-1740	-2100	144	
		Pull	131	360	654	1007	2054	2283	2492	2878	3146	16655	17799	15994
	2nd	Push	-366	-497	-595	-667	-811	-1079	-1289	-1577	-1962	-150	844	
		Pull	118	334	635	975	1864	2211	2466	2976	3225	15000	15091	
33	1st	Push	-484	-706	-909	-1047	-1531	-1832	-2231	-2466	-2453	1276	1838	
		Pull	275	674	1040	1387	2388	2577	3022	5567	21436	25962	32713	26394
	2nd	Push	-491	-713	-870	-1073	-1603	-2015	-2276	-2420	1263	1832	3990	
		Pull	281	661	975	1302	2237	2590	3114	9511	20376	26950	28768	
34	1st	Push	-569	-824	-1060	-1289	-1832	-2009	-2140	-2218	-2860	-222	131	
		Pull	366	785	1060	1296	2388	2755	2945	3403	18734	22130	27045	24074
	2nd	Push	-589	-857	-1073	-1328	-1813	-1976	-2107	-2192	-46	124	1571	
		Pull	340	726	995	1198	2362	2775	3056	8795	17452	22373	23439	
35	1st	Push	-353	-478	-582	-681	-910	-949	-1126	-1250	-1525	-1021	582	
		Pull	209	543	805	962	1924	2160	2395	2788	3449	15000	17539	15039
	2nd	Push	-366	-504	-602	-759	-890	-1060	-1191	-1414	-1800	419	1054	
		Pull	209	524	759	877	1806	2107	2408	2906	7598	14640	14044	

Table A-24 HCPP longitudinal bar strain gages 40-44

Strain Gage	Cycle	Loading Action	Drift [%]											
			0.25	0.5	0.75	1	2	3	4	5	6	8	10	12
40	1st	Push	124	418	706	1013	1889	2517	2530	2719	3020	8452	15694	
		Pull	-379	-634	-889	-1196	-2085	-3347	-4177	-4961	-5510	-7909	-8275	-5360
	2nd	Push	150	451	745	1039	2118	2262	2405	2673	3124	8190	5713	
		Pull	-425	-641	-948	-1209	-2183	-3334	-4327	-5079	-5765	-8144	-5059	
41	1st	Push	137	438	707	995	2179	2591	2886	4129	6425	8702	12255	
		Pull	-471	-739	-1086	-1361	-1924	-2676	-4122	-5882	-6779	-7590	-7361	-6079
	2nd	Push	203	445	680	988	2290	2578	3259	4469	5961	8558	4829	
		Pull	-484	-779	-1145	-1354	-1943	-2781	-4613	-6386	-6936	-7407	-5954	
42	1st	Push	72	275	550	845	1807	2462	2638	2796	2907	3385	7882	
		Pull	-445	-707	-1015	-1251	-1892	-2239	-2573	-3345	-3588	-4125	-6625	-4675
	2nd	Push	79	321	563	864	2016	2350	2527	2697	2894	3490	3221	
		Pull	-471	-727	-1048	-1264	-1944	-2246	-2606	-3418	-3738	-4269	-4583	
43	1st	Push	-386	-641	-897	-1008	-1499	-1551	-1774	-1957	-2239	-2402	-196	
		Pull	46	242	936	1355	2559	2893	3083	3194	3286	15232	15912	12103
	2nd	Push	-412	-681	-805	-903	-1303	-1604	-1839	-2095	-2219	-380	1388	
		Pull	46	275	877	1276	2468	2841	3044	3175	3384	14498	13922	
44	1st	Push	-458	-753	-1047	-1270	-1767	-1853	-1944	-1997	-2134	-2396	-2586	
		Pull	92	380	1178	1499	3129	3581	3849	4216	4478	12608	12987	11115
	2nd	Push	-478	-812	-1041	-1231	-1656	-1787	-1885	-1984	-2298	-2618	-1322	
		Pull	98	412	1159	1479	3070	3522	3816	4170	4661	11541	11141	

Table A-25 HCPP longitudinal bar strain gages 49-53

Strain Gage	Cycle	Loading Action	Drift [%]											
			0.25	0.5	0.75	1	2	3	4	5	6	8	10	12
49	1st	Push	85	426	772	1080	2029	2330	2442	2533	2573	2651	2749	
		Pull	-543	-838	-1165	-1453	-2167	-2422	-2474	-2553	-2573	-2605	-2592	-2344
	2nd	Push	72	452	759	1054	1964	2239	2357	2481	2566	2651	1165	
		Pull	-550	-884	-1198	-1466	-2226	-2376	-2481	-2540	-2566	-2573	-2468	
50	1st	Push	85	262	183	137	79	229	327	393	452	419	347	
		Pull	-570	-661	-563	-517	-419	-386	-295	-255	-223	-111	59	-563
	2nd	Push	92	249	157	151	190	321	367	432	504	622	-1604	
		Pull	-537	-622	-530	-491	-412	-367	-301	-275	-223	118	-825	
51	1st	Push	131	340	622	831	1421	1748	1905	2082	2206	2311	2461	
		Pull	-498	-681	-910	-1100	-1617	-1853	-1944	-1925	-1931	-2029	-1977	-1663
	2nd	Push	111	301	628	812	1407	1702	1879	2036	2147	2344	975	
		Pull	-498	-661	-936	-1119	-1637	-1833	-1885	-1892	-1925	-2016	-1820	
52	1st	Push	-687	-976	-1257	-1467	-2023	-2121	-2167	-2167	-2207	-2311	-2357	
		Pull	39	255	485	779	1630	1840	1964	2062	2010	2200	2462	884
	2nd	Push	-707	-1008	-1244	-1447	-1958	-2056	-2108	-2141	-2128	-2265	-2043	
		Pull	13	236	478	746	1578	1827	1945	2017	2069	2233	2351	
53	1st	Push	-702	-1023	-1344	-1652	-2256	-2361	-2367	-2328	-2308	-2348	-2393	
		Pull	33	249	466	754	1849	2197	2367	2538	2610	2715	3036	2807
	2nd	Push	-715	-1069	-1371	-1639	-2223	-2269	-2289	-2256	-2256	-2321	-2079	
		Pull	26	243	472	754	1830	2184	2380	2525	2616	2734	2951	

Table A-26 HCPP transverse bar strain gages 16-19

Strain Gage	Cycle	Loading Action	Drift [%]											
			0.25	0.5	0.75	1	2	3	4	5	6	8	10	12
16	1st	Push	-33	-20	7	26	105	144	386	569	635	563	334	
		Pull	39	72	98	150	177	497	837	1001	1008	1145	1093	249
	2nd	Push	-26	-7	13	39	98	196	451	556	550	406	92	
		Pull	26	65	111	144	177	504	733	798	792	896	262	
17	1st	Push	-13	0	52	79	111	46	124	164	124	183	177	
		Pull	-46	-92	-111	-111	-33	20	-7	33	137	137	399	622
	2nd	Push	-7	0	65	79	131	111	157	144	105	170	59	
		Pull	-39	-98	-124	-111	-26	13	-39	98	124	151	753	
18	1st	Push	0	46	105	118	295	484	399	347	373	707	897	
		Pull	-20	-26	-7	52	131	183	255	340	445	635	792	949
	2nd	Push	-7	59	98	118	223	314	190	216	393	550	681	
		Pull	-20	-20	7	72	137	190	242	367	458	622	1113	
19	1st	Push	26	46	124	144	177	190	452	366	386	419	380	
		Pull	-20	-52	-7	46	52	118	242	366	563	739	844	1335
	2nd	Push	26	52	118	164	183	275	425	353	366	347	111	
		Pull	-20	-46	7	59	79	131	249	373	556	733	1433	

Table A-27 HCPP transverse bar strain gages 25-28

Strain Gage	Cycle	Loading Action	Drift [%]											
			0.25	0.5	0.75	1	2	3	4	5	6	8	10	12
25	1st	Push	-5	20	54	20	79	30	183	337	401	510	574	
		Pull	30	64	94	99	183	233	253	297	352	376	406	203
	2nd	Push	-5	25	40	20	109	149	223	352	436	500	168	
		Pull	35	69	84	94	178	223	262	302	332	361	233	
26	1st	Push	-4154	-2015	-1491	-366	752	2361	-16104	-11362	-8778	-14109	2531	
		Pull	-2146	-4376	-1171	373	478	2630	-32045	-18243	-9857	-19362	-7470	-
	2nd	Push	-4343	-2008	-1439	-222	-137	3231	-12605	-18119	-10302	-20676	-31502	
		Pull	-1675	-2060	-2283	-177	471	2643	-12225	981	-11408	-3421	-	
27	1st	Push	52	72	79	65	105	46	39	39	20	-59	46	
		Pull	13	-13	-46	-59	-203	-203	-209	-98	13	118	242	203
	2nd	Push	59	65	59	59	0	46	39	0	-59	-144	-111	
		Pull	7	-7	-39	-72	-242	-196	-203	-46	59	170	236	
28	1st	Push	0	-33	-33	-26	399	504	399	373	373	327	301	
		Pull	13	-26	-33	-7	164	255	281	314	380	268	151	105
	2nd	Push	0	-33	-33	0	425	432	380	360	314	308	196	
		Pull	0	-33	-26	7	190	255	275	360	301	222	170	

Table A-28 HCPP transverse bar strain gages 36-39

Strain Gage	Cycle	Loading Action	Drift [%]											
			0.25	0.5	0.75	1	2	3	4	5	6	8	10	12
36	1st	Push	-20	-13	20	13	209	177	183	242	209	419	602	
		Pull	39	52	79	98	216	249	294	353	432	550	641	766
	2nd	Push	-20	-7	7	20	236	190	242	209	196	465	203	
		Pull	33	52	79	92	196	249	301	366	432	550	779	
37	1st	Push	-13	-26	-33	-13	98	380	753	844	864	844	910	
		Pull	20	0	0	26	262	524	635	740	766	785	726	510
	2nd	Push	-13	-33	-33	-20	203	517	766	844	844	844	340	
		Pull	0	-7	7	39	275	537	668	740	753	746	596	
38	1st	Push	39	52	85	98	-589	-1166	-2036	-1519	-1683	-419	354	
		Pull	-13	0	7	20	-2403	-4151	-1526	-1303	-2193	-1054	-229	-622
	2nd	Push	46	72	79	92	-2645	-1794	-5506	-1107	-1879	-98	164	
		Pull	-13	0	0	26	-1198	-3817	-3870	-1382	-2357	-275	-236	
39	1st	Push	33	33	7	-20	353	726	936	1041	1080	1231	1231	
		Pull	13	46	72	216	766	1132	1126	1152	1368	1368	1302	1060
	2nd	Push	39	46	39	-7	491	733	857	949	949	1015	929	
		Pull	13	33	105	229	851	1100	1113	1191	1257	1250	1198	

Table A-29 HCPP transverse bar strain gages 45-48

Strain Gage	Cycle	Loading Action	Drift [%]											
			0.25	0.5	0.75	1	2	3	4	5	6	8	10	12
45	1st	Push	7	20	52	72	124	236	216	236	242	340	465	
		Pull	52	65	85	111	340	451	504	530	595	615	674	608
	2nd	Push	0	26	72	79	203	216	229	229	255	373	216	
		Pull	46	52	79	144	399	465	484	536	556	595	602	
46	1st	Push	7	-13	-33	-26	-26	13	137	353	438	478	589	
		Pull	20	-7	-13	-26	-39	26	124	177	229	295	314	393
	2nd	Push	7	-13	-39	-39	-26	39	190	380	438	524	510	
		Pull	13	0	-20	-46	-26	46	137	203	255	288	373	
47	1st	Push	65	92	118	131	242	301	288	314	340	439	524	
		Pull	20	13	85	144	301	347	406	465	517	497	524	596
	2nd	Push	59	92	111	131	229	262	288	295	360	465	406	
		Pull	0	20	85	151	308	367	439	484	517	517	615	
48	1st	Push	33	33	7	-39	-46	-13	59	98	209	321	425	
		Pull	-7	-33	0	20	137	281	360	445	484	537	497	491
	2nd	Push	46	39	7	-39	-46	26	79	144	216	347	321	
		Pull	-20	-33	-20	0	177	294	366	438	478	504	465	

Table A-30 HCPP transverse bar strain gages 54-57

Strain Gage	Cycle	Loading Action	Drift [%]											
			0.25	0.5	0.75	1	2	3	4	5	6	8	10	12
54	1st	Push	-14	-7	27	89	179	227	227	227	213	247	296	
		Pull	48	48	96	131	220	247	220	234	234	234	316	289
	2nd	Push	0	14	62	96	186	227	234	213	227	227	158	
		Pull	41	76	76	144	227	220	206	220	220	261	302	
55	1st	Push	59	92	137	216	268	353	405	458	477	543	569	
		Pull	78	131	320	419	589	641	700	759	772	844	902	778
	2nd	Push	98	131	190	229	314	379	425	471	517	556	438	
		Pull	92	157	353	419	589	647	700	732	778	844	824	
56	1st	Push	13	33	98	137	262	314	340	340	353	393	432	
		Pull	7	20	65	105	222	255	281	301	314	307	321	321
	2nd	Push	20	59	92	137	262	307	321	327	366	373	327	
		Pull	0	52	65	118	242	262	288	307	314	334	314	
57	1st	Push	26	20	137	288	406	471	491	524	543	583	615	
		Pull	20	7	203	386	563	609	642	648	668	681	714	615
	2nd	Push	26	65	216	314	419	471	498	537	557	589	491	
		Pull	26	46	268	432	576	596	629	635	661	681	642	

Table A-31 GCNP longitudinal bar strain gages 1-5

Strain Gage	Cycle	Loading Action	Drift [%]											+6 3rd cycle	-6 3rd cycle	+8 1st cycle
			0.25	0.5	0.75	1	2	3	4	5	6					
1	1st	Push	26	465	1106	1708	3574	13509	22430	30126	37594					
		Pull	-569	-733	-877	-1001	-1695	-556	229	1126	1525					
	2nd	Push	7	458	1080	1728	3685	15505	22364	30657	37902					
		Pull	-596	-733	-877	-1001	-1780	7	655	1656	3364					
2	1st	Push	59	550	1145	1707	3029	13391	20227	28195	36149					
		Pull	-576	-792	-994	-1210	-2146	-2591	-2538	-2263	-2355					
	2nd	Push	59	550	1106	1688	3317	14281	20809	29379	37255					
		Pull	-569	-798	-1001	-1210	-2290	-2152	-2192	-1564	-1557					
3	1st	Push	79	498	1080	1584	2789	12366	17086	23162	29584					
		Pull	-537	-727	-897	-1061	-1683	-982	-1237	-1244	-727					
	2nd	Push	65	511	1054	1584	2854	12779	17577	23895	34710					
		Pull	-543	-727	-884	-1047	-1761	-694	-1080	-727	989					
4	1st	Push	-367	-570	-740	-877	-1381	-1545	-1349	-936	-295					
		Pull	602	1178	1722	2180	7148	13622	18584	22590	27355					
	2nd	Push	-367	-583	-740	-923	-1440	-1257	-903	-301	648					
		Pull	602	1165	1702	2114	8228	13773	18126	22865	-					
5	1st	Push	-399	-641	-870	-1073	-1799	-2009	-1708	-1256	-838					
		Pull	615	1256	1865	2362	10004	16874	23313	25243	24150					
	2nd	Push	-393	-641	-877	-1152	-1695	-1505	-1171	-674	-111					
		Pull	622	1230	1826	2290	10436	17175	22331	23110	90595					

Table A-32 GCNP longitudinal bar strain gages 6-10

Strain Gage	Cycle	Loading Action	Drift [%]										+6 3rd cycle	-6 3rd cycle	+8 1st cycle
			0.25	0.5	0.75	1	2	3	4	5	6				
6	1st	Push	46	851	1532	2108	12753	16582	6612	5898	4511	1008	-6861	910	
		Pull	-890	-1146	-1355	-1519	445	2907	4249	3771	-1322				
	2nd	Push	20	812	1427	2049	12537	10055	6010	5630	2822				
		Pull	-890	-1146	-1342	-1545	720	4550	4183	1709	-3856				
7	1st	Push	222	1054	1682	2205	12602	20592	20605	5614	2846	746	-12203	380	
		Pull	-929	-1269	-1564	-1852	-1813	-2591	2277	903	-3409				
	2nd	Push	183	981	1551	2146	12753	21154	10665	4031	2068				
		Pull	-929	-1269	-1538	-1845	-1426	-2349	3422	-1603	-6066				
8	1st	Push	203	942	1472	1891	11331	18247	25221	29173	29304	22231	-11502	19739	
		Pull	-851	-1165	-1433	-1662	-1315	-2002	-3625	-3867	-4776				
	2nd	Push	170	896	1374	1806	11292	18561	23958	27295	24403				
		Pull	-870	-1145	-1426	-1662	-981	-2074	-3409	-4043	-7517				
9	1st	Push	-569	-890	-1151	-1374	-2257	-654	5220	7026	6771	5476	-64084	-	
		Pull	726	1531	2283	3081	17637	20097	8132	7968	8190				
	2nd	Push	-569	-877	-1145	-1328	-216	3866	6895	6987	6005				
		Pull	733	1511	2224	3147	16904	13084	7746	7955	16041				
10	1st	Push	-288	-740	-1159	-1525	-3660	-2894	7993	7980	7116	5126	217400	3398	
		Pull	1296	2239	3241	5290	21433	32117	8936	8897	8399				
	2nd	Push	-262	-753	-1133	-1080	-1401	8445	8111	7725	5591				
		Pull	1296	2187	3162	5525	20530	9348	8877	8687	7686				

Table A-33 GCNP longitudinal bar strain gages 29-33

Strain Gage	Cycle	Loading Action	Drift [%]										+6 3rd cycle	-6 3rd cycle	+8 1st cycle
			0.25	0.5	0.75	1	2	3	4	5	6				
29	1st	Push	-46	596	1165	1649	7271	12389	16721	20864	24870	-	-	-	
		Pull	-746	-988	-1230	-1446	-2677	-3200	-5720	-9104	-				
	2nd	Push	-72	589	1113	1617	7736	11702	15707	19686	-				
		Pull	-740	-988	-1217	-1466	-2696	-3547	-6990	-9994	-				
30	1st	Push	20	746	1367	1910	4377	11220	5424	2081	314	-1969	-4789	-229	
		Pull	-896	-1289	-1662	-2048	-6974	-8649	-1943	-3566	-14864				
	2nd	Push	7	746	1322	1858	7524	7910	2224	942	-1518				
		Pull	-903	-1276	-1662	-2081	-7923	-6503	-1564	-7864	-10651				
31	1st	Push	39	615	1178	1656	2644	8470	11840	15597	18720	16514	-9543	21266	
		Pull	-622	-903	-1145	-1407	-2088	-4673	-7946	-12056	-14544				
	2nd	Push	33	622	1139	1630	2618	8162	11566	14609	17797				
		Pull	-635	-877	-1172	-1420	-2180	-4844	-9294	-12318	-13084				
32	1st	Push	-327	-746	-1139	-1499	-2513	-6408	-8293	-1034	-59	-727	2441	-1604	
		Pull	857	1577	2232	2756	10636	13404	10348	3835	3135				
	2nd	Push	-314	-766	-1119	-1499	-3534	-5884	-857	609	-452				
		Pull	864	1545	2180	2684	9667	11964	5701	3325	2972				
33	1st	Push	-406	-864	-1250	-1603	-2644	-6171	-8410	-2284	-7474	-13422	-3233	-11747	
		Pull	812	1538	2219	2742	12964	15504	9385	4018	2035				
	2nd	Push	-412	-870	-1243	-1597	-3253	-5792	-1021	-3704	-12735				
		Pull	831	1518	2160	2657	11688	14476	4470	2958	648				

Table A-34 GCNP longitudinal bar strain gages 38-42

Strain Gage	Cycle	Loading Action	Drift [%]										+6 3rd cycle	-6 3rd cycle	+8 1st cycle
			0.25	0.5	0.75	1	2	3	4	5	6				
38	1st	Push	-52	412	929	1426	2558	8747	11861	16819	21719	20947	-334	23904	
		Pull	-621	-831	-1027	-1204	-1714	-2211	-1950	-2852	-3278				
	2nd	Push	-65	412	909	1393	2499	8838	12279	17330	22033				
		Pull	-621	-811	-1008	-1197	-1779	-1930	-2146	-2957	-2185				
39	1st	Push	DEAD												
		Pull													
	2nd	Push													
		Pull													
40	1st	Push	13	445	968	1466	2559	9940	12583	14212	6112	4227	105	4417	
		Pull	-648	-877	-1106	-1296	-1898	-2382	-2258	-713	-1799				
	2nd	Push	-7	438	968	1453	2500	9436	12576	8572	5248				
		Pull	-641	-870	-1099	-1309	-1963	-2035	-1826	-589	-1204				
41	1st	Push	-295	-694	-1041	-1362	-2344	-3810	-3555	956	1990	2867	3816	2861	
		Pull	714	1329	1970	2599	4032	14964	16614	4137	4170				
	2nd	Push	-295	-707	-1047	-1375	-2645	-2880	1342	1715	2488				
		Pull	707	1316	1951	2540	4438	13727	4281	4091	4006				
42	1st	Push	-321	-694	-1008	-1289	-2147	-4294	-3286	-2585	-4032	-4241	1041	-3201	
		Pull	661	1257	1839	2369	3619	11859	14844	12769	5688				
	2nd	Push	-340	-700	-1001	-1289	-2553	-2808	-2834	-2592	-6388				
		Pull	661	1237	1800	2317	5315	11270	13862	8430	1754				

Table A-35 GCNP transverse bar strain gages 25-28

Strain Gage	Cycle	Loading Action	Drift [%]										+6 3rd cycle	-6 3rd cycle	+8 1st cycle
			0.25	0.5	0.75	1	2	3	4	5	6				
25	1st	Push	-26	39	144	177	282	367	406	367	419	550	917	793	
		Pull	138	197	223	269	485	793	924	1002	1061				
	2nd	Push	-7	46	157	203	314	373	367	393	498				
		Pull	151	203	223	275	485	839	884	996	924				
26	1st	Push	-13	0	13	46	111	183	288	399	465	556	916	602	
		Pull	0	7	0	7	-39	-39	13	124	216				
	2nd	Push	0	-7	26	52	144	262	353	445	471				
		Pull	7	0	7	-13	-33	-7	59	157	360				
27	1st	Push	DEAD												
		Pull													
	2nd	Push													
		Pull													
28	1st	Push	26	0	-13	33	157	236	524	851	1061	1192	655	910	
		Pull	46	98	131	190	288	380	413	465	544				
	2nd	Push	20	13	-7	33	183	341	662	924	1015				
		Pull	46	85	124	183	282	380	406	458	537				

Table A-36 GCNP transverse bar strain gages 34-37

Strain Gage	Cycle	Loading Action	Drift [%]										+6 3rd cycle	-6 3rd cycle	+8 1st cycle
			0.25	0.5	0.75	1	2	3	4	5	6				
34	1st	Push	20	13	65	131	334	582	602	811	903	870	922	824	
		Pull	85	144	209	235	392	563	1001	1367	1694				
	2nd	Push	20	46	98	157	386	523	582	870	962				
		Pull	98	137	209	242	406	576	975	1269	1328				
35	1st	Push	-13	-26	7	33	196	485	733	1002	1048	864	720	792	
		Pull	0	0	7	33	242	393	491	766	904				
	2nd	Push	-13	-13	7	26	314	524	825	1008	936				
		Pull	7	7	13	39	295	406	471	760	661				
36	1st	Push	150	-1269	-595	-1740	-2008	-2126	-22565	-35267	-52678	-47740	-70344	-95878	
		Pull	-975	-1446	-1498	-1485	-2368	-3368	-6214	-38302	-74445				
	2nd	Push	46	-1589	-1452	-1773	-2387	-3741	-8889	-43207	-39505				
		Pull	-477	-1642	-1223	-1923	-2642	-1746	-11564	-64313	-21819				
37	1st	Push	65	59	46	190	543	720	727	635	491	406	615	432	
		Pull	33	33	33	124	367	439	707	635	550				
	2nd	Push	59	46	59	242	563	740	655	537	406				
		Pull	39	26	65	131	334	478	615	543	367				

Table A-37 GCNP transverse bar strain gages 43-46

Strain Gage	Cycle	Loading Action	Drift [%]										+6 3rd cycle	-6 3rd cycle	+8 1st cycle
			0.25	0.5	0.75	1	2	3	4	5	6				
43	1st	Push	26	39	52	137	249	458	799	975	753	491	550	59	
		Pull	118	177	223	268	432	589	825	1008	988				
	2nd	Push	39	52	65	157	347	530	890	805	353				
		Pull	118	177	209	268	452	576	838	916	799				
44	1st	Push	20	-26	13	33	183	321	432	680	968	883	739	713	
		Pull	7	13	39	144	504	752	1014	1073	1152				
	2nd	Push	-13	-13	20	79	229	334	478	772	942				
		Pull	7	13	52	170	504	733	994	1047	779				
45	1st	Push	79	131	196	210	380	524	635	773	949	884	393	845	
		Pull	39	39	65	98	210	170	419	478	557				
	2nd	Push	98	138	183	223	386	517	648	766	917				
		Pull	46	59	59	111	236	314	426	511	236				
46	1st	Push	39	20	-13	-13	236	386	366	380	360	353	445	334	
		Pull	39	39	72	196	340	484	811	1093	1165				
	2nd	Push	39	33	-7	20	229	327	386	353	347				
		Pull	26	52	79	222	360	543	896	1027	517				

Table A-38 GCNP grouted coupler strain gages 11-17

Strain Gage	Cycle	Loading Action	Drift [%]										+6 3rd cycle	-6 3rd cycle	+8 1st cycle
			0.25	0.5	0.75	1	2	3	4	5	6				
11	1st	Push	-164	20	190	294	595	766	955	1008	1080	995	-615	811	
		Pull	-465	-582	-680	-779	-909	-857	-739	-687	-811				
	2nd	Push	-164	20	164	281	543	831	896	995	1027				
		Pull	-458	-576	-687	-766	-870	-798	-739	-707	-576				
12	1st	Push	DEAD												
		Pull													
	2nd	Push													
		Pull													
13	1st	Push	-39	249	661	916	1715	1833	1748	1735	1800	1702	-3266	2343	
		Pull	-628	-858	-1041	-1191	-2023	-3266	-4405	-4615	-4739				
	2nd	Push	-79	268	589	877	1414	1290	1414	1427	1623				
		Pull	-635	-844	-1041	-1159	-2003	-3417	-4176	-4458	-3987				
14	1st	Push	-190	-301	-360	-406	-393	-131	20	85	59	13	2555	170	
		Pull	242	465	681	891	1572	1854	2097	2326	2568				
	2nd	Push	-190	-282	-367	-380	-347	-144	7	85	59				
		Pull	242	432	662	871	1553	1835	2070	2333	2536				
15	1st	Push	-229	-537	-798	-988	-1525	-1636	-1806	-2101	-2081	-1590	661	-1734	
		Pull	504	857	1185	1486	1826	2147	2369	2565	2794				
	2nd	Push	-223	-530	-759	-949	-1355	-1466	-1715	-1904	-1832				
		Pull	510	838	1165	1479	1832	2107	2330	2533	864				
16	1st	Push	-236	-465	-648	-844	-949	-517	-164	-59	7	-59	569	-52	
		Pull	380	648	936	1165	1453	1551	1603	1675	1715				
	2nd	Push	-229	-478	-648	-805	-746	-406	-118	-59	0				
		Pull	386	641	903	1139	1440	1525	1597	1669	353				
17	1st	Push	-281	-537	-753	-962	-1715	-2409	-3377	-4045	-4339	-3430	281	-3731	
		Pull	452	792	1139	1492	2369	2841	3246	3633	4130				
	2nd	Push	-268	-556	-766	-929	-1735	-2494	-3476	-3953	-4058				
		Pull	471	779	1119	1492	2317	2756	3109	3554	2114				

Table A-39 GCNP grouted coupler strain gages 18-24

Strain Gage	Cycle	Loading Action	Drift [%]										+6 3rd cycle	-6 3rd cycle	+8 1st cycle
			0.25	0.5	0.75	1	2	3	4	5	6				
18	1st	Push	-59	269	591	873	1562	1844	2199	2606	3006	3255	-1011	4115	
		Pull	-545	-715	-866	-998	-1227	-1260	-1352	-1352	-1405				
	2nd	Push	-66	263	551	860	1542	1884	2264	2658	3137				
		Pull	-564	-722	-860	-998	-1188	-1273	-1306	-1313	-984				
19	1st	Push	26	432	766	1067	1675	2062	2343	2657	2991	2965	-903	1460	
		Pull	-543	-772	-969	-1086	-1067	-949	-929	-988	-1073				
	2nd	Push	33	412	733	1034	1780	2062	2363	2729	2971				
		Pull	-563	-772	-956	-1067	-982	-903	-903	-982	-956				
20	1st	Push	52	321	714	969	1689	1931	2088	2298	2612	2448	288	2658	
		Pull	-353	-491	-622	-687	-478	-13	262	360	484				
	2nd	Push	39	340	687	962	1722	1885	2095	2402	2645				
		Pull	-367	-484	-596	-655	-419	52	190	340	524				
21	1st	Push	-307	-353	-425	-471	-438	-321	-307	-406	-504	-477	648	-373	
		Pull	92	249	392	497	778	962	994	1020	1040				
	2nd	Push	-281	-373	-412	-451	-445	-392	-366	-451	-477				
		Pull	92	242	373	477	772	922	962	968	1105				
22	1st	Push	-253	-431	-589	-679	-619	-367	-545	-753	-812	376	1095	104	
		Pull	243	446	619	763	887	906	986	1119	1204				
	2nd	Push	-238	-431	-560	-649	-495	-480	-530	-693	-718				
		Pull	233	426	609	733	867	892	1006	1110	2992				
23	1st	Push	-321	-668	-975	-1270	-2585	-3652	-4568	-5184	-5236	-3659	-812	-4156	
		Pull	439	792	1093	1407	1643	1669	1649	1839	2088				
	2nd	Push	-301	-668	-956	-1244	-2409	-3495	-4470	-4824	-4811				
		Pull	432	766	1060	1368	1571	1604	1466	1695	733				
24	1st	Push	-170	-301	-366	-399	-255	124	542	765	915	549	784	608	
		Pull	248	457	634	804	1216	1314	1431	1484	1640				
	2nd	Push	-163	-307	-353	-386	-209	255	614	778	935				
		Pull	242	431	621	797	1118	1327	1379	1497	706				

Table A-40 GCPP longitudinal bar strain gages 1-5

Strain Gage	Cycle	Loading Action	Drift [%]										-6 3rd cycle	+8 1st cycle	-8 1st cycle
			0.25	0.5	0.75	1	2	3	4	5	6				
1	1st	Push	236	805	1283	1715	2539	9908	15202	21078	28100	6021	43236	36189	
		Pull	-393	-563	-733	-897	-1531	-982	-445	255	1309				
	2nd	Push	255	255	1270	1708	2533	10693	16118	22230	30168				
		Pull	-419	-419	-746	-903	-1610	-739	-79	707	2245				
2	1st	Push	308	929	1499	2022	2657	10523	14312	16052	7977	-203	4901	-	
		Pull	-478	-759	-1008	-1250	-1773	-1662	-1198	969	975				
	2nd	Push	288	288	1479	1976	2670	10614	14547	12362	4823				
		Pull	-504	-504	-1034	-1276	-1813	-1315	-720	1623	1793				
3	1st	Push	229	752	1191	1584	1708	5922	7172	6072	4109	-1498	2624	2689	
		Pull	-412	-550	-667	-641	-602	275	739	733	-432				
	2nd	Push	229	229	1191	1472	1688	5889	6596	5196	2172				
		Pull	-412	-412	-654	-452	-641	523	838	523	-327				
4	1st	Push	-530	-740	-943	-1172	-1833	-2324	-2390	-1918	4570	-	-	-	
		Pull	301	877	1486	2036	2828	12976	18685	18286	9480				
	2nd	Push	-524	-524	-949	-1192	-2030	-2311	-2023	3516	-6613				
		Pull	301	301	1460	2043	3084	13035	19137	11091	-				
5	1st	Push	-576	-818	-1021	-1237	-1931	-2612	-2343	-2212	-1041	6604	1217	79	
		Pull	353	910	1519	2088	6225	13751	20172	27948	27863				
	2nd	Push	-583	-583	-1021	-1257	-2101	-2029	-2062	-1512	5793				
		Pull	353	353	1525	2075	7213	13981	20644	28596	9412				

Table A-41 GCPP longitudinal bar strain gages 6-10

Strain Gage	Cycle	Loading Action	Drift [%]											-6 3rd cycle	+8 1st cycle	-8 1st cycle
			0.25	0.5	0.75	1	2	3	4	5	6					
6	1st	Push	412	1244	1813	2298	11030	15723	21687	27467	33391	-5558	-47641	31885		
		Pull	-550	-779	-1008	-1218	-1113	-1277	-2651	-5368	-7894					
	2nd	Push	425	425	1761	2206	10421	15959	21379	26832	33005					
		Pull	-556	-556	-1015	-1257	-910	-1748	-2448	-4805	-7083					
7	1st	Push	DEAD													
		Pull														
	2nd	Push														
		Pull														
8	1st	Push	497	1315	1891	2382	12512	18741	26103	32647	37797	4214	48345	49111		
		Pull	-524	-785	-1067	-1296	-1296	-1767	-3134	-5811	-6387					
	2nd	Push	504	504	1832	2323	11982	19095	25926	31488	36802					
		Pull	-530	-530	-1067	-1322	-1027	-1747	-2840	-5333	-3553					
9	1st	Push	-687	-1027	-1309	-1616	-2657	-4364	-6740	-8827	-16633	62095	-4070	-4279		
		Pull	609	1191	1858	2382	12622	19263	26441	26238	8689					
	2nd	Push	-700	-700	-1335	-1616	-2185	-4391	-6406	-11771	-19760					
		Pull	576	576	1793	2297	11634	18485	25198	16548	-4750					
10	1st	Push	-689	-991	-1286	-1601	-2631	-5262	-7546	-9272	-13149	40656	-14324	-12329		
		Pull	577	1161	1798	2316	11555	18464	25859	31955	33149					
	2nd	Push	-696	-696	-1293	-1621	-2703	-5118	-6621	-9252	-12152					
		Pull	564	564	1739	2231	10787	17841	24960	29822	38261					

Table A-42 GCPP longitudinal bar strain gages 11-15

Strain Gage	Cycle	Loading Action	Drift [%]											-6 3rd cycle	+8 1st cycle	-8 1st cycle
			0.25	0.5	0.75	1	2	3	4	5	6					
11	1st	Push	347	1028	1552	2056	2900	13316	17460	21918	26141	1820	24236	12386		
		Pull	-740	-1034	-1336	-1558	-2586	-6134	-8327	-10023	-9761					
	2nd	Push	360	360	1545	2030	3090	12321	16838	21362	23863					
		Pull	-733	-733	-1309	-1539	-2881	-6056	-8629	-10075	-7529					
12	1st	Push	DEAD													
		Pull														
	2nd	Push														
		Pull														
13	1st	Push	288	917	1460	1925	2724	9769	14162	17600	21594	-14293	22334	20186		
		Pull	-746	-1107	-1441	-1755	-3889	-7982	-11301	-13246	-15609					
	2nd	Push	288	288	1441	1905	5179	9533	13206	16926	19617					
		Pull	-760	-760	-1460	-1761	-5775	-8257	-11321	-13521	-13586					
14	1st	Push	-792	-1302	-1734	-2114	-10555	-11831	-13978	-15627	-16615	-	-	52122		
		Pull	353	1191	1878	2447	7447	12512	17518	19115	8363					
	2nd	Push	-798	-798	-1721	-2114	-8638	-11046	-12898	-13546	-16432					
		Pull	393	393	1839	2382	6727	12250	16085	11615	-					
15	1st	Push	-700	-1106	-1498	-1825	-6542	-8380	-10755	-13117	-15190	31997	-17748	-16342		
		Pull	393	1204	1838	2368	7752	13077	18684	23629	28850					
	2nd	Push	-700	-700	-1479	-1825	-5809	-8158	-10559	-12554	-14772					
		Pull	432	432	1806	2316	7294	12835	18108	23296	30374					

Table A-43 GCPP longitudinal bar strain gages 20-24

Strain Gage	Cycle	Loading Action	Drift [%]										-6 3rd cycle	+8 1st cycle	-8 1st cycle
			0.25	0.5	0.75	1	2	3	4	5	6				
20	1st	Push	491	1289	1905	2409	12448	16487	22717	28628	34773	1191	41645	31579	
		Pull	-753	-1041	-1329	-1564	-3397	-3279	-3142	-2356	-1610				
	2nd	Push	478	478	1813	2330	11388	16074	22272	28333	34597				
		Pull	-740	-740	-1322	-1558	-3122	-2945	-2775	-1996	-458				
21	1st	Push	DEAD												
		Pull													
	2nd	Push													
		Pull													
22	1st	Push	491	1230	1865	2415	11499	14470	14791	5373	3652	1466	3521	3423	
		Pull	-740	-1067	-1368	-1649	-5039	-4791	-2297	668	1833				
	2nd	Push	478	478	1806	2330	9706	8986	4241	3580					
		Pull	-740	-740	-1381	-1675	-4522	-4064	628	1224	2395				
23	1st	Push	151	183	46	183	517	838	1002	1139	1270	1525	1028	910	
		Pull	105	33	196	301	569	831	1002	1231	1434				
	2nd	Push	26	26	170	177	641	1113	1191	1283	1375				
		Pull	0	0	105	105	694	943	916	1348	1381				
24	1st	Push	-890	-1257	-1603	-1754	-4823	-1702	-131	170	170	1859	281	438	
		Pull	569	1139	1721	2166	2526	1014	1257	1198	1342				
	2nd	Push	-870	-870	-1453	-1656	-1669	151	275	236	216				
		Pull	543	543	1662	2055	2049	1054	1145	1172	1669				

Table A-44 GCPP longitudinal bar strain gages 47-51

Strain Gage	Cycle	Loading Action	Drift [%]										-6 3rd cycle	+8 1st cycle	-8 1st cycle
			0.25	0.5	0.75	1	2	3	4	5	6				
47	1st	Push	111	582	1124	1523	2300	2634	2928	4320	7169	-1666	8352	6071	
		Pull	-392	-601	-758	-908	-1274	-1497	-1640	-2032	-2300				
	2nd	Push	124	124	1104	1470	2196	2490	2875	5163	7084				
		Pull	-399	-399	-778	-908	-1287	-1483	-1653	-2059	-1908				
48	1st	Push	209	798	1361	1754	2631	2912	8710	9312	10522	-1112	11824	9037	
		Pull	-458	-720	-988	-1217	-1780	-1872	-2336	-2205	-2316				
	2nd	Push	216	216	1322	1708	2546	2866	8500	9004	10319				
		Pull	-478	-478	-1008	-1243	-1767	-1852	-1989	-2133	-1616				
49	1st	Push	118	727	1211	1656	2579	2992	7842	10068	12038	33	13733	11900	
		Pull	-465	-733	-962	-1198	-1623	-1839	-1918	-1689	-1506				
	2nd	Push	118	118	1204	1637	2487	3024	7842	10087	11887				
		Pull	-478	-478	-969	-1185	-1623	-1872	-1656	-1473	-655				
50	1st	Push	-510	-766	-995	-1210	-1649	-1845	-1937	-2094	-2231	1852	-2198	-1871	
		Pull	196	674	1165	1577	2421	2715	2977	3173	3350				
	2nd	Push	-491	-491	-1014	-1204	-1603	-1773	-1891	-2074	-2277				
		Pull	203	203	1138	1525	2323	2637	2964	3167	2100				
51	1st	Push	-432	-694	-969	-1192	-1683	-1972	-1998	-609	65	3858	347	622	
		Pull	190	675	1120	1546	2312	2502	5954	5607	6013				
	2nd	Push	-459	-459	-963	-1199	-1670	-1795	-865	-33	616				
		Pull	203	203	1094	1480	2234	2476	5011	5522	4592				

Table A-45 GCPP longitudinal bar strain gages 56-60

Strain Gage	Cycle	Loading Action	Drift [%]											
			0.25	0.5	0.75	1	2	3	4	5	6	-6 3rd cycle	+8 1st cycle	-8 1st cycle
56	1st	Push	707	884	576	884	1094	1756	1651	1900	1887	288	1834	1638
		Pull	177	-308	177	157	-131	-138	-216	-164	-485			
	2nd	Push	59	59	773	668	1369	2090	2312	2299	2214			
		Pull	-236	-236	-216	-531	79	105	-649	-26	-347			
57	1st	Push	177	530	1041	1630	2500	2703	2696	2945	9050	-897	10215	7611
		Pull	-491	-766	-1008	-1224	-1702	-1865	-1983	-2114	-2716			
	2nd	Push	151	151	1073	1603	2415	2605	2690	3279	8861			
		Pull	-510	-510	-1014	-1237	-1656	-1832	-1989	-2343	-1643			
58	1st	Push	79	381	822	1164	1897	1773	1848	2100	4315	-84	4988	4320
		Pull	-357	-530	-694	-837	-1055	-941	-1016	-1134	-1025			
	2nd	Push	74	74	817	1154	1828	1724	1808	2383	4335			
		Pull	-357	-357	-708	-812	-872	-921	-1011	-1144	-481			
59	1st	Push	-438	-700	-896	-1093	-1518	-1727	-1878	-1937	-2663	1963	-2441	-2048
		Pull	190	582	968	1315	1904	2074	2316	5392	7682			
	2nd	Push	-425	-425	-883	-1080	-1479	-1669	-1767	-2388	-2107			
		Pull	183	183	955	1296	1793	1943	2264	6681	3494			
60	1st	Push	-223	-308	-373	-380	-432	-347	-255	-255	-216	2252	-79	59
		Pull	105	295	563	844	1447	1617	1846	2147	3286			
	2nd	Push	-216	-216	-340	-314	-295	-281	-196	-223	-72			
		Pull	92	92	596	851	1394	1597	1866	2258	2599			

Table A-46 GCPP transverse bar strain gages 16-19

Strain Gage	Cycle	Loading Action	Drift [%]											
			0.25	0.5	0.75	1	2	3	4	5	6	-6 3rd cycle	+8 1st cycle	-8 1st cycle
16	1st	Push	46	137	190	209	281	177	170	366	491	1440	831	720
		Pull	72	151	190	209	530	936	1322	1590	1911			
	2nd	Push	59	59	190	229	268	190	295	465	589			
		Pull	105	105	164	203	484	903	1296	1577	1669			
17	1st	Push	-20	-52	-72	-52	-26	118	203	314	458	65	975	968
		Pull	0	13	33	111	268	536	530	595	772			
	2nd	Push	-7	-7	-39	-26	59	164	242	386	595			
		Pull	7	7	72	137	281	464	484	635	510			
18	1st	Push	DEAD											
		Pull												
	2nd	Push												
		Pull												
19	1st	Push	-20	-52	-46	-33	-26	79	170	249	321	1014	576	510
		Pull	-13	92	157	196	249	281	380	478	654			
	2nd	Push	-33	-33	-39	-20	52	157	216	308	380			
		Pull	0	0	157	203	229	301	386	504	910			

Table A-47 GCPP transverse bar strain gages 25-28

Strain Gage	Cycle	Loading Action	Drift [%]											
			0.25	0.5	0.75	1	2	3	4	5	6	-6 3rd cycle	+8 1st cycle	-8 1st cycle
25	1st	Push	13	52	65	111	190	170	229	327	478	393	773	603
		Pull	59	144	183	242	262	478	648	753	897			
	2nd	Push	13	13	98	151	216	190	282	386	570			
		Pull	59	59	203	236	269	452	576	720	570			
26	1st	Push	7	20	46	85	164	151	249	399	458	85	478	223
		Pull	26	39	72	105	249	334	452	537	615			
	2nd	Push	20	20	72	111	118	118	301	386	465			
		Pull	26	26	72	124	236	314	432	517	79			
27	1st	Push	33	98	131	144	203	373	576	772	890	661	1066	824
		Pull	13	52	92	131	157	190	314	432	536			
	2nd	Push	52	52	137	150	216	366	536	693	975			
		Pull	7	7	105	137	157	203	327	445	674			
28	1st	Push	DEAD											
		Pull												
	2nd	Push												
		Pull												

Table A-48 GCPP transverse bar strain gages 43-46

Strain Gage	Cycle	Loading Action	Drift [%]											
			0.25	0.5	0.75	1	2	3	4	5	6	-6 3rd cycle	+8 1st cycle	-8 1st cycle
43	1st	Push	0	26	65	98	183	307	491	635	792	510	942	909
		Pull	59	98	137	183	353	425	517	621	693			
	2nd	Push	7	7	59	118	236	379	556	713	844			
		Pull	65	65	131	196	347	425	517	621	556			
44	1st	Push	-20	-20	-20	0	177	452	713	916	1014	824	1027	779
		Pull	-7	-20	-39	7	353	694	962	1256	1394			
	2nd	Push	-7	-7	-20	39	314	563	805	955	995			
		Pull	0	0	-39	26	484	779	1099	1302	844			
45	1st	Push	DEAD											
		Pull												
	2nd	Push												
		Pull												
46	1st	Push	151	183	46	183	517	838	1002	1139	1270	1525	1028	910
		Pull	105	33	196	301	569	831	1002	1231	1434			
	2nd	Push	26	26	170	177	641	1113	1191	1283	1375			
		Pull	0	0	105	105	694	943	916	1348	1381			

Table A-49 GCPP transverse bar strain gages 52-55

Strain Gage	Cycle	Loading Action	Drift [%]										-6 3rd cycle	+8 1st cycle	-8 1st cycle
			0.25	0.5	0.75	1	2	3	4	5	6				
52	1st	Push	491	523	105	268	236	425	288	641	805	1079	118	504	
		Pull	340	118	517	661	667	746	641	837	608				
	2nd	Push	13	13	334	150	373	785	831	1079	1093				
		Pull	13	13	281	144	733	850	373	798	471				
53	1st	Push	79	72	39	105	196	367	419	471	471	510	458	425	
		Pull	33	59	92	183	510	687	785	798	753				
	2nd	Push	52	52	65	137	308	412	458	458	491				
		Pull	79	79	79	177	563	713	753	726	530				
54	1st	Push	79	144	170	229	321	380	432	484	511	236	439	380	
		Pull	-20	20	46	85	164	196	216	262	314				
	2nd	Push	79	79	183	216	321	380	458	478	445				
		Pull	-20	-20	59	92	164	183	262	314	216				
55	1st	Push	26	26	52	196	491	589	694	785	877	510	864	497	
		Pull	26	65	157	236	406	471	530	602	700				
	2nd	Push	33	33	92	209	504	609	700	798	857				
		Pull	33	33	157	249	406	471	517	596	550				

Table A-50 GCPP grouted coupler strain gages 29-35

Strain Gage	Cycle	Loading Action	Drift [%]										-6 3rd cycle	+8 1st cycle	-8 1st cycle
			0.25	0.5	0.75	1	2	3	4	5	6				
29	1st	Push	131	491	799	1074	1820	2049	2200	2390	2593	-543	2717	1257	
		Pull	-327	-465	-602	-720	-871	-871	-864	-838	-812				
	2nd	Push	131	131	786	1061	1787	2017	2226	2396	2586				
		Pull	-314	-314	-609	-733	-825	-818	-792	-779	-648				
30	1st	Push	216	288	144	131	-209	-340	-386	-556	-393	-995	-412	3416	
		Pull	-275	-497	-576	-668	-825	-687	-890	-1047	-1257				
	2nd	Push	131	131	249	26	-275	-229	-380	-412	-111				
		Pull	-327	-327	-733	-812	-726	-622	-1047	-1106	-1152				
31	1st	Push	72	275	465	622	1021	1191	1328	1466	1590	-79	1721	1001	
		Pull	-281	-334	-471	-523	-609	-609	-523	-451	-419				
	2nd	Push	65	65	458	622	1021	1191	1361	1466	1590				
		Pull	-255	-255	-478	-517	-550	-523	-451	-386	-190				
32	1st	Push	-308	-406	-478	-556	-661	-740	-720	-700	-687	903	-635	-596	
		Pull	46	340	589	805	1420	1643	1806	2022	2238				
	2nd	Push	-281	-281	-471	-543	-674	-707	-707	-674	-615				
		Pull	46	46	589	812	1368	1597	1820	2055	805				
33	1st	Push	-406	-609	-766	-916	-1185	-1191	-1139	-1054	-929	982	-799	-655	
		Pull	118	458	785	1021	1381	1564	1728	1951	2134				
	2nd	Push	-380	-380	-753	-864	-1034	-1034	-962	-884	-812				
		Pull	164	164	746	988	1348	1564	1754	1983	1100				
34	1st	Push	-438	-687	-910	-1067	-1433	-1446	-1348	-1302	-1230	2251	-1060	-812	
		Pull	131	524	890	1237	1787	1977	2264	2566	2808				
	2nd	Push	-432	-432	-877	-1034	-1257	-1250	-1172	-1126	-1014				
		Pull	157	157	890	1224	1747	1996	2291	2572	2461				
35	1st	Push	-380	-563	-713	-831	-1041	-1047	-988	-923	-825	2651	-674	-419	
		Pull	118	412	700	1008	1728	1990	2369	2880	3155				
	2nd	Push	-393	-393	-687	-792	-923	-910	-870	-792	-628				
		Pull	111	111	707	982	1702	1996	2500	2913	2867				

Table A-51 GCPP grouted coupler strain gages 36-42

Strain Gage	Cycle	Loading Action	Drift [%]										-6 3rd cycle	+8 1st cycle	-8 1st cycle
			0.25	0.5	0.75	1	2	3	4	5	6				
36	1st	Push	92	393	543	380	419	412	517	576	641	-190	622	1433	
		Pull	-262	-367	-406	-406	-380	-347	-327	-327	-308				
	2nd	Push	111	111	360	334	367	406	530	596	628				
		Pull	-249	-249	-367	-386	-334	-314	-308	-295	-203				
37	1st	Push	125	465	904	1212	1645	2025	2320	2556	2805	308	2890	721	
		Pull	-288	-419	-550	-564	-485	-446	-295	-170	-20				
	2nd	Push	131	131	937	1160	1638	2103	2320	2621	2857				
		Pull	-288	-288	-557	-531	-419	-347	-216	-13	170				
38	1st	Push	124	321	386	452	602	714	648	615	530	26	419	452	
		Pull	-216	-360	-445	-347	-321	-412	-354	-190	-131				
	2nd	Push	124	124	354	478	635	674	615	583	537				
		Pull	-216	-216	-465	-380	-249	-321	-327	-111	-52				
39	1st	Push	-294	-393	-491	-550	-707	-720	-615	-517	-412	1106	-203	-98	
		Pull	52	262	504	713	1354	1550	1734	1766	1878				
	2nd	Push	-288	-288	-484	-530	-648	-615	-504	-438	-353				
		Pull	59	59	497	707	1335	1518	1668	1766	1079				
40	1st	Push	-196	-275	-360	-340	-406	-439	-288	-209	-111	1146	478	530	
		Pull	118	295	517	700	1028	1257	1368	1388	1401				
	2nd	Push	-203	-203	-308	-340	-353	-353	-255	-157	471				
		Pull	137	137	491	668	1002	1231	1303	1335	1204				
41	1st	Push	-340	-510	-648	-733	-864	-818	-713	-628	-510	2434	-353	-183	
		Pull	131	458	772	1093	1878	2140	2408	2624	2814				
	2nd	Push	-334	-334	-602	-680	-726	-654	-609	-530	-399				
		Pull	150	150	772	1119	1858	2166	2408	2617	2532				
42	1st	Push	-229	-314	-347	-366	-353	-314	-229	-164	-92	1505	-65	92	
		Pull	39	268	504	674	1315	1557	1694	1714	1747				
	2nd	Push	-216	-216	-314	-340	-321	-268	-203	-131	-92				
		Pull	39	39	497	661	1223	1564	1668	1681	1583				